A STUDY OF THE MICROCHEMISTRY OF NANOCRYSTALLINE $BaTiO_3$ WITH TETRAGONAL AND PSEUDOCUBIC ROOM TEMPERATURE SYMMETRIES

BY

ROBERT A. LACEY

A THESIS
SUBMITTED TO THE FACULTY OF

ALFRED UNIVERSITY

IN PARTIAL FULFILLMENT OF THE REQUIREMENTS
FOR THE DEGREE OF

DOCTOR OF PHILOSOPHY

IN

CERAMICS

ALFRED, NEW YORK

SEPTEMBER, 2007

A STUDY OF THE MICROCHEMISTRY OF NANOCRYSTALLINE $BaTio_3$ WITH TETRAGONAL AND PSUEDOCUBIC ROOM TEPMERATURE SYMMETRIES

BY

ROBERT A. LACEY

B.S. ALFRED UNIVERSITY (2000)

SIGNATURE OF AUTHOR (Signature on file)

APPROVED BY (Signature on file)
WALTER A. SCHULZE, ADVISOR

(Signature on file)
ROBERT A. CONDRATE, ADVISORY COMMITTEE

(Signature on file)
STEVEN M. PILGRIM, ADVISORY COMMITTEE

(Signature on file)
SCOTT T. MISTURE, ADVISORY COMMITTEE

(Signature on file)
DOREEN D. EDWARDS, CHAIR, ORAL THESIS DEFENSE

ACCEPTED BY (Signature on file)
ALASTAIR N. CORMACK, DEAN,
KAZUO INAMORI SCHOOL OF ENGINEERING

ACCEPTED BY (Signature on file)
WILLIAM M. HALL, ASSOCIATE PROVOST
FOR GRADUATE AND PROFESSIONAL PROGRAMS
ALFRED UNIVERSITY

ACKNOWLEDGEMENTS

My earnest appreciation to Fran Williams and Ward Votava for their generous assistance and guidance during the studies set forth in this tome.

Special thanks to Dr. Walter Schulze for supplying the material and new instrumentation that made this study possible, and the thoughtfulness to allow students to find their own path.

Raymond Lewis… nanopowders and XPS… time enjoyed with your assistance in the complex issues that were at times baffling during this phase of the study.

James Ovenstone… for assistance with unusual results obtained with HT-XRD that were fascinating… are there more hours in a day?

To my family, friends and colleagues who supported my work and discoveries through this journey, my deepest appreciation.

The humbling truth is that with all my learning and discoveries I feel that I am one of many who reside on the fringe of knowledge.

TABLE OF CONTENTS

LIST OF TABLES

LIST OF FIGURES

ABSTRACT

The investigation of possible effects of undesired surface species on barium titanate, one of the most utilized ferroelectric ceramics, constitutes the focus of this work. Six commercial barium titanate powders from three manufacturers representing two different synthesis processes, with average particle sizes from 40 nm to 470 nm, were analyzed in this study. Four of the nanopowders exhibited pseudocubic room temperature symmetry. Diffuse Reflectance Infrared Fourier Transform (DRIFT) spectroscopic analysis of the nanopowders was conducted in ambient atmosphere at room temperature. High temperature DRIFT followed incorporating four avenues of analysis: moisture adsorption studies, deuterium oxide exchange studies, carbon dioxide adsorption studies, and high temperature analysis under dry air and UHP nitrogen atmospheres. At the highest temperature used in this study, 1173K, moisture and the accompanying incorporated protonic impurities were still present. The powders readily readsorbed moisture during rapid cooling, 170K/minute, to room temperature. The smallest powder, as received, formed spherical agglomerates up to 10 μm diameter. These sintered as separate units attaining diameters up to 60 μm during intermediate stage sintering. X-ray photoelectron spectroscopy indicated a surface contamination layer of 10 Å to 18 Å; 50 – 70% of which was barium carbonate, the balance being atmospheric adsorbed species. Samples cooled at 3K/minute after an 1173K calcine retained cubic symmetry as indicated with high temperature X-ray diffraction. However, spectral evidence was obtained indicating that upon the rapid cooling from the 1173K calcine, a reorientation to the room temperature tetragonal symmetry was observed. Further, SEM and TEM supported this finding with visual evidence of interfacial rearrangement including corroborating electron diffraction analysis. This data, therefore, substantiated the hypothesis that the cause of the room temperature pseudocubic structure was strain due to the presence of point defects from protonic impurities in conjunction with the strain between the barium carbonate contamination layer and the barium titanate core.

1 The Barium Titanate Nanopowders

1.1 Overview

Barium titanate is an important commercial dielectric material. Over 100 billion pieces per year are manufactured.[1] In the ferroelectric and dielectric industries the surface properties of barium titanate powders have great influence on the quality and reproducibility of the final products. Generally, the surface properties of particles strongly influence the sintering behavior of the resulting product. The influence of the composition and structural variations on dielectric properties was noticed long ago by several investigators.[2-4] Reliability problems of multilayer ceramic capacitors (MLCCs) due to undesirable impurities incorporated during the manufacturing and post-aging process of barium titanate raw materials have been reported.[4-9] Control of the raw materials is, therefore, vital in the complex process of MLCC production in achieving reproducible high quality final products. As industry moves closer to developing products using nanoscale precursors, a better understanding of the physiochemical nature of nano-barium titanate is desirable.

As the particle size of a powder decreases below one micron the surface area of the powder and the volume fraction of the outermost layer of ions on the surface increase quite significantly. This would be expected to play an increasingly important role in the processing of the powders as the particle size decreases. Submicron powders have high activity and tend to agglomerate. The surface area and surface chemistry are the characteristics that have the most important influence in processing. This increased surface area and its structure will have an important influence on surface phenomena during sintering, especially with regard to surface species that may be present. The surface chemistry of the nanopowders, therefore, can also have direct influence on the densification and microstructural evolution during the sintering process.

The structure of nanoscale crystallites may be described as composed of two components; a crystalline component having atoms in normal lattice positions, and an interfacial component denoted by atoms situated within the

interfaces. The interface situated atoms are of higher free energy due to unsaturated bonding and a more disordered state.

These nanocrystallites frequently show features distinct from those of the bulk due to the high percentage of surface state atoms.[10-12] Properties of nanocrystallites are therefore different from bulk crystals of the same composition. The bulk behavior of the material will then be significantly influenced by the properties of the interface regions.[13-17]

During sintering these surfaces become the grain boundaries and interfaces that act as sources and sinks for diffusion. Densification will be controlled by the structure and composition of these grain boundaries. Impurity species on the surfaces of the starting nanopowder may alter grain boundary composition and the resultant microstructure of the sintered product. For many electroceramic applications, the manipulation of the surface chemistry of the starting powder aids in the control of the grain boundaries, the structure of the final product, and is an important consideration in processing.

It has been previously known that oxide surfaces absorb atmospheric molecules that alter their surface charge.[18] The investigation of possible effects of undesired surface species on barium titanate, one of the most utilized ferroelectric ceramics, constitutes the focus of this investigation. Six commercial barium titanate powders from three manufacturers representing two different synthesis processes were analyzed in this study as shown in Table 1.1. The effects of residual moisture and carbonate content on the intermediate stage of sintering of compacts were investigated.

The nanopowders were initially analyzed in ambient atmosphere at room temperature using BET specific surface area (SSA), thermogravimetric analysis (TGA), differential thermal analysis (DTA), optical microscopy, scanning electron microscopy (SEM), transmission electron microscopy (TEM) and x-ray diffraction (XRD).

Table 1.1. Commercial Barium Titanate Powders Used in this Study

	Powder Preparation	Manufacturer	Lot #
A	solid state synthesis	Ferro Corp., Penn Yan, NY	992800
B	solid state synthesis	Ferro Corp., Penn Yan, NY	992480
C	hydrothermal synthesis	Cabot Corp., Boyertown, PA	PE06010917
D	hydrothermal synthesis	Cabot Corp., Boyertown, PA	OJ00010965
E	hydrothermal synthesis	Cabot Corp., Boyertown, PA	OE00010930
F	hydrothermal synthesis	TPL, Inc., Albuquerque, NM	BTA020516AC

Infrared vibrational spectroscopic analysis was conducted in several formats. Diffuse reflectance infrared Fourier Transform (DRIFT) spectroscopy of the nanopowders was conducted in ambient atmosphere at room temperature. High temperature DRIFT spectroscopy followed incorporating four avenues of experimentation: moisture adsorption studies, deuterium oxide adsorption studies, carbon dioxide adsorption studies, and high temperature analysis under dry air and nitrogen atmospheres with soaks at 473K, 773K and 1173K to relate moisture and carbonate content to the subsequent calcining studies.

The nanopowders were calcined at 473K, 773K and 1173K for one hour in ambient atmosphere. Analysis of morphology and particle size of the products was accomplished with optical microscopy, SEM and TEM. The “as-received” and calcined nanopowders were pressed into compacts for the intermediate stage sintering study. No processing additives were used in forming the pellets to preclude the introduction of further moisture or carbonate species to the nanopowders. Pellets were sintered for one hour at 1473K in ambient atmosphere. The fired compacts were analyzed with SEM for grain size, grain

morphology and porosity. Volumetric density was calculated by weighing and measuring the fired compacts. Archimedes density testing was not utilized after the failure of most pellets to remain whole during the testing of an initial run.

Previously, extensive work had been carried out in regard to the effect of particle size and the structure of barium titanate nanocrystallites. Several questions were raised in the literature: (1) Is there a critical size below which the cubic phase is stable at room temperature? (2) Are the nanocrystallites a true cubic phase without tetragonality when they appear to be cubic according to XRD? (3) Can stabilization of the anomalous room temperature cubic phase occur through the ubiquitous incorporation of hydroxyl groups in hydrothermally derived barium titanate? (4) Is there a constricting effect of the surface state of the nanopowders (i.e. a strain that exists between a large volume contamination layer with respect to a barium titanate core)? and (5) Can stabilization of the anomalous room temperature cubic phase occur through virtue of the nanoscale of the grains (i.e. through the residual strain in the crystallites from synthesis)?

The critical crystalline particle size expressed by some researchers was less than 49nm[19], 120nm[20], 30nm[21] and 190nm[22]; each showed no tetragonal phase at room temperature as analyzed with X-ray diffraction. The discrepancy in the critical particle size results from differing synthesis methods and conditions in preparation of the barium titanate nanopowder with each investigator.

In regard to there being a true cubic phase present, Cho[23] and Clark[24] argued that the nanocrystalline barium titanate particles are tetragonal rather than cubic according to the presence of Raman active modes for the tetragonal phase.

Uchino indicated that the high temperature cubic phase in barium titanate could be stabilized at room temperature by virtue of the nanoscale of the grains (i.e. through residual strain in the crystallites).[20] Hennings argued for the stabilization through the ubiquitous incorporation of hydroxyl groups in hydrothermally derived barium titanate.[25]

Clarification of these structure issues with barium titanate nanopowders raised in the literature is the focus of this work in an attempt to provide a solution to the question: Can stabilization of the anomalous room temperature cubic phase occur through the ubiquitous incorporation of hydroxyl groups in hydrothermally derived barium titanate through virtue of the nanoscale grains (i.e. through the residual strain due to point defects in the nanocrystallites from synthesis)?

2 Analysis of Nanopowders in Ambient Atmosphere and at Room Temperature

2.1 BET Specific Surface Area (BET), Thermogravimetric Analysis (TGA) & Differential Thermal Analysis (DTA)

2.1.1 Introduction

Initial testing of the nanopowders involved surface area analysis and dynamic thermogravimetric and differential thermal analysis. These techniques are widely used techniques in studying the kinetics of thermal decomposition reactions and for specific surface area determination. Thermogravimetric analysis (TGA) was used to examine the weight loss/gain due to moisture desorption/adsorption and the carbonate reduction released in the form of carbon dioxide. This provided an indicator of the temperatures at which the hydroxyl and carbonate species decomposition reactions occurred. The differential thermal analysis (DTA) was used in evaluating whether these reactions were endothermic or exothermic.

2.1.2 Experimental Procedure

The BET nitrogen adsorption specific surface area (BET) measurements were performed on the nanopowders. (Micromeritics Gemini 2375, Flow Prep 060, Micromeritics Corp., Norcross, GA) The nanopowders were outgassed at 425K for 45 minutes prior to nitrogen adsorption testing.

The TGA and DTA procedures were accomplished using a simultaneous DSC-TGA (TA Instruments model SDT2960, New Castle, DE) with alumina pans and an ultra high purity (UHP) nitrogen atmosphere (moisture content <6ppm) at a flow rate of 100 ml/minute. The TGA experiments used 16-18 mg of sample nanopowder with a one hour purge time prior to beginning each experiment. The powders were heated at 10K/minute from room temperature to 1560K. The DTA experiments used 16-18 mg of sample nanopowder and 16-18 mg of Al_2O_3 (TA Instruments lot #12617CR) in the alumina reference pan, a UHP nitrogen

atmosphere at a flow rate of 100 ml/minute and purged one hour prior to beginning a sample run.

2.1.3 Results and Discussion

2.1.3.1 BET Specific Surface Analysis

Equivalent particle sizes were calculated using the equation:

$$Diameter = \frac{6}{(cellvolume)(SSA)} \tag{2.1}$$

assuming a spherical shape factor, the specific surface area from BET testing and a theoretical density of 6012 Kg/m^3 using the room temperature tetragonal structure of barium titanate. The unit cell dimensions used in the calculations were taken from the PDF file (#81-2201) for tetragonal $BaTiO_3$, the room temperature stable phase. The results in table 2.1, with the calculated particle size, place the largest nanopowder to at 469 nm and the smallest at 66 nm. Surface area increases dramatically as particle diameter decreases below 130 nm.

The manufacturer specifications for Nanopowder F indicated an average particle size of 40 nm. Calculating the SSA using the above formula with 40 nm as a spherical particle diameter and the cell volume of the tetragonal structure, a value closer to 25 m^2/g should have resulted from BET analysis. A possible explanation for the lower specific surface area result for Nanopowder F could be that the nanopowder is highly agglomerated with a large volume of trapped porosity yielding a lower than accurate specific surface area during BET analysis. The volume of trapped porosity will be discussed further in Section 2.5. Singular nanocrystallites may also incorporate trapped porosity as a result of synthesis, similar to the findings of Hennings, et al.[25]

Table 2.1. BET Specific Surface Area and Resultant Spherical Particle Diameter

Nanopowder	SSA (m^2/g)	Diameter (nm)
A	2.13	469
B	2.29	436
C	5.89	169
D	7.79	128
E	15.14	66
F	14.85	67

2.1.3.2 Thermogravimetric Analysis and Differential Thermal Analysis

TGA traces obtained for the as-received nanopowders, upon heating in a UHP nitrogen atmosphere, show several nanopowders that exhibited a mass increase at elevated temperatures. This increase was indicative of the dissolution of moisture in the lattice and chemisorbed on vacant oxygen sites according to:

$$H_2O_{(g)} + V_O^{\cdot\cdot} \rightarrow 2H_i^{\cdot} + O_O \qquad (2.2)$$

which formed protonic defects. The adsorption exhibited in the TGA traces in this study was analogous to the water incorporation studies on barium cerate perovskites by Kruth and Irvine[26] and the high temperature protonic conductors study by Bonanos.[27]

Kruth and Irvine were able to show that the cerate perovskites structure would adsorb moisture between 450K and 1075K. The upper limit of adsorption was prompted by the reduction of Ce^{4+} to Ce^{3+} through an oxygen deficiency yielding further sites for hydroxyl incorporation. The Bonanaos TGA study in a moist N_2 atmosphere showed evolution of oxygen and a subsequent adsorption

of moisture on heating to 1175K with a molar fraction of moisture adsorbed at 1175K of 0.9%. These studies provided previous experimental validation of the adsorption of moisture to vacant oxygen lattice sites at high temperatures.

The protonic defect, an interstitial proton, is an extremely small point charge that due to its size is incapable of occupying a regular interstitial position.[28] It therefore is attracted to an oxygen ion forming hydroxide ions on oxide ion sites ($OH_O^{\cdot}$). These are positively charged defects competing with other positively charged defects, electron holes ($h^{\cdot}$) and oxygen vacancies ($V_O^{\cdot\cdot}$), that are charge compensated by major negatively charged defects, which may include electrons, metal ion vacancies, or oxygen interstitials.

Electronic hole formation occurs through the annihilation of protonic defects as temperature increases according to the equation:

$$2OH_O^{\cdot} + \tfrac{1}{2}O_2 \rightarrow H_2O_{(g)} + 2h^{\cdot} + 2O_O \qquad (2.3)$$

through the dehydration of the hydroxide defects. At higher temperatures the reformation of oxygen vacancies occurs at the expense of the electronic holes and liberation of oxygen gas according to:

$$2h^{\cdot} + O_O \rightarrow V_O^{\cdot\cdot} + \tfrac{1}{2}O_2\ . \qquad (2.4)$$

These competing charge carrying defects, especially the hydroxide ions, are present upon cooling to room temperature from sintering level temperatures.

The drier the powder was prior to thermogravimetric analysis the more moisture that was adsorbed. Nanopowder B had the lowest moisture content of all nanopowders tested (see Figure 3.2 in the Infrared Vibrational Characterization section) and exhibited the largest moisture gain (see Figure 2.2). One powder was an exception to this pattern. Nanopowder F having the largest specific surface area, and third driest sample, exhibited the second highest level of moisture adsorption (see Figure 2.6). This was a result of the

large number of available surface sites for additional moisture attachment and subsequent hydroxide ion incorporation into the lattice.

The percent mass loss ranged between 0.42% and 2.03% (see Table 2.2). The loss was represented in the loss of moisture and carbon dioxide over the temperature range examined. The surface adsorbed hydroxyl groups are bound with various energy levels indicative of the local site of attachment. These hydroxyls are desorbed over a large temperature range. The oxygen lattice bound proton, as $OH_O^{\cdot}$, have specific binding energies respective of the location of attachment within the lattice. These hydroxyls are desorbed over a narrower temperature range, 690K – 715K for the hydrothermal nanopowders. This was in agreement with Abicht et al who attained a similar specific lattice desorption at 675K.[29] Valdivieso et al also realized desorption of lattice bound hydroxyls at 688K through mass spectrometry.[30] The temperature range for lattice hydroxyl desorption for the solid state powders was 1015K – 1030K. This deviation will be discussed further in a later section.

Table 2.2. TGA Mass Loss Results of the Nanopowders from Room Temperature to 1560K

Nanopowder	Initial Mass (mg)	Loss Mass (mg)	Percent Loss (%)
A	17.2850	0.1283	0.74
B	17.1439	0.0721	0.42
C	16.6866	0.1439	0.86
D	17.8573	0.3621	2.03
E	17.7035	0.2700	1.53
F	17.3505	0.1244	0.72

Three nanopowders had shown moisture level gains of 31.62%, 14.31%, and 1.33% of the entire mass ultimately lost during experimental analysis, representing the B, F and A nanopowders (see Figures 2.7, 2.8 and 2.9, respectively and Table 2.3). The moisture adsorption in these three samples occurred between 400K and 650K and is suspected to be related to surface carbonate loss and moisture incorporation on the open sites and will be addressed further in a later section. Each moisture gain exhibited by the nanopowders was endothermic as shown in the accompanying DTA traces. Nanopowders C, D and E exhibit no mass increase whatsoever indicating a possible maximum in moisture incorporation in the lattice which is lost at high temperatures.

The higher the initial moisture content of the nanopowder the lower the adsorption of moisture. This indicates an equilibrium moisture level in barium titanate nanopowders in the 400K to 600K temperature region. This anomaly will be addressed further in Section 3, the Vibrational Spectroscopic Characterization of the nanopowders.

Table 2.3. TGA Mass Gain Results of the Nanopowders in Various Thermal Regimes between Room Temperature and 1560K

Nanopowder	Gain Mass (mg)	Percent Gain (%)	Percent of total mass loss (%)	Temp Regime (K)
A	0.0017	0.01	1.33	530-630
B	0.0228	0.13	31.62	435-725
C	-----	-----	-----	-----
D	-----	-----	-----	-----
E	-----	-----	-----	-----
F	0.0178	0.11	14.31	420-690

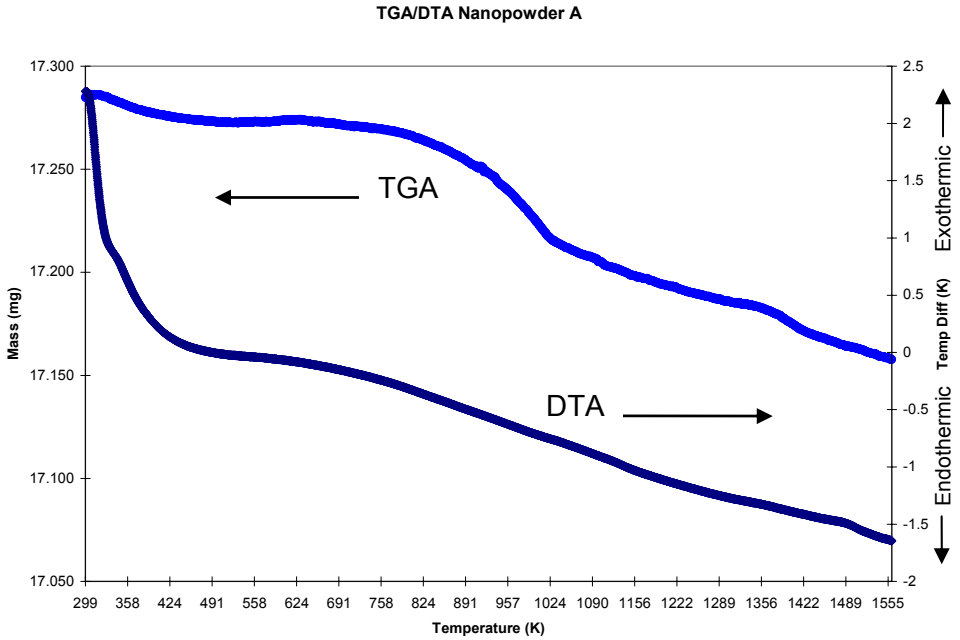

Figure 2.1. Thermogravimetric and Differential Thermal Analysis plots of Nanopowder A.

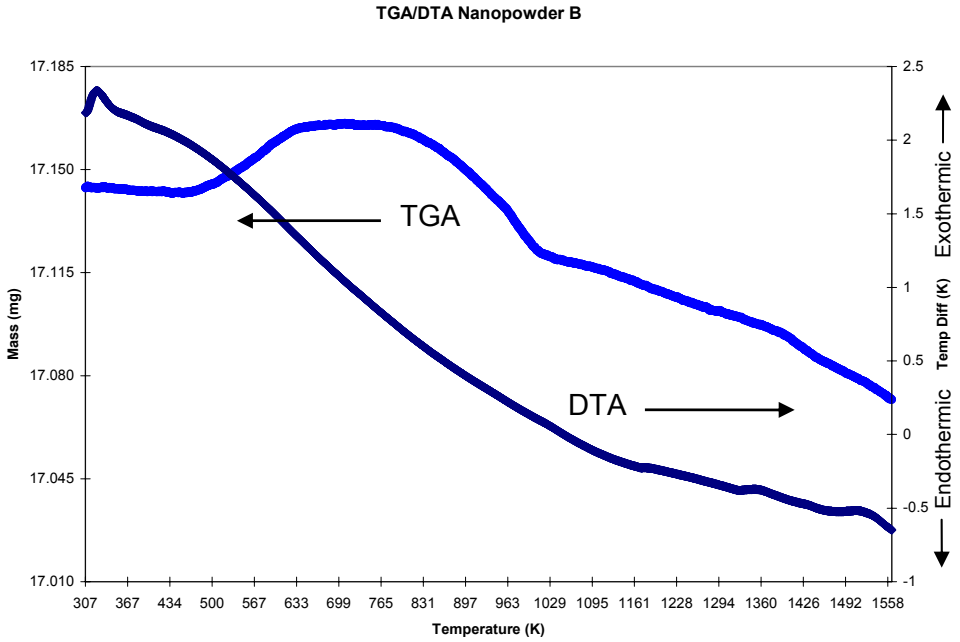

Figure 2.2. Thermogravimetric and Differential Thermal Analysis plots of Nanopowder B.

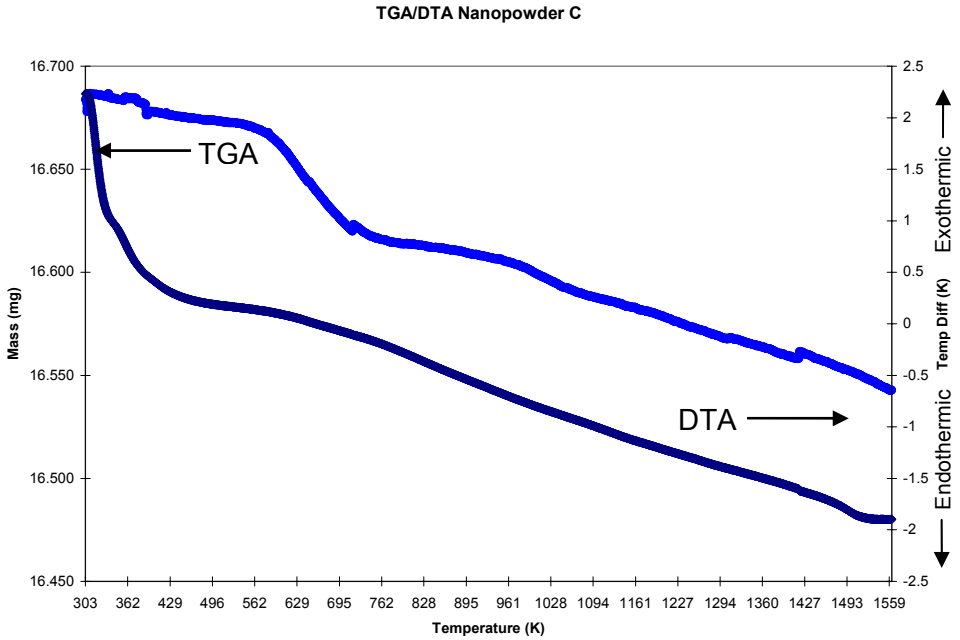

Figure 2.3. Thermogravimetric and Differential Thermal Analysis plots of Nanopowder C.

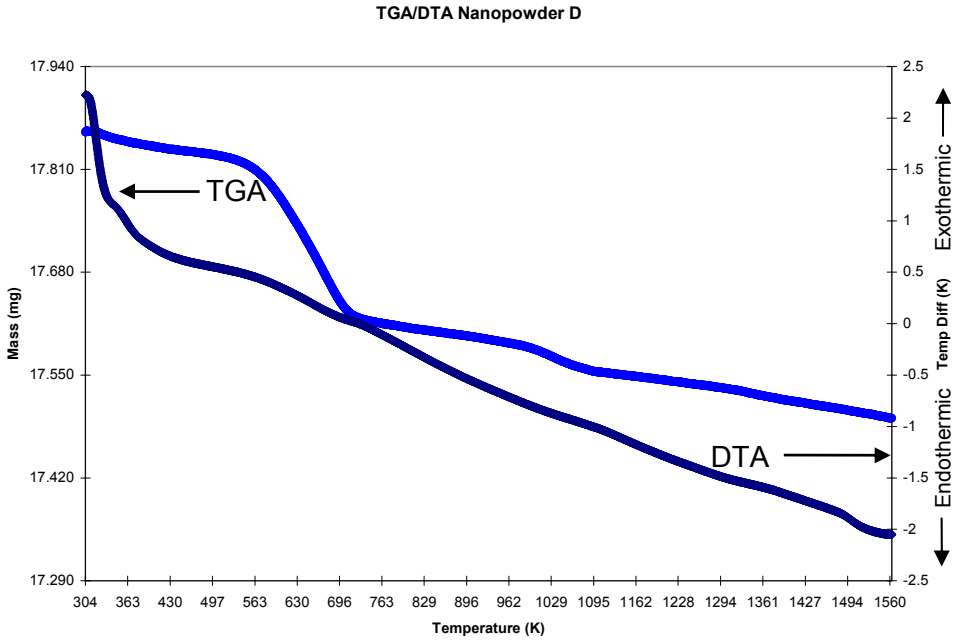

Figure 2.4. Thermogravimetric and Differential Thermal Analysis plots of Nanopowder D.

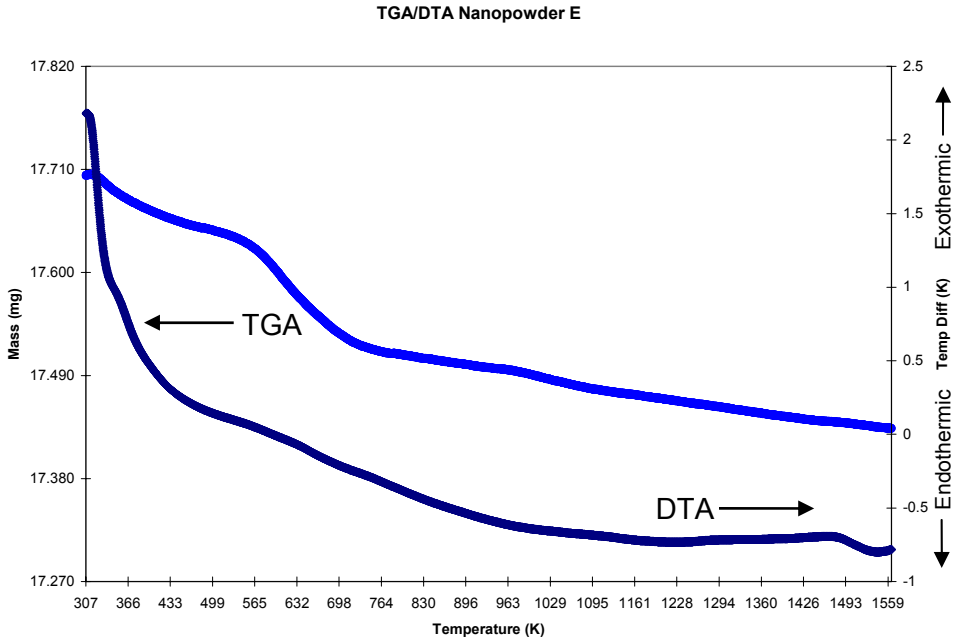

Figure 2.5. Thermogravimetric and Differential Thermal Analysis plots of Nanopowder E.

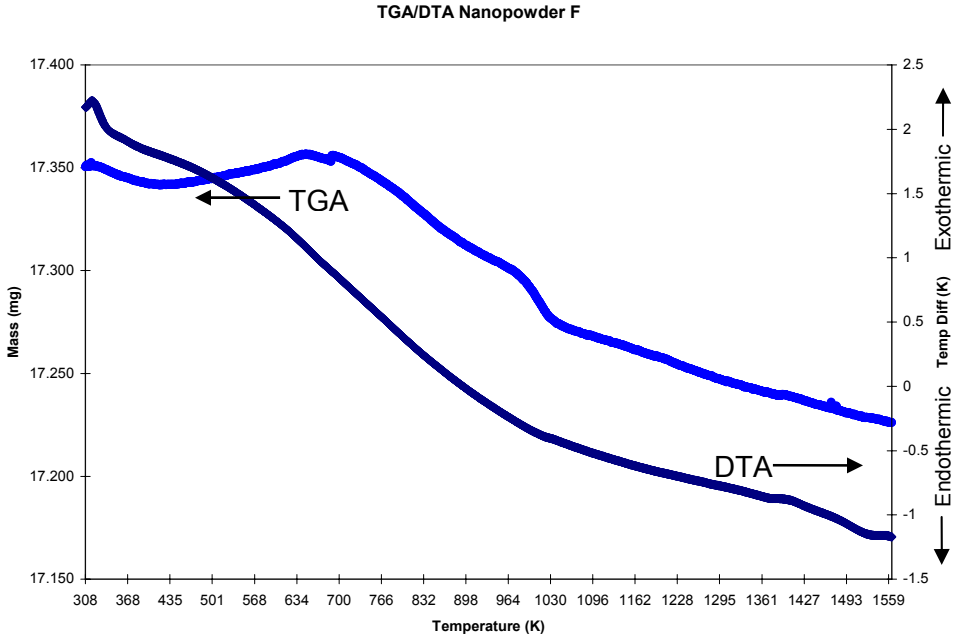

Figure 2.6. Thermogravimetric and Differential Thermal Analysis plots of Nanopowder F.

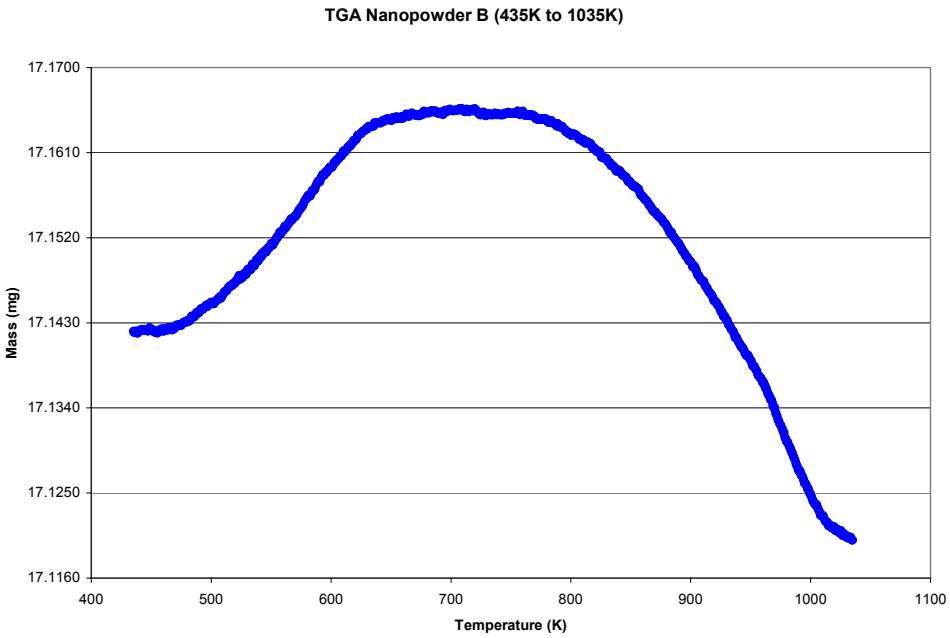

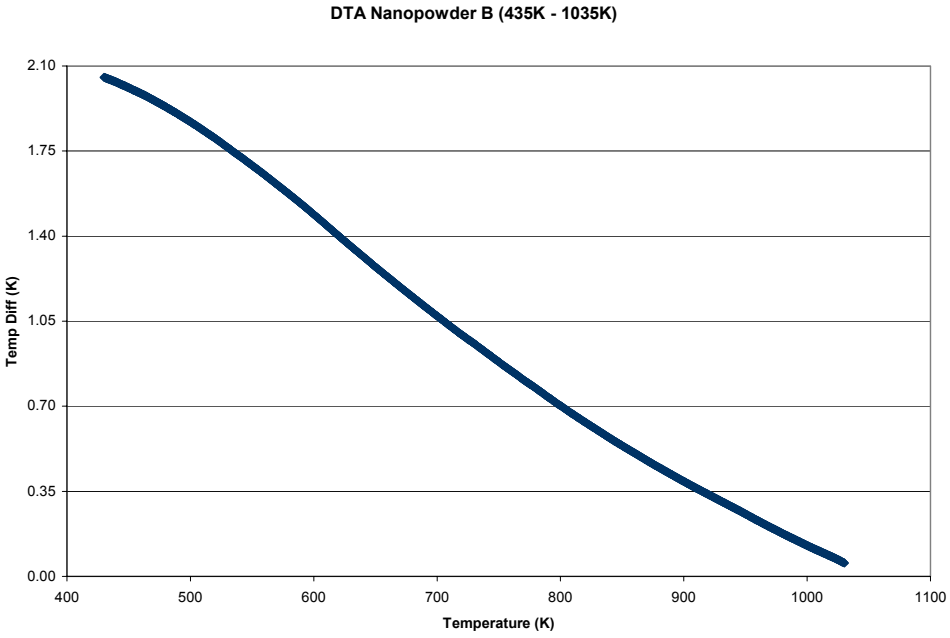

Figure 2.7. TGA and DTA traces of Nanopowder B in the region of moisture adsorption between 430K and 1030K.

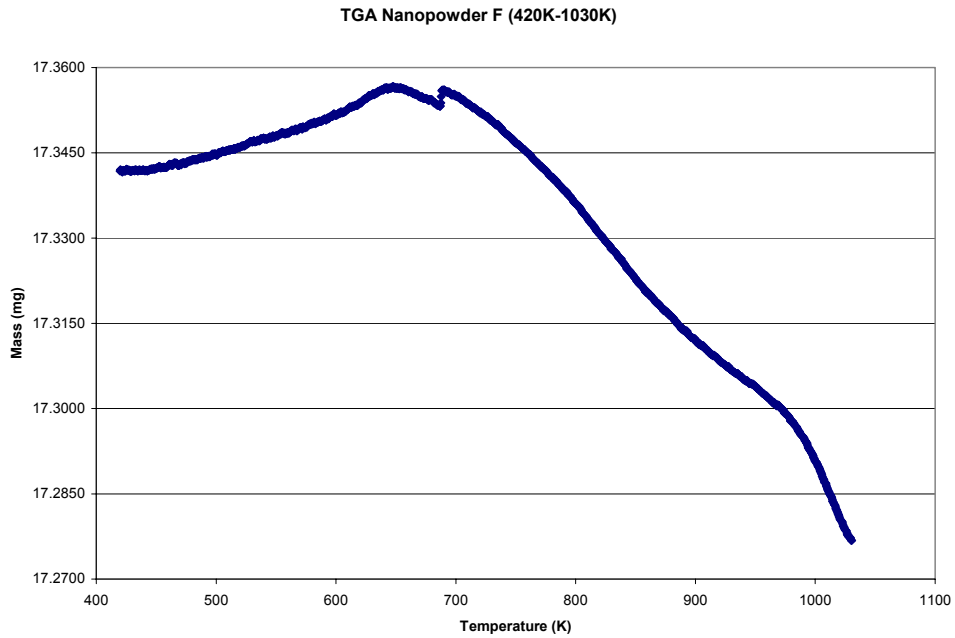

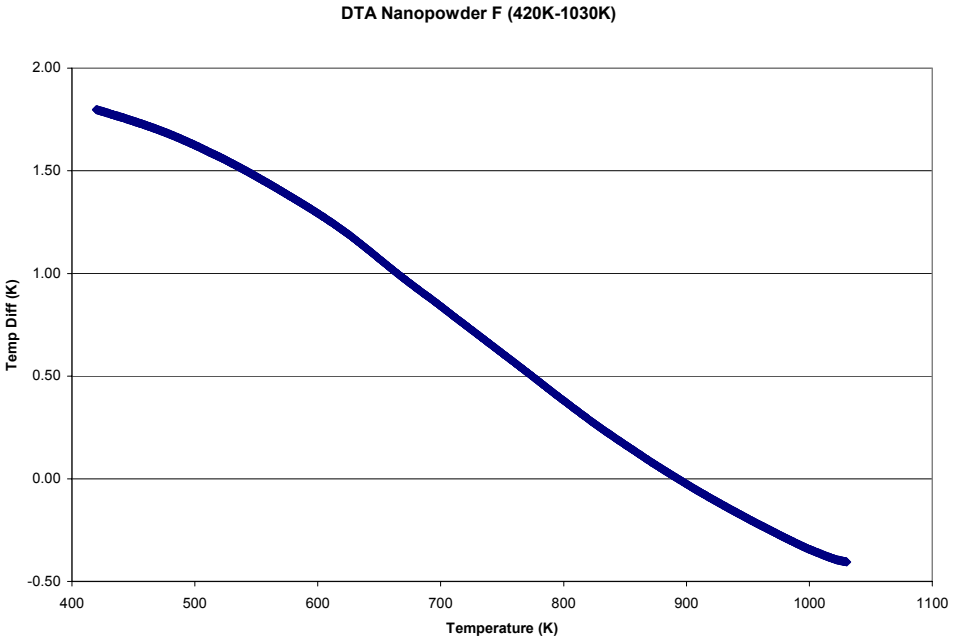

Figure 2.8. TGA and DTA traces of Nanopowder F in the region of moisture adsorption between 420K and 1030K.

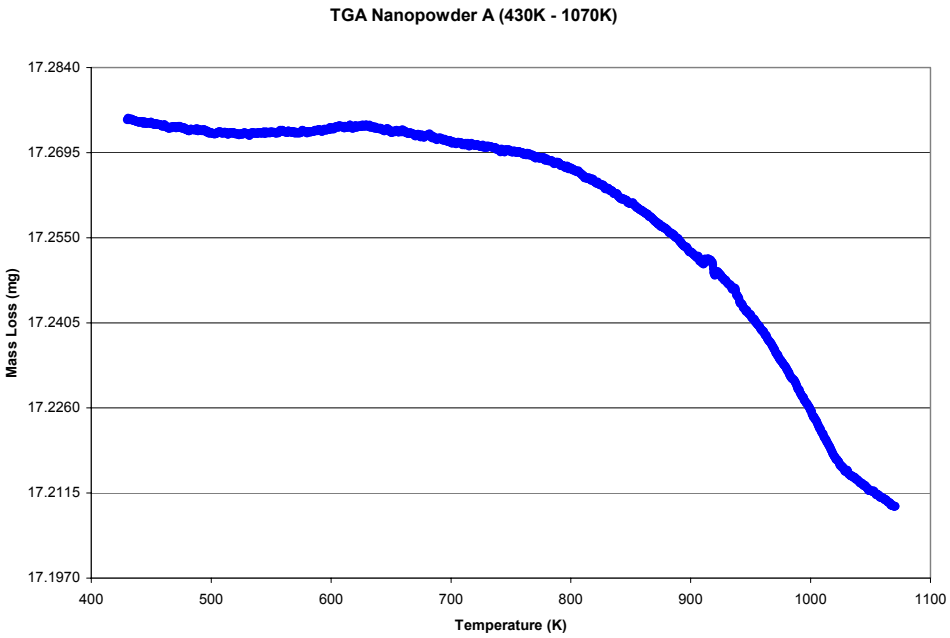

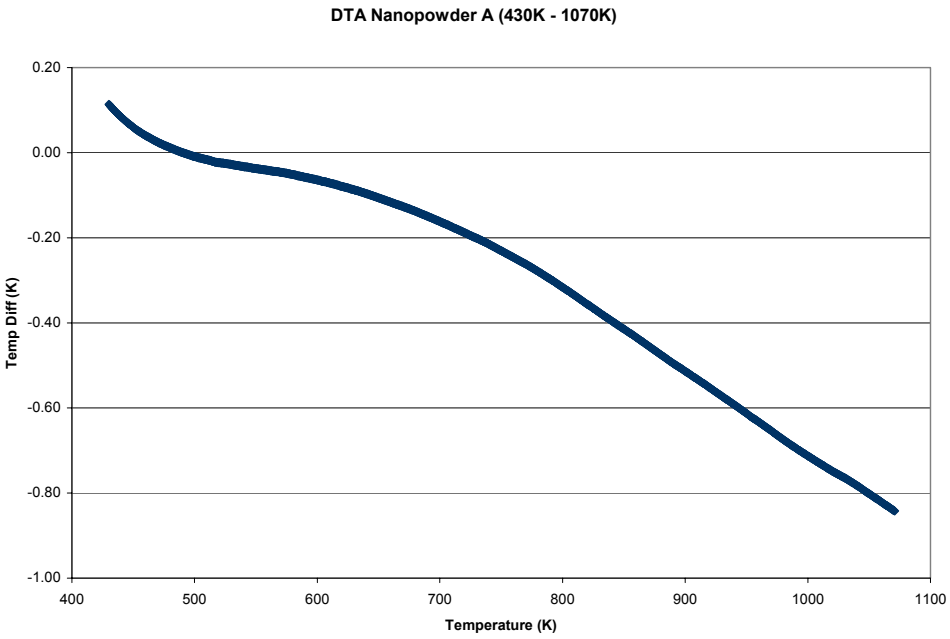

Figure 2.9. TGA and DTA traces of Nanopowder A in the region of moisture adsorption between 430K and 1070K.

2.1.4 Summary

The six nanopowders being reviewed in this work have specific surface areas of 2 to 15 m^2/g. Their particle size as calculated from their respective specific surface areas range from 469 nm to 66 nm. The TGA traces depicted an increase in mass for four of the nanopowders examined; the other nanopowders exhibited no mass increase. The increase in mass occurred due to water vapor adsorption within the 400K to 650K region for the hydrothermal nanopowders and was in agreement with previous studies. The solid state synthesized nanopowders exhibited gains at higher temperatures and was believed to be related to carbonate loss and subsequent hydroxyl incorporation. This anomaly will be addressed in Section 3, the Vibrational Spectroscopic Characterization of the nanopowders.

Equations in Kröger-Vink notation have been written to depict the possible defects from the adsorption of water vapor by the nanopowders. The hydroxyl ion is incorporated on a vacant oxygen lattice site. The interstitial proton ($H_i^{\cdot}$), which may also bond to an oxygen ion, forms the hydroxyl ion ($OH_o^{\cdot}$) point defect. This highly mobile charge carrier is incorporated in the lattice at high temperatures. The TGA data indicated an equilibrium concentration of water vapor adsorbed in the form of the hydroxyl ion within the barium titanate structure at elevated temperatures. This will also be addressed further in Section 3, the Vibrational Spectroscopic Characterization of the nanopowders.

2.2 Optical Microscopy

2.2.1 Introduction

Optical microscopy of nanopowders was accomplished expressly to observe the state of agglomeration of the powders used in this study. The motivation for looking at the powders optically came about through the preparation of powder samples for transmission electron microscopy (TEM). The support grid with an accompanying sample was viewed under an optical microscope to verify proper coverage of the powder on the support grid for TEM observation. The agglomeration of the powders was interesting and the scope of the study was expanded to include optical microscopic observation of the nanopowder agglomerates.

2.2.2 Experimental Procedure

Sample preparation for optical microscopy began by dispersing 0.05 g of each of the as-received nanopowders in 10 ml of acetone in a 50 ml beaker and ultrasonicating for 15 minutes. (Brandon Ultrasonics Corp., model 2510, Danbury, CT) A pipette was used to draw a sample from near the surface of the solution and applying a single drop onto a sample slide.

Analysis was performed using a Leitz optical microscope (Leitz, Laborlux 11 POL, Wetzlar, Germany) under reflected light conditions using a digital camera with SPOT software, version 4.1 (Diagnostic Instruments, Inc., Sterling Heights, MI) for processing the photomicrographs. Due to the interesting images observed with powder F, additional optical images were analyzed after calcining the powder at 475K, 775K and 1175K, at a rate of 10K/minute, for a soak period of one hour at each temperature in ambient atmosphere. Optical results of this calcining are included in section 4.1

2.2.3 Results and Discussion

The photomicrographs in Figure 2.10 are of each of the as-received nanopowders at room temperature in ambient atmosphere at 200X magnification. Varying degrees of agglomeration were evident with each of the powders.

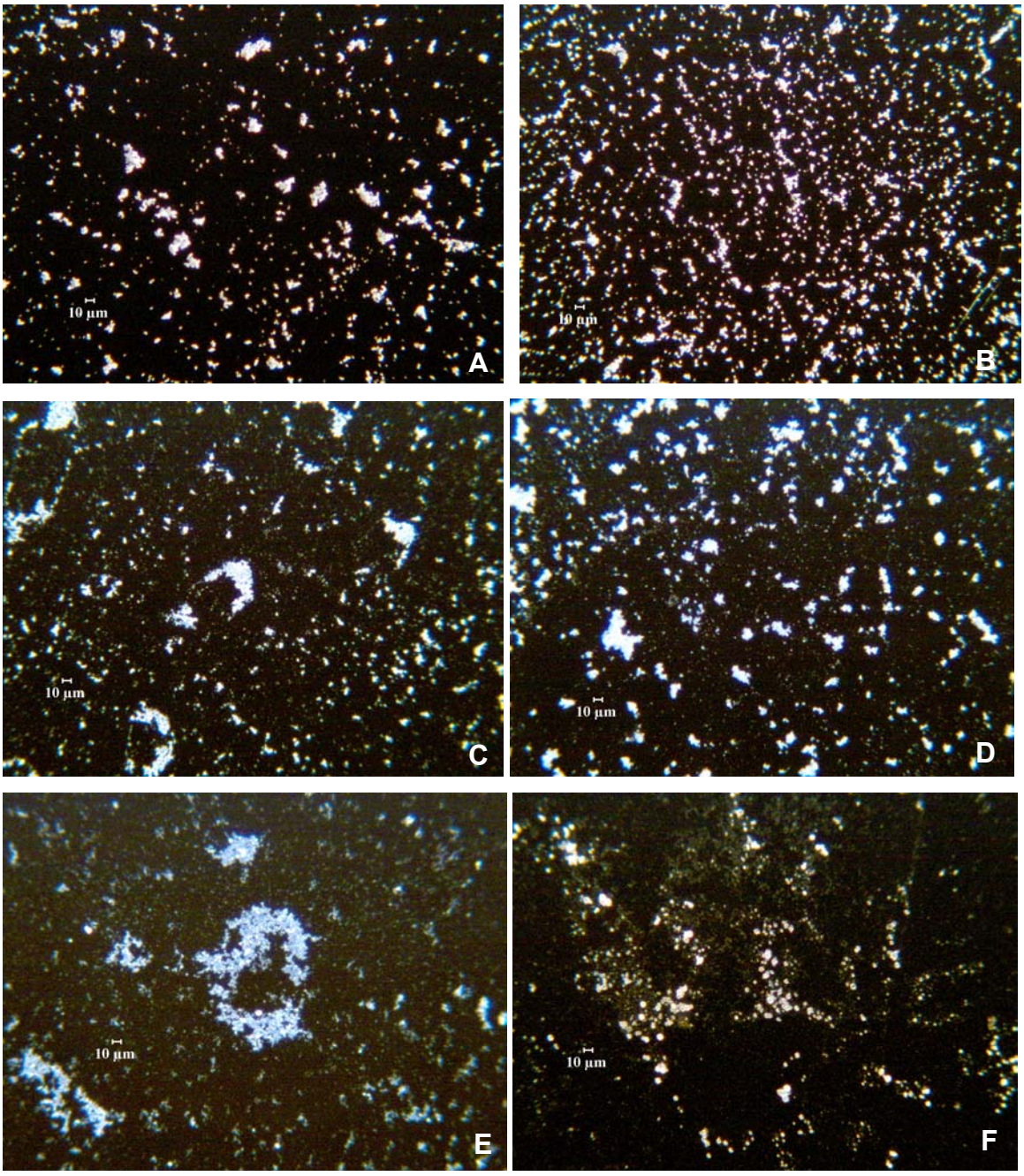

Figure 2.10. Optical photomicrographs of Nanopowders A-F under reflected light at 200X magnification. Size bars in each photomicrograph indicate 10μm distance.

Nanopowder D exhibited the greatest amount of agglomeration of the powders studied. The most interesting aspect of the agglomeration of the nanopowders was observed with Nanopowder F. The agglomerates were in the form of

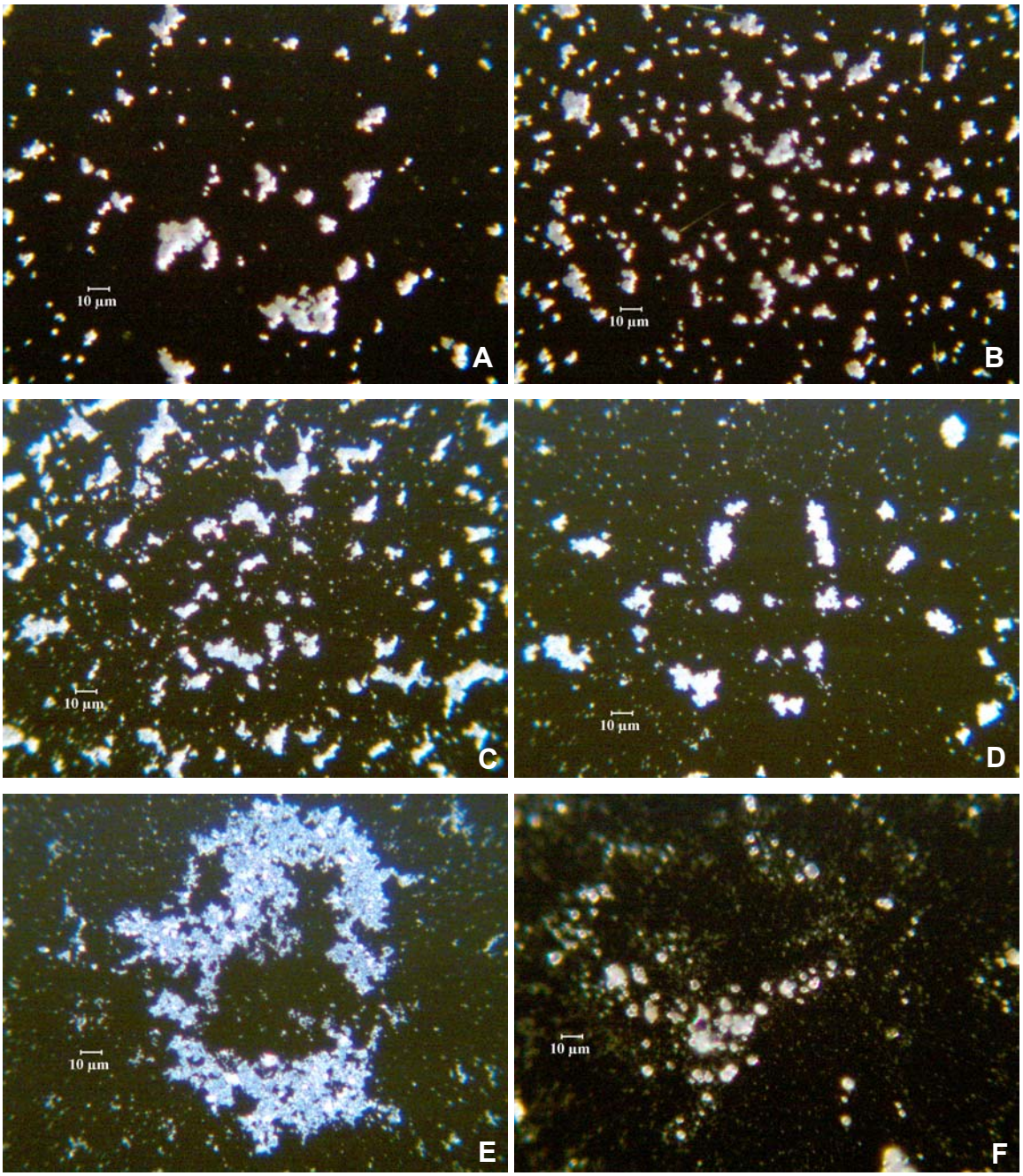

Figure 2.11. Optical photomicrographs of Nanopowders A-F under reflected light at 500X magnification. Size bars in each photomicrograph indicate 10μm distance.

spheres as opposed to the irregular shaped agglomerates observed with the other powders.

Under higher magnification (500X in Figure 2.11) the spherical shapes of Nanopowder F were far more evident. These spheres have the appearance of small opalescent pearls with a smooth spherical surface. The varying degrees of agglomeration of the other five nanopowders were observed more readily under the increased magnification. Nanopowders D and B exhibited the greatest degree of exaggerated agglomeration, respectively, of all samples.

2.2.4 Summary

Optical microscopic analysis of the as-received nanopowders reveals all nanopowders to be agglomerated to varying degrees. Nanopowder D was observed to have the largest degree of agglomeration, containing the largest agglomerates of all the nanopowders in the study. The second most agglomerate populated nanopowder was powder B, although through visual inspection, does not contain agglomerates as large as that of Nanopowder D.

The arrangement of the agglomerates of Nanopowder F was spherical. The excess surface space charge of the <70nm particle size nanopowder is being compensated for with the agglomerates assuming the lowest energy shape, the sphere. Considering particle size alone, it would be expected that agglomerates of Nanopowder E, also <70nm, would exhibit the tendency to assume a similar spherical shape as well. The optical images refute this assumption. A secondary conclusion may be that the particle size of Nanopowder F was far smaller than that calculated from the specific surface area analysis. A smaller particle size is indicated, with an associated higher reactive surface. In addition, the proposed smaller nanocrystallites would form these spherical agglomerates to reduce their higher surface energy and in the process likely formed regions of trapped microporosity. This microporous structure would yield a higher specific surface area result than would be expected for a powder containing smaller crystallites.

2.3 X-ray Diffraction

2.3.1 Introduction

The structure of a barium titanate crystal depends upon the temperature. Above its Curie temperature (T_c), the unit cell is cubic and nonpolar. The unit cell becomes tetragonal below the Curie temperature, where the structure is distorted with an accompanying polarization in the <100> direction. Barium titanate is usually tetragonal at room temperature and changes to the cubic phase at approximately 403K, its Curie temperature.

X-ray diffraction (XRD) was utilized in this study to verify the crystallinity of the nanopowders as well as discern their crystal structure. The x-ray diffraction patterns, along with transmission electron microscopic diffraction patterns that follow in section 2.5, were used to verify the phase of each of the as-received nanopowders used in this study.

2.3.2 Experimental Procedure

The “as-received” nanopowders were lightly packed in a side-drift holder. The scans were set at 20º to 70º 2-theta with a step size of 0.04 and dwell of 3 seconds per step. Copper K_α radiation of wavelength 1.5406Å was used.

2.3.3 Results and Discussion

The results of the scans of each of the nanopowders are presented in Figures 2.12 through 2.17, A through F respectively. All of the nanopowders were crystalline; no amorphous attributes were exhibited in the diffraction patterns. Each of the major peaks has been annotated with the diffraction planes using the PDF’s #31-0174 (the cubic phase) and #05-0626 (the tetragonal phase) of barium titanate. Nanopowders A and B exhibited several peak splittings that can be attributed to the tetragonal phase of barium titanate. The most noticeable of these was near 45º 2-theta, the (002)/(200) peaks.

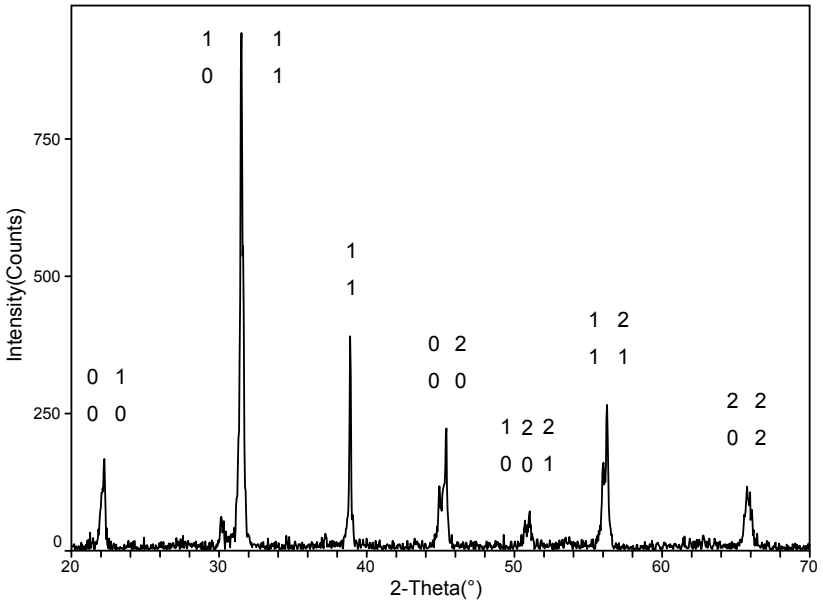

Figure 2.12. Full scan x-ray diffraction pattern of Nanopowder A in the range 20º to 70º 2-theta.

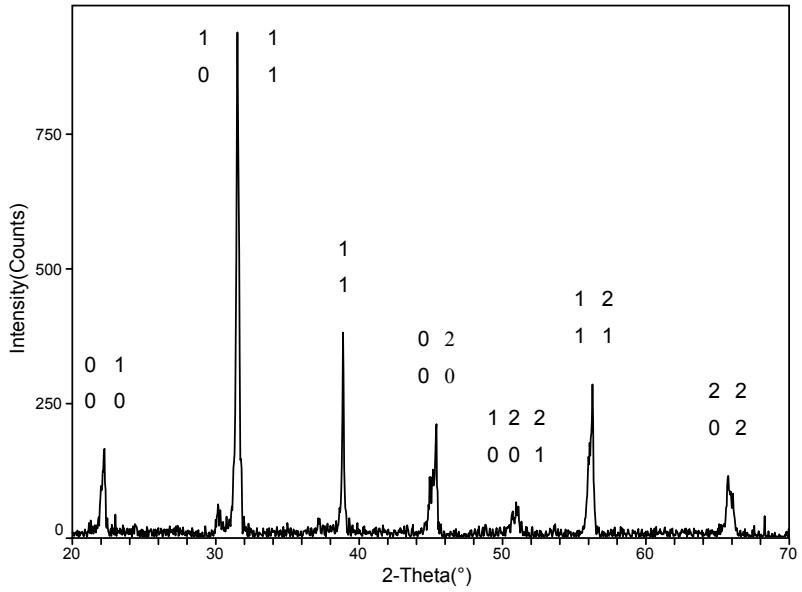

Figure 2.13. Full scan x-ray diffraction pattern of Nanopowder B in the range 20º to 70º 2-theta.

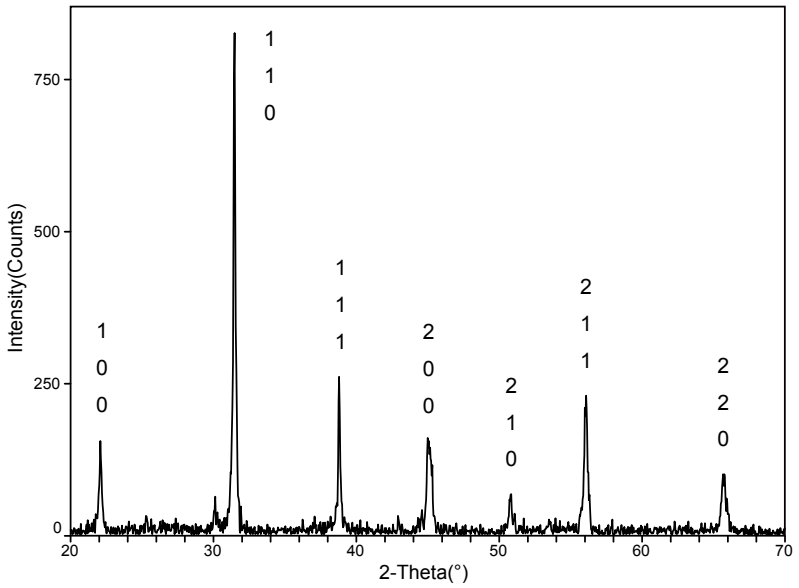

Figure 2.14. Full scan x-ray diffraction pattern of Nanopowder C in the range 20º to 70º 2-theta.

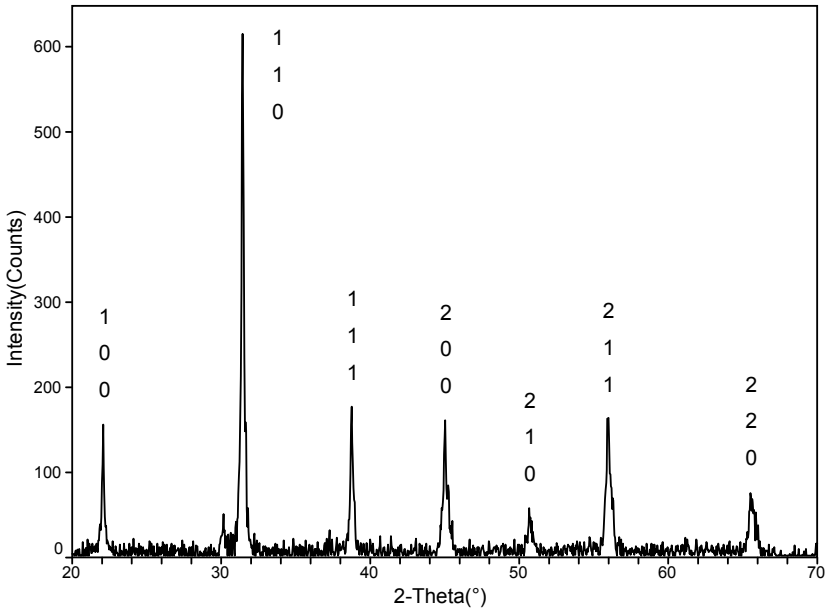

Figure 2.15. Full scan x-ray diffraction pattern of Nanopowder D in the range 20º to 70º 2-theta.

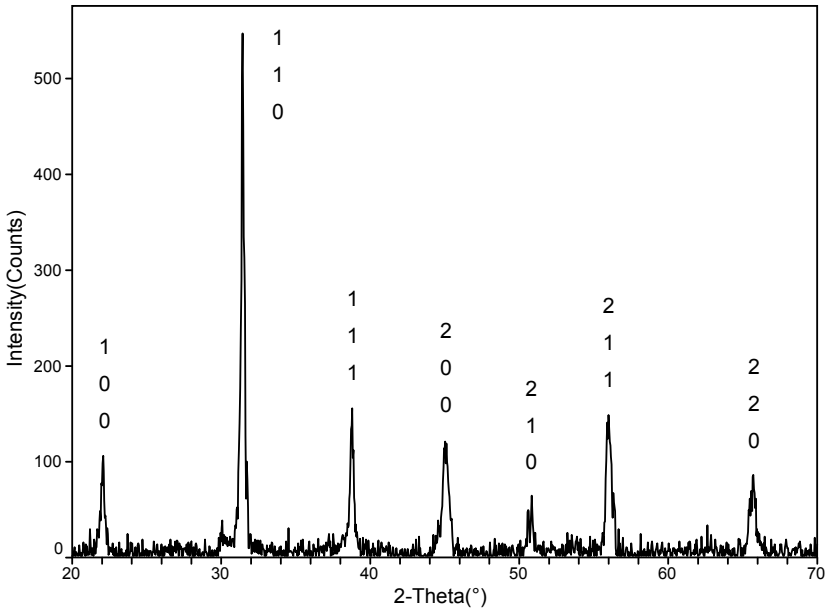

Figure 2.16. Full scan x-ray diffraction pattern of Nanopowder E in the range 20º to 70º 2-theta.

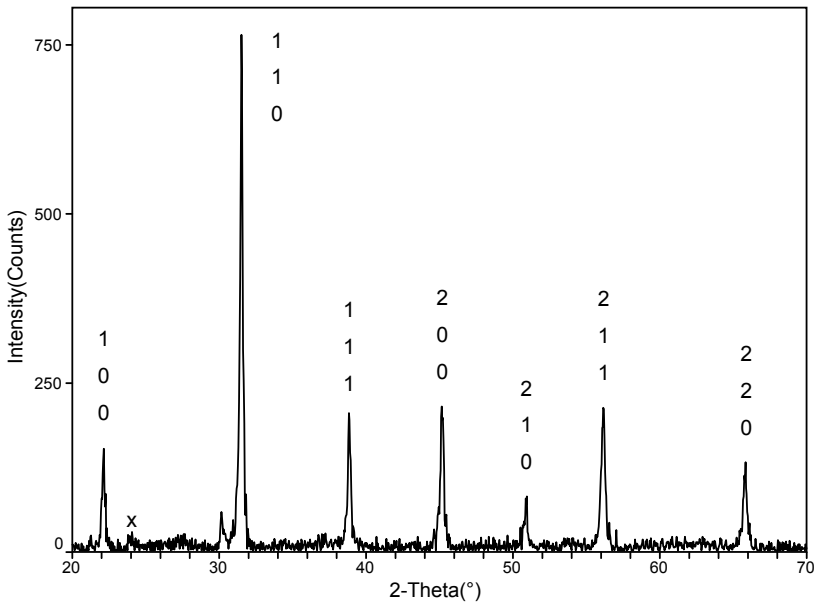

Figure 2.17. Full scan x-ray diffraction pattern of Nanopowder F in the range 20º to 70º 2-theta.

A closer examination of the 45º 2-theta peak in each of the diffraction patterns revealed the difference between the nanopowders exhibiting the cubic phase from those of the tetragonal phase. The cubic phase shows a single peak at 44.926º 2-theta (200), while the tetragonal phase exhibits a dual peak of 44.855º and 45.377º 2-theta (002)/(200). The relative intensity of the two peaks, (002)/(200), being 12/37 respectively. This dual peak was seen with Nanopowders A and B, but is absent in the patterns of the other four nanopowders, Figures 2.18 through 2.23. The structure of Nanopowders A and B were tetragonal through analysis of the x-ray diffraction patterns. The structure of Nanopowders C through F exhibited the anomalous room temperature cubic phase as observed by others through XRD analysis.[31] No peak splitting is observed in the diffraction patterns of these nanopowders.

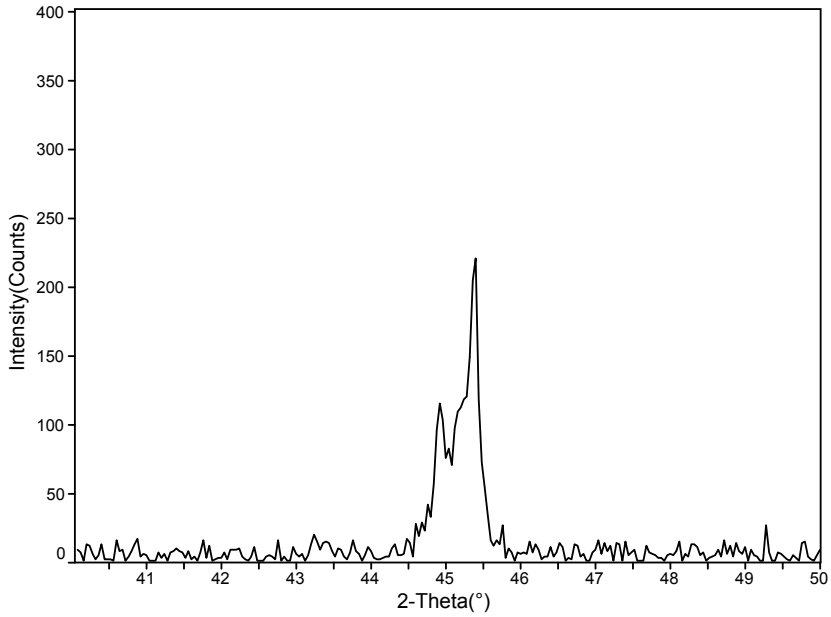

Figure 2.18. Enlarged section of the x-ray diffraction pattern at 45º 2-theta of Nanopowder A depicting the split peaks of the (002)/(200) planes of the tetragonal phase of barium titanate.

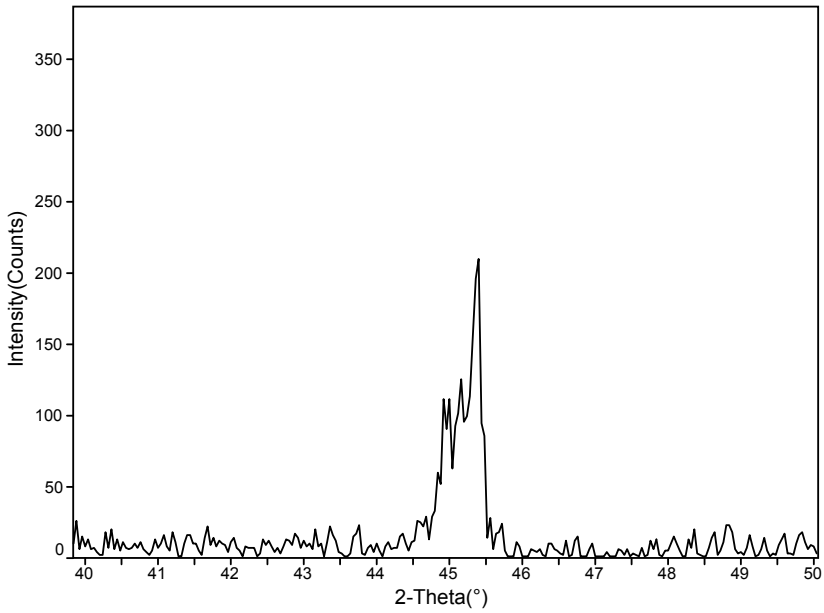

Figure 2.19. Enlarged section of the x-ray diffraction pattern at 45º 2-theta of Nanopowder B depicting the split peaks of the (002)/(200) planes of the tetragonal phase of barium titanate.

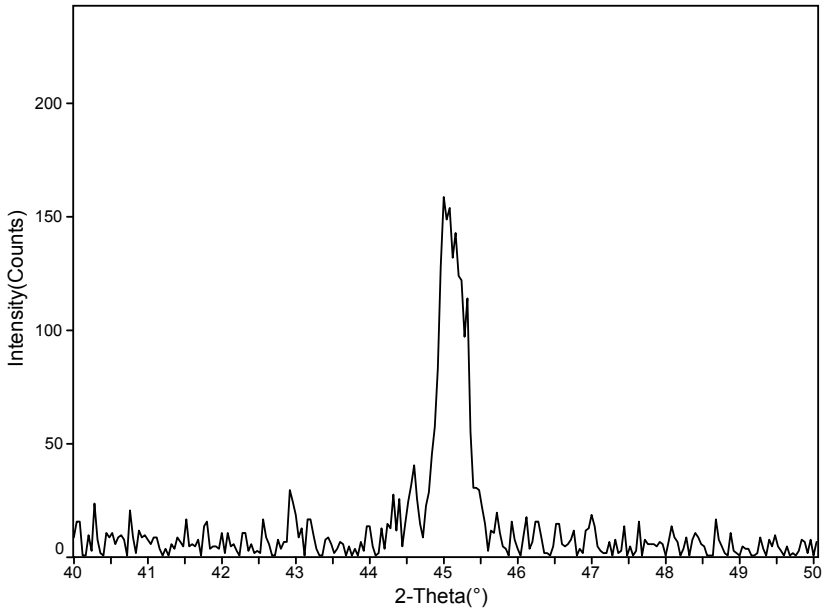

Figure 2.20. Enlarged section of the x-ray diffraction pattern at 45º 2-theta of Nanopowder C depicting the single peak of the (200) plane of the cubic phase of barium titanate.

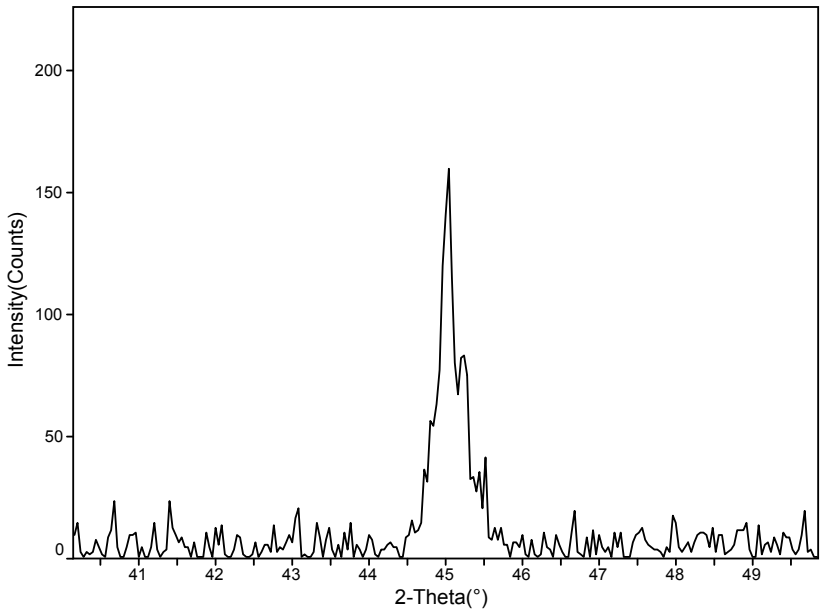

Figure 2.21. Enlarged section of the x-ray diffraction pattern at 45º 2-theta of Nanopowder D depicting the single peak of the (200) plane of the cubic phase of barium titanate.

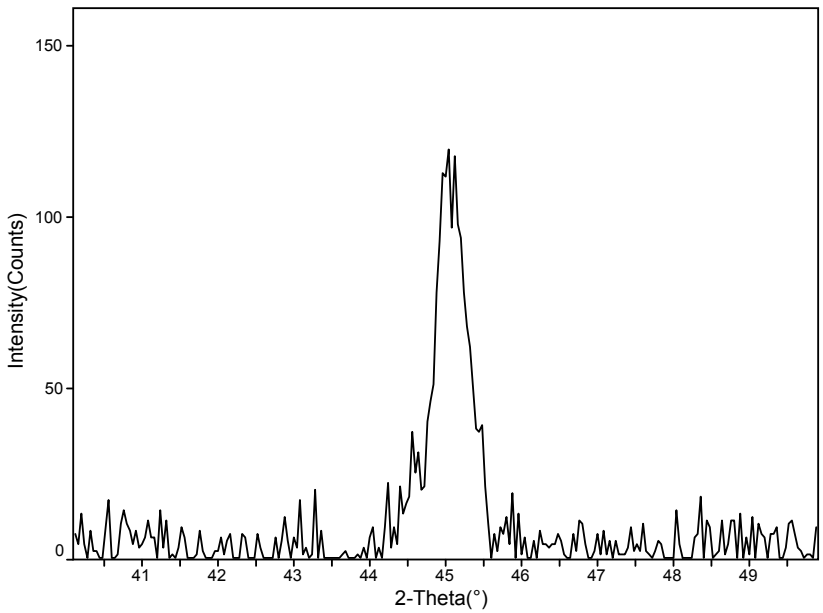

Figure 2.22. Enlarged section of the x-ray diffraction pattern at 45º 2-theta of Nanopowder E depicting the single peak of the (200) plane of the cubic phase of barium titanate.

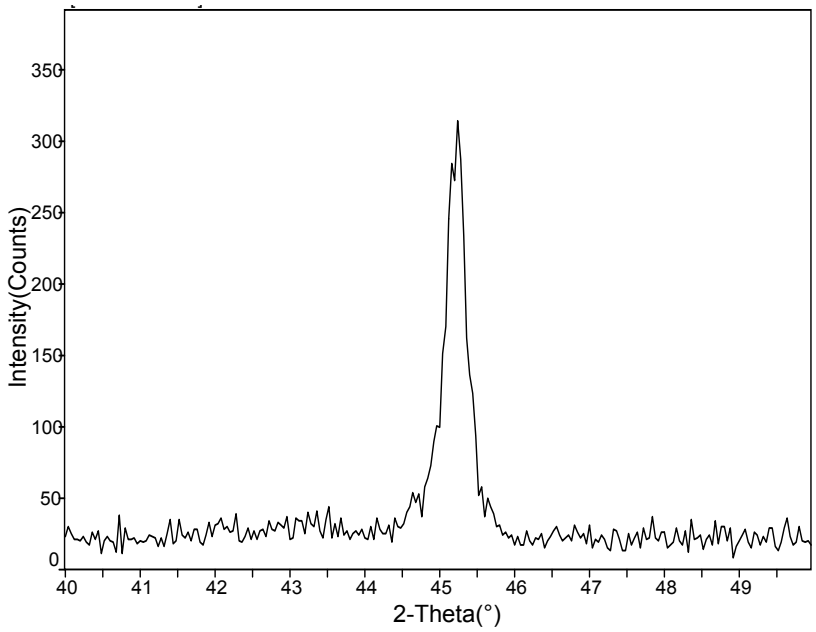

Figure 2.23. Enlarged section of the x-ray diffraction pattern at 45º 2-theta of Nanopowder F depicting the single peak of the (200) plane of the cubic phase of barium titanate.

The relative intensity of the (111) peak was also included in the distinction between cubic and tetragonal crystal structures. The (111) peak intensity for a cubic structure is 30 while that for the (111) tetragonal structure is 46. This difference was large enough to aid in the differentiation between the two structure types. The relative intensity of this peak in the patterns from Nanopowders A and B were 40.5 and 40.25, respectively. The relative intensities of the Nanopowders C through F were 31.2, 28.4, 28.6 and 27.2, respectively. The former two correlated with a tetragonal structure intensity while the latter four correlated with the cubic structure intensity, supplementary evidence to verify the crystal structures of the nanopowders examined.

Takeuchi et al. described a combination of both cubic and tetragonal structures present during XRD analysis.[32] They stipulated that the crystallites were tetragonal cored with a cubic surface layer. The thickness of this cubic layer was proposed to be consistent, 5 nm, irrespective of the particle size. As

the particle size decreased, with the cubic surface layer remaining constant, the cubic content of the crystallites increased. Li and Shih also described observing both cubic and tetragonal peaks with XRD analysis.[33] They described three peaks near 45º 2-theta, both cubic and tetragonal peaks since the cubic peak lies between the split tetragonal peaks. Their conclusion was that clustering of the crystallites had an effect on the tetragonal-cubic transformation of the barium titanate crystallites. Small individual crystallites would be cubic if alone but could be tetragonal when contained in a cluster.

The smallest nanopowder (F) included in this study averaged <70 nm in size. The nanopowder was highly agglomerated with the agglomerates obtaining a spherical shape as observed optically and by SEM. The nanopowder did not exhibit the combination cubic/tetragonal structure through XRD analysis that was observed by Li and Takeuchi. None of the nanopowders exhibited this cubic/tetragonal dual nature.

Table 2.4. Positions of the (002) and (200) Peaks of Each Nanopowder from Analysis of XRD Patterns

Nanopowder and Peak	Peak Position (º 2-theta)
PDF, tetragonal, (002)/(200)	44.855 and 45.377
PDF, cubic, (200)	44.926
A (002)/(200)	44.859 and 45.346
B (002)/(200)	44.849 and 45.355
C (200)	45.018
D (200)	45.060
E (200)	45.069
F (200)	45.212

A small peak near 24º 2-theta was observed upon close examination of the full scan pattern for Nanopowder F (see 'x' in Figure 2.17). Data from PDF #071-2394 of witherite ($BaCO_3$), the (111) peak is observed at 23.9º 2-theta and is the most intense peak. The weak peak observed at 24º 2-theta in the pattern for Nanopowder F was therefore assigned to the presence of barium carbonate in the sample. As will be shown later in Section 3.1, vibrational spectroscopy of nanopowder F indicated a large amount of carbonate present. The amount was just within the detection limits of XRD.

The patterns were examined for peak shifting that may indicate a level of residual strain that may be present in the nanopowders. The results, shown in Table 2.4, specify the positions of the (002)/(200) peaks observed in the patterns of Nanopowders A and B compared well with the (002)/(200) PDF card values. The (200) peaks of other four nanopowders, however, exhibited shifting to varying degrees. The smallest of the nanopowders, F, exhibited the largest shift, 0.286º 2-theta. This observed shift is a possible indication of residual strain from the synthesis process. The issue of residual strain will be addressed further in Section 2.5, Transmission Electron Microscopy.

2.3.4 Summary

The "as-received" nanopowders have been examined by means of x-ray diffraction. All nanopowders exhibited a crystalline structure; no amorphous attributes were displayed in the diffraction patterns. A tetragonal structure was confirmed through the diffraction patterns for Nanopowders A and B. The balance of the nanopowders showed evidence of having the anomalous room temperature cubic phase.

The data corroborate previous literature in answering the question: Is there a critical size below which the cubic phase is stable at room temperature? The tetragonal nanopowders, A and B, were the largest in this study, being in excess of any of the previously published critical particle sizes for anomalous room temperature cubic phase. However, these two powders were synthesized

through the solid state method. The other nanopowders (C through F) exhibited the anomalous room temperature cubic structure and are in agreement with the literature since all were below the largest critical particle size reported (190 nm). This critical size though may be coupled to synthesis methods that incorporate water in their processes. The water content, from the synthesis process, may be distorting the lattice causing residual strain in the crystallites. Residual strain in the crystallites may therefore be the cause of the anomalous room temperature cubic phase. This hypothesis will be explored during transmission electron characterization of the nanopowders.

The data also corroborates previous literature in answering the question: Can stabilization of the anomalous room temperature cubic phase occur through the ubiquitous incorporation of hydroxyl groups in hydrothermally derived barium titanate? Each of the nanopowders that exhibited the anomalous room temperature cubic phase had incorporated water as a result of the synthesis process. The TGA traces showed evidence of the removal of this water from each of the Nanopowders C through F at an elevated temperature consistent with lattice bound water.

The data do not definitively support an answer to the questions: Are the nanocrystals a true cubic phase as they appear to be according to XRD? Are the hydrothermally synthesized nanopowders pseudo-cubic structures as referred to in the literature? The discussion of this topic is therefore deferred to the section on transmission electron microscopic characterization of the nanopowders. The electron diffraction studies may generate an answer to this question.

2.4 Scanning Electron Microscopy

2.4.1 Introduction

The first true scanning electron microscope was built by von Ardenne in 1938.[34] The image was recorded photographically on a rotating drum. The instrument was designed for the study of very thin specimens by means of transmitted electrons (actually a transmission electron microscope).

Improvements were introduced by McMullan with his microscope built at Cambridge.[34] These improvements were made possible by the achievement of a much better signal to noise ratio than had been obtained previously. The improvement in signal/noise ratio thus enabled visual images which greatly facilitated focusing and selection of an appropriate area of the specimen.

Smith, also at Cambridge, made improvements to McMullan's microscope, in particular altering the position of the collector and by keeping it at a positive potential with respect to the specimen. Smith was thus able to ensure the collection of slow secondary electrons as well as faster backscattered electrons. This improved the signal/noise ratio and gave better contrast in the image.[34]

By this time, the possibilities of the instrument were beginning to be appreciated by researchers with numerous specimens being examined. One specimen in particular, a spruce fiber, aroused great interest in the Pulp and Paper Research Institute of Canada which led to the support of the work at Cambridge. The Institute requested the construction of a microscope for its own use which was constructed by Cambridge in 1958.[35] It will be appreciated that, by 1958, the scanning electron microscope had been established as a useful research tool.

Scanning electron microscopy (SEM) provided a closer examination of the nanopowders subsequent to the optical study. SEM was employed to view the morphology of the nanopowders and the agglomerates that were present. The diameter of the smallest of the nanopowders was smaller than the resolving capability of the SEM and precluded the viewing of individual crystallites.

2.4.2 Experimental Procedure

The nanopowders were prepared for viewing by ultrsonicating approximately 50 mg in 10 ml of acetone in a 100 ml beaker for a period of 10 minutes. Using a pipette, a drop of this solution was deposited on a carbon-disc coated long stem pin support and allowed to air dry. The nanopowders were then coated for a period of 1.5 minutes by plasma sputtering with 70:30, by weight, gold-palladium with an operating voltage of 25 kV. The pin supports were then placed in the SEM (Amray 1810, Amray Inc., Bedford, MA) utilizing a short working distance to allow well resolved high magnification viewing. All micrographs are imaged in secondary electron mode.

2.4.3 Results and Discussion

The two solid state synthesized powders, Nanopowders A and B, exhibited irregular morphology. It was difficult to judge from the micrographs whether agglomerates or individual crystallites were present. The morphology of Nanopowder A (see Figure 2.24) appeared to be irregular, flattened clusters of approximate 500 nm average diameter with a few appearing to approach 1 μm.

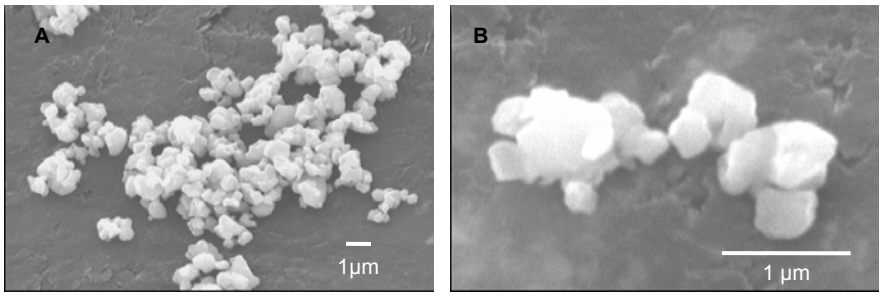

Figure 2.24. SEM micrographs of Nanopowder A at 6,800X (A) and 35,500X (B).

Nanopowder B (see Figure 2.25) was similar in morphology to Nanopowder A. The crystallites had an irregular shape, flattened and chunky. The sizes ranged from approximately a micron to 200 nm which yielded a large crystallite size distribution.

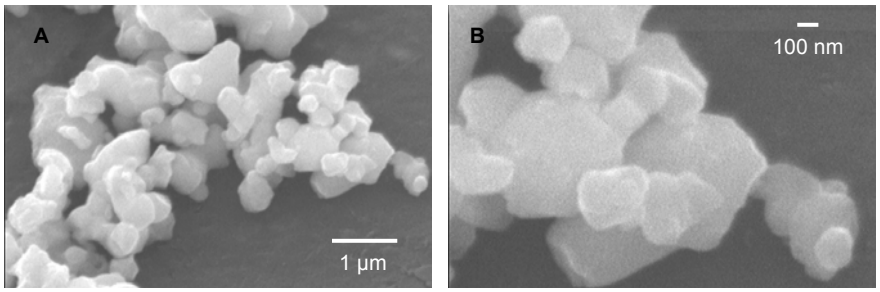

Figure 2.25. SEM micrographs of Nanopowder B at 18,000X (A) and 48,000X (B).

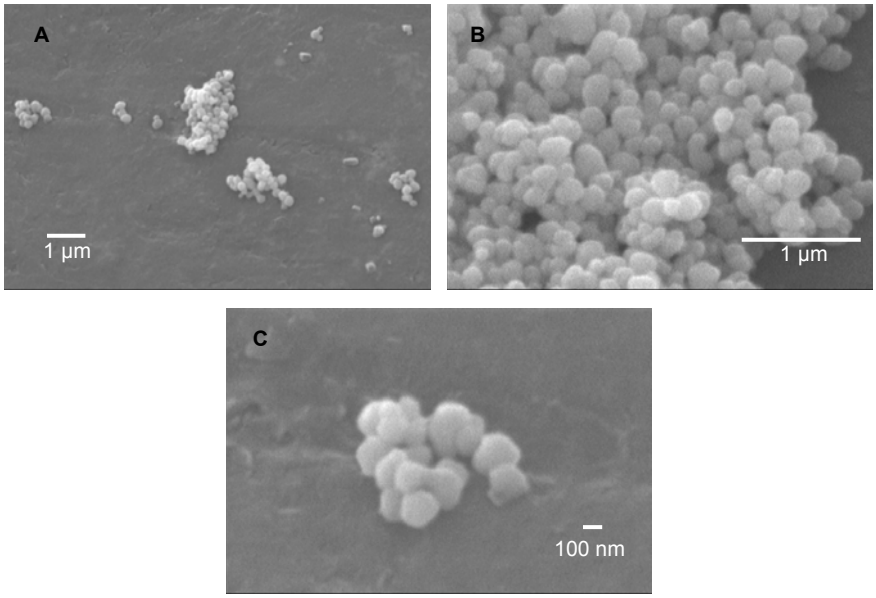

Figure 2.26. SEM micrographs of Nanopowder C at 10,500X (A), 33,000X (B) and 49,000X (C).

The morphology of Nanopowder C (see Figure 2.26) was nearly spherical with a narrower size distribution. The crystallites approximate average diameter appeared to be 150 nm to 200 nm. Agglomeration was sporadic on the pin support with small to very large groupings of crystallites.

The low magnification micrograph of Nanopowder D (see Figure 2.27, micrograph A) showed the extent of the agglomeration present in the sample. A view of one of the larger agglomerated regions at 35,500X showed a uniform crystallite size (see micrograph B). The crystallites were 120 nm to 150 nm in diameter and of nearly spherical shape as seen in micrograph C.

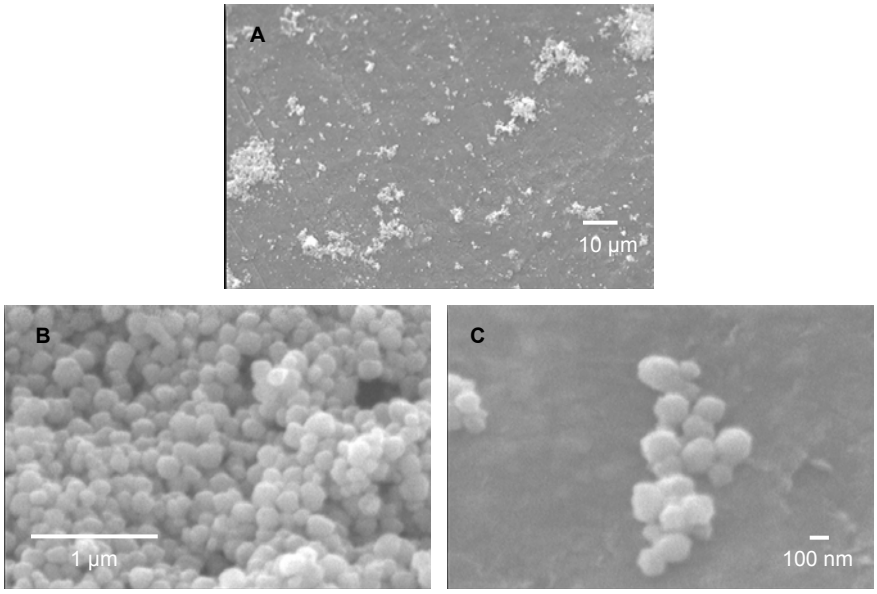

Figure 2.27. SEM micrographs of Nanopowder D at 1000X (A), 35,500X (B) and 48,500X (C).

Nanopowder E (see Figure 2.28) was extremely agglomerated and proved to be difficult in obtaining a well resolved high magnification image. The crystallites were too small to resolve any of the few small groups that were present on the pin support. The crystallites appeared to be of spherical morphology. The crystallite size was difficult to ascertain from the highest magnification image available. The size distribution as well could not be deduced from the micrographs.

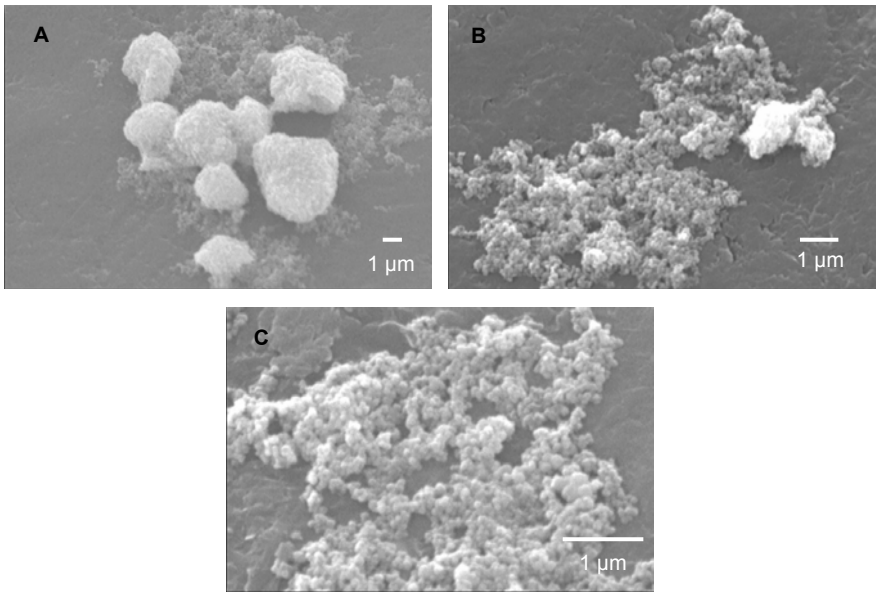

Figure 2.28. SEM micrographs of Nanopowder E at 4,800X (A), 10,000X (B) and 21,500X (C).

A large difference was observed with Nanopowder F. As with Nanopowder E, the crystallite size was indistinguishable with this nanopowder. The interesting aspect of the morphology was the true spherical shape of the agglomerates. In Figure 2.29 micrograph A, sphere sizes of 5 µm to 10 µm were observed. The irregular shaped agglomerate in micrograph C was not the norm with what was observed on the pin support. The surface of the 10 µm sphere in micrograph B, was viewed at a higher magnification of 33,500X (see micrograph D). The nanoscale crystallites were soft-packed into a perfect sphere which would result in a large reduction of surface energy from the sum of the individual crystallites.

Insuring that the acetone had no effect during the preparation of the nanopowder, a sample was viewed neat, as-received. A minute amount of the nanopowder was placed on the pin support with a spatula and sputter coated in the same manner as the previous specimens. Similar spherical agglomerates were observed (see Figure 2.30) as were seen with the acetone ultrasonicated samples.

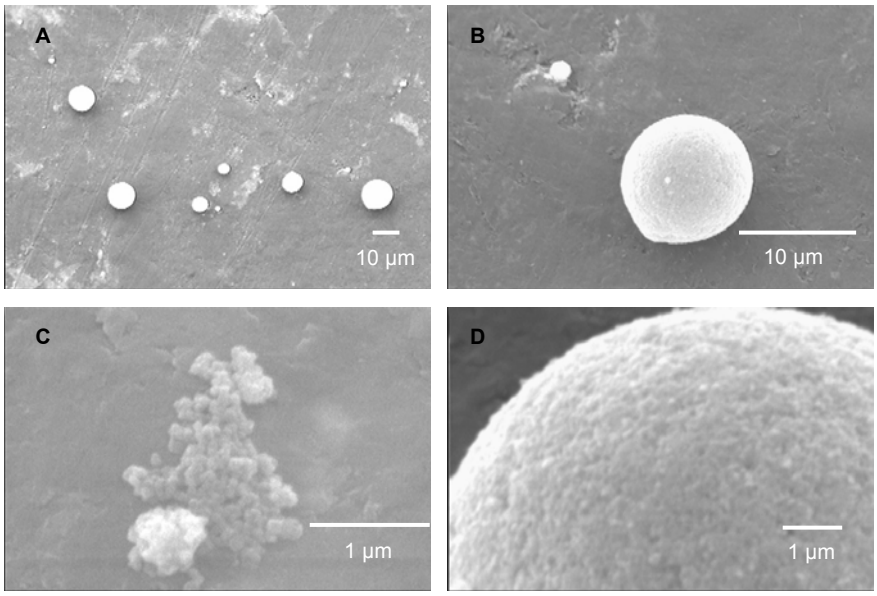

Figure 2.29. SEM micrographs of Nanopowder F at 1,000X (A), 3,300X (B), 16,000X (C) and 33,500X (D).

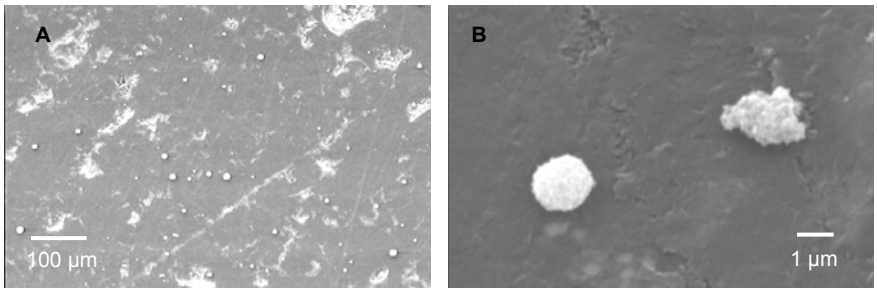

Figure 2.30. SEM micrographs of Nanopowder F, without acetone ultrasonication preparation, at 500X (A) and 10,000X (B).

2.4.4 Summary

Scanning electron microscopic examination of each of the nanopowders was accomplished. A general estimate of particle size and distribution was made for all but the smallest nanopowders, E and F. The largest degree of agglomeration was observed with Nanopowders E and F. Unusual spherical agglomerates were seen in the micrographs of Nanopowder F. It is suggested that this spherical agglomerate form is achieved through inter-particle attractions due to van der Waals interactions in an attempt of the crystallites to reduce large individual surface energy through sphere formation.

2.5 Transmission Electron Microscopy

2.5.1 Introduction

The primary reason for using transmission electron microscopy is the vast increase in resolving capabilities compared to SEM. This is due to the wavelength of the illumination produced by the energized beam of electrons. In 1924 de Broglie hypothesized on the wave nature of electrons and other particles exhibiting wave properties. He combined Einstein's relativity formula and the formula for the photoelectric effect to achieve his hypothesis for the electron. Known as the de Broglie wavelength, $\lambda = \frac{h}{p} = \frac{h}{mv}$, it proposed a wave nature for the electron.

In 1927, Davisson and Germer experimentally confirmed de Broglie's hypothesis on the wave nature of the electron.[36,37] The transmission electron microscope (TEM) soon followed taking advantage of this new finding on the electron. Ernst Ruska and Max Knoll developed the first working TEM in 1932. They were awarded the Nobel Prize in 1986 for their accomplishment. By the 1940's, usage of the TEM extended beyond metal foils, to include other branches of scientific research.[38]

The transmitted beam of electrons in a TEM is of uniform intensity; however, interaction with a specimen changes this intensity. The path of the electrons is changed through interaction with the specimen thus producing interference and diffraction. The contrast that provides imaging of a specimen arises from these scattering events as intensity of the electrons varies in different parts of the image. The bright areas of an image occur in regions of high transmittance and dark areas from regions where scattering and absorption of the beam within the specimen occurs.

Contrast observed in an image is generally the result of the thickness of a specimen and the atomic number of the elements present. The higher the atomic number the greater the absorption of the electrons. Uniform atomic

number specimens produce contrast due to thickness; the thicker the specimen, the darker the image.

Crystallography of the specimen can be analyzed through electron diffraction techniques. The scattering events occur from the interaction between the beam of electrons and the planes of atoms in the specimen producing a pattern of spots, i.e. a diffraction pattern. Each spot in the diffraction pattern represents diffraction from a specific plane of atoms. Upon solving the diffraction pattern produced by the specimen, the crystallographic information provided includes an index of diffracting planes, the zone axis, the crystal system and characteristic symmetry of the specimen.

2.5.2 Experimental Procedure

The nanopowders were prepared, as-received, for TEM analysis by ultrasonicating 5-10 milligrams in 15 ml of acetone in a 50 ml beaker for 20 minutes. Formvar coated copper grids were carbon coated for proper conductivity and were used to support the nanopowders during analysis. Needle-point tweezers were used to quick-dip the support grid into the nanopowder-acetone solution. A small quantity of nanopowder adhered to the grid and was inspected under an optical microscope to assure proper coverage.

The nanopowder coated copper grid was placed in a double tilt holder and inserted into position in the TEM. The accelerating voltage used was 120 kV with a beam current of 70 μA. Initially, several grid locations were viewed to image representative crystallites for particle size and distribution. Smaller groups were imaged at higher magnifications to locate single crystallites for analysis. Single crystallites, separate from others, were imaged by convergent beam electron diffraction. The double tilt holder allows tilting of the sample along two axes. Particular attention had to be made to the eucentric position of the crystallite of interest. Tilting at high magnifications had the distinction of losing the crystallite of interest unless the crystallite was at the exact eucentric position. Brightfield

(BF) images, darkfield (DF) images and selected area diffraction patterns were obtained.

2.5.3 Results and Discussion

Brightfield images are presented to elucidate the size and size distribution of the crystallites of the nanopowders studied. Low magnification images provided a sample view of the morphology of the nanopowders. Figure 2.31 verified the SEM images seen previously. Nanopowder A was highly irregular in shape with a large distribution of crystallite size. The micrograph on the right depicts a sub-500 nm crystallite along with a one micron crystallite.

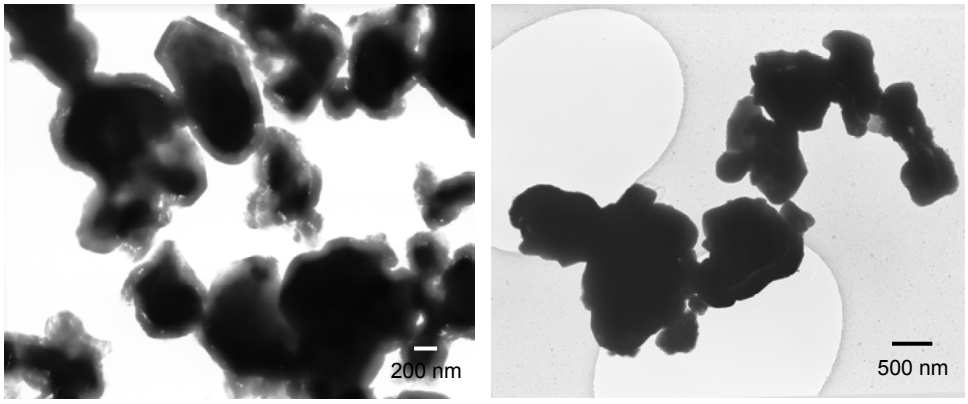

Figure 2.31. TEM Brightfield micrographs of Nanopowder A.

Nanopowder B as seen in Figure 2.32 exhibits similar crystallite morphology as A. The size distribution observed was narrower than that of Nanopowder A. Few crystallites were of one micron size, the majority of the larger crystallites being approximately 750 nm in size.

The specific surface area results for Nanopowders A and B were 469 nm and 436 nm respectively. The crystallites observed by TEM appeared to substantiate the specific surface area findings.

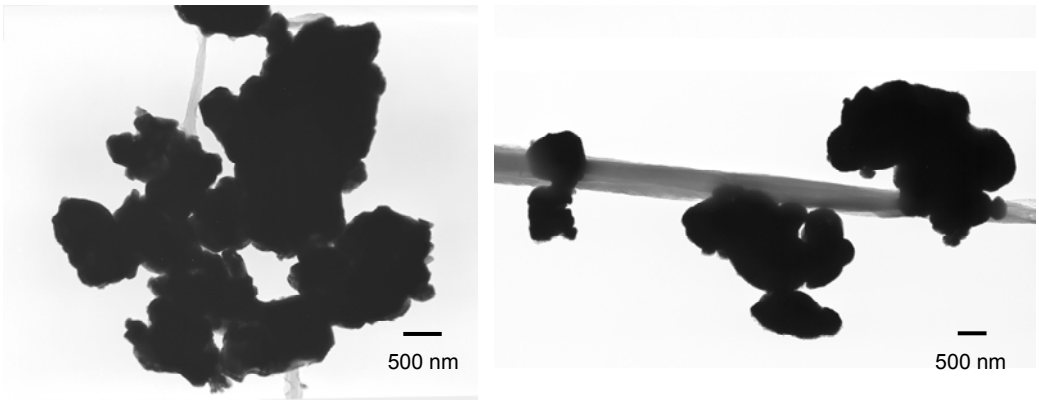

Figure 2.32. TEM Brightfield micrographs of Nanopowder B.

The hydrothermally synthesized nanopowders, C through E, were uniform and nearly spherical crystallites. The size of the largest of the crystallites of Nanopowder C was approximately 150 nm with a narrow distribution of the sizes; the smallest being around 75 nm (see Figure 2.33). Nanopowder C also exhibited crystallites having trapped porosity, the light spots within the crystallites, as seen in Figures 2.33 and 2.34. This trapped porosity, or possibly trapped residual moisture from the synthesis of the nanopowder, was observed within the necked crystallites, the large crystallite in the right micrograph and with the small 25 nm crystallite in the right micrograph (see Figure 2.34). The issue of trapped porosity or moisture will be examined in greater detail in later sections.

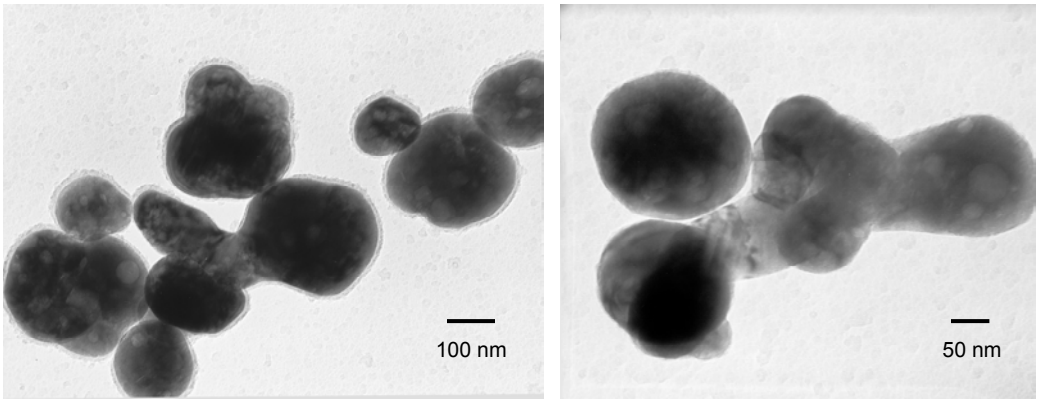

Figure 2.33. TEM Brightfield micrographs of Nanopowder C.

A discussion regarding crystallite strain due to the distortion of the unit cell follows in the darkfield imaging.

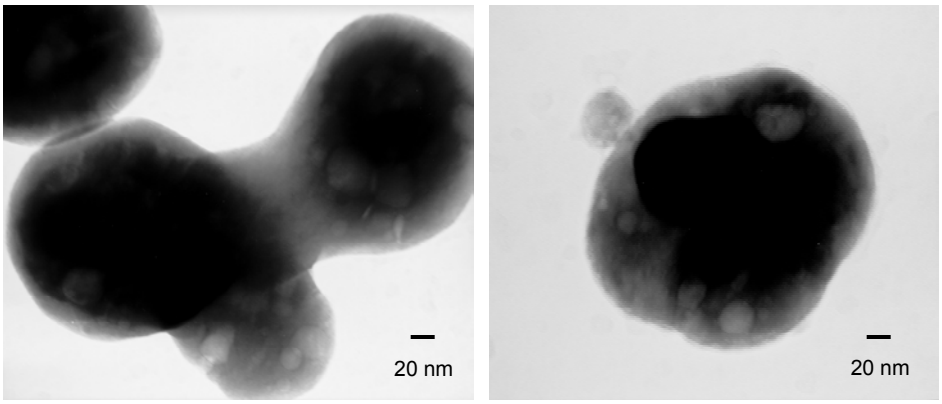

Figure 2.34. TEM Brightfield micrographs of Nanopowder C exhibiting trapped porosity.

The second hydrothermally synthesized Nanopowder, D, had a wider crystallite size distribution and an approximate average crystallite size of 125 nm (see Figure 2.35). This value agrees well with the specific surface area findings. This nanopowder did not exhibit the trapped porosity observed in Nanopowder C.

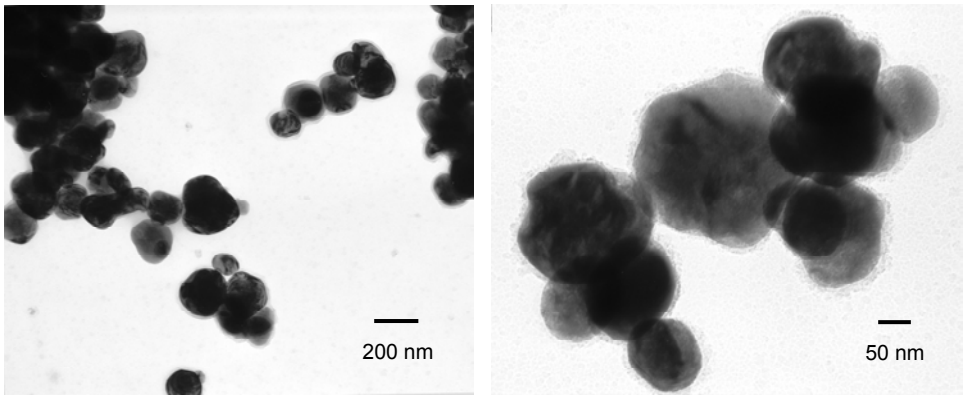

Figure 2.35. TEM Brightfield micrographs of Nanopowder D.

In the following higher magnification set of micrographs of Nanopowder D (see Figure 2.36) a pair of crystallites was observed in the later stage of necking along with five other individual crystallites, all confirming the lack of trapped porosity as was observed with the crystallites of Nanopowder C.

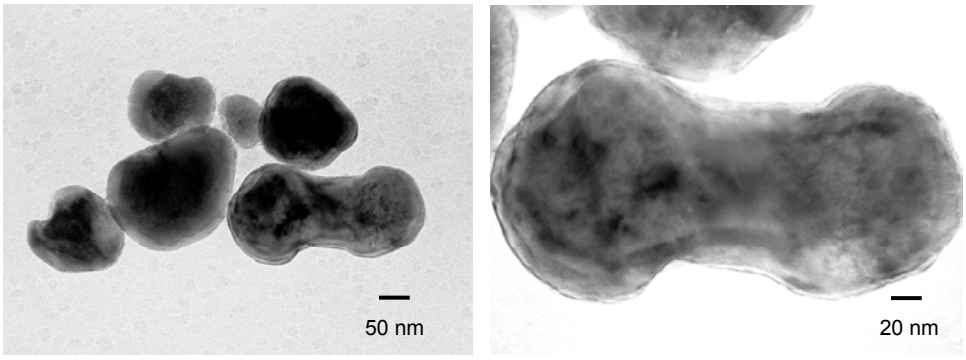

Figure 2.36. TEM Brightfield micrographs of Nanopowder D confirming no observable trapped porosity.

The third hydrothermally synthesized nanopowder, E, had an observable average crystallite size of 70 nm. Crystallites were as small as 30 nm with the largest observed being 100 nm. No trapped porosity was exhibited in the crystallites. Crystallite size agreed with the specific surface area analysis. A

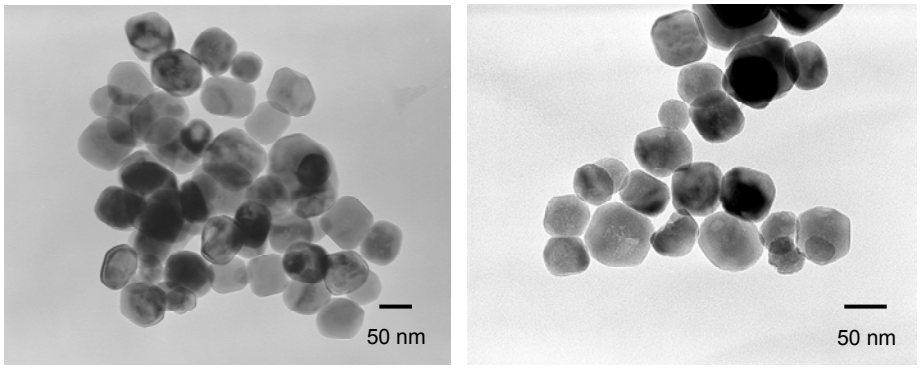

Figure 2.37. TEM Brightfield micrographs of Nanopowder E.

high magnification micrograph of a 60 nm x 70 nm crystallite (see Figure 2.38) exhibited no observable trapped porosity. Faceting of the edges, a phenomenon that was observed with some samples in the sintering section of this study, is observed.

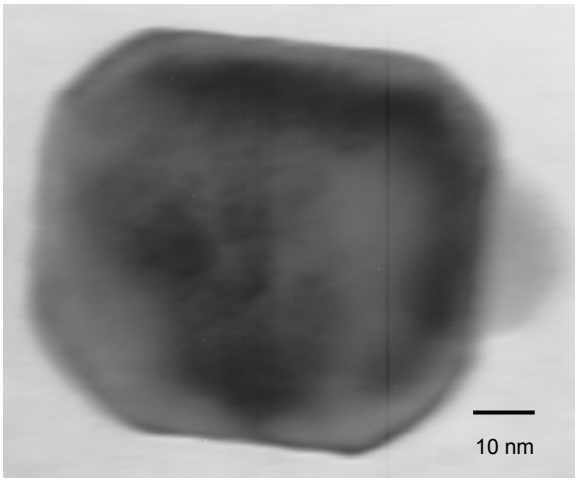

Figure 2.38. TEM Brightfield micrograph of a nanocrystallite of Nanopowder E at 800,000X exhibiting faceted edges.

Nanopowder F was smaller than predicted through the specific surface area analysis. Calculations using the surface area yielded a crystallite diameter of 67 nm. The crystallite size observed by TEM, micrographs in Figure 2.39, was 40-45 nm. A narrow size distribution, with the smallest crystallites of 20 nm size, was observed. The individual crystallites do not exhibit the trapped porosity that was observed with Nanopowder C.

The difference between the crystallite diameter calculated from the BET analysis, 67 nm, and that observed by TEM, 40-45 nm, may be explained by examining the agglomeration exhibited in the SEM analysis. This crystallite size difference can be associated with porosity trapped within the spherical agglomerates. A calculation for an expected specific surface area from a 43 nm average particle size may be made with a result of 23.21 m^2/g. The difference in

this calculated value and that from the BET analysis, 14.85 m^2/g, yields a large trapped surface area within the agglomerates. Approximately one-third of the surface area of the particles was encapsulated within the agglomerates during the BET analysis. The agglomerates therefore seemingly behaved as large individual crystals during the BET surface analysis.

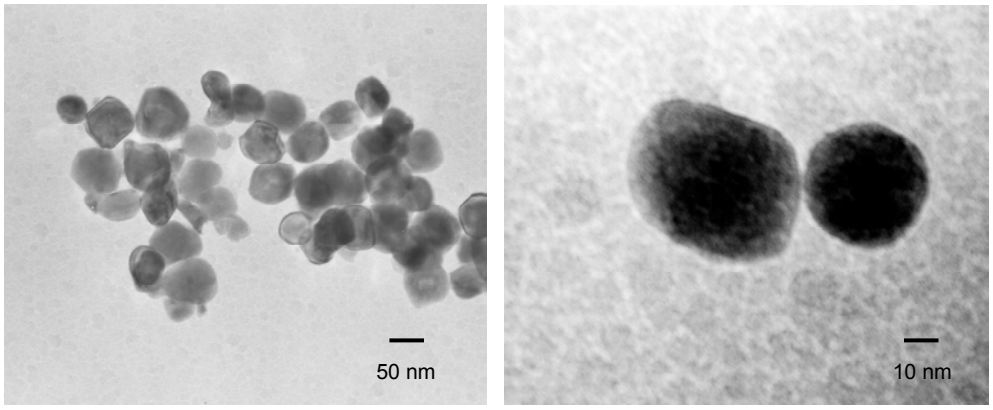

Figure 2.39. TEM Brightfield micrographs of Nanopowder F.

Darkfield images were examined to explore the extent of residual strain, from the synthesis process, in the crystallites. A crystallite without residual strain would present uniform contrast. An exception would be contrast variations due to inconsistent thickness. The residual strain, when present, affects the diffraction behavior of electrons resulting in contrast changes in the image. Darkfield images present the greatest available contrast. The darkfield images, therefore, are high magnification maps of the intensity distribution across the diffracted beams produced by the interaction between the crystallite and electron beam.

Image contrast arises from point to point differences in the region of the crystallite under study. The amplitudes of the transmitted beam and the diffracted beam are coupled in a specimen. When the transmitted beam propagates through the crystal its amplitude will decrease by diffraction while the amplitude of the diffracted beam will increase correspondingly. The amplitude

and phase of waves is therefore altered when passing through the crystal where the crystal has been distorted.

Specimens may contain a number of defects: dislocations, stacking faults, impurities, etc. Using a dislocation as an example, the displacement arising from the strain field of the dislocation is $\Re$ and g is the reciprocal lattice vector for the reflecting plane. The distortion in the lattice causes a phase factor exp(-iα) where $\alpha = 2\pi g \cdot \Re$, to be superimposed on the normal scattering process. If the atom is displaced by $\Re$, the phase of the scattered wave is changed by exp(-$2\pi g \cdot \Re$). Therefore, when a BF image is formed of a distorted crystal, dark regions arise from the enhanced diffraction by the strain field of the crystal defect. The corresponding DF image would present the greatest available contrast of the strain effect. One of the main advantages of the DF image is that it allows the strain field to be viewed with less ambiguity than with the BF image.

The displacements in atom positions, $\Re$, caused by strain fields around defects, provide diffraction contrast in TEM mages. Specifically, the local displacements of the unit cells near a defect, $\Re(x,y,z)$, cause the phase $2\pi g \cdot \Re$ to vary with z. This variation alters the diffracted intensity. The diffraction contrast from the defect therefore varies across the image as determined by the local displacements $\Re(x,y,z)$. The direction of the streaks in the darkfield image represents the direction of maximum strain.[39]

Darkfield imaging was included to show the extent of strain in the crystallites of the nanopowders studied. The elastic strain of the lattice is clearly shown through the contrast variations in the DF images. The magnitude of $g \cdot \Re$ must be sufficiently large to change the local intensity from the background level so that contrast is visible in the image. This criterion is adequate for the analysis of diffraction contrast from many defects in materials: dislocations, precipitates, domain boundaries, and grain and interface boundaries.

Fringe contrast is light and dark regions due to thickness variations along the edge of the specimen and occurs with planar specimens. As the thickness of a specimen varies, the intensity of both the transmitted and the diffracted beams vary. The separation distance between fringes depends on the extinction

distance, ξ_g, and the thickness of the edge of the specimen. The thicker the specimen the closer the fringes will be and as the length of the vector ξ_g decreases, the closer the fringes. This effect, therefore, is different from the strain effects described previously that are of concern with the nanopowders.

Bend contours, another feature of crystalline specimens, also vary the contrast observed and appear as dark contour lines on the edge of a crystal. These contour lines are a result of the specimen being curved such that a given set of planes (*hkl*) are not all at the Bragg condition (i.e. due to the curvature), values of (±*hkl*) are considered and provide contrast, the contour line effect. These curved lines are different from the effects observed due to strain.

Examination of the micrograph of Nanopowder A, a darkfield image (see Figure 2.40) no strain is evident. The consistency in contrast variation (the darker regions are in the center sections of the crystallites) is due to the thickness of the crystallite. The contrast variation between the edges and center of the crystallites is evidence of the decreasing thickness from the center of the crystallite to the edge.

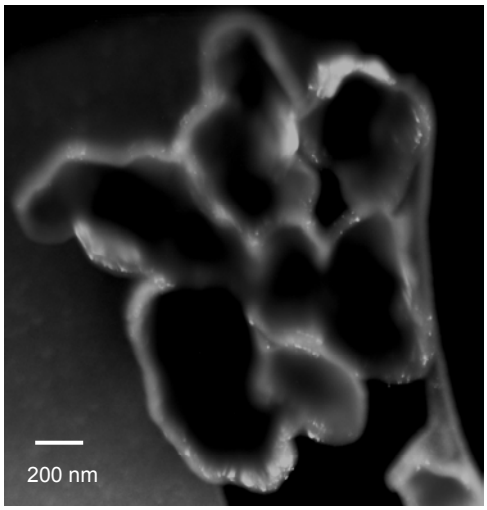

Figure 2.40. TEM Darkfield micrograph of Nanopowder A with no strain exhibited.

The results of the examination of the micrographs of Nanopowder B are similar to that of the previous nanopowder. The lighter contrast crystallites (see Figure 2.41) are due to their being smaller and thinner than the others. No large deviations in contrast within the crystallites are exhibited. Both of the solid state synthesized nanopowders exhibited contrast only of the form dt/dz, that due to variations in thickness.

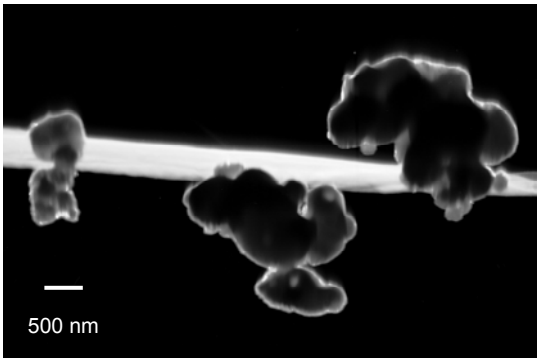

Figure 2.41. TEM Darkfield micrograph of Nanopowder B with no strain exhibited.

The hydrothermally synthesized nanopowders exhibited varying levels of residual strain. Nanopowder C (see Figure 2.42) showed several crystallites exhibiting deviations in contrast within the crystallite. The varying degrees of contrast, dark to bright, represented levels of strain within the crystallites. The crystallites were within a narrow size distribution; therefore, the variation in contrast is not due to thickness variations between individual crystallites. Nanopowder C exhibited trapped porosity; regions near these pockets would exhibit the requisite strain field ($\Re$), and the deviation dδr/dz, producing some of the contrast variant observed.

Nanopowder D (see Figure 2.43) exhibited crystallite strain, streaking of the contrast within individual crystallites. Although the size distribution was broader with this nanopowder, only two fully bright crystallites are observed in the micrograph, a possible indication of their being thicker than the other crystallites

present. Others did exhibit variation of contrast across the crystallite, an indication of strain fields ($\Re$) present within the crystallite.

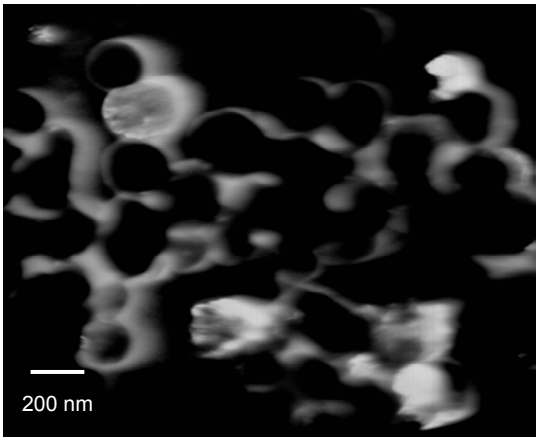

Figure 2.42. TEM Darkfield micrograph of Nanopowder C with crystallites exhibiting strain.

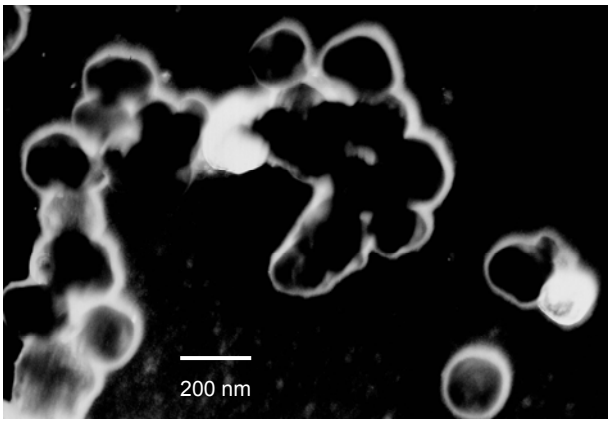

Figure 2.43. TEM Darkfield micrograph of Nanopowder D with crystallites exhibiting strain.

In the darkfield micrograph of nanopowder E (see Figure 2.44) there was variation in the levels of contrast within the crystallites. Several exhibit variation in contrast within the crystallites. As with the previous two chemically synthesized nanopowders, strain fields ($\Re$) were present to satisfy dδr/dz and produced the contrast variation observed.

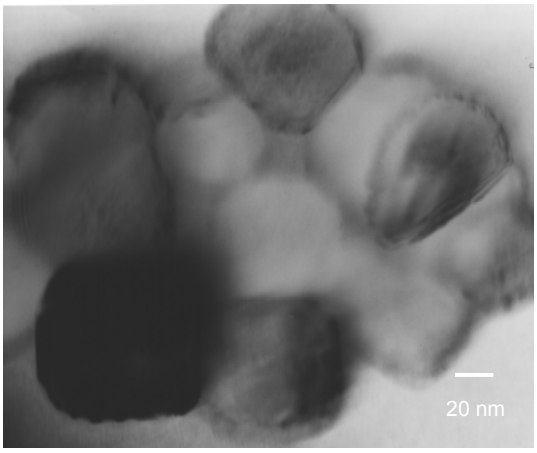

Figure 2.44. TEM Darkfield micrograph of Nanopowder E with crystallites exhibiting strain.

Nanopowder F (see Figure 2.45) exhibited some residual strain within the crystallites. The crystallite on the left exhibits nearly half bright and half dark contrast. The accompanying brightfield image, right micrograph, shows the crystallite with only slight variation in intensity resulting from a variation in thickness. The contrast in the darkfield image, therefore, is a consequence of residual strain in the crystallite.

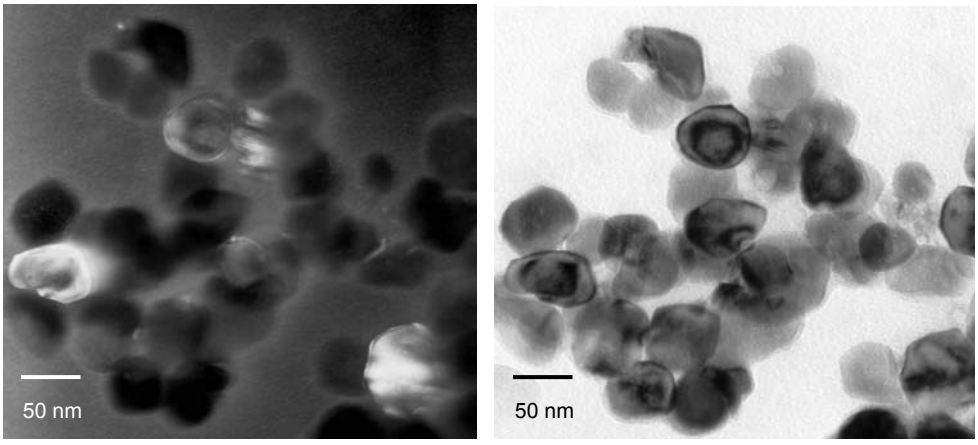

Figure 2.45. TEM Darkfield and Brightfield micrographs of Nanopowder F with crystallites exhibiting strain.

The TiO_6 octahedron need be distorted in the <100> direction with a displacement of the Ti^{4+} ion for the lattice to assume the tetragonal structure. The physical sizes of the nanocrystals, that contain defects, prevent completion of the cubic-tetragonal phase transition at room temperature leading to strains within the crystallites. These internal strains are from defects in the nanopowders formed during the chemical and hydrothermal synthesis, primarily in the form of lattice hydroxyls and their compensation by cation vacancies. As will be shown in a later section, the solid state synthesized nanopowders contained far lower levels of moisture and, therefore, should exhibit tetragonal crystal symmetry. Their tetragonal structure, as shown by XRD and TEM electron diffraction, along with low levels of moisture results in the observed lack of residual strain in the darkfield images.

Viekanandan and Kutty suggested that strain in the crystallites were related to the point defects in the lattice.[40] Compensation of the residual hydroxyl ions in the oxygen sublattice by cation vacancies results in strains leading to the presence of a metastable cubic phase at room temperature. Shi et al. also reported the stabilization of the cubic phase in hydrothermal synthesized barium titanate and were caused by surface defects that included hydroxyl defects and barium vacancies.[41] Clark et al. observed that as-prepared powders contained many defects, primarily in the form of lattice hydroxyl ions.[24]

During the process of obtaining the darkfield micrographs, the observance of changes in the observed variation in contrast occurred. A crystallite exhibiting suspected levels of strain could be altered by partially condensing the beam of electrons to cover only the crystallite of interest in brightfield mode. This alteration was readily observable and resulted in a different appearance of the crystallite under darkfield conditions. The exhibited contrast variation across the crystallite from residual strain became of uniform contrast, through the relieving of the lattice strain, after the electron beam was condensed on it then spread out to cover the entire view screen. Ostrander observed a reduction in lattice strain of fine barium titanate powders after heat treatment.[42] Numerous crystallites could be altered by observation at higher magnifications, where the electron

beam is also further condensed, which produced the same results with some crystallites. This process made difficult the capture of the residual strain in darkfield mode.

The energy of the electrons was of high enough order to produce a reduction of lattice strain within many of the crystallites. A rearrangement of the crystallite structure, through the observance of rapidly changing contrast within the crystallites during imaging, was hypothesized. This rearrangement possibly from the reorientation of small trapped moisture pockets within the crystallites, quite possibly included the loss of moisture as vapor in the process, which allowed the crystallite structure to relax, and thereby reduced the observable strain in darkfield mode.

Crystallography of the specimen can be analyzed through electron diffraction techniques.[43] The information provided by a diffraction pattern will determine whether the specimen is crystalline and provide the crystal system and characteristic symmetry of the specimen if it is crystalline. Using the separation between the diffraction spots of the diffraction pattern, the interplanary spacings in the crystallite can be determined.

A diffraction pattern was recorded for each of the as-received nanopowders. The method of solving the patterns is described in detail in the appendix. A diffraction pattern of each nanopowder follows including a brightfield micrograph of the crystallite from which the pattern was taken. The patterns were solved and indexed, the zone axis stipulated, and the crystal system noted.

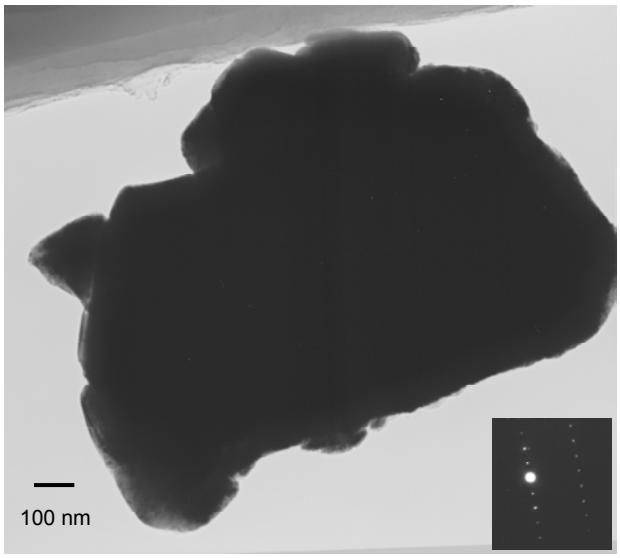

Figure 2.46. TEM Brightfield micrograph of Nanopowder A with diffraction pattern (inset).

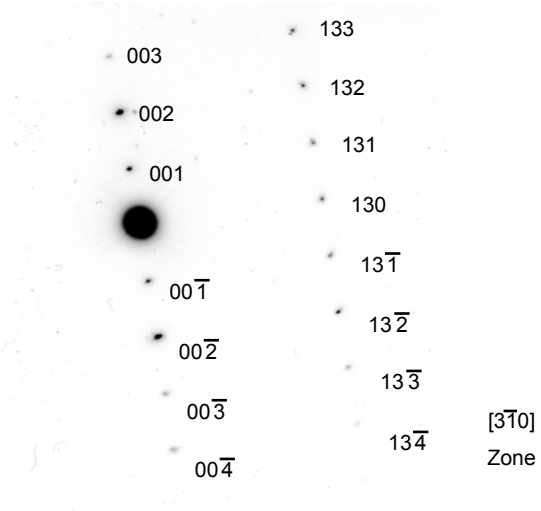

Figure 2.47. Indexed TEM electron diffraction pattern of Nanopowder A with zone axis denoted; tetragonal crystal system.

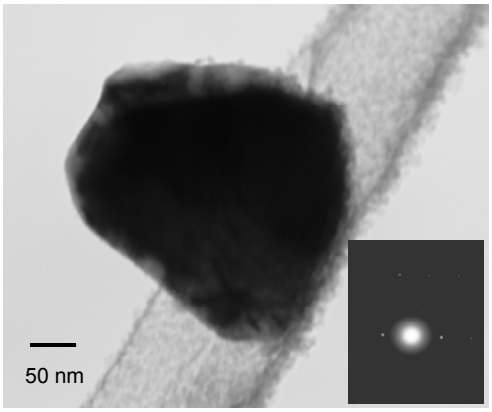

Figure 2.48. TEM Brightfield micrograph of Nanopowder B with diffraction pattern (inset).

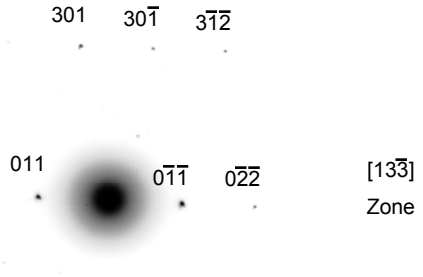

Figure 2.49. Indexed TEM electron diffraction pattern of Nanopowder B with zone axis denoted; tetragonal crystal system.

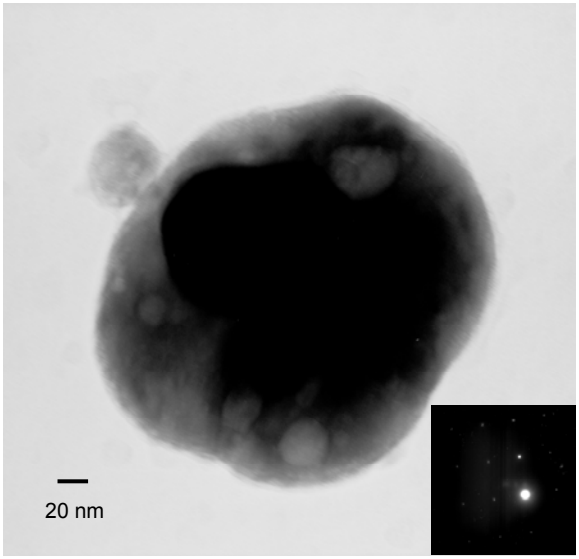

Figure 2.50. TEM Brightfield micrograph of Nanopowder C with diffraction pattern (inset).

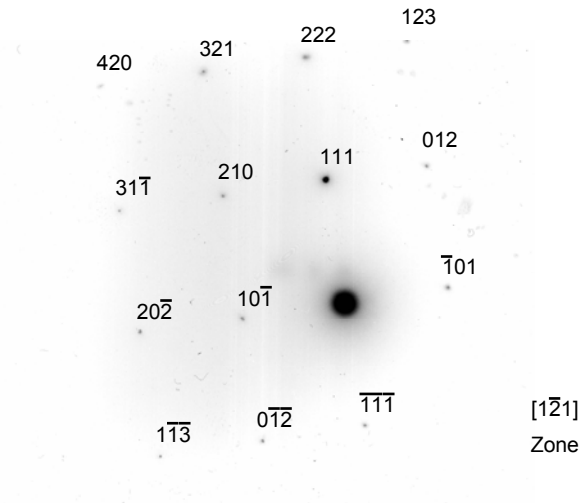

Figure 2.51. Indexed TEM electron diffraction pattern of Nanopowder C with zone axis denoted; cubic crystal system.

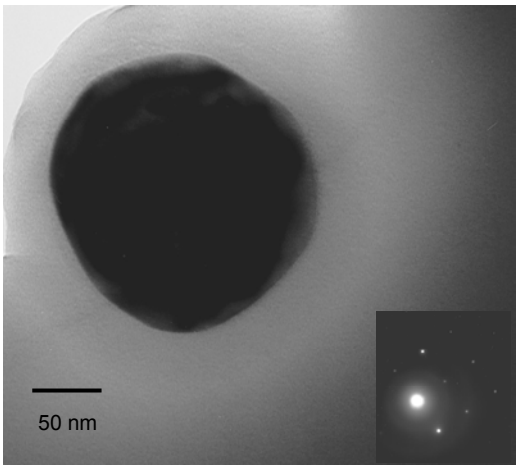

Figure 2.52. TEM Brightfield micrograph of Nanopowder D with diffraction pattern (inset).

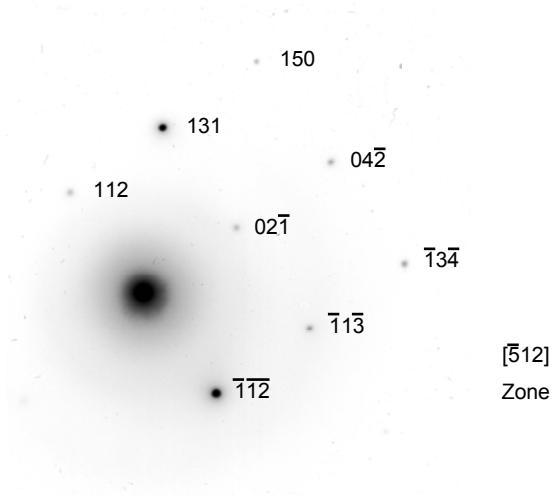

Figure 2.53. Indexed TEM electron diffraction pattern of Nanopowder D with zone axis denoted; cubic crystal system.

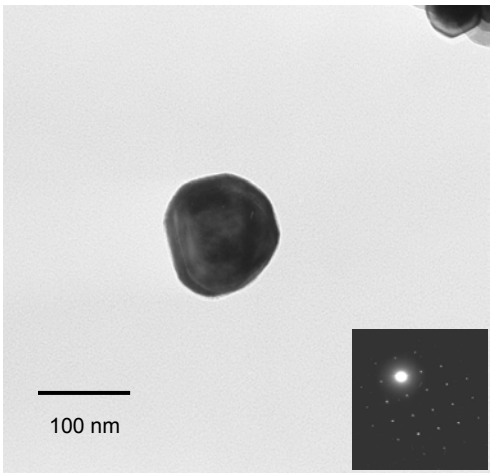

Figure 2.54. TEM Brightfield micrograph of Nanopowder E with diffraction pattern (inset).

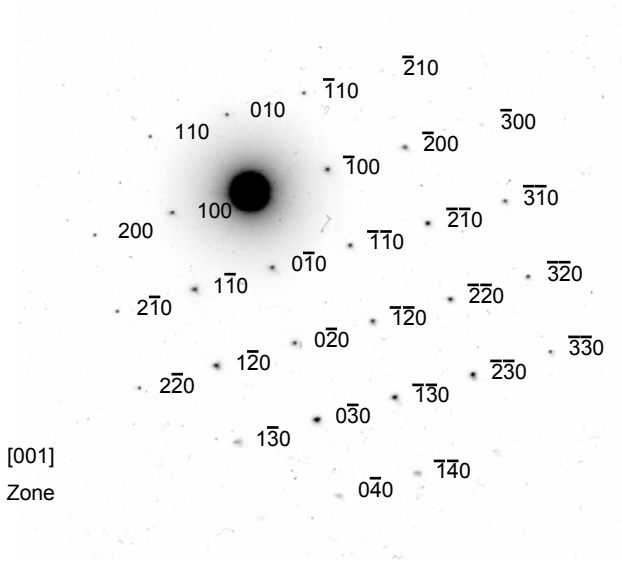

Figure 2.55. Indexed TEM electron diffraction pattern of Nanopowder E with zone axis denoted; crystal system indistinguishable due to zone axis.

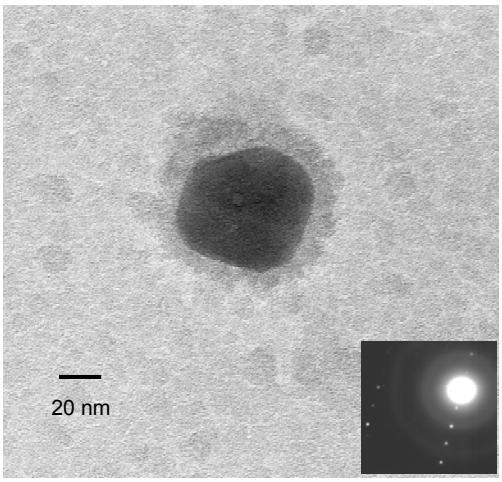

Figure 2.56. TEM Brightfield micrograph of Nanopowder F with diffraction pattern (inset).

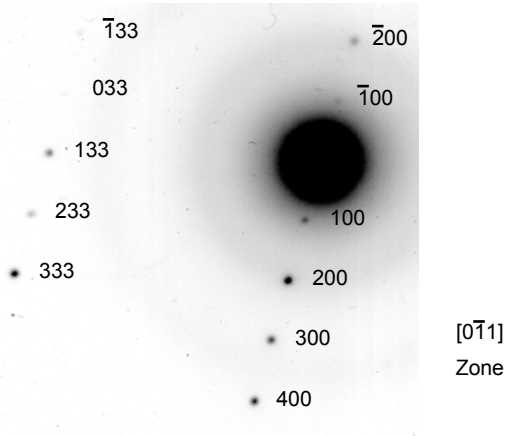

Figure 2.57. Indexed TEM electron diffraction pattern of Nanopowder F with zone axis denoted; cubic crystal system.

The indexed electron diffraction patterns indicated that the solid state synthesized nanopowders (A and B) had tetragonal symmetry. The hydrothermally synthesized nanopowders (C through F) were cubic in symmetry. An exception exists with Nanopowder E; two diffraction patterns were photomicrographed, both having a [001] zone axis. Since this direction is along the z-axis, the direction of unit cell distortion, no difference in angles would be detected between tetragonal and cubic symmetries although XRD analysis supported cubic symmetry. The electron diffraction results, therefore, substantiate the data observed with the XRD data presented previously. The accumulated data, therefore, confirms a room temperature metastable cubic phase for the hydrothermally derived barium titanate nanopowders as previously noted by others.

2.5.4 Summary

The TEM study confirmed the particle size of the nanopowders as calculated from the BET analysis with the exception of nanopowder F. The crystallite size as observed by TEM was 40-45 nm as opposed to the BET calculated value of 67 nm. This size difference could be associated with porosity trapped within the spherical agglomerates. The agglomerates, therefore, could be considered as large individual crystals during the BET analysis.

In the brightfield micrographs of Nanopowder C, trapped porosity within individual crystallites was observed, possibly trapped moisture. This hypothesis will be discussed in the vibrational spectroscopic characterization section of this study.

In the darkfield micrographs residual strain was observed with the hydrothermal nanopowders. The solid state nanopowders exhibited no contrast variation that would present evidence for residual strain. The strain is proposed to be a result of defects in the nanopowders formed during their hydrothermal synthesis, primarily in the form of lattice hydroxyls. The nanocrystals are so small that structural defects prevent the completion of the room temperature

tetragonal phase, which leads to high strains within the crystallites. The internal strain then is due to the tetragonal to cubic deformation observed with XRD and TEM electron diffraction as a result of the incorporated hydroxyl defect.

The diffraction patterns were indexed and confirmed the tetragonal phase for the solid state synthesized nanopowders. The cubic phase was confirmed for the chemically hydrothermal nanopowders, and was in agreement with the XRD analysis.

3 Vibrational Spectroscopic Characterization

3.1 Diffuse Reflectance Infrared Fourier Transform (DRIFT)

3.1.1 Introduction

The discovery of "invisible light" occurred in 1800.[44] Visible light was explored with a prismatic spectrum as projected on a table using a mercury thermometer as a heat detector. Sir William Herschel discovered that the heating power increased towards the red end of the spectrum but it did not reach a maximum until the thermometer was moved beyond the limit of the visible spectrum, hence his term of "invisible light." The existence of radiant energy to which the eye was insensitive lay dormant for thirty years following Sir Herschel's discovery due to the lack of a suitable detector other than the mercury thermometer.

A phonon is a single quantum of vibrational energy in the crystal lattice. Atoms in solid materials are constantly vibrating at high frequencies. The vibrations are coupled due to the bonding of neighboring atoms. The vibrations therefore are coordinated in a way that traveling lattice waves are produced which propagate through the crystal. There are generally three modes, or polarizations, of the atomic vibrations: acoustic or longitudinal waves, with the atoms vibrating along the line of atoms, and two optical or transverse waves, with the atoms vibrating perpendicular to the line of atoms.[45]

Infrared spectroscopy examines the absorption of light whose wavelength corresponds to the bond energy of a molecule. By plotting the degree of absorption as a function of wavelength, one obtains the infrared spectrum of the molecule which allows the distinction between the bonds that are present. The wavenumber ($\tilde{\upsilon}$) in units of reciprocal centimeter (cm^{-1}) is the unit most commonly used in vibrational spectroscopy. This unit is derived from energy and is related to the frequency and wavelength by:

$$E = nh\nu \qquad c/\lambda = \nu \tag{3.1}$$

$$\text{substituting, } E = nh\left(c/\lambda\right) = nhc\tilde{\upsilon} \tag{3.2}$$

where, $\tilde{\upsilon} = 1/\lambda = \nu/c = E/hc$. (3.3)

Note the distinction between the symbol for frequency (ν, nu) and the symbol for the wavenumber ($\tilde{\upsilon}$).[46]

The surface of any material, regardless of the particle size, is expected to have properties that are different from that of the bulk. The exposed plane of atoms at the surface encounter a loss of periodicity in one dimension which result in changes in electronic states at the surface. This implies that different properties exist for the surface with respect to the bulk. The lack of nearest neighbors of the surface atoms leaves chemical bonds free and available for chemical reactivity. Surfaces adsorb atomic and molecular species to minimize the energy at the interface.

Relaxation, reconstruction, structural imperfections, as well as adsorbed molecules and atoms cause drastic changes in the electrical properties at the surface by modifying the affinity of the surface for electrons.[47-48] The nature of the impurities adsorbed on the surface is partly related to the synthesis history of the nanopowders. It should also be noted that the molecules or atoms adsorbed on the surface can originate either from the atmosphere or from the interior of the nanopowder through diffusion processes. The most common and abundant component of the surface layer is atmospheric water, whose molecules can strongly adsorb and dissociate to form hydroxyl groups.

Consider the barium titanate nanopowders to have a density of 6012 Kg/m^3, cubic morphology and packing of atoms, and a one micron particle size. The percent of atoms that reside at the surface is ~0.14%. Reduce the particle size to 25 nm and the percent of atoms that reside at the surface increases to ~5.4%, more than an order of magnitude increase in the number of atoms that reside at the surface. The number of surface atoms increases with increasing specific surface area of the nanopowder. This leads to a higher surface reactivity of the nanopowders compared to a micron-sized counterpart. A decreased surface energy occurs with the preferential adsorption of atoms and/or molecules to these surfaces of the nanopowders.[49] Therefore, when processing the nanopowders into their final solid state while exposed to air, the surface

adsorbed molecules, most prevalently atmospheric water and carbonate, will be trapped in the grain boundaries in the sintering process and major difficulties may be encountered.[50-52]

As a consequence of the surface reactivity, the interaction of the nanopowder surface with its environment, the atmosphere or the gaseous reactants from synthesis, will yield chemical surface species. It is important, therefore, that the nature and properties of the surface itself are key issues in understanding the interactions between solid surfaces. A comprehension of the surface structure on the molecular level is required for control of technical properties (i.e. control of properties through the purposeful additions of surface chemistry modifying impurities). It is the understanding of these impurity species incorporated in the barium titanate nanopowders that are of interest during the vibrational characterization using diffuse reflectance.

The scattered radiation is the essential effect of the diffuse reflectance mode of infrared characterization.[53-54] The first advantage of this mode over the transmission technique is that loose powders can be analyzed without the need for pressing small quantities of the powder into a KBr pellet thereby leaving the surfaces undisturbed. A second advantage is the high sensitivity of diffuse reflectance to surface species due to the multiple reflection and diffraction of the beam at the surfaces of the powders.

In general, it has been found that the principles useful in interpreting the infrared spectra of compounds are applicable to species on the surfaces of solids also. Thus, the concept of group vibrational frequencies, where particular structural groups of atoms are associated with characteristic vibrational frequencies, applies well on surfaces as it does in molecules. Minor variations in the group vibrational frequency associated with a particular group of atoms may often be attributed to interactions either within the molecule, between adsorbed molecules, or between the molecule and a surface.

From the point of view of surface chemistry, the main reason for measuring the vibrational spectra of a surface is to study adsorbates and to infer

information about their structure and mode of bonding. Infrared spectroscopy has been widely used in this way on polycrystalline oxides.[55]

The use of IR spectroscopy in the studies of the adsorbed surface species on the barium titanate nanopowders was to determine their chemical nature. Two types of adsorption are usually distinguished: physical adsorption (physisorption) and chemical adsorption (chemisorption). Physisorption is the physical interaction between molecules that may include London, Keesom and Debye forces known collectively as van der Waals forces. The binding energy is typically 0.25 eV or less.[50,56] The chemisorption interaction is stronger and may be dissociative or reactive. It must be noted, however, that no clear division is stipulated separating chemisorption from physisorption. When a molecule is physisorbed or chemisorbed on the surface, the electronic distribution in the molecule is perturbed with respect to the gas phase. Therefore, changes in its vibrational state can be observed, according to the nature and strength of the adsorption.

3.1.2 Experimental Procedure

In this work, structural investigation of crystalline barium titanate nanopowders was performed with DRIFT analysis to indicate the presence of defects such as H_2O, OH^- and carbonate ions. The diffuse reflectance accessory (Collector, Model 0030-005, Thermo Spectra-Tech, Stanford, CT) was used in a Nicolet Nexus 670 mid-infrared FT-IR (Thermo Nicolet Corp., Madison, WI). The FT-IR was equipped with a nitrogen cooled mercury cadmium telluride (MCT-A) detector, KBr beam splitters and a GloBar element as the source of infrared radiation. Continuous flow of water and CO_2 free purge gas was provided through a Type 75-60 air generator (Balston Filter Products, Lexington, MA). Spectra were obtained at a resolution of 1 cm^{-1} with 500 cumulative scans to form the final spectrum between 650 cm^{-1} and 4000 cm^{-1}.

The nanopowders were examined at room temperature, neat (i.e. “as-received”) so as not to disturb the surface layers and to improve the surface

sensitivity of the technique. A micro-cup was used to hold the nanopowders during sampling. A background was taken using an aluminum coated mirror and auto subtracted from the final sample spectrum by the Omnic 6.0 software package. (Thermo Nicolet Corp., Madison, WI)

3.1.3 Results and Discussion

The major absorption bands of all six nanopowders are summarized in Table 3.1 as obtained during the 1 cm^{-1} resolution DRIFT analysis. The surfaces of the hydrothermally derived nanopowders exhibit large concentrations of physisorbed water (see Figures 3.1 – 3.6). The ~3685 cm^{-1} band is the typical region for the surface -OH groups on metal oxides, and in particular, on anatase and rutile TiO_2.[57-59] The strong ~3510 cm^{-1} band is typical for both binary and ternary metal oxides. Similar bands observed in the hydrothermally derived nanopowders correspond as well with the 3505 cm^{-1} band of CsI disk prepared $BaTiO_3$ and the 3480 cm^{-1} band of $BaTiO_3$ monocrystals.[60-62] The 3510 cm^{-1} band is therefore assigned to lattice hydrogen impurities due to the OH stretching mode of the OH groups in the bulk. An OH deformation mode would also be expected near 530 cm^{-1} but may overlap with a $BaTiO_3$ fundamental mode at 540 cm^{-1}, although this region is outside the capabilities of the mercury cadmium telluride detector utilized in this study.

It is well known that hydrogen impurities can penetrate several ternary oxides with perovskite structure as H^+ bonded to a lattice oxygen in the form of OH^-.[62] These protons can be compensated for by a cation charge defect, either reduced centers such as Ti^{3+} or cation vacancies in nonstoichiometric samples. These lattice hydroxyls will be examined further in the following section.

The large broad band between 3600 – 2700 cm^{-1}, observed in varying degrees with all of the nanopowders, is indicative of OH stretching of molecular water physisorbed to the surface of the nanopowders. Berg noted that oxide surfaces could all be described as hydroxylated surfaces.[63] These surfaces adsorb and strongly retain several layers of bound water. Bradley worked out the

theory of the formation of multiple layers based upon the view that the induced dipoles in the initial adsorbed layer will themselves induce dipoles in the layers above.[64] This occurs through the nondissociative adsorption of hydroxyl ions via hydrogen bonding and is spectrally observed as the broad 3600 – 2700 cm^{-1} band.

In the case of a perfectly ordered surface coverage, an even distribution of adsorbed molecules, and a low surface coverage, a perfectly symmetric, sharp band would be observed. A more random orientation of adsorbed molecules would produce more random oscillating species resulting in weaker band intensity with broadening of the band at the low frequency end. The low frequency adsorption tail is characteristic of vibrational coupling within a random molecular distribution.[65] The broad 3600 – 2700 cm^{-1} band is evidence of the numerous variations of possible planes at surface terminations.

The broad weak band at 2090 cm^{-1} is also indicative of physisorbed molecular water in conjunction with a weak barium carbonate band. Additionally, the strong band at ~1625 cm^{-1} is assigned to the OH bending mode of water. The major molecular water bands as related to the nanopowders are easily observed in Figure 3.9, a combination of molecular water with Nanopowder A.

Nanopowder F (the smallest average crystallite sized powder) does not exhibit a large concentration of adsorbed water as do the other three hydrothermally synthesized nanopowders, ranking 4^{th} in moisture concentration. Tables 3.2 and 3.3 summarize the peak areas related to moisture and carbonate content of the nanopowders. The peak area tool of the Omnic 6.0 software package was used to obtain the area within the peaks of interest. The lower moisture content observed with Nanopowder F is due to the large concentration of carbonate, ranking first with the highest concentration, which reduces the number of available sites for the adsorption of hydroxyls and molecular water.

The concentration of physisorbed water is much lower on the solid state synthesized nanopowders than for the other nanopowders. The temperature of

Table 3.1. Infrared Band Wavenumbers and Assignments at 1 cm^{-1} Resolution

Location (cm^{-1})						Assignment	Comment	Reference
A	B	C	D	E	F			
3687w	3686w	minor	minor	3683b	3685b	ν_{asym}, OH	surface	79,104
3600-2700b	3600-2700b	3600-2700b	3600-2700b	3600-2700b	3600-2700b	$\nu_{sym} + \nu_{asym}$	weak bound H_2O	81,91,98
_	_	3510	3512	3510	3509	ν_{asym}, OH	lattice	79,104
_	_	_	_	_	3492	ν_{asym}, OH	lattice	104
_	_	_	_	_	3451	ν_{asym}, OH	lattice	104
_	_	_	_	_	3340	ν_{asym}, OH	lattice gas	104
2887w	2887w	minor	minor	minor	2887		$BaCO_3$	_
2823w	2823w	minor	minor	minor	2823		$BaCO_3$	_
2451	2451	2451	2451	2451	2451	$\nu_{sym} + \nu_{asym}$	$BaCO_3$	79,101
_	_	_	_	_	2340	ν_{asym}, CO_2^-	adsorbed to cation	81,83,84, 85,93,94,
2090 b,w	2090 b,w	2090b	2090b	2090b	2090b		$BaCO_3$ + water	_
1749 sp	1749 sp	1749 sp	1749 sp	1749 sp	1749 sp	$\nu_{sym} + \delta_{ip}$	$BaCO_3$	79,82,94,95, 96,99,100, 103,108
1625 b,w	1625 b,w	1629	1631	1626	1618	δ, OH bend	H_2O	99
1466	1469	1469	1463	1461	1456	ν_{asym}, CO_3^{2-}	lattice as $BaCO_3$	79,94,100, 101
1431	1426	1410	1433	1423	1429	ν_{asym}, CO_3^{2-}	surface	79,94,100,101
1375w	1375w	1375w	1375w	1375w	wb	ν_{asym}, C=O	surface CO_3^{2-}	79
1369w	1370w	1369	1369w	1370 vw	wb	ν_{sym}, CO_3^{2-}	unidentate ligand	94
1059w	1059w	1059w	1059w	1059w	1059	ν_{sym}, C=O	$BaCO_3$	79, 99,102
860vw	860	858vw	856vw	_	860	δ_{oop}	$BaCO_3$	79, 99,102
785	830	782	796	794	794	ν_1, TiO_6 octahedron	$BaTiO_3$ lattice mode	81,92,97

ν – stretching modes, δ – deformation modes, sym – symmetric, asym – antisymetric, ip – in-plane, oop – out-of-plane, b – broad, sp – sharp, w – weak, vw – very weak

the synthesis reactions for the hydrothermally derived nanopowders are only moderate and include the dehydration of OH, which is a slow process, leading to partial retention of H_2O and OH^- in the nanopowders.[66] Since the aliovalent OH^- groups replacing the O^{2-} ions have to be compensated by an equivalent number of cation vacancies to maintain electroneutrality, the presence of these framework modifying impurities enhances the lattice defects and the

Table 3.2. Relative Moisture Content of the Nanopowders

Moisture related bands		
Nanopowder	1630 cm^{-1} Band Area	3600 – 2700 cm^{-1} Band Area
A – solid state	1.57	32.19
B – solid state	1.24	31.57
C – hydrothermal	9.05	174.26
D – hydrothermal	10.43	192.27
E – hydrothermal	13.51	199.32
F – hydrothermal	7.32	118.29

Table 3.3. Relative Carbonate Content of the Nanopowders

Carbonate related bands		
Nanopowder	1749 cm^{-1} Band Area	2451 cm^{-1} Band Area
A – solid state	0.117	1.213
B – solid state	0.098	1.037
C – hydrothermal	0.041	0.629
D – hydrothermal	0.051	0.700
E – hydrothermal	0.034	0.438
F – hydrothermal	0.140	2.100

accompanying microstrains in the nanopowders such that the cubic phase remains metastable at room temperature.

Nanopowder F exhibits a unique set of lattice incorporated OH stretching modes: 3509 cm^{-1} (assigned as previously discussed), 3492 cm^{-1} and 3451 cm^{-1} (see Figure 3.6). These three bands could be interpreted as a distribution of the hydrogen population into localized positions throughout the mesoscopic surface. The intensities of these bands are more pronounced with Nanopowder F than the other nanopowders and may be explained since: 1) band intensity increases as particle size decreases,[67-68] 2) the bands are not obscured by the broad molecular water band since the concentration of molecular water in Nanopowder F is lower than that observed with nanopowders C – E, and 3) the greater surface area provides expanded regions for higher relative volumes of OH bonding.

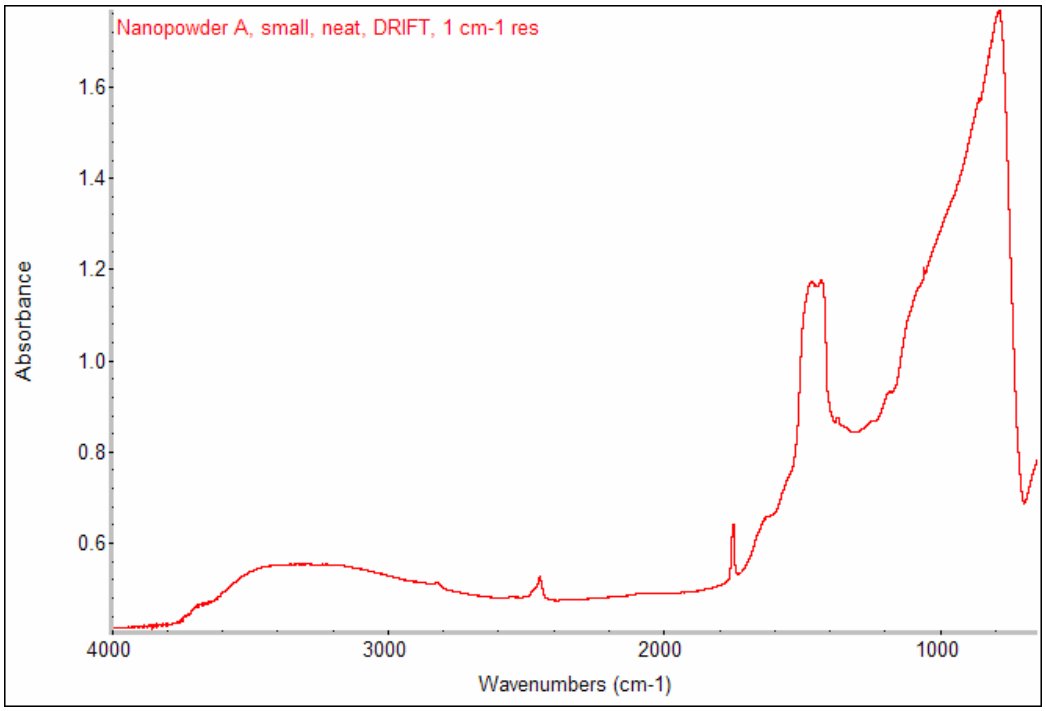

Figure 3.1. DRIFT spectrum of Nanopowder A at 1 cm^{-1} resolution.

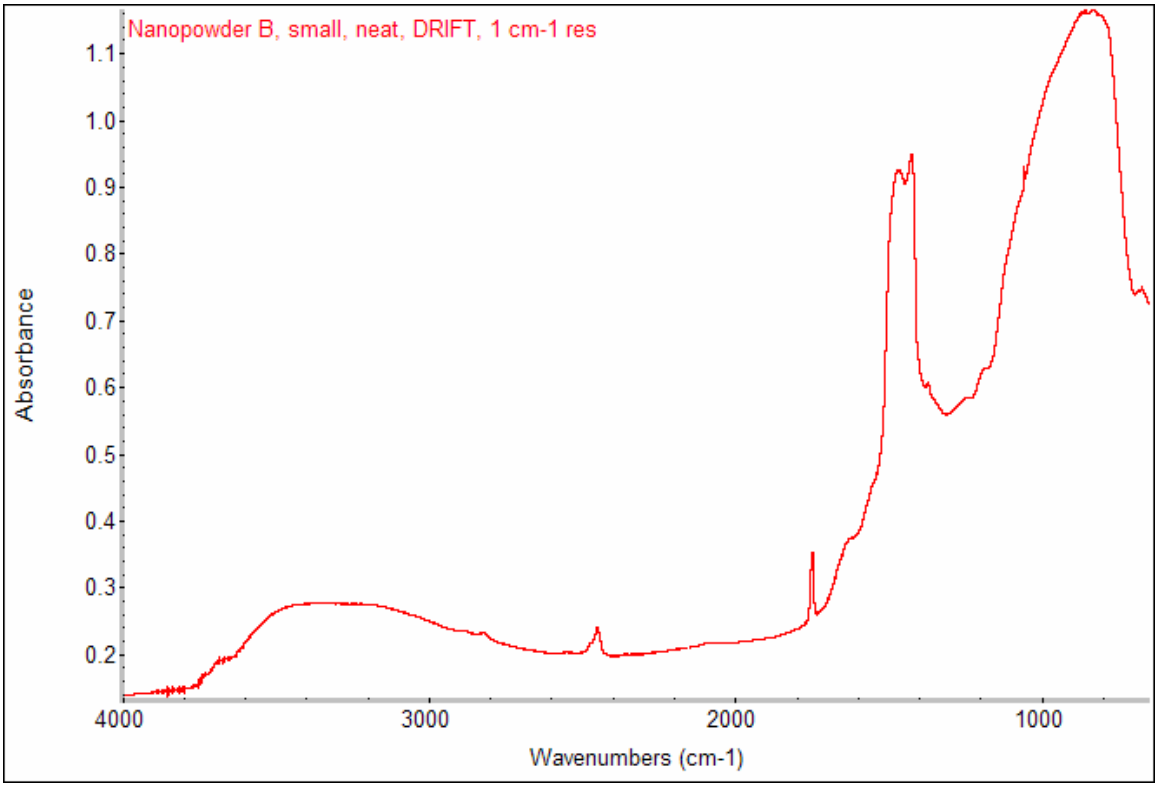

Figure 3.2. DRIFT spectrum of Nanopowder B at 1 cm^{-1} resolution.

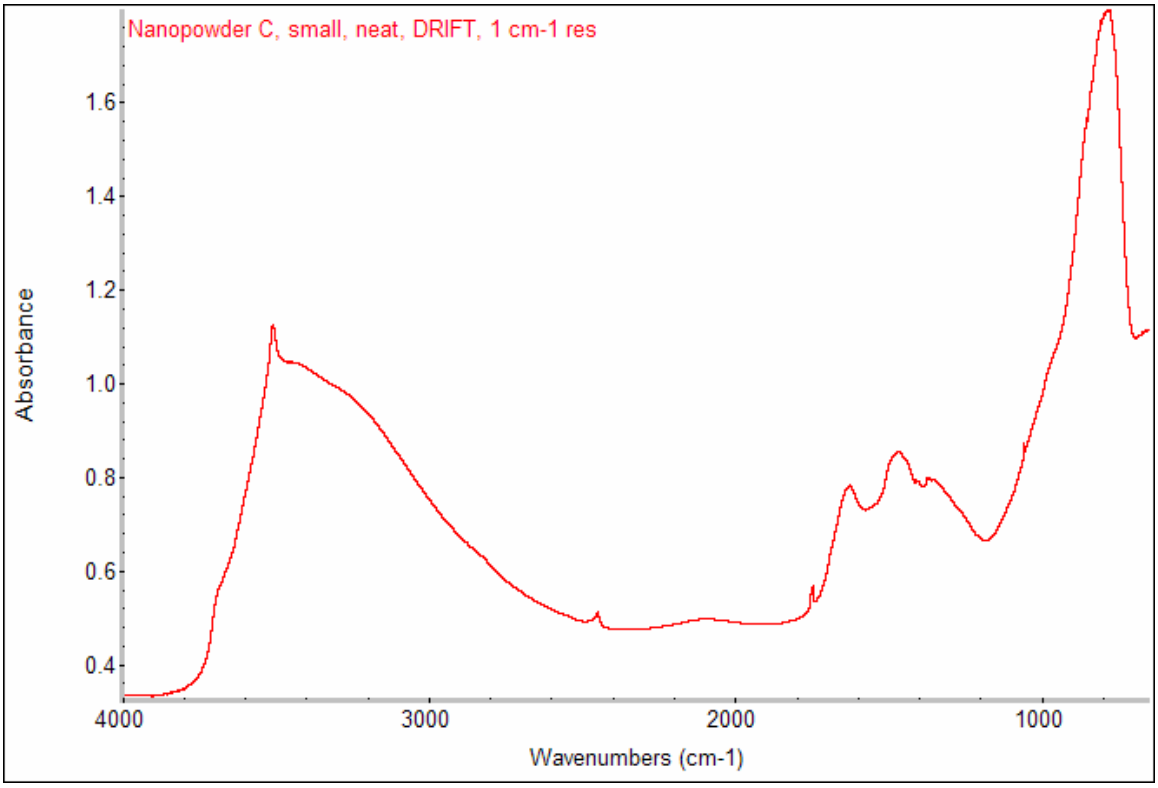

Figure 3.3. DRIFT spectrum of Nanopowder C at 1 cm^{-1} resolution.

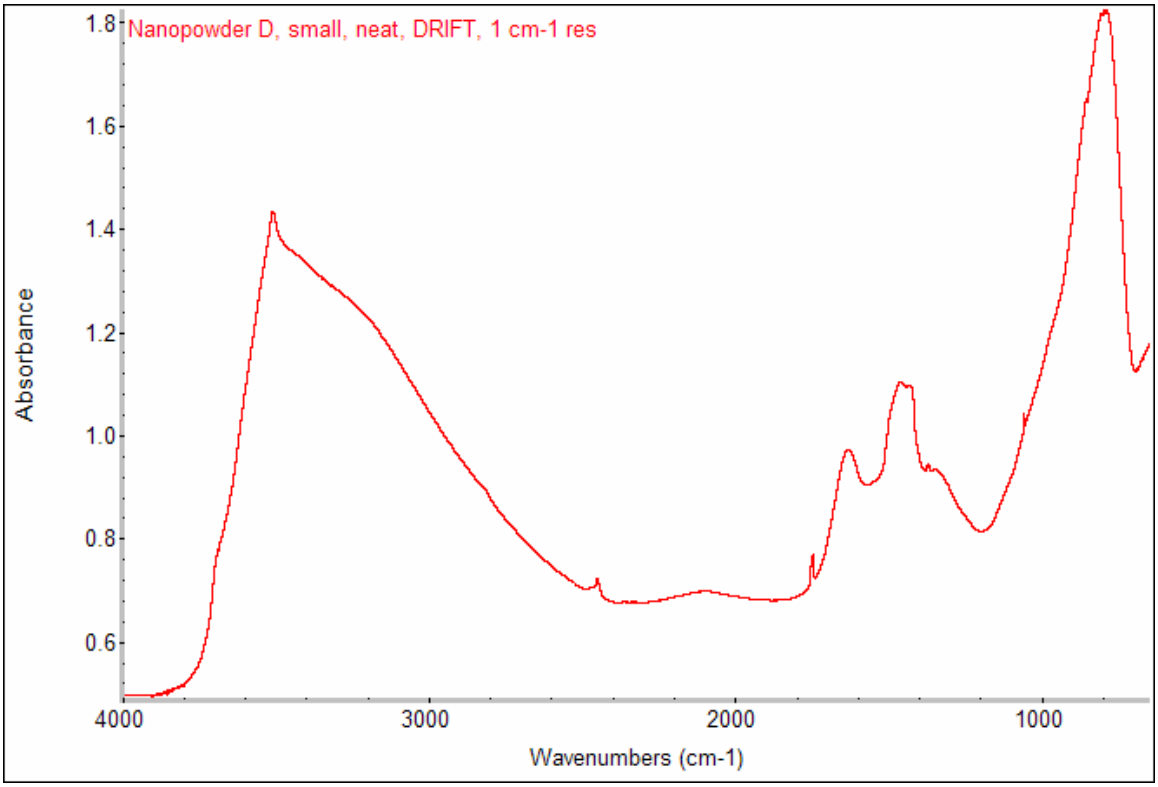

Figure 3.4. DRIFT spectrum of Nanopowder D at 1 cm^{-1} resolution.

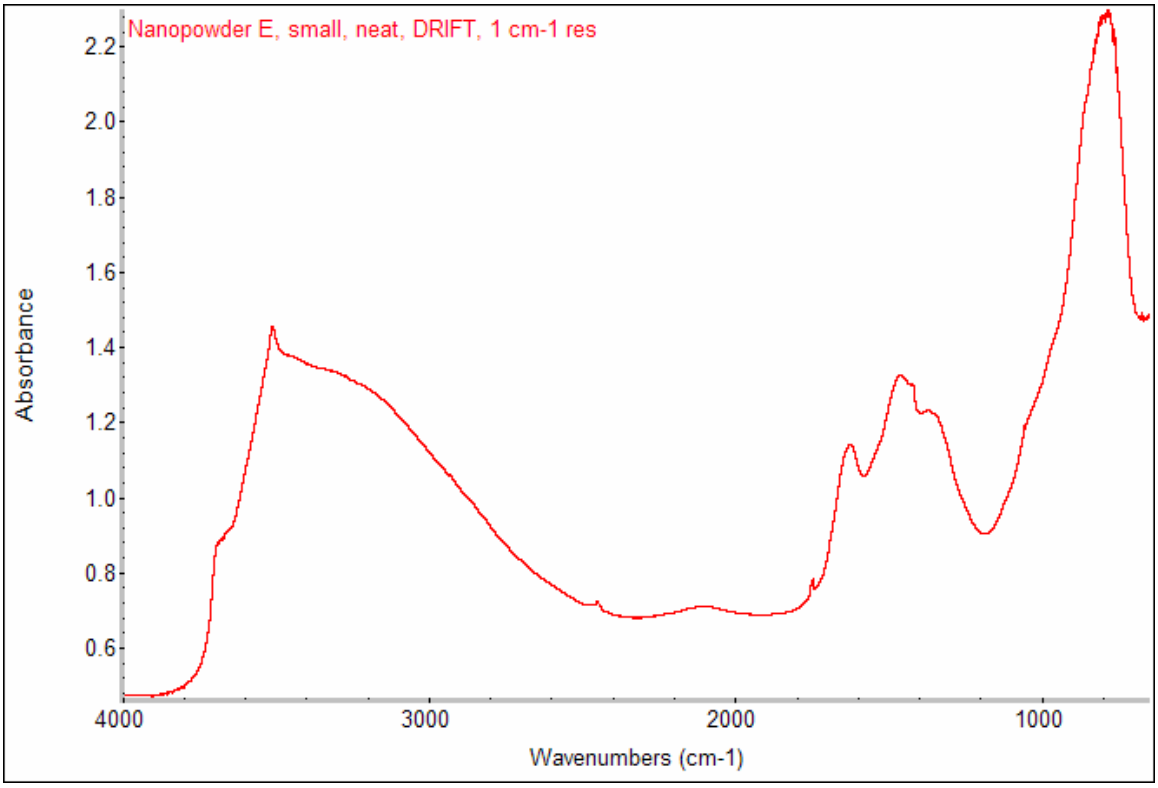

Figure 3.5. DRIFT spectrum of Nanopowder E at 1 cm^{-1} resolution.

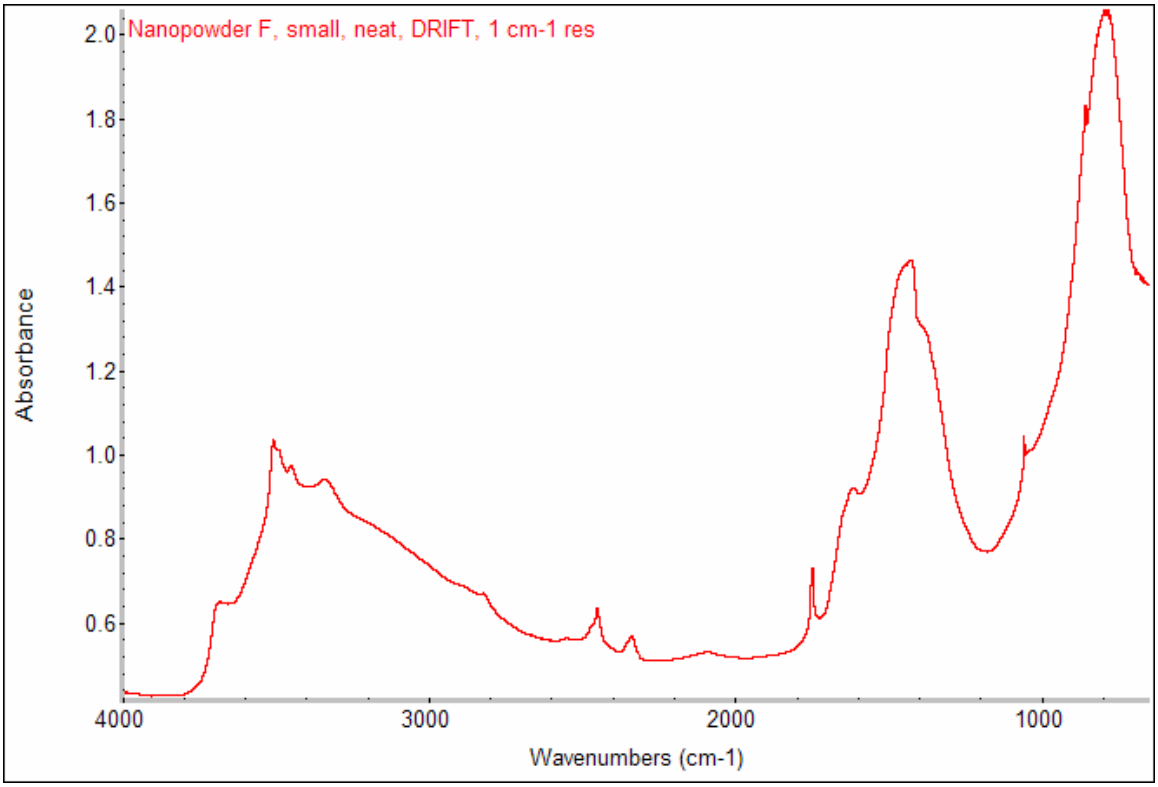

Figure 3.6. DRIFT spectrum of Nanopowder F at 1 cm^{-1} resolution.

Within the temperature range 273K and 403K, barium titanate has a distorted perovskite structure with noncentrosymmetric titanium ions. The distortion of the unit cell is due to the displacement of the Ti^{4+} and O^{2-} ions in different directions. The resulting Ti-O dimensions[69] (1.86 Å, 2.17 Å and 2.0 Å) present three possible H^+ host sites, Type I, Type II, and Type III, respectively (see Figure 3.7). It is well established that both titanium ion and oxygen octahedron move in opposite directions with the barium ion remaining in an undisturbed position.[69,70] This leads to a large change in the Ti-O bond lengths, and very little change in the Ba-O bond lengths.[71-73]

The structure of Nanopowder F had been identified with cubic symmetry. The assignments, therefore, for the bands observed in nanopowder F, 3509 cm^{-1}, 3492 cm^{-1} and 3451 cm^{-1}, can be associated with the barium titanate nanopowder having a mesoscopic surface. Kotomin et al. indicated that the relaxation of $BaTiO_3$ surfaces produced considerable dipole moments

perpendicular to the surface.[74] The mesoscopic surfaces produced charged surfaces for definitive absorption of OH groups. Each of the three assignments described herein can be related to the lattices of three distinctive surface states.

The band width observed with the three wavenumbers indicates moderately localized oscillators with moderate broadening due to disordered hydrogen bonding. This is similar to the case of OH stretching bands in $SrTiO_3$ in the work by Kapphan.[75]

The larger hydrothermally synthesized nanopowders, C through E, exhibited a single OH band at 3510 cm^{-1}. Allowing for the cubic symmetry derived from both XRD and electron diffraction, the single band was most probably related to a distribution of the hydrogen population into localized positions within the lattice in relation to the six degenerate bonds displayed by the Ti^{4+} ion in the oxygen octahedron. An in-depth discussion of these bands will follow in the high temperature DRIFT investigations.

The highly disordered state of the interfaces, from the previously proposed mesoscopic state for Nanopowder F, and the spectral evidence examined indicated interfaces with states similar to tetragonal symmetry. The high ratio of surface area to bulk volume provided large regions of varied bond states along the interfaces due to the large number of dangling-bond atoms. Additionally, these surfaces are composed of different atoms (i.e. Ba, Ti, and O atoms). The atoms of these surfaces and interfaces of the nanocrystallites, therefore, possessed various unsaturated coordination states. The nature of these regions assumed a pseudo-tetragonal symmetry or a relaxed state along the interfaces in an attempt at a reduction in their free surface energy. The position of the protonic impurities in the "as-received" nanopowder, therefore, produced oscillators similar to tetragonal symmetry. The bulk crystallites, however, had cubic symmetry.[76]

The 3340 cm^{-1} band, which is also observed only with Nanopowder F, can be attributed to an additional OH^- band due to lattice gas. When adsorbed surface layer mobility is enhanced repulsive forces increase giving rise to a weaker, symmetric band. The molecules try to maximize their intermolecular

distances forming a stable cluster right above the surface which is termed a lattice gas.[63] The presence of these regions of lattice gas resulted in the appearance of this additional band since there exists an equilibrium between the lattice gas regions and the adsorbed layer. The lattice gas was a consequence of the previously proposed mesoscopic state for Nanopowder F, a state which provided highly disordered interfacial regions.

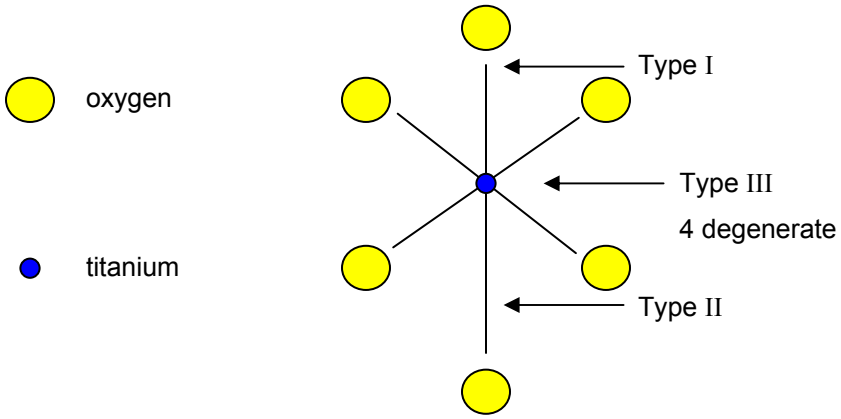

Figure 3.7. Titanium – oxygen bond H^+ host types in the TiO_6 octahedron of tetragonal barium titanate.

The spectra of all of the nanopowders, as examined with 1 cm^{-1} resolution DRIFT, exhibit residual barium carbonate. The common reaction for CO_2 with oxygen atoms at the surface is the acid/base interaction to give surface carbonate, CO_3^{2-}, through the following reaction:

$$CO_2 + O^{2-} \rightarrow CO_3^{2-} . \qquad (3.4)$$

On the BaO plane, this may proceed to yield bulk carbonate. The reaction is so favorable that complex oxides containing barium, such as barium titanate, may be covered with a layer of $BaCO_3$.[77] The presence of $BaCO_3$ in the spectra of the nanopowders supports the premise of a barium carbonate layer. Additionally, the presence of unreacted Ba^{2+} in solution from synthesis can react with

atmospheric CO_2 forming $BaCO_3$ and become mixed into the crystallites during posttreatment.[78]

A comparison of the spectra for the four hydrothermal nanopowders, in regard to the two carbonate bands at 1429 cm^{-1} and 1456 cm^{-1}, revealed the effect of crystallite size. As the crystallite size decreased there was a softening of the vibrations arising from the lattice carbonates. The vibrations arising from the surface carbonate thus increased with decreasing crystallite size. This spectral evidence, therefore, signified that as the crystallite size decreases the ratio of surface atoms to atoms in the bulk increases. The lattice related band at 1456 cm^{-1}, broadened and diminished as the surface related band, 1429 cm^{-1}, increased (see Figure 3.8). The values of the peak heights of the two bands for each of the four nanopowders numerically illustrate this finding (see Table 3.4). As the crystallite size decreased from Nanopowder C through Nanopowder F, the

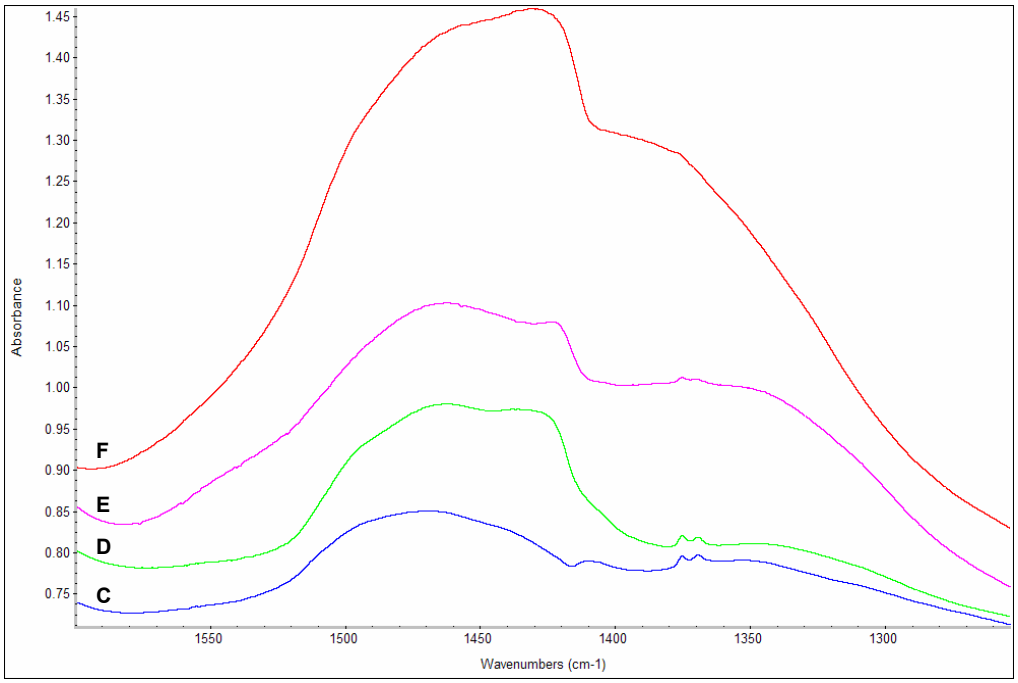

Figure 3.8. DRIFT spectrum of Nanopowders C, D, E, and F in the spectral region 1600 cm^{-1} to 1255 cm^{-1} at 1 cm^{-1} resolution; stacked common scale.

Table 3.4. Relative Heights of Lattice and Surface Carbonate Related Bands.

Nanopowder	1456 cm^{-1}	1429 cm^{-1}	ratio 1429/1456
C	0.757	0.768	1.0145
D	0.496	0.463	0.933
E	0.335	0.309	0.922
F	0.257	0.182	0.708

ratio of surface carbonate (1429 cm^{-1}) versus lattice carbonate (1456 cm^{-1}) increased.

The $BaCO_3$ related bands (860 cm^{-1}, 1059 cm^{-1}, 1429 cm^{-1}, 1749 and 2451 cm^{-1}) are well documented in the literature as noted in Table 3.I. The two bands at 2887 cm^{-1} and 2823 cm^{-1}, however, have been previously assigned in the literature to hydrocarbon related groups.[79] A careful comparison of these bands, as observed with all of the nanopowders, with a spectrum of barium carbonate, as shown in Figure 3.9, show that these two bands are carbonate related bands. The matching of the 2451 cm^{-1} and 1749 cm^{-1} were included to corroborate this finding. In addition, Figure 3.10 exhibits the subtraction result of the Nanopowder F spectrum minus a barium carbonate spectrum with excellent alignment and intensities of these bands.

In addition, the broad weak band observed with all nanopowders at 2090 cm^{-1} was also a barium carbonate/water related band. The comparison with the barium carbonate spectrum was also seen in Figure 3.9 and 3.10. A spectrum of Nanopowder A with the addition of molecular water corroborates the assertion of the affect of molecular water on the bands of interest (see Figure 3.11) and exhibited the broad adsorption band around the 2090 cm^{-1} carbonate band.

The carbonate bands were barely distinguishable within the intensities of the broad molecular water bands. The intensities of the three carbonate related bands was, therefore, lower than that seen in the $BaCO_3$ spectrum due to incorporation within the broad molecular water bands in the two spectral regions

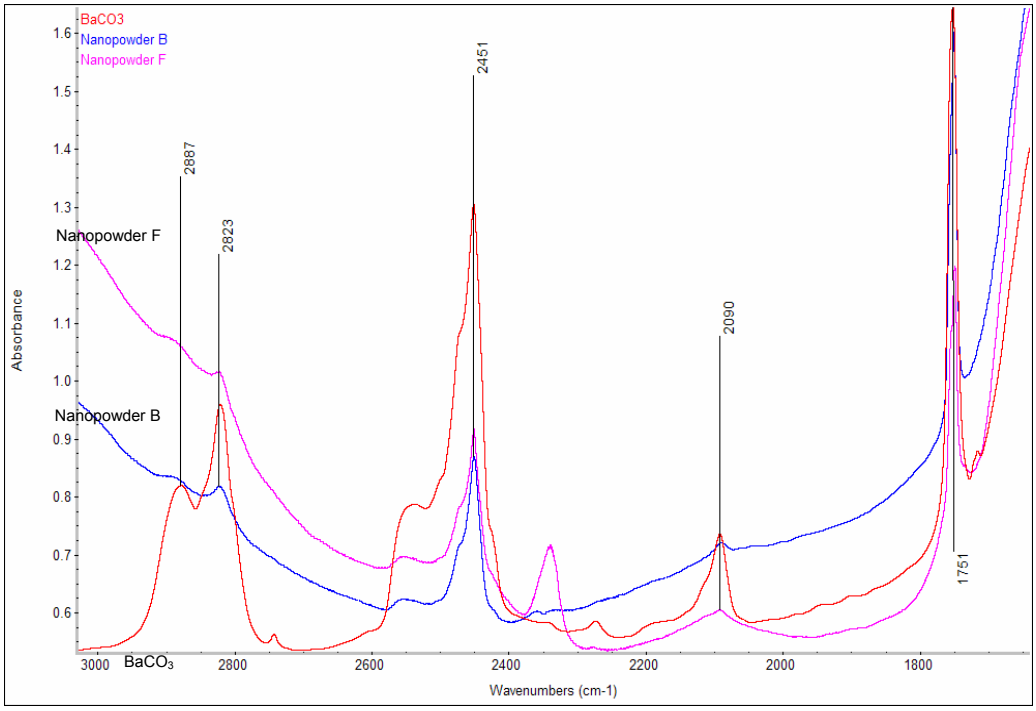

Figure 3.9. Spectra in the region 3030 cm^{-1} to 1640 cm^{-1} of the barium carbonate related bands in the barium titanate nanopowders B and F; common scale.

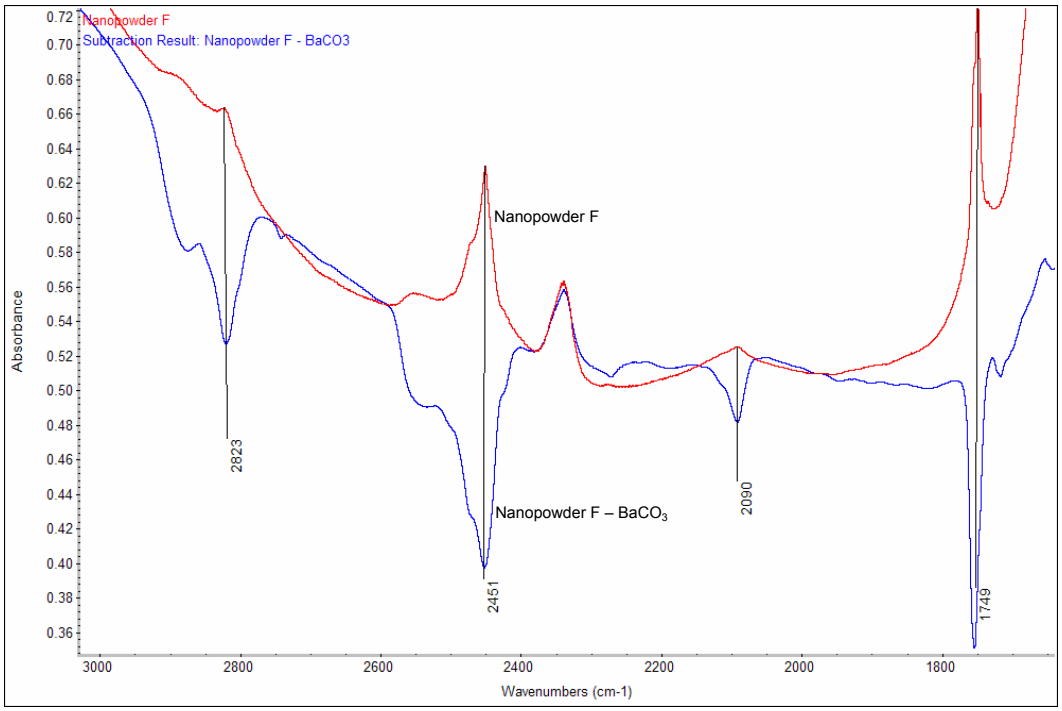

Figure 3.10. Subtraction spectra in the region 3030 cm^{-1} to 1640 cm^{-1} of the carbonate related bands in barium carbonate from Nanopowder F.

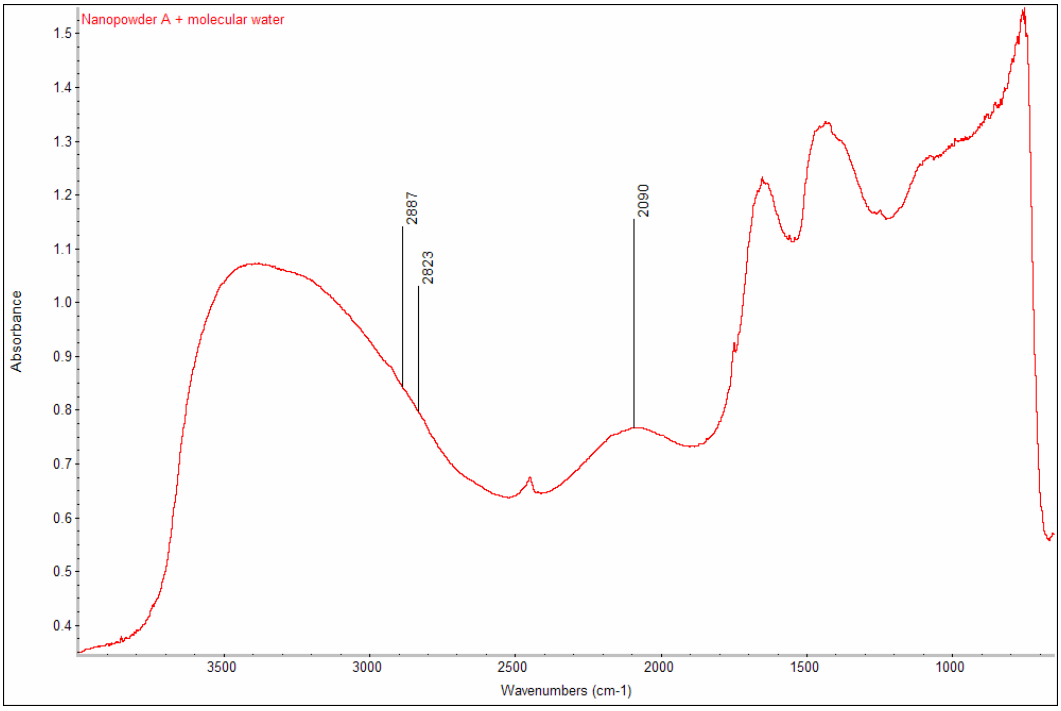

Figure 3.11. Spectrum in the region 4000 cm^{-1} to 400 cm^{-1} of Nanopowder A with additional molecular water.

and further due to the concentration of barium carbonate present in each of the nanopowders. Barium carbonate existed, therefore, as a molecular constituent in all of the nanopowders examined.

Nanopowder F exhibited a band at 2340 cm^{-1} that was not observed with the other nanopowders. This band was assigned to the attachment of the linear CO_2 molecule to B-cations (see Figures 3.12 and 3.13). Occasionally the CO_2 molecule may accept a single electron and form the CO_2^- species coordinated to metal cations near an oxygen vacancy through the reaction:

$$CO_2 + e^- \rightarrow CO_2^- \qquad (3.5)$$

Freund suggested that spectral evidence supports a bent CO_2^- from the gain of the electron, yielding a 45º deviation from the free molecule linearity which results in a 135º angle.[80-81] This bending was described as being accompanied by an elongation of the C-O bond length, nearest the cation attachment, with respect to the free molecule which leads to a drastic lowering of the asymmetric

C-O stretching mode at 2350 cm^{-1} to 1867 cm^{-1}.[63,82] This drastic red-shift effect is not observed in the spectrum of Nanopowder F.

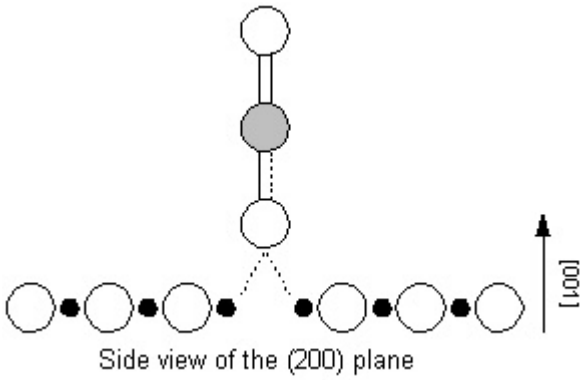

Figure 3.12. Linear carbon dioxide molecule bidentate attachment to surface B-cations at an oxygen vacancy site.

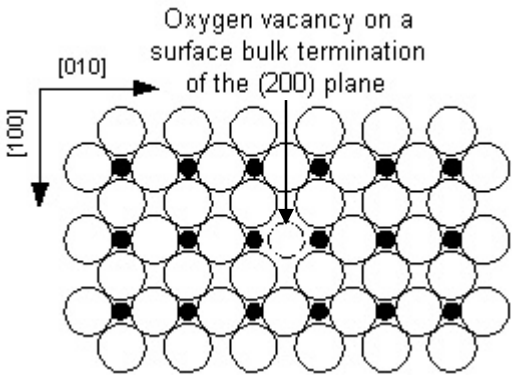

Figure 3.13. Oxygen vacancy site on the bulk termination surface of the (200) plane; bidentate attachment with the two opposite titanium atoms at vacancy site.

More recently, evidence of CO_2 adsorption in its linear form has been shown. Souter and Andrews[83] have shown spectral evidence of linear CO_2 adsorption on Group 6 metals with isotropic substituted oxygen forms of CO_2.

Their observed spectra exhibited bands suggesting the presence of two inequivalent oxygen atoms both of which come from the same CO_2 molecule. Adsorption with uranium complex also resulted in carbon dioxide remaining in a linear state and being spectrally observed at 2347.6 cm^{-1}.[84-85] The angle of attachment is stipulated at 171.1º with the carbon dioxide molecule angle being 178º, very close to linear.

Jeung calculated energy states for Cr- and Ti-(CO_2) complexes, examining four coordination types of the 135° bent non-linear molecule.[86-87] Type III (the bent molecule end-on mode of adsorption) had the lowest calculated energy state. Gibson[88] suggested a linear attachment since the bending of the linear CO_2 molecule requires an energy adsorption. A lower energy state was calculated for the end-on attachment and was more stable for the Cr-complex. This work supports the earlier work of Souter and Andrews.

The titanium atom coordinates with six oxygen atoms to form a saturated six-coordination octahedron in the bulk phase. On the surface of the crystallites, if the titanium atom is situated at the corner, it coordinates with three oxygen atoms; or if situated at the edge, it coordinates with four oxygen atoms; if the titanium atom is situated on the surface, it coordinates with five oxygen atoms (see Figure 3.14). All of these sites are unsaturated coordination states. Since the surface component is different from the bulk phase, the incomplete molecules situated at the surface or interfaces of the crystallites will possess different unsaturated coordination atoms and some properties of the crystallite will be influenced by all of the incomplete molecules that are present. The effect allows the adsorption of the linear CO_2 molecule to these unsaturated titanium sites.

The linear molecule was more strongly bound to the unsaturated defect sites that arose from the mesoscopic surface states.[89] This stronger bond state was observed with the higher vibrational wavenumber. The stretching mode of gaseous CO_2, 2350 cm^{-1}, is slightly perturbed to 2340 cm^{-1} due to bidentate ligand attachment.[77,90-91] Nakamoto indicated that attachment would occur only when surfaces were atomistically rough or a high defect chemistry existed.[92] When a species is adsorbed to a surface a new geometry is established and new

vibrational selection rules are created. A gas molecule attached to a surface undergoes transition from gas state to adsorbed state on a solid surface. The previously free moving gas molecule, after attachment at one or more ends, has a restricted motion or loss of a rotational degree of freedom. The adsorption of carbon dioxide will be further explored in a following section.

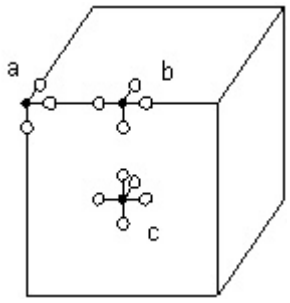

Figure 3.14. Model for the coordination of the titanium atom when situated at (a) the corner, (b) the edge and (c) the surface.

3.1.4 Summary

The surfaces of the nanopowders exhibited spectral evidence of the presence of these adsorbates: carbon dioxide, carbonate ion, barium carbonate, molecular water and surface and lattice hydroxyl groups. The vibrational wavenumbers of these adsorbates has been assigned and tabulated. Barium carbonate existed as a molecular constituent in all of the nanopowders examined, which may be considered a formation from the common reaction of carbon dioxide with oxygen on the BaO surface to produce surface carbonate, CO_3^{2-}. Formation of barium carbonate then proceeds to yield a layer of $BaCO_3$. This surface layer will be investigated further in Section 5, X-ray Photoelectron Spectroscopic Analysis.

Nanopowder F exhibited cubic symmetry through XRD and electron diffraction data. Spectral evidence thus existed for a highly disordered state of the surfaces and interfaces. The spectral evidence indicated interfaces with

states associated with the barium titanate nanopowder having a mesoscopic surface.

As discussed previously in Section 2.1, equilibrium existed between the nanopowder surface and the concentration of adsorbed water for each of the nanopowders, which were temperature, specific surface area and adsorbate species specific. The nanopowder surfaces exposed a regular pattern of their constituent ions. The crystallites possessed not only tremendous surface area, but also had a large number of surface atoms which lacked periodicity in one dimension and changed electronic states at the surface. The surfaces, therefore, were potentially highly dynamic. The lack of nearest neighbors at the surface left the chemical bonds of the surface atoms free and available for chemical reactivity.

Spectral evidence existed for the hydroxylation of surface oxygen atoms on crystallographic planes that contain oxide layers. The oxygen atoms of oxide surfaces that have been hydroxylated adsorb and strongly retain several layers of bound water, as was observed spectrally with all of the nanopowders. This adsorption phenomenon is the precursor to the availability of the ensuing mobile lattice proton and the lattice hydroxyl defect.

The unintentional incorporation of hydrogen, among other adsorbed contaminants, during device processing will gain more attention as critical dimensions are scaled down to the nanometer regimes. These factors mean that a small amount of contaminant may have a relatively larger effect on miniaturized devices than with the current larger devices.

3.2 High Temperature DRIFT

3.2.1 Introduction

The exposure of the nanopowder surfaces to ambient atmosphere causes a hydrolysis reaction with humidity. Hydroxyl groups are formed which in turn form hydrogen bonds with surrounding molecular water. The surface, therefore, becomes covered with several layers of hydrogen bonded water. In addition, other contaminants can react with the surfaces such as carbon dioxide leading to the carbonate ion (CO_3^{2-}) and formation of $BaCO_3$.

The cubic phase of barium titanate (the high temperature thermodynamically stable form) was observed at room temperature when the crystallite size was smaller than a critical size. Different values for this critical size of the crystallite, for the transition from cubic to tetragonal phase, have been suggested and discussed previously. This critical size varied for different preparation methods.

Uchino et al. found that the cubic phase was stable with crystallites smaller than 90 nm synthesized through the hydrothermal method and suggested that the surface tension of the small particles and the particle size affected the soft mode phonon with a resultant cubic phase.[21]

The discussion on the room temperature crystallite structure of nanocrystalline barium titanate included not only the effect of particle size but also residual strain as discussed previously. Begg et al. suggested two possible mechanisms to explain the anomalous cubic room temperature phase: 1) the strains imposed by the presence of hydroxyl ion content, and 2) the role of surface effects.[22] Begg found difficulty in accepting how the charge compensating cation vacancies could be retained once the hydroxyl ions had been removed from the lattice. Begg believed therefore that the hydroxyl ion/cation vacancy model of imposed strain did not adequately explain the stabilization of the cubic phase. The HT-FT-IR studies that follow indicate that readsorption of lattice hydroxyl ions occurs with <6 ppm available moisture in the

gas flows utilized in this study and, therefore, hydroxyl related strain may still explain the stabilization of the cubic phase.

The role of surface tension (hydrostatic pressure) was suggested to be sufficient to lower the Curie temperature of nanocrystallites to below room temperature and thereby stabilize the cubic phase. This possibility was suggested by Uchino; a pressure of 2 GPa was required in barium titanate crystallites to decrease the Curie temperature to room temperature using a critical particle size of 100 nm.[21] The T_c of small cubic crystallites has not been measured to validate this hypothesis, although Begg suggests that a combination of surface energy and particle size is the plausible explanation for the anomalous room temperature cubic phase.

Takeuchi et al. discussed the presence of both cubic and tetragonal phases coexisting in crystallites as shown by XRD. Two explanations were suggested: that a core-shell model existed with crystallites having a tetragonal core with a 5 nm thick cubic shell; that the two phases coexisted. The content of $BaCO_3$ exhibited by the nanopowders herein studied, and as expressed by others as being a surface phenomenon as well as being confirmed spectrally, would tend to refute the core shell hypothesis. Additionally, no evidence of a core-shell structure was observed during the TEM study.

The presence of hydroxyl ions affecting the structure of barium titanate nanocrystallites is still debated.[21,40,105-07] The affinity of the water molecule to dissociate at the surface of barium titanate was apparently underestimated. As observed in the HT-FT-IR spectra of all of the non-solid state nanopowders, and to a lesser degree with the solid state nanopowders, the readsorption of molecular water and hydroxyl ions readily occurred under the flowing ultra high purity nitrogen gas used in this study. The effects of the residual impurity constituents from synthesis (molecular water, hydroxyl ions, protons, molecular barium carbonate and the carboxyl ion) need to be characterized allowing clarification of these issues.

To identify the characteristics of these adsorbing species, the surfaces of the nanopowders must first be ‘cleaned’ of the contaminants. This was partially

achieved by a thermal treatment or activation process for removal. Some of the contaminating species were removed, but it was possible for some to remain, depending upon the activation temperature. Data from the literature indicates that the uppermost layers of molecular water were eliminated at low temperatures. The hydrogen bonded species, e.g. lattice hydroxyls, were removed by moderate temperatures, ~725K. This higher temperature removal of water incorporated in the lattice was typical of hydrothermally synthesized powders.[25] Depending on the strength of the interactions, other contaminants such as the carbonates were released at a series of higher temperatures. The usual activation temperatures of carbonate removal from barium titanate powders were 873K, 1150K and 1525K.[108]

Upon removal of the contaminating species, the surface sites became available for selected probe molecules. The surfaces were highly reactive after the contaminant removal. The exposed planes of atoms at the surfaces encountered a loss of periodicity which resulted in changes in electronic states at the surface. The lack of nearest neighbors of the surface atoms left chemical bonds free and available for chemical reactivity. Therefore, when any probe molecule came in contact with the 'cleaned' surface, an adsorption or possible chemical reaction occurred to minimize the surface energy. Surfaces adsorbed atomic and molecular species to minimize the energy at the interface. This activation, thermal desorption and probe molecule additions were the essential steps in the vibrational characterization of adsorbates present in the nanopowders.

The nature of H_2O, OH groups and carbonate groups that may be incorporated in the lattice of the barium titanate nanopowders as residual components from the powder synthesis was investigated. The removal of the molecular water, surface and lattice hydroxyls, and carbonates was investigated in the preliminary high temperature DRIFT (HT-DRIFT) study, Section 3.2.2. The readsorption of H_2O and OH groups was investigated in the H_2O study, Section 3.2.3. The exchange reaction between the incorporated OH groups and OD groups during treatment with deuterium oxide (D_2O) was investigated; Section

3.2.4, the D_2O study. The readsorption of carbonate groups was investigated in the CO_2 study, Section 3.2.5.

3.2.2 Preliminary High Temperature Study

3.2.2.1 Experimental Procedure

To examine these processes *in situ* HT-DRIFT spectra were obtained of all nanopowders up to 1173K. A Spectra-Tech Smart Collector (Model 0031-999, Thermo Spectra-Tech, Stanford, CT) with an optional environmental cell (Model 0030-005, Thermo Spectra-Tech, Stanford, CT) was used in conjunction with the Nicolet Nexus 670 FT-IR to make the *in situ* high temperature measurements. Figure 3.16A illustrates the positioning of the entire assembly as mounted in the FT-IR. The temperature controller and cooling pump is seen to the right of the FT-IR. Figure 3.16B illustrates the environmental cell with the gas line connections that allow selective atmosphere control during analysis. Figure 3.16C illustrates the environmental cell, open, with sample in place prior to analysis.

The nanopowders were examined through the temperature range room temperature to 1173K, neat (i.e. as-received so as not to disturb the surface layers and to improve the surface sensitivity of the technique). The heating chamber of the environmental cell has dimensions of 5 mm diameter by 3 mm depth and accommodated ~50 milligrams of the nanopowders. A background spectrum was taken using the polished aluminum coated mirror in the standard Smart Collector sample holder, similar to the previous DRIFT technique, and auto subtracted from the final sample spectrum by the Omnic 6.0 software package. Spectra were obtained at a resolution of 4 cm^{-1} with 500 cumulative scans to form the final spectrum between 650 cm^{-1} and 4000 cm^{-1}. A continuous flow of ultra high purity (UHP) nitrogen gas was provided at a rate of 150 ml/minute. A heating rate of 10K/minute was used.

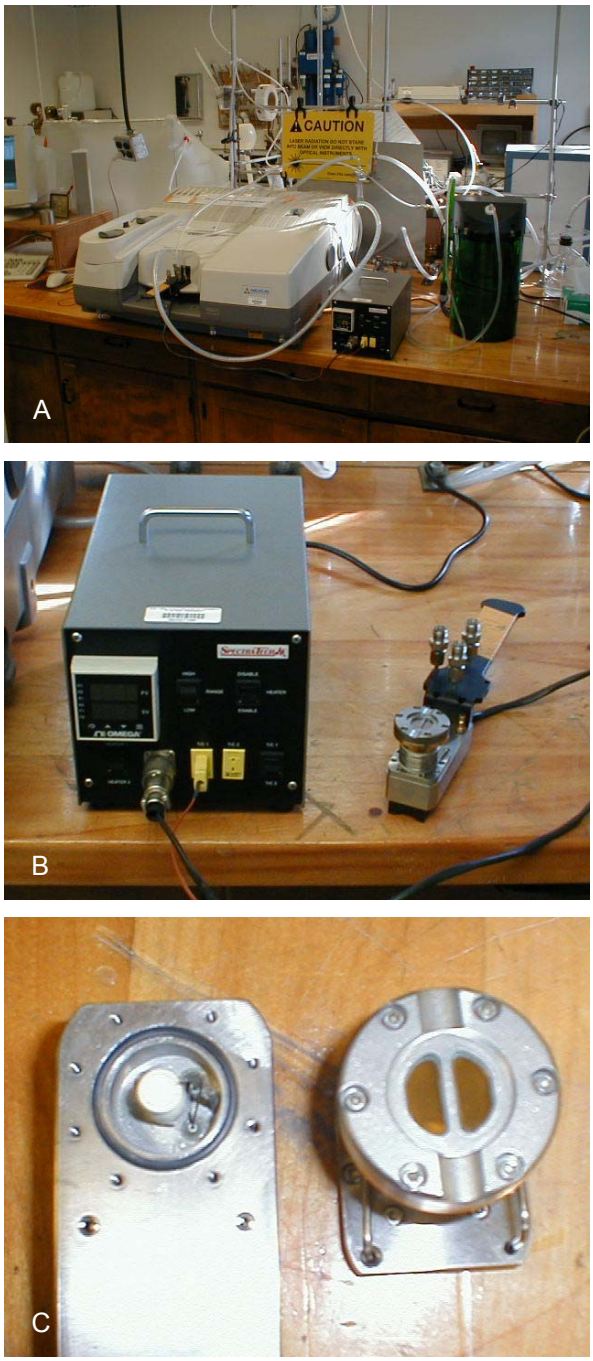

Figure 3.15. Photographs of A, the environmental cell in position in the Smart Collector and mounted in the Nexus 670; B, the environmental cell and temperature controller; and C, the environmental cell, open, with sample in place.

Spectra for each nanopowder were obtained at room temperature and at 100K increments over the range 373K to 1173K, the maximum temperature limit of the environmental cell. A final spectrum was obtained after the sample was cooled to room temperature. The time to cool a sample to 310K was approximately 5 minutes or 170K/minute.

3.2.2.2 Results and Discussion

Figures 3.16 through 3.21 display the *in situ* high temperature spectra of Nanopowders A through F respectively. All of the nanopowders exhibited a reduction of moisture and carbonate levels through the temperature range studied. Two additional bands were observed in the spectra of each of the nanopowders at 2340 cm^{-1} and 2360 cm^{-1} which can be attributed to the presence of CO_2 gas from the desorption of lattice and surface carbonate species.[109] The presence of CO_2 gas was first observed at 573K, 300 Kelvin lower than previously noted in the literature. All of the nanopowders exhibited evidence of readsorption of moisture upon cooling. The intensity of the broad 2700 - 3600 cm^{-1} band and the 1640 cm^{-1} band, the OH related wavenumbers and molecular H_2O bending wavenumber, being greater upon cooling than the intensity of these bands observed at 673K during the heat treatments. The spectral evidence clearly showed the affinity of the nanopowder surfaces for the readsorption of moisture. This readsorption was from ultra high purity (UHP) nitrogen gas with a stated purity of 3ppm moisture content.

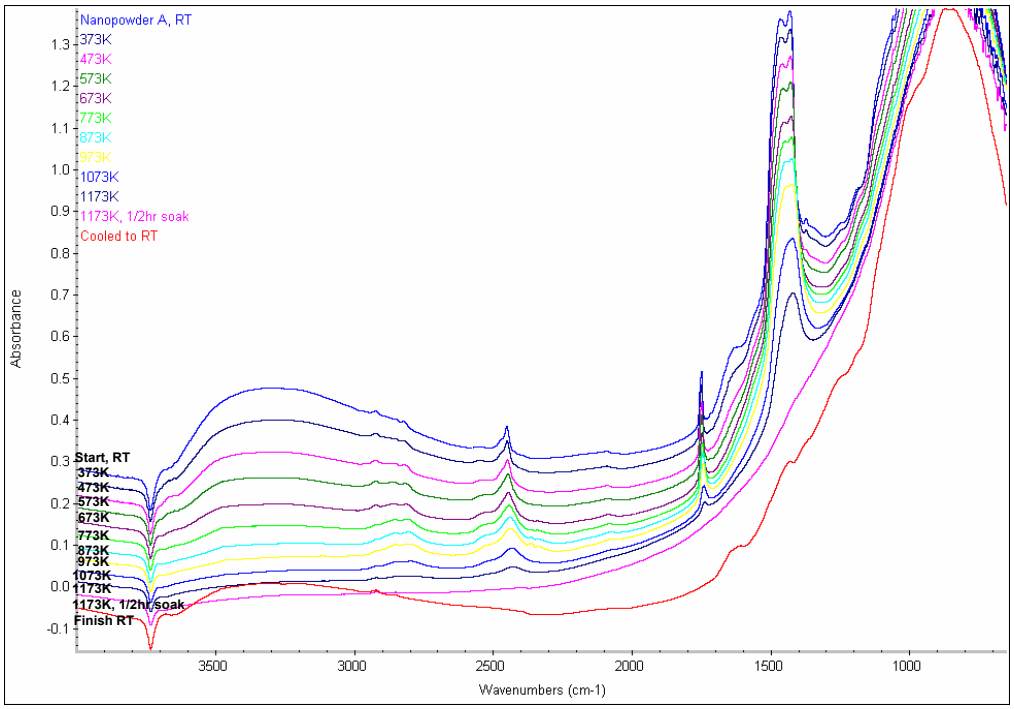

Figure 3.16. *In situ* HT-DRIFT spectra of Nanopowder A through the temperature range 298K to 1173K, and after cooling to 298K; stacked common scale.

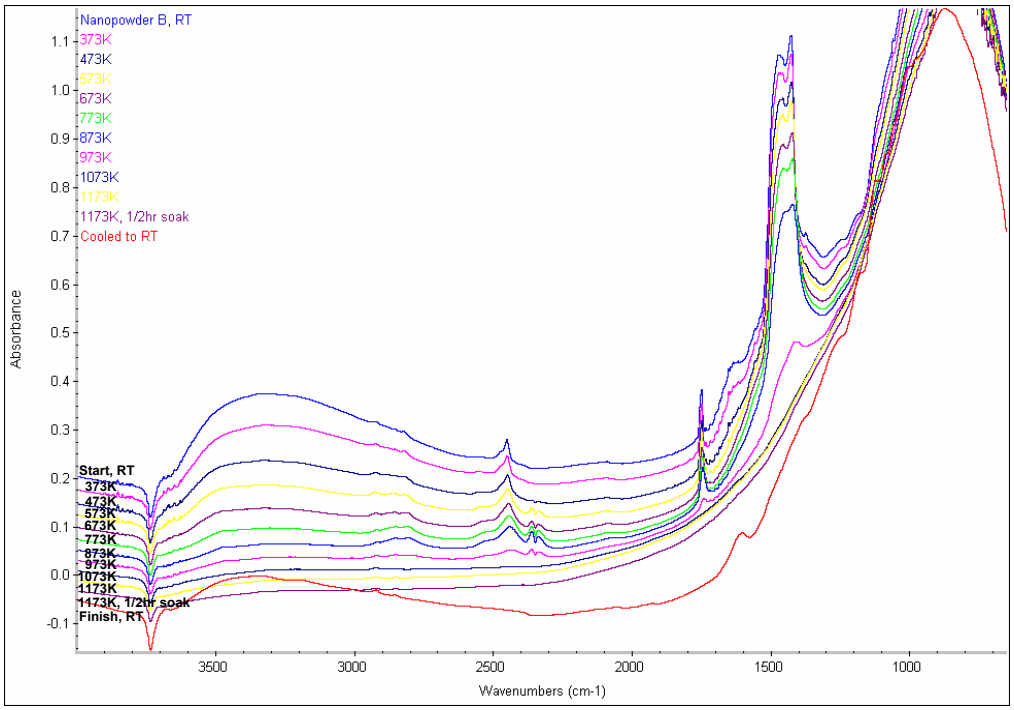

Figure 3.17. *In situ* HT-DRIFT spectra of Nanopowder B through the temperature range 298K to 1173K, and after cooling to 298K; stacked common scale.

The solid state nanopowders, A and B, contained a higher concentration of moisture after heat treatment than was observed in the room temperature spectra. The intensity of the broad 2700 - 3600 cm^{-1} band and the 1640 cm^{-1} band was greater after the heat treatment than prior to the heat treatment. The majority of the carbonate present in the two nanopowders was removed after a half-hour at 1173K. The removal of the carbonate in addition to moisture loss during the heat treatment provided open sites for the readsorption of moisture during the cooling phase.

The hydrothermally synthesized nanopowders (C through E) also exhibited spectral evidence of moisture readsorption during the cooling phase. The vibrational frequency related to the bend deformation of H_2O at 1630 cm^{-1} had dissipated by 873K with each of the nanopowders. The band was observed in the cooled spectra of each of the nanopowders signifying the readsorption of molecular moisture to the surfaces of the nanopowders.

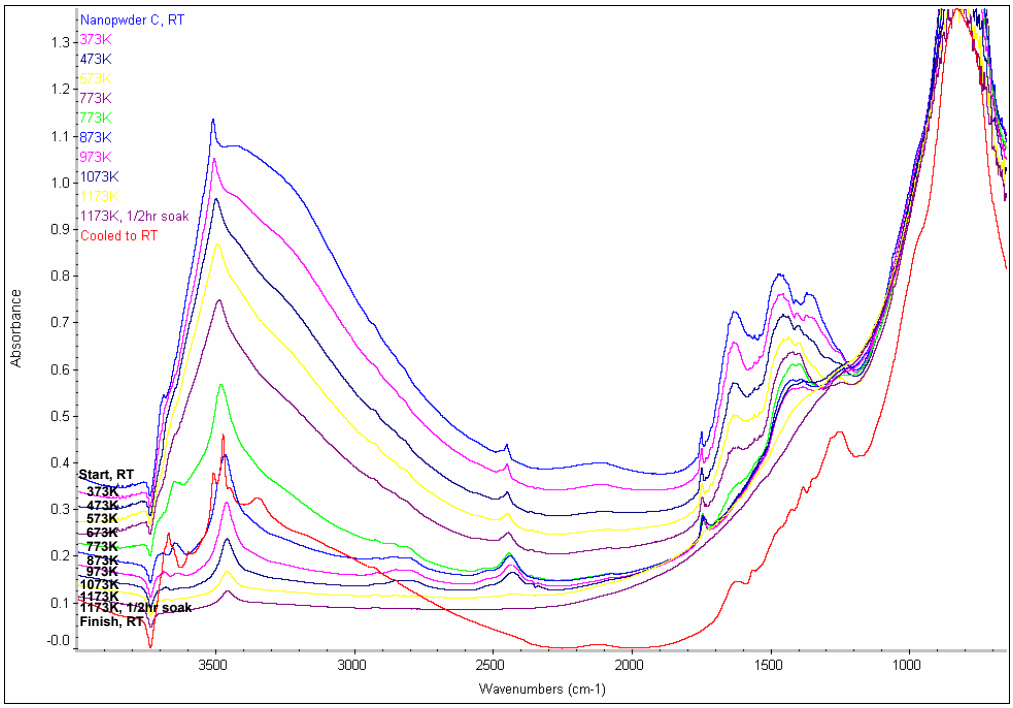

Figure 3.18. *In situ* HT-DRIFT spectra of Nanopowder C through the temperature range 298K to 1173K, and after cooling to 298K; stacked common scale.

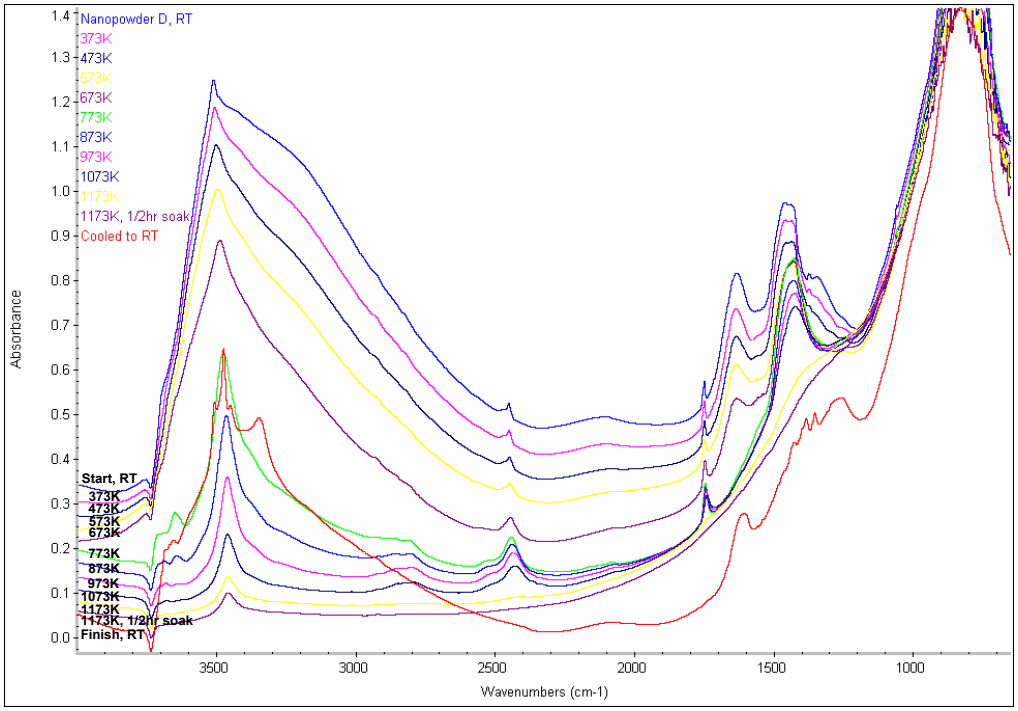

Figure 3.19. *In situ* HT-DRIFT spectra of Nanopowder D through the temperature range 298K to 1173K, and after cooling to 298K; stacked common scale.

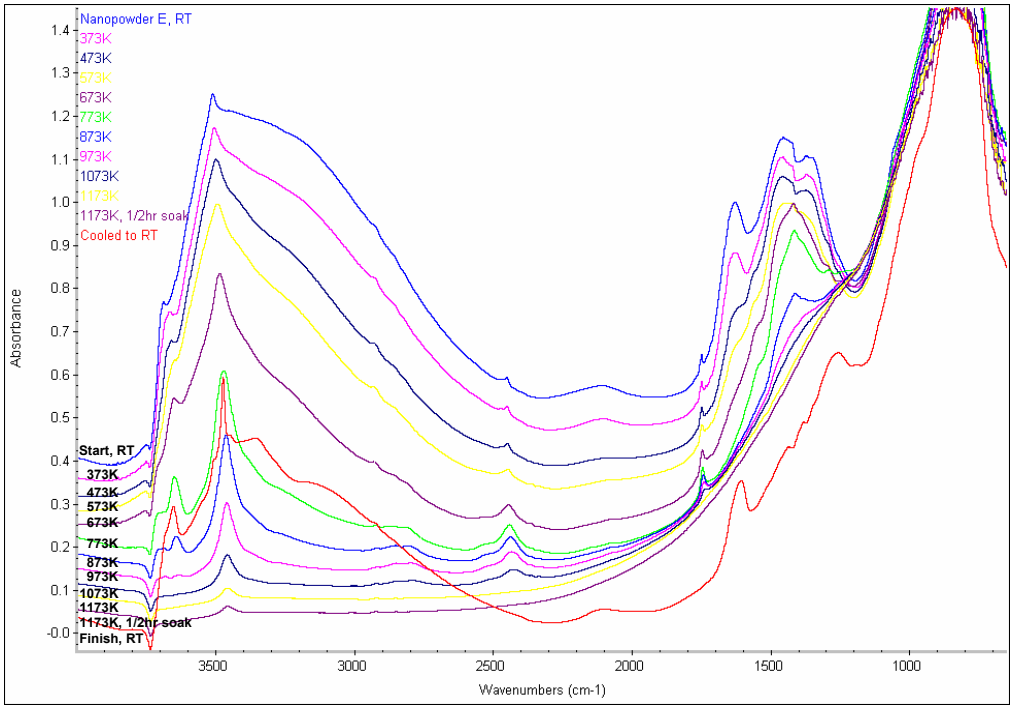

Figure 3.20. *In situ* HT-DRIFT spectra of Nanopowder E through the temperature range 298K to 1173K, and after cooling to 298K; stacked common scale.

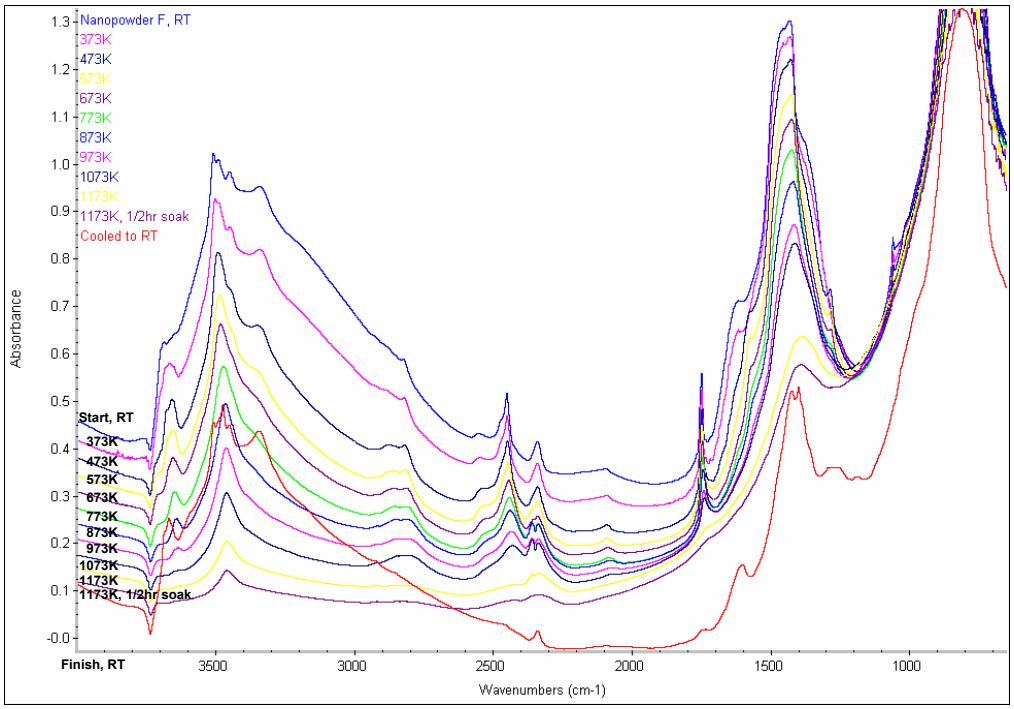

Figure 3.21. *In situ* HT-DRIFT spectra of Nanopowder F through the temperature range 298K to 1173K, and after cooling to 298K; stacked common scale.

Nanopowders C through E readsorbed a large amount of moisture upon cooling. The concentration was close to that observed with the 673K spectrum of the heating phase of each of the nanopowders. The carbonate levels of the three nanopowders had been reduced, only minor intensities of carbonate related bands were observed in the cooled spectra of each of the nanopowders.

Nanopowder F exhibited a large concentration of both carbonate species and moisture in the room temperature spectrum. After a half-hour at 1173K, the level of moisture had diminished in similar fashion to Nanopowders C through E. Upon cooling, the concentration of moisture was similar to that observed in the 473K spectrum of the heating phase. This moisture level was a large percentage of that contained prior to analysis, which indicated a preferential adsorption of moisture to the surfaces of the nanopowder.

The carbonate, however, was still observed in the 1173K spectrum after a half-hour soak. The 1429 cm^{-1} band of the lattice carbonate species remained present with nanopowder F, whereas this band was not observed at 1173K with

all other nanopowders. When cooled to room temperature, considerable remaining carbonate was observed in the final spectrum. The most intense barium carbonate band was observed at 1749 cm^{-1}. This band, observed with all of the room temperature spectra of the nanopowders, remained in the final cooled spectrum of Nanopowder F after heat treatment, while being absent from the cooled spectra of all other nanopowders.

The amount of residual carbonate and moisture observed with the cooled spectrum of Nanopowder F in regard to the other nanopowders can be attributed to the Nanopowder F's larger surface area and the state of this surface area. The crystallites of Nanopowder F, which had the smallest average crystallite size of the nanopowders examined, resided in the form of incomplete molecules with various unsaturated coordinations, or broken bonds. The nanocrystalline powder may therefore have resided in a transition state of mesomolecules/molecules along the interfaces to a fully crystalline material within the bulk, or a mesoscopic state.[110-13] Nanopowder F, therefore, consisted of a saturated coordination bulk phase with mesoscopic surfaces of unsaturated coordinations.

This mesoscopic state of perovskite type compounds was revealed in IR and Raman spectra[112-14] displaying molecular vibrational characteristics with band vibrations assigned to various incomplete mesomolecules. The studies examined the spectral changes over a range of nanoparticle sizes and observed new bands, most noticeably in the far IR, when the nanoparticles sizes were <50 nm.

This disordered mesoscopic surface state would account for the concentration of carbonate and moisture observed not only in the initial spectrum but of that observed in the final spectrum after heat treatment. This disordered surface would accept the large concentration of adsorbates to stabilize its surface state. The high temperature limit of the HT-DRIFT study, 1173K with short duration soaks, does not permit a large amount of diffusion of Ba and Ti cations for the restructuring of this mesoscopic surface state; hence the large residual concentration of carbonate and moisture in the final spectrum of Nanopowder F.

It is interesting to note that, in observing the spectral region 3350 cm^{-1} to 3600 cm^{-1}, the distribution of OH groups in the lattice had changed significantly with Nanopowders C through F. A single OH related band was observed at ~3509 cm^{-1} in the room temperature spectra of Nanopowders C through E. Upon cooling after heat treatment three bands were observed at 3509 cm^{-1}, 3475 cm^{-1} and 3451 cm^{-1} in the final spectra of Nanopowders C through E. The three bands observed with the room temperature spectrum of Nanopowder F (3509 cm^{-1}, 3492 cm^{-1} and 3451 cm^{-1}) transformed to 3509 cm^{-1}, 3475 cm^{-1} and 3451 cm^{-1} upon cooling after heat treatment, the same bands as observed in the final spectrum of the other three nanopowders. This was indicative of a cubic to tetragonal phase transition for Nanopowders C through E as a result of the heat treatment and a redistribution of the OH groups into a tetragonal phase related attachment of Nanopowder F. Klauer and Wöhlecke described similar results with strontium titanate.[115] They observed a single band, due to OH related to the cubic structure, split into three bands when strontium titanate transformed to tetragonal symmetry below 105K.

Reviewing the previous data with regard to the crystal structure of the nanopowders, XRD and electron diffraction indicated a cubic symmetry for Nanopowders C through E. This corroborated the HT-DRIFT data. The single, cubic related band of the room temperature spectra of Nanopowders C through E was indicative of the six degenerate Ti-O bonds in the oxygen octahedron of the cubic unit cell. The cooled spectra that exhibited three tetragonal related bands were indicative of the three different H^+ host sites in the distorted oxygen octahedron of the tetragonal unit cell (see Figure 3.22). The previous data for Nanopowder F indicated cubic symmetry by XRD and by electron diffraction. The HT-DRIFT indicated evidence of a mesoscopic structure with the three bands at room temperature, a single band at higher temperatures indicative of cubic symmetry, and three bands upon cooling from high temperature indicative of tetragonal symmetry.

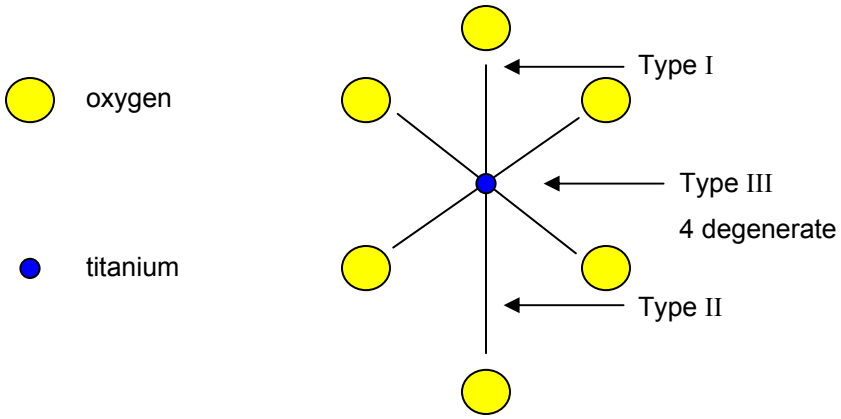

Figure 3.22. H^+ host site types of the Ti-O bonds in the oxygen octahedron of the barium titanate tetragonal unit cell.

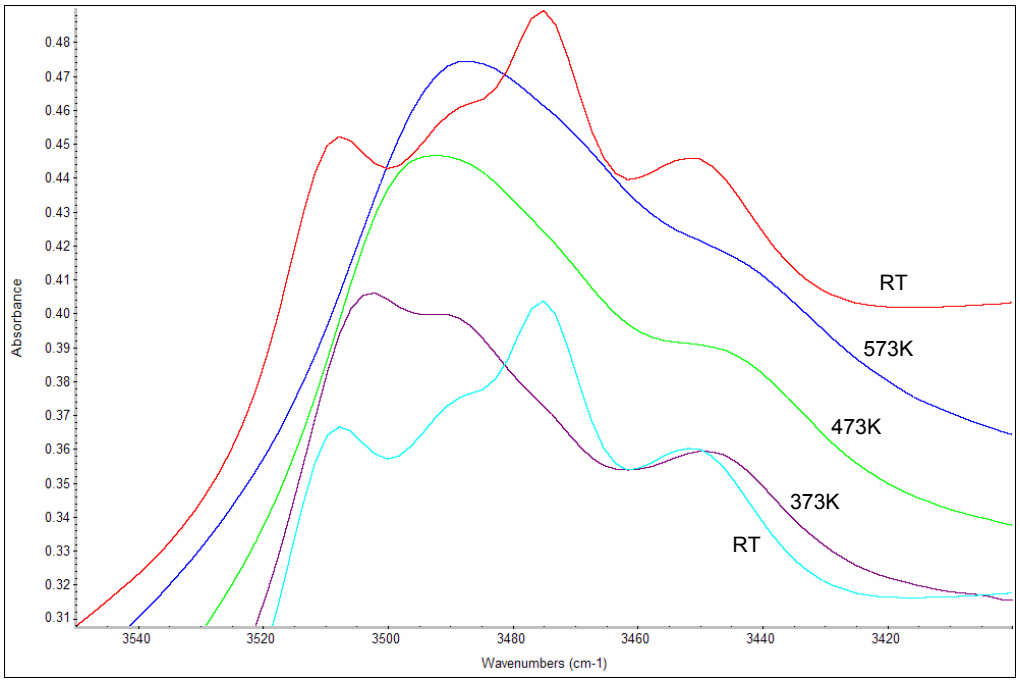

Figure 3.23. *In situ* HT-DRIFT spectra of Nanopowder F, cycled through the temperature range 298K to 573K, exhibiting the tetragonal - cubic transition; stacked common scale.

The shift from several bands to a single band during the *in situ* high temperature study was examined. This phenomenon was cyclic as temperature was raised and lowered (see Figure 3.23) which indicated the incorporated hydroxyl bands were related to the tetragonal to cubic transition. The nanopowders were initially heated to 773K in the HT-DRIFT chamber. Temperature was then cycled between room temperature and 573K. The single band appeared during the high temperature with the multiple bands reappearing upon return to room temperature. This was evidence for the structural transition between the tetragonal and cubic phases of barium titanate.

Observing the room temperature spectrum of Nanopowder F between 3600 cm^{-1} and 3350 cm^{-1}, the central band at 3492 cm^{-1} had transformed to 3475 cm^{-1} after heat treatment. A shoulder, of frequency equal to the room temperature 3492 cm^{-1} band, was observed at the high wavenumber side of the 3475 cm^{-1} band in the cooled spectrum. This indicated that four oscillators were active in the unit cell after the 573K heat treatment. Table 3.5 indicates assigned positions of the hydroxyl defects with regard to their vibrational modes and is depicted schematically in Figure 3.24.

To clarify the discrepancies with the OH related bands Nanopowders C through F were heat treated at 773K and 1173K. Spectra of the cooled nanopowders after treatment (see Figures 3.25 and 3.26), clearly exhibited structural changes had occurred. The bands exhibited after each heat

Table 3.5. Spectroscopic Data for OH – Oscillators: Position Assignments.

Stretching Vibration	Wavenumber (cm^{-1})	Site	Assignment
A	3509	◦	Type III host site
B	3451	▫	Type I host site
C	3492	•	axial, Ti-O-Ti plane
D	3475	▪	Type II host site

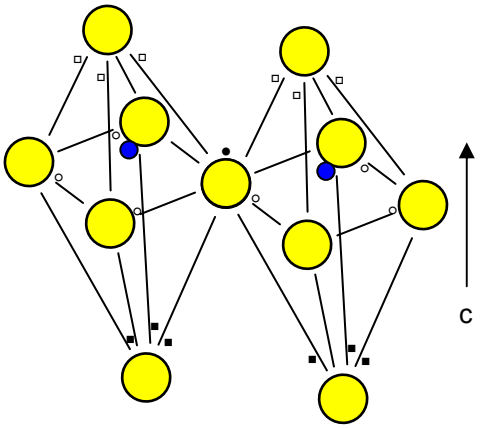

Figure 3.24. Schematic depiction of the proton position in the TiO_6 octahedron in the tetragonal phase unit cell of barium titanate. Barium atoms omitted for clarity. (See Table 3.5.)

treatment was different. The 773K cooled nanopowders exhibited the spectral bands 3509 cm^{-1}, 3492 cm^{-1}, 3475 cm^{-1}, and 3451 cm^{-1}. The 1173K cooled nanopowders exhibited the spectral bands 3509 cm^{-1}, 3475 cm^{-1}, and 3451 cm^{-1}. The 3492 cm^{-1} band observed only as a minor shoulder to the 3475 cm^{-1} band with Nanopowder F after the 1173K treatment.

The development of these bands in Nanopowders C through E occurred only after the 773K temperature level. The single band observed with the room temperature spectrum of each remained after lower temperature heat treating.

Structural changes occurred with the mesoscopic state of the interfaces of Nanopowder F after the 773K treatment. The 3509 cm^{-1} band observed with the room temperature spectrum had decreased in intensity with the 3492 cm^{-1} band of highest intensity. Structural changes continued to occur with all four nanopowders during the 1173K treatment. The 3475 cm^{-1} band was of highest intensity of the three bands observed with all of the nanopowders upon cooling.

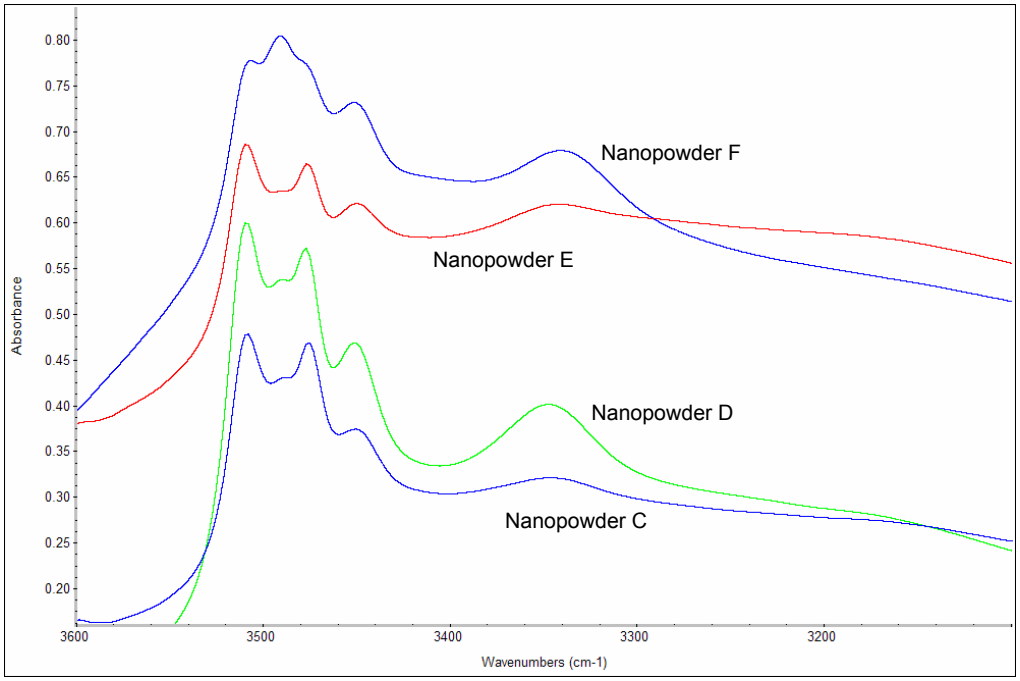

Figure 3.25. *In situ* HT-DRIFT spectra of Nanopowders C through F cooled after the 773K heat treatment; stacked common scale.

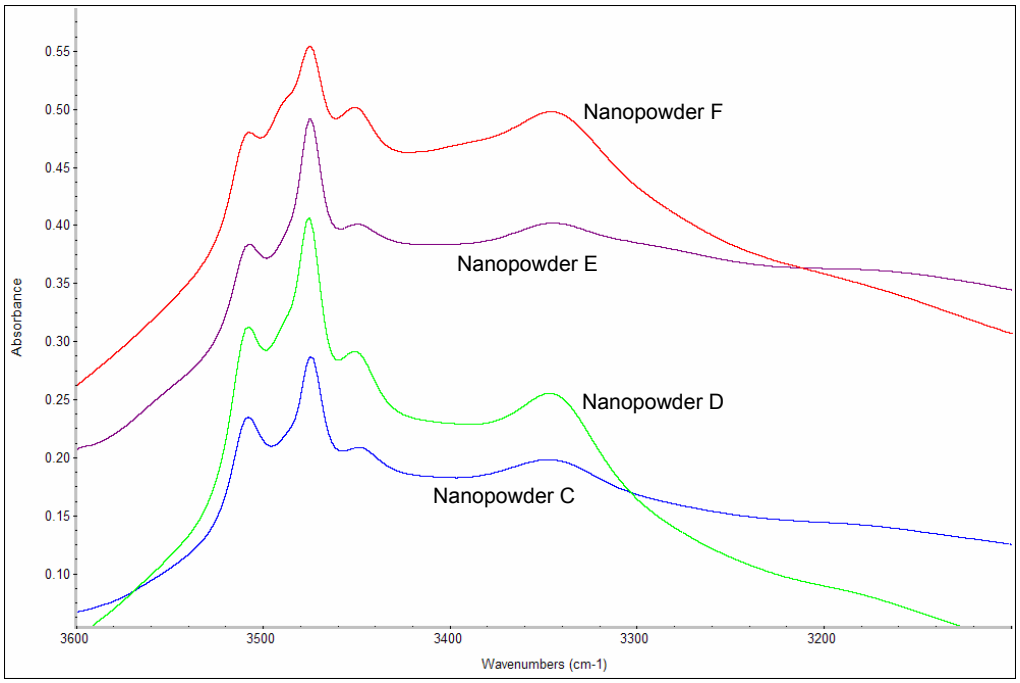

Figure 3.26. *In situ* HT-DRIFT spectra of Nanopowders C through F cooled after the 1173K heat treatment; stacked common scale.

Nanopowders C through E exhibited a single band with their room temperature spectra. This was indicative of the protonic defect bonded with oxygen ions in a lattice of cubic symmetry. The band positions changed during the heat treatments as the formation of crystallites with tetragonal symmetry occurred. The 773K spectra indicated positions of similar dimensions to cubic symmetry barium titanate, the shorter type I, and III bonds depicted in Figure 3.22. Both were represented with the 3509 cm^{-1} band and 3451 cm^{-1} band respectively. The highest temperature treatment produced structure changes that generated a large population of crystallites with tetragonal symmetry. The type II bond depicted in Figure 3.24 would yield the most open position for the incorporation of the protonic defect in the room temperature tetragonal structure. This was spectrally confirmed; the 3475 cm^{-1} band had the highest intensity after the 1173K treatment.

The 3509 cm^{-1} band observed in Nanopowders C through F was therefore related to the 4 degenerate oxygen bonds. These assignments are based upon the $OH^{\bullet}$ – Ti bond length and the work by Bellamy and Owen.[76] The longer the $OH^{\bullet}$ – X bond length the smaller the change in wavenumber $\Delta\tilde{\upsilon}$ and the inverse for shorter bond lengths, a larger $\Delta\tilde{\upsilon}$ was observed.

Nanopowder F exhibited three bands with the room temperature spectrum. These were related to the tetragonal symmetry observed after the 773K and 1173K heat treatments. The most populated band (3509 cm^{-1}) was related to cubic symmetry. The other two bands (3492 cm^{-1} and 3451 cm^{-1}) were tetragonal symmetry related.

The highly disordered state of the interfaces, in the previously proposed mesoscopic state for Nanopowder F, and the spectral evidence examined indicated interfaces with states similar to tetragonal symmetry. The high ratio of surface area to bulk volume provided large regions of varied bond states along the interfaces. The nature of these regions assumed a pseudo-tetragonal symmetry or a relaxed state along the interfaces in an attempt at a reduction in their free surface energy. The position of the protonic impurities in the “as-received” nanopowder, therefore, produced oscillators related to tetragonal

symmetry. The bulk crystallites, however, had cubic symmetry as evidenced with XRD and electron diffraction. The room temperature bands remained; however, they exhibited changes in intensity as related to the change in population density of the repositioned protonic impurity. This repositioning was due to the changed interfaces during the heat treatments.

The 773K heat treatment produced changes in the interfaces of the four nanopowders. The surfaces would be the first to exhibit change to the tetragonal symmetry that was spectrally observed. As treatment temperature increased to 1173K a more stable tetragonality was observed. These structural changes were addressed in Section 6 during the study of calcining in an ambient atmosphere.

Kapphan and Weber studied the adsorption of the hydrogen impurity in $BaTiO_3$.[116] They reported high resolution wavenumber values (0.1 cm^{-1} resolution) for OH vibrational frequencies in single crystals. The polarization pattern yielded a possible picture of the hydrogen positions in the lattice, with both axial and parallel sites along the O-O directions of the oxygen octahedron. The five OH stretching wavenumbers were reported as 3509 cm^{-1}, 3501 cm^{-1}, 3492 cm^{-1}, 3485 cm^{-1} and 3462 cm^{-1}. These wavenumbers reflect favorably on the wavenumbers observed with the polycrystalline nanopowders as reported in this study: 3509 cm^{-1}, 3492 cm^{-1}, 3475 cm^{-1}, 3451 cm^{-1} and 3340 cm^{-1}. This latter wavenumber, due to its intensity and position with regard to the other four bands in both studies, was believed to emerge due to the lattice gas observed in this study and as reported by others.[62,104]

The four higher wavenumber bands reported by Kapphan and Weber were attributed to the proton parallel, perpendicular and isotropically positioned around the oxygen atoms of the oxygen octahedron. The designations were accomplished using polarized light parallel and perpendicular to the c-axis of single crystal barium titanate and the observed resultant spectra. The bands transforming into a broad double band at 411K were also reported, whereas a transformation to a single band was observed in this study.

Pirc and Blinc applied a mesoscopic model of barium titanate in describing the position of the titanium atom in the unit cell.[117] In their description of the

paraelectric phase, the Ti – ion occupied one of eight off-center positions in the unit cell; a non-centrosymmetric position towards the oxygen octahedron face in the [111] direction. The result would, however, only produce two different bond lengths between the titanium and oxygen atoms, hence two different oscillators would be active.

The 773K heat treatment resulted in four bands with each of Nanopowders C through F upon cooling. These results may be indicative of a local atomic displacement from cubic symmetry; distortion of the titanium atom away from the c-axis in the direction of a face of the oxygen octahedron, however, not in a [111] direction. The observed four bands would be indicative of the resultant four bond lengths of the distorted cubic unit cell as described by Pirc and Blinc, but slightly off from the [111] direction. A Ti-ion position of (0.51, 0.51, 0.53) would yield four Ti – O bond lengths and the associated four bands observed. Eight possible regions would exist, for a displaced Ti-ion towards an oxygen octahedral face. It was presumed therefore, that the titanium atoms were displaced from their cubic centrosymmetric positions which resulted in local tetragonal-type distortions (see Figure 3.27). This suggested that after the 773K treatment the minimum potential for the Ti-ion was a non-centrosymmetric location in a cubic unit cell.

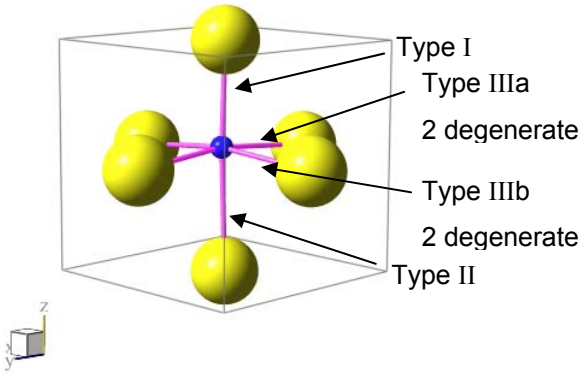

Figure 3.27. H^+ host site types of the Ti-O bonds in the oxygen octahedron of a distorted barium titanate cubic unit cell.

The protonic defect, in its position in the barium titanate structure, points to a neighboring oxygen ion. The proton, therefore, can migrate through the structure according to the Grotthuss mechanism, which is the predominant migration mechanism in perovskite type oxides.[118-19] The rate of diffusional reorientation is dependent upon the hydrogen bonding between the hydroxyl ion and the neighboring oxygen ion. Münch et. al., in quantum molecular dynamic simulations, depicted the position of the proton as a rotational diffusion around an oxygen ion in the plane perpendicular to the Ti-O-Ti plane at 1200K, as shown in Figure 3.28.[120] Münch calculated the time scale of this proposed rotation as 10^{-12} seconds for one complete turn, placing the rotational wavenumber beyond the near infrared capability of the HT-FT-IR used.

The high temperature spectra exhibited band broadening and shifting to lower wavenumber as well as baseline shifting at lower wavenumbers. This was a result of the effect that heat has on the KBr beam splitter and the detector window.[121-22] Although continuously cooled, the environmental chamber dissipates residual heat that affects these components. Slight aberrations in the beam splitter cause the shifting of bands to lower wavenumbers and a rising baseline at the low wavenumber side of the spectrum. These effects were considered when assessing the position of the bands of interest.

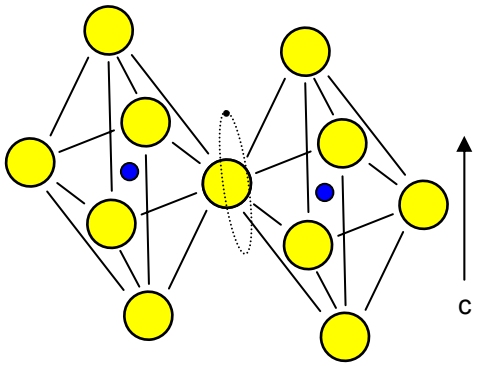

Figure 3.28. Schematic depiction of the rotational position of the proton near the TiO_6 octahedron in the cubic phase unit cell of barium titanate. Barium atoms omitted for clarity.

A large shift can be noted with the 3509 cm^{-1} room temperature band during the heating phase of the nanopowders between 573K and 873K. The shift was observed with the four non-solid state nanopowders. The room temperature band broadens while shifting to lower wavenumber as temperature increased. The band is broadest at 773K, whereupon it begins to narrow perceptively through the temperature maxima. This narrowing of the band is indicative of well localized oscillators. The spectra of nanopowder E for example, exhibited this shift (see Figure 3.29). In comparison, the shift due to temperature observed with the band at 2439 cm^{-1} is shown for comparison (see Figure 3.30). This band shift accompanied with narrowing of the band is believed to be the result of the diffusional reorientation of the protonic impurities into the axial positions around the corner oxygen ions of the TiO_6 octahedron. The high temperature phase of barium titanate is cubic and, therefore, a proton at each of the eight corner oxygen ions would be in degenerate energy states. Thus, these localized oscillators, as predicted by Münch, would produce the narrower, lower wavenumber shifted band at higher temperature.

It should be noted that the proton undergoes reorientation as the temperature cools, the unit cell becomes tetragonal and Ti-O and O-O bond lengths become modified. The axial position was, at room temperature, the most populated position occupied by the protonic defect, as observed with the intensity of the 3475 cm^{-1} band in the final spectrum of each of the non-solid state nanopowders.

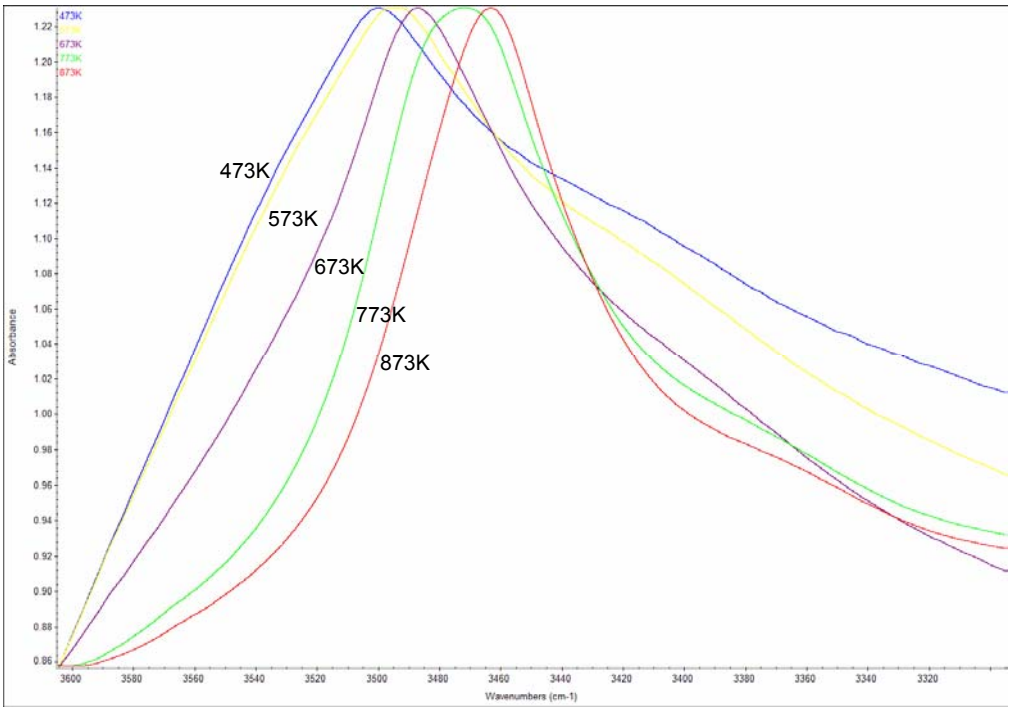

Figure 3.29. *In situ* HT-DRIFT spectra of nanopowder E. Temperature induced shift of the 3509 cm^{-1} band through the temperature range 473K to 873K.

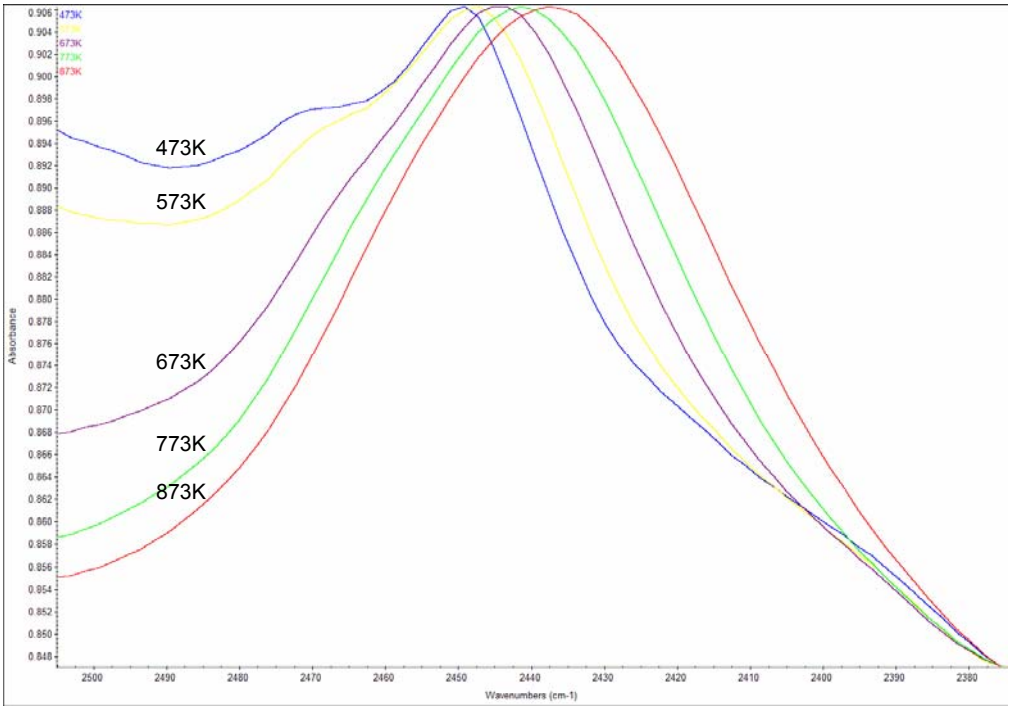

Figure 3.30. *In situ* HT-DRIFT spectra of nanopowder E. Temperature induced shift of the 2439 cm^{-1} band through the temperature range 473K to 873K.

3.2.3 H_2O Study

3.2.3.1 Experimental Procedure

The H_2O study incorporated the same high temperature set up as the preliminary study. The nanopowders were examined neat (i.e. as-received so as not to disturb the surface layers and to improve the surface sensitivity of the technique). A background spectrum was taken using the polished aluminum coated mirror in the standard Smart Collector sample holder, similar to the previous HT-DRIFT technique, and auto subtracted from the final sample spectrum by the Omnic 6.0 software package. Spectra were obtained at a resolution of 4 cm^{-1} with 500 cumulative scans to form the final spectrum between 650 cm^{-1} and 4000 cm^{-1}. A continuous flow of ultra high purity nitrogen gas was provided at a rate of 150 ml/minute.

The nanopowders were quickly heated, a fast ramping of the temperature to 773K over a period of a few minutes. The temperature was held at 773K for two hours. The temperature was then reduced to 383K and held for a period of 60 minutes after which the temperature was increased to 473K and held for an additional 30 minutes. Temperature was then returned to room temperature.

A room temperature spectrum was taken of the nanopowders prior to heat treatment, after the two hour soak at 773K, and at 5 minute intervals at the 383K and 473K temperature soaks. A final spectrum was taken after returning the sample to room temperature.

Two different methods were used in accessing the readsorption of moisture by the nanopowders, both following the same procedure. The first utilized the continuous flow of UHP nitrogen gas, provided at a rate of 150 ml/minute, as in the previous preliminary study. The UHP N_2 provides 3 ppm H_2O content, the maximum allowed for UHP gas as stipulated by the supplier. The second method utilized dry air providing 6 ppm H_2O, the maximum allowed for dry air as stipulated by the supplier, provided at the same flow rate.

3.2.3.2 Results and Discussion

The following discussions compared the results of the adsorption of moisture under flowing UHP N_2 with adsorption under flowing dry air. The adsorption at both temperature levels studied (383K and 473K) were included. The asymmetric stretching band of the hydroxyl (OH_{vasym}) was examined with all of the nanopowders. Additionally, the molecular water bend mode (OH_{δ}) was also examined with the hydrothermally derived nanopowders (C through F). The amount of adsorbed moisture was qualitatively examined through band area analysis using the Omnic 6.0 software package.

The spectra for the adsorption of moisture under the flow of UHP N_2 on Nanopowder A during the 60 minutes at 383K (see Figure 3.31a) and for 30 minutes at 473K in Figure 3.31b. As anticipated only a low amount of moisture was adsorbed. The available sites for adsorption were relatively unchanged from the initial room temperature state. The 773K soak was not high enough to liberate any substantial quantity of carbonate from the nanopowder, which resulted in few new sites for moisture attachment.

The dry air experiment with Nanopowder A resulted in similar results, with only a slight increase in the moisture adsorbed. Although the dry air contained a qualitatively higher amount of moisture, the lack of new sites for attachment was suspected of limiting the level of moisture adsorption. Figure 3.32a and 3.32b show adsorbed moisture levels from dry air at 383K and 473K respectively.

The spectra for the adsorption of moisture on Nanopowder B during the 60 minutes at 383K is shown in Figure 3.33a, and for 30 minutes at 473K in Figure 3.33b. Similarly, Nanopowder B did not exhibit a high level of moisture adsorption after moderate heat treatment. Both of the solid state synthesized nanopowders contained strongly bound carbonate impurities that remained intact after the moderate heat treatment.

The dry air experiment with Nanopowder B, similar to Nanopowder A, resulted in only a slight increase in the moisture adsorbed over that from UHP N_2. Figure 3.34a and 3.34b show adsorbed moisture levels from dry air at 383K and 473K respectively.

The surfaces of the hydrothermal nanopowders were more reactive in their adsorption of moisture. After the moderate heat treatment at 773K, all readsorbed moisture in excess of their initial content. These nanopowders had higher initial moisture content than the solid state derived nanopowders, and in addition their higher specific surface area also aided in providing a greater number of possible sites for readsorption.

Nanopowder C exhibited the three tetragonal related bands in the 3400 cm^{-1} to 3500 cm^{-1} region during the 60 minute soak at 383K, slightly below the 403K Curie transition temperature, during the study of moisture readsorption from UHP N_2. The readsorption of moisture was continuous over the 60 minute time period as shown with the OH bands, in the 3400 cm^{-1} to 3500 cm^{-1} region, and with the 1640 cm^{-1} molecular water bending mode (see Figures 3.35a and 3.35b, respectively).

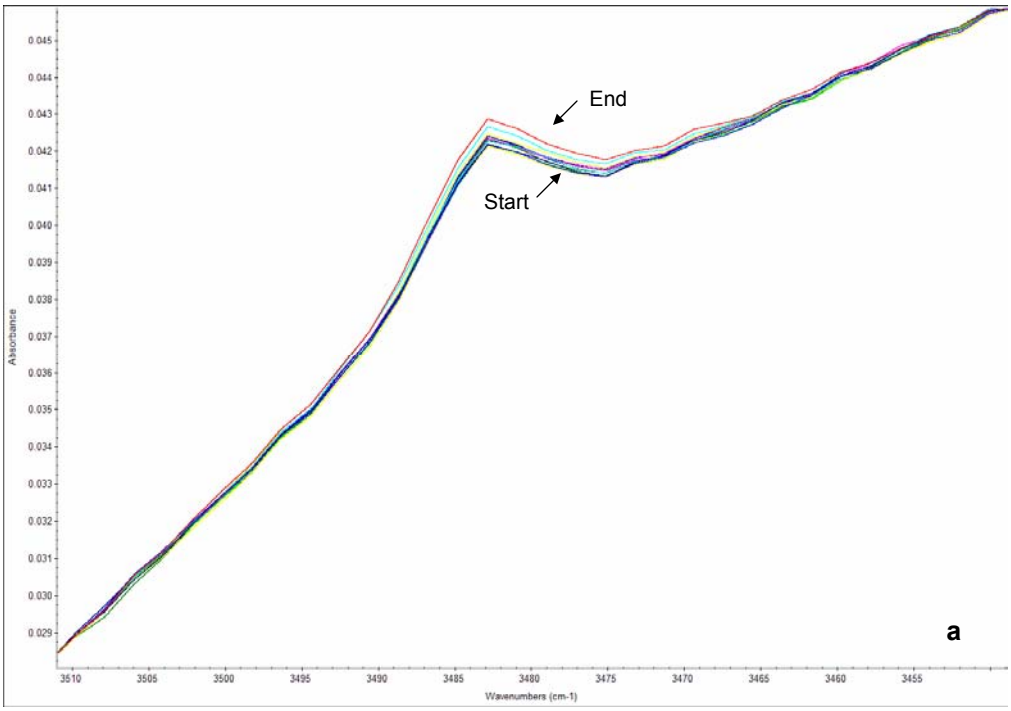

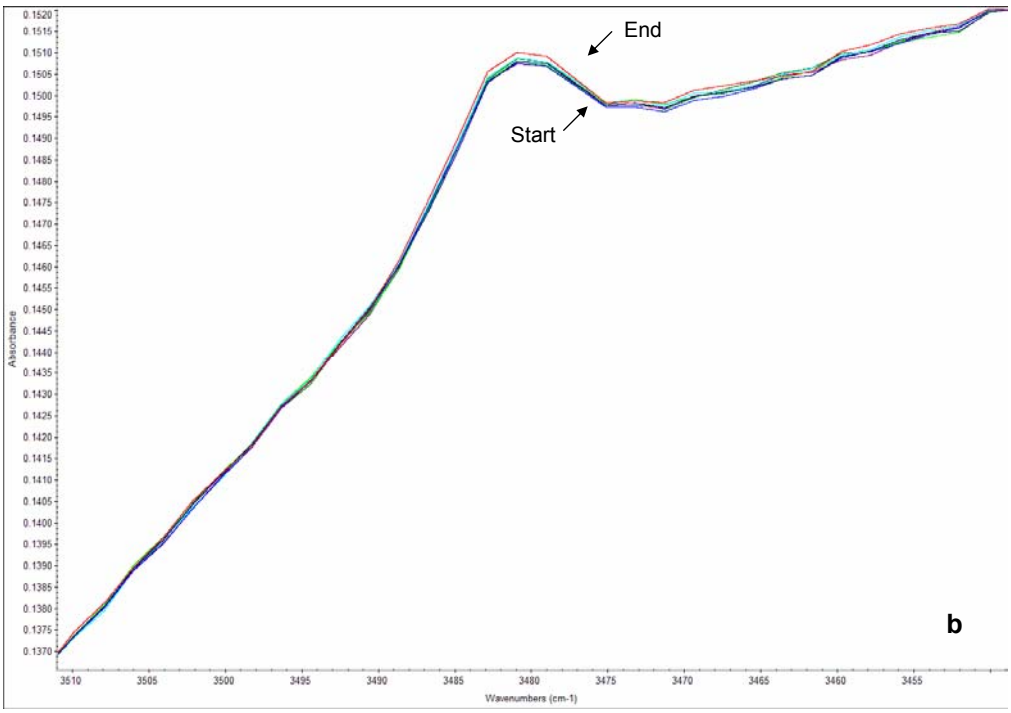

Figure 3.31. *In situ* HT-DRIFT spectra of Nanopowder A: moisture adsorption from UHP N_2 (a) during 60 minutes at 383K, (b) during 30 minutes at 473K.

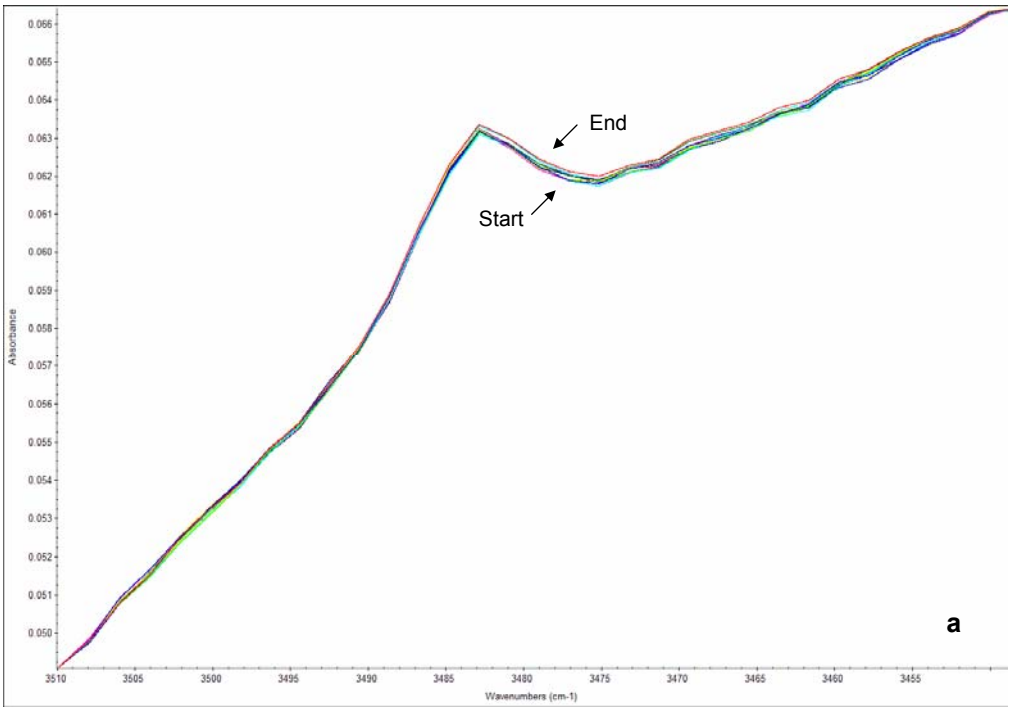

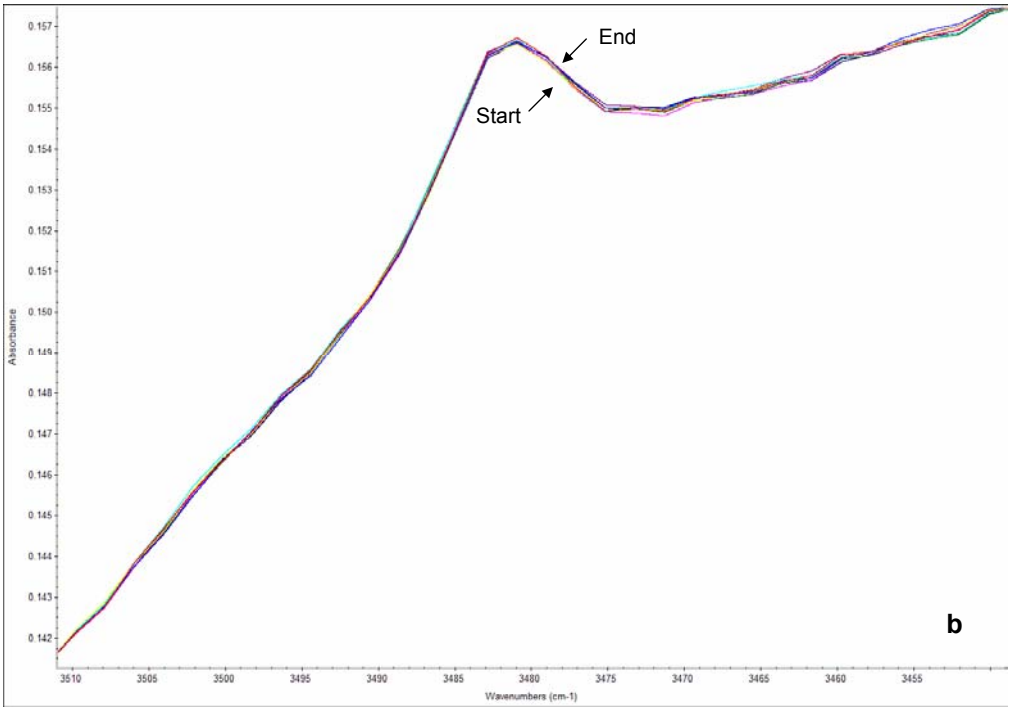

Figure 3.32. *In situ* HT-DRIFT spectra of Nanopowder A: moisture adsorption from Dry Air (a) during 60 minutes at 383K, (b) during 30 minutes at 473K.

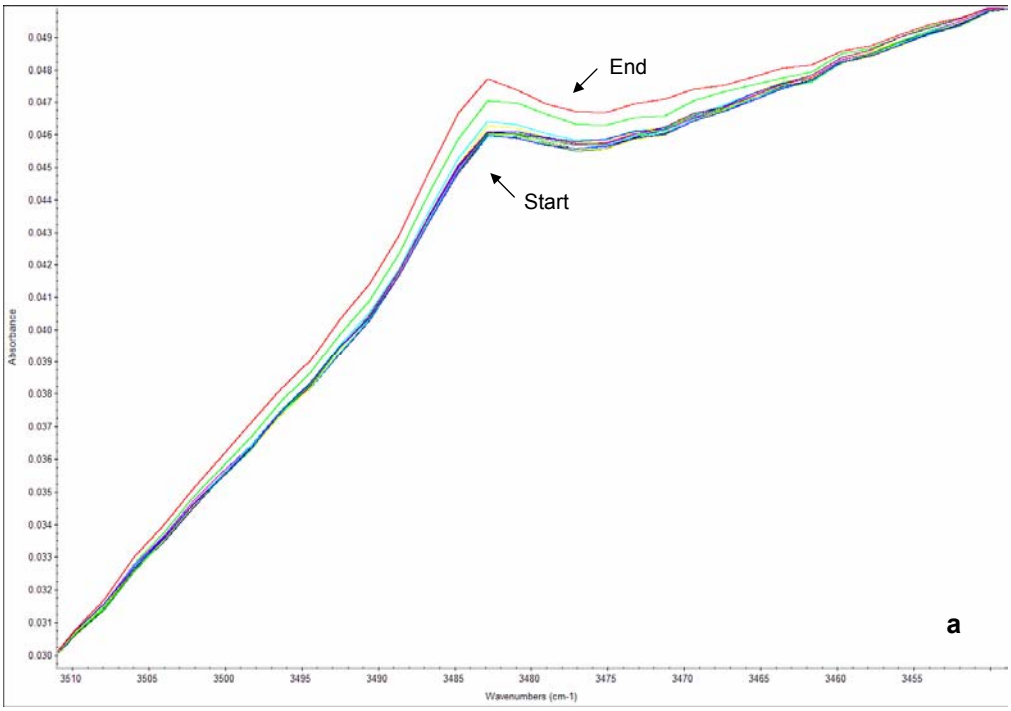

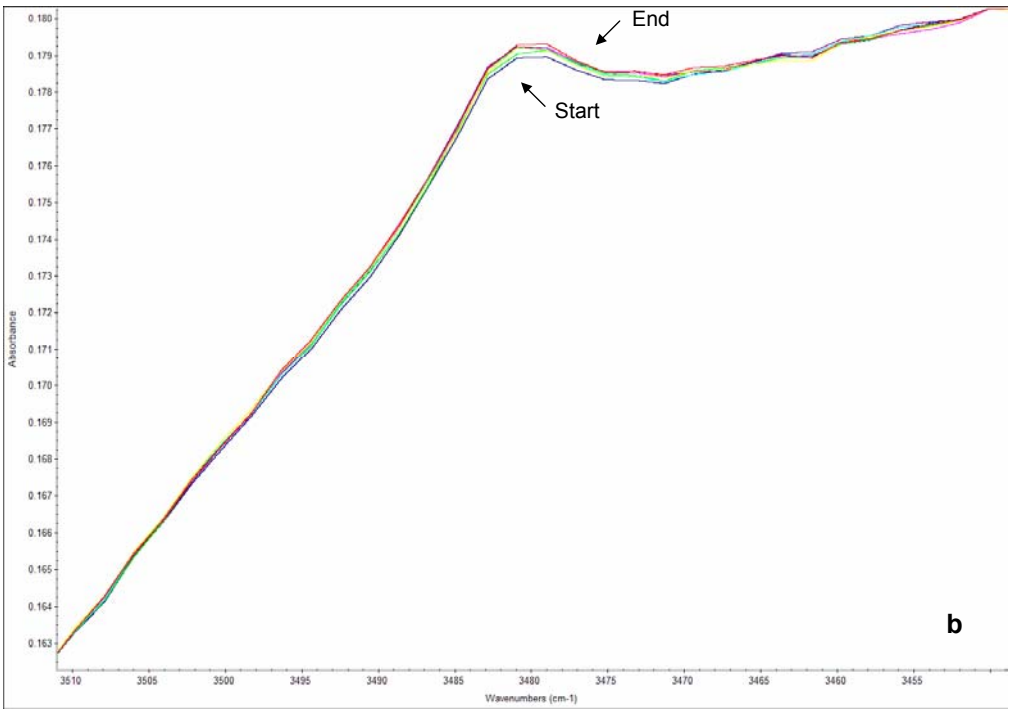

Figure 3.33. *In situ* HT-DRIFT spectra of Nanopowder B: moisture adsorption from UHP N_2 (a) during 60 minutes at 383K, (b) during 30 minutes at 473K.

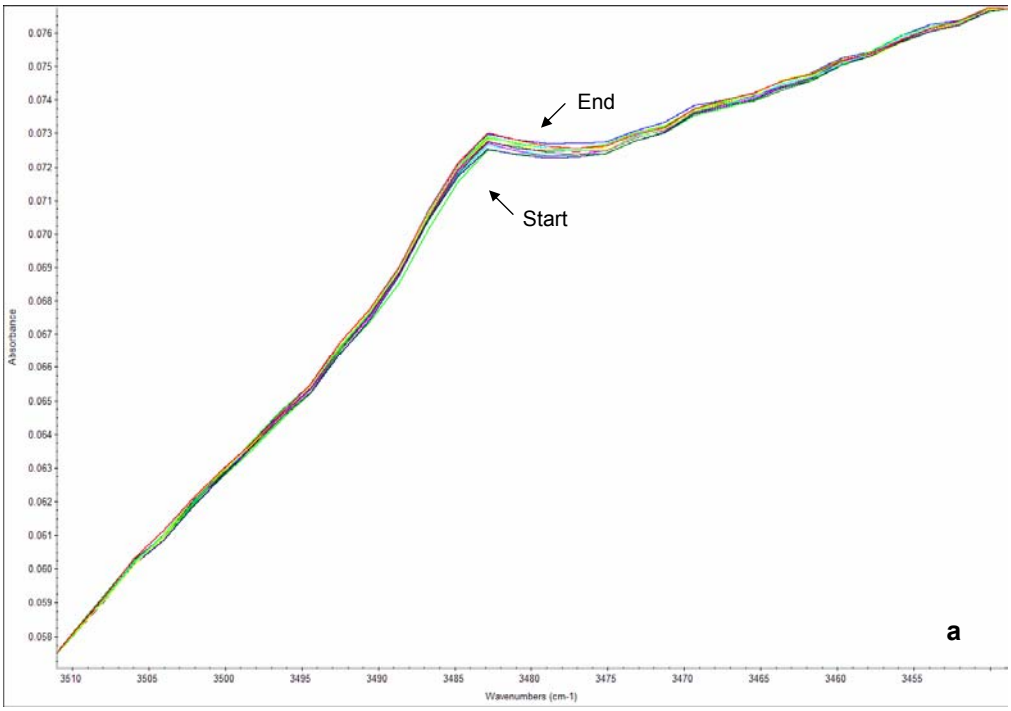

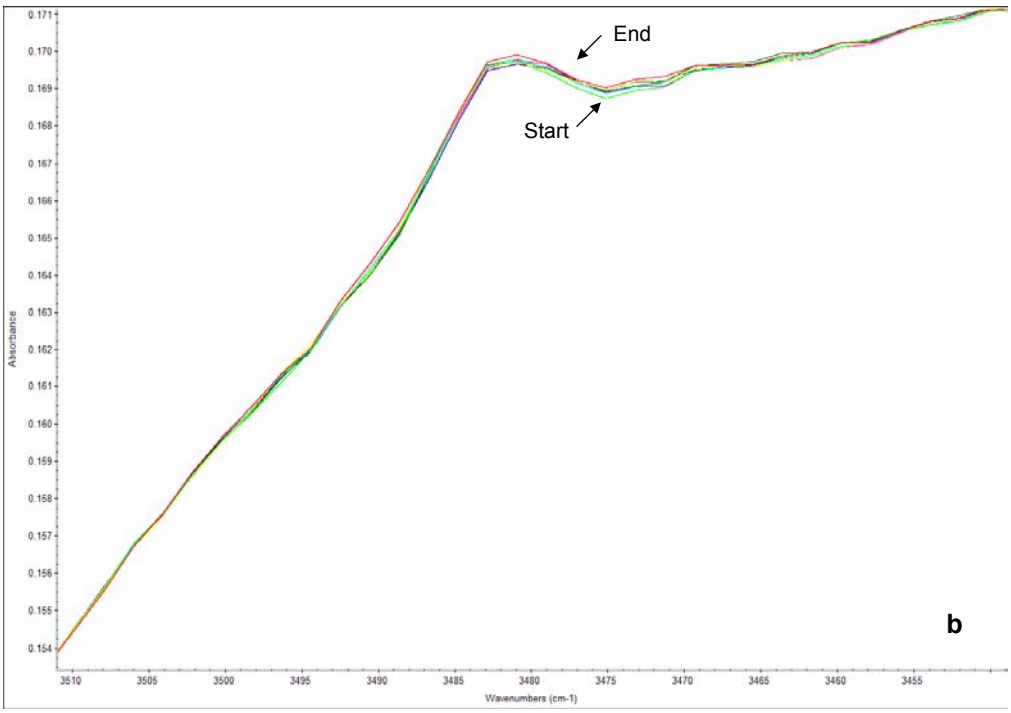

Figure 3.34. *In situ* HT-DRIFT spectra of Nanopowder B: moisture adsorption from Dry Air (a) during 60 minutes at 383K, (b) during 30 minutes at 473K.

The moisture adsorption studied at 383K and the higher soak temperature of 473K, above the Curie temperature, is shown in Figures 3.35a and 3.36b, respectively. A reorientation of the OH groups, as previously described in the preliminary study, had progressed. A reduction of the intensities of the high and low wavenumber bands in the 3400 cm^{-1} to 3500 cm^{-1} region was observed, in relation to the 383K temperature spectra, related to the tetragonal to cubic structure transition. Additionally, an overall reduction was observed in the intensities of all three OH related bands in the 3400 cm^{-1} to 3500 cm^{-1} region at 473K (see Figure 3.36a). However, an increase in the intensity of the molecular water bend at 1640 cm^{-1} was observed (see Figure 3.36b). The reduced levels of the OH related bands at 473K and the increase observed with the 1640 cm^{-1} band indicates that the equilibrium concentration of the OH ion was lower at this temperature than by the nanopowder at 383K.

The moisture adsorption spectra of Nanopowder C from the dry air supply during the 60 minute soak at 383K is shown with the OH bands, in the 3400 cm^{-1} to 3500 cm^{-1} region, and with the 1640 cm^{-1} molecular water bending mode, in Figures 3.37a and 3.37b, respectively. The allowable moisture content of the dry air supply (6 ppm) was twice that of the allowed content in the UHP N_2 supply (3 ppm). A continued desorption is observed in the hydroxyl region while an increase was observed in the molecular water band.

Continued moisture desorption was observed with the three OH related bands, the tetragonal related bands in the 3400 cm^{-1} to 3500 cm^{-1} region. The molecular water bending mode (1640 cm^{-1}) band, was moderately broad but well defined over the time period displayed. An increase in adsorption by the nanopowder was exhibited. Additionally, broad overtones were also observed through 1200 cm^{-1}.

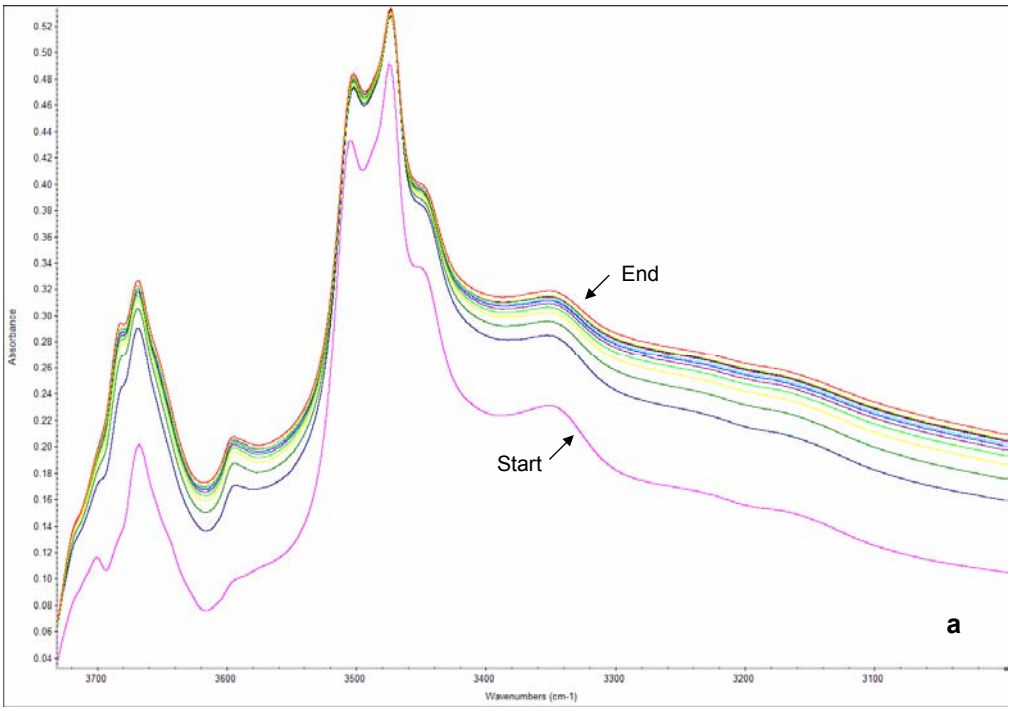

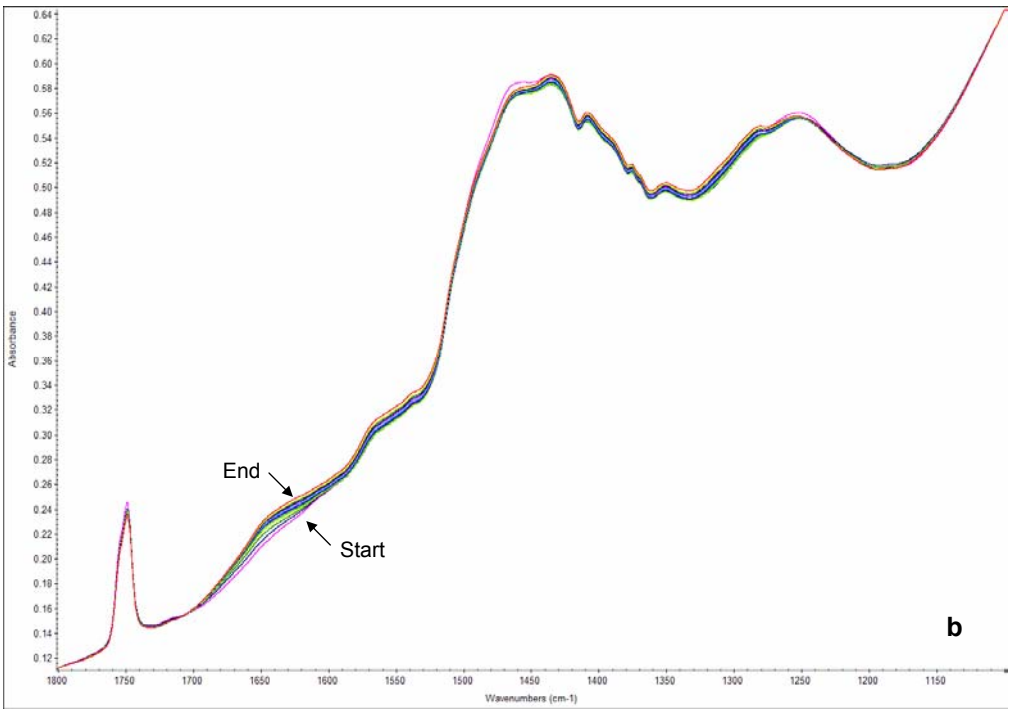

Figure 3.35. *In situ* HT-DRIFT spectra of moisture adsorption from UHP N_2 on Nanopowder C during 60 minutes at 383K: (a) OH_{vasym}, the asymmetric stretching band region of the hydroxyl, (b) HOH_{δ}, the molecular water bending mode region.

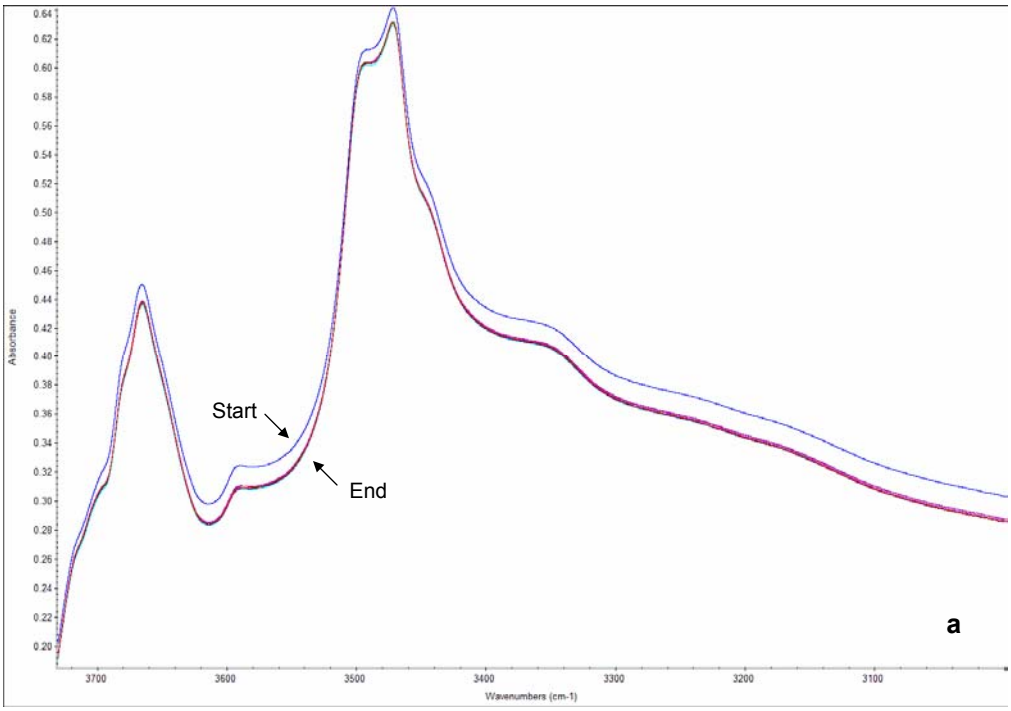

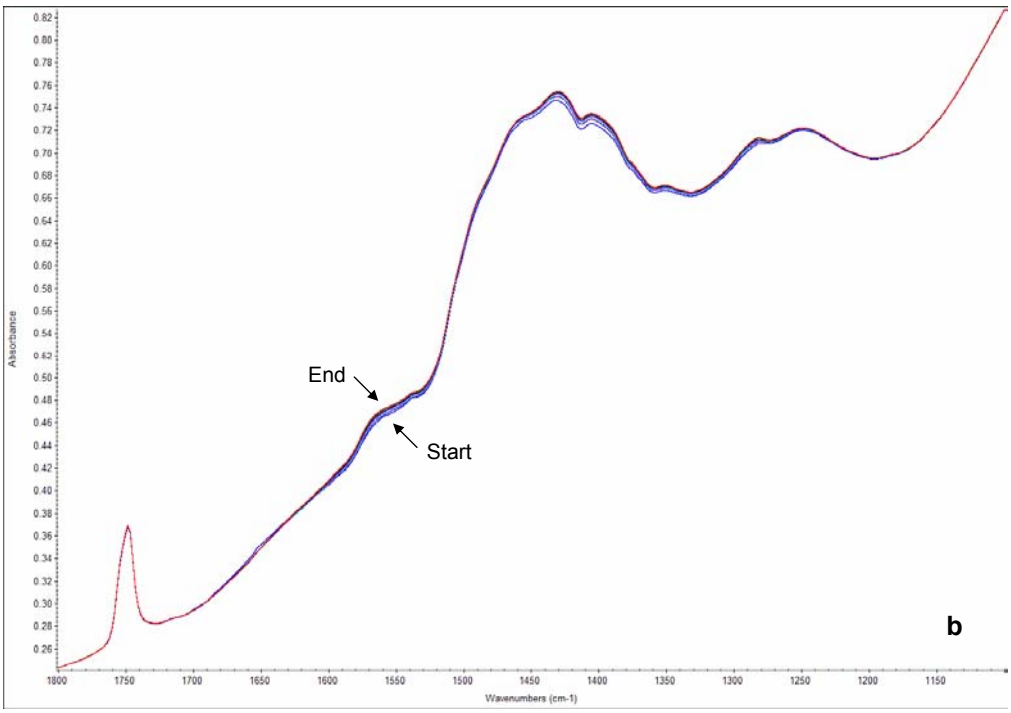

Figure 3.36. *In situ* HT-DRIFT spectra of moisture adsorption from UHP N_2 on Nanopowder C during 30 minutes at 473K: (a) OH_{vasym}, the asymmetric stretching band region of the hydroxyl, (b) HOH_{δ}, the molecular water bending mode region.

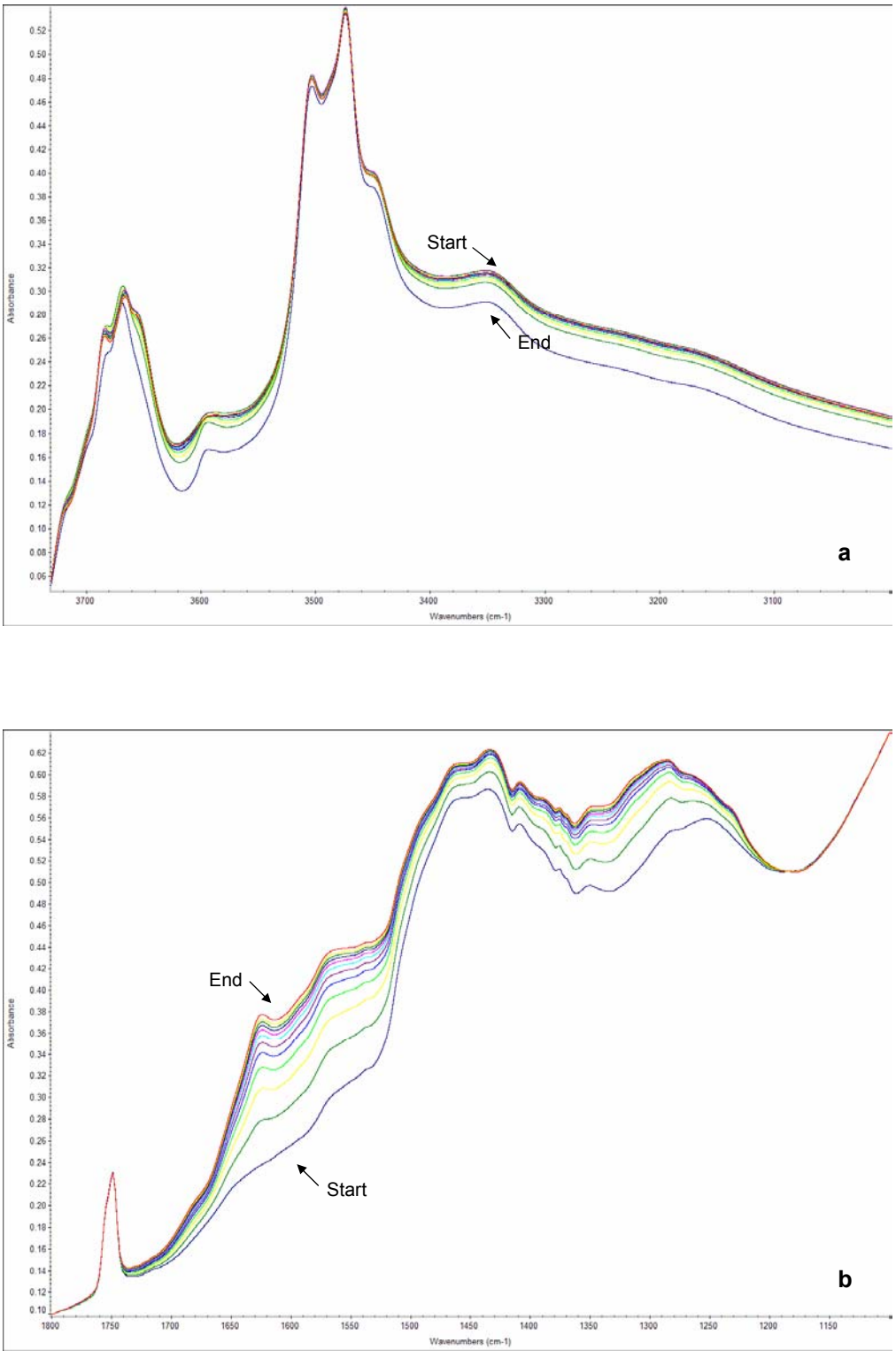

Figure 3.37. *In situ* HT-DRIFT spectra of moisture adsorption from dry air on Nanopowder C during 60 minutes at 383K: (a) OH_{vasym}, the asymmetric stretching band region of the hydroxyl, (b) HOH_{δ}, the molecular water bending mode region.

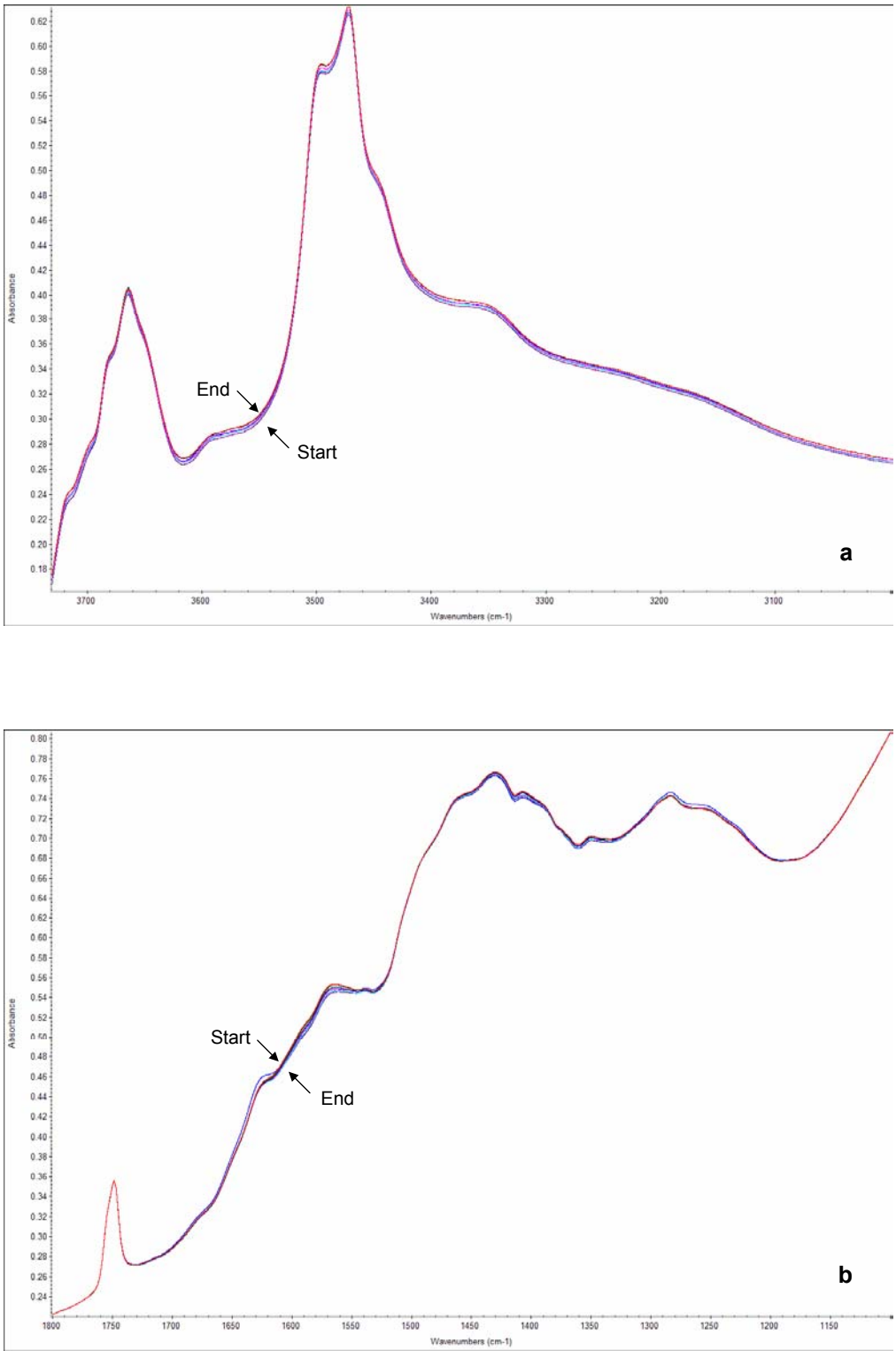

Figure 3.38. *In situ* HT-DRIFT spectra of moisture adsorption from dry air on Nanopowder C during 30 minutes at 473K: (a) OH_{vasym}, the asymmetric stretching band region of the hydroxyl, (b) HOH_{δ}, the molecular water bending mode region.

At the 473K soak over the 30 minute time period, a slight increase was observed with the OH related bands while a slight decrease was observed with the molecular water band. This finding was opposite the results observed with the adsorption under UHP N_2 at 473K where a decrease in the OH related bands was observed. The equilibrium concentration of the OH ion was greater under the higher moisture level provided with the dry air supply as opposed to the UHP N_2 supply.

The moisture adsorption spectra of Nanopowder D from the UHP N_2 supply during the 60 minute soak at 383K is shown with the OH bands in the 3400 cm^{-1} to 3500 cm^{-1} region and with the 1640 cm^{-1} molecular water bending mode in Figures 3.38a and 3.38b, respectively. The readsorption of moisture was continuous over the 60 minute time period as shown with the hydroxyl bands in the 3400 cm^{-1} to 3500 cm^{-1} region and with the molecular water bending mode (1640 cm^{-1}).

The moisture adsorption studied at the higher soak temperature of 473K, above the Curie temperature, is shown in Figures 3.40a and 3.40b, respectively. A reorientation of the OH groups, as previously described in the preliminary study, had progressed. A reduction of the intensities of the high and low wavenumber bands in the 3400 cm^{-1} to 3500 cm^{-1} region was observed, in relation to the 383K temperature spectra, related to the tetragonal to cubic structure transition. The level of hydroxyl at 473K was lower than that observed at the lower 383K soak, a reduction in the OH levels was observed in this region. A minor level of increase was shown in the molecular water bending mode during the 473K soak. This was a similar trend as with Nanopowder C, each showing a reduction of hydroxyl level and a minor increase in molecular water.

There existed a 3340 cm^{-1} band with both Nanopowders C and D, which was observed only with Nanopowder F in the DRIFT study, which can be attributed to an additional OH^- band due to lattice gas. When adsorbed surface layer mobility was enhanced repulsive forces increased giving rise to a weaker, symmetric band.

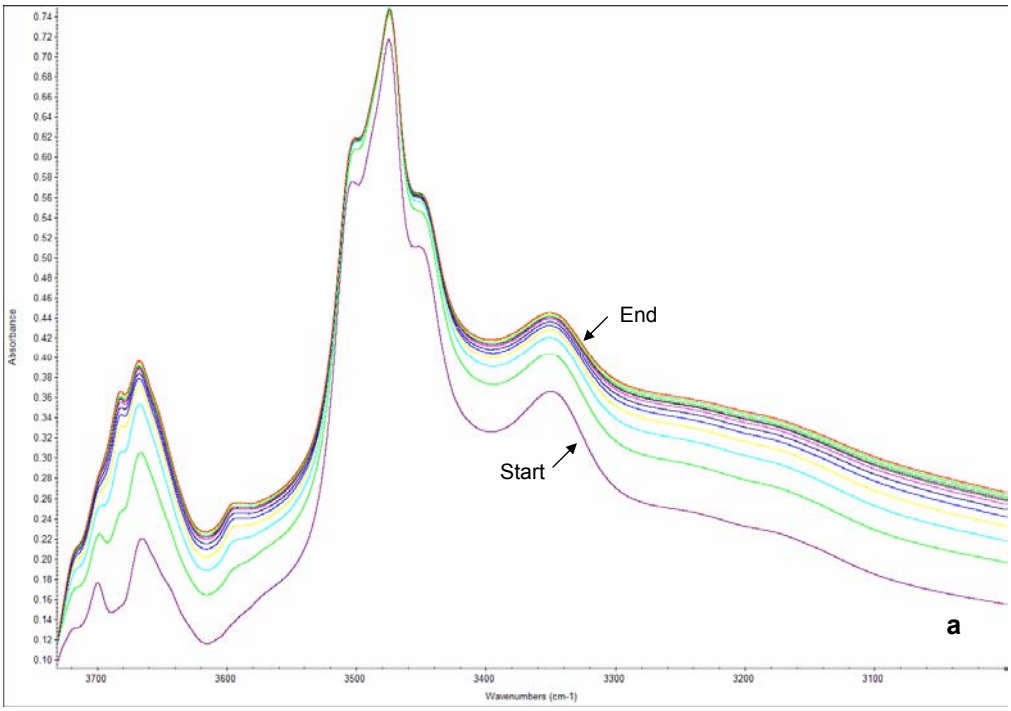

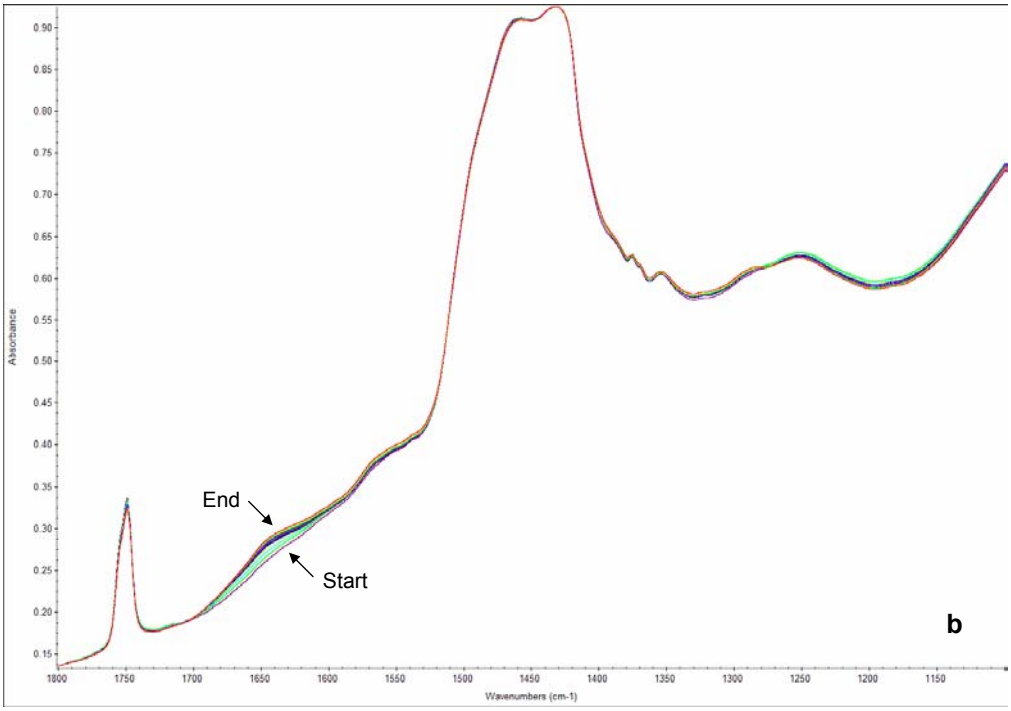

Figure 3.39. *In situ* HT-DRIFT spectra of moisture adsorption from UHP N_2 on Nanopowder D during 60 minutes at 383K: (a) OH_{vasym}, the asymmetric stretching band region of the hydroxyl, (b) HOH_{δ}, the molecular water bending mode region.

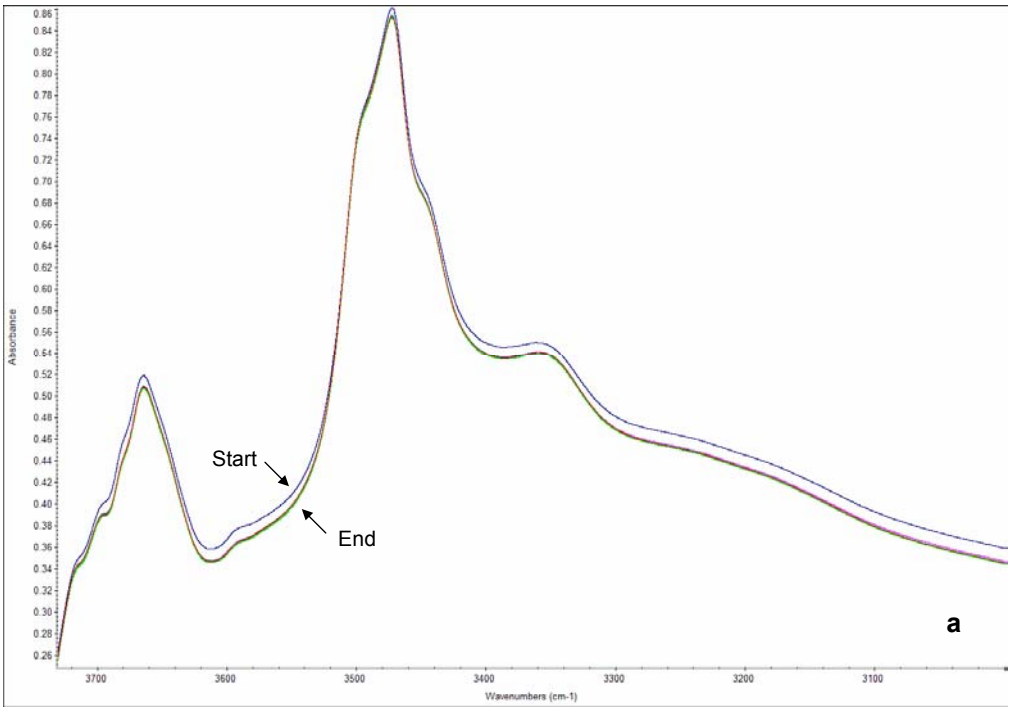

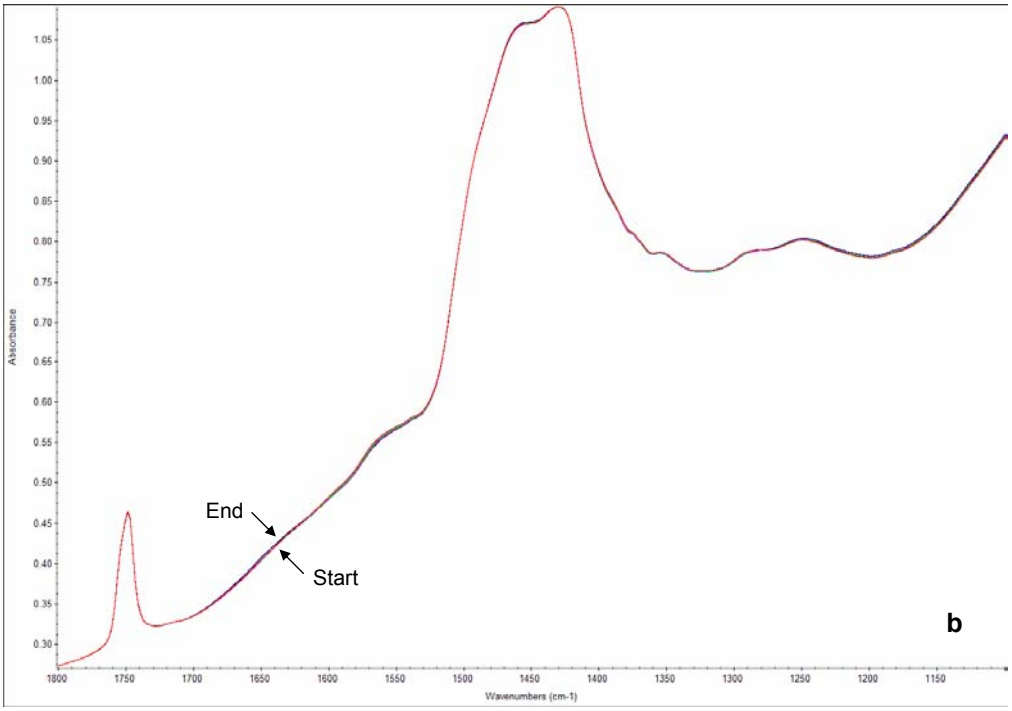

Figure 3.40. *In situ* HT-DRIFT spectra of moisture adsorption from UHP N_2 on Nanopowder D during 30 minutes at 473K: (a) OH_{vasym}, the asymmetric stretching band region of the hydroxyl, (b) HOH_{δ}, the molecular water bending mode region.

The presence of these regions of lattice gas resulted in the appearance of this additional band since there existed equilibrium between the lattice gas regions and the adsorbed layer.

The moisture adsorption spectra of Nanopowder D from the dry air supply during the 60 minute soak at 383K is shown with the OH bands, in the 3400 cm^{-1} to 3500 cm^{-1} region, and with the molecular water bending mode (1640 cm^{-1}), in Figures 3.41a and 3.41b, respectively. Moisture readsorption was observed with the three OH related bands, the tetragonal related bands in the 3400 cm^{-1} to 3500 cm^{-1} region. The molecular water bending mode (1640 cm^{-1}) band, was moderately broad but well defined over the time period displayed also indicating an increase in adsorption by the nanopowder. Additional broad overtones were also observed through 1200 cm^{-1}. The 3340 cm^{-1} band due to the lattice gas, was also observed during the time period at 383K under the flowing dry air supply.

The moisture adsorption spectra of Nanopowder D from the dry air supply during the 30 minute soak at 473K is shown with the OH bands in the 3400 cm^{-1} to 3500 cm^{-1} region and with the molecular water bending mode (1640 cm^{-1}) in Figures 3.42a and 3.42b, respectively. Similarly to Nanopowder C, a loss was observed in hydroxyl levels and a minor increase in the level of molecular water.

The moisture adsorption spectra of Nanopowder E from the UHP N_2 supply during the 60 minute soak at 383K is shown with the OH bands in the 3400 cm^{-1} to 3500 cm^{-1} region and with the molecular water bending mode (1640 cm^{-1}) in Figures 3.43a and 3.43b, respectively. A large increase was observed in the hydroxyl region showing the bands for tetragonal symmetry. The lattice gas band that was observed at 3340 cm^{-1} is broadening and reducing in intensity. The molecular water bending mode (1640 cm^{-1}) was broad yet increasing.

At the higher temperature 473K soak under flowing UHP N_2, Nanopowder E exhibited a reduction in hydroxyl level and a small increase in molecular water (see Figures 3.44a and 3.44b). The lattice gas contribution was present as a broad low intensity band. The high and low wavenumber hydroxyl related bands were reduced, exhibiting a reorientation of the OH groups to the cubic symmetry

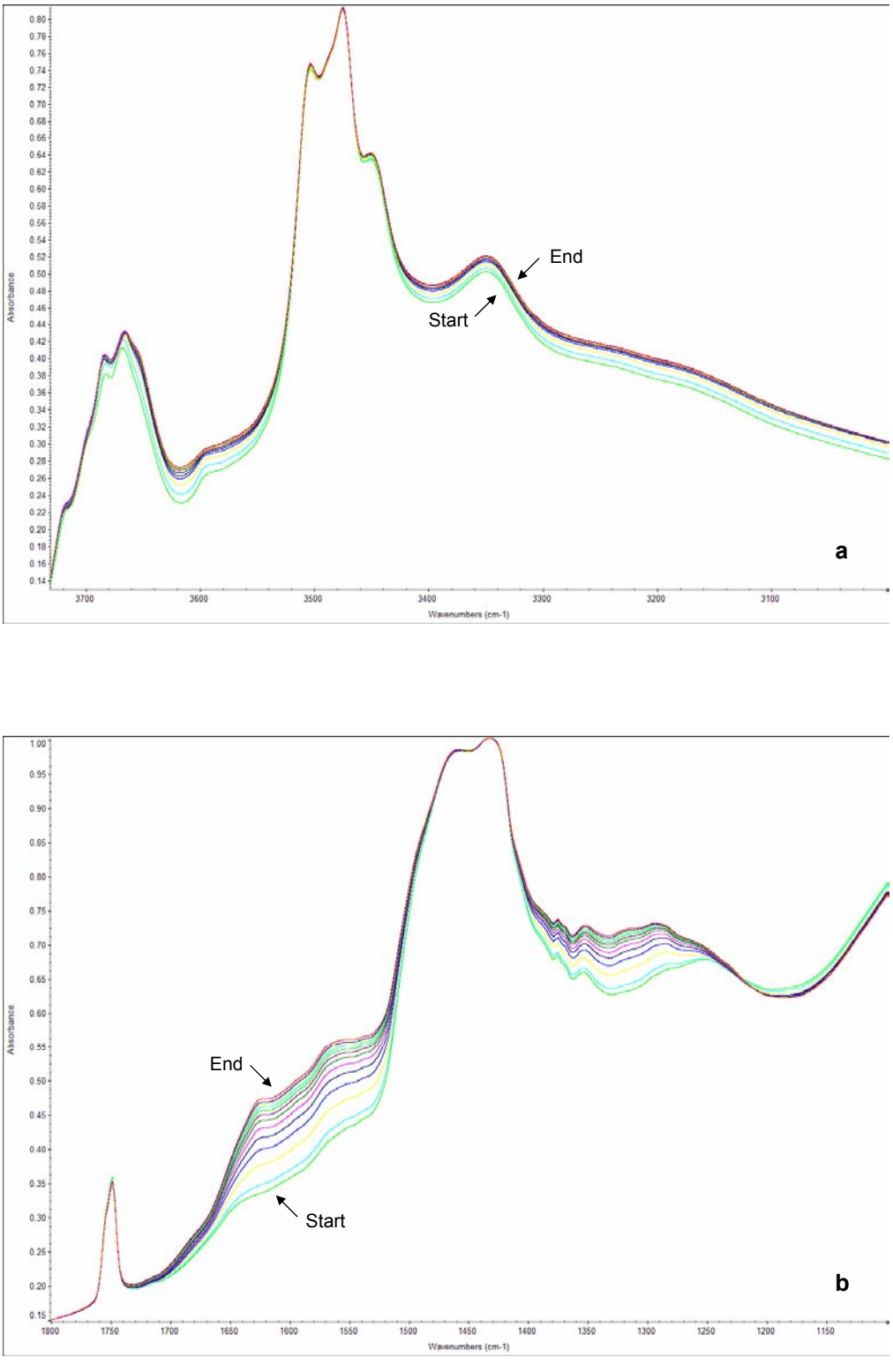

Figure 3.41. *In situ* HT-DRIFT spectra of moisture adsorption from dry air on Nanopowder D during 60 minutes at 383K: (a) OH_{vasym}, the asymmetric stretching band region of the hydroxyl, (b) HOH_{δ}, the molecular water bending mode region.

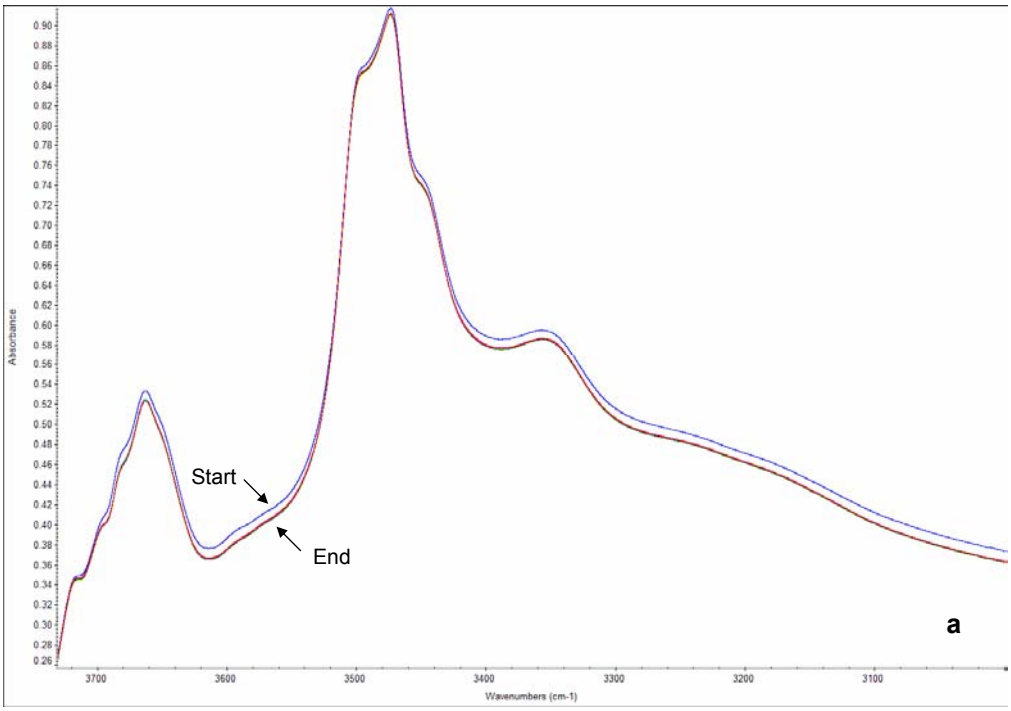

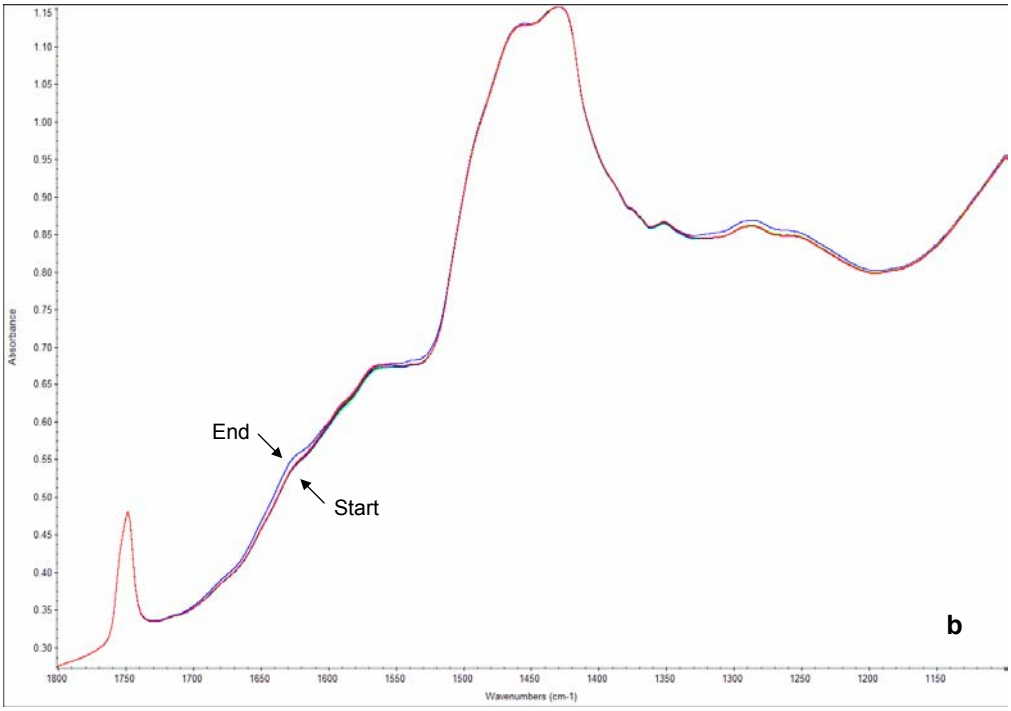

Figure 3.42. *In situ* HT-DRIFT spectra of moisture adsorption from dry air on Nanopowder D during 30 minutes at 473K: (a) OH_{vasym}, the asymmetric stretching band region of the hydroxyl, (b) HOH_{δ}, the molecular water bending mode region.

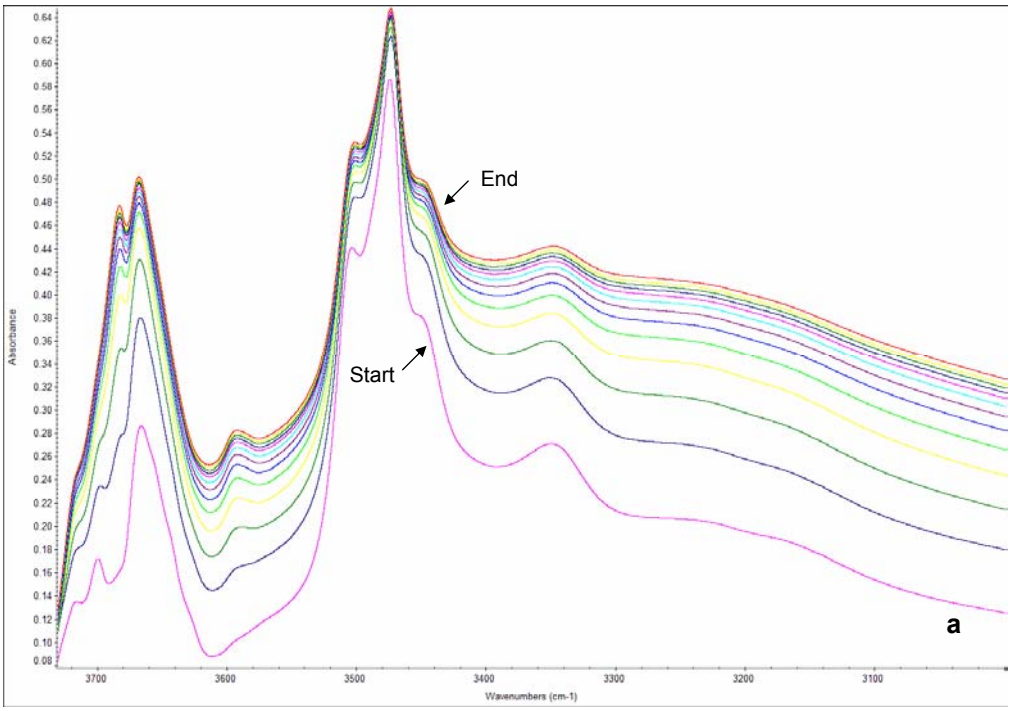

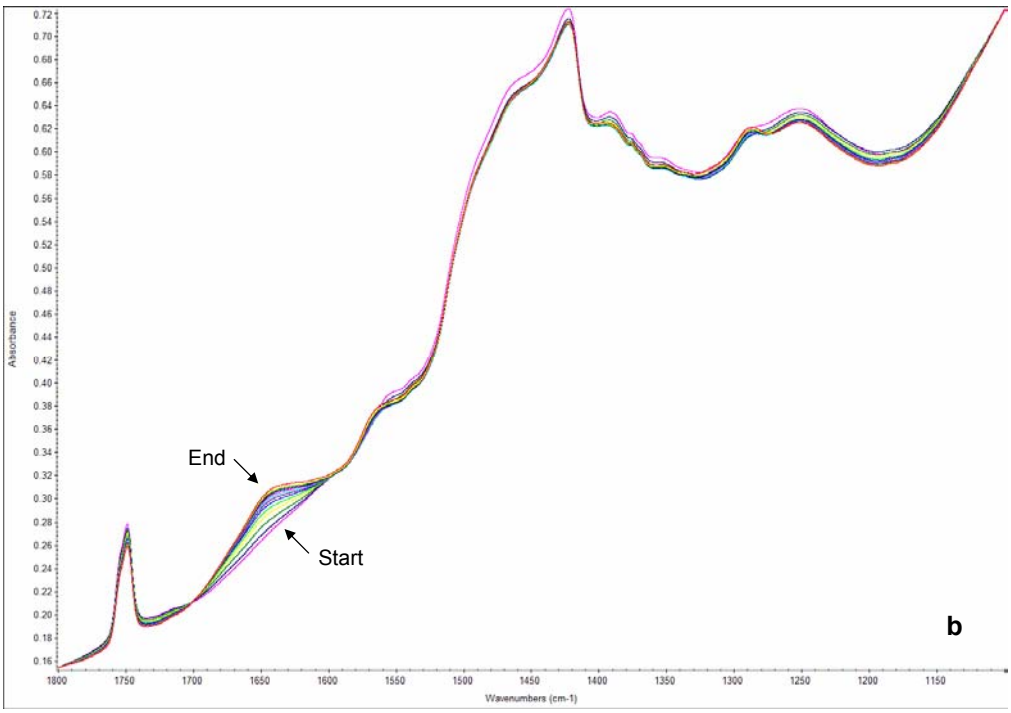

Figure 3.43. *In situ* HT-DRIFT spectra of moisture adsorption from UHP N_2 on Nanopowder E during 60 minutes at 383K: (a) OH_{vasym}, the asymmetric stretching band region of the hydroxyl, (b) HOH_{δ}, the molecular water bending mode region.

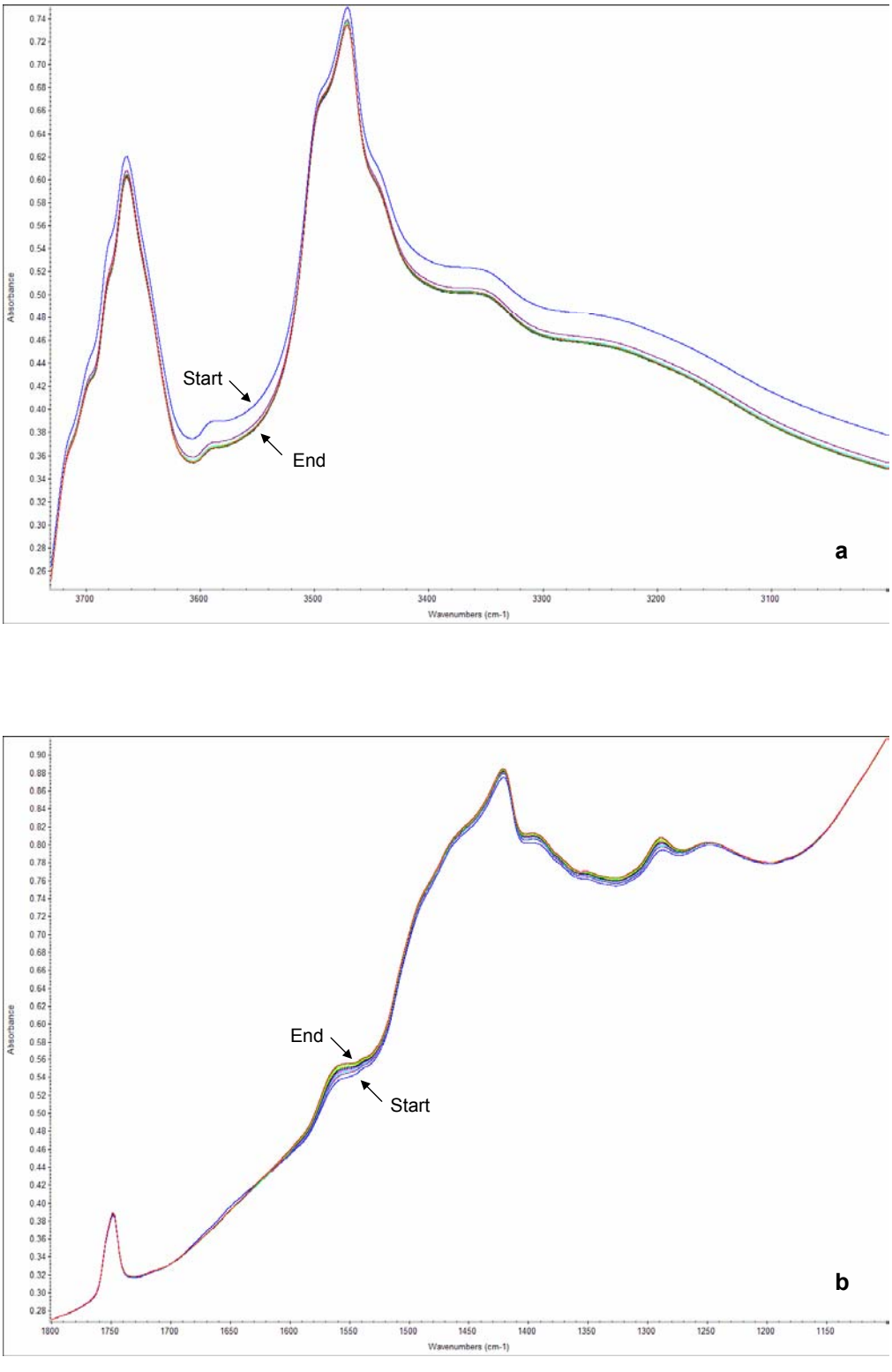

Figure 3.44. *In situ* HT-DRIFT spectra of moisture adsorption from UHP N_2 on Nanopowder E during 30 minutes at 473K: (a) $OH_{\nu asym}$, the asymmetric stretching band region of the hydroxyl, (b) HOH_{δ}, the molecular water bending mode region.

orientation.

The moisture adsorption spectra of Nanopowder E from the dry air supply during the 60 minute soak at 383K is shown with the OH bands, in the 3400 cm^{-1} to 3500 cm^{-1} region, and with the molecular water bending mode (1640 cm^{-1}) in Figures 3.45a and 3.45b, respectively. In contrast with Nanopowders C and D, Nanopowder E exhibited a reduction in hydroxyl levels in the 3400 cm^{-1} to 3500 cm^{-1} region. The lattice gas contribution was observed and was unchanged throughout the time duration. The molecular water, observed at 1640 cm^{-1} and overtones continuing through 1200 cm^{-1}, showed a moderate increase. Nanopowder E exhibited the highest concentration of hydroxyl and moisture of the nanopowders tested. The surfaces were most likely still saturated at the start of the readsorption testing, yielding the resultant continued loss in hydroxyl content.

The moisture adsorption spectra of Nanopowder E from the dry air supply during the 30 minute soak at 473K is shown with the OH bands in the 3400 cm^{-1} to 3500 cm^{-1} region and with the molecular water bending mode (1640 cm^{-1}) in Figures 3.46a and 3.46b, respectively. Similarly to Nanopowders C and D, a loss was observed in hydroxyl levels and a minor increase in the level of molecular water.

The moisture adsorption spectra of Nanopowder F from the UHP N_2 supply during the 60 minute soak at 383K is shown with the OH bands in the 3400 cm^{-1} to 3500 cm^{-1} region and with the molecular water bending mode (1640 cm^{-1}) in Figures 3.47a and 3.47b, respectively. The tetragonal bands were observed as well as the lattice gas contribution. An increase in hydroxyl level was seen, but a reduction in the level of molecular water, likely due to the greater surface area of this nanopowder that yielded an increased number of possible sites for hydroxyl adsorption during the heating period.

At the higher temperature (473K) soak under flowing UHP N_2, Nanopowder F exhibited a reduction in hydroxyl level and a small increase in molecular water (see Figures 3.48a and 3.48b). The lattice gas contribution was present as a broad low intensity band. The high and low wavenumber hydroxyl

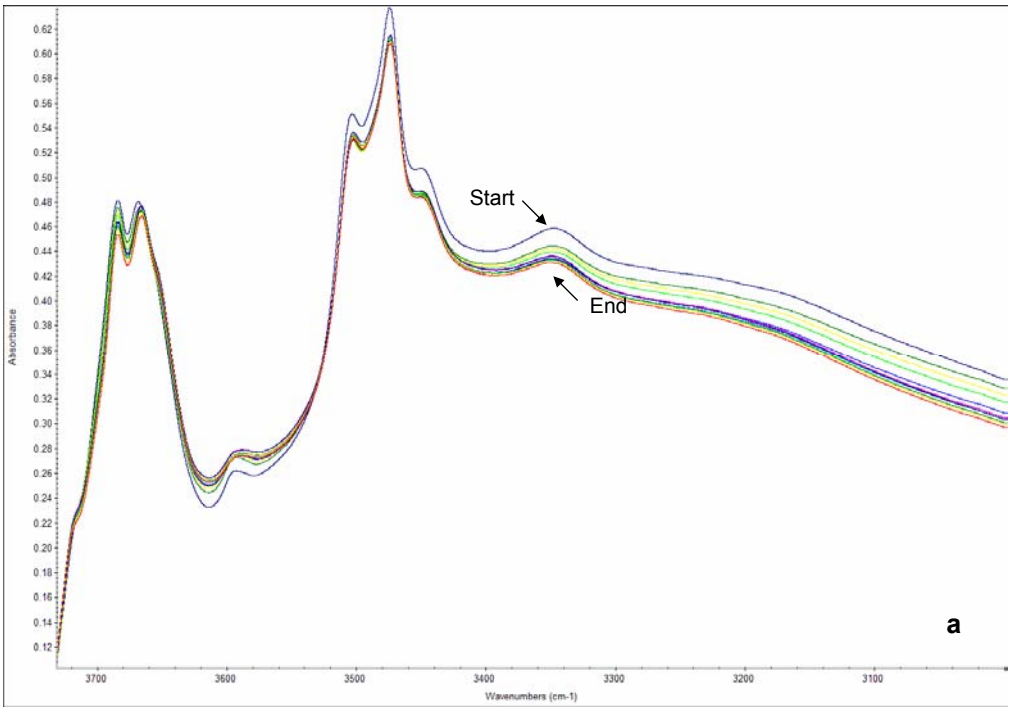

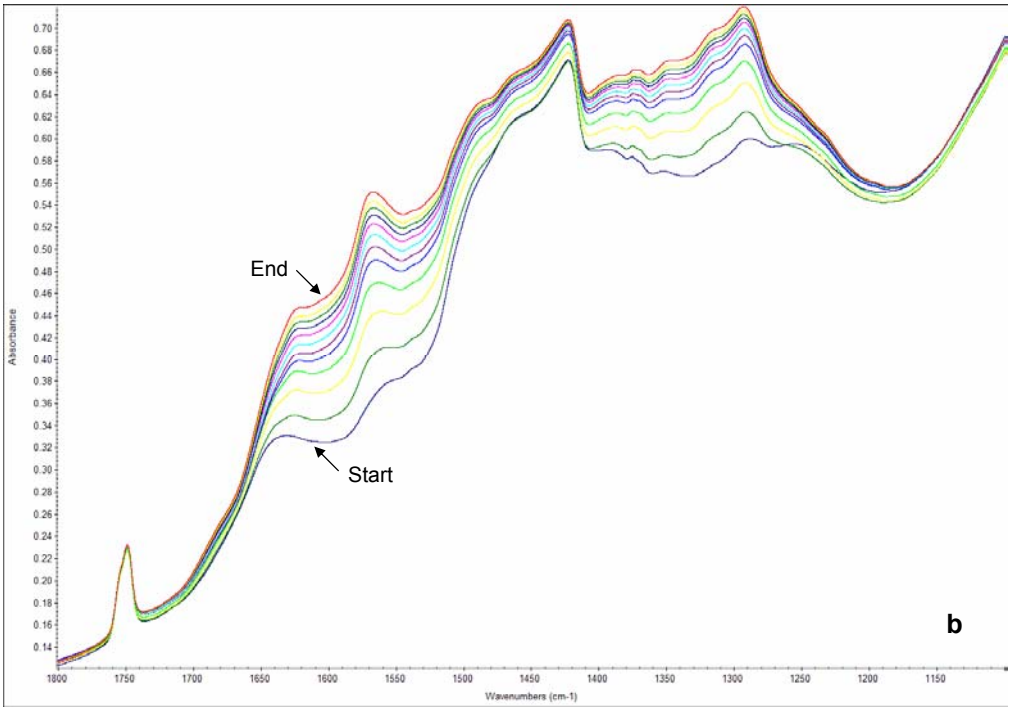

Figure 3.45. *In situ* HT-DRIFT spectra of moisture adsorption from dry air on Nanopowder E during 60 minutes at 383K: (a) OH_{vasym}, the asymmetric stretching band region of the hydroxyl, (b) HOH_{δ}, the molecular water bending mode region.

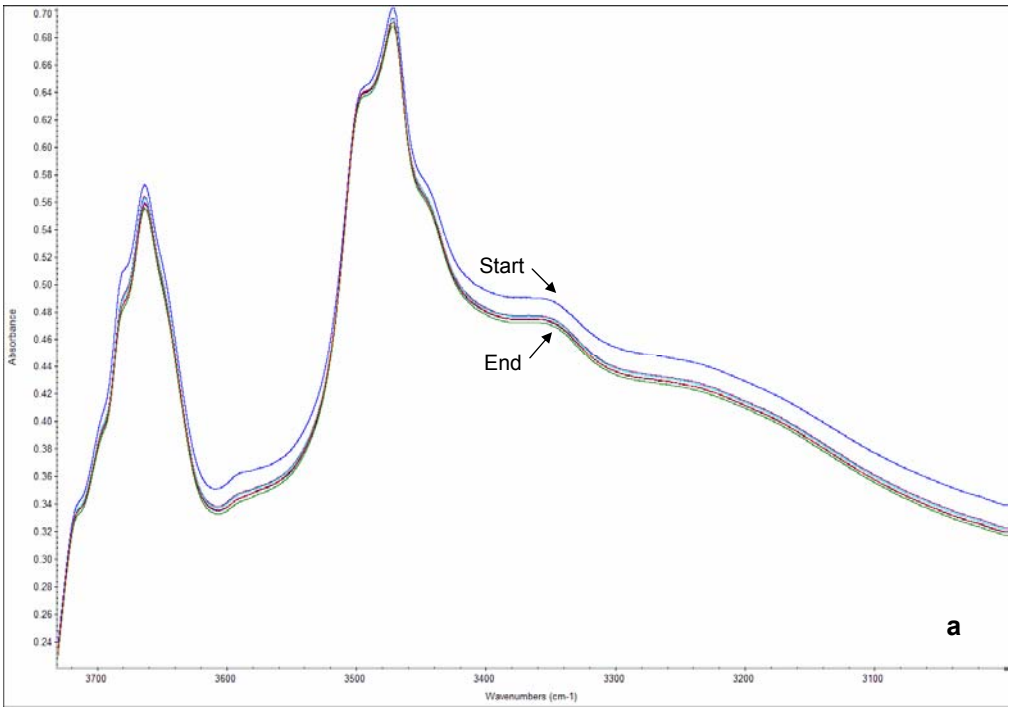

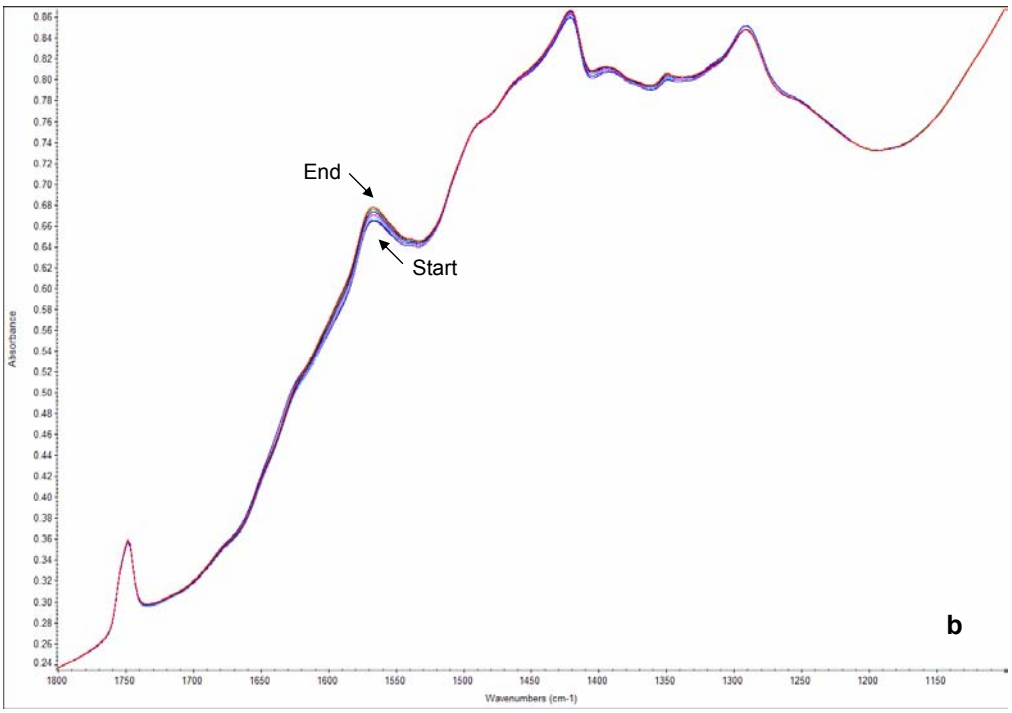

Figure 3.46. *In situ* HT-DRIFT spectra of moisture adsorption from dry air on Nanopowder E during 30 minutes at 473K: (a) OH_{vasym}, the asymmetric stretching band region of the hydroxyl, (b) HOH_{δ}, the molecular water bending mode region.

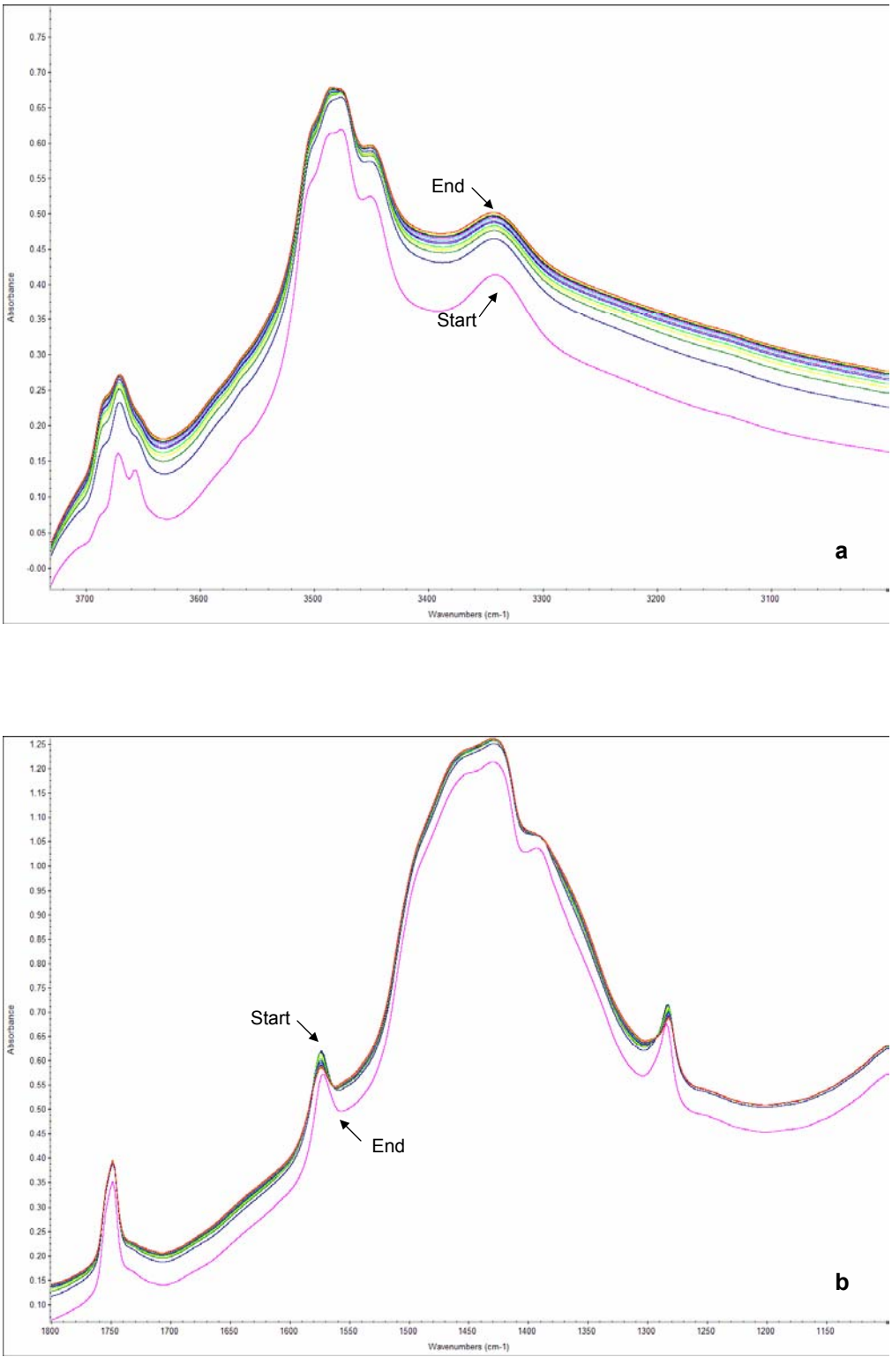

Figure 3.47. *In situ* HT-DRIFT spectra of moisture adsorption from UHP N_2 on Nanopowder F during 60 minutes at 383K: (a) OH_{vasym}, the asymmetric stretching band region of the hydroxyl, (b) HOH_{δ}, the molecular water bending mode region.

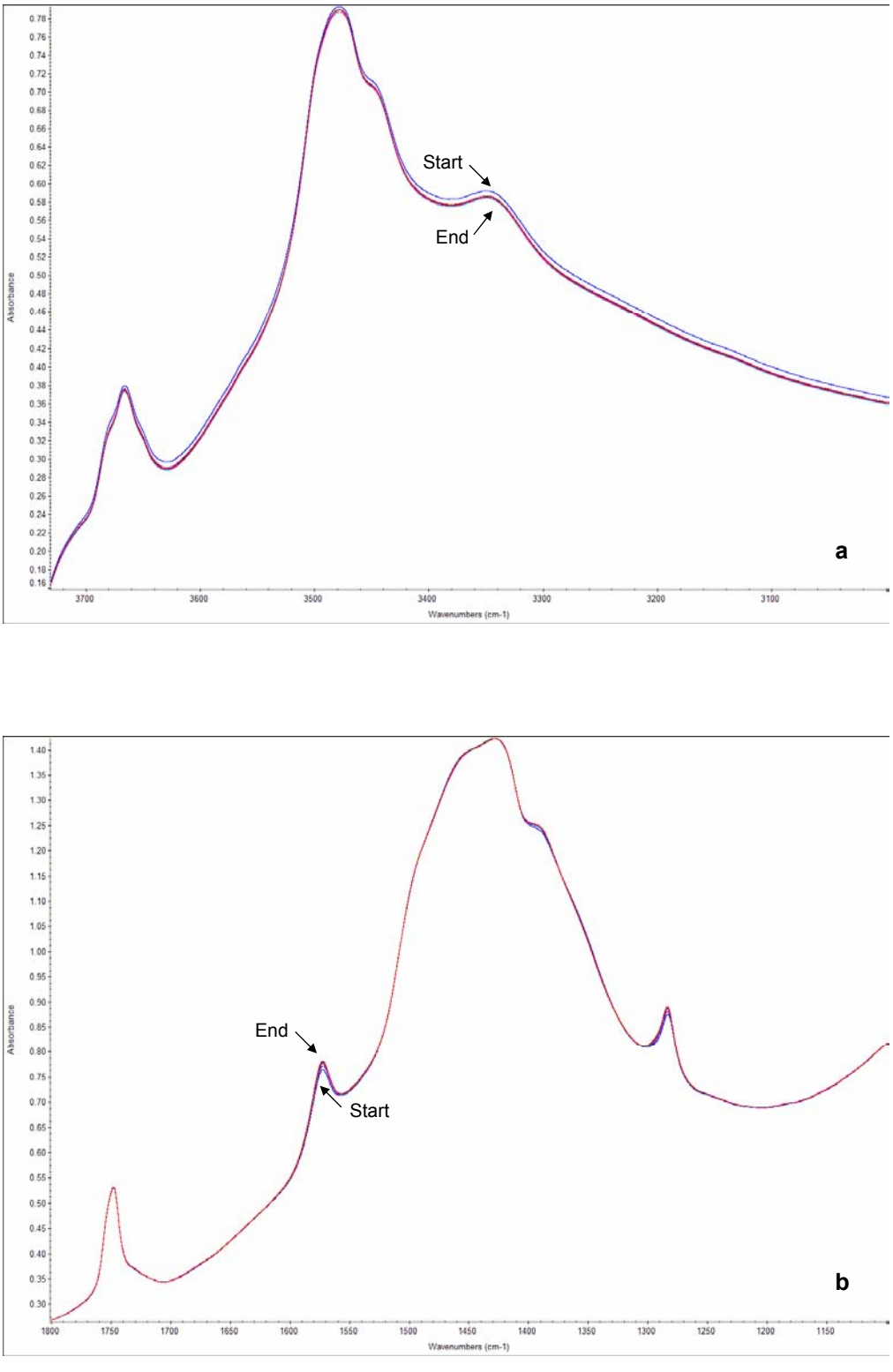

Figure 3.48. *In situ* HT-DRIFT spectra of moisture adsorption from UHP N_2 on Nanopowder F during 30 minutes at 473K: (a) OH_{vasym}, the asymmetric stretching band region of the hydroxyl, (b) HOH_{δ}, the molecular water bending mode region.

related bands were reduced, exhibiting a reorientation of the OH groups to the cubic symmetry orientation. These observations were similar to the three previous hydrothermal nanopowders.

The moisture adsorption spectra of Nanopowder F from the dry air supply during the 60 minute soak at 383K is shown with the OH bands in the 3400 cm^{-1} to 3500 cm^{-1} region and with the molecular water bending mode (1640 cm^{-1}) in Figures 3.49a and 3.49b, respectively. Increased hydroxyl concentration and molecular water are observed. The lattice gas was also observed and remains constant throughout the heating period.

The moisture adsorption spectra of Nanopowder F from the dry air supply during the 30 minute soak at 473K is shown with the OH bands in the 3400 cm^{-1} to 3500 cm^{-1} region and with the molecular water bending mode (1640 cm^{-1}) in Figures 3.50a and 3.50b, respectively. An increase was observed in both hydroxyl and molecular water during the heating period. The lattice gas band had broadened but remained constant throughout the time period.

Similar responses had been observed in the adsorption of moisture from the UHP N_2 and the dry air supplies by the nanopowders examined. The solid state nanopowders adsorbed far less than the hydrothermal nanopowders. Their surfaces were more stable, had a far lower initial moisture content and the available surface sites already bound by carbonate species. The lower initial heat treatment to clean the surfaces removed only a small amount of carbonate which allowed few new sites for moisture readsorption. The hydrothermal nanopowders had larger initial moisture content and with removal of some carbonate species during the initial heat treatment, provided a larger number of free surfaces for the readsorption of moisture.

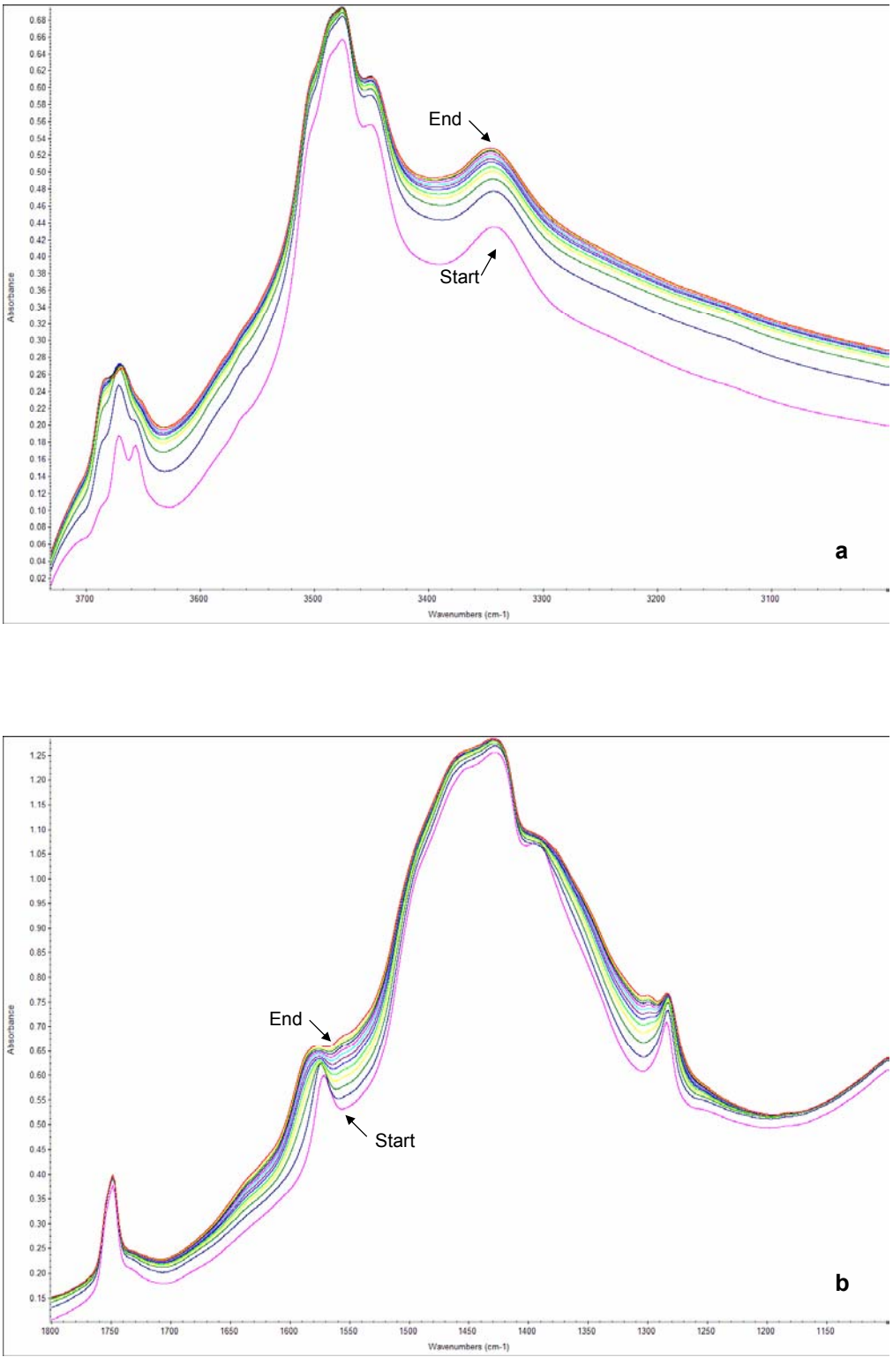

Figure 3.49. *In situ* HT-DRIFT spectra of moisture adsorption from dry air on Nanopowder F during 60 minutes at 383K: (a) OH_{vasym}, the asymmetric stretching band region of the hydroxyl, (b) HOH_{δ}, the molecular water bending mode region.

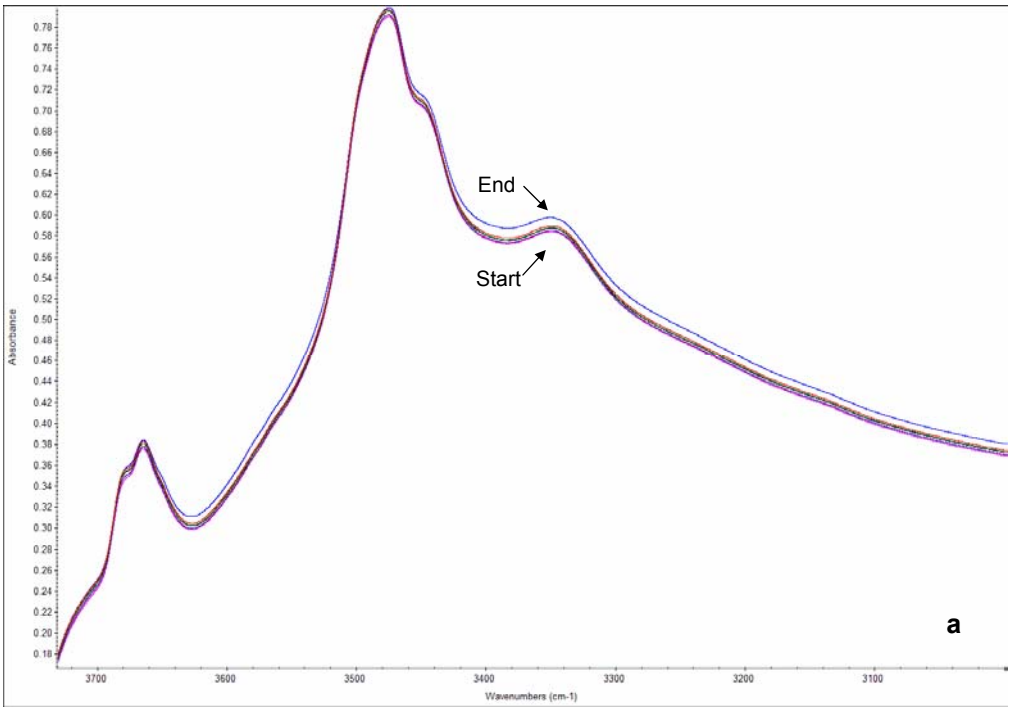

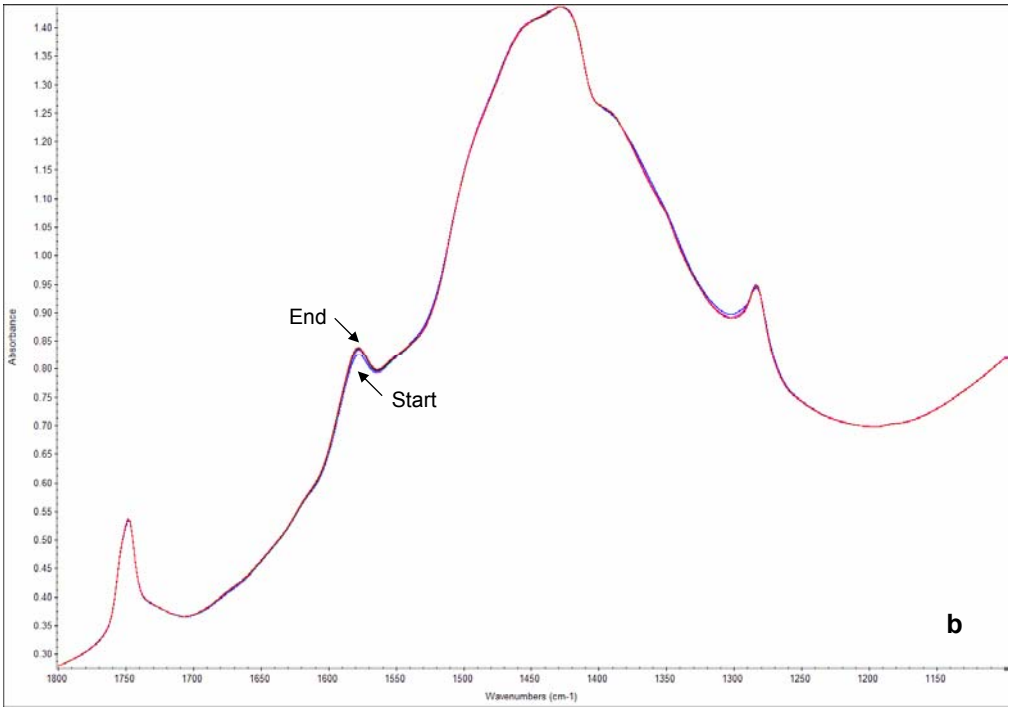

Figure 3.50. *In situ* HT-DRIFT spectra of moisture adsorption from dry air on Nanopowder F during 30 minutes at 473K: (a) OH_{vasym}, the asymmetric stretching band region of the hydroxyl, (b) HOH_{δ}, the molecular water bending mode region.

3.2.4 D_2O Study

3.2.4.1 Experimental Procedure

The hydrogen impurities that had been shown to exist in the nanopowders in fairly large amounts gave rise to the infrared adsorption bands 3509 cm^{-1}, 3475 cm^{-1} and 3451 cm^{-1} due to the OH stretching vibrations related to the Ti-O bonds in the oxygen octahedron. These modes had been shown to be sensitive to the cubic - tetragonal structural phase transition. In order to more closely study behavior of these modes, the exchange reaction between the incorporated OH groups and OD groups during treatment with deuterium oxide was investigated.

The large relative change in the mass of the hydrogen atom between OH and OD has a strong influence on the wavenumber of the vibrational modes. Calculating the shift in vibrational wavenumber between $\tilde{\upsilon}_{OH}$ and $\tilde{\upsilon}_{OD}$ using reduced masses results in a ratio of $\tilde{\upsilon}_{OH}/\tilde{\upsilon}_{OD} \approx \sqrt{2}$.[123-25] The actual shift will be slightly lower than this 1.41 value since the assumption that the force constants $k_H = k_D$ is reasonable for making the calculations. The OH/OD vibrational wavenumbers have experimentally been found to approximate this ratio.[123-24] The exchange of OD for OH at the sites of interest should therefore be observed in the 2500 – 2600 cm^{-1} region.

To examine these processes *in situ* HT-DRIFT spectra were obtained of all nanopowders up to 1173K. A Spectra-Tech Smart Collector (Model 0031-999, Thermo Spectra-Tech, Stanford, CT) with an optional environmental cell (Model 0030-005, Thermo Spectra-Tech, Stanford, CT) was used in conjunction with the Nicolet Nexus 670 FT-IR to make the *in situ* high temperature measurements.

The nanopowders were examined neat (i.e. as-received, so as not to disturb the surface layers and to improve the surface sensitivity of the technique). The heating chamber of the environmental cell has dimensions of 5 mm diameter by 3 mm depth and accommodates ~50 milligrams of nanopowder. A background spectrum was taken using the polished aluminum coated mirror in

the standard Smart Collector sample holder, similar to the previous HT-DRIFT technique, and auto subtracted from the final sample spectrum by the Omnic 6.0 software package. Spectra were obtained at a resolution of 4 cm^{-1} with 500 cumulative scans to form the final spectrum between 650 cm^{-1} and 4000 cm^{-1}. A continuous flow of ultra high purity (UHP) nitrogen gas was provided at a rate of 150 ml/minute.

A bubbler was added to the gas flow system to introduce D_2O to the nanopowder samples. Figure 3.51 indicates the system used for controlling the flow of gas into the environmental cell. Two switching valves were incorporated in controlling the introduction of D_2O to the samples in the environmental cell during the exchange process.

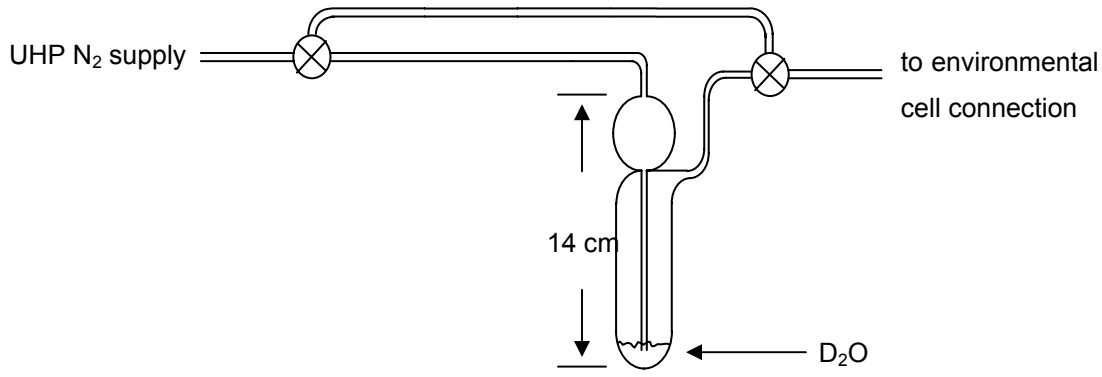

Figure 3.51. Set up for the control of gas flow into the *in situ* high temperature environmental chamber during the D_2O Study.

The nanopowders were initially heat treated at 773K for 2 hours under the UHP N_2 gas flow. Temperature was then reduced to 383K and gas flow through the D_2O bubbler initiated. After one hour, while still under D_2O flow, the temperature was increased to 473K and held for an additional hour. After this time the D_2O was stopped, the temperature in the environmental cell reduced to room temperature and the UHP N_2 flow reinitiated for a period of 30 minutes to purge the system of D_2O.

Spectra for each nanopowder were obtained at room temperature and at 5 minute intervals through the 60 minute duration of each temperature soak (383K and 473K). A final spectrum was obtained after the sample was cooled to room temperature under a 30 minute UHP N_2 purge.

3.2.4.2 Results and Discussion

The spectra for the deuterium exchange are exhibited in Figures 3.52 through 3.57 for Nanopowders A through F, respectively. Exchange of D_2O and the OD groups for H_2O and OH groups was observed in each of the nanopowders. The exchange was seen as a reduction of the OH related bands and the subsequent increase in the OD bands.

As expected, due to their low initial moisture content, the deuterium exchange for Nanopowders A and B showed minor increases in the expected wavenumber range of 2500 – 2600 cm^{-1}. A weak broad band was observed between 2600 cm^{-1} and 2200 cm^{-1}. The weakly bound H_2O was observed in these nanopowders as a very broad band between 3600 cm^{-1} and 2700 cm^{-1} during the initial DRIFT characterization. This wavenumber shift was within the predicted calculated range. This lower wavenumber band, therefore, was attributed to weakly bound D_2O.

The remaining nanopowders, having larger initial moisture content than the solid state nanopowders, exhibited a greater exchange of D_2O for H_2O. The weakly bound D_2O was observed as the broad band between 2600 cm^{-1} and 2200 cm^{-1}. Three OD bands were observed in the 2600 cm^{-1} to 2570 cm^{-1} region indicating the presence of the three Ti – O bond lengths of the tetragonal structure. These room temperature tetragonal Ti – O bond related OD bands were very prominent (see Figure 3.58). The presence of an OD lattice gas was also observed as a band near 2480 cm^{-1} for each of the nanopowders.

Molecular water was observed prior to the deuterium exchange, as listed in Table 3.1.1. Molecular deuterium oxide was observed along with molecular water after cooling the nanopowders under the UHP N_2 flow, seen in Figure 3.59. The low relative absorbance observed was related to a small amount of the

adsorbed molecular species. This was a reasonable finding considering the manner of introduction of D_2O to the nanopowders.

The shift in wavenumber between $\tilde{\upsilon}_{OH}$ and $\tilde{\upsilon}_{OD}$ is approximately 1.35 and, as predicted, slightly lower than the calculated 1.41 value. All three Ti – O related OD bands, the OD lattice gas and the molecular D_2O band exhibited this value for the shift in vibrational wavenumber. Table 3.6 lists the relevant bands and their subsequent wavenumber shifts for the four hydrothermal nanopowders.

Table 3.6 D_2O Exchange Infrared Band Wavenumbers and Their Shifts

Band	C	D	E	F
Lattice OH	3508	3507	3500	3498
Lattice OD	2595	2595	2595	2593
ν_{shift}	1.352	1.351	1.349	1.349
Lattice OH	3475	3477	3476	3477
Lattice OD	2583	2583	2582	2583
ν_{shift}	1.345	1.346	1.346	1.346
Lattice OH	3451	3451	3449	3451
Lattice OD	2573	2573	2573	2571
ν_{shift}	1.341	1.341	1.340	1.342
Lattice Gas_{OH}	3343	3343	3339	3338
Lattice Gas_{OD}	2476	2481	2479	2477
ν_{shift}	1.350	1.347	1.347	1.348
Molecular H_2O	1629	1631	1626	1618
Molecular D_2O	1208	1209	1206	1201
ν_{shift}	1.348	1.349	1.342	1.347

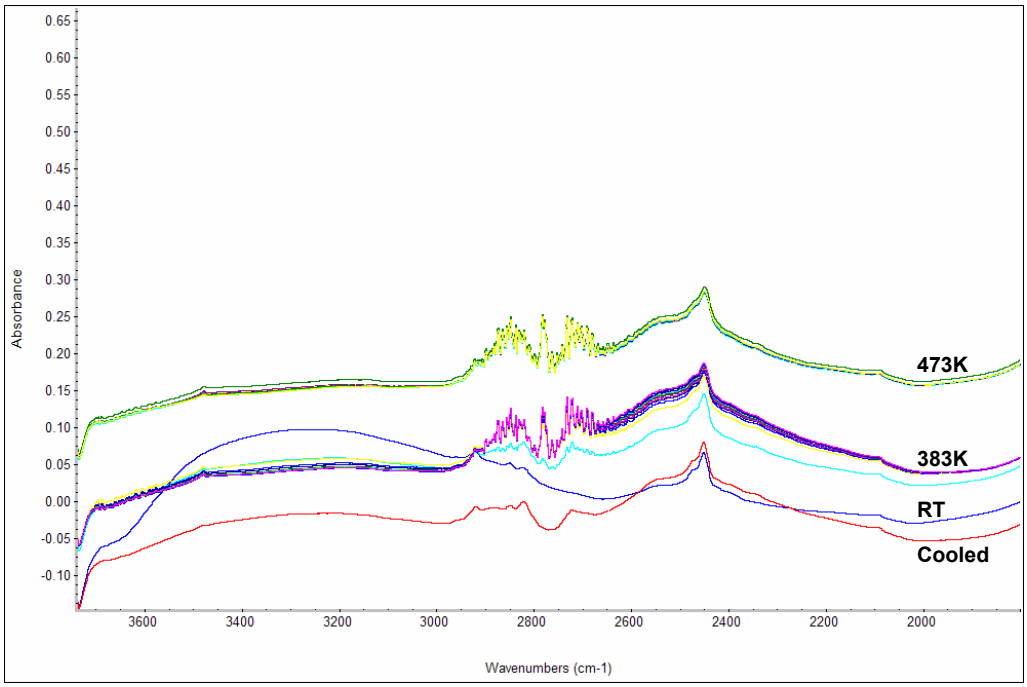

Figure 3.52. *In situ* HT-DRIFT spectra of Nanopowder A under D_2O at 383K and 473K temperature soaks; also under UHP N_2 flow at RT and after cooling to 298K.

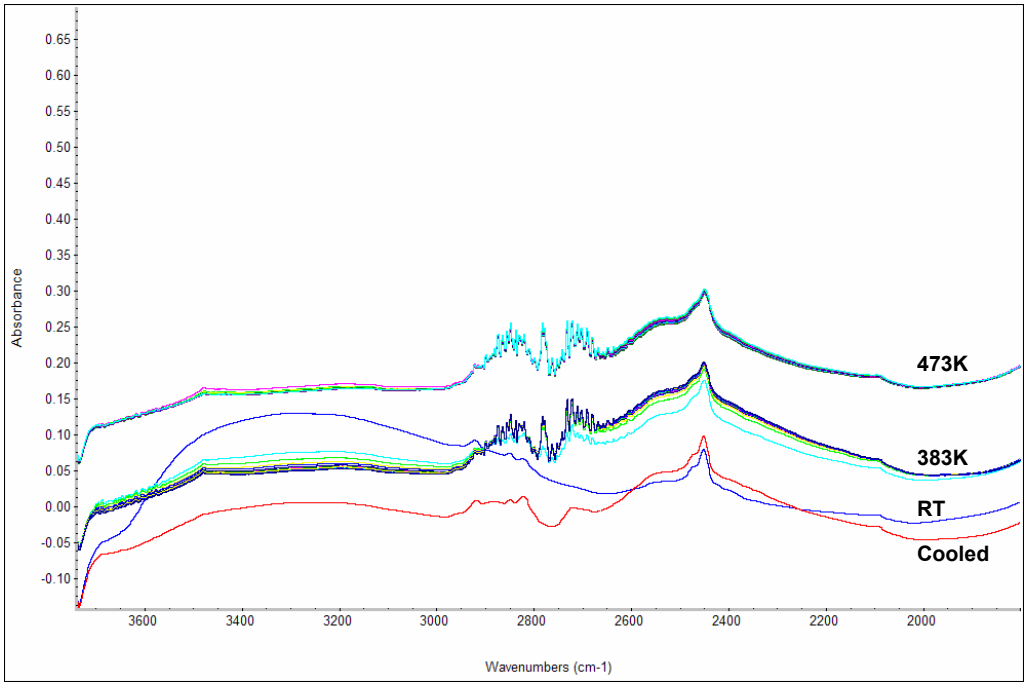

Figure 3.53. *In situ* HT-DRIFT spectra of Nanopowder B under D_2O at 383K and 473K temperature soaks; also under UHP N_2 flow at RT and after cooling to 298K.

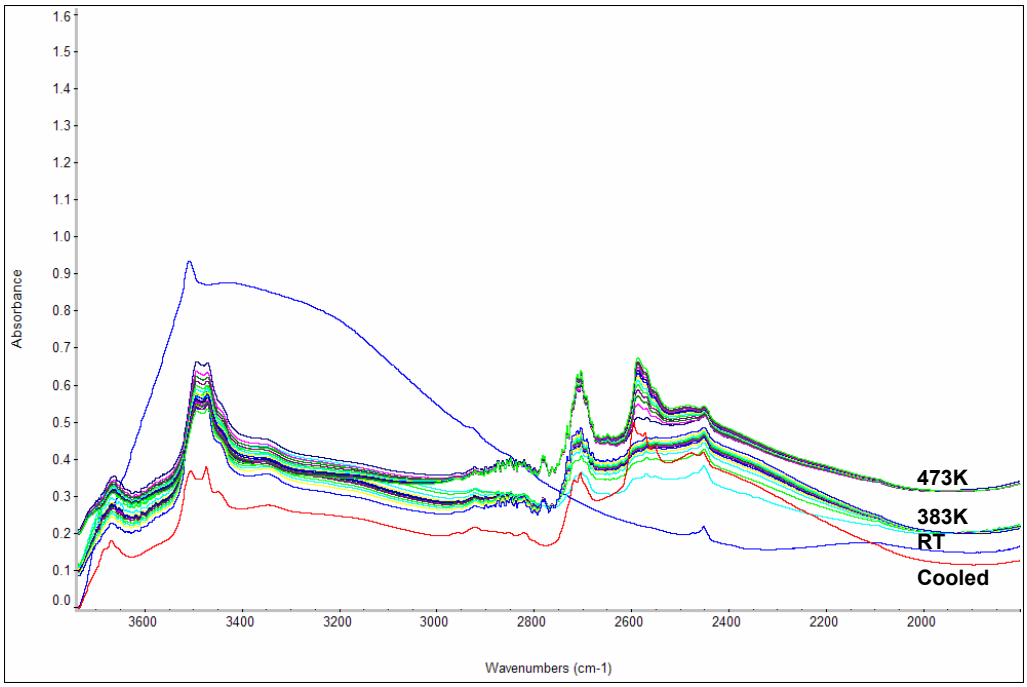

Figure 3.54. *In situ* HT-DRIFT spectra of Nanopowder C under D_2O at 383K and 473K temperature soaks; also under UHP N_2 flow at RT and after cooling to 298K.

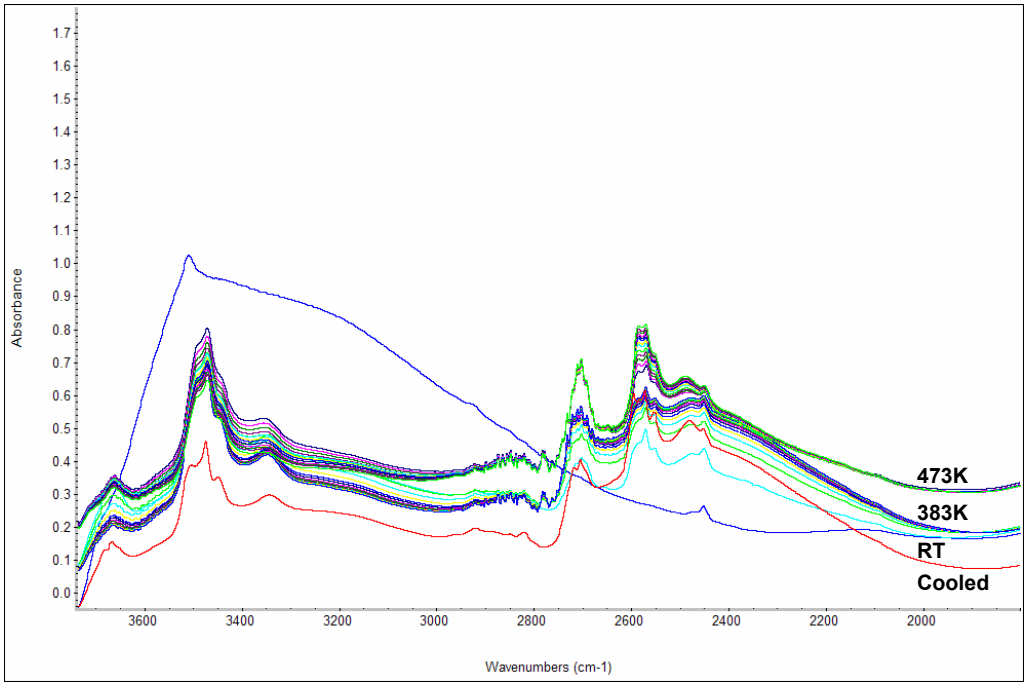

Figure 3.55. *In situ* HT-DRIFT spectra of Nanopowder D under D_2O at 383K and 473K temperature soaks; also under UHP N_2 flow at RT and after cooling to 298K.

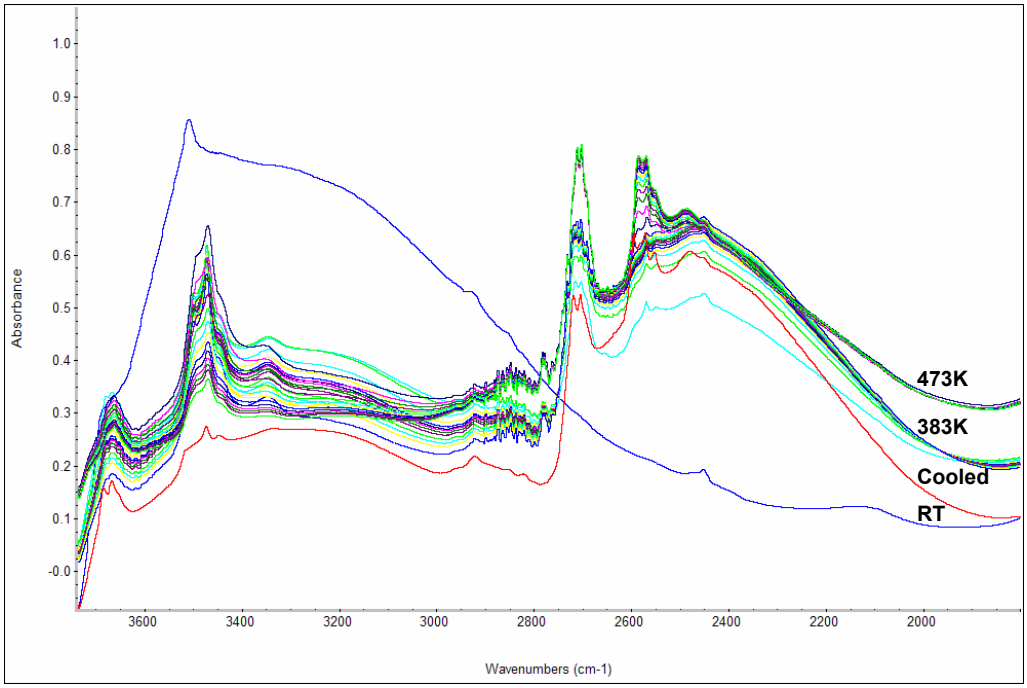

Figure 3.56. *In situ* HT-DRIFT spectra of Nanopowder E under D_2O at 383K and 473K temperature soaks; also under UHP N_2 flow at RT and after cooling to 298K.

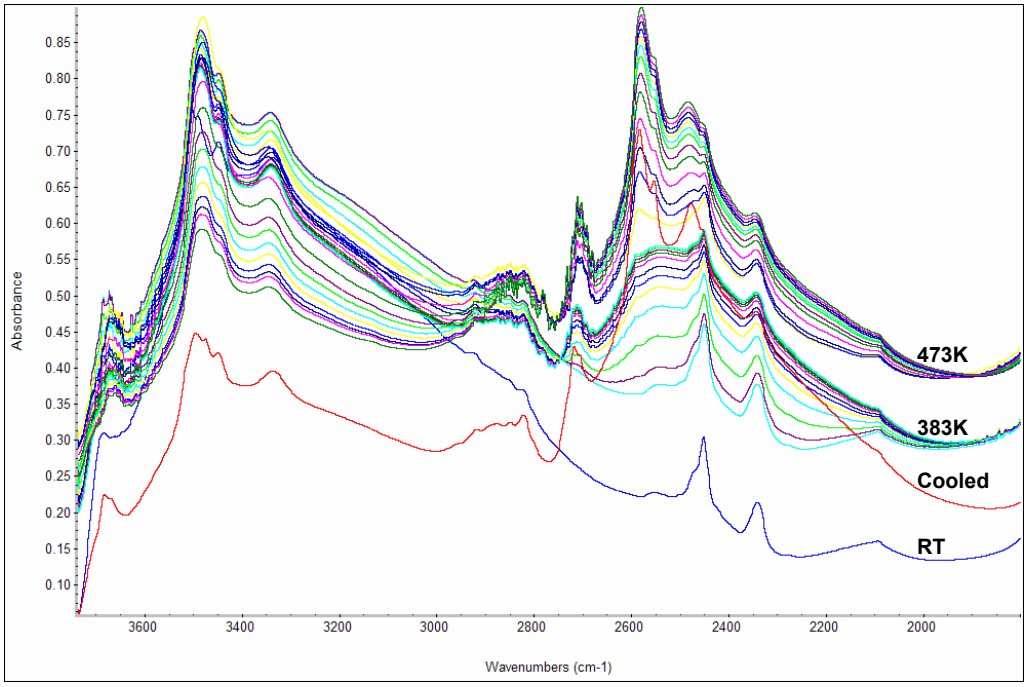

Figure 3.57. *In situ* HT-DRIFT spectra of Nanopowder F under D_2O at 383K and 473K temperature soaks; also under UHP N_2 flow at RT and after cooling to 298K.

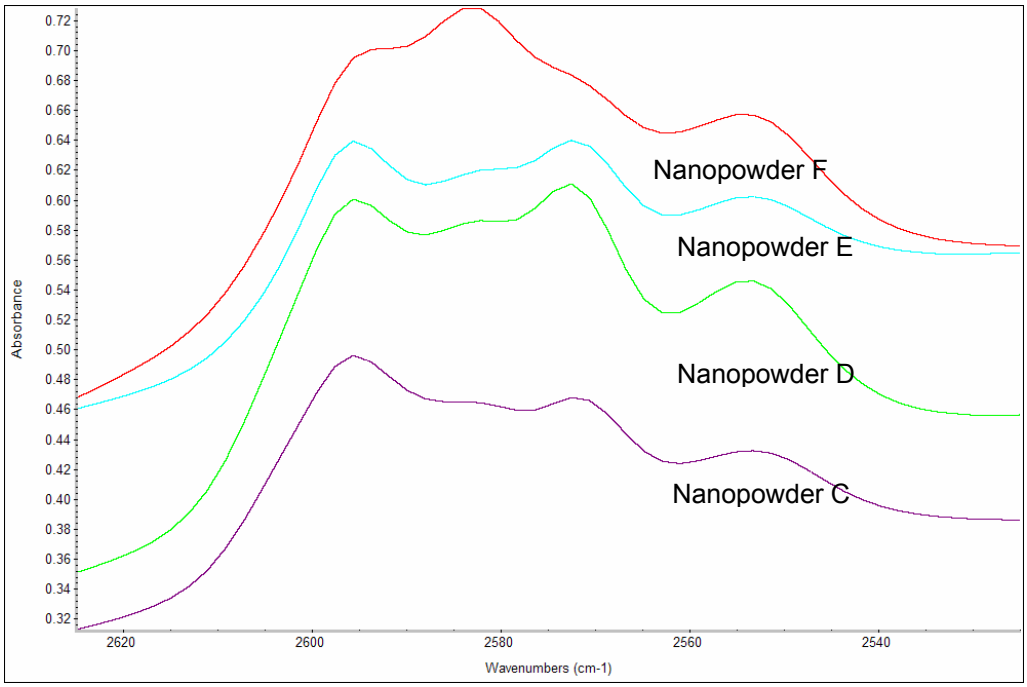

Figure 3.58. *In situ* HT-DRIFT spectra of the tetragonal related OD bands and the accompanying lattice gas band after cooling to room temperature under UHP N_2 flow for each of the hydrothermal nanopowders; stacked common scale.

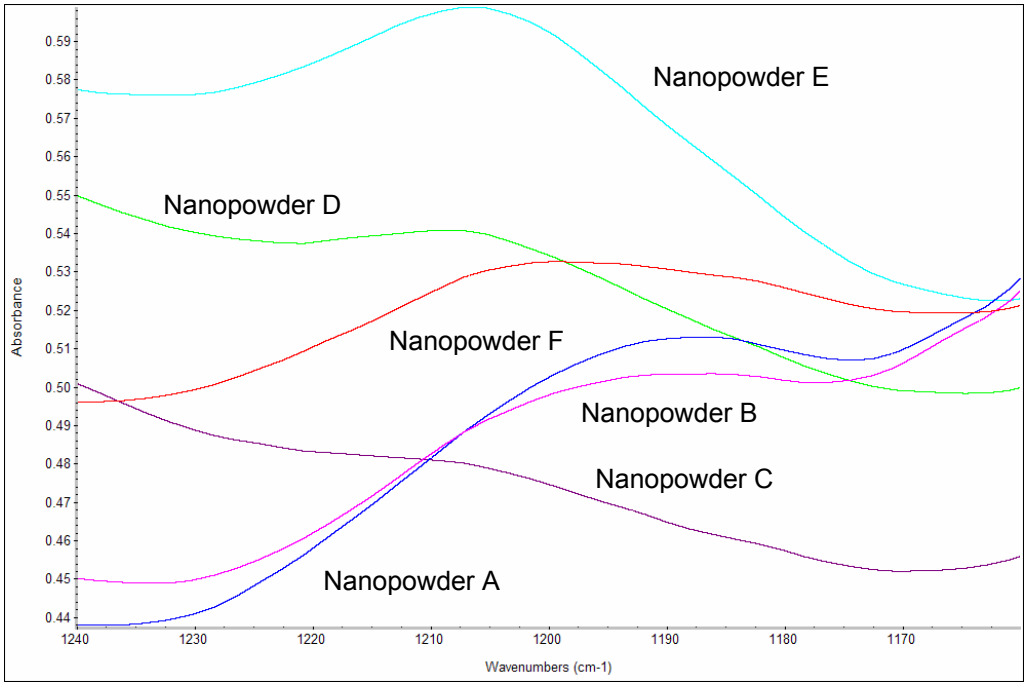

Figure 3.59. *In situ* HT-DRIFT spectra of molecular D_2O bands after cooling to room temperature under UHP N_2 flow for each of the nanopowders; stacked common scale.

The OD group's affinity for the nanopowders during the deuterium exchange was similar to that of the OH groups during the readsorption study. The deuterium exchange produced three OD bands observed at the predicted frequency shift from the three Ti – O related OH bands previously described. Therefore, the presence of these three OD bands also indicates a room temperature tetragonal structure for the heat treated nanopowders.

3.2.5 CO_2 Study

3.2.5.1 Experimental Procedure

Carbonate groups, along with the hydroxyl groups, represented the major impurity species in the nanopowders analyzed. The carbon dioxide molecule is normally linear; however, the molecule may become bent increasing its acceptor character. This leads to a Lewis acid/base reaction allowing the formation of the surface carbonate CO_3^{2-}. Along a BaO plane this may proceed in the formation of bulk carbonate as $BaCO_3$.[77,86,126-27] The chemisorption of the linear CO_2^- is generally formed when surfaces are anatomically rough or when the surface contains a high concentration of defects. The Ti-(CO_2) linear complex was shown to be the lowest energy form of attachment.[82,87] This section attempts to investigate the affinity of the carbonate species for the barium titanate nanopowders.

A dry air supply was utilized as a source of CO_2 for the study. The CO_2 concentration of ambient air is 0.038 vol%.[128(p.14-19)] The moisture content of the dry air utilized was <6 ppm. This level was shown in previous sections to be a high enough concentration for OH adsorption to occur. The reaction temperature was, therefore, held at 523K to alleviate the issue of moisture and carbonate competing for adsorption on available sites. The temperature also provides the thermal energy necessary for carbonate adsorption.

The nanopowders were subjected to a two hour soak at 1173K, the environmental cell's upper temperature limit, under flowing UHP N_2 at a rate of 150 ml/minute. The temperature was then reduced to 523K, a flowing dry air initiated to replace the UHP N_2 and held at this temperature for one hour. The temperature of the environmental cell was then reduced to room temperature and returned to the flowing UHP N_2. A schematic representation of the gas flow set up is shown in Figure 3.60.

The nanopowders were, as in previous studies, examined neat, i.e. as-received, so as not to disturb the surface layers and to improve the surface sensitivity of the technique. A background spectrum was taken using the polished aluminum coated mirror in the standard Smart Collector sample holder,

similar to the previous HT-DRIFT technique, and auto subtracted from the final sample spectrum by the Omnic 6.0 software package. Spectra were obtained at a resolution of 4 cm^{-1} with 500 cumulative scans to form the final spectrum between 650 cm^{-1} and 4000 cm^{-1}.

Spectra for each nanopowder were obtained at room temperature, at the end of the 1173K soak, and at 5 minute intervals through the 60 minute duration of the 523K temperature soak. A final spectrum was obtained after the sample was cooled to room temperature under a 30 minute UHP N_2 purge.

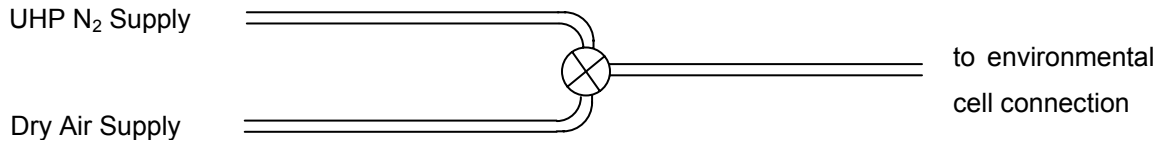

Figure 3.60. Schematic of the gas atmosphere supply to the environmental cell.

3.2.5.2 Results and Discussion

The readsorption of the carbonate species proved less probable than the readsorption of moisture. The two hour soaks at 1173K under flowing dry air (see Figures 3.61, 63, 65, 67, 69 and 71) indicated the resultant carbonate levels greatly reduced from their initial levels. The major carbonate bands, 2451 cm^{-1} and 1751 cm^{-1}, were no longer apparent. The lattice and surface carbonate species, between 1420 cm^{-1} and 1470 cm^{-1}, were also no longer apparent. Nanopowder F was the exception; after 2 hours at the 1173K soak carbonate remained as a moderate, broad band in the 1400 cm^{-1} region. The lattice and surface carbonates were seen as weak, broad bands.

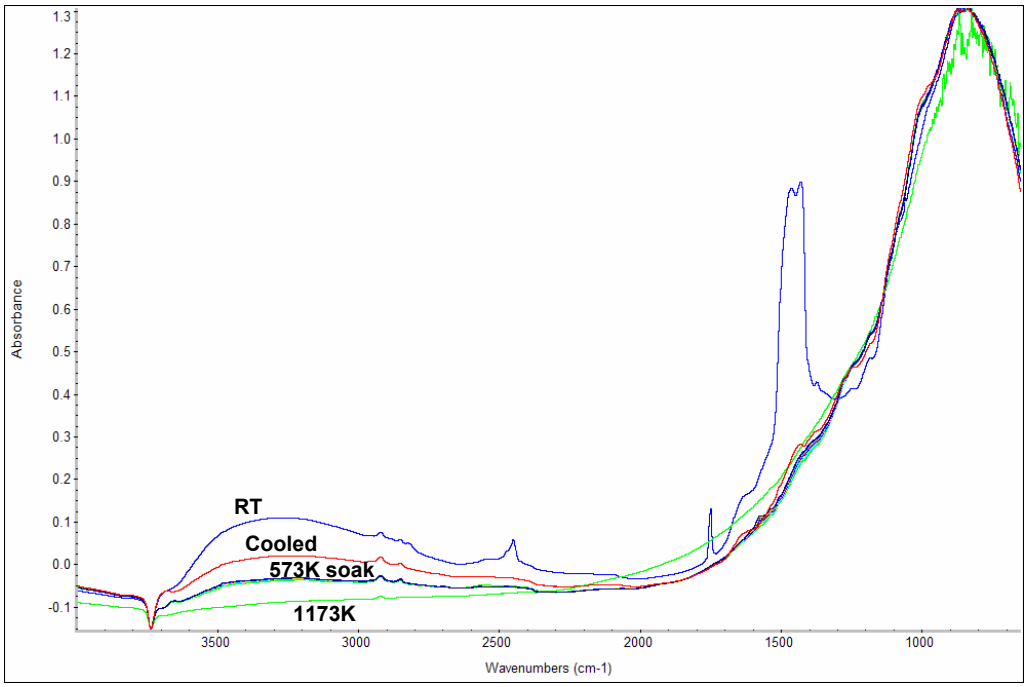

Figure 3.61. *In situ* HT-DRIFT spectra of Nanopowder A under flowing dry air at a 523K temperature soak; also under UHP N_2 flow at RT and after cooling to 298K.

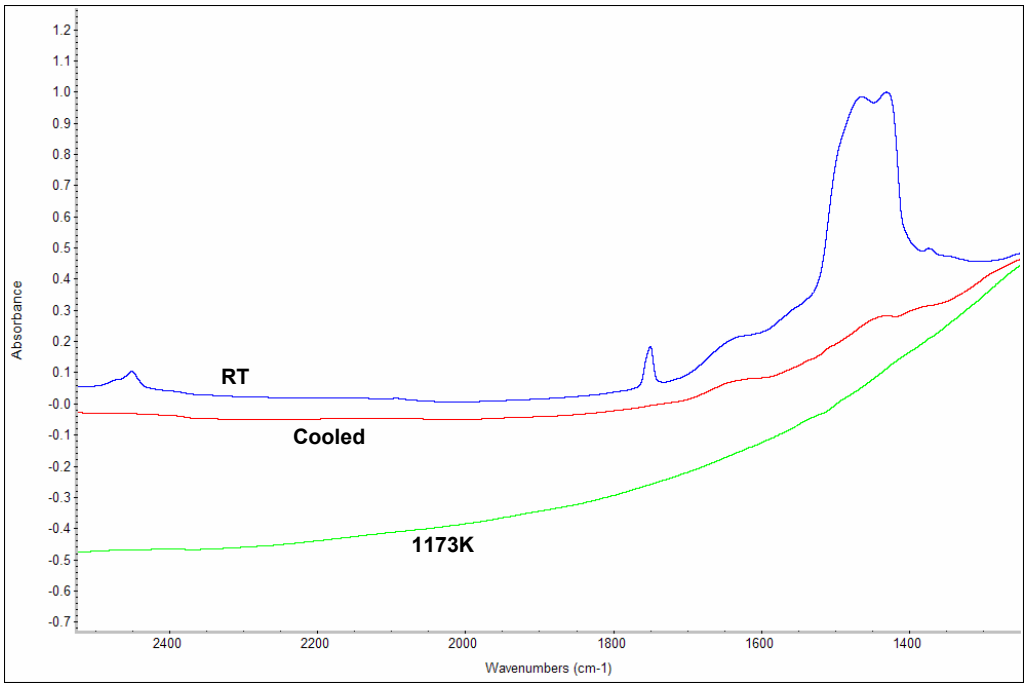

Figure 3.62. *In situ* HT-DRIFT spectra of Nanopowder A under UHP N_2 flow at RT, 1173K and after cooling to 298K in the spectral range 2525 cm^{-1} to 1250 cm^{-1}; stacked, common scale.

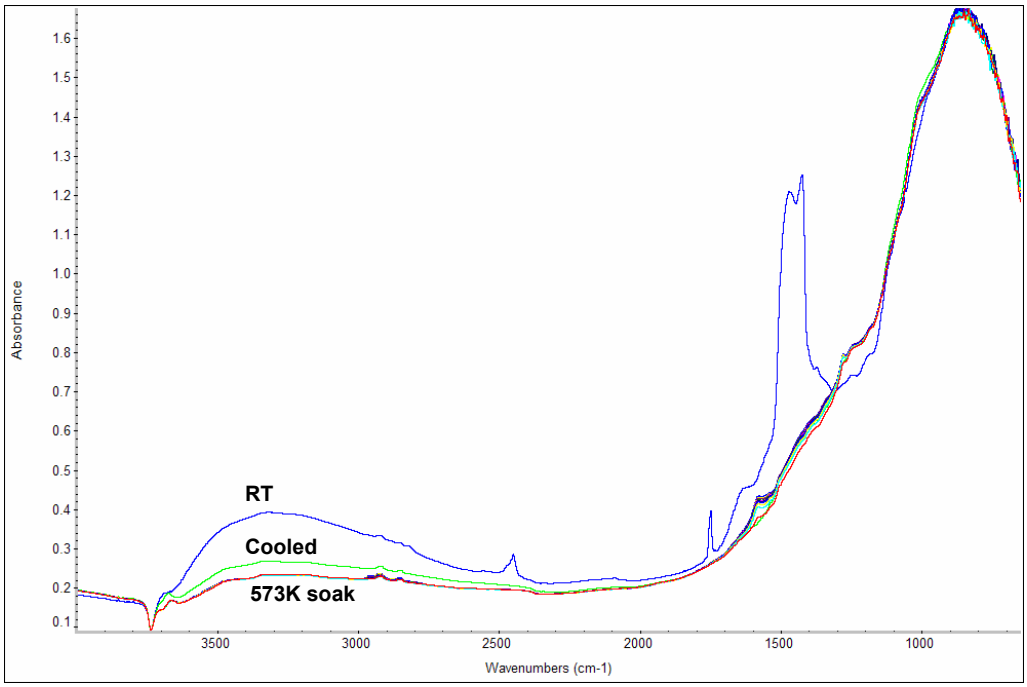

Figure 3.63. *In situ* HT-DRIFT spectra of Nanopowder B under flowing dry air at a 523K temperature soak; also under UHP N_2 flow at RT and after cooling to 298K.

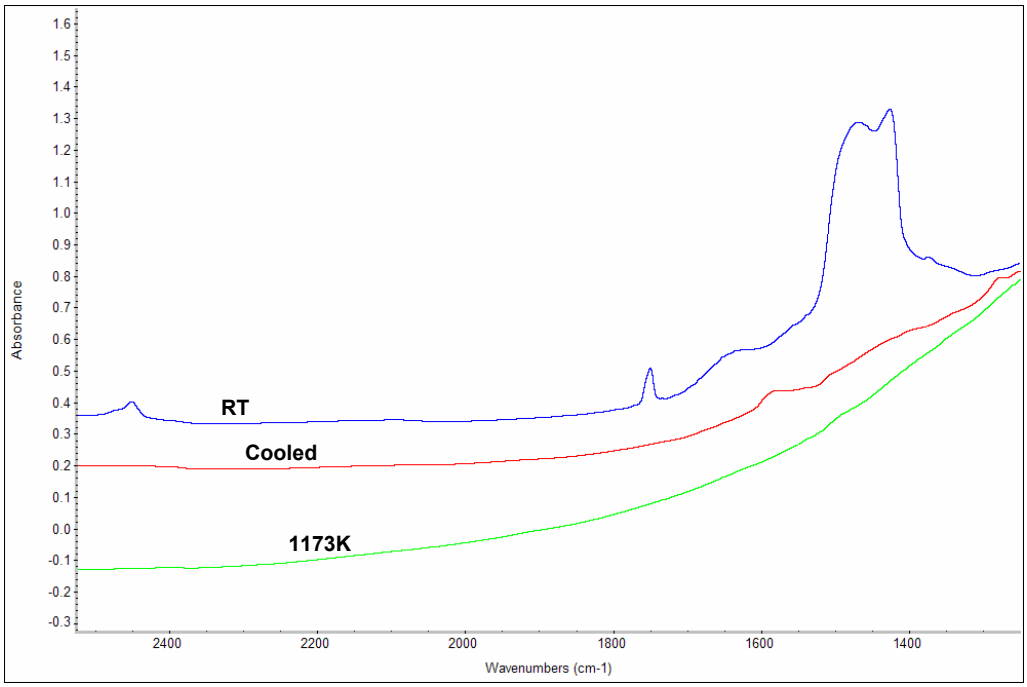

Figure 3.64. *In situ* HT-DRIFT spectra of Nanopowder B under UHP N_2 flow at RT, 1173K and after cooling to 298K in the spectral range 2525 cm^{-1} to 1250 cm^{-1}; stacked, common scale.

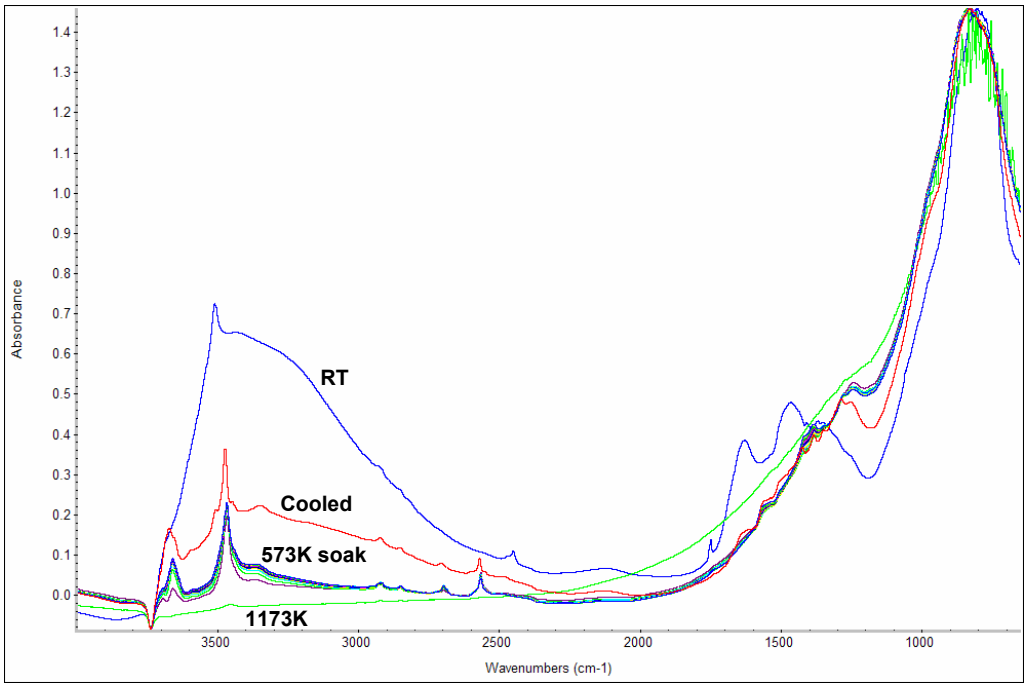

Figure 3.65. *In situ* HT-DRIFT spectra of Nanopowder C under flowing dry air at a 523K temperature soak; also under UHP N_2 flow at RT and after cooling to 298K.

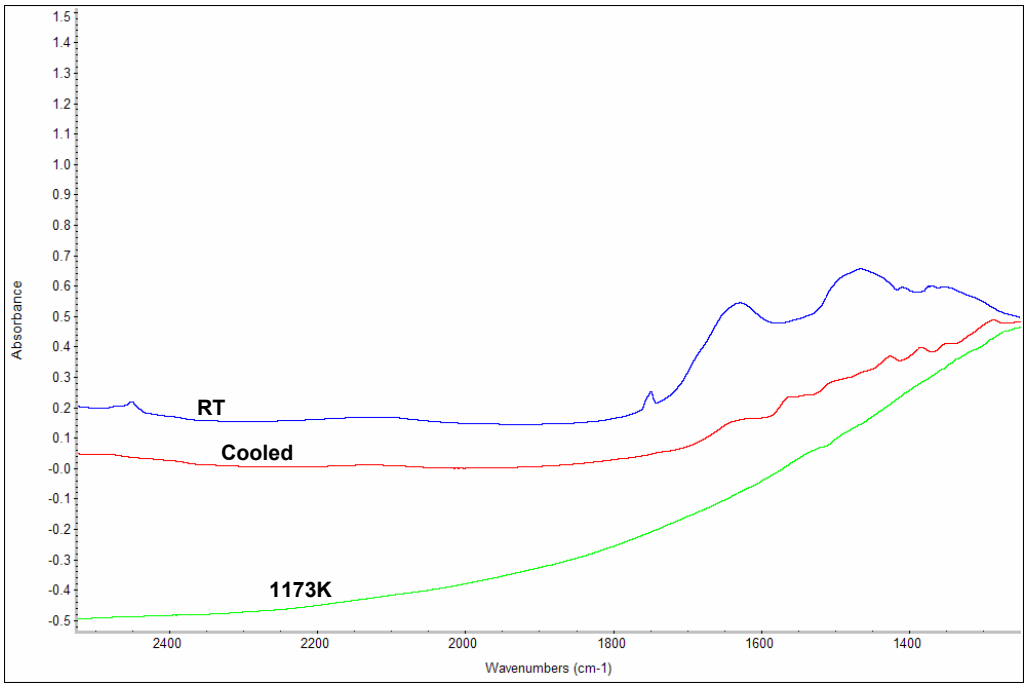

Figure 3.66. *In situ* HT-DRIFT spectra of Nanopowder C under UHP N_2 flow at RT, 1173K and after cooling to 298K in the spectral range 2525 cm^{-1} to 1250 cm^{-1}; stacked, common scale.

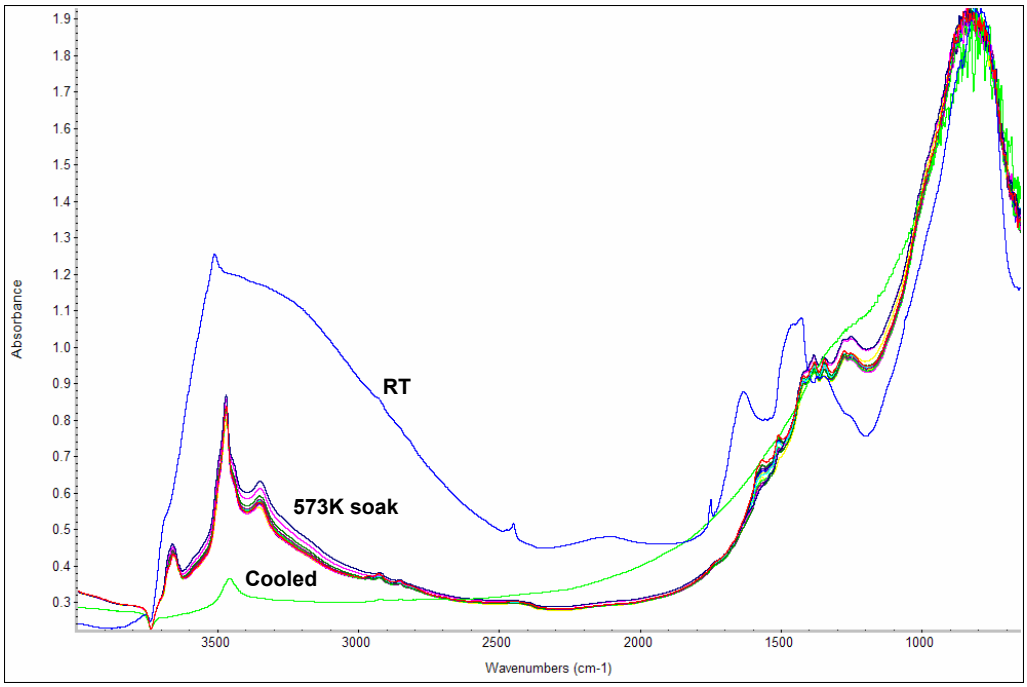

Figure 3.67. *In situ* HT-DRIFT spectra of Nanopowder D under flowing dry air at a 523K temperature soak; also under UHP N_2 flow at RT and after cooling to 298K.

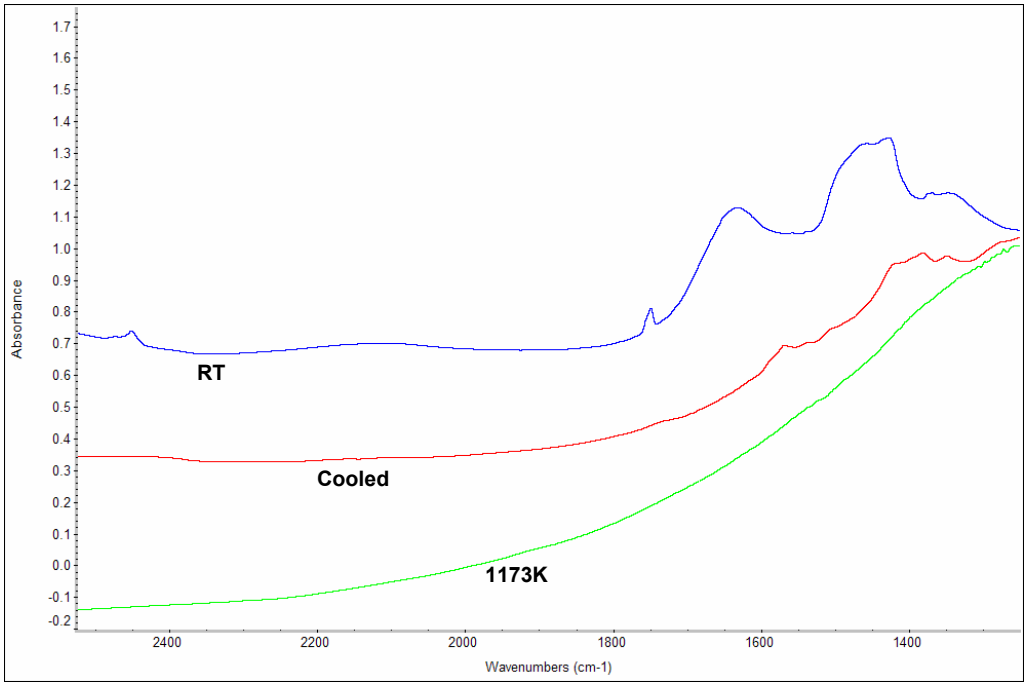

Figure 3.68. *In situ* HT-DRIFT spectra of Nanopowder D under UHP N_2 flow at RT, 1173K and after cooling to 298K in the spectral range 2525 cm^{-1} to 1250 cm^{-1}; stacked, common scale.

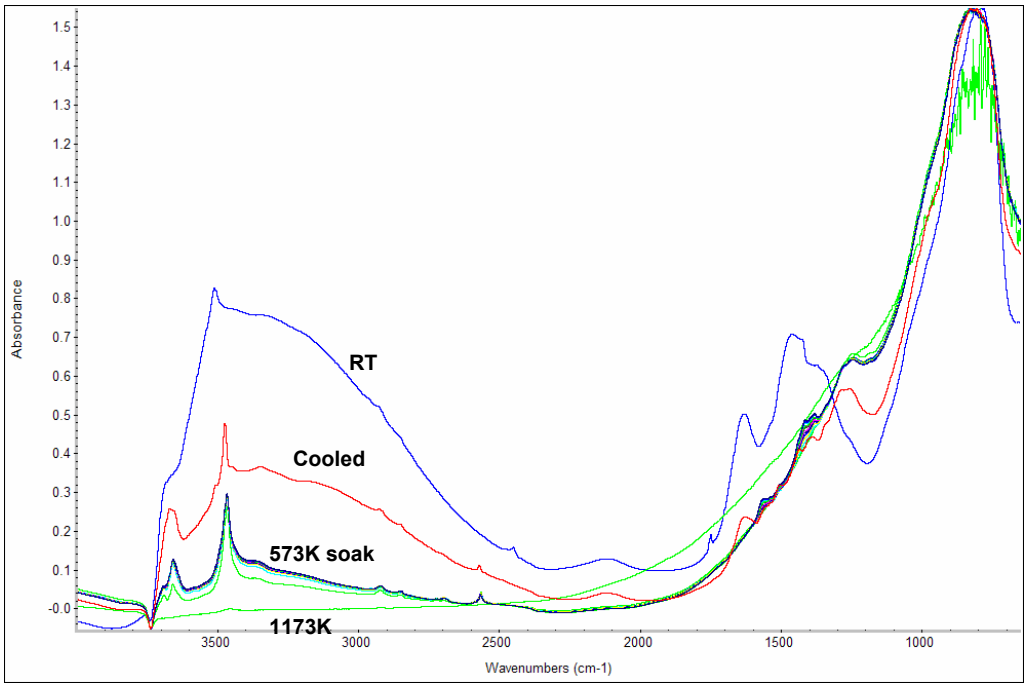

Figure 3.69. *In situ* HT-DRIFT spectra of Nanopowder E under flowing dry air at a 523K temperature soak; also under UHP N_2 flow at RT and after cooling to 298K.

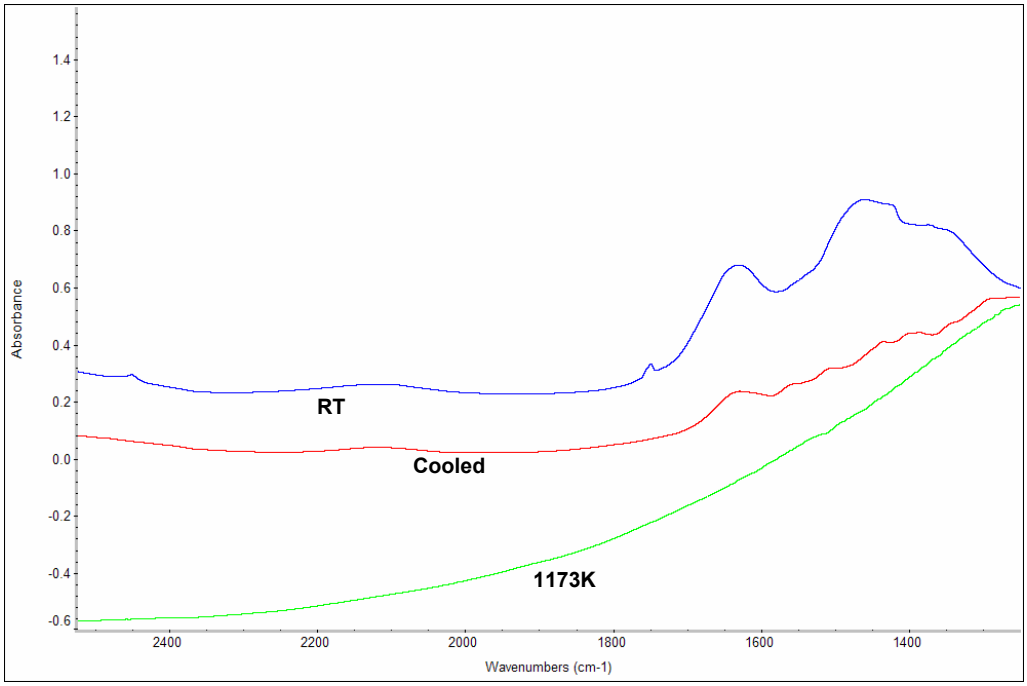

Figure 3.70. *In situ* HT-DRIFT spectra of Nanopowder E under UHP N_2 flow at RT, 1173K and after cooling to 298K in the spectral range 2525 cm^{-1} to 1250 cm^{-1}; stacked, common scale.

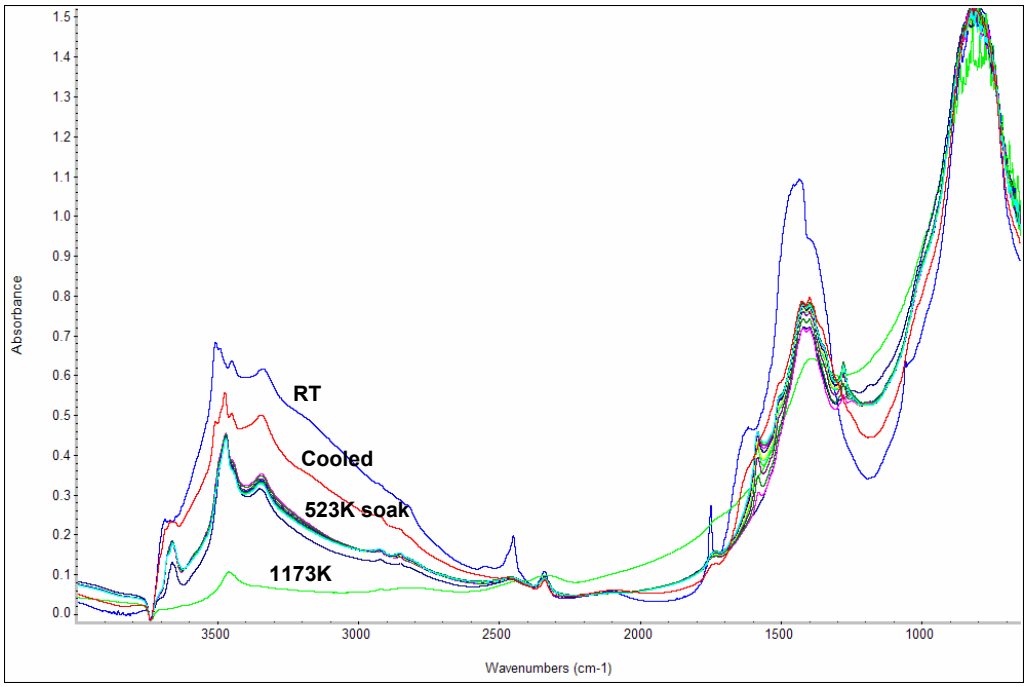

Figure 3.71. *In situ* HT-DRIFT spectra of Nanopowder F under flowing dry air at a 523K temperature soak; also under UHP N_2 flow at RT and after cooling to 298K.

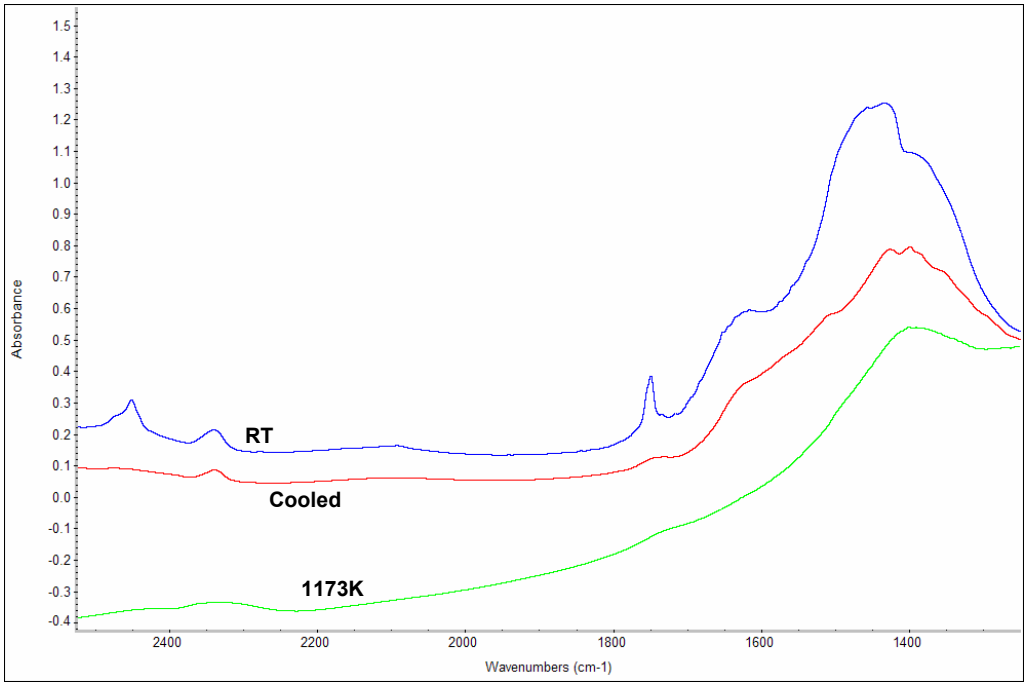

Figure 3.72. *In situ* HT-DRIFT spectra of Nanopowder F under UHP N_2 flow at RT, 1173K and after cooling to 298K in the spectral range 2525 cm^{-1} to 1250 cm^{-1}; stacked, common scale.

Looking in the spectral region 2525 cm^{-1} through 1250 cm^{-1} (the region containing the major carbonate bands) for the spectra of the nanopowders at room temperature, after two hours at 1173K and cooled after dry air treatment is shown (see Figures 3.62, 64, 66, 68, 70 and 72). As was observed, the readsorption of carbonate was negligible. A closer examination of the spectra regarding Nanopowder F in the 1400 cm^{-1} region was accomplished. Using the Omnic 6.0 software package the peak areas in the 1400 cm^{-1} region were measured of three spectra: the room temperature spectrum, the spectrum taken after two hours at 1173K and the cooled spectrum after the dry air soak. The analysis shows that the level of carbonate is unchanged after the dry air soak. Therefore, negligible readsorption occurred on Nanopowder F.

This study indicated that negligible readsorption of carbonate will occur after treating the nanopowders at an elevated temperature thereby removed the majority of initial carbonate content. However, similar to the H_2O study, moisture freely adsorbed during this study from the <6 ppm moisture content of the dry air used. Each of the nanopowder spectra exhibited some amount of moisture readsorption after the 1173K heat treatment. Moisture was again shown to be a pervasive contaminant for the nanopowders studied.

3.2.6 Summary

It has been previously known that oxide surfaces absorb atmospheric molecules that alter their surface charge.[129] The exposure of the nanopowder surfaces to ambient atmosphere causes a hydrolysis reaction with the humidity. Hydroxyl groups are formed which in turn form hydrogen bonds with the nanopowder surface and with surrounding molecular water. The surface, therefore, becomes covered with several layers of hydrogen bonded water. The proton may then be incorporated within the lattice through the Grotthuss mechanism becoming a protonic impurity with associated localized point defects, i.e. cation vacancies. In addition, other contaminants can react with the surfaces

such as carbon dioxide during synthesis leading to the carbonate ion, CO_3^{2-} and formation of $BaCO_3$.

All of the nanopowders were examined with *in situ* HT-DRIFT vibrational spectroscopy. All of the nanopowders exhibited a reduction of moisture and carbonate levels through the temperature range studied. Bands were observed in the spectra of each of the nanopowders at 2340 cm^{-1} and 2360 cm^{-1} which can be attributed to the presence of CO_2 gas from the desorption of lattice and surface carbonate species.

The uppermost layers of molecular water were eliminated at low temperatures and the hydrogen bonded species, lattice hydroxyls, were removed by moderate temperatures, ~725K. All of the nanopowders exhibited evidence of readsorption of moisture upon cooling. The intensity of the broad 2700 - 3600 cm^{-1} band and the 1640 cm^{-1} band (the OH related frequencies and molecular H_2O bending mode) were greater upon cooling than the intensity of these bands observed at 673K during the heat treatments. The spectral evidence clearly shows the affinity of the nanopowder surfaces for the readsorption of moisture.

The presence of CO_2 gas was first observed at 573K, 300 degrees lower than previously noted in the literature. The majority of the carbonate present in the two nanopowders was removed after a half-hour at 1173K. The carbonate levels of the three nanopowders C, D and E were nearly completely reduced, only minor intensities of carbonate related bands were observed in the spectra of each of the nanopowders. The removal of the carbonate in addition to moisture during the heat treatment provided open sites for the readsorption of moisture during the cooling phase.

The carbonate, however, was still observed in the 1173K spectrum of Nanopowder F after a half-hour soak. The 1429 cm^{-1} band of the lattice carbonate species remained present, whereas this band had diminished nearly completely with all other nanopowders. When cooled to room temperature, considerable remaining carbonate was observed in the final spectrum. The most intense barium carbonate band was observed at 1749 cm^{-1}. This band, observed in the room temperature spectra of all of the nanopowders, remained in the final

cooled spectrum of nanopowder F after heat treatment, while being absent from the cooled spectra of all other nanopowders.

The presence of this level of residual carbonate in Nanopowder F may be a result of the structural barium carbonate species. The amount of residual carbonate and moisture observed with the cooled spectrum of Nanopowder F in regard to the other nanopowders can be attributed to the nanopowder F's larger surface area and the state of this surface area. The atoms situated at the surfaces and interfaces of Nanopowder F, having the smallest average particle size of the nanopowders examined, are in the form of incomplete molecules with various unsaturated coordinations, or broken bonds. The nanocrystalline powder may therefore reside in a transition state of incomplete molecules to a fully crystalline material, or a mesoscopic state. Nanopowder F, therefore, consists of a saturated coordination bulk phase of barium titanate and barium carbonate with mesoscopic surfaces of unsaturated coordinations.

This disordered mesoscopic surface state would account for the concentration of carbonate, and moisture, observed not only in the initial spectrum but of that observed in the final spectrum after heat treatment. This disordered surface would accept the large concentration of adsorbates to stabilize its surface state. The high temperature limit of the HT-DRIFT study, 1173K with short duration soaks, does not permit a large amount of diffusion of Ba and Ti cations for the restructuring of this mesoscopic surface state; hence the large residual concentration of carbonate is observed in the final spectrum of Nanopowder F.

The readsorption of H_2O and OH groups was investigated in the H_2O study. All of the nanopowders exhibited evidence of readsorption of moisture upon cooling. The HT-FT-IR studies indicated that readsorption of lattice hydroxyl ions occurs with <6 ppm available moisture in the gas flow utilized in this study. The spectral evidence clearly showed the affinity of moisture for the readsorption onto the nanopowder surfaces. The solid state nanopowders (A and B) contained a higher concentration of moisture after heat treatment than was present initially. The vibrational wavenumber related to the bend

deformation of H_2O at 1630 cm^{-1} dissipated by 873K with each of the nanopowders. This band was observed in the cooled spectra of each of the nanopowders signifying the readsorption of moisture to the surfaces of the nanopowders.

It is interesting to note that, in observing the spectral region 3350 cm^{-1} to 3600 cm^{-1}, the distribution of OH groups in the lattice had changed significantly with Nanopowders C through F. A single OH related band was observed at ~3509 cm^{-1} in the room temperature spectra of nanopowders C through E. Upon cooling after heat treatment, three bands were observed at 3509 cm^{-1}, 3475 cm^{-1} and 3451 cm^{-1} in the final spectra of Nanopowders C through E. The three bands observed with the room temperature spectrum of Nanopowder F (3509 cm^{-1}, 3492 cm^{-1} and 3451 cm^{-1}) transformed to 3509 cm^{-1}, 3475 cm^{-1} and 3451 cm^{-1} upon cooling after heat treatment, the same bands as observed in the final spectrum of the other three nanopowders. These OH related bands were indicative of a cubic to tetragonal phase transition for Nanopowders C through E as a result of the heat treatment and a redistribution of the OH groups in a tetragonal phase of Nanopowder F. The singular OH band near 3509 cm^{-1} observed with the spectra of the hydrothermal nanopowders indicated the possibility of multiple degenerate Ti – O bond related positions for these hydroxyls prior to elevated temperature treatment, therefore denoting a room temperature cubic structure. Three separate OH bands of differing intensities were observed in the spectra of these nanopowders after elevated heat treatment. This provides evidence for the concept of a repositioning of the hydroxyls into energy states associated with Ti – O bond related positions having three different bond lengths. This data, the single OH band at room temperature, a single OH band observed above T_c and the three OH bands observed at room temperature after heat treatment, may substantiate the hypothesis that the cause of the room temperature cubic phase is a hydroxyl strain stabilized pseudocubic structure.

Although dehydroxylation occurs at the temperatures utilized in this study, defects are not completely eliminated, as observed in the mesoscopic structure

of Nanopowder F. The complete elimination of lattice strains arising from the removal of the hydroxyl content and subsequent lattice rearrangement of residual point defects may not occur. The lattice strains issue will be addressed in the following section. The elimination of these lattice strains is important in stabilizing the room temperature tetragonal phase. The presence of hydroxyl ions affecting the structure of barium titanate nanocrystallites is still debated.

The protonic defect (an interstitial proton) is an extremely small point charge that due to its size is attracted to an oxygen ion forming hydroxyl ions on oxide ion sites ($OH_O^{\cdot}$). These are positively charged defects competing with other positively charged defects, electron holes ($h^{\cdot}$) and oxygen vacancies ($V_O^{\cdot\cdot}$), that are charge compensated by major negatively charged defects, which may include electrons, metal ion vacancies, or oxygen interstitials. The annihilation of protonic defects occurs as temperature increases through the dehydration of the hydroxyl defects according to the equation:

$$2OH_O^{\cdot} + \tfrac{1}{2}O_2 \rightarrow H_2O_{(g)} + 2h^{\cdot} + 2O_O \,. \qquad (3.6)$$

It was shown, however, that the readsorption of moisture readily occurs with the hydrothermally derived nanopowders upon return to room temperature.

The deuterium exchange studies had shown the OD group's affinity for the nanopowders during the deuterium exchange. This was similar to that of the OH groups during the readsorption study. The deuterium exchange produced three OD bands observed at the predicted wavenumber shift from the three Ti – O related OH bands previously described. Therefore, the presence of these three OD bands also indicates a room temperature tetragonal structure for the treated nanopowders.

The usual activation temperatures of carbonate removal from barium titanate powders were 873K, 1150K and 1525K.[104] The highest temperature achieved in this study was 1173K (the temperature limit of the HT-DRIFT environmental cell) and well below the 1575K upper temperature necessary to release the tightly bound lattice carbonates. The presence of CO_2 gas was first

observed at 573K, 300 degrees lower than the previously noted 873K temperature. The carbonates were released continuously beginning at 573K and continued through the higher temperatures studied. This study indicated that negligible readsorption of carbonate would occur after treating the nanopowders at an elevated temperature which removed the majority of initial carbonate content. Residual carbonate was observed with all of the nanopowders.

Heat treating the hydrothermally synthesized nanopowders (C, D, and E) at 1173K and subsequent cooling produced a shift to several OH bands from a single OH band during the *in situ* high temperature study. This phenomenon was cyclic as temperature was raised and lowered, which indicated the incorporated hydroxyl bands were related to the tetragonal to cubic transition. The nanopowders were initially heated to 1173K in the HT-DRIFT chamber. Temperature was then cycled between room temperature and 573K. The single band appeared at high temperature with the multiple bands reappearing upon return to room temperature. This was evidence for the structural transition between the tetragonal and cubic phases of barium titanate.

The discussion on the room temperature crystallite structure of nanocrystalline barium titanate includes not only the effect of particle size but also residual strain as discussed previously. Begg et al. suggested two possible mechanisms to explain the anomalous cubic room temperature phase: 1) the strains imposed by the presence of hydroxyl ion content, and 2) the role of surface effects.

The HT-FT-IR studies herein indicated that after the nanopowders were subjected to heat treatment of 773K that the beginning of tetragonal symmetry was observed. However, readsorption of lattice hydroxyl ions occurred with <6 ppm available moisture in the gas flows utilized in this study and, therefore, hydroxyl related strain in conjunction with cation vacancies may still be the reason for the stabilization of the pseudocubic phase.

The observance of tetragonal symmetry after the 773K treatment was likely the observed surface state of the nanopowders, not the bulk state. The spectral results indicated a restructuring of the interfaces at this temperature.

Reviewing the previous data with regard to the as-received crystal structure of the nanopowders (see Table 3.7), XRD and electron diffraction indicated a cubic symmetry for nanopowders C through E. This corroborated the HT-DRIFT data. The single, cubic related band of the room temperature spectra of Nanopowders C through E was indicative of the six degenerate Ti-O bonds in the oxygen octahedron of the cubic unit cell. The cooled spectra that exhibited three tetragonal related bands were indicative of the three different bonds in the distorted oxygen octahedron of the tetragonal unit cell. The previous data for Nanopowder F indicated cubic symmetry by XRD and by electron diffraction. The HT-DRIFT, however, indicated evidence of a mesoscopic structure at room temperature.

Table 3.7. Symmetry of the Nanopowders as Denoted with Each Technique

	Nanopowder and Symmetry Indicated					
Technique	A	B	C	D	E	F
XRD	tetragonal	tetragonal	cubic	cubic	cubic	cubic
TEM	tetragonal	tetragonal	cubic	cubic	-------	cubic
HT-IR	-------	-------	cubic	cubic	cubic	meso

The highly disordered state of the interfaces, in the previously proposed mesoscopic state for Nanopowder F, and the spectral evidence examined indicated interfaces with states similar to tetragonal symmetry. The high ratio of surface area to bulk volume provided large regions of varied bond states along the interfaces. The nature of these regions assumed a pseudo-tetragonal symmetry or a relaxed state along the interfaces in an attempt at a reduction in their free surface energy. The position of the protonic impurities in the “as-

received" nanopowder, therefore, produced oscillators indicative of this mesoscopic state. The room temperature bands remained; however, they exhibited changes in intensity as related to the change in population density of the repositioned protonic impurity. This repositioning was due to the changed interfaces during the heat treatments.

These structural changes occurred with the mesoscopic state of the interfaces of Nanopowder F after the 773K treatment. The 3509 cm^{-1} band observed in the room temperature spectrum had decreased in intensity with the 3492 cm^{-1} band of highest intensity. The 3475 cm^{-1} band was of highest intensity of the three bands observed with all of the nanopowders upon cooling.

The 773K heat treatment produced changes in the interfaces of the four nanopowders. The 773K heat treatment resulted in four bands with each of Nanopowders C through F. The observed four bands would be indicative of the resultant four bond lengths of the distorted cubic unit cell as described by Pirc and Blinc, but slightly off from the [111] direction. A Ti-ion position of (0.51, 0.51, 0.53) would yield four Ti – O bond lengths and the associated four bands observed. Eight possible regions would exist, for a displaced Ti-ion towards an oxygen octahedral face. The suggested, therefore, that after the 773K treatment the minimum potential for the Ti-ion was a non-centrosymmetric location in a cubic unit cell.

This study is in partial agreement with Begg. The possible mechanisms to explain the stabilization of the anomalous cubic room temperature phase are 1) the strains imposed by the presence of point defects: the protonic impurities and their associated cation vacancies, and 2) the role of surface states and structural changes. The two issues will be further considered in Section 4, the study of calcining in ambient atmosphere.

At the highest temperature used in this study (1173K) moisture and the accompanying hydroxyls were removed. Further, spectral evidence was obtained indicating that the reorientation of surface states occurred. Although this temperature level does not allow a high degree of cation diffusion, the

reorientation of the crystallite interfaces was observed in conjunction with the presence of tetragonal symmetry.

The affinity of the water molecule to dissociate at the surface of barium titanate nanopowders has been previously underestimated. As observed in the HT-FT-IR spectra of all of the non-solid state nanopowders, and to a lesser degree with the solid state nanopowders, the readsorption of molecular water and hydroxyl ions readily occurs under the flowing ultra high purity nitrogen gas used in this study in the low temperature regimes used herein.

4 High Temperature X-ray Diffraction

4.1 Introduction

The structure of a barium titanate crystal depends upon the temperature. Above its Curie temperature (T_c) the unit cell is cubic and nonpolar. The unit cell becomes tetragonal below the Curie temperature, where the structure is distorted with an accompanying polarization in a [100] direction. Barium titanate's Curie temperature is ~403K.

The vibrational spectroscopic studies have indicated that the pseudocubic nanopowders began reorienting at 773K and after the 1173K calcine were tetragonal at room temperature. This room temperature tetragonality was confirmed with other techniques.

High temperature X-ray diffraction (HT-XRD) was utilized in this study to verify the symmetry of the nanopowders. Additionally, it is proposed that HT-XRD would determine the calcine temperature from which these nanopowders would cool to room temperature in tetragonal symmetry, the normal variant.

4.2 Experimental Procedure

The pseudocubic nanopowders, 0.5 gram of each, were mixed with acetone in a small crucible. The amount of nanopowder and acetone was adjusted until a light slurry was formed. Slurry was transferred to an alumina sample holder to produce a thin layer of nanopowder on the substrate.

The samples were then placed in the high temperature diffractometer. Cobalt excitation radiation was used at a 40 kV, 24 mA setting. Scans were taken between 25º and 80º 2-theta with a 0.05º step size. A room temperature pattern was taken prior to beginning the high temperature run. The runs were set for a hold at elevated temperature with a ramp rate of 10K/minute under flowing nitrogen (100ml/minute). Additional patterns were taken upon reaching the high

temperature set point, again after the half-hour soak, and lastly below T_c, at 373K.

4.3 Results and Discussion

The first sample run was completed with Nanopowder F. The resulting patterns in Figures 4.1 and 4.2, for the initial room temperature scan and the cooled 373K scan, respectively, indicated no change in the symmetry of the sample. The soak temperature was 873K, which was above the temperature noted in vibrational analysis when reorientation to tetragonal symmetry began. There was no evidence of peak splitting in either pattern, and the relative intensity of the (111) peak also indicates cubic symmetry for both patterns. The only evidence of the heating cycle is the diminished barium carbonate peak annotated in each pattern, which indicated the partial removal of the carbonate surface layer.

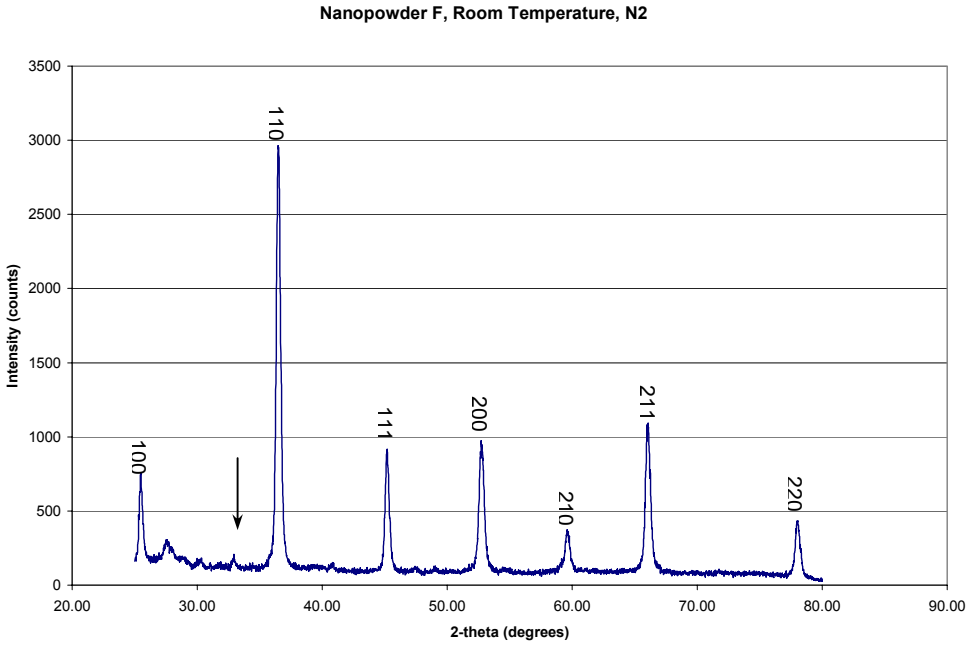

Figure 4.1. HT-XRD room temperature pattern of Nanopowder F prior to heat treatment to 873K.

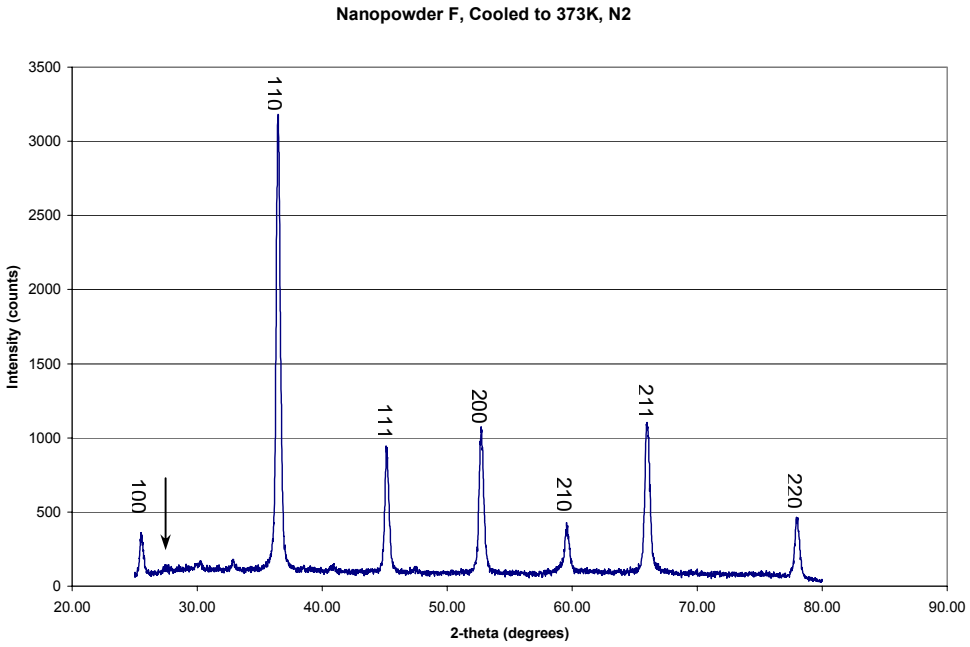

Figure 4.2. HT-XRD pattern of Nanopowder F cooled to 373K after a half-hour soak at 873K.

Another run was made with the same nanopowder with a soak temperature of 1173K, which was the upper limit for vibrational analysis. The cooled spectra for Nanopowder F indicated well defined bands that represented tetragonal symmetry. Similar results were expected with the HT-XRD.

The patterns from this run had results duplicating the first run. The room temperature pattern was again indicative of the pseudocubic symmetry with the barium carbonate peak present (see Figure 4.3). No peak splitting to indicate tetragonal symmetry was observed in the cooled pattern after the half-hour soak at 1173K (see Figure 4.4). The relative intensity of the (111) peak was again indicative of cubic symmetry. The barium carbonate peak was reduced further than was observed after the lower temperature treatment. A low intensity, broad peak is observed in Figure 4.2, whereas no peak is observed in Figure 4.4.

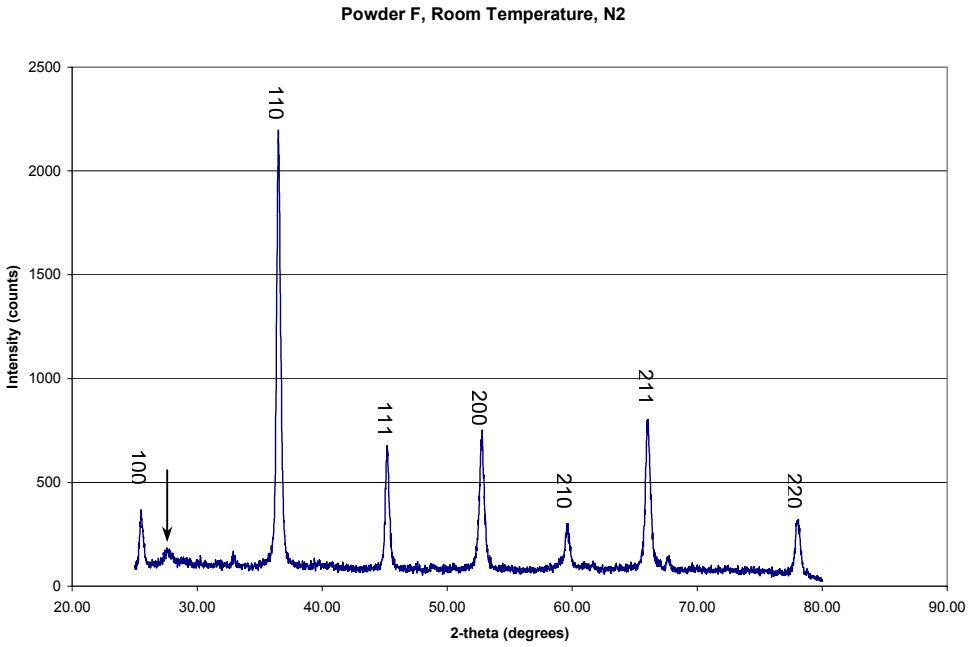

Figure 4.3. HT-XRD room temperature pattern of Nanopowder F prior to heat treatment to 1173K.

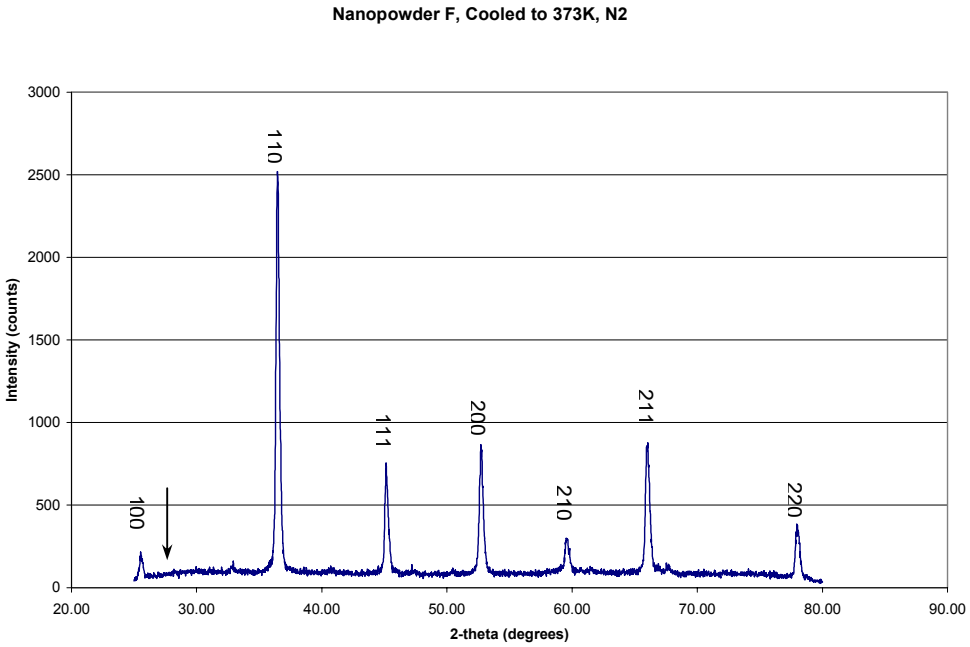

Figure 4.4. HT-XRD pattern of Nanopowder F cooled to 373K after a half-hour soak at 1173K.

A last experiment was attempted that tried to match the conditions of the vibrational analysis technique. During the vibrational experiments, the samples were cooled quickly, i.e., 130K/minute. The cooling rate that can be achieved with the high temperature x-ray diffractometer had a far lower rate, 3K/minute below 473K. The presumption was that during the slow cooling the samples were re-adsorbing moisture that affected the ability of reordering to tetragonal symmetry. No method existed for cooling the sample chamber any quicker than the previous cooling rates. Therefore, the highest N_2 flow rate that could be safely used was initiated in hopes of drawing released moisture out of the sample chamber.

This also failed to produce a different result than that previously encountered in the other experiments. It was, however, an indication that the readsorption of moisture was affecting the room temperature symmetry of the samples. This evidence assists in confirming that the cause of the room temperature cubic phase was a hydroxyl strain stabilized pseudocubic structure.

4.4 Summary

Nanopowder F was analyzed with HT-XRD. The results of the experiments were indicative of cubic symmetry at room temperature subsequent to the high temperature calcines. The HT-XRD cooling rate was far slower than that incorporated in the vibrational studies. The vibrational spectroscopic studies had indicated that the pseudocubic nanopowders began reorienting at 773K and after an 1173K calcine were tetragonal at room temperature. This room temperature tetragonality was confirmed with other techniques.

The slow cooling rate of the HT-XRD apparently allowed the readsorption of moisture by the samples. This had the effect of impeding the transition to tetragonal symmetry, and resulted in cubic symmetry upon cooling through T_c to room temperature.

5 X-ray Photoelectron Spectroscopic Analysis

5.1 Introduction

All solids interact with their surroundings along their surfaces. The composition of the surface layer dictates the nature of any interactions that may occur. Surfaces influence many important properties of solids, more so when nanoscale processes are involved due to the large surface to volume ratio. It is this importance of surface layers, especially involving nanoscale materials, that X-ray Photoelectron Spectroscopy (XPS) was utilized to analyze the nanopowders.

XPS is a surface analytical technique; the depth of the analysis is dependent upon the inelastic mean free path (IMFP) of the core level electrons ejected from the surface of a sample, generally less than a few nanometers. The barium 4d electron IMFP in barium titanate as calculated using the Tanuma, Powell, and Penn equation[130] is 2.9 nm. Similarly, the IMFP for the other elements of interest are: carbon 1s – 2.6 nm, oxygen 1s – 2.2 nm, and titanium 2p – 2.3 nm.

Since XPS is a surface sensitive technique, the surfaces of the nanopowders may be probed to answer: 1) Which elements are present near the surface? 2) What chemical state(s) of these elements are present? and 3) How much of each element is present? This data would provide the basis for calculating the thickness of the layer of contamination on the nanopowders.

5.2 Experimental Procedure

The nanopowders, 0.5 gram of each, were weighed and pressed in a double action cylindrical steel die at 44 MPa to form compacts measuring 1.25 cm in diameter. No processing additives were employed in the production of the compacts. A small piece of tape, adhesive on both sides, was used to securely attach the compacts to the XPS sample stage. A second set of analytical runs were later accomplished with samples lightly packed in an aluminum sample stub

(see Figure 5.1). The stubs were attached to the sample stage in the same manner as the pressed compacts.

The samples were then slowly degassed in the introductory chamber for a weekend, and then moved into the high vacuum chamber of the XPS spectrometer (Phi Quantera SXM, Physical Electronics USA, Chanhassen, MN). Monochromatic Al K_α at 25.1 Watts was utilized to generate the electron signal -- the ejected core level electrons. The spectra were collected from a 100 μm diameter spot size using a hemispherical electron energy analyzer with pass energy of 26 eV, a 0.05 eV step size, and 10 cumulative scans to form the final spectra. A survey spectrum was obtained of each sample prior to depth profile sputtering. Sputtering of the sample surfaces was accomplished over a 3 mm x 3mm area using Ar^+ with a 1 kV potential at a 45º incidence angle with respect to the sample surfaces for 1 minute. The peaks were fitted using the MultiPak Spectrum software program with Gaussian peak approximation and Shirley background reduction. Calibration was accomplished using copper, silver, and gold foil standards.

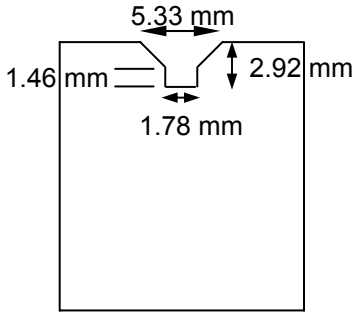

Figure 5.1. Dimensional drawing of the cylindrical aluminum sample stub used in XPS analysis of the nanopowders.

5.3 Results and Discussion

All of the survey spectra of the nanopowders were found to contain barium, titanium, oxygen, and carbon peaks (see Figures 5.2 – 5.7). The carbon peaks were generally of poor resolution due to high noise levels. The survey spectra were not an accurate representation of the electron escape peaks. The barium 4d peak at 90 eV appears to be a single peak in each of the survey spectra. However, narrowing the abscissa to 10 eV above and below the 90 eV peak, 4 distinctive peaks are observed. The barium 4d5 and 4d3 transitions will be analyzed later in the chapter. The two sets of doublet peaks for the 4d5 and 4d3 transitions each corresponded to a different chemical bonding state.

Each of the samples was examined in similar specific energy windows for each of the elements present. Titanium was observed to have a 2p3 and 2p1 doublet set for each sample. A shoulder to the oxygen peaks was also observed for each sample at a 1.5 eV higher binding energy. Carbon was represented by two, and at times three, peaks: a ubiquitous contaminant carbon and a carbonate

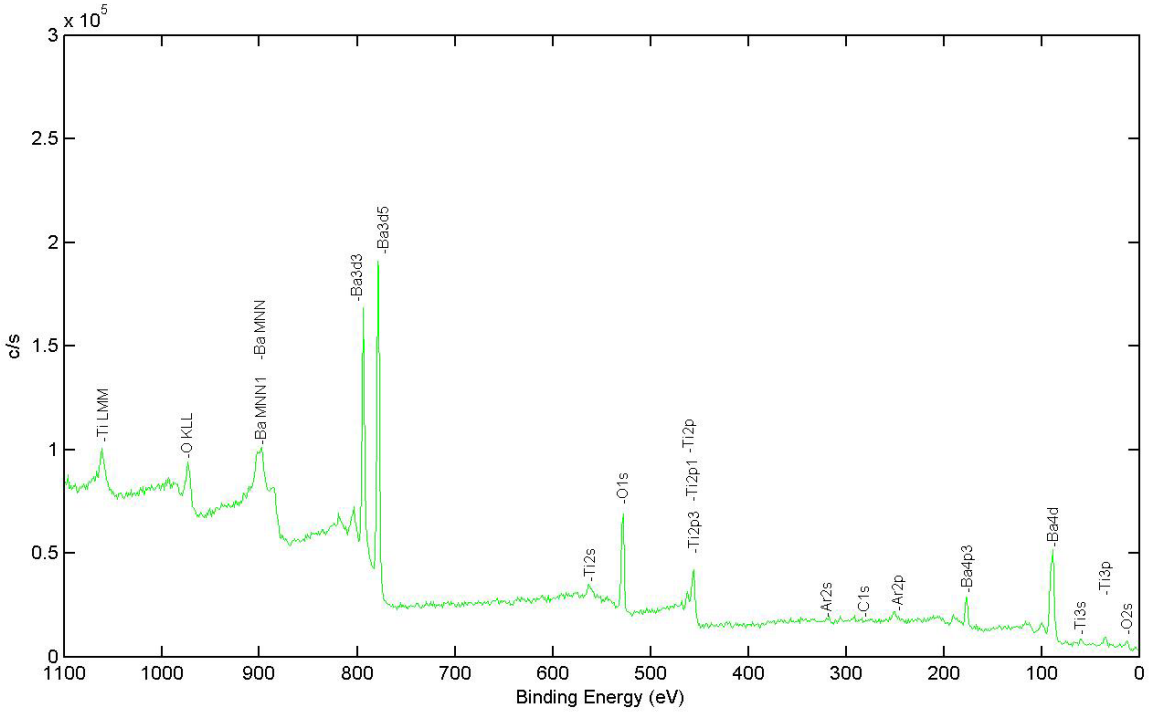

Figure 5.2. XPS survey spectrum of Nanopowder A with peaks identified.

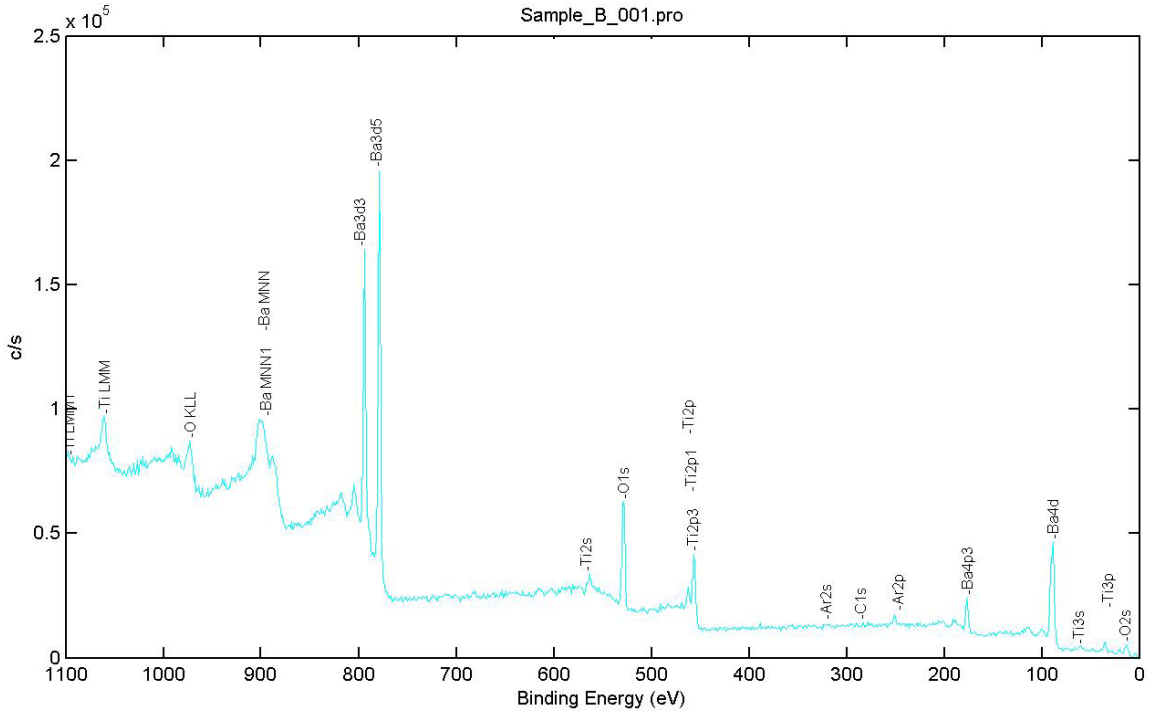

Figure 5.3. XPS survey spectrum of Nanopowder B with peaks identified.

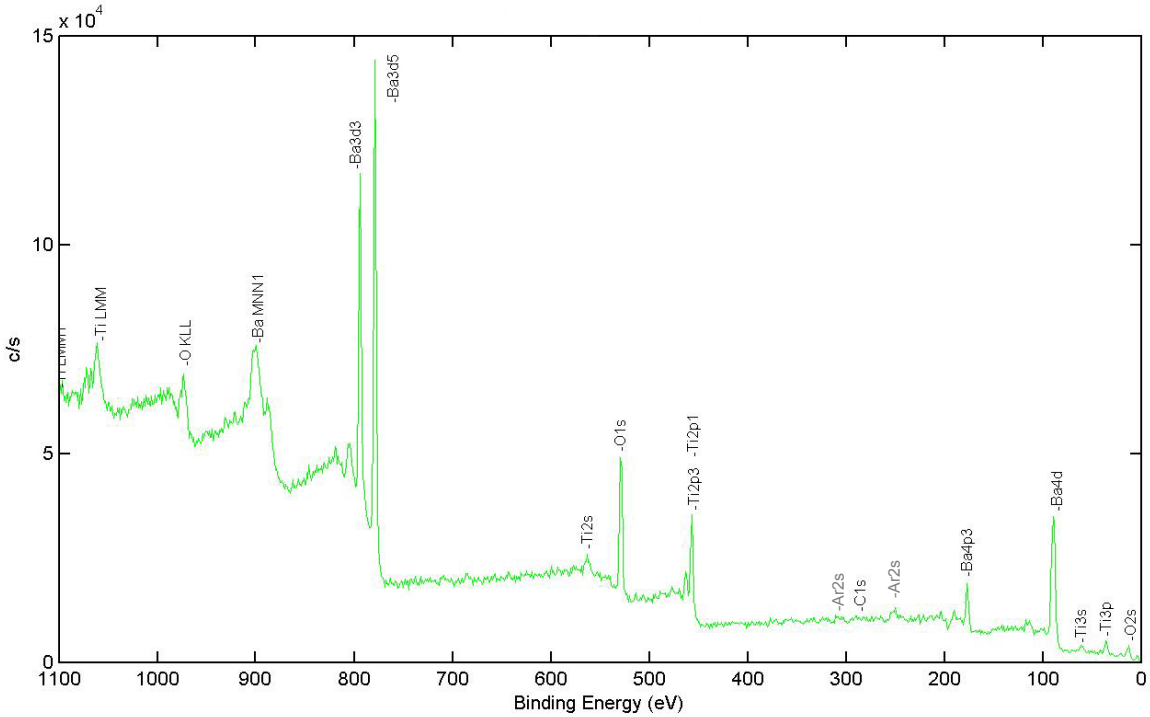

Figure 5.4. XPS survey spectrum of Nanopowder C with peaks identified.

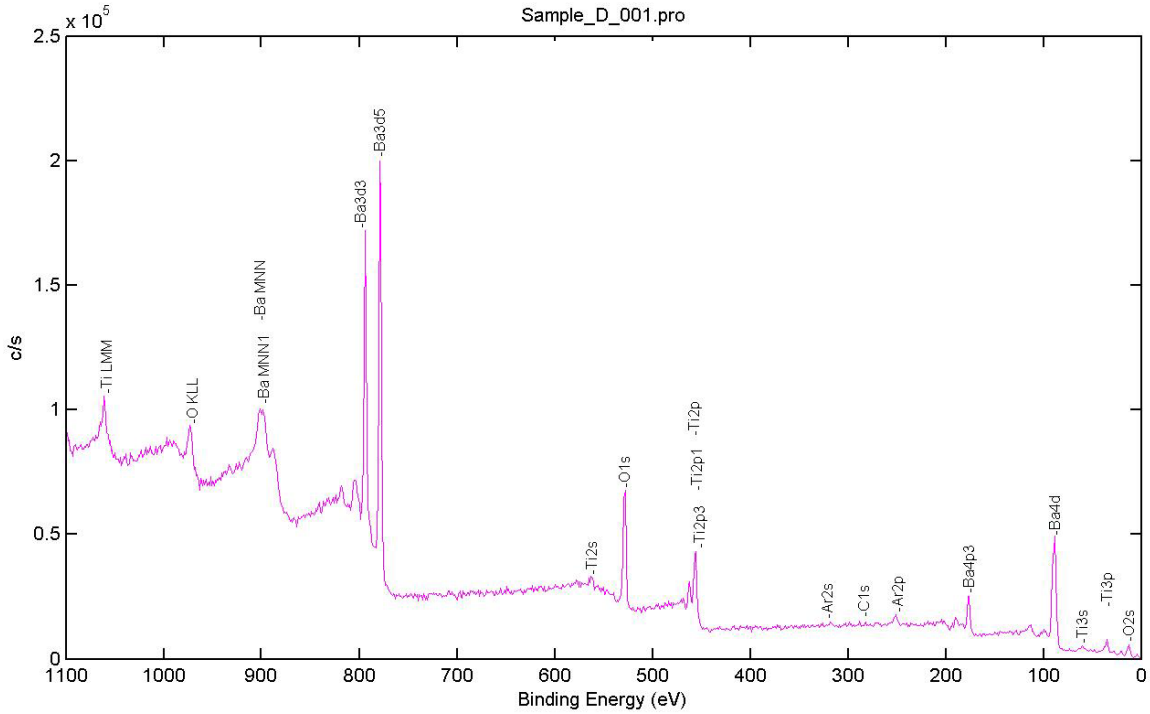

Figure 5.5. XPS survey spectrum of Nanopowder D with peaks identified.

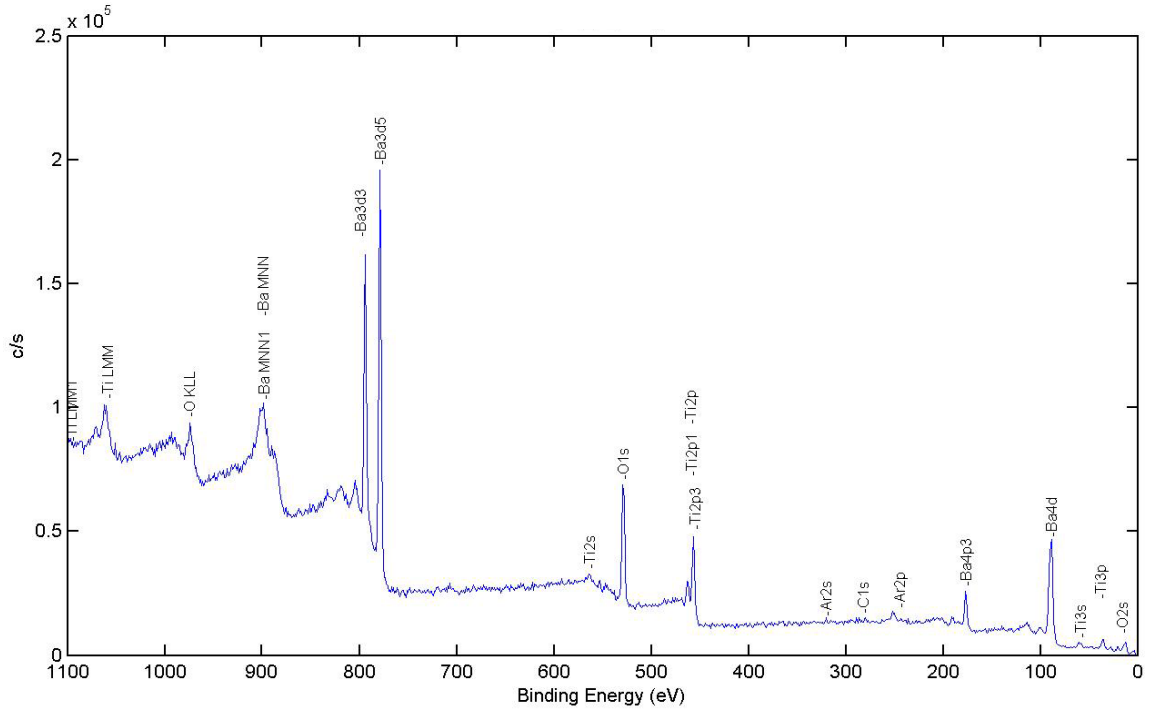

Figure 5.6. XPS survey spectrum of Nanopowder E with peaks identified.

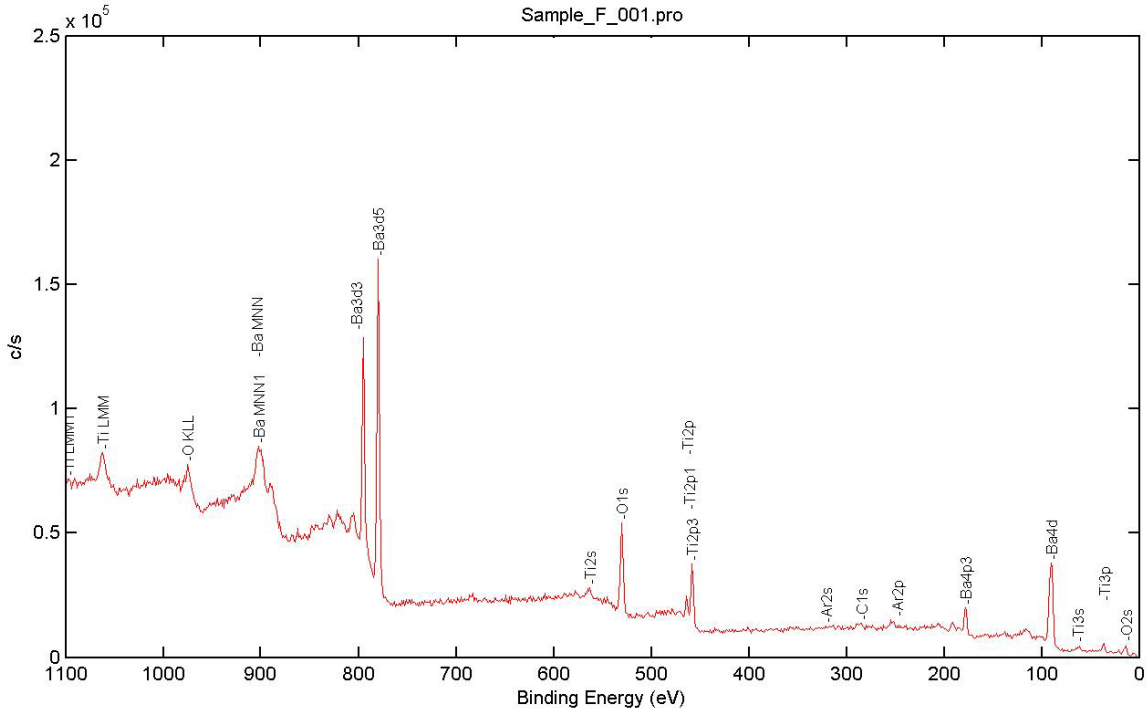

Figure 5.7. XPS survey spectrum of Nanopowder F with peaks identified.

related peak at slightly higher energy, and another that was infrequently observed at a binding energy between the previously mentioned peaks.

The shift between the doublet pairs of the 4d5 and 4d3 barium peaks was 1.15 eV to 1.45 eV depending upon the depth within the samples (see Figure 5.8). The spin orbital splitting for the 4d transition was 2.6 eV, in agreement with the literature value reported by Ford (2.47 eV) and by van Doveren (2.1 – 3.0 eV).[131-32] The shift between the titanium doublet pairs 2p3 and 2p1 was 2 eV (see Figure 5.9). The spin orbital splitting for the titanium 2p peaks was between 5.42 eV and 5.74 eV; in close agreement with the literature value of 5.54 eV.[133(p.138)] These values were highly dependent upon the software package's integrity in peak fitting and the level of noise in the spectra.

The barium binding energy shifts can be explained through chemical bonding models. In nearly completely ionic compounds barium can be assumed to be in the 2^+ state at all times. Therefore, chemical shifts are primarily the result of local potential changes caused by different anion coordination.[134] In the

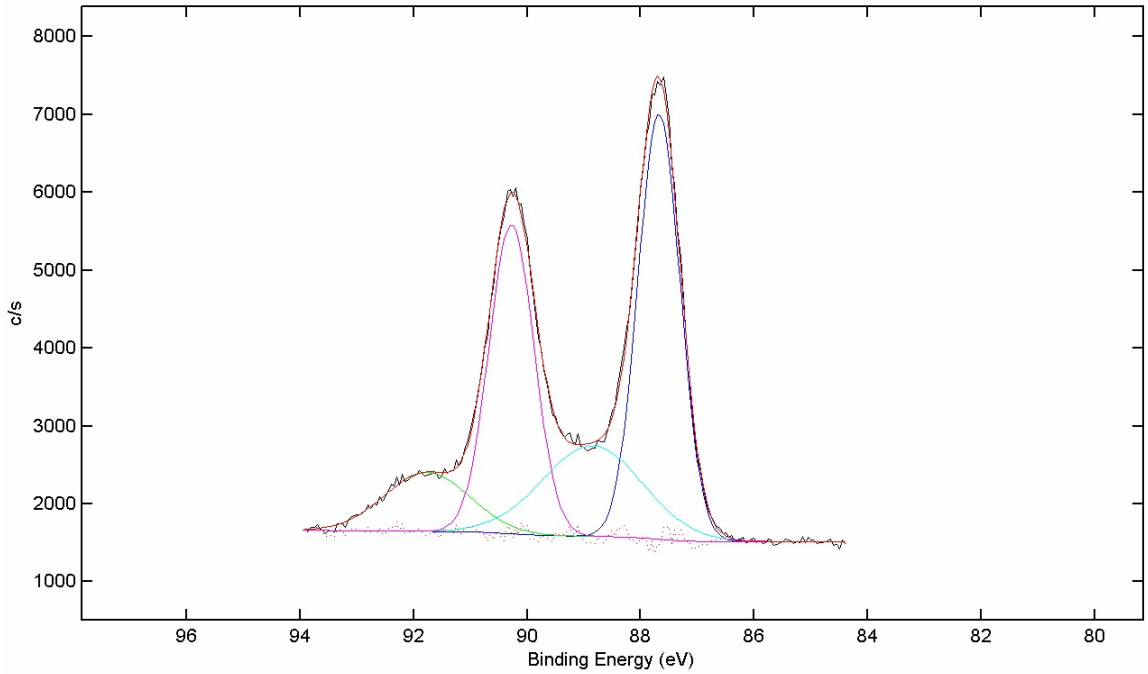

Figure 5.8. XPS detail spectrum of the barium 4d5 and 4d3 peaks of Nanopowder A, each with a higher energy shoulder. Spectrum obtained prior to surface sputtering.

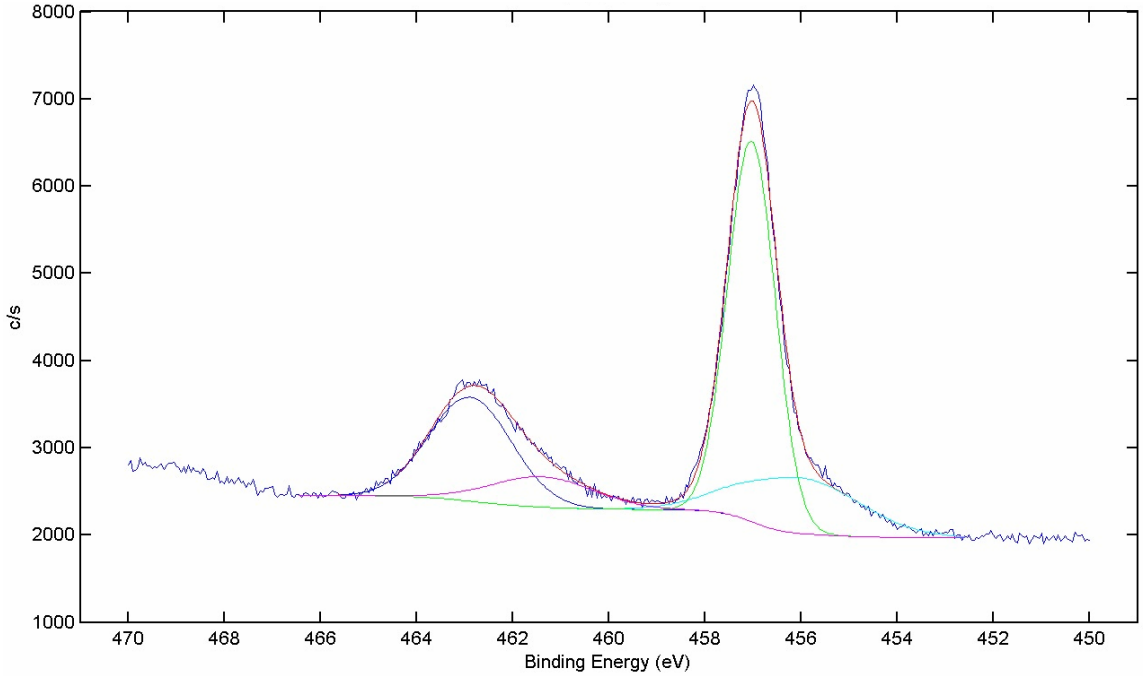

Figure 5.9. XPS detail spectrum of the titanium 2p3 and 2p1 peaks of Nanopowder A, each with lower energy shoulders. Spectrum is representative of all nanopowders.

perovskite structure for barium titanate, barium is in 12-fold coordination.[135] In comparison, barium in barium carbonate is in 9-fold coordination.[136] The barium in the perovskite had a higher binding energy, and in the carbonate a lower binding energy.

Vibrational spectroscopy has indicated the presence of barium carbonate in each of the nanopowders. XRD on Nanopowder F confirmed the presence of carbonate. The doublet pairs of the barium 4d5 and 4d3 transitions may therefore be assigned as belonging to two different chemical states. The lower energy 4d transition pair was assigned as barium in barium titanate, and the higher energy 4d transition pair was assigned as barium in barium carbonate.

The shoulder on the oxygen peaks at 1.5 eV higher binding energy can be assigned to either hydrogen bound to oxygen or carbon bound to oxygen in carbonate coordination.[137] Since it was not possible to differentiate between these two species, no in depth study was performed with respect to this region of the spectra (see Figure 5.10). It may be noted, however, that this shoulder was always present in all of the spectra, including the depth profiling studies.

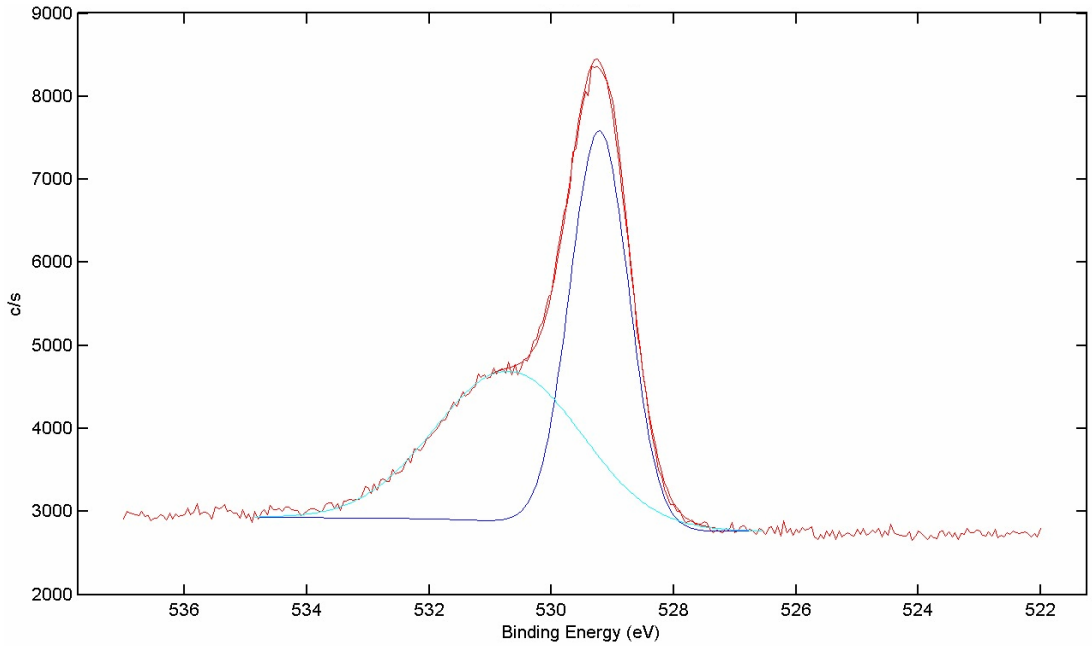

Figure 5.10. XPS detail spectrum of the oxygen 1s peak of Nanopowder A with a higher energy shoulder. Spectrum obtained prior to surface sputtering.

Iterations in depth were achieved where no carbon signal was recorded; however, the higher energy shoulder of the oxygen peak was yet present. The data may therefore be considered indicative of the continued presence of both species: new surface carbonate species as sputtering uncovered surface area of new particles, and the presence of lattice hydroxyl as sputtering exposed particle cores.

Carbon was observed in each of the nanopowder spectra and was represented with two, and at times three, peaks. These were assigned as ubiquitous contaminant carbon at the lowest binding energy; the second major peak assigned as a carbonate related peak located at the highest binding energy; and another that was infrequently observed at a binding energy between the previously mentioned peaks, and was assigned to C-O bonding. This latter peak was solved while observing similar carbon related energy peaks on the metal foil calibration standards.

In addition to being used as peak position standards, the copper, silver and gold foil standards were examined to verify the binding energy peak position of the ubiquitous carbon observed on the nanopowder samples. The binding energy of the ubiquitous carbon was observed in each foil sample spectrum (see Figures 5.11 – 5.13) and was of a similar binding energy as that found in the lowest carbon related peak for each of the nanopowders. Table 5.1 lists the binding energies of this carbon contaminant with the metal foil detail spectra shown in Figures 5.14 through 5.16.

The composition of the surface of the foil standards is shown in Table 5.2. The ubiquitous carbon was the majority constituent of the surface of each foil. Oxygen was the second major surface component. The gold foil standard survey spectrum was compromised by the sputtering of the other two standards prior to examination. Weak peaks for the copper 3p and silver 3d transitions were denoted in the gold foil spectrum. This was a result of the sputtering of their representative foils and the presence of these sputtered atoms adsorbed to the already contaminated gold foil surface.

Table 5.1. Binding Energies of the Ubiquitous Carbon Contaminant

Sample	Binding Energy (eV)
Copper	284.35
Silver	284.57
Gold	284.37
A	284.54
B	284.48
C	284.53
D	284.43
E	284.31
F	284.43

The percentage of the metal component represented in each foil spectrum can be further separated into its constituent signals: metal and metal oxide. The percentage of the total signal from the elemental metal in each foil sample was 8%, 16.2%, and 15.4%, corresponding to Cu, Ag, and Au respectively. The copper peak was separated into two different energy peaks; the lower peak at 932.6 eV is indicative of the element Cu, the higher 934.2 eV peak is indicative of the oxide CuO.

The silver and gold peaks, however, do not specifically denote the presence of an oxide. Both of these peaks were fitted with three different Gaussians: a broad peak and two narrow peaks. The broad peak and the mid-energy narrow peak of each foil were indicative of escape electrons from the representative metal. The high energy narrow peak of the silver foil and the low energy narrow peak of the gold foil were representative of a perturbed state on

the metal surface related to an oxygen attachment.[133(p.121,183)] Although these peaks were not representative of an energy for their metal oxides such as the CuO peak, the energies were near the ranges of energy for each of the respective metal oxides. As such, these peaks were incorporated in the calculations of the contamination layer thickness as representing an oxide layer.

Table 5.2. Surface Composition of the Metal Foil Standards

Sample	Element	Percentage (%)
Copper Foil	C	67.9
	O	22.5
	Cu	9.6
Silver Foil	C	58.4
	O	17.3
	Ag	24.3
Gold Foil	C	59.6
	O	23.6
	Au	16.8

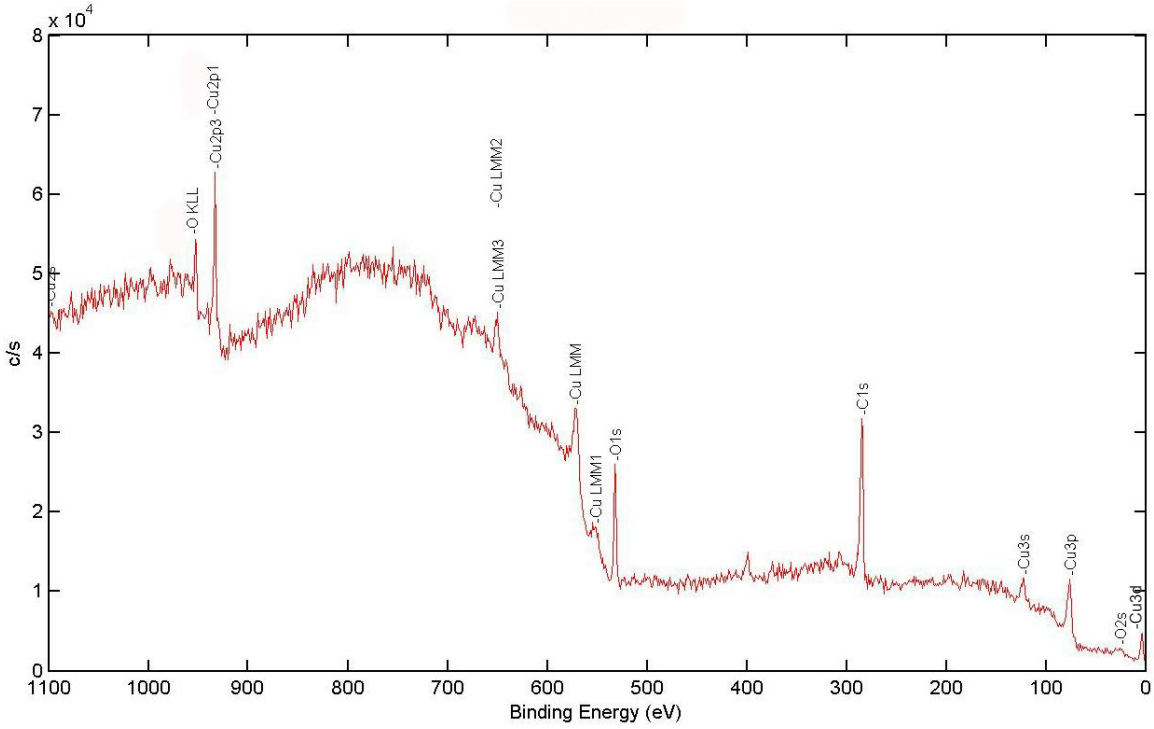

Figure 5.11. XPS survey spectrum of the copper foil standard with carbon and oxygen surface contamination peaks assigned.

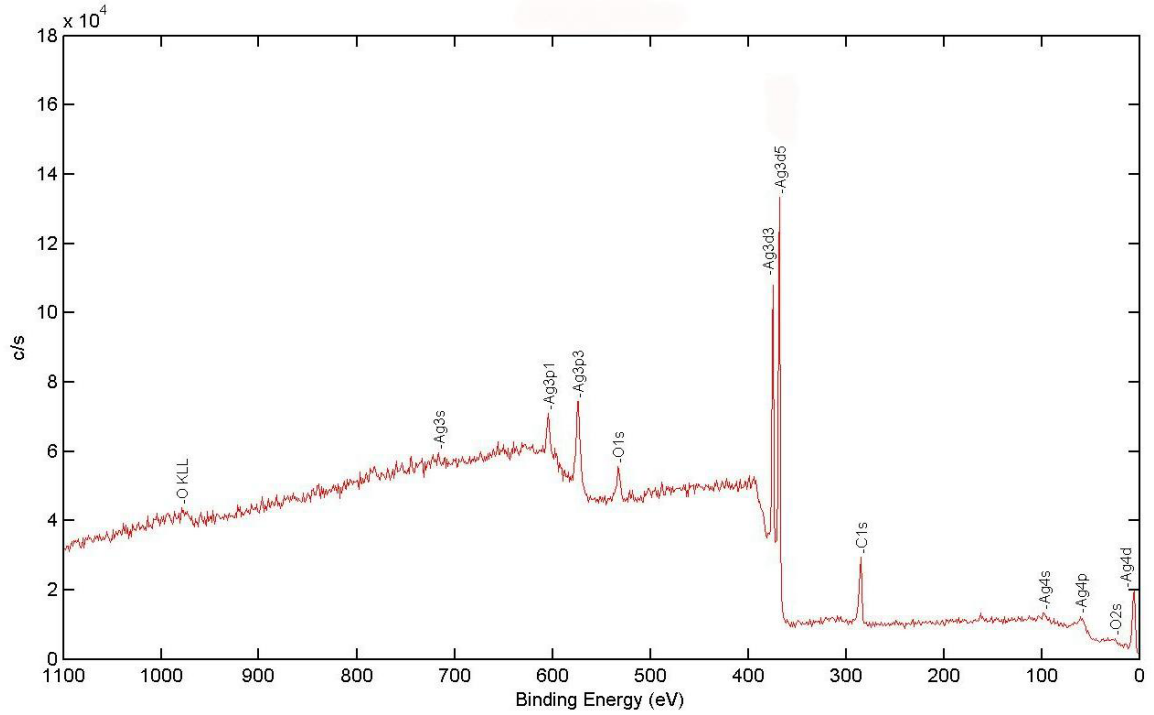

Figure 5.12. XPS survey spectrum of the silver foil standard with carbon and oxygen surface contamination peaks assigned.

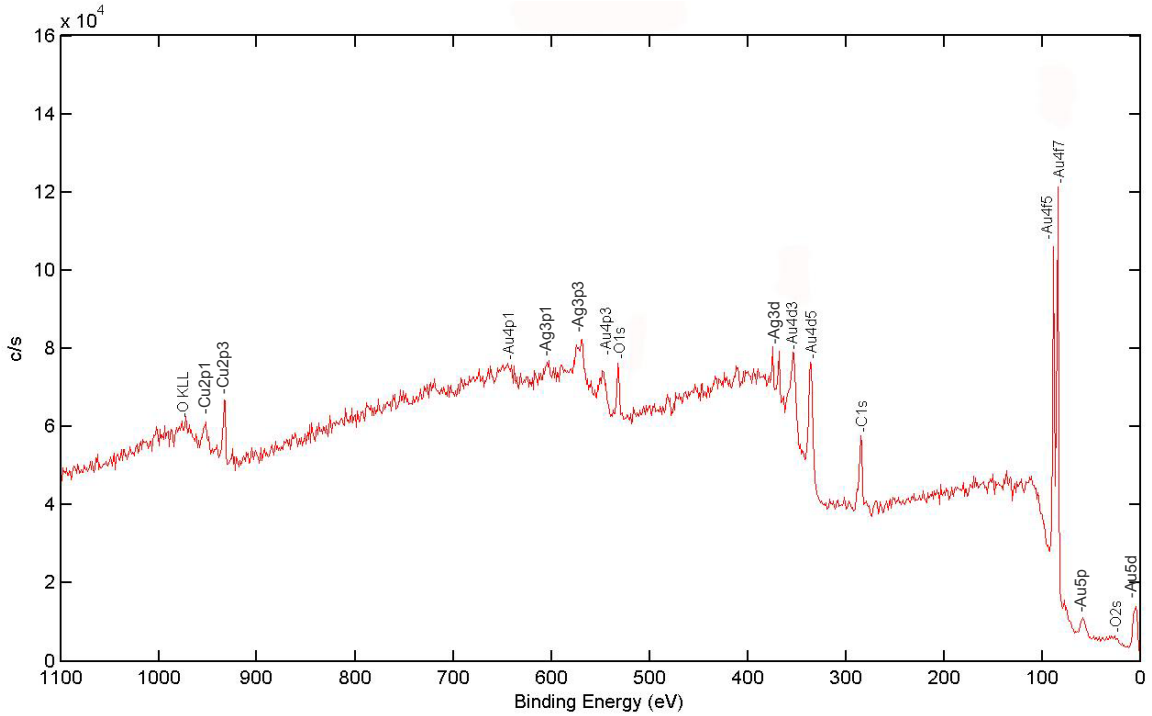

Figure 5.13. XPS survey spectrum of the gold foil standard with copper, silver, carbon, and oxygen surface contamination peaks assigned.

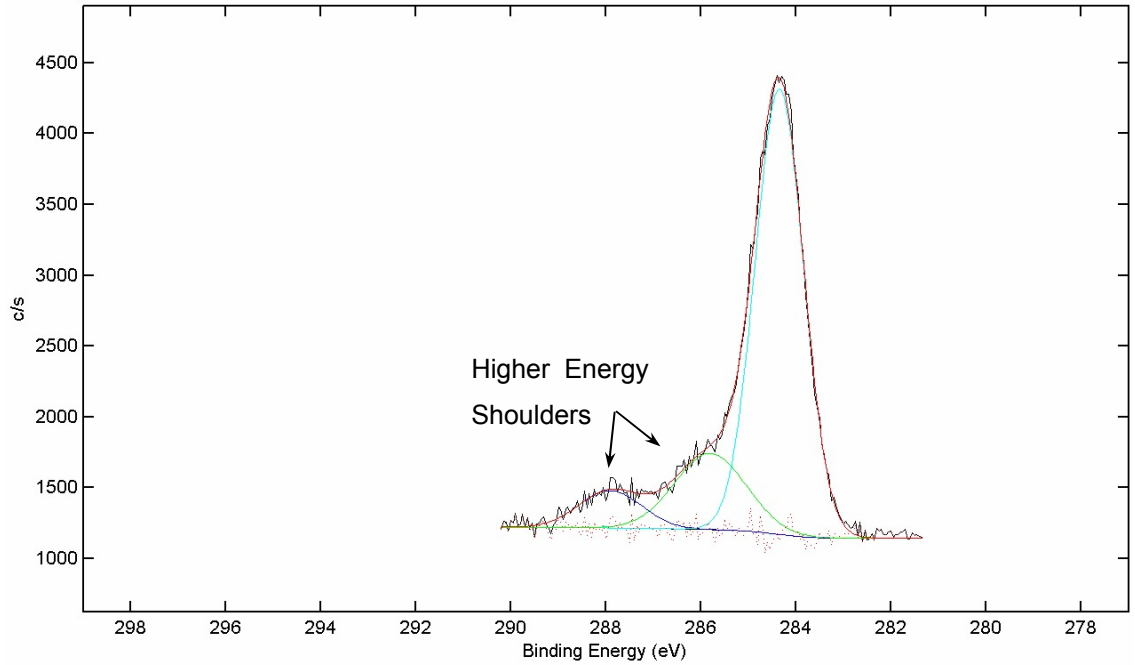

Figure 5.14. XPS detail spectrum of the ubiquitous carbon peak with two higher energy shoulders on the copper foil standard.

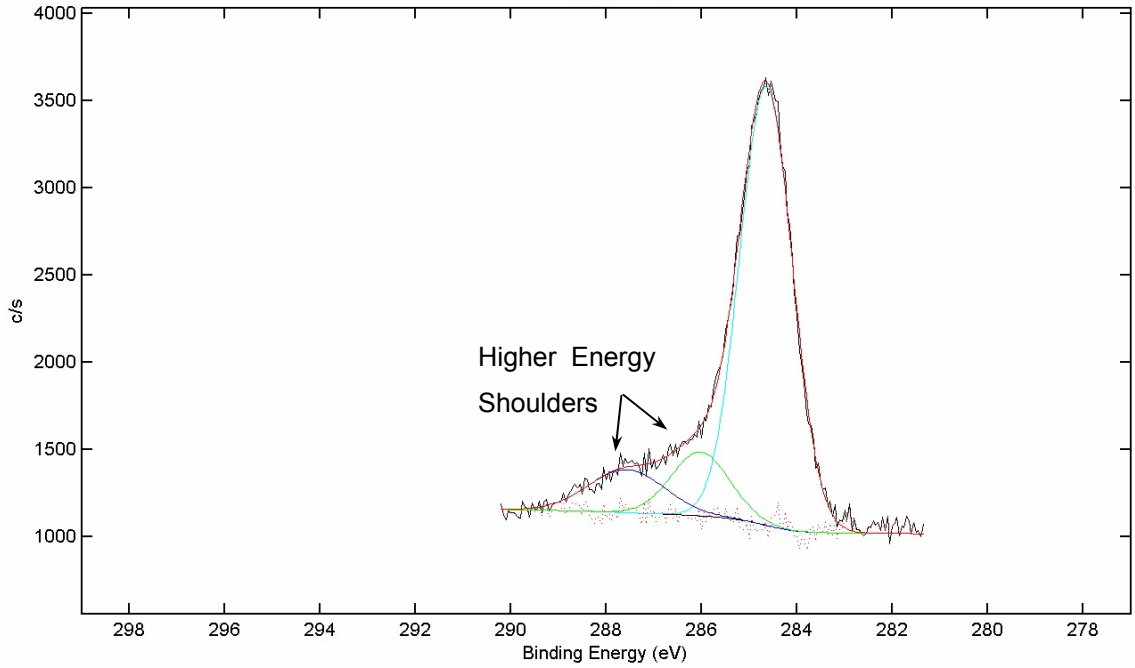

Figure 5.15. XPS detail spectrum of the ubiquitous carbon peak with two higher energy shoulders on the silver foil standard.

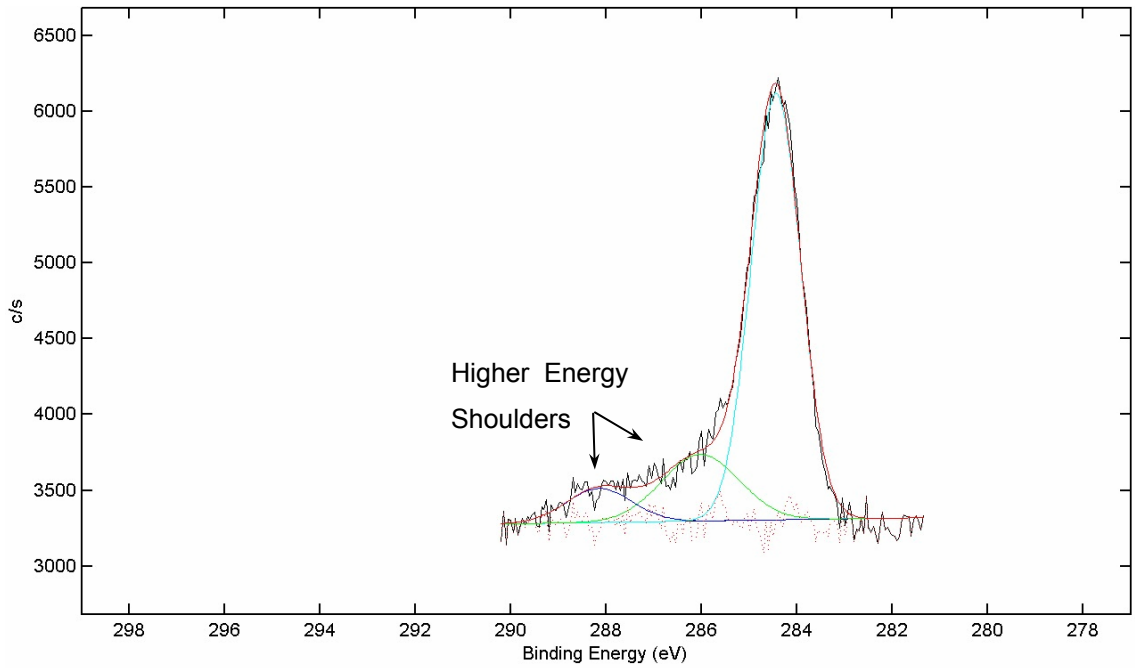

Figure 5.16. XPS detail spectrum of the ubiquitous carbon peak with two higher energy shoulders on the gold foil standard.

Considering the IMFP of the electrons from the elemental metal and the observed percentage present in each foil standard, the thickness of the contamination layer may be calculated. The large percentage of contamination with respect to the percentage of each elemental metal was indicative of a thick layer of adsorbed contamination. Calculations that included the IMFP of the ejected electrons yielded a representative thickness of these contamination layers on each of the foil standards and are listed in Table 5.3 with the process described in Section A.3. The contamination layer thicknesses are consistent with the XPS data obtained and the IMFP of the ejected electrons of each element present. The copper foil had been used more often as can be inferred from the thin oxide layer thickness and the reduced level of adsorbed contamination.

Each of the carbon components of the foil surfaces shown in Table 5.2 included higher energy peaks (see Figures 5.14 – 5.16). The broad mid-energy peak was also representative of ubiquitous carbon 1s electrons, however, from a broader energy distribution than the narrow lower energy peak. The highest energy peak observed with each of the metal foil spectra, located at a 2.4 – 3.5 eV higher binding energy position, was assigned to C – O bonding.[133(p.41)] Each oxygen peak observed in the foil spectra included higher energy shoulders. These are related to a combination of C – O and O – H bonding of carbon dioxide and moisture adsorbed as surface contaminants.[137]

Table 5.3. Calculated Thickness of Surface Layer Contamination on the Metal Foil Standards

Foil Standard	Oxide Layer	Contamination Layer
copper	26.5 pm	14.7 Å
silver	45.3 pm	23.3 Å
gold	45.3 pm	26.9 Å

The high energy shoulders of the oxygen and carbon peaks are indicative of the presence of moisture and carbon dioxide adsorbed to the foil surfaces. Pawelec had extensively shown the presence of a high energy shoulder on oxygen peaks in XPS analysis of metal oxides which could be attributed to different species such as carbonates, hydroxyls.[137] The energy shift of these oxygen shoulders was observed to be 1.5 eV. This agrees with the data obtained with the metal foils and with the observed shoulders on each oxygen peak of the nanopowder spectra.

Using a hot stage in the XPS analysis of samples, Pawelec was able to show that this oxygen shoulder was related to moisture adsorption, through exposure to moisture or a reducing hydrogen environment. Carbonate species also reveal themselves in XPS spectra as a high energy shoulder of oxygen and carbon peaks. Heating of samples at increasing temperature led to a progressive decrease in the intensity of the high energy oxygen shoulder component. This observation indicated that these oxygen species were partially eliminated upon thermal treatment under vacuum. Similar behavior was observed in the high energy carbon peak, although the decrease in peak intensity with temperature was less pronounced than with the high energy oxygen peak.

The oxygen peaks in the nanopowder spectra each included a high energy shoulder, shifted 1.5 eV from the lattice oxygen peak. The nanopowder spectra also included a high energy carbon peak. This data was indicative of the presence of moisture and carbonate species. It was not possible to differentiate between these two species since there was no technique available for higher temperature *in situ* analysis with XPS. Moisture and carbonate species, however, were observed in the vibrational spectra of the nanopowders, and thus corroborated the XPS findings.

After a survey spectrum was obtained of each sample, depth profile sputtering began. A spectrum was obtained after each one minute sputter, with 30 iterations obtained for each nanopowder. Spectra were obtained after each sputtering iteration within a narrow binding energy window, ±10 eV of an

expected peak, for the elements of interest: barium, titanium, oxygen, and carbon.

Potassium peaks were observed near the carbon peak of the spectra of Nanopowders C, D, and E (see Figures 5.17 – 5.19). The observed potassium 2p1 and 2p3 peaks, annotated in the previously noted figures, were at positions within reference values.[133(p.67)] The peak positions observed in the spectra of Nanopowders C and D are indicative of the potassium impurity bonded with oxygen. The peak observed in the spectrum of Nanopowder E, however, was observed at a lower binding energy. This was representative of elemental potassium in a K – K bonding state of a larger assemblage of the impurity. The potassium peaks were sporadically observed during the depth profiling of these three nanopowders, which would be expected for an impurity constituent. The presence of this impurity perturbed the position of carbon peaks, and affected the slope of the spectral background.

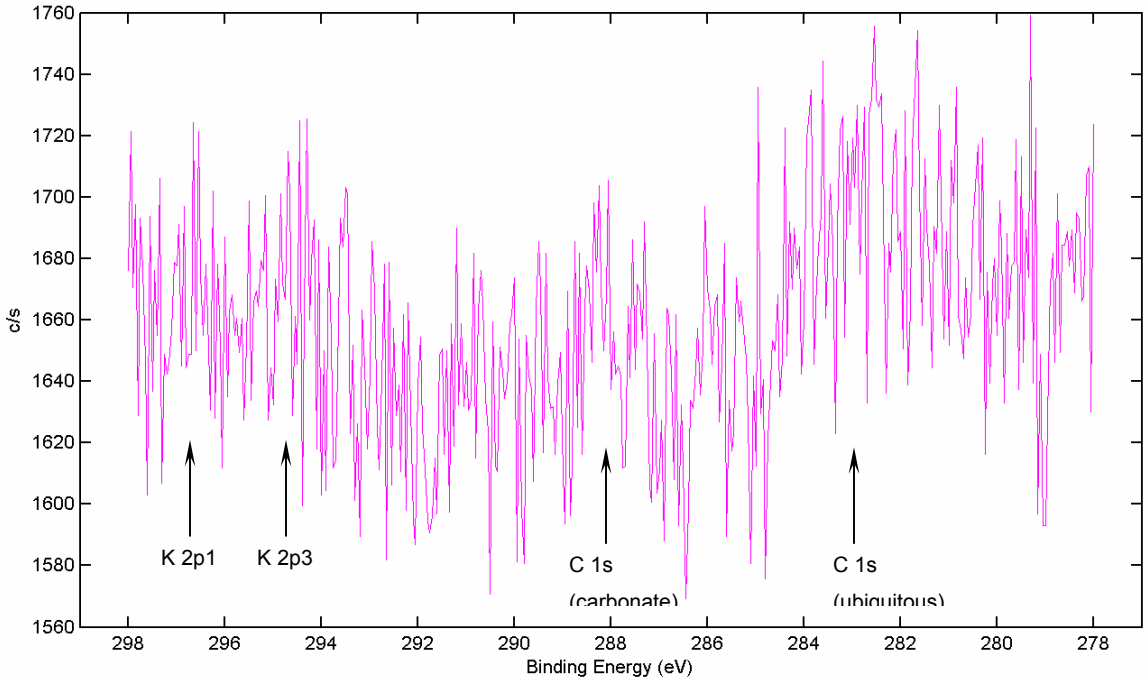

Figure 5.17. XPS detail spectrum of the carbon peaks and potassium impurity for Nanopowder C.

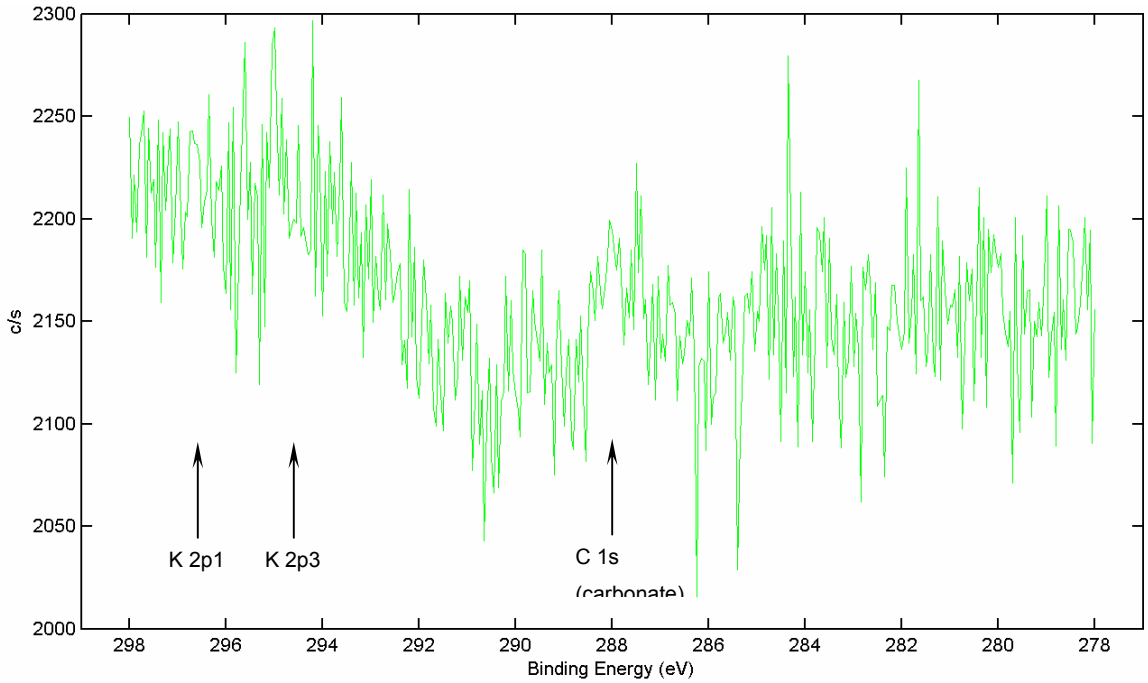

Figure 5.18. XPS detail spectrum of the carbon peak and potassium impurity for Nanopowder D.

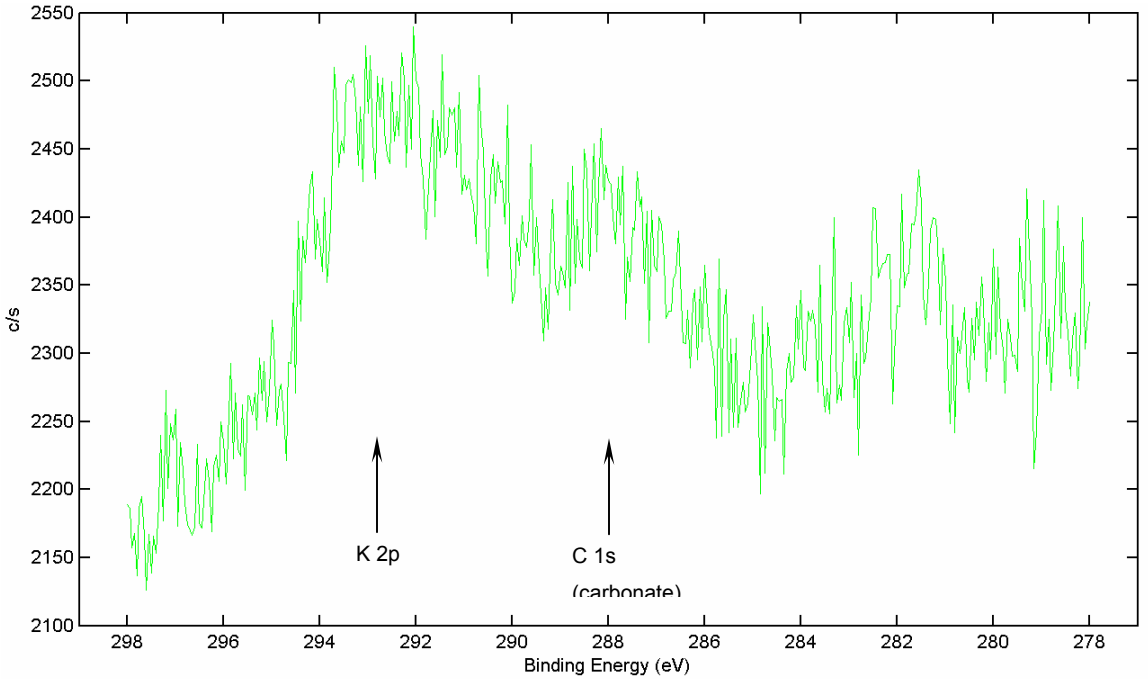

Figure 5.19. XPS detail spectrum of the carbon peak and potassium impurity for Nanopowder E.

The vibrational data in Section 3.1 indicated the presence of the compound barium carbonate with all of the nanopowders. The barium peaks observed in the XPS analysis indicated that two chemical states existed. Prior to the first sputtering, two pairs of barium peaks were observed in the spectra of all of the samples. These barium peak pairs were observed throughout the entire series of depth iterations with all of the nanopowders. Initially, the barium 3d transitions were observed since a reference for the binding energy of the barium 3d5 transition in barium carbonate was known. The binding energies of the two 3d5 transitions were observed to be 777.8 eV and 779.2 eV. The lower binding energy agreed with the reference energy for barium in barium carbonate.[133(p.139)] The higher binding energy was therefore assigned to barium in barium titanate.

The detail spectra of barium 4d transitions of each of the nanopowders in compact form are shown in Figures 5.20 through 5.25. Each figure begins with an un-sputtered spectrum and continues with the next 15 successive depth iterations. The initial spectra of Nanopowders A, B, and F exhibit a larger

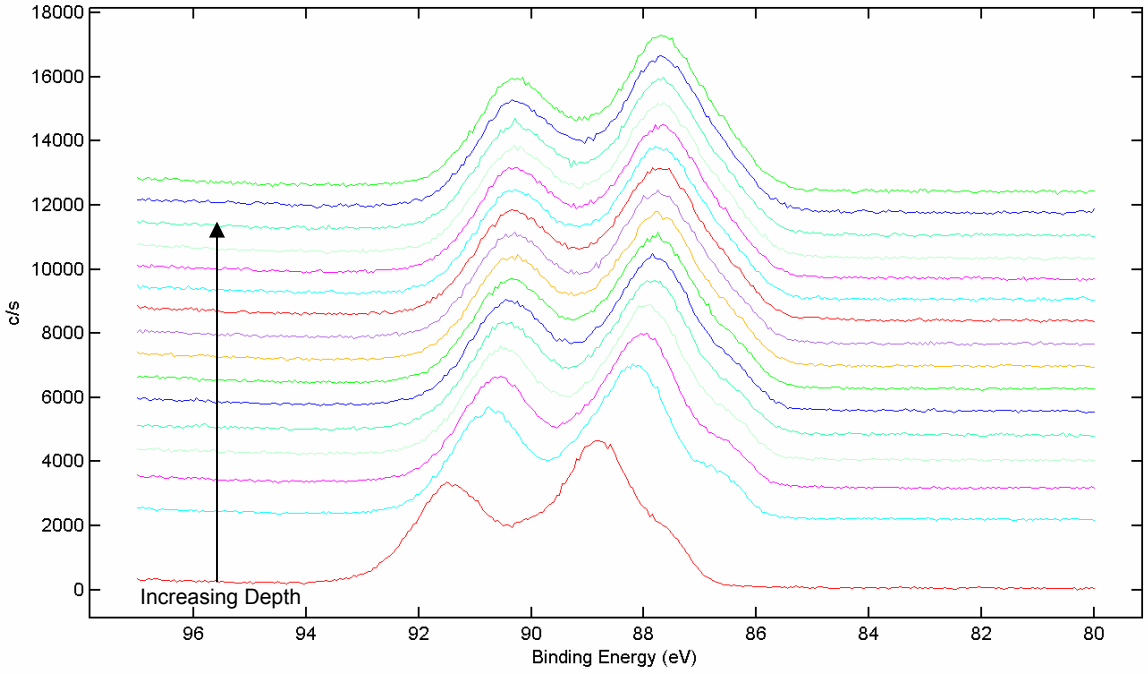

Figure 5.20. XPS detail spectrum of the barium 4d peaks of the pressed compact of Nanopowder A.

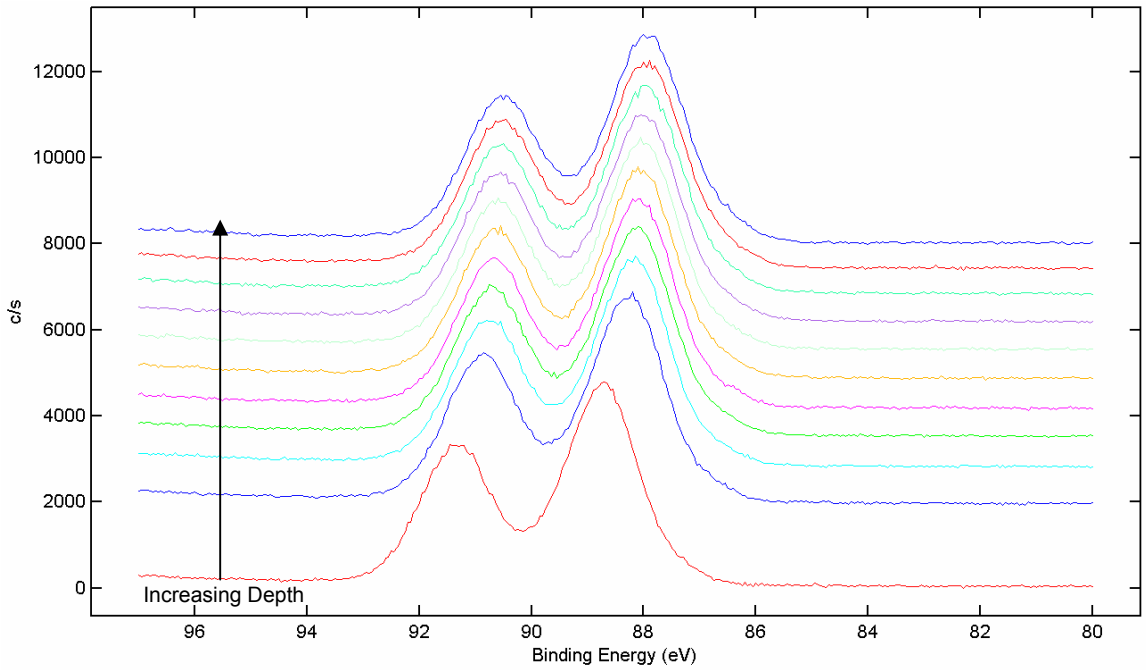

Figure 5.21. XPS detail spectrum of the barium 4d peaks of the pressed compact of Nanopowder B.

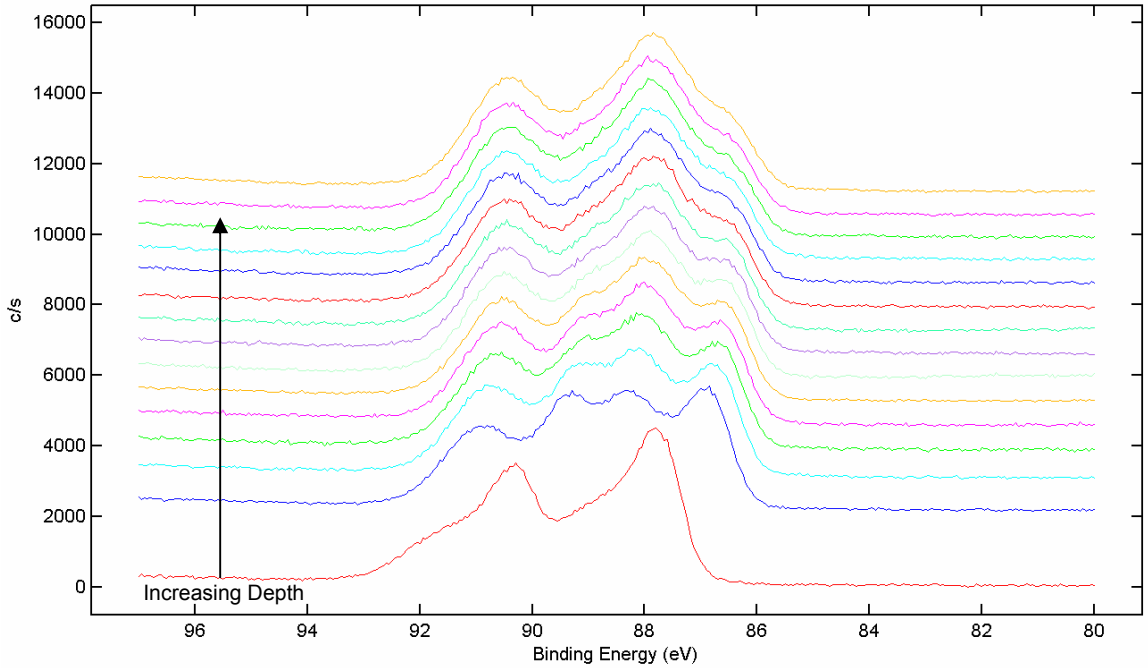

Figure 5.22. XPS detail spectrum of the barium 4d peaks of the pressed compact of Nanopowder C.

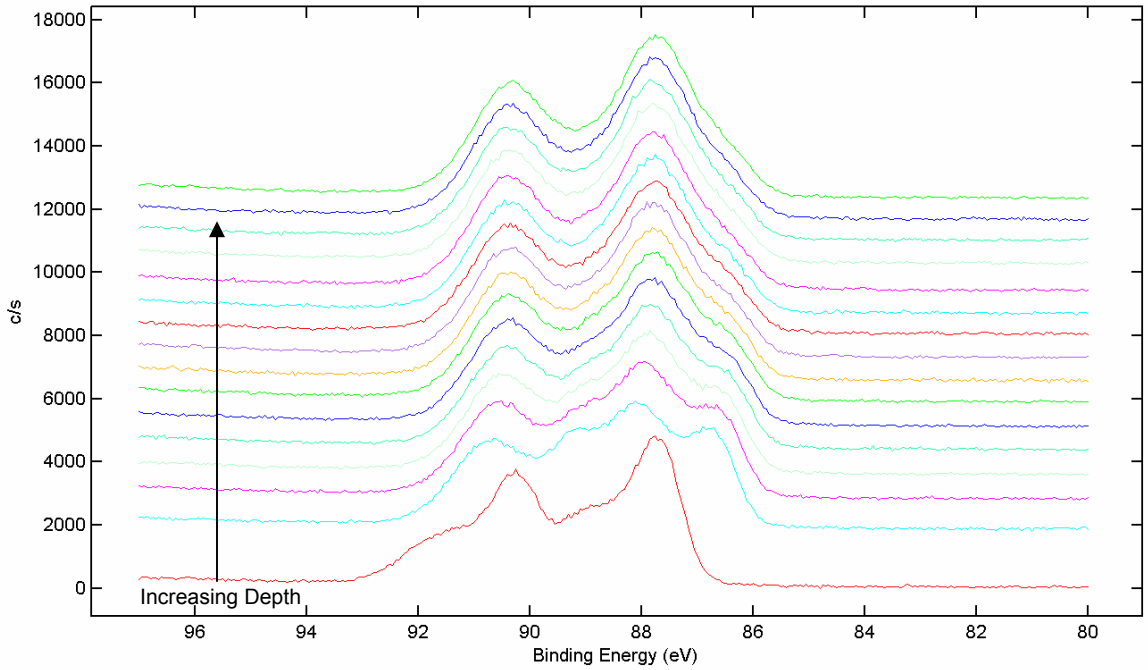

Figure 5.23. XPS detail spectrum of the barium 4d peaks of the pressed compact of Nanopowder D.

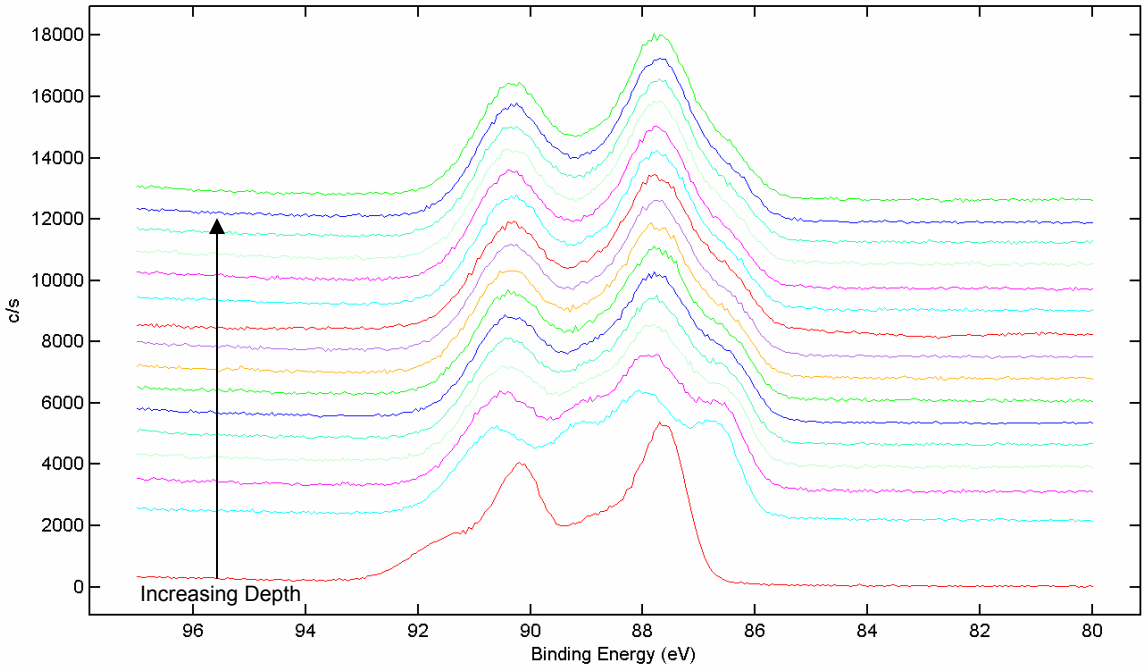

Figure 5.24. XPS detail spectrum of the barium 4d peaks of the pressed compact of Nanopowder E.

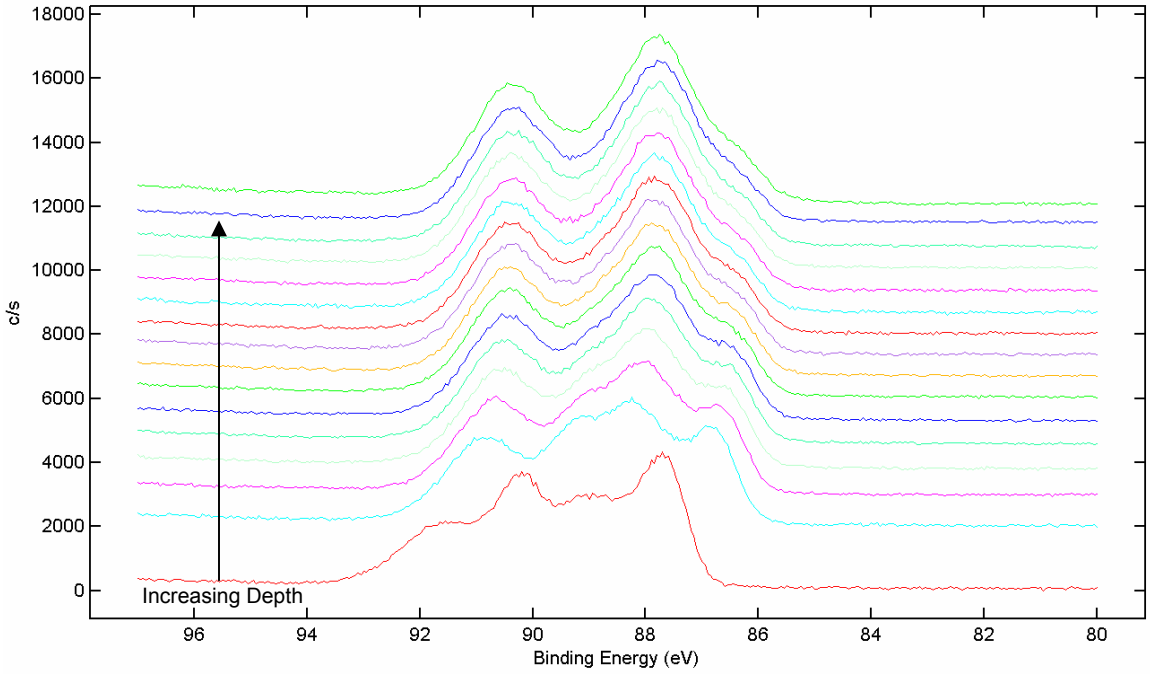

Figure 5.25. XPS detail spectrum of the barium 4d peaks of the pressed compact of Nanopowder F.

peak area for the pair of high binding energy peaks than the peak areas of the lower binding energy peak pair. This was indicative of a larger percentage of carbonate at the surfaces of these nanopowders. The spectra of the three remaining nanopowders, (C, D, and E), each had similar percentages of carbonate present, but were much less than that observed with the previous three nanopowders. Table 5.4 lists the percentage of the barium 4d transitions related to titanate (high binding energy, Ba_H) and carbonate (low binding energy, Ba_L) as represented in the initial spectra for each nanopowder.

In Section 3.2 of the vibrational analysis, a mesoscopic state was suggested for the surfaces of Nanopowder F. All of the peaks in the initial spectrum of Nanopowder F were broader and less well defined than that observed with the other nanopowders. This indicated a much broader energy distribution of all of the 4d transitions and supported the presumption of the mesoscopic state for the surfaces of this nanopowder.

Table 5.4. Percentage of Barium 4d Transitions Related to Titanate (Ba_H) and Carbonate (Ba_L) Compounds of the Compacts Prior to Sputtering

Sample	Ba_H (%)	Ba_L (%)	Sample	Ba_H (%)	Ba_L (%)
A	84.7	15.3	D	49.5	50.5
B	95.0	5.0	E	46.7	53.3
C	57.9	42.1	F	58.4	41.6

Each of the nanopowder spectra exhibited a large shift, ~0.8 eV in binding energy, after the first sputtering of the surfaces. The peaks continued to shift to lower energy with succeeding iterations through the eighth iteration, totaling 1.0 to 1.25 eV. Large reductions were observed with the high energy shoulder to the oxygen peaks, the lower energy barium peak pairs, and the carbon peaks with all nanopowders after the first sputtering. This first sputter also produced the greatest shift in peak energy. Further sputtering removed the ubiquitous carbon and the majority of carbonate related carbon after five to eight iterations for all samples. The high energy oxygen shoulder also diminished during this period. The carbonate related barium peak pairs also diminished during these iterations. The spectral peak shifting was, therefore, considered to be the effect of the removal of the contamination layer from the surfaces.

The approximate sputter rate for SiO_2 is 3.55 Å/minute under the same sputtering conditions. Using the data from Nanopowder F, (the smallest nanopowder), the carbon peaks, oxygen shoulder, and Ba_L peak pair were relatively unchanged after the eighth iteration. The calculated contamination layer thickness was 18.57 Å. The approximate sputter rate was 2.32 Å/minute. The calculated contamination layer of Nanopowder A, (the largest nanopowder), had a thickness of 11.97 Å. The aforementioned peaks were relatively unchanged after the fifth iteration.

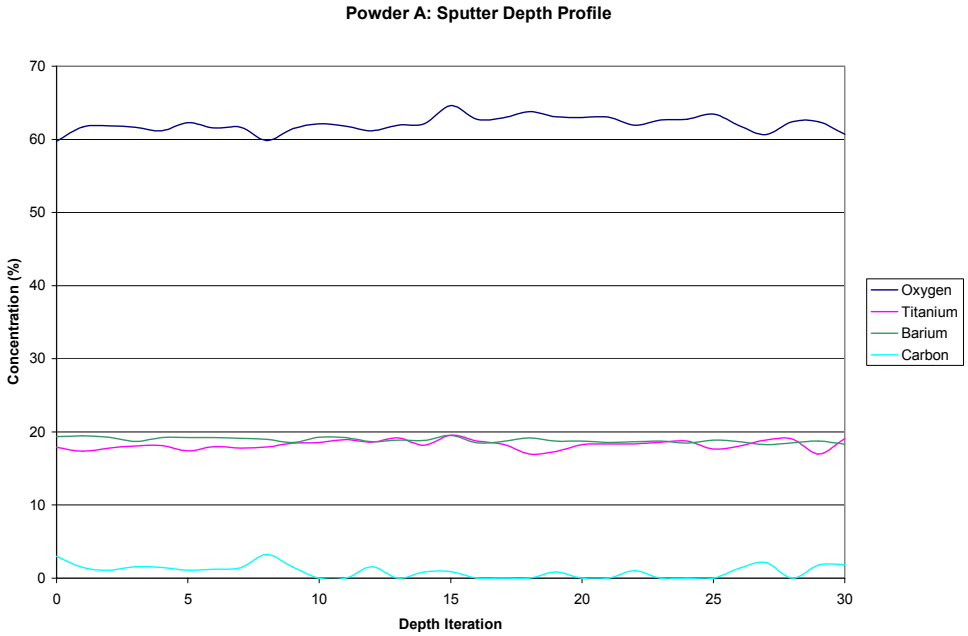

Figure 5.26. XPS sputter depth profile indicating percentage of elements present in the pressed compact of Nanopowder A after each of the 30 sputtering iterations.

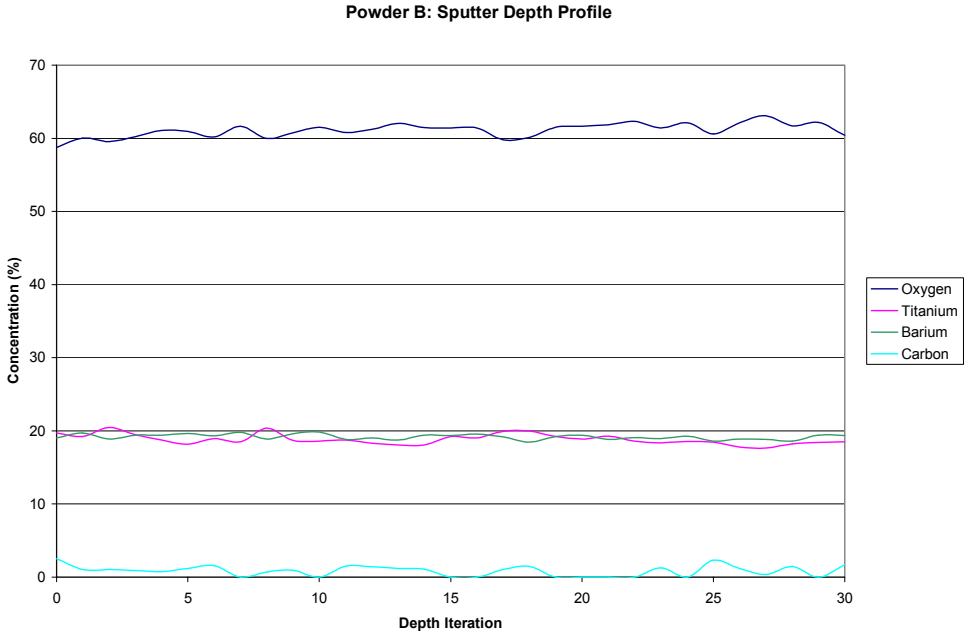

Figure 5.27. XPS sputter depth profile indicating percentage of elements present in the pressed compact of Nanopowder B after each of the 30 sputtering iterations.

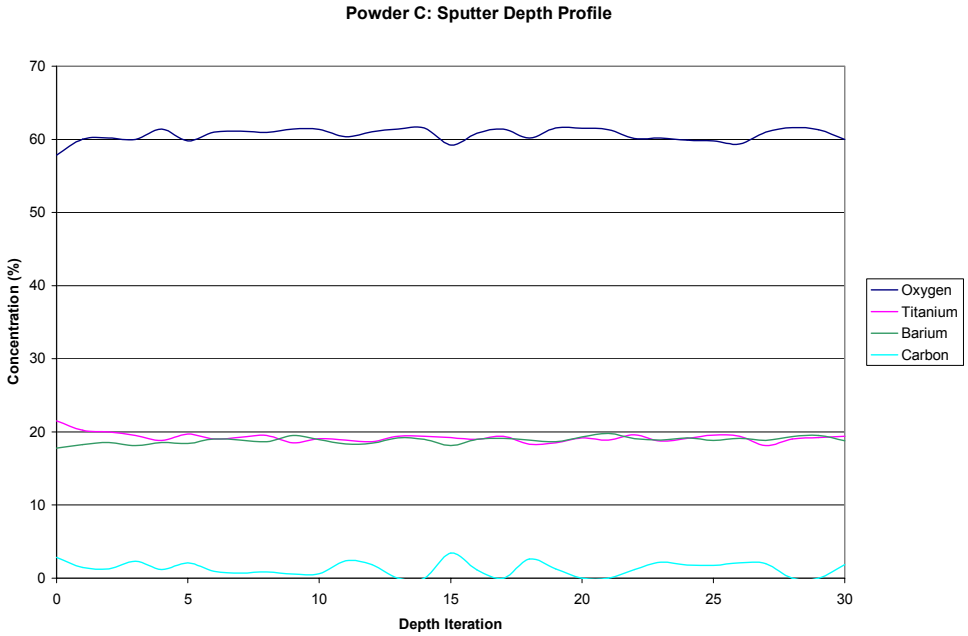

Figure 5.28. XPS sputter depth profile indicating percentage of elements present in the pressed compact of Nanopowder C after each of the 30 sputtering iterations.

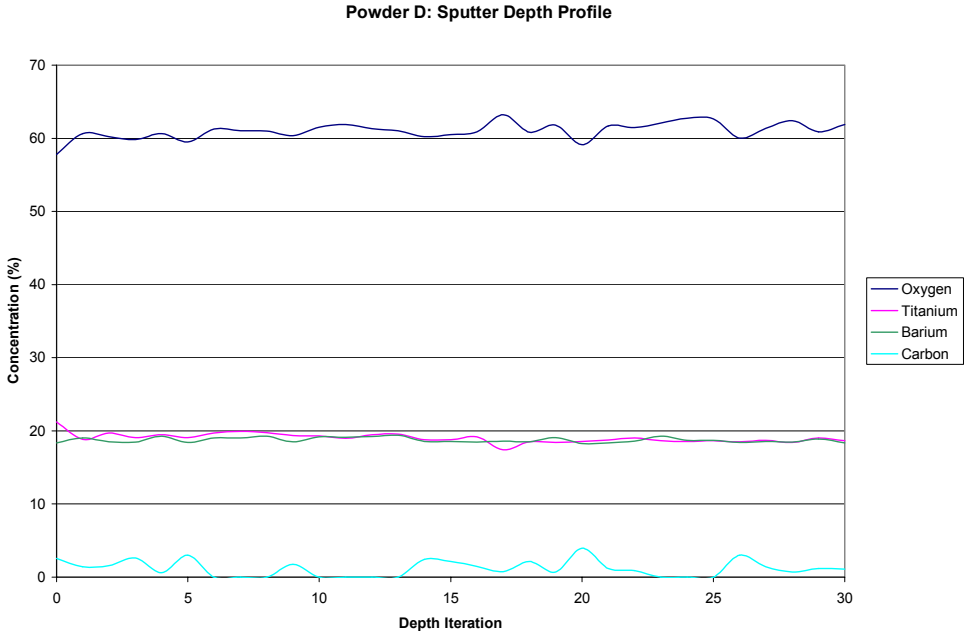

Figure 5.29. XPS sputter depth profile indicating percentage of elements present in the pressed compact of Nanopowder D after each of the 30 sputtering iterations.

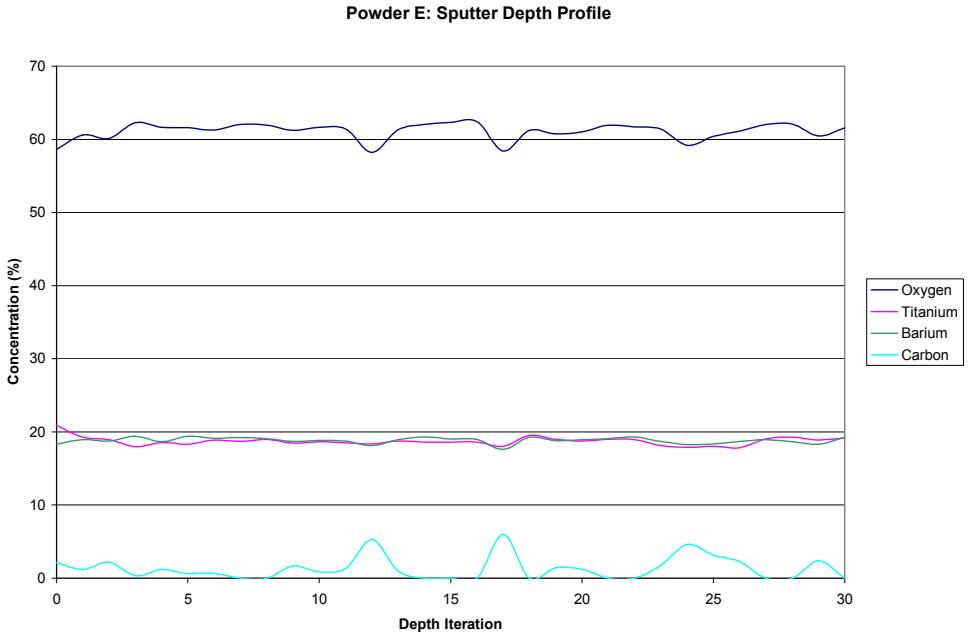

Figure 5.30. XPS sputter depth profile indicating percentage of elements present in the pressed compact of Nanopowder E after each of the 30 sputtering iterations.

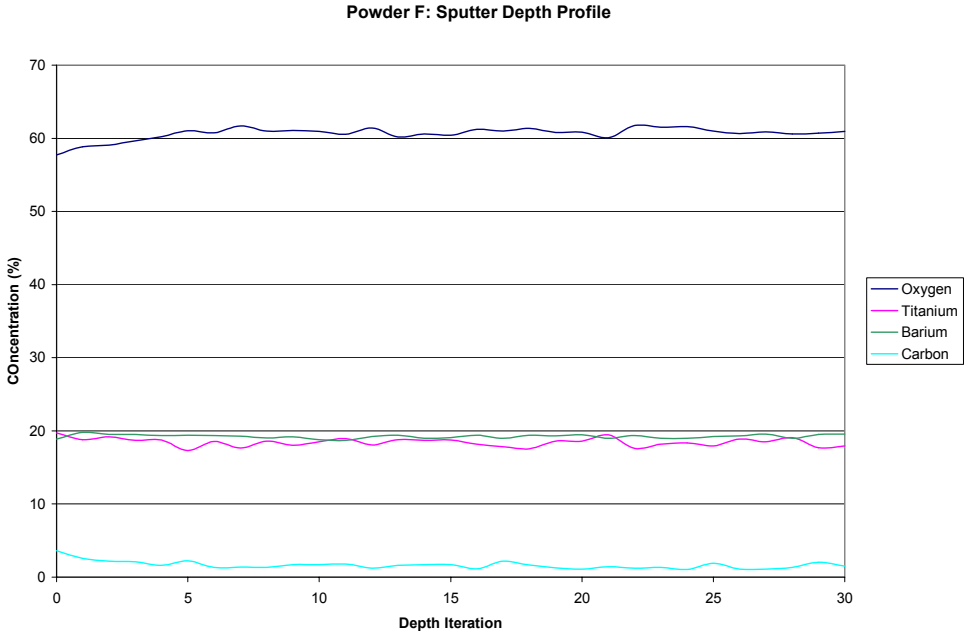

Figure 5.31. XPS sputter depth profile indicating percentage of elements present in the pressed compact of Nanopowder F after each of the 30 sputtering iterations.

The approximate sputter rate was 2.4 Å/minute, close to that calculated for the other nanopowders.

The percentage of the elements present in the nanopowder pressed compacts after each sputtering iteration exhibited slight variations in the Ba/Ti ratios (see Figures 5.26 – 5.31). The variations in these values were highly dependent upon the software package's integrity in peak fitting and the level of noise in the spectra. It was not possible, therefore, to calculate specific Ba/Ti ratios of the nanopowders. However, general trends in the relation between the elements present were observed.

The ratio of oxygen to barium and titanium in barium titanate or to barium and carbon in barium carbonate is 3:1. There was a slightly higher ratio than this observed with each of the nanopowder samples. Vibrational analysis indicated the presence of surface carboxyl groups and moisture in each of the samples. The ratio observed with the XPS analysis was indicative of additional oxygen bound possibly in carboxyl groups or as moisture, as indicated with the vibrational results. Additionally, carbon was observed discontinuously through all sputtering iterations in Nanopowders A through E, which also gave support to this premise. However, carbon was observed continuously with Nanopowder F; a reasonable finding considering that this nanopowder had the highest percentage of carbonate.

Throughout the depth profiling, only Nanopowders A and B showed little change in the Ba_L peaks and the associated high percentage of barium carbonate at the surfaces of these nanopowders. Since XPS is a surface sensitive technique, the continued presence of the lower energy peaks was indicative of a carbonate surface layer.

Table 5.5 shows the calculated thickness of the barium carbonate present in the nanopowder compacts, and the additional thickness due to surface contamination. This contamination included any adsorbed moisture, carbon dioxide, and ubiquitous carbon present. The listed volume percentages were the amount of an average sized nanoparticle represented by barium titanate. The XPS results are consistent with the results obtained during vibrational analysis.

The amount of barium carbonate present in Nanopowder F, which contained the largest percentage of carbonate, was just above the detection limit of x-ray diffraction. The XRD analysis of Nanopowder F exhibited a minor peak representing this amount.

Table 5.5 evidences the trend that the volume percentage of surface species increased as the nanopowder size decreased. The volume percentages were representative of an average sized particle of each of the nanopowders. Considering a particle of 20 nm radius of nanopowder F for example, the smallest of the samples in this study, would have been encapsulated by a 1.23 nm layer of barium carbonate, and an additional 0.6 nm of adsorbed contaminant from ambient atmosphere. The barium titanate within the layers of carbonate and adsorbed species would only have a radius of slightly more than 18 nm. Further, considering the density of barium carbonate and barium titanate, the density ratio of carbonate to titanate would be 1 to 6. For batch calculations this would represent approximately 84% barium titanate by weight basis, the balance represented by carbonate and atmospheric surface contamination! Compounds formed through the use of nanopowders of a similar contamination layer thickness would have an inaccurate resultant stoichiometry, affecting processes such as thin film production.

A second series of samples were examined using the sample holder shown in Figure 5.1. Results were comparable with the first series. The detail spectra of the barium 4d transitions showed a smaller shift, 0.2 eV to 0.65 eV in binding energy, after the first sputtering of the surfaces. The peaks continued to shift to lower energy with succeeding iterations through the seventh iteration, totaling 0.5 to 1.0 eV. The calculated contamination layer for Nanopowder F was thinner than that of the previous series and exhibited smaller peak shifting. This shift was also observed with the peaks for the other elements.

The barium 4d transition peaks of nanopowder F in the second series did not follow the same trend. The peaks were also broad and ill-defined as with the first series. However, the peaks shifted to both higher and lower positions during the sputtering iterations (see Figure 5.32). This again indicated a much broader

Table 5.5. Calculated Volume Percentage and Layer Thickness of the Surface Contamination on the Nanopowder Compacts Prior to Sputtering

Powder	Barium Titanate Volume %	Carbonate Layer Thickness	Surface Contamination	Total Layer Thickness
A	98.48	9.06 Å	2.91 Å	11.97 Å
B	98.40	8.32 Å	3.37 Å	11.69 Å
C	95.89	5.20 Å	6.54 Å	11.74 Å
D	95.02	4.68 Å	6.12 Å	10.80 Å
E	90.90	5.48 Å	4.84 Å	10.32 Å
F	77.23	12.31 Å	6.26 Å	18.57 Å

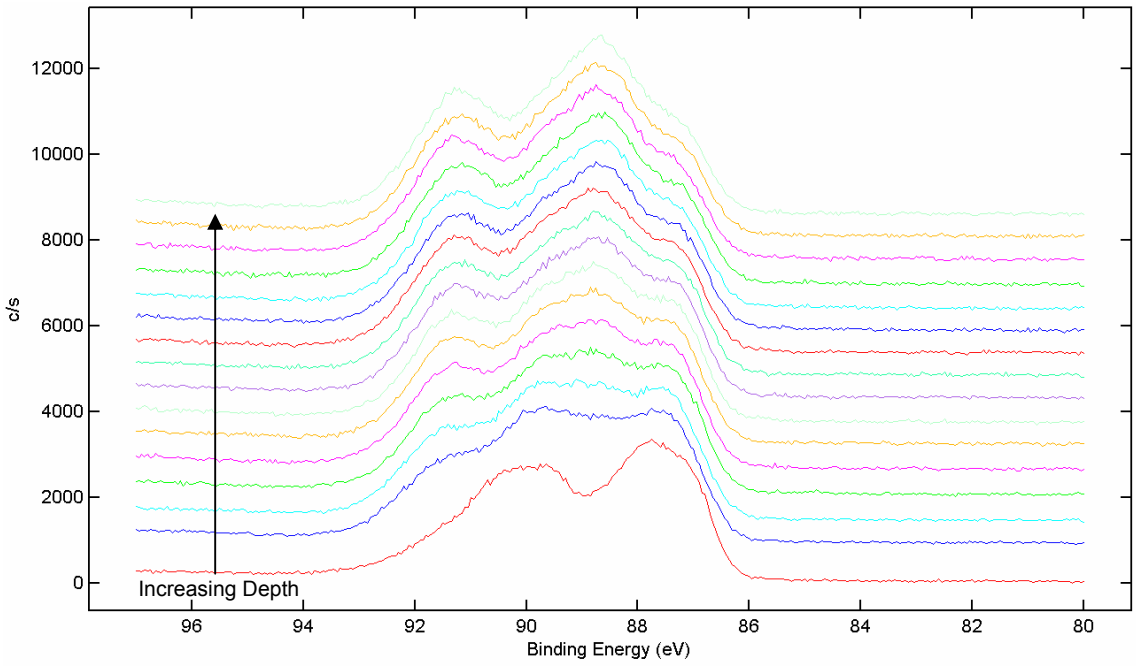

Figure 5.32. XPS detail spectrum of the barium 4d peaks of Nanopowder F lightly tamped in the sample holder.

energy distribution of all of the 4d transitions and further supported the presumption of the mesoscopic state for the surfaces of this nanopowder.

Table 5.6 shows the calculated thickness of the barium carbonate present in the nanopowders of the second series, and the additional thickness due to surface contamination. The data were consistent with the data from the first series, and again evidence the trend that the volume percentage of surface species increased as the nanopowder size decreased. The adsorbed surface layer was, however, of increased thickness. The pressed compacts were stored in small zip-lock bags prior to placement on the sample stage and entry into the introductory chamber of the spectrometer. The second series of samples were lightly tamped in their respective holders, and then placed in an open hood without protection from ambient atmosphere for several days. The samples were then placed on the sample stage and entered into the introductory chamber. The additional exposure was evidenced by the increased thickness of the layer of surface contamination.

The data from this second series of samples were compatible with the first set and were also consistent with the data from the previous analysis techniques. Plotting average particle size of the nanopowders sampled versus the percent of the particle comprised of barium titanate from the XPS results of the second series, provided interesting results (see Figure 5.33). The barium titanate content diminished sharply after reaching an average particle radius of 30 nm. The graph predicts that extremely small particles, radii below 10 nm, would conceivably be comprised of half barium titanate with the balance comprised of barium carbonate and adsorbed contamination.

Table 5.6. Calculated Volume Percentage and Layer Thickness of the Surface Contamination on the Second Series of Nanopowders Prior to Sputtering

Powder	Barium Titanate Volume %	Carbonate Layer Thickness	Surface Contamination	Total Layer Thickness
A	98.00	9.22 Å	6.55 Å	15.77 Å
B	97.85	9.15 Å	6.59 Å	15.74 Å
C	95.82	5.14 Å	6.80 Å	11.94 Å
D	93.95	6.55 Å	6.64 Å	13.19 Å
E	89.10	6.14 Å	6.31 Å	12.45 Å
F	80.21	9.82 Å	6.12 Å	15.94 Å

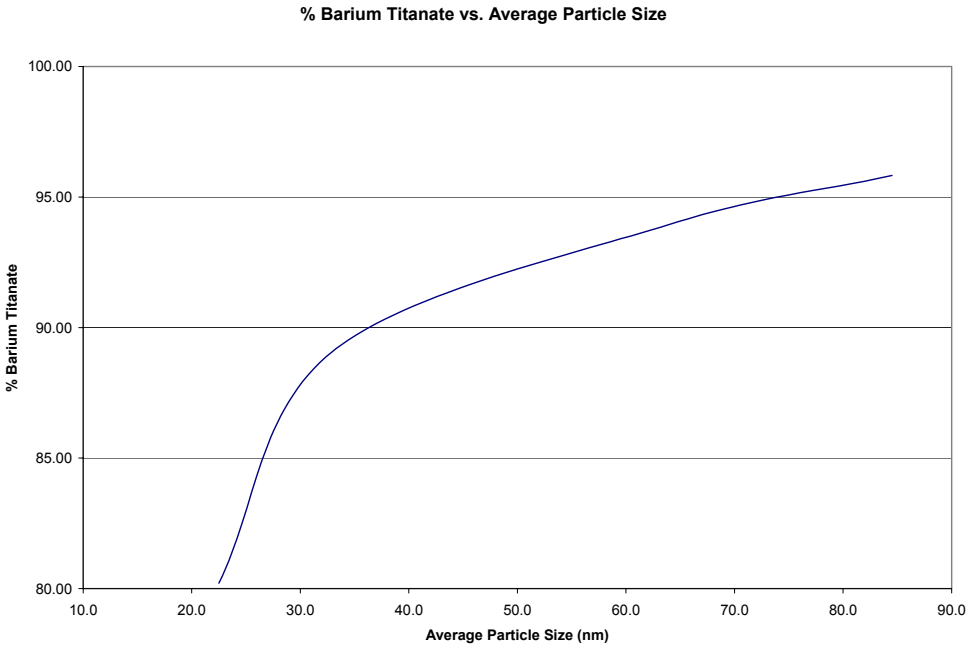

Figure 5.33. Percentage of barium titanate contained by the nanopowders of the second series based on the XPS data.

5.4 Summary

All of the XPS survey spectra of the nanopowders were found to contain barium, titanium, oxygen, and carbon peaks. Nanopowders C, D, and E contained a potassium impurity that was occasionally encountered during depth profiling. Carbon was represented by peaks assigned to ubiquitous carbon and a carbonate related peak. The peak related to oxygen was accompanied by a 1.5 eV higher binding energy shoulder. This shoulder was representative of either hydrogen bound to oxygen or carbon bound to oxygen in carbonate coordination.

The peak position for the ubiquitous carbon was solved using the spectra of metal foil standards. The peak position was 284.44 ±0.13 eV for the metal foil standards and the nanopowders. The percentage of the total signal from the elemental metal in each foil sample was 8%, 16.2%, and 15.4%, corresponding to Cu, Ag, and Au respectively. This highlighted the fact that a large percentage of the metal foil surfaces were comprised of adsorbed surface contamination.

XPS revealed that the barium titanate bonding state could be distinguished from a barium carbonate state on the basis of the barium 3d and 4d transitions' peak shifts. The barium carbonate bond state was assigned to peaks located at a 1.5 eV lower binding energy than the position of the barium titanate peaks. Justification for the peak assignments was supported by values referenced in literature and by other analysis techniques performed previously.

The nanopowders followed trends that were substantiated by the data from XPS and previously performed techniques. XPS identified the carbonate impurity phase that, by XRD, was faintly present with Nanopowder F and absent in the other nanopowders. As the average particle size decreased the percentage of the particles comprised by barium titanate decreased non-linearly. Moisture was indicated with XPS and vibrational techniques.

All of the peaks in the initial spectrum of Nanopowder F were broader and less well defined than that observed with the other nanopowders. This indicated a much broader energy distribution of all of the 4d transitions. This data corroborated the vibrational analysis in Section 3.2, and supported the presumption of a mesoscopic state for the surfaces of Nanopowder F.

As analyzed by XPS, the nanopowders in contact with ambient atmosphere had a surface layer of barium carbonate and adsorbed carbon dioxide, moisture, and ubiquitous carbon. Comparison of the barium 3d and 4d transitions allowed the calculation of the depth of the layer of barium carbonate and the adsorbed species layer. The nanopowders were encapsulated by a layer of surface carbonate that ranged between 4.68 Å and 12.31 Å and a total contamination layer that ranged between 10.32 Å and 18.57 Å.

A plot of the percentage of barium titanate versus average particle radius revealed that the percentage of barium titanate diminished sharply below a radius of 30 nm. This plot predicts that extremely small particles, radii below 10 nm, would conceivably be comprised of half barium titanate and half barium carbonate with additional adsorbed surface contamination. Further, batch calculations would contain a low percentage of barium titanate. Compounds formed through the use of nanopowders having a similar contamination layer thickness as observed here, would have an inaccurate resultant stoichiometry that could affect processes such as thin film production.

The unintentional incorporation of adsorbed contaminants during device processing will gain more attention as critical dimensions are scaled down to the nanometer regimes. These factors mean that a small amount of contaminant may have a relatively larger effect on miniaturized devices than with the current larger devices.

6 Calcining in an Ambient Atmosphere

6.1 Optical Microscopy

6.1.1 Introduction

Due to the interesting images observed with Nanopowder F in ambient conditions, additional optical images were analyzed after calcining the nanopowder at 473K, 773K and 1173K. The agglomeration of the nanopowder was an interesting aspect of Nanopowder F and the scope of the study was expanded to include optical microscopic observation of the calcined samples. The nanopowder was viewed optically to study the degree of agglomeration, shape and possible growth after calcination.

6.1.2 Experimental Procedure

Samples were calcined at 473K, 773K and 1173K, at a rate of 10K/minute, for a soak period of one hour at each temperature in ambient atmosphere. An amount of 50 mg of each nanopowder sample was dispersed in 10 ml of acetone in a 50 ml beaker and ultrasonicated for 15 minutes. (Brandon Ultrasonics Corp., model 2510, Danbury, CT) A pipette was used to draw a sample from near the surface of the solution and apply a single drop onto a sample glass slide. Analysis was performed using a Lietz optical microscope (Leitz, Laborlux 11 POL, Wetzlar, Germany) under reflected light conditions. Optical photomicrographs were taken and stored digitally.

6.1.3 Results and Discussion

After one hour at 473K in an ambient atmosphere (see Figure 6.1) the spherical agglomeration was still evident. The size of these spheres was visibly larger than those observed at room temperature. The degree of growth of the agglomerates was visually extensive through comparison of both 500X magnified

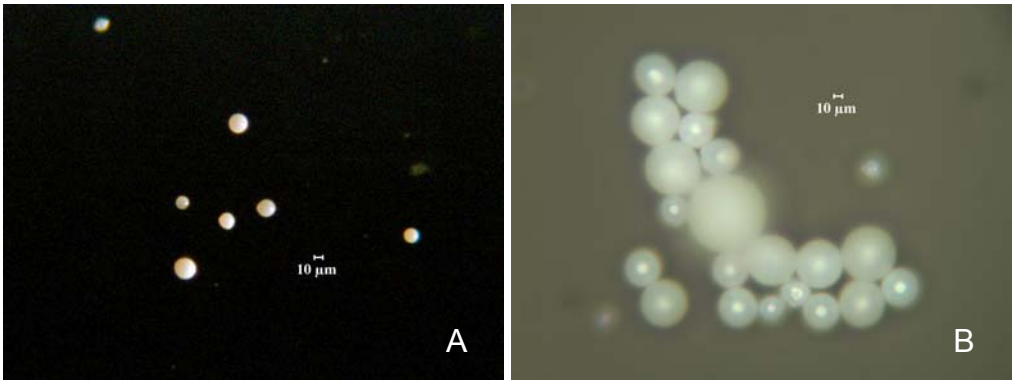

Figure 6.1. Optical photomicrograph of Nanopowder F under reflected light at 200X (A) and 500X (B) magnification after calcining at 473K for one hour in an ambient atmosphere.

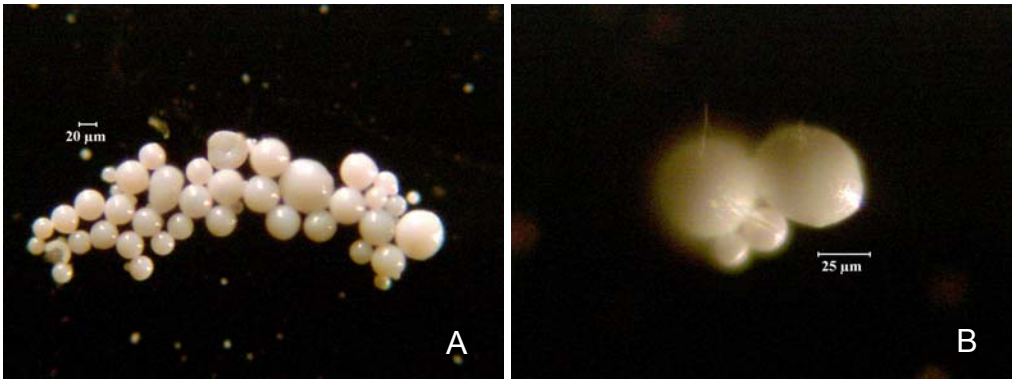

Figure 6.2. Optical photomicrographs of Nanopowder F under reflected light at 200X (A) and 500X (B) magnification after calcining at 773K for one hour in an ambient atmosphere.

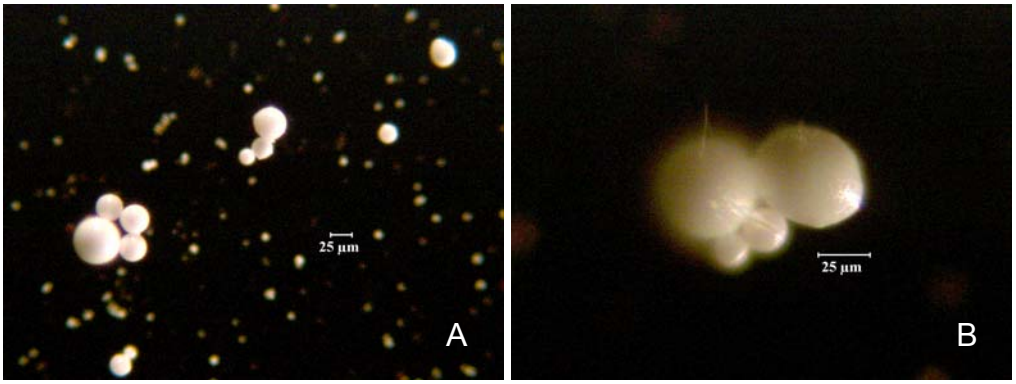

Figure 6.3. Optical photomicrographs of Nanopowder F under reflected light at 200X (A) and 500X (B) magnification after calcining at 1173K for one hour in an ambient atmosphere.

images: at room temperature (see Figure 2.3 micrograph F) and at 473K (see micrograph B in Figure 6.1).

After one hour at 773K in an ambient atmosphere (see Figure 6.2) the spherical agglomeration was again still evident. A larger number of the spherical agglomerates had grown to 20 microns in diameter as opposed to the number achieving this size after the 473K calcine.

After one hour at 1173K in an ambient atmosphere (see Figure 6.3) the spherical agglomeration was still evident. A marked difference is observed between the 1173K calcined sample versus all other samples. The 1173K calcined sample exhibited a smaller number of larger spheres accompanied with a larger number of smaller spheres. This indicates that an equilibrium agglomerate diameter, approximately 25 microns in diameter, had been reached for the larger spheres. However, growth continued with the remaining smaller spheres.

6.1.4 Summary

The arrangement of the agglomerates of Nanopowder F, the smallest of the study, was spherical. The excess surface space charge of the 40 nm average particle size nanopowder was being compensated for with the agglomerates assuming the lowest energy volumetric shape, the sphere. These spheres retained their shape and increased in diameter during calcination in ambient atmosphere. The spheres appeared to reach a maximum size at 773K, possibly the equilibrium agglomerate diameter. The 1173K calcined sample appearing visually to be of similar dimensions as the 773K calcined sample with a larger number of smaller spheres of increased diameter. There was no deviation from the spherical shapes during the calcining and visual microscopic analysis.

6.2 Scanning Electron Microscopy

6.2.1 Introduction

Scanning electron microscopy (SEM) provided a closer examination of the calcined nanopowders subsequent to the optical study at room temperature. SEM was employed to view the morphology of the nanopowders, and the agglomerates that were present, subsequent to calcination. The diameter of the smallest of the nanopowders was smaller than the resolving capability of the SEM used and precluded the viewing of individual crystallites.

6.2.2 Experimental Procedure

Nanopowders were calcined in small alumina boats at 473K, 773K and 1173K, at a rate of 10K/minute, in a muffle furnace (Centurion Q50, Degussa-Ney, Yucaipa, CA) for a soak period of one hour at each temperature in ambient atmosphere. Samples of the nanopowders were then prepared for viewing by ultrsonicating approximately 50 mg in 10 ml of acetone in a 100 ml beaker for a period of 10 minutes. Using a pipette, a drop of this solution from the top of the solution was deposited on a carbon-disc coated long stem pin support and allowed to air dry. The nanopowders were then coated for a period of 1.5 minutes by plasma sputtering with 70:30, by weight, gold-palladium with an operating voltage of 25 kV. The pin supports were then placed in the SEM (Amray 1810, Amray Inc., Bedford, MA) utilizing a short working distance to allow well resolved high magnification viewing with an acceleration voltage of 25 kV to 30 kV.

6.2.3 Results and Discussion

6.2.3.1 Nanopowders Calcined at 473K

The two solid state synthesized powders, Nanopowders A and B, exhibited irregular morphology. It was difficult to judge from the micrographs whether agglomerates or interconnected individual crystallites were present. The

morphology of Nanopowder A (see Figure 6.4) appeared to be irregular, flattened clusters of approximate 750 nm average diameter with a few appearing to just exceed 1 μm in diameter.

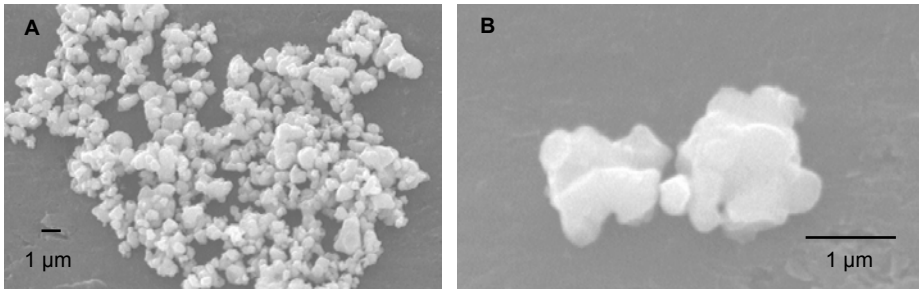

Figure 6.4. SEM micrographs of Nanopowder A after one hour at 473K at 4,800X (A) and 25,000X (B).

The crystallites of Nanopowder B (see Figure 6.5) had an irregular shape, flattened and chunky. The sizes ranged from over a micron to 250 nm which yielded a large size distribution. The micron plus sized crystallites observed were of the minority. Interconnected crystallites were observed; the initiation of necking is part of crystal growth.

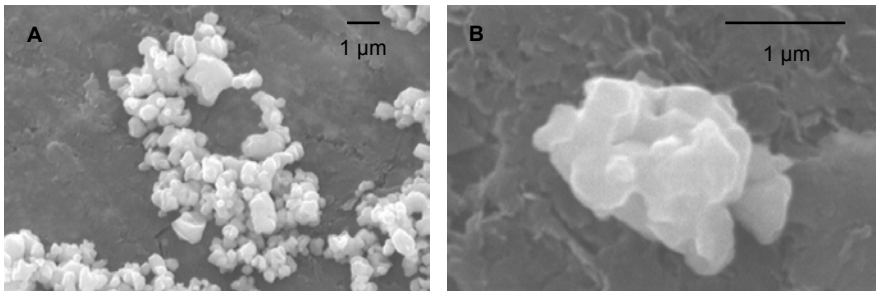

Figure 6.5. SEM micrographs of Nanopowder B after one hour at 473K at 8,000X (A) and 32,000X (B).

The morphology of Nanopowder C (see Figure 6.6) was nearly spherical with a narrower size distribution than that observed with Nanopowders A and B. The majority of the crystallites approximate average diameter appeared to be 200 nm; however, necking and crystallite growth can be seen in the center of the image (see Figure 6.6, micrograph B). Agglomeration was sporadic on the pin support with small to very large groupings of crystallites observed.

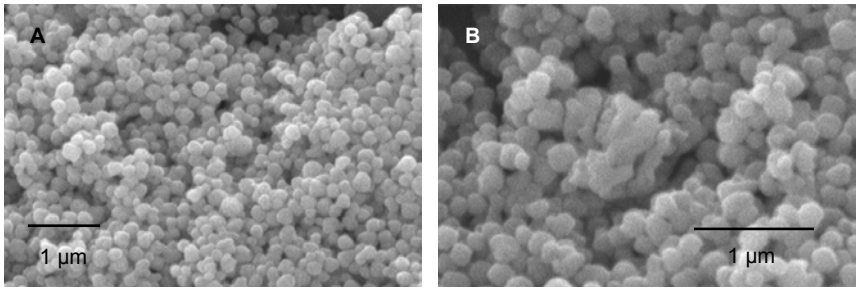

Figure 6.6. SEM micrographs of Nanopowder C after one hour at 473K at 19,000X (A) and 32,000X (B).

Nanopowder D (see Figure 6.7) showed a narrow crystallite size distribution. The crystallites were 120 nm to 150 nm in diameter, with a small number of slightly larger crystallites, and of nearly spherical shape. Necking of crystallites that was observed with Nanopowder C appeared to be absent with this nanopowder.

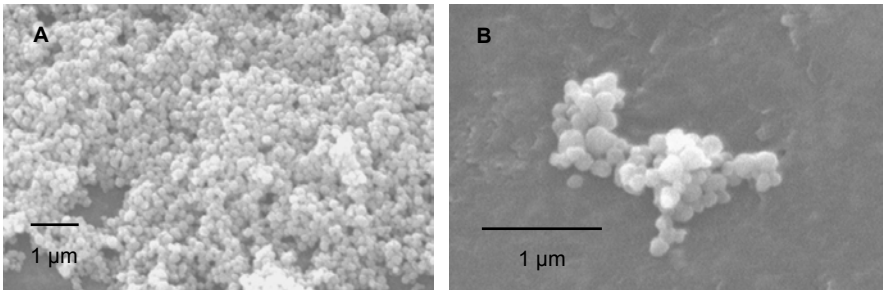

Figure 6.7. SEM micrographs of Nanopowder D after one hour at 473K at 13,000X (A) and 30,000X (B).

Nanopowder E (see Figure 6.8) had large agglomerates and, due to the small particle size, proved difficult in obtaining a well resolved high magnification image. The crystallites were too small to resolve any of the few small groups that were present on the pin support. The crystallites appeared to be of spherical morphology. The crystallite size was difficult to ascertain from the highest magnification image available. The size distribution as well could not be well deduced from the micrographs. Exaggerated growth was evident, however, in the low magnification micrograph A, with several very large clusters present. A higher magnification micrograph was taken of one of the large clusters (see micrograph C). The micrograph showed that the cluster appeared to be a developing large crystal. Small crystallites were interconnected to form the larger crystal. Large flat appearing areas are observed along the edge, the beginning of a faceted structure.

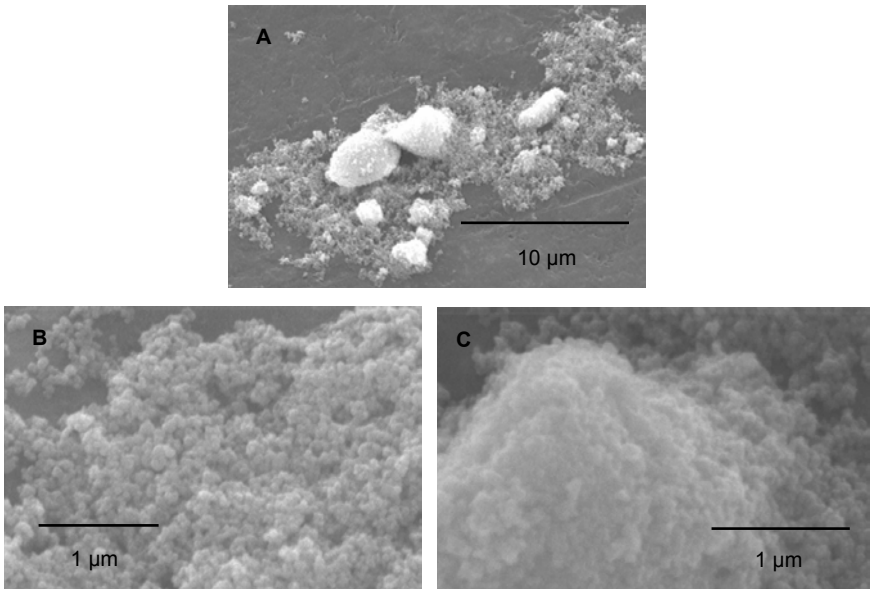

Figure 6.8. SEM micrographs of Nanopowder E after one hour at 473K at 3,300X (A), 27,000X (B) and 30,000X (C).

A large difference was observed with Nanopowder F (see Figure 6.9). As with Nanopowder E, the individual crystallite size was indistinguishable from this nanopowder. The interesting aspect of the morphology was the true spherical shape of the agglomerates. Sphere sizes of 1 μm to 10 μm were observed. The surface of the 8 μm sphere in micrograph C shows the method of growth of the agglomerates. The larger agglomerate is in the process of absorbing another 3 μm spherical agglomerate. The nanoscale crystallites were soft-packed along the surfaces of the spheres; however, there appears to be solidification of the larger spheres resulting in a large reduction of surface energy as the smaller individual crystallites disappear.

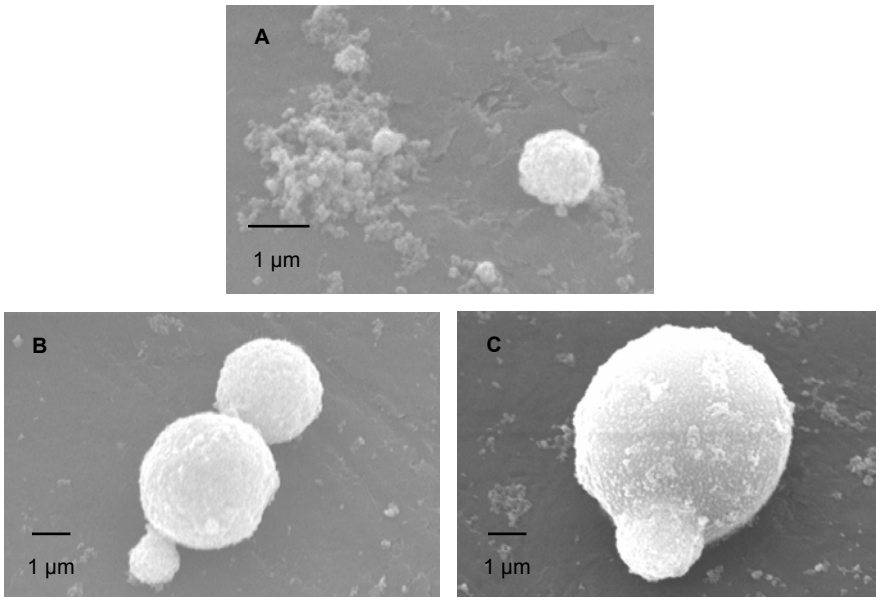

Figure 6.9. SEM micrographs of Nanopowder F after one hour at 473K at 12,000X (A), 7,500X (B) and 7,500X (C).

6.2.3.2 Nanopowders Calcined at 773K

During the one hour soak at 773K, Nanopowder A exhibited evidence of larger crystallites necking and absorbing smaller crystallites (see Figure 6.10). The joining of crystallites appears to occur through the joining of stacked

crystallites that retain their irregular morphological shape. Average particle size appears relatively unchanged from the 473K calcined sample.

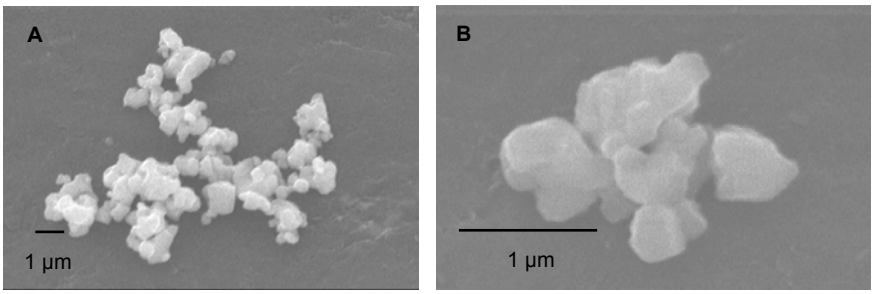

Figure 6.10. SEM micrographs of Nanopowder A after one hour at 773K at 7,500X (A) and 39,000X (B).

Nanopowder B (see Figure 6.11) exhibits necking similar to Nanopowder A. A broad size distribution still remains with crystallites of 250 nm to 1 micron observed. The irregular morphology remains with larger crystallites necking and absorbing the smaller crystallites.

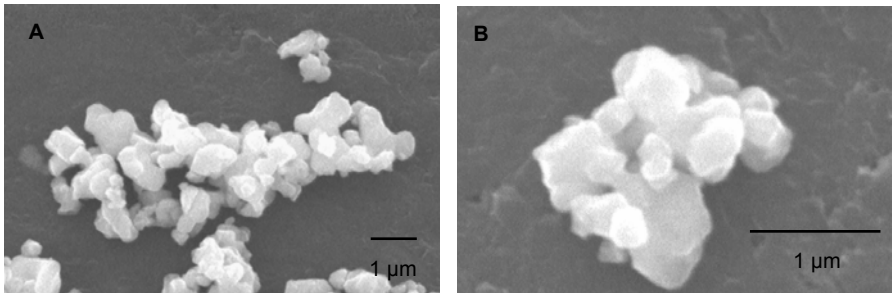

Figure 6.11. SEM micrographs of Nanopowder B after one hour at 773K at 12,000X (A) and 35,000X (B).

In the SEM micrographs of Nanopowder C (see Figure 6.12) the spherical morphology of the nanopowder is observed. The nanopowder crystallites have sizes of 150 nm to 200 nm with some crystallite necking being exhibited, as seen in the right edge of micrograph A, with an apparently narrowed size distribution.

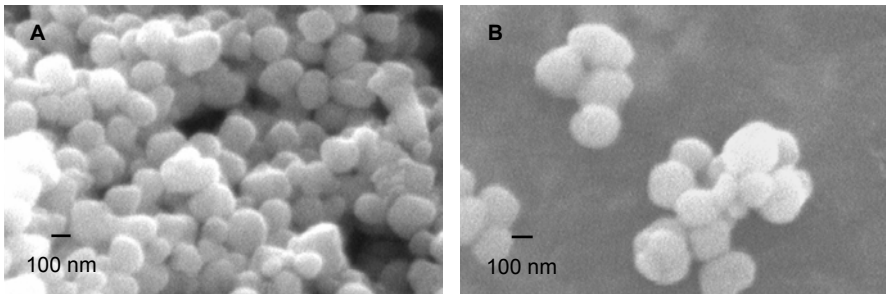

Figure 6.12. SEM micrographs of Nanopowder C after one hour at 773K at 48,000X (A) and 55,000X (B).

Nanopowder D (see Figure 6.13) exhibits crystallites of an apparent 150 nm to 200 nm size with a narrow distribution. Crystallite growth is atypical, a few larger crystallites are observed, however, and necking and growth is less apparent than with Nanopowder C. The morphology remains somewhat spherical, however, faceting is observed in micrograph B.

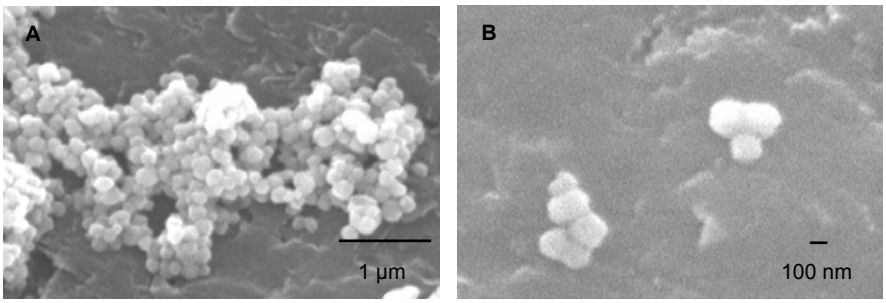

Figure 6.13. SEM micrographs of Nanopowder D after one hour at 773K at 25,000X (A) and 48,000X (B).

Nanopowder E (see Figure 6.14) exhibits crystallites of 100 nm size, a narrow distribution and, as with Nanopowder D, insignificant apparent necking and growth as compared to Nanopowder C. The exaggerated growth that was evident in the 443K calcine is not observed here. Little change in morphology is observed. Large agglomerates were observed (see micrograph C) in sizes to several microns.

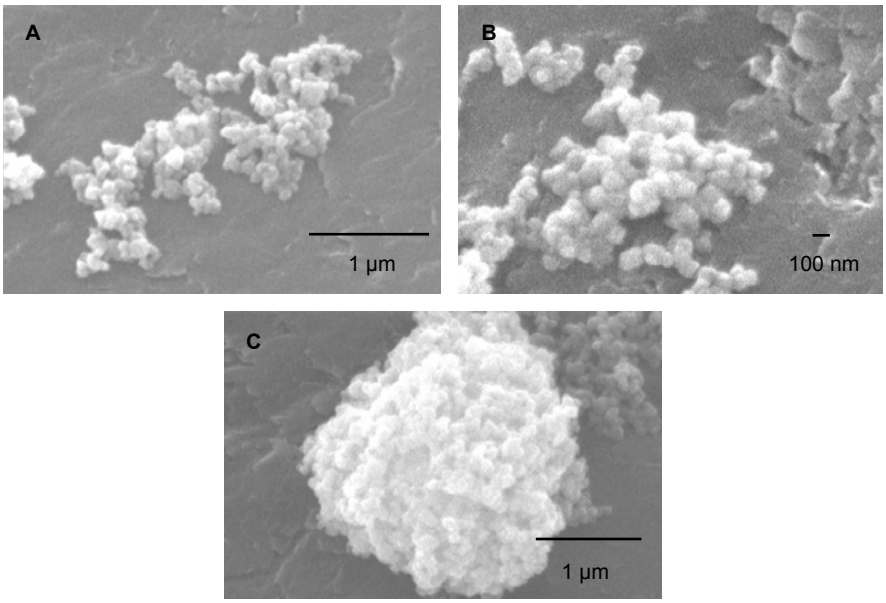

Figure 6.14. SEM micrographs of Nanopowder E after one hour at 773K at 33,000X (A), 49,000X (B) and 30,000X (C).

The smallest average particle sized Nanopowder F (see Figure 6.15) exhibits the anomalous growth of large spherical agglomerates. As with the 473K calcine of this nanopowder, these large spherical agglomerates coarsened and became large individual crystals. The driving force of this densification was the reduction of the large free surface energy of the sub-100 nm nanopowder. The largest of these spheres nears 10 microns as seen in micrograph A. A large developing sphere, observed in micrograph B, resided among the small separate nanocrystallites. There was evidence of consolidation of these larger spheres through necking between large and small spheres in micrograph C, with the larger spheres absorbing smaller spheres. Individual nanocrystallites were observed separate from the large spheres in micrograph D.

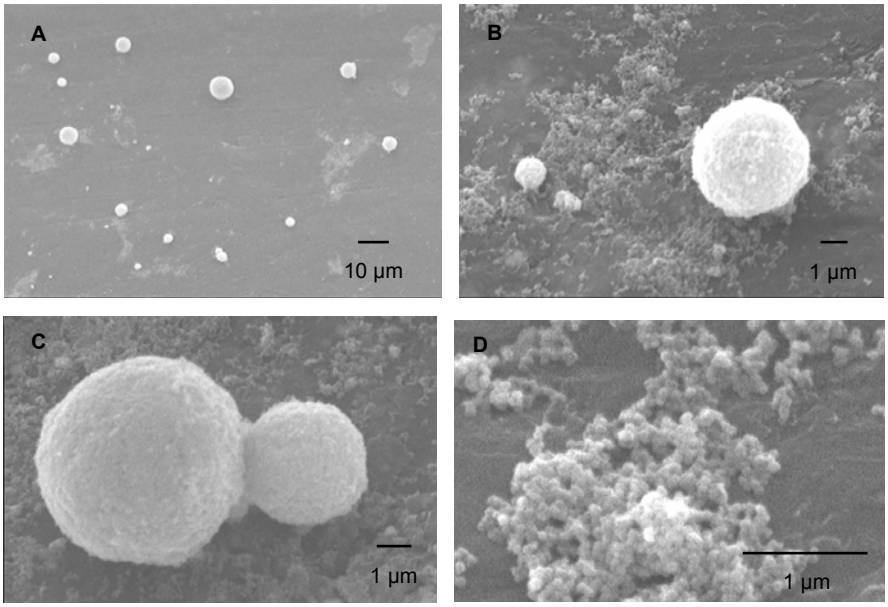

Figure 6.15. SEM micrographs of Nanopowder F after one hour at 773K at 1,000X (A), 7,500X (B), 10,000X (C) and 34,000X (D).

6.2.3.3 Nanopowders Calcined at 1173K

During the one hour soak at 1173K, Nanopowder A exhibited evidence of larger crystallites necking and absorbing smaller crystallites (see Figure 6.16). The irregular shapes observed with the samples calcined at 473K and 773K were absent here. The crystallite edges are less abrupt having smoothed during the higher temperature calcine. The crystallites are larger than with the previous calcined samples and joined crystallites are frequently observed in the sample, as seen in micrographs B and C. Neck growth is well marked between the two crystallites, denoted with an arrow in micrograph C, and the shape of the smaller crystallite is still evident.

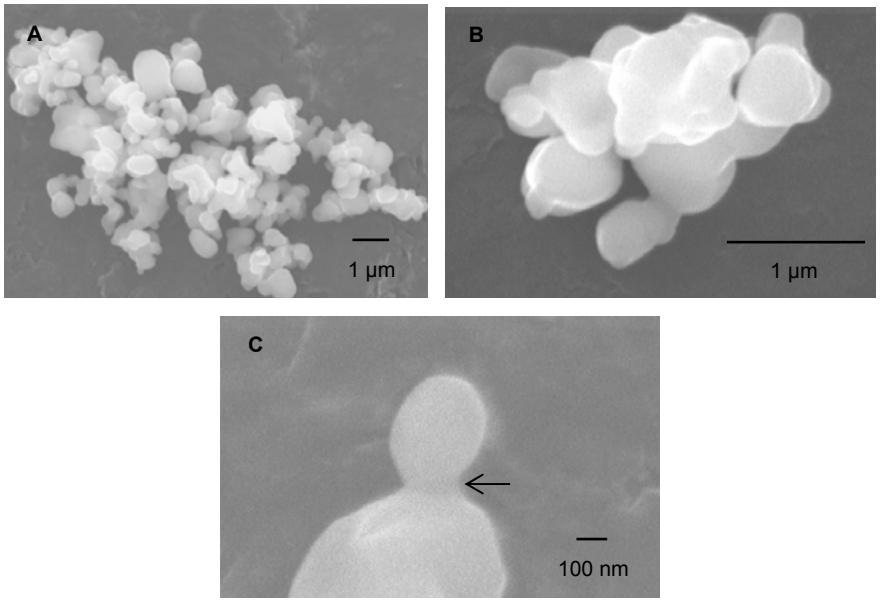

Figure 6.16. SEM micrographs of Nanopowder A after one hour at 1173K at 10,000X (A), 37,000X (B) and 88,000X (C).

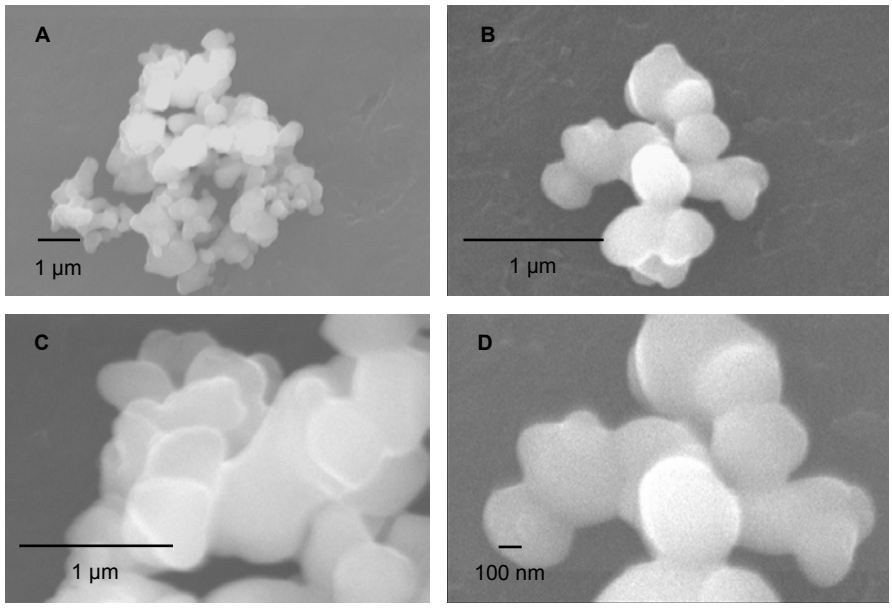

Figure 6.17. SEM micrographs of Nanopowder B after one hour at 1173K at 11,000X (A), 38,000X (B), 41,000X (C) and 64,000X (D).

Nanopowder B (see Figure 6.17) also exhibits larger growth of the crystallites than with the previous calcined samples. The flattened morphology of the crystallites is still evident in micrograph C. This nanopowder differs from nanopowder A in that groups have formed of several crystallites joined together. The group seen in micrograph B, and at higher magnification in micrograph D, appears to be a single group formed from numerous 500 nm crystallites. Necking is seen between the crystallites yielding the appearance of a single disorganized crystal. A longer time at the current calcine temperature would likely produce a single micron sized crystal.

The micrographs of Nanopowder C (see Figure 6.18) show an increased amount of crystallites joining together through necking as opposed to the 773K calcined sample. Necking was readily evident among the sample as imaged in the SEM; the small group in micrograph A is a representative group. The spherical nature of this nanopowder is no longer observed due to the vast amount of growth occurring. The irregular shape is the common morphology of the crystallites, micrographs B and C.

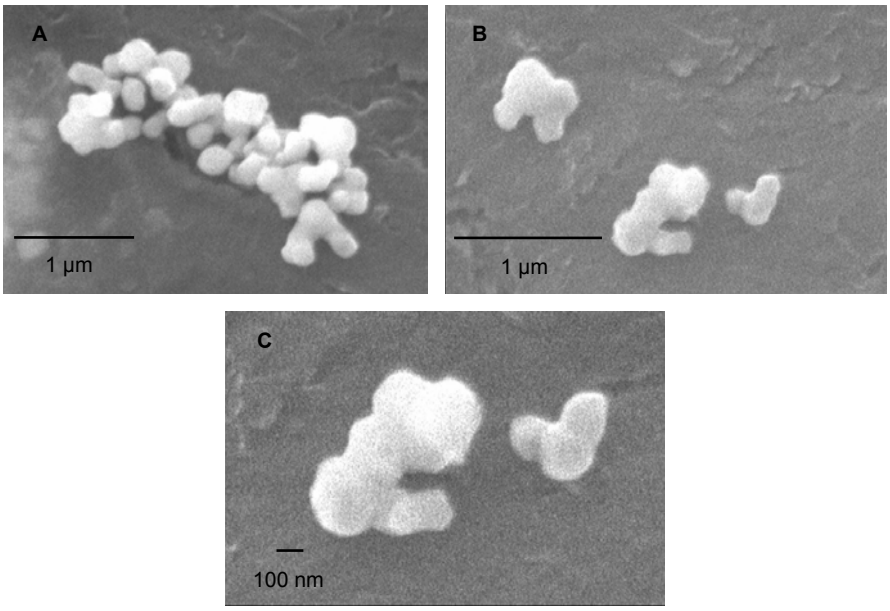

Figure 6.18. SEM micrographs of Nanopowder C after one hour at 1173K at 33,000X (A), 40,000X (B) and 72,000X (C).

Nanopowder D after calcining for one hour at 1173K (see Figure 6.19) exhibited abnormal growth of the crystallites unlike the previous three nanopowders. Crystals in excess of one micron are observed among the smaller crystallites, denoted by arrows in micrographs A and B. These anomalous crystals are a factor of ten times larger than the average appearing crystallites. In the highest magnified micrograph, C, the growth illustrates the extent of this anomalous growth. The anomalous growth was first observed after the 1173K temperature. Close inspection of the area denoted with the arrows shows evidence of a rapid coarsening of the crystallites. A large anomalous nonporous crystal was in development with well defined surfaces. This anomalous growth was also observed with nanopowder E; however, the size of the developed anomalous crystals was not as large as those observed here.

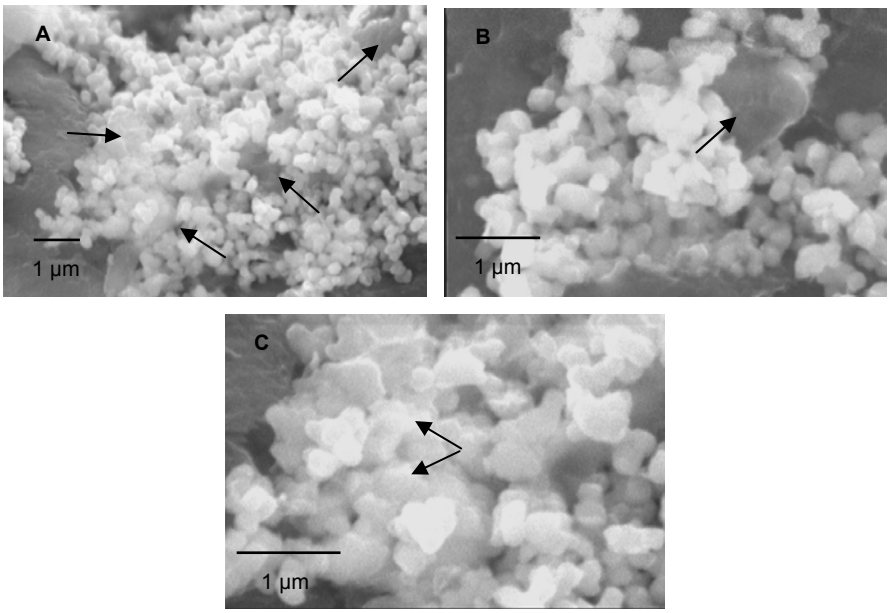

Figure 6.19. SEM micrographs of Nanopowder D after one hour at 1173K at 12,000X (A), 22,000X (B) and 28,000X (C).

Nanopowder E (see Figure 6.20) also indicated anomalous crystal growth during the 1173K calcine. The first pair of micrographs, A and B, illustrates the size of these abnormal crystals as compared to the majority of the crystallites viewed by SEM. A large, smooth surfaced ovate structure formed from the initial mostly spherical shape of the nanopowder. This anomalous growth is similar to that observed with Nanopowder D, however, large anomalous growth was also observed with this nanopowder. As seen in micrograph C, an apparent agglomerate with the approximate dimension of three microns by five microns in a columnar structure is observed. At higher magnification, micrograph D, this was a developing single crystal with an interconnected porous structure.

This large anomalous crystal growth was an uncommon observance. The development of this structure, along with the other smaller anomalous growths, may also be the result of a moisture assisted liquid calcining process.[139] The release of moisture is observed in the spectra throughout the HT-DRIFT FT-IR study of the nanopowders. The combination of high moisture content, small

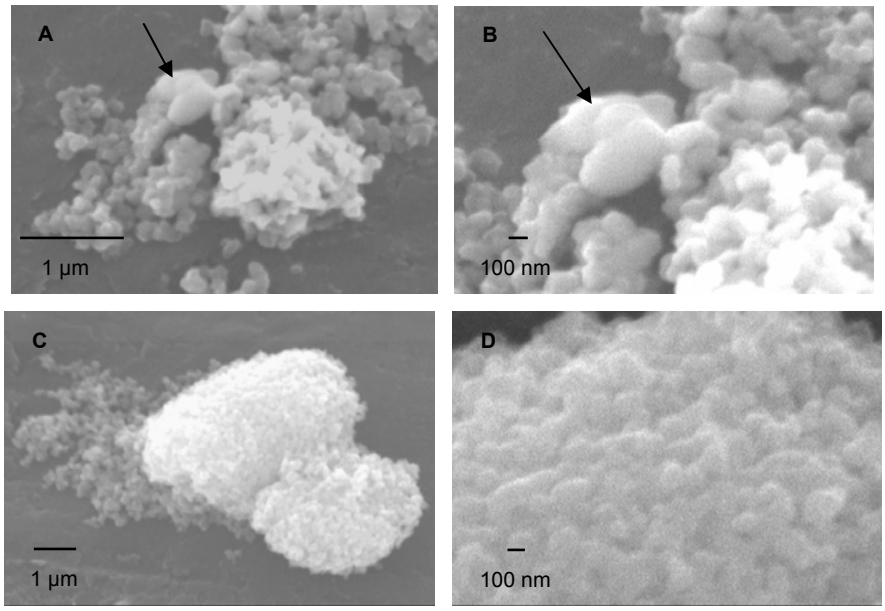

Figure 6.20. SEM micrographs of Nanopowder E after one hour at 1173K at 28,000X (A), 51,000X (B), 12,000X (C) and 49,000X (D).

crystallite size and the accompanying high reactive surface area may account for the growths observed.

The results from calcining the smallest of the nanopowders (F) were quite interesting (see Figure 6.21). The growth of the spherical agglomerates, observed with the previous calcinations, continues during the 1175K calcine with sintered sphere diameters nearing 50 to 60 microns. There exists evidence of large spheres necking and absorbing smaller spheres in micrographs C and D. The spheres are an amalgam of the still small crystallites joined in an initial sintering condition and, therefore, appear porous under higher magnification. This anomalous spherical growth is the combined result of the high surface energy of the nanoscale crystallites, the initial morphology of the agglomerates and enough thermal energy to initiate the initial stage of sintering.

There are numerous spheres with diameters above 10 microns also observed (see Figure 6.21 micrographs A and B, and Figure 6.22 micrograph A). The formation of these spheres is observed in Figure 6.22, micrographs C and D. The nanocrystallites join and assume a spherical morphology during the

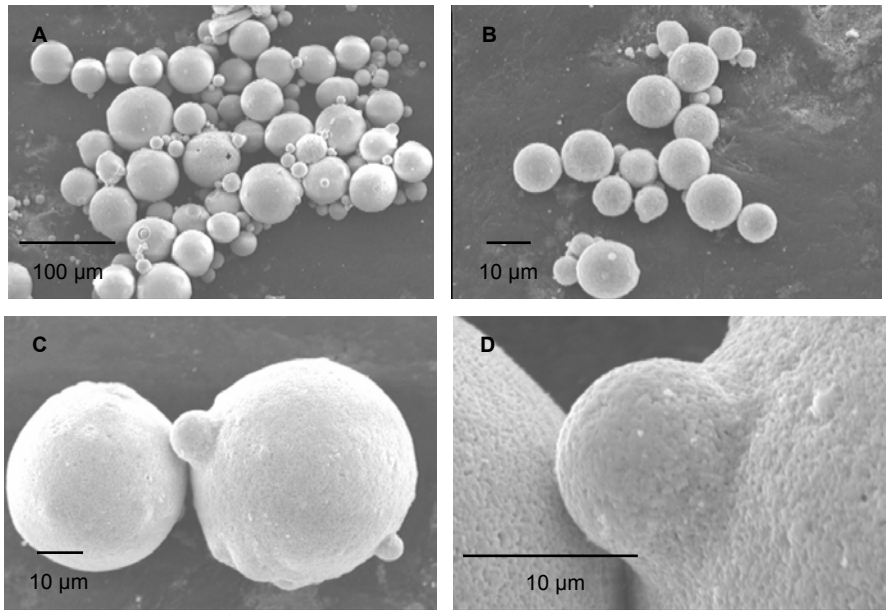

Figure 6.21. SEM micrographs of Nanopowder F after one hour at 1173K at 260X (A), 1,000X (B), 12,000X (C) and 49,000X (D).

continued addition of more nanocrystallites. Porosity is also evident in these developing spheres.

Additional evidence is observed in Figure 6.22, micrograph B, where a large sphere has necked and nearly fully absorbed a smaller sphere. The diameter of the larger sphere is approximately 50 microns and the diameter of the smaller sphere being about 8 microns. The larger sphere's growth has nearly encompassed the smaller sphere. This micrograph indicates an origin of internal porosity of a solid. As one developing region absorbs another the boundary between them incorporates a quantity of porosity. The elimination of these vacant regions from within the bulk will be necessary during densification at the higher temperatures of sintering for a high density compact solid. The porous nature of these spheres is also shown in the micrographs in Figure 6.22. This microporosity is observed in the initial grouping of numerous nanocrystallites in micrographs C and D, through the developed large agglomerate spheres in micrographs A and B. Individual crystallite sizes increased and necking was observed in Figure 6.22.

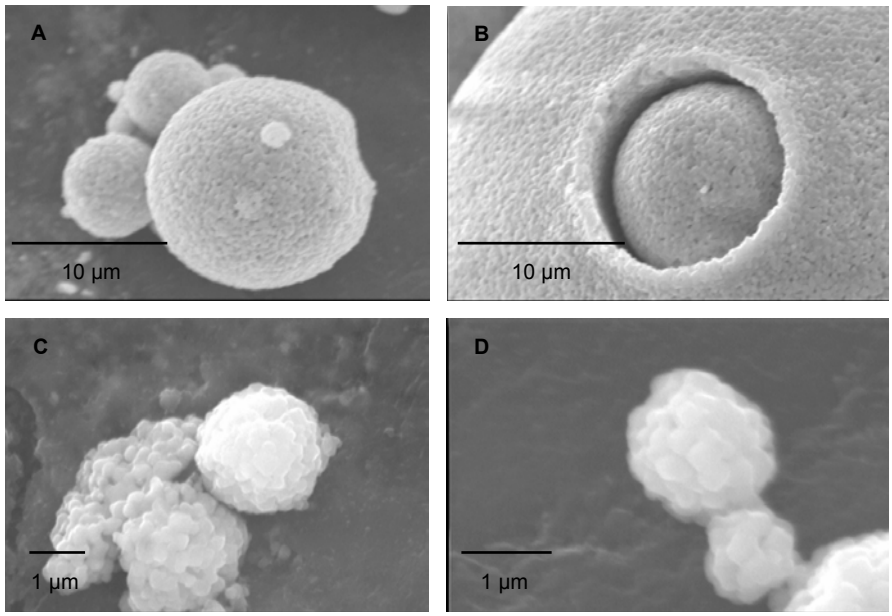

Figure 6.22. SEM micrographs of Nanopowder F after one hour at 1173K at 4000X (A), 15,000X (B), 24,000X (C) and 46,000X (D).

6.2.4 Summary

SEM enabled a closer examination of the calcined nanopowders subsequent to the optical study at room temperature. SEM was employed to view the morphology of the nanopowders, and the agglomerates that were present, subsequent to calcination at three different temperatures.

The solid state synthesized nanopowders exhibited necking and growth at all calcine temperatures. Their irregular morphology remained throughout the lower two calcine temperatures; however, the morphology observed after the highest calcine temperature was less irregular and indicated a more faceted structure of the crystallites. This growth appeared to be accomplished through a stacking of the flattened and chunky crystallites.

Nanopowders C and D exhibited different behavior during calcination. These nanopowders showed little to no necking and growth at the two lowest calcine temperatures. At the highest calcine temperature, Nanopowder C began to show evidence for necking and growth. The morphology was atypical; from an initially spherical form that changed to irregularly shaped growths. Since initiation of necking and growth took place only at the highest calcine temperature, higher activation energy was apparently necessary for this nanopowder as compared with the others.

At the highest calcine temperature Nanopowder D exhibited anomalous growth of crystals that were a factor of ten times larger than the average appearing crystallites. The SEM micrographs showed evidence for a liquid coarsening of the crystallites. Large anomalous nonporous crystals were in development with a glassy appearing surface. This nanopowder contained the second highest concentration of molecular water of all of the nanopowders. Moisture assisted liquid sintering may explain the appearance of these developing crystals.

Nanopowder E displayed exaggerated growth during calcine at the lowest and the highest temperatures. Large, smooth surfaced ovate structures formed from the initial, mostly spherically shaped nanopowder. This anomalous growth was similar to that observed with Nanopowder D, however, large anomalous

growth was also observed with this nanopowder. An agglomerate with the approximate dimensions of three microns by five microns in a columnar structure was observed. At higher magnification, however, this was observed to be a developing single crystal with an interconnected porous structure. This large anomalous crystal growth was an uncommon observance in the 1173K sample. This type of growth was not observed in the sample after the 773K calcine.

The development of this type of structure, along with the other smaller anomalous growths, may be the result of a moisture assisted liquid calcining process. Valdivieso, et al.[139] indicated that barium titanate samples that were calcined at 1123K in a moist flowing atmosphere had an accelerating effect in the reduction of specific surface area of the samples. Water vapor partial pressure of 133 to 2133 Pa was used. In conclusion, Valdivieso indicated that to control and inhibit coarsening, it was important to maintain a very low partial pressure of water vapor during calcining and sintering. The release of moisture was observed in the spectra of nanopowder D throughout the temperature regime used in the HT-DRIFT FT-IR study. The combination of static air during calcining, high moisture content, small crystallite size and the accompanying high reactive surface area may account for the growths observed.

Nanopowder F exhibited much different behavior than the other nanopowders. Sphere formation was the predominant morphological evolution during the calcinations. At the lowest calcine temperature spherical growth was observed to a diameter of 10 microns. As the calcine temperature increased, growth of this spherical morphology continued with diameters reaching 50 to 60 microns. These spheres originate from the spherical agglomerates that were observed at room temperature under optical and SEM observation of this nanopowder. Spheres also developed during the necking and growth of individual nanocrystallites as observed in the nanopowder after the 1173K calcine.

The possibility of a tremendous amount of excess surface energy in the nanocrystallites of Nanopowder F could explain this sphere formation; an attempt to reduce their high energy level through sphere formation. A high concentration

of mesomolecules, i.e. incomplete barium titanate unit cells, comprising the structure of the nanocrystallites would account for an elevated excess surface energy. In addition, remnant strain from synthesis would also add available energy for crystallite growth during calcination.

The sintered spheres observed after the 1173 calcine can be considered large solid agglomerates. These sintered agglomerates are predominantly much larger than the matrix of smaller crystallites. These spheres will likely resist fracture and breakdown during compaction for the sintering studies.

6.3 Transmission Electron Microscopy

6.3.1 Introduction

The primary reason for using transmission electron microscopy (TEM) is that the vast increase in resolving capabilities over SEM providing a closer examination of the calcined nanopowders. TEM is employed to view the morphology of the nanopowders, and the agglomerates that may be present, subsequent to calcination. The diameter of the smallest of the nanopowders was smaller than the resolving capability of the SEM used and precluded the viewing of individual crystallites. TEM, however, will provide higher magnification micrographs that will elucidate the morphological evolution of the crystallites during their respective calcinations.

6.3.2 Experimental Procedure

Nanopowders were calcined at 473K, 773K and 1173K, at a rate of 10K/minute, for a soak period of one hour at each temperature in ambient atmosphere. Samples of the nanopowders were then prepared for TEM analysis by ultrasonicating 5-10 milligrams in 15 ml of acetone in a 50 ml beaker for 20 minutes. Formvar coated copper grids were carbon coated for proper conductivity and were used to support the nanopowders during analysis. Needle-point tweezers were used to quick-dip the support grid into the nanopowder-acetone solution. A small quantity of nanopowder adhered to the grid and was inspected under an optical microscope to assure proper coverage.

The nanopowder coated copper grid was placed in a double tilt holder and inserted into position in the TEM. The accelerating voltage used was 120 kV with a beam current of 70 μA. Initially several grid locations were viewed to image representative crystallites for particle size and distribution. Smaller groups were imaged at higher magnifications to locate single crystallites for analysis. These crystallites, separate from groups, allowed analysis of size and morphology, and after the 1173K calcine, selected area diffraction patterns. Brightfield (BF) and darkfield (DF) images were obtained of the nanopowders calcined at 473K, 773K

and 1173K. Selected area diffraction patterns were obtained from the nanopowders after the 1173K calcine.

Brightfield images were examined to identify the crystallite size and morphology generally through the examination of larger groups. Darkfield images were examined to explore the extent of residual strain, from the synthesis process, in the crystallites and its possible reduction through calcination. A crystallite without residual strain would present uniform contrast. An exception would be contrast variations due to inconsistent thickness and bend contours, another feature of crystalline specimens. The attenuation of transmitted electron beam intensity is dependent upon the thickness of a crystallite and causes contrast variance different from the effects observed due to strain. The contrast variations due to bend contours appear as dark contour lines along the edge of a crystal. These contour lines are a result of the specimen being curved such that a given set of planes (*hkl*) are not all at the Bragg condition (i.e. due to the curvature, values of (±*hkl*) are considered and provide contrast). These curved lines are different from the effects observed due to strain.[140]

The residual strain, when present, affects the diffraction behavior of electrons resulting in contrast changes in the image. Darkfield images present the greatest available contrast. The darkfield images, therefore, are high magnification maps of the intensity distribution across the diffracted beams produced by the interaction between the crystallite and electron beam. The elastic strain of the lattice is clearly shown through the contrast variations in the DF images.

The selected area diffraction patterns were solved to elucidate the structure of the crystallites after the highest temperature calcine. These were then compared to the results from the room temperature study of the nanopowders.

6.3.3 Results and Discussion

6.3.3.1 Nanopowders Calcined at 473K

TEM brightfield micrographs of Nanopowder A, Figure 6.23, indicated negligible change over that observed with the room temperature TEM study in Section 2.5. No necking of crystallites was observed and the irregular morphology remains unchanged. This nanopowder did, however, have a narrow average size distribution after initially viewing several grid locations to image representative crystallites for particle size and distribution.

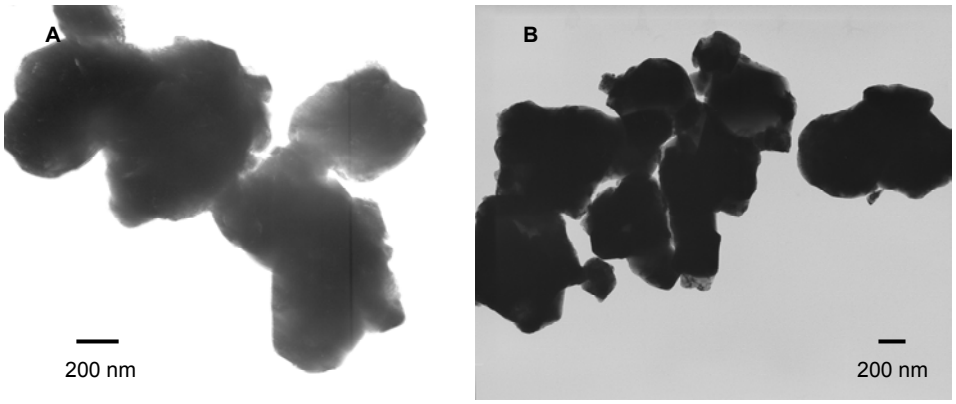

Figure 6.23. TEM Brightfield micrographs of Nanopowder A after a one hour calcine at 473K.

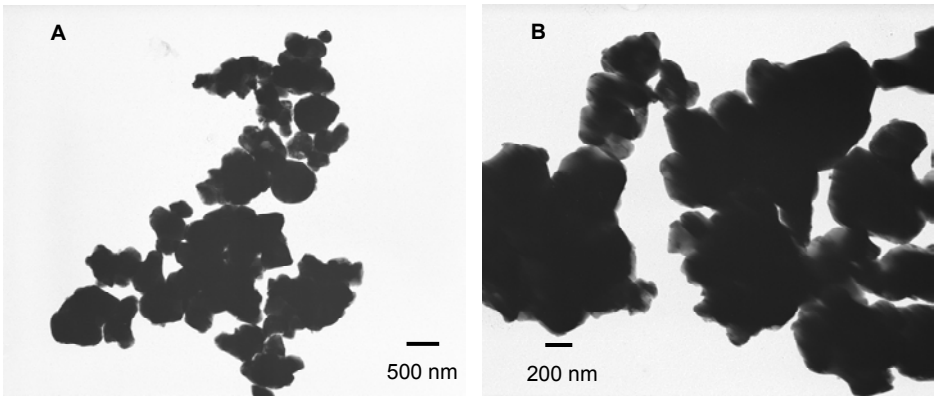

Figure 6.24. TEM Brightfield micrographs of Nanopowder B after a one hour calcine at 473K.

Comparing the micrographs for Nanopowder B, Figure 6.24, with those from the room temperature study negligible changed was observed. Necking of crystallites was not observed and the irregular morphology remains. This solid state nanopowder contained a broader crystallite size distribution than Nanopowder A.

Nanopowder C, the first of the hydrothermally synthesized nanopowders, exhibited crystallites having trapped porosity remaining after the 473K calcine; the light spots within the crystallites as seen in Figure 6.25. This trapped porosity, or trapped residual moisture from the synthesis of the nanopowder, was observed in individual crystallites as well as within the necked crystallites, micrographs B, C and D. Various stages of necking of crystallites were readily observed, however, the apparent growth in crystallite size was negligible.

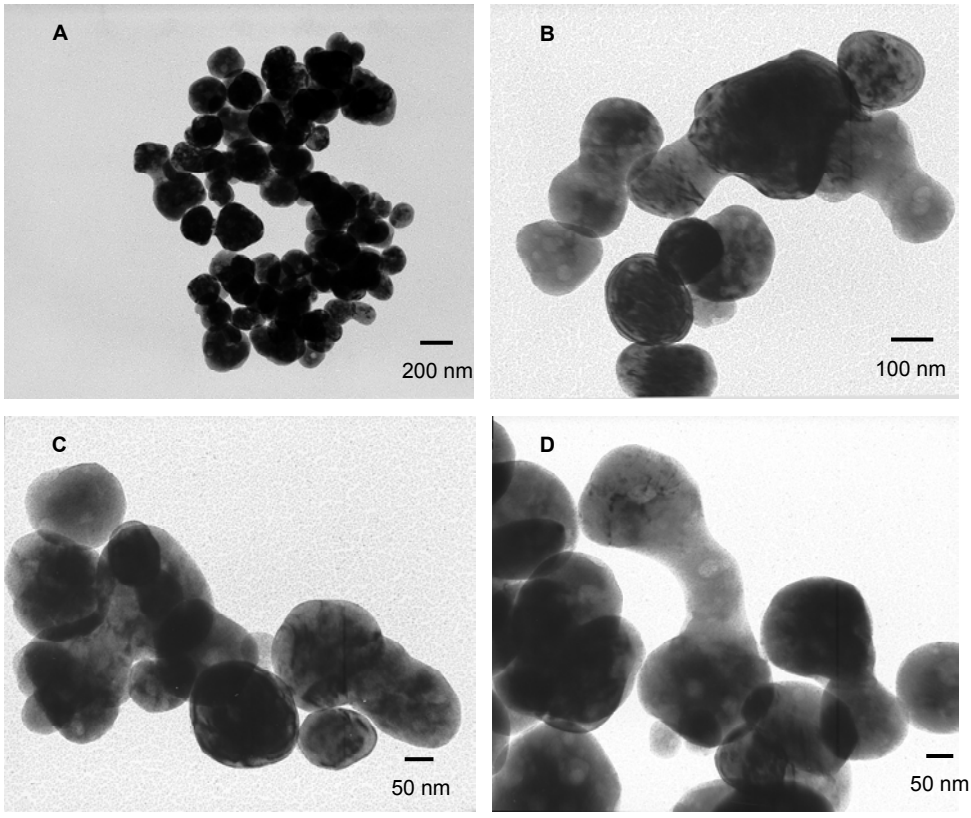

Figure 6.25. TEM Brightfield micrographs of Nanopowder C after a one hour calcine at 473K.

The second hydrothermally synthesized nanopowder, D, had a wider crystallite size distribution than Nanopowder C. This nanopowder did not exhibit the trapped porosity observed in Nanopowder C, Figure 6.26. In the following higher magnification set of micrographs, C and D, the apparent size of the crystallites was similar to that observed in the as-received samples and all confirmed the lack of trapped porosity that was observed with the crystallites of Nanopowder C.

The uncalcined sample of Nanopowder E had an observable average crystallite size of 70 nm with crystallites as small as 30 nm and the largest observed being approximately 100 nm. The 473K calcined sample exhibited atypical growth of a minority number of crystallites of size 125 to 150 nm (Figure 6.27). A comparison of apparent size between the average sized crystallites and an atypical crystallite is shown in micrograph C. Entrained moisture was not

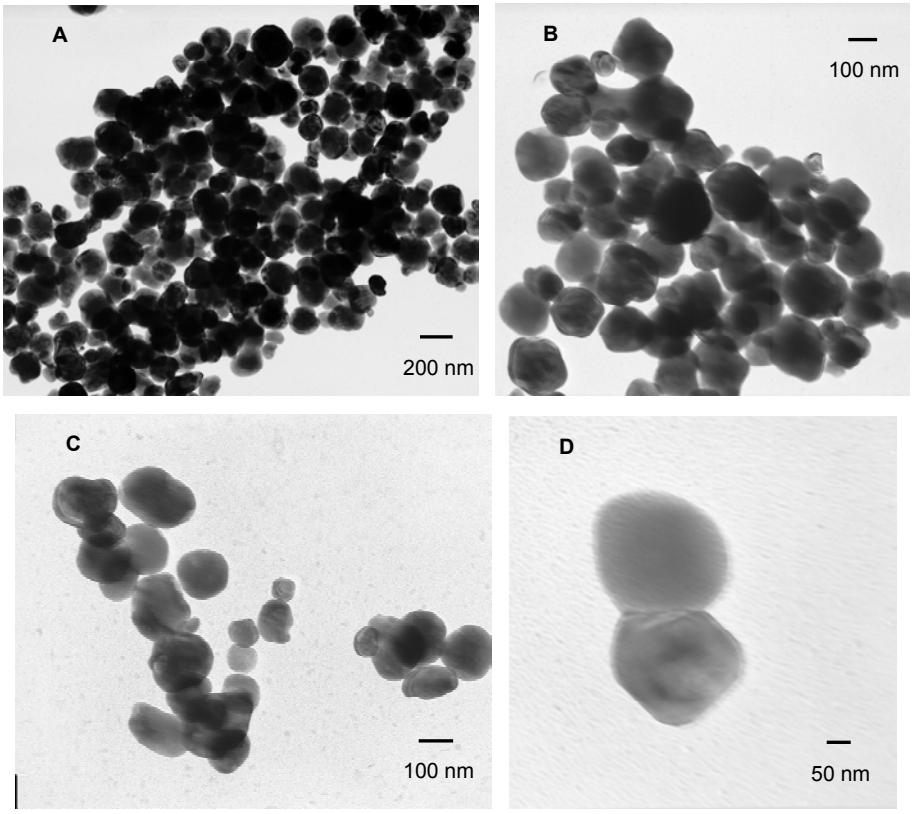

Figure 6.26. TEM Brightfield micrographs of Nanopowder D after a one hour calcine at 473K.

exhibited in the uncalcined crystallites, nor with the 473K calcined crystallites.

The crystallite size of the as-received Nanopowder F as observed by TEM, micrographs in Figure 2.42, was 40-45 nm, with the smallest crystallites nearing 20 nm. The apparent average size of the 473K calcined sample nears 50 to 70 nm, Figure 6.28. The crystallites are nearly opaque; the formvar film is observable beneath the crystallites, micrograph C. The crystallite growth observed with the low temperature calcine supports the premise of a highly reactive state of this nanopowder. The previously proposed mesostructure, or high concentration of incompletely bonded unit cell constructs, provides reactive surfaces for the growth of the crystallites. This growth or rearrangement of the structure allows the completion of these incompletely bonded unit cell constructs.

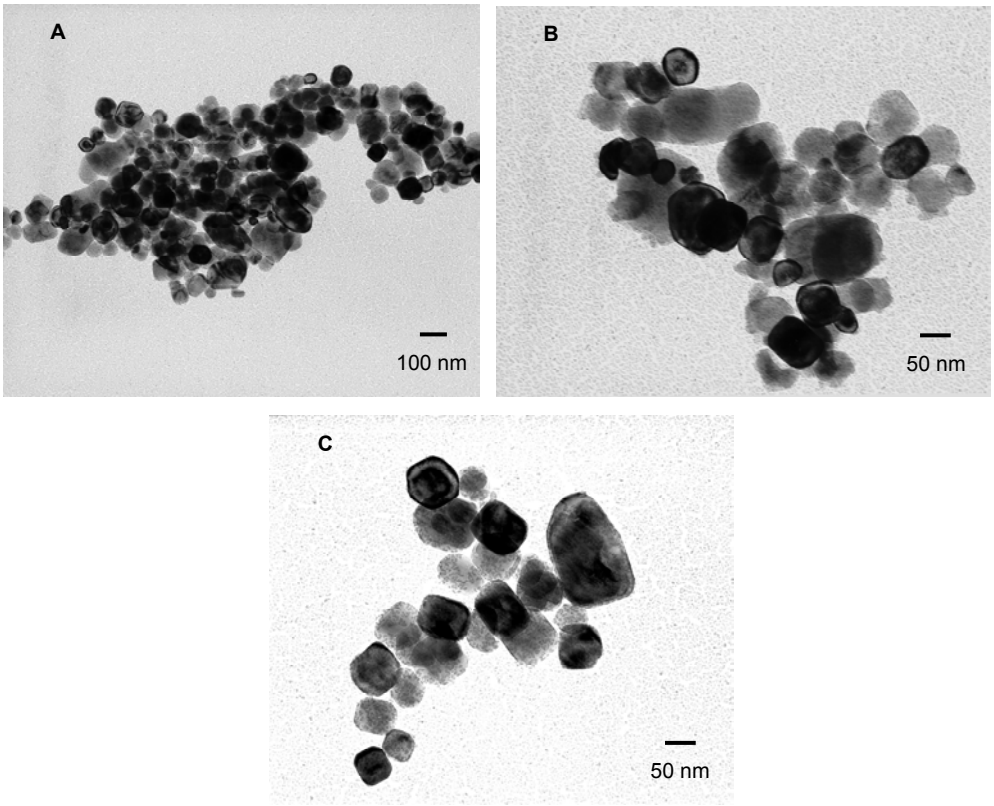

Figure 6.27. TEM Brightfield micrographs of Nanopowder E after a one hour calcine at 473K.

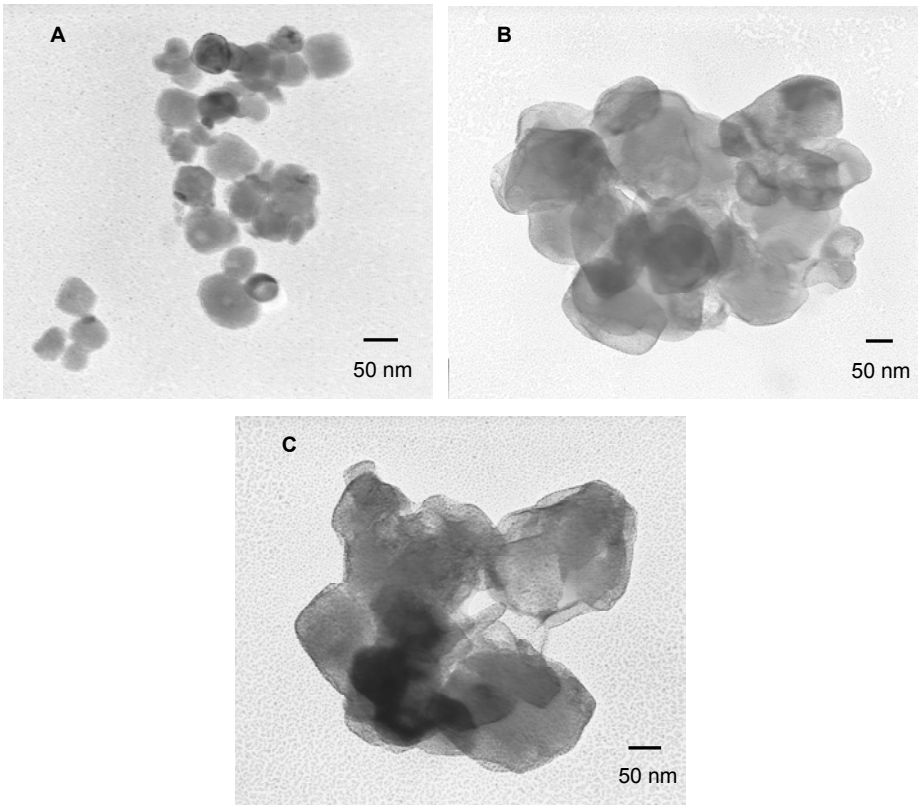

Figure 6.28. TEM Brightfield micrographs of Nanopowder F after a one hour calcine at 473K.

Darkfield images were examined to explore the extent of residual strain in the crystallites after the one hour at 473K calcine. A crystallite without residual strain would present uniform contrast. Examination of the darkfield micrograph of Nanopowder A, Figure 6.29, shows no strain was evident. The contrast variation, i.e. the darker regions are in the center sections of the crystallites with the lighter contrast outer edges, was due to the thickness of the crystallite. The contrast variation between the edges and center of the crystallites was evidence of the decreasing thickness from the center of the crystallite to the edge. No invariant contrast was observed to support the premise that residual strain is present.

The results of the examination of the micrograph of Nanopowder B are similar to that of the previous nanopowder. The lighter contrast crystallites, Figure 6.30, are due to their being smaller and thinner than Nanopowder A. No large deviations in contrast within the crystallites are exhibited. Both of the solid state synthesized nanopowders exhibited contrast only in the form of that due to variations in thickness.

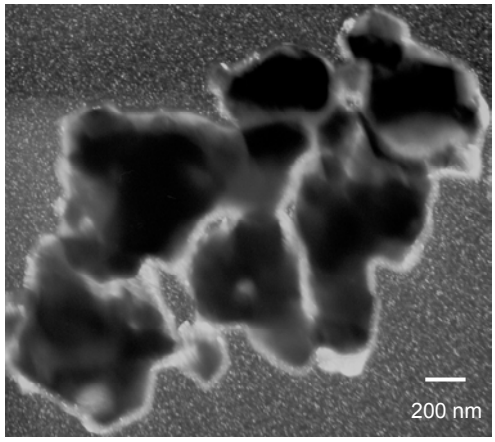

Figure 6.29. TEM Darkfield micrograph of Nanopowder A after a one hour calcine at 473K.

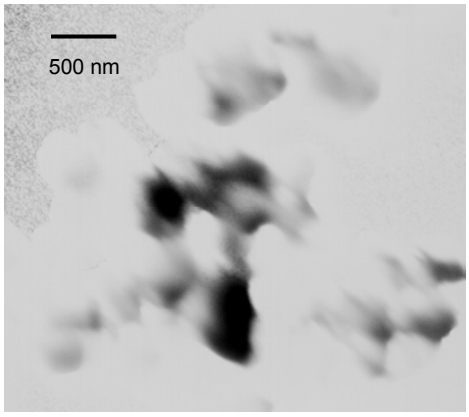

Figure 6.30. TEM Darkfield micrograph of Nanopowder B after a one hour calcine at 473K.

The hydrothermally synthesized nanopowders exhibited varying levels of residual strain after the 473K calcine. Nanopowder C, Figure 6.31, showed several crystallites exhibiting deviations in contrast within the crystallite; however, the number was reduced from that observed in the as-received sample. The varying degrees of contrast, dark to bright, represented levels of strain within the crystallites. The crystallites were within a narrow size distribution; therefore, the variation in contrast is not due to thickness variations between individual crystallites. Nanopowder C exhibited trapped porosity; regions near these pockets would exhibit the requisite strain field, producing some of the contrast variation observed.

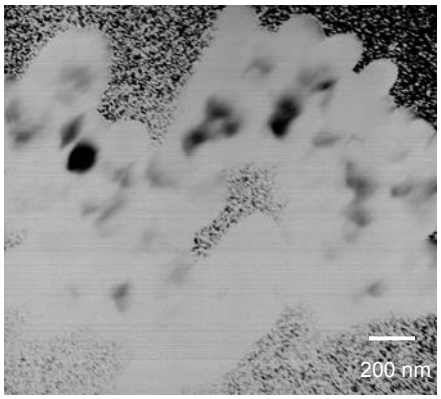

Figure 6.31. TEM Darkfield micrograph of Nanopowder C after a one hour calcine at 473K.

Nanopowder D, Figure 6.32, exhibited crystallite strain -- streaking of the contrast within individual crystallites. The size distribution was broader with this nanopowder than with the previous nanopowder, as seen by the fully bright crystallites observed in the micrograph as well as fully dark crystallites an indication of the presence of thick and thin crystallites present. Others did exhibit variation of contrast across the crystallite, an indication of strain fields present within the crystallite.

In the darkfield micrograph of Nanopowder E, Figure 6.33, there was variation in the levels of contrast within the crystallites; the swirling effect observed in the crystallites on the right as well as others. Several exhibited variation in contrast within the crystallites. As with the previous two hydrothermally synthesized nanopowders, strain fields were present to produce the contrast variation observed.

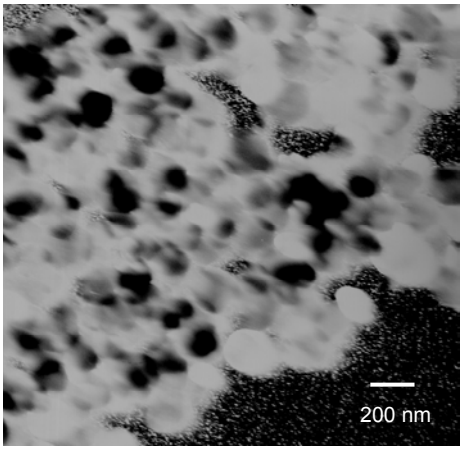

Figure 6.32. TEM Darkfield micrograph of Nanopowder D after a one hour calcine at 473K.

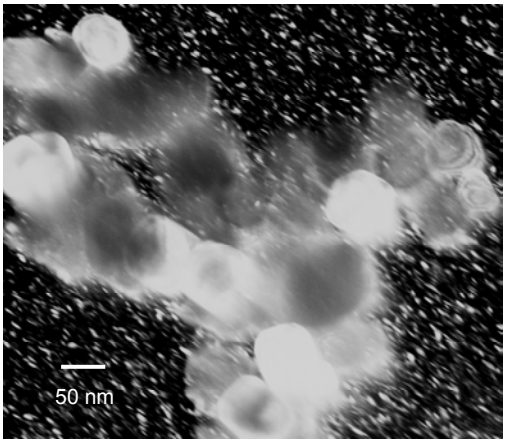

Figure 6.33. TEM Darkfield micrograph of Nanopowder E after a one hour calcine at 473K.

Nanopowder F, also hydrothermally derived, exhibited no apparent residual strain within the crystallites, Figure 6.34. No large deviations in contrast within the crystallites were exhibited. Nanopowder F exhibited contrast only of the form of that due to variations in thickness; the bright crystallites being thicker than the darker appearing crystallites. The spotted appearance is due to the observance of crystallites adsorbed to the opposite side of the formvar, i.e. observing them through the formvar.

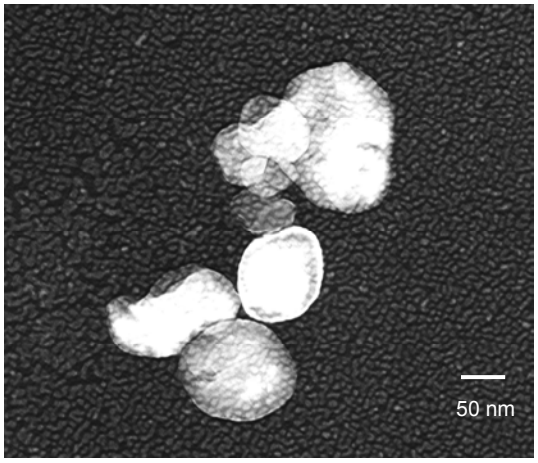

Figure 6.34. TEM Darkfield micrograph of Nanopowder F after a one hour calcine at 473K.

6.3.3.2 Nanopowders Calcined at 773K

TEM brightfield micrographs of Nanopowder A, Figure 6.35, indicated noticeable change over that observed with the 473K calcined sample in Figure 6.23. Crystallite necking was observed adding to the irregular morphology previously observed. After initially viewing several grid locations to view representative crystallites for particle size and distribution, the nanopowder exhibited a broadened average size distribution due to the growth of the larger crystallites. These larger crystallites had nearly doubled in size as compared to those observed in the 473K calcined sample. The number of the smaller crystallites was small and the growth of abnormally large crystals was observed.

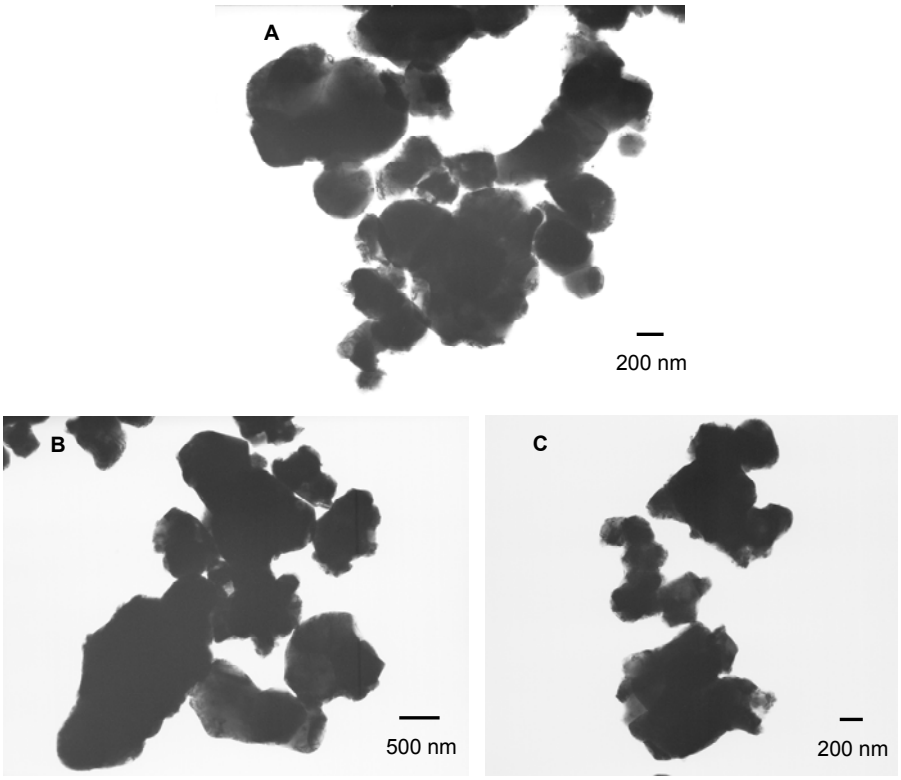

Figure 6.35. TEM Brightfield micrographs of Nanopowder A after a one hour calcine at 773K.

Nanopowder B, after the one hour calcine at 773K, exhibited inconsequential growth when compared to the 473K calcined sample; the crystallite size appeared only slightly changed; Figure 6.36. The broad size distribution remains and necking between crystallites was observed. A morphological change was, however, observed. The irregular shape had diminished with a more regular profile detected. This observed dimensional change was apparently at the expense of growth in crystal size.

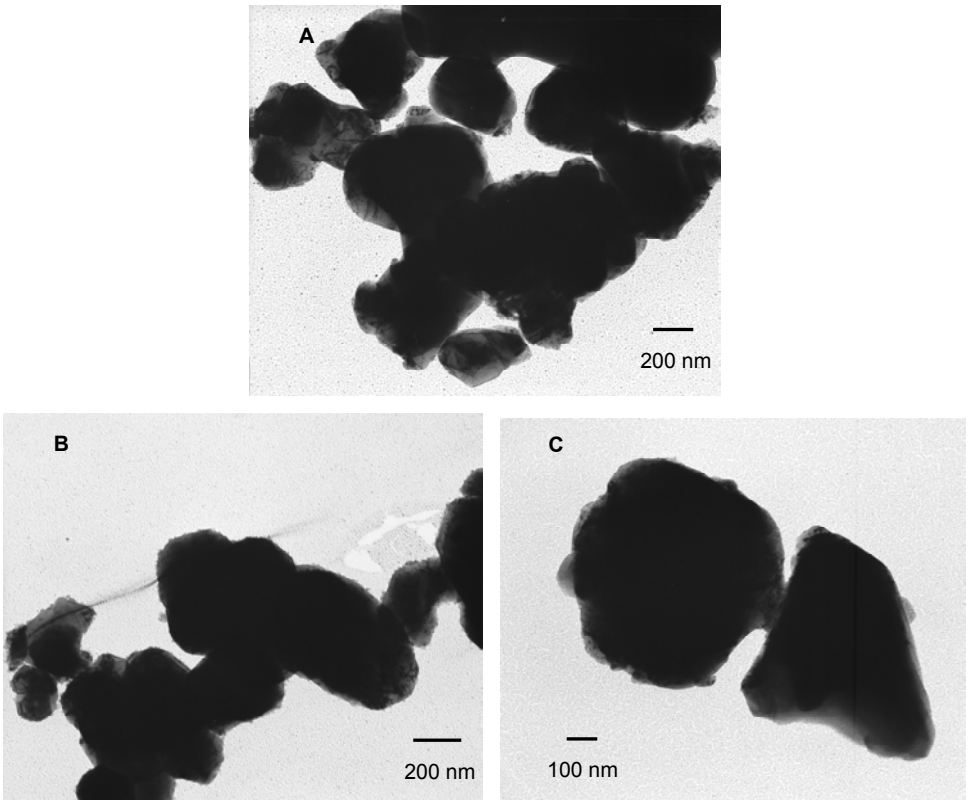

Figure 6.36. TEM Brightfield micrographs of Nanopowder B after a one hour calcine at 773K.

Trapped porosity was still evident in the crystallites of Nanopowder C, the largest of the hydrothermally synthesized nanopowders, Figure 6.37 micrographs A and B. The necking between small crystallites was observed in all micrographs and was well represented with the dog bone shaped crystal observed in micrograph C. The extended necking occurred as an intermediate stage in the development of a single crystal from the blending of smaller crystallites. The apparent size of the crystallites at this stage of calcine was moderately changed from that observed after the previous lower temperature calcine. The degree of trapped porosity did, however, appear to have diminished.

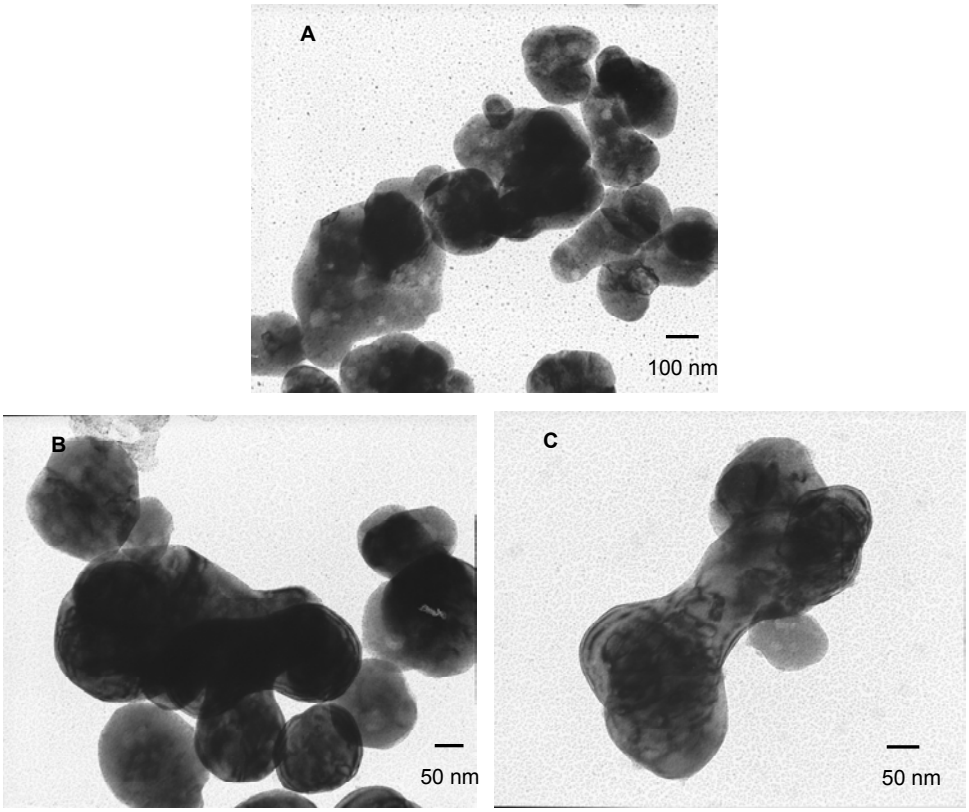

Figure 6.37. TEM Brightfield micrographs of Nanopowder C after a one hour calcine at 773K.

The 773K calcine of Nanopowder D produced a noticeable degree of growth in the form of necked crystallites that was observed in all micrographs in Figure 6.38. The previous lower temperature calcine did not produce any significant neck growth. Dog bone shaped constructs as well as the necking of large and small crystallites was observed. However, the individual crystallite size appeared to have remained nearly constant after one hour at this temperature level.

The micrographs of Nanopowder E, Figure 6.39, again exhibited the atypical crystal growth similar to that observed with the previous lower temperature calcine. These abnormally large crystals were easily spotted during the initial low magnification viewing of various grids prior to higher magnification

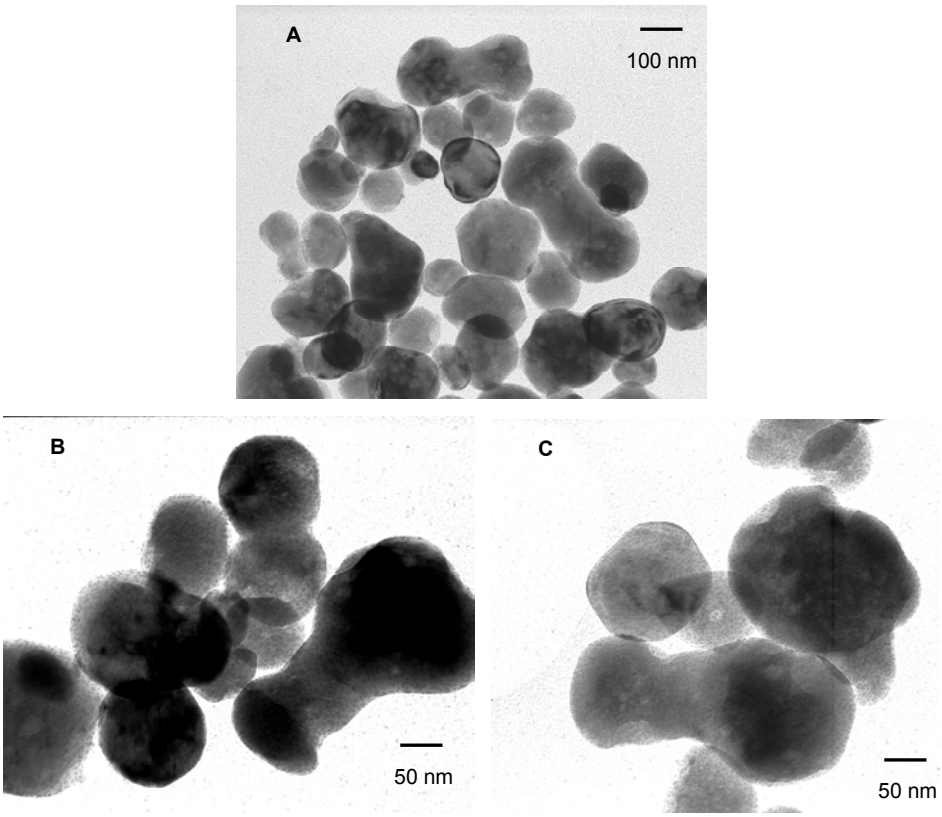

Figure 6.38. TEM Brightfield micrographs of Nanopowder D after a one hour calcine at 773K.

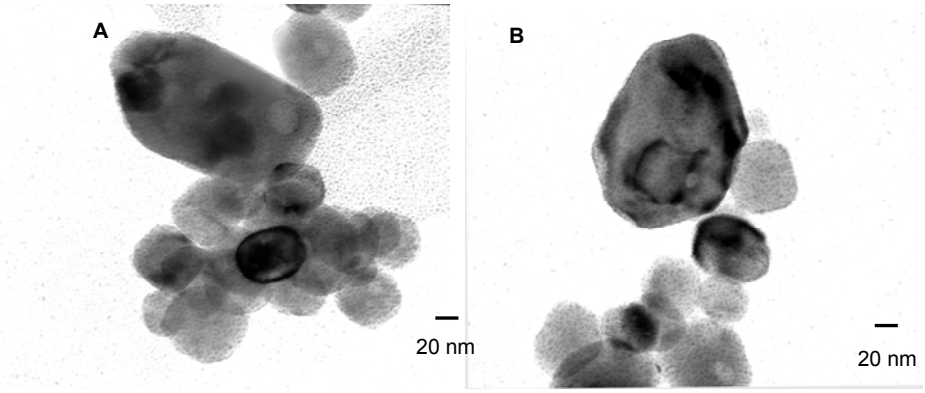

Figure 6.39. TEM Brightfield micrographs of Nanopowder E after a one hour calcine at 773K.

imaging within individual grids. The largest of these atypical crystals exceeded 100 nm. There was no development of small crystallite necking as observed with the other nanopowders.

The apparent average size of the 473K calcined sample of Nanopowder F was 50 to 70 nm, Figure 6.28, which was similar to that observed here with the 773K calcine. The crystallites were nearly translucent; the formvar film was observable beneath the crystallites in micrograph C. The crystallite growth observed with the two different temperature calcinations supported the premise of a highly reactive state of this nanopowder. The previously proposed mesostructure, or a high concentration of incompletely bonded unit cell constructs, provided reactive surfaces for the growth of the crystallites. The growth or rearrangement of the structure during the higher temperature calcine allowed the completion of these incompletely bonded unit cell constructs. The

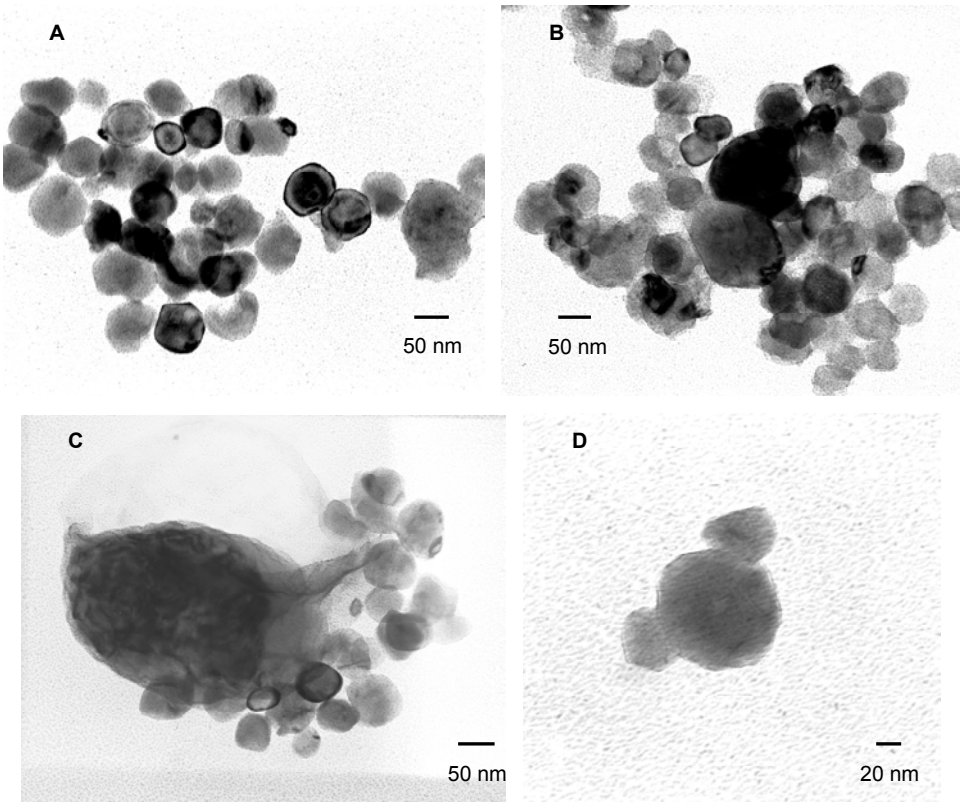

Figure 6.40. TEM Brightfield micrographs of Nanopowder F after a one hour calcine at 773K.

773K calcine sample, Figure 6.40, continued this type of growth as observed in micrographs A and C. The appearance at this stage was of a yet incomplete form or an amorphous appearing phase, as seen branching off of the right edge of the large crystal in micrograph C.

Darkfield images were examined after the 773K calcine to again explore the extent of residual strain in the crystallites. A crystallite without residual strain would present uniform contrast. Examination of the darkfield micrograph of Nanopowder A, Figure 6.41, shows that no strain was evident. The contrast variation with the darker regions in the center sections of the crystallites and the lighter contrast outer edges was due to the thickness of the crystallite. The contrast variation between the edges and center of the crystallites was evidence of the decreasing thickness from the center of the crystallite to the edge. No invariant contrast is observed to support the premise that crystal residual strain was present.

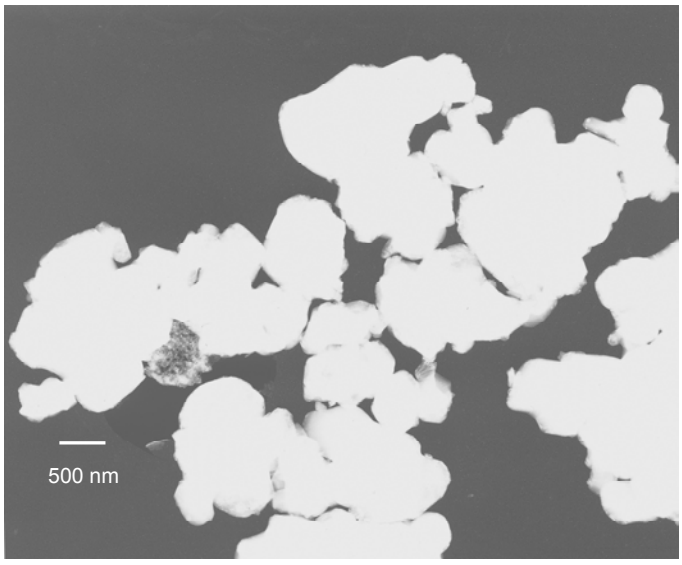

Figure 6.41. TEM Darkfield micrograph of Nanopowder A after a one hour calcine at 773K.

The darkfield micrograph of Nanopowder B, Figure 6.42, also exhibited no variance in contrast. The contrast variation along the edges of the crystals was evidence of the decreasing thickness from the center of the crystallite to the edge where thickness variation is most noticeable. Therefore no residual strain was evident in the crystals of Nanopowder B.

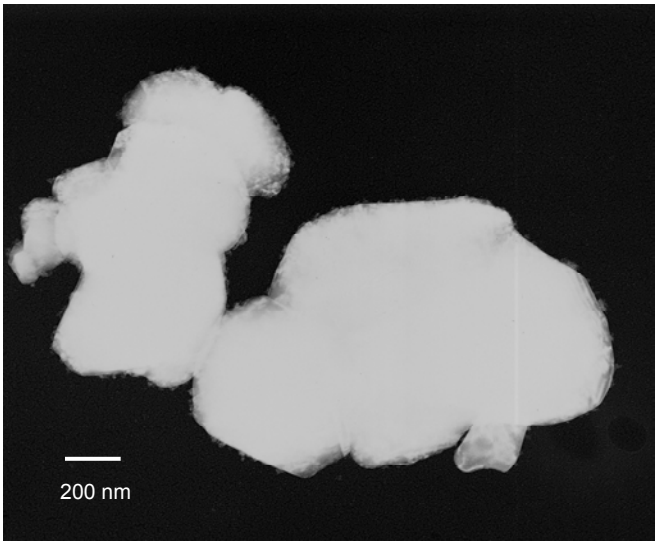

Figure 6.42. TEM Darkfield micrograph of Nanopowder B after a one hour calcine at 773K.

After the one hour calcine at 773K a few of the crystallites of Nanopowder C still exhibited contrast variation throughout, Figure 6.43. The number of such crystallites was greatly reduced and was not readily observed. The crystallites were observed within a narrow size distribution; therefore, the variation in contrast was not due to thickness variations between individual crystallites. Nanopowder C previously exhibited trapped porosity; regions near these pockets exhibited the requisite strain field, producing some of the contrast variation observed. There were a reduced number of crystallites having some degree of trapped porosity. The reduction of trapped porosity led to a reduction in the accompanying residual strain. The degree of trapped porosity having diminished and the contrast invariance also diminished gave evidence for the premise of a

connection between residual strain, and porosity produced high concentration of incompletely bonded unit cell constructs within the crystallites.

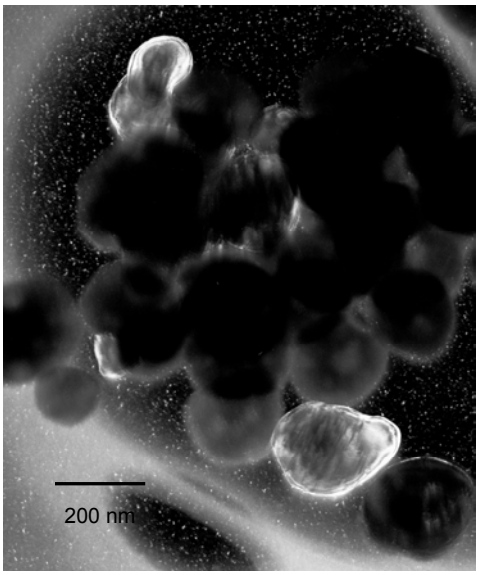

Figure 6.43. TEM Darkfield micrograph of Nanopowder C after a one hour calcine at 773K.

Nanopowder D, Figure 6.44, exhibited crystallite strain -- streaking of the contrast within individual crystallites. However, it was much reduced from the previous lower temperature calcine. The size distribution was broader with this nanopowder than with the previous nanopowder, as seen by the fully bright crystallites observed in the micrograph as well as fully dark crystallites, an indication of the presence of thick and thin crystallites present. Others did exhibit variation of contrast across the crystallite, an indication of strain fields present within the crystallite.

In the darkfield micrograph of Nanopowder E, Figure 6.45, there was variation in the levels of contrast within the crystallites; the swirling effect observed in the crystallites in the upper right and lower left. Several crystallites exhibited variation in contrast. The number of crystallites exhibiting contrast variation was much reduced from that observed after the previous lower

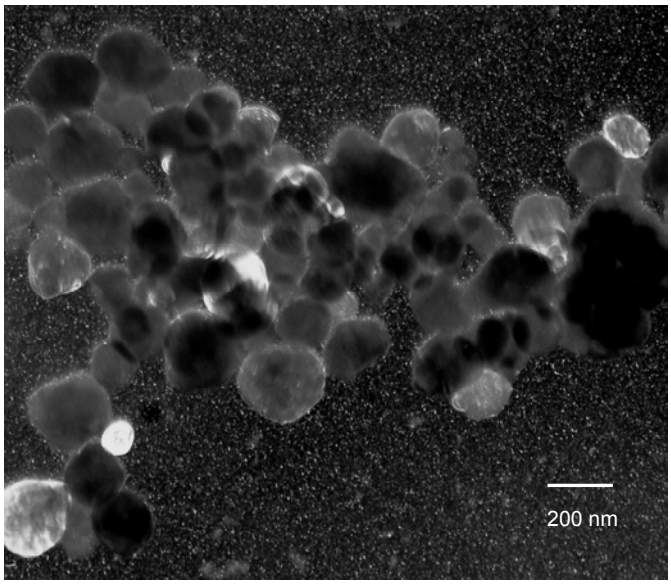

Figure 6.44. TEM Darkfield micrograph of Nanopowder D after a one hour calcine at 773K.

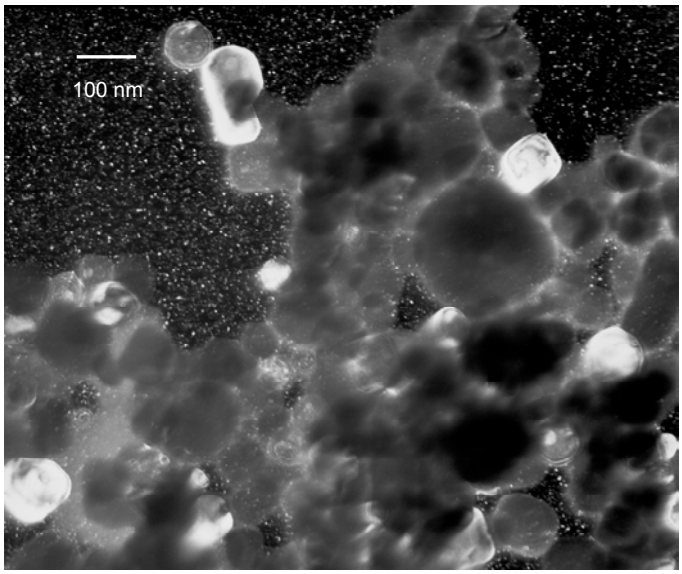

Figure 6.45. TEM Darkfield micrograph of Nanopowder E after a one hour calcine at 773K.

temperature calcine. As with the previous two hydrothermally synthesized nanopowders, strain fields were present to produce the contrast variation observed.

Nanopowder F, also hydrothermally derived, exhibited no apparent residual strain within the crystallites after the 773K calcine. The deviations in contrast within the micrograph, Figure 6.46, are exhibited due to thickness variations among the crystallites with the bright crystallites being thicker than the darker appearing crystallites. No swirling contrast variation was observed nor striated contrast across the crystallites. The incomplete crystallite form or an amorphous glassy phase along the crystallite surfaces, as observed in Figure 6.28, was a high concentration of incompletely bonded unit cell constructs. The bright edges observed in the micrograph are thicker sections and are observed with numerous crystallites. This effect was due to the rearrangement of the high disorder surfaces during the higher temperature calcine which allowed the completion of incompletely bonded unit cell constructs surrounding the surfaces.

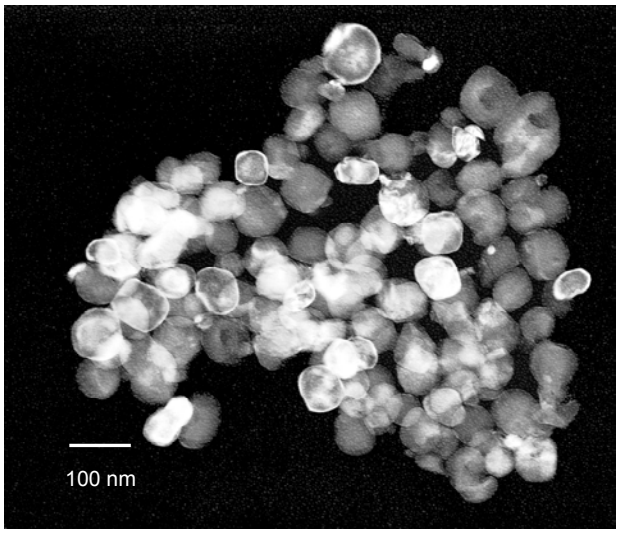

Figure 6.46. TEM Darkfield micrograph of Nanopowder F after a one hour calcine at 773K.

6.3.3.3 Nanopowders Calcined at 1173K

The TEM brightfield micrograph of Nanopowder A (see Figure 6.47) indicated negligible change in crystallite size over the two previous calcines. The lack of necking as a prelude to crystallite growth led to the conclusion that this solid state nanopowder required a higher temperature to induce surface reactivity.

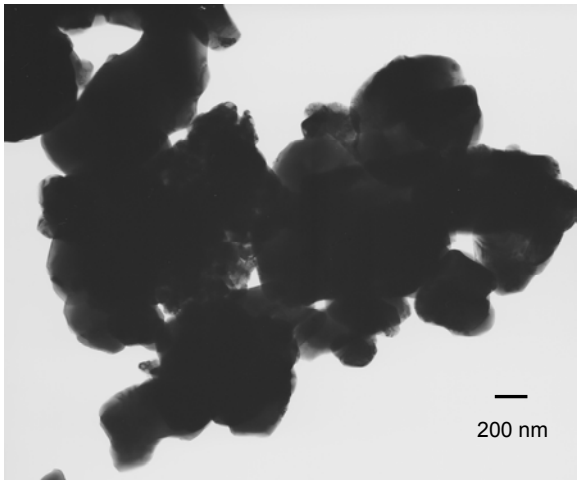

Figure 6.47. TEM Brightfield micrograph of Nanopowder A after a one hour calcine at 1173K.

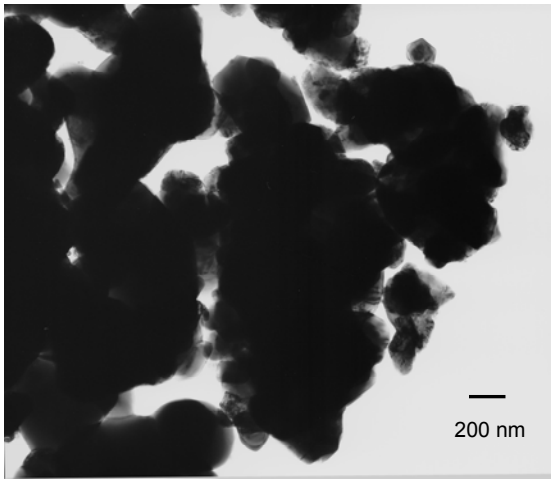

Figure 6.48. TEM Brightfield micrograph of Nanopowder B after a one hour calcine at 1173K.

Comparing the micrographs for Nanopowder B (see Figure 6.48) with those from the previous temperature studies revealed negligible change was observed. However, additional necking of crystallites was observed and the irregular morphology reduced. This solid state nanopowder contained a broader crystallite size distribution than Nanopowder A.

Nanopowder C, the first of the hydrothermally synthesized nanopowders, exhibited some crystallites having trapped porosity remaining after the 1173K calcine; the light spots within the crystallites as seen in Figure 6.49. This trapped porosity, or trapped residual moisture from the synthesis of the nanopowder, was observed in individual crystallites. The spherical shape of the crystallites exhibited a change to more facet edged crystallites, with a small apparent growth in crystallite size.

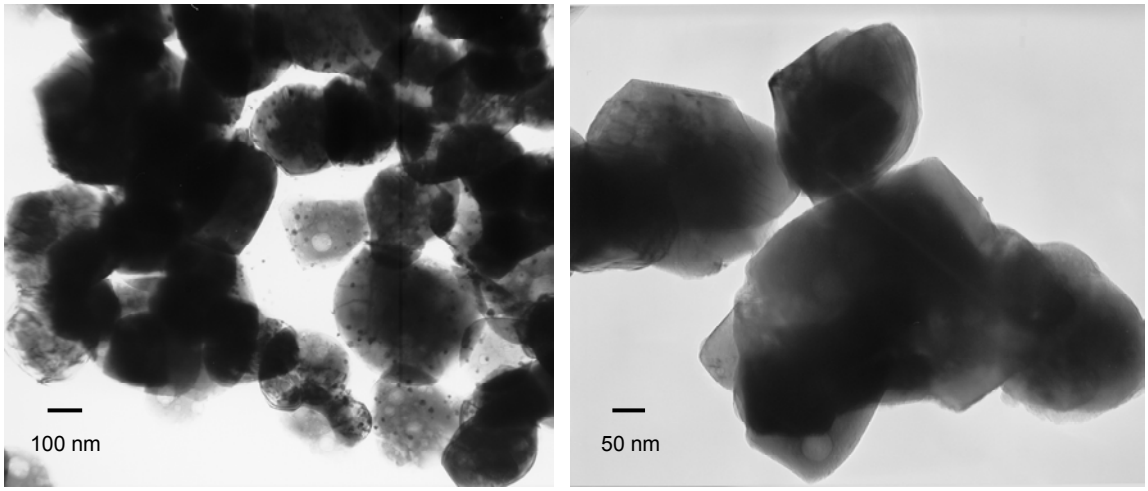

Figure 6.49. TEM Brightfield micrographs of Nanopowder C after a one hour calcine at 1173K.

The second hydrothermally synthesized Nanopowder, D (see Figure 6.50) had a wider crystallite size distribution than Nanopowder C. This nanopowder did not exhibit the trapped porosity observed in Nanopowder C. In the following set of micrographs the apparent size of the crystallites was larger than the lower temperature calcine. This confirmed the lack of trapped porosity that was

observed with the crystallites of Nanopowder C. The largest of the crystallites neared 200 nm with necked and near fully joined crystallites observed.

The uncalcined sample of Nanopowder E had an observable average crystallite size of 70 nm with crystallites as small as 30 nm and the largest observed being approximately 100 nm. The 1173K calcined sample exhibited atypical growth of a minority number of crystallites of size 125 to 150 nm (see Figure 6.51). The spherical morphology of the room temperature nanopowder was not observed here. The morphology exhibited was more irregular facet edged crystallites.

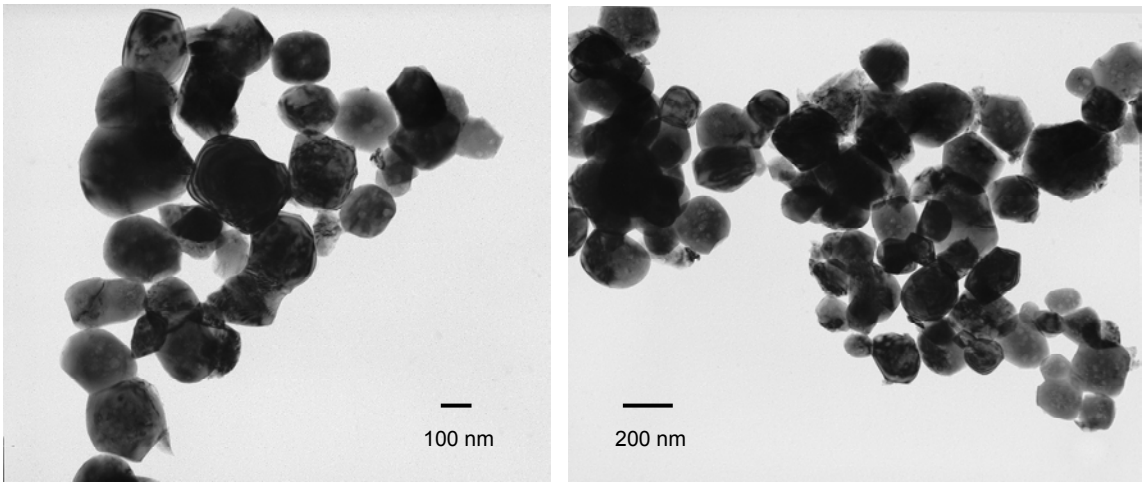

Figure 6.50. TEM Brightfield micrographs of Nanopowder D after a one hour calcine at 1173K.

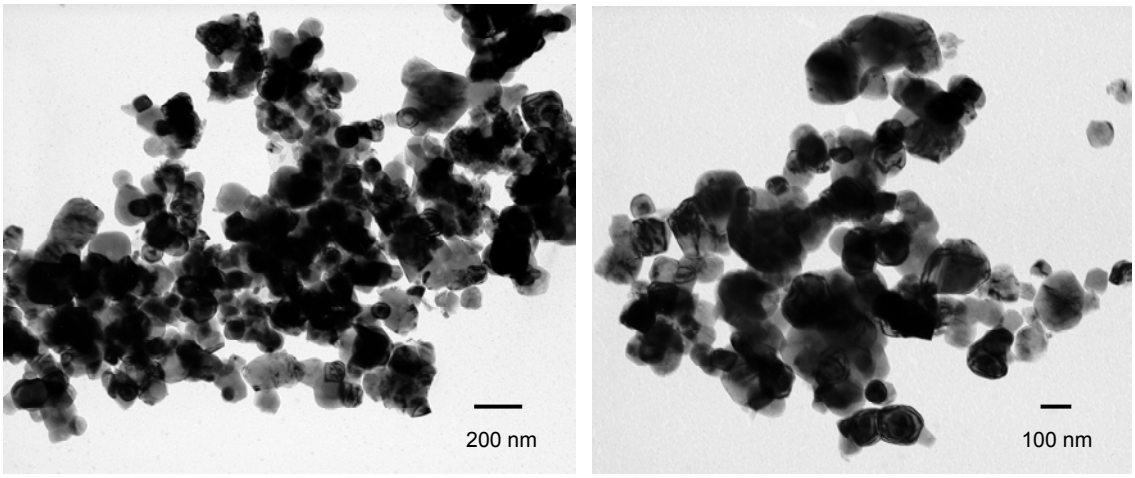

Figure 6.51. TEM Brightfield micrographs of Nanopowder E after a one hour calcine at 1173K.

The crystallite size of the as-received hydrothermally synthesized nanopowder as observed by TEM micrographs in Figure 2.42 was 40-45 nm, with the smallest crystallites nearing 20 nm. The apparent average size of the 1173K calcined sample neared 100 nm (see Figure 6.52). The crystallites were no longer spherical; faceted surfaces were readily observed. The continued crystallite growth observed supported the premise of a highly reactive state of this nanopowder. The previously proposed mesostructure, or high concentration of incompletely bonded unit cell constructs, provided reactive surfaces for the growth of the crystallites. This growth or rearrangement of the structure allowed the completion of these incompletely bonded unit cell constructs.

Nanopowder F was prone to forming spherical agglomerates as shown previously with the optical and SEM observations. These agglomerates were not observed with TEM prior to this calcine series. The size of the agglomerates and the method of preparing sample grids usually precluded the possibility of a spherical agglomerate attaching to a grid. However, it was observed that these agglomerates, after the one hour calcine at 1173K, were composed of individual particles necked together to form this spherical morphology (see Figure 6.52).

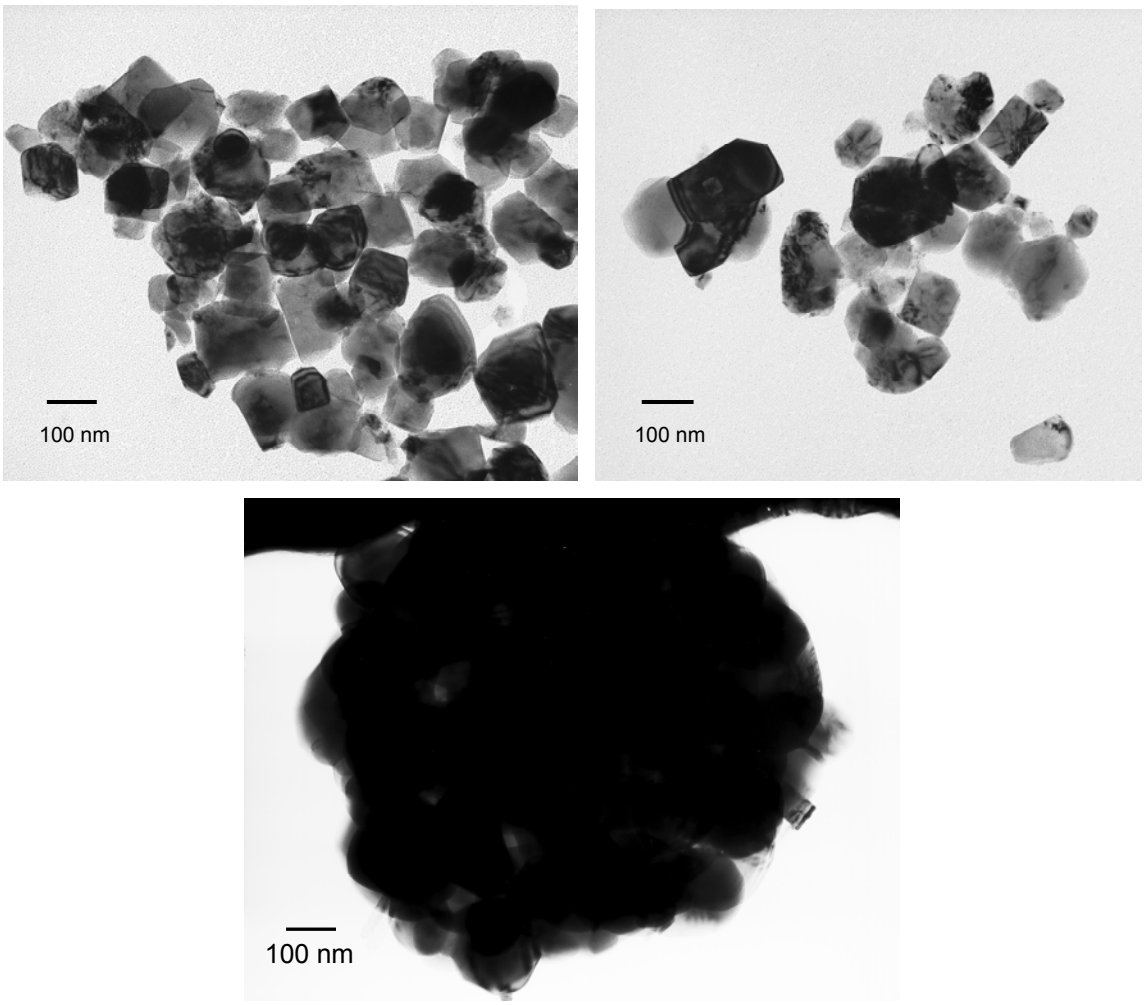

Figure 6.52. TEM Brightfield micrographs of Nanopowder F after a one hour calcine at 1173K.

Darkfield images were examined after the 1173K calcine to again explore the extent of residual strain in the crystallites. A crystallite without residual strain would present uniform contrast. Examination of the darkfield micrograph of Nanopowder A (see Figure 6.53) and Nanopowder B (see Figure 6.54) no strain was evident in either sample. The contrast variation, the darker regions were in the center sections of the crystallites with the lighter contrast outer edges, was due to the thickness of the crystallite. The contrast variation between the edges and center of the crystallites was evidence of the decreasing thickness from the

center of the crystallite to the edge. No invariant contrast was observed to support the premise that crystal residual strain was present.

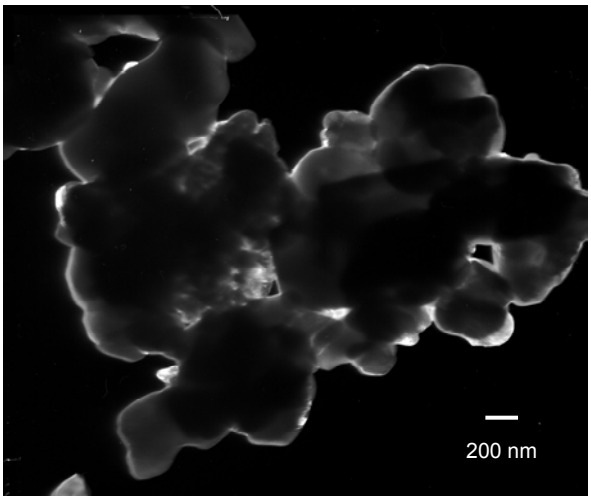

Figure 6.53. TEM Darkfield micrograph of Nanopowder A after a one hour calcine at 1173K.

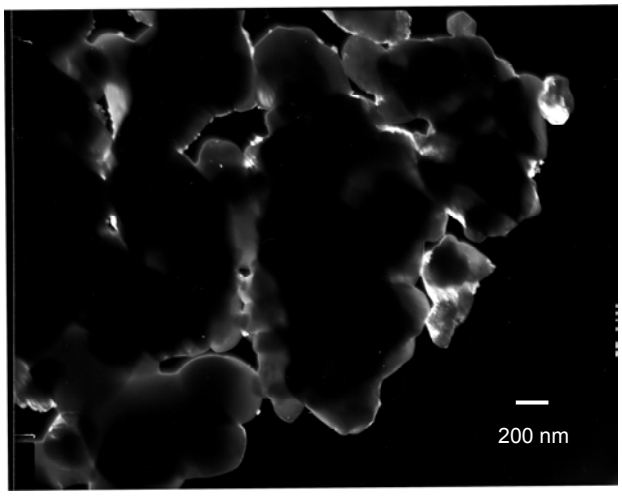

Figure 6.54. TEM Darkfield micrograph of Nanopowder B after a one hour calcine at 1173K.

After the one hour calcine at 1173K none of the crystallites of Nanopowder C still exhibited contrast variation throughout (see Figure 6.55). Nanopowder C previously exhibited trapped porosity; regions near these pockets would exhibit the requisite strain field, producing some of the contrast variation observed. This higher temperature calcine had greatly reduced the number of crystallites having some degree of trapped porosity as observed with the brightfield micrograph (see Figure 6.49). The reduction of the number of crystallites with trapped porosity would lead to a reduction in the number observed in the darkfield micrograph. The degree of trapped porosity had diminished and the contrast invariance also diminished gave evidence for the premise of a connection between residual strain and porosity. These high energy regions were eliminated during the higher temperature calcine and produced complete bonded unit cell constructs within the crystallites without residual strain.

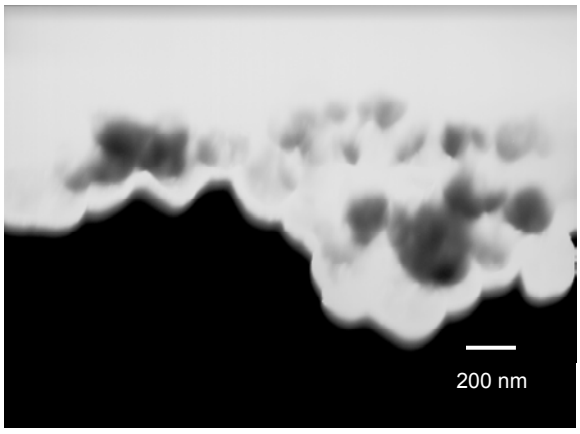

Figure 6.55. TEM Darkfield micrograph of Nanopowder C after a one hour calcine at 1173K.

Nanopowder D (see Figure 6.56) exhibited no observable crystallite strain. The size distribution was broader with this nanopowder than with the previous nanopowder, as seen by the fully bright crystallites observed in the micrograph as well as fully dark crystallites an indication of the presence of thick and thin crystallites present.

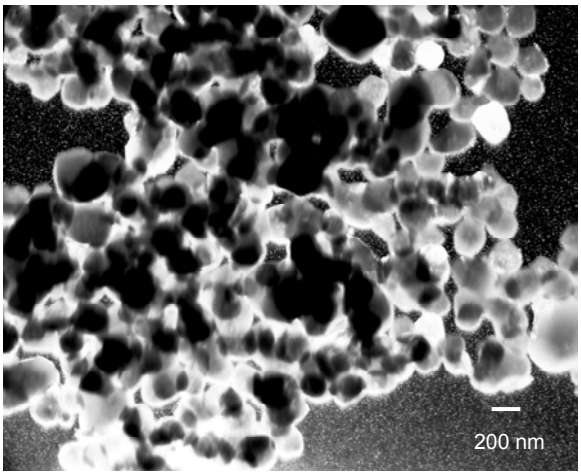

Figure 6.56. TEM Darkfield micrograph of Nanopowder D after a one hour calcine at 1173K.

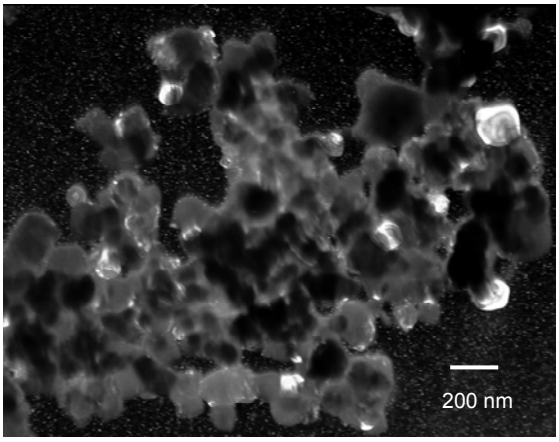

Figure 6.57. TEM Darkfield micrograph of Nanopowder E after a one hour calcine at 1173K.

In the darkfield micrograph of Nanopowder E (see Figure 6.58) there was no variation in the levels of contrast within the crystallites. The bright contrast observed was due to the larger crystallites grown during the 1173K calcine. There was fewer light contrast crystallites as observed with previous calcinations. The growth observed was the reason for the lack of smaller crystallites.

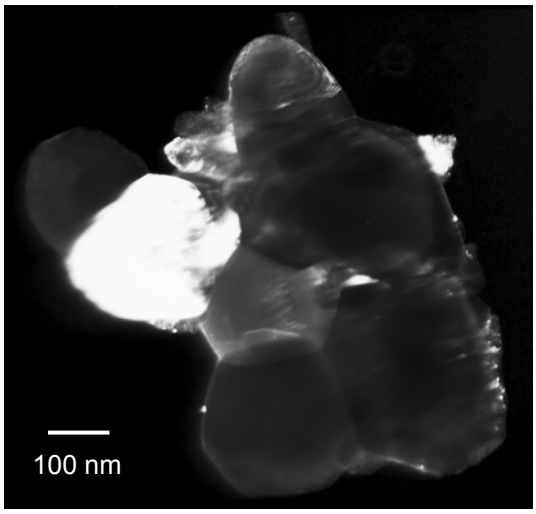

Figure 6.58. TEM Darkfield micrograph of Nanopowder F after a one hour calcine at 1173K.

A diffraction pattern was recorded for each of the 1173K calcined nanopowders. The method of solving the patterns is described in detail in the appendix. A diffraction pattern of each nanopowder follows including a brightfield micrograph of the crystallite from which the pattern was taken. The patterns were solved and indexed, the zone axis stipulated, and the crystal system noted.

The indexed electron diffraction patterns indicated that there was no change from the tetragonal symmetry observed with the room temperature solid state synthesized Nanopowders A and B. The hydrothermally synthesized nanopowders, C through E, each exhibited tetragonal symmetry after the 1173k calcine. The pseudocubic structure previously observed with the room temperature nanopowders was no longer evident. Nanopowder F, the last hydrothermally derived nanopowder, also exhibited tetragonal symmetry after the 1173K calcine. The data, therefore, confirms a stabilized tetragonal symmetry for all of the barium titanate nanopowders subsequent to the 1173K calcine.

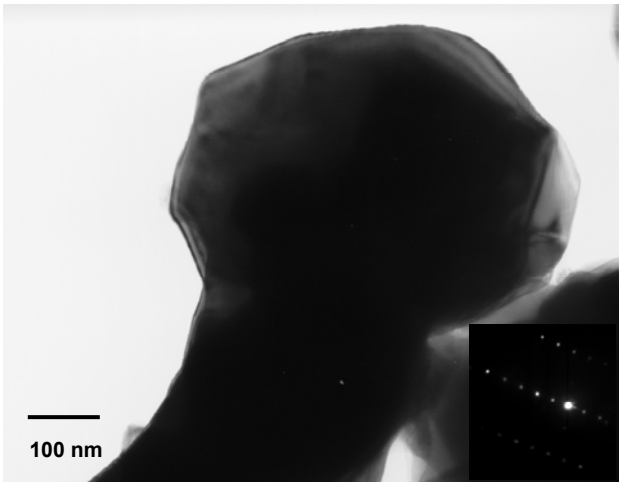

Figure 6.59. TEM Brightfield micrograph of Nanopowder A with diffraction pattern (inset).

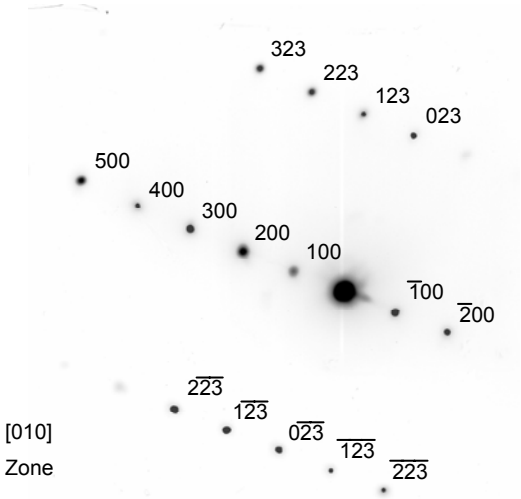

Figure 6.60. Indexed TEM electron diffraction pattern of Nanopowder A with zone axis denoted; tetragonal crystal system.

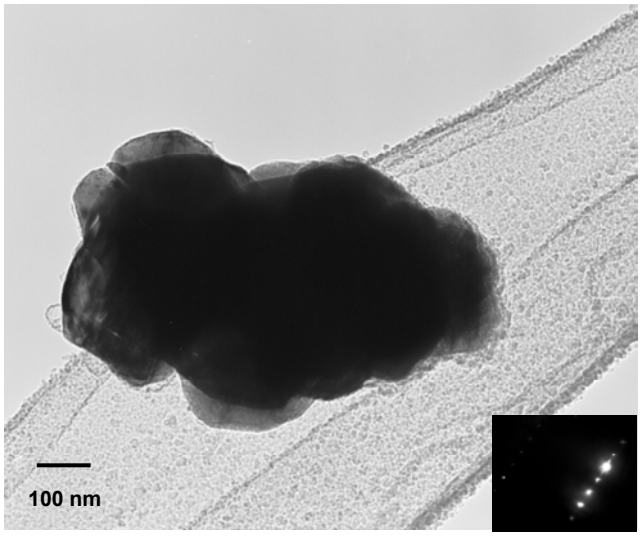

Figure 6.61. TEM Brightfield micrograph of Nanopowder B with diffraction pattern (inset).

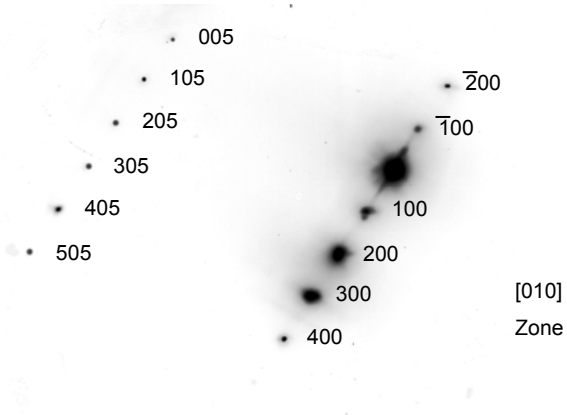

Figure 6.62. Indexed TEM electron diffraction pattern of Nanopowder B with zone axis denoted; tetragonal crystal system.

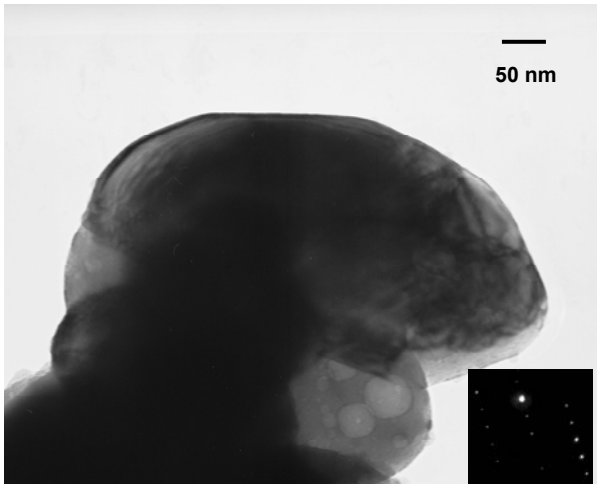

Figure 6.63. TEM Brightfield micrograph of Nanopowder C with diffraction pattern (inset).

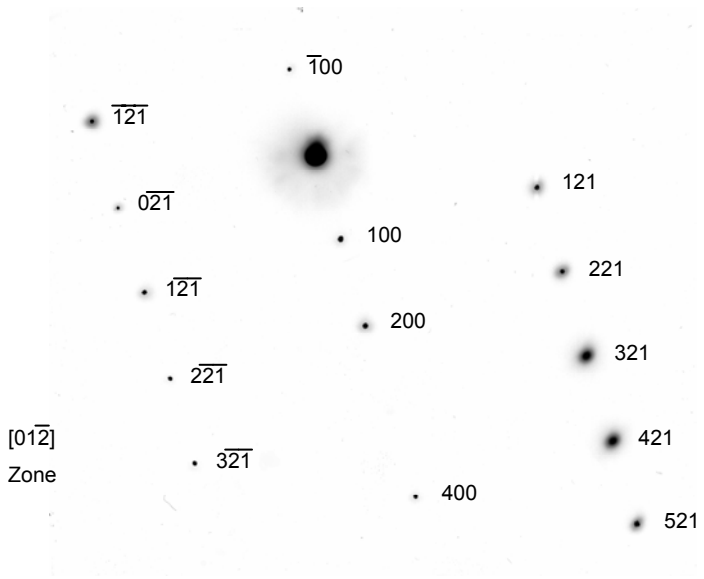

Figure 6.64. Indexed TEM electron diffraction pattern of Nanopowder C with zone axis denoted; tetragonal crystal system.

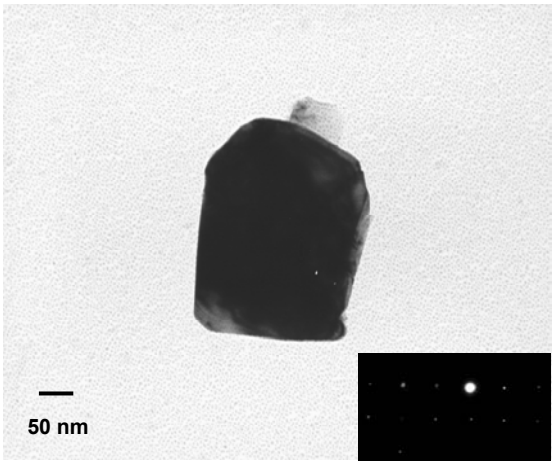

Figure 6.65. TEM Brightfield micrograph of Nanopowder D with diffraction pattern (inset).

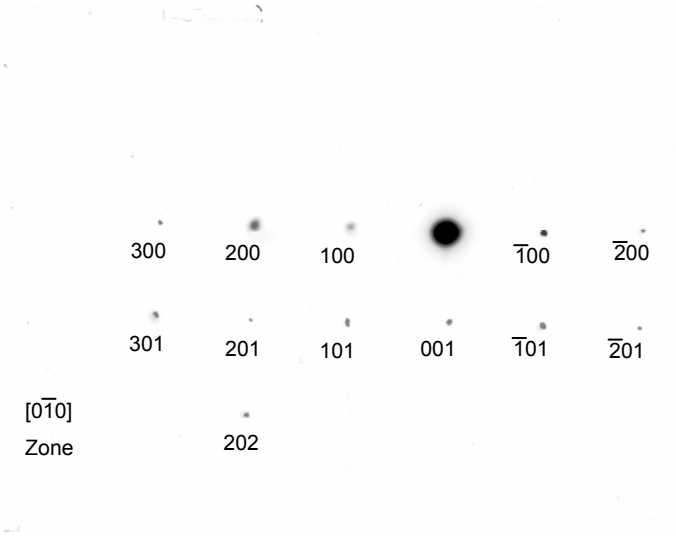

Figure 6.66. Indexed TEM electron diffraction pattern of Nanopowder D with zone axis denoted; tetragonal crystal system.

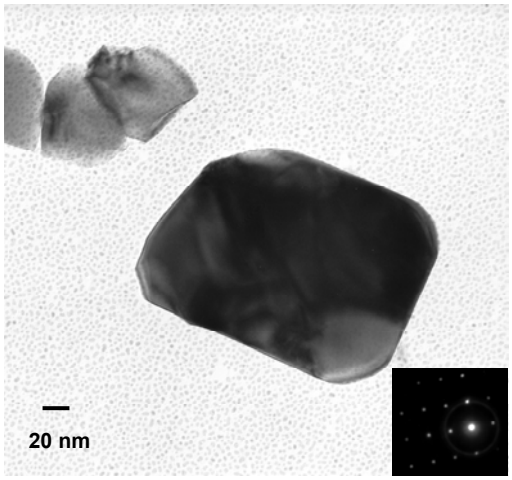

Figure 6.67. TEM Brightfield micrograph of Nanopowder E with diffraction pattern (inset).

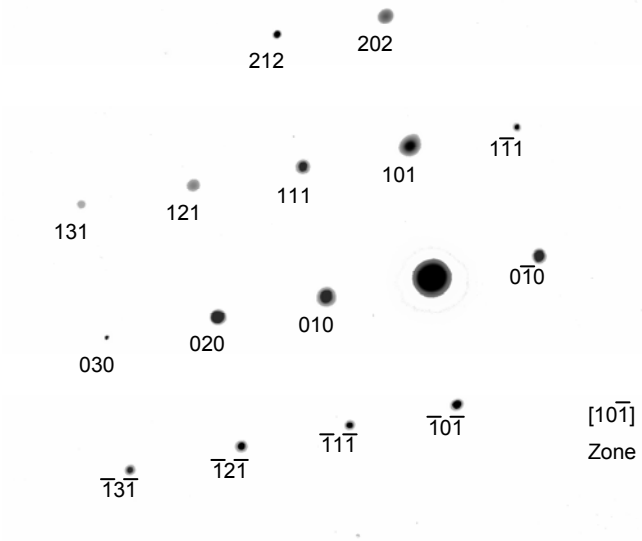

Figure 6.68. Indexed TEM electron diffraction pattern of Nanopowder E with zone axis denoted; tetragonal crystal system.

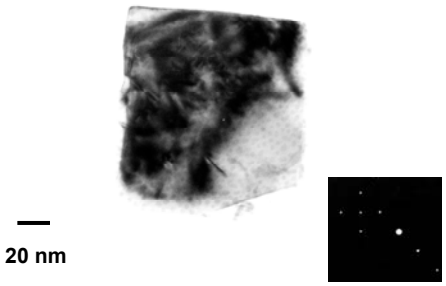

Figure 6.69. TEM Brightfield micrograph of Nanopowder F with diffraction pattern (inset).

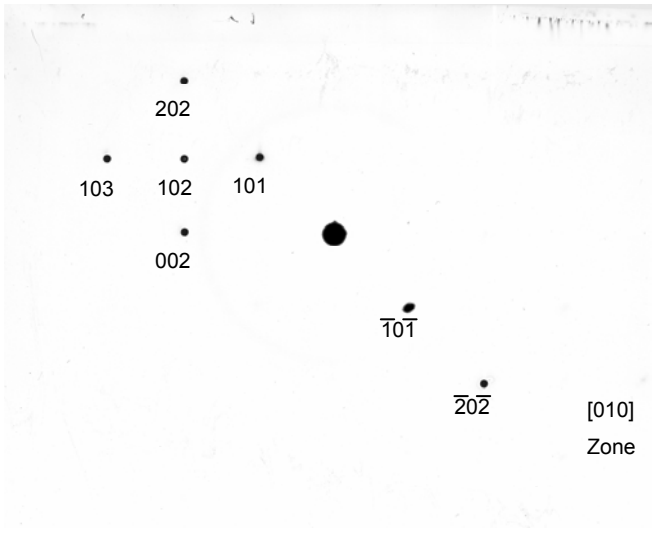

Figure 6.70. Indexed TEM electron diffraction pattern of Nanopowder F with zone axis denoted; tetragonal crystal system.

6.3.4 Summary

Each of the nanopowders examined in this study were calcined at 473K, 773K and 1173K for a period of one hour in ambient atmosphere. Samples were subsequently examined by TEM using brightfield and darkfield imaging. Diffraction patterns were obtained from the 1173K calcined samples. The patterns were solved and indexed, a zone axis stipulated, and the crystal system noted.

The two solid state nanopowders, A and B, exhibited negligible necking and growth after the 473K calcine. A small degree of necking was observed after the 773K calcine and growth was observed after the 1173K calcine. Their irregular morphology remained throughout the lower two calcine temperatures. However, the morphology observed after the highest calcine temperature was less irregular and indicated a more faceted structure of the crystallites. This growth appeared to be accomplished through a stacking of the flattened and chunky crystallites. Large atypical grains developed during the 773K and 1173K calcines of Nanopowder A. This atypical growth was not observed with nanopowder B. The morphology of Nanopowder B changed during the 773K and 1173K calcines. The irregularity observed with the uncalcined nanopowder slowly diminished as growth altered the crystallites. No strain was evident after examination of the darkfield micrographs. Both of these solid state synthesized nanopowders exhibited tetragonal symmetry upon indexing of their respective diffraction patterns prior to calcination and after the 1173K calcine.

The largest average crystallite sized hydrothermally synthesized nanopowder, C, exhibited some degree of necking of crystallites after each calcine. Crystallite growth was observed after each calcine, however, only to a small degree. Growth largely existed as an increase in interconnected crystallites. The number of necked crystallites increased with increasing calcine temperature. Crystallite morphology changed from the “as-received” spherical shape to a more facet edged shape after the 1173K calcine.

Porosity was observed within the crystallites of the “as-received” Nanopowder C. This porosity decreased as calcine temperature increased. The

number of crystallites containing this trapped porosity after the 1173K calcine was very small. Several grid sections needed to be examined to locate crystallites of this type. Crystallites of the “as-received” nanopowder with trapped porosity were observed in all grid sections viewed.

Examination of the darkfield micrographs for Nanopowder C revealed that residual strain was evident after the two lower temperature calcines. Only after the 1173K calcine was strain no longer evident in the darkfield micrograph. As trapped porosity declined the evidence of residual strain also diminished. It was therefore concluded that this residual strain observed was the result of the porous regions within the crystallites. As temperature of calcining increased, vacancy transport from porous regions to the surface of the crystallites occurred. As the vacancies reached the surface they were annihilated, thereby reducing the accompanying strain observed within the crystallites.

Nanopowder D had a larger crystallite size distribution than Nanopowder C. No porosity was observed in the “as-received” nanopowder nor with any of the samples calcined. Negligible crystallite growth occurred during the 473K and 773K calcines. Necked crystallites were first observed with the 773K calcine, but were absent with the 473K calcine and negligible with the 1173K calcine. At the highest calcine temperature, Nanopowder D exhibited anomalously grown crystals that were a factor of ten times larger than the average appearing crystallites. Therefore, noticeable growth in the form of the necking of crystallites was initiated during the 773K calcine and crystallite growth occurred at a temperature thereafter during the 1173K calcine. However, larger crystallites were observed after the 1173K calcine. The morphology of the grown crystallites, after the 1173K calcine, was no longer spherical. As with Nanopowder C, facet edged crystallites developed.

The presence of residual strain was observed during examination of the darkfield micrographs of the 473K and 773K calcined Nanopowder D. No evidence of residual strain was apparent in the darkfield micrograph of the 1173K calcined nanopowder. The degree of growth was minimal at the lower two temperature calcines. Necking was not observed to initiate until after the 773K

calcine. The reduction of residual strain occurred after the highest temperature calcine where necking and crystallite growth had proceeded. The higher energy regions around strain fields were reduced during this necking and growth. The diffraction pattern obtained after the 1173K calcine indicated tetragonal symmetry.

Nanopowder E exhibited a large average crystallite size distribution. At the lowest calcine temperature atypical growth was observed. The largest crystallites absorbed smaller crystallites forming atypically large crystallites. The 773K calcine had similar results with larger atypical crystallites formed. During both calcines no small necked crystallites were observed. Large, smooth surfaced ovate structures formed from the initial mostly spherical shape of the nanopowder. After the 1173K calcine, the original spherical morphology no longer existed. Irregular facet edged crystallites were the norm with numerous atypical growths. The larger crystallites grew atypically with small crystallites still easily observable.

This anomalous growth was similar to that observed with Nanopowder D, however, large anomalous growth was also observed with this nanopowder. An idiomorphic agglomerate with the approximate dimensions of three microns by five microns, was observed. At higher magnification, however, this was observed to be a developing single particle with an interconnected porous structure. The development of this type of structure, along with the other smaller anomalous growths, may be the result of a moisture assisted liquid calcining process that was investigated by Valdivieso. The release of moisture was observed in the spectra throughout the HT-DRIFT FT-IR study. The combination of static air during calcination, the high moisture content, small crystallite size and the accompanying high reactive surface area may account for the observed growths.

Residual strain was evidenced in the darkfield micrographs of the two lower temperature calcined samples. Crystallites with residual strain were rare after the 1173K calcine. As with Nanopowder D, the reduction in residual strain observed here was associated with the large crystallite growth observed. The

diffraction pattern obtained after the 1173K calcine indicated tetragonal symmetry.

Nanopowder F exhibited much different behavior than the other nanopowders. Sphere formation was the predominant morphological evolution during the calcinations. The excess surface space charge of the 40 nm particle size nanopowder was being compensated for with the agglomerates assuming the lowest energy volumetric shape, the sphere. These spheres retained their shape and increased in diameter during calcination in ambient atmosphere. The spheres appeared to reach a maximum size at 773K, possibly the equilibrium agglomerate diameter. The 1173K calcined sample appeared optically to be of similar dimensions as the 773K calcined sample with a larger number of smaller spheres of increased diameter. There was no deviation from the spherical shapes during the calcining and optical microscopic analysis.

At the lowest calcine temperature sphere growth was observed to reach a diameter of 10 microns under SEM analysis. As the calcine temperature increased, growth of this spherical morphology continued with diameters reaching 50 to 60 microns. These spheres originate from the spherical agglomerates that were observed at room temperature under optical and SEM observation of this nanopowder. Spheres also developed during the necking and growth of individual nanocrystallites as observed in the nanopowder after the 1173K calcine.

The possibility of a tremendous amount of excess surface energy in the nanocrystallites of Nanopowder F could explain this sphere formation; an attempt to reduce their high surface energy through sphere formation. A high concentration of mesomolecules near the surfaces, incomplete barium titanate unit cells, comprising the structure of the nanocrystallites would account for an elevated excess surface energy. In addition, residual strain from synthesis would also add available energy for crystallite growth during calcination.

The TEM analysis revealed that crystallites were still small, opaque, and some had an amorphous appearing edge after the 473K calcine. The 773K calcine produced similar results with a larger number of particles with edges

having an amorphous appearance. Negligible growth over that observed with the 473K calcine was observed as the crystallites remained opaque. This amorphous appearance may be the result of the annihilation of the mesoscopic surfaces during calcination; surface reordering at the expense of necking and growth.

The sintered spheres observed after the 1173 calcine can be considered large solid agglomerates. These sintered agglomerates are predominantly much larger than the matrix of smaller crystallites. These spheres will likely resist fracture and breakdown during compaction for the sintering studies.

The spherical morphology which was typical with the samples of this nanopowder had diminished after the 1173K calcine, although the spheres were still observed. The crystallites were more idiomorphic with sizes above 100 nm easily observed. The amorphous appearing morphology observed after the previous two calcines was no longer present. The highest temperature calcine produced the faceted idiomorphic crystallites.

Residual strain, as evidenced with darkfield imaging, was not exhibited after the lowest temperature calcine. The low temperature reduction of strain was attributable to the apparent lack of crystallite growth and the reduction in the amorphous appearing regions that were observed. The fluidic nature of mass transport of the small crystallites during the low temperature calcine was aided by the proposed mesoscopic surfaces. The observed rearrangement of these surfaces diminished any localized residual strain present. The diffraction pattern obtained after the 1173K calcine indicated tetragonal symmetry.

The primary driving force for growth of strain free crystallites was reduction in the interfacial energy. The crystallite growth and shape evolution observed with the nanopowders provide evidence for a reduction in total interfacial volume and an associated reduction in interfacial energy.

The tetragonal symmetry exhibited by Nanopowders C through F, after the 1173K calcine, was the expected symmetry for unstrained barium titanate below the curie temperature of 403K. The pseudocubic symmetry that was observed with these nanopowders in “as-received” condition was no longer present.

7 Intermediate Stage Sintering Studies

7.1 Introduction

The term sintering relates to the phenomena that occur as a compacted powder is transformed into a dense solid. The development of solid structures at an intermediate stage of sintering was studied. The changes occurring in the compacts, porosity changes, grain sizes, presence of a formed glassy phase, and density, were topics of interest during this section of the barium titanate nanopowder study.

Sintering allows a system to attain a state of lowest free enthalpy. The nanopowders have high surface areas and an accompanying high surface energy. Sintering reduces the surface area through the joining of crystallites, grain growth, and a reduction of porosity which allows a decrease in the overall grain boundary surface energy.

This section investigates the state of the nanopowder compacts at an intermediate stage of sintering at varying levels of moisture and carbonate content. Calcining the nanopowders at three different temperatures that can be related to the vibrational spectroscopic investigations allows insight to the effects of the differing levels of impurity constituents.

An intermediate stage of sintering is typified by the necking of grains between adjacent particles of the compacted powder. Densification at this stage begins as grains neck and porosity is reduced. The porosity may be thought of as an interconnected network of channels along the developing grain boundaries. It is during this stage of sintering that densification occurs through the reduction of this large porous network. Only in the latter stage of sintering does grain growth, the growth of larger grains at the expense of smaller grains, become the determining factor in densification.

The degree of porosity and its morphology was examined. The degree of grain necking and grain growth during sintering was also of interest. The presence of atypical grain growth, glassy phases and the density of the sintered compacts complete the areas investigated.

7.2 Experimental Procedure

Samples, 0.5 gram, of each nanopowder were weighed and pressed in a double action cylindrical steel die at 44 MPa to form compacts measuring 1.25 cm in diameter. No processing additives were employed in the production of the compacts. Four sets of compacts of each of the nanopowders were pressed: "as-received", 473K calcine, 773K calcine and 1173K calcine. The calcining was accomplished in ambient atmosphere for one hour at each of the stipulated temperatures. Five compacts were prepared of each nanopowder from each of the four sets. Sintering was in ambient atmosphere conditions at 1473K (below the 1605K eutectic temperature of barium titanate) for one hour at a ramp rate of 5 K/min (Centurion Q50, Degussa-Ney, Yucaipa, CA). The samples were allowed to slowly cool to room temperature.

Each compact was weighed and dimensionally measured. Density was calculated from these values. The Archimedes method of calculating density was not used due to the frangible nature of the compacts. A majority of the compacts disintegrated during the first attempt at calculating density by the Archimedes method.

Samples were examined using scanning electron microscopy (Amray 1810, Amray Inc., Bedford, MA and Philips SEM 515, Philips Electron Optics, Eindhoven, Netherlands). Fracture edges and compact surfaces of each nanopowder type were studied. Polishing was initially attempted with the "as-received" lots. This lot was polished and 2% hydrofluoric acid (HF) etched. The etched surfaces of the compacts were then examined. The frangible nature of the compacts after an intermediate stage of sintering made this a difficult process. If a compact surface disintegrated at the start of polishing, no further attempt to achieve a polished surface was made. The surfaces of these compacts were examined "as-sintered." The fracture surfaces were of greater interest in studying the state of densification and the nature of structural development within the compacts after an intermediate stage of sintering.

7.3 Results and Discussion

7.3.1 Calculated Densities of Sintered Compacts

Compacts were weighed and dimensionally measured after sintering. The diameter of each compact was measured across two diameters perpendicularly opposed. Thickness was measured in three separate regions. These values were averaged and density was calculated from the resulting values. The lots of each type of compact were totaled and an average density value for each tabulated.

Table 7.1 Calculated Densities of 1473K Sintered Compacts

	Nanopowder Compact / Average Density (g/cm^3) [Std. Dev.]					
Sample Type	A	B	C	D	E	F
as received	3.69[0.08]	3.54[0.06]	5.22[0.24]	4.19[0.06]	3.56[0.18]	4.74[0.27]
473K calcine	3.86[0.12]	3.60[0.15]	4.91[0.18]	4.19[0.12]	4.19[0.19]	4.62[0.16]
773K calcine	4.57[0.25]	4.29[0.47]	4.97[0.20]	4.17[0.19]	4.20[0.12]	4.27[0.09]
1173K calcine	4.30[0.11]	4.45[0.15]	4.46[0.12]	4.11[0.14]	3.86[0.21]	4.33[0.20]

The solid state Nanopowder B was the only set of compacts that the calcination exhibited beneficial effects with improved densification. The density continued to increase with increasing calcination temperature. Compacts formed from Nanopowder D were unaffected by the calcine process, the densities were consistent for all compact types. Nanopowder C compacts in “as-received”

condition produced the densest sample of all lots examined; 86.7% of the theoretical density (D_{th}) of 6.02 g/cm^3.[141]

7.3.2 Sintered Compacts of "as-received" Nanopowders

The HF acid etch was initially attempted on polished surfaces of compacts formed from each of the "as-received" nanopowders. The results were interesting, but led to the examination of the balance of compacts without using

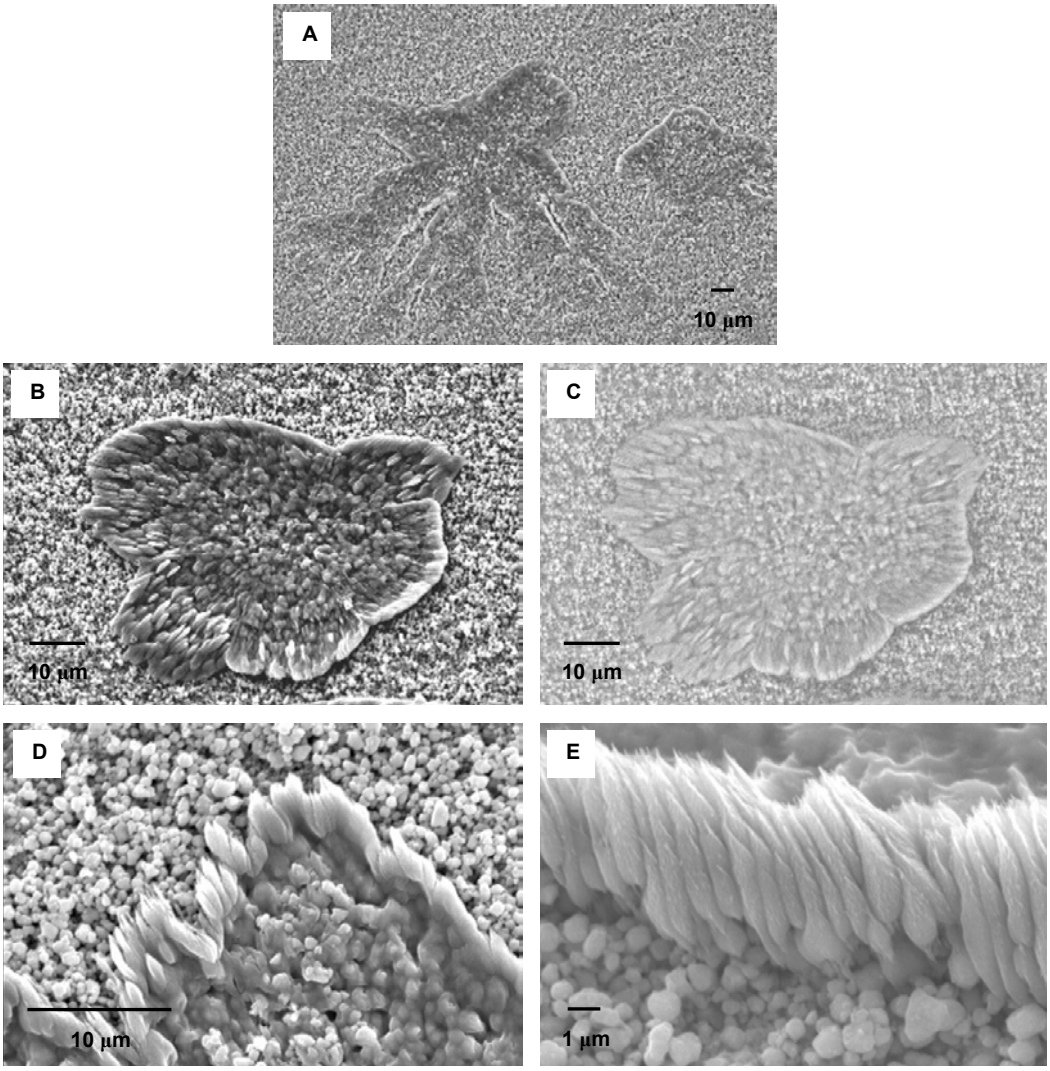

Figure 7.1. SEM micrographs of a sintered compact of "as-received" Nanopowder A, 2% HF etched, at 500X SE (A), 1,300X SE (B), 1,300X BSE (C), 3,300X SE (D), and 7,500X SE (E).

an etchant on their polished surfaces. The formation of a new phase, as a result of the etching of these samples, was discovered with all of the compacts examined.

The new phase, white in appearance, was viewed under secondary electron mode (SE) and backscatter mode (BSE). Average atomic number contrast is discernable under backscatter mode with the SEM. This variance in average atomic number was difficult to discern, however, in the micrographs which follow.

The compact formed from the “as-received” Nanopowder A (see Figure 7.1) which was HF etched, exhibits the formation of another phase on the surface. This new phase has a striated feathery morphology. Micrographs B and C are of the same area under secondary electron mode (B) and backscatter mode (C). Micrographs D and E are higher magnification images of the rim of the formation. These formations were at various locations on the surface of the compact, micrograph A.

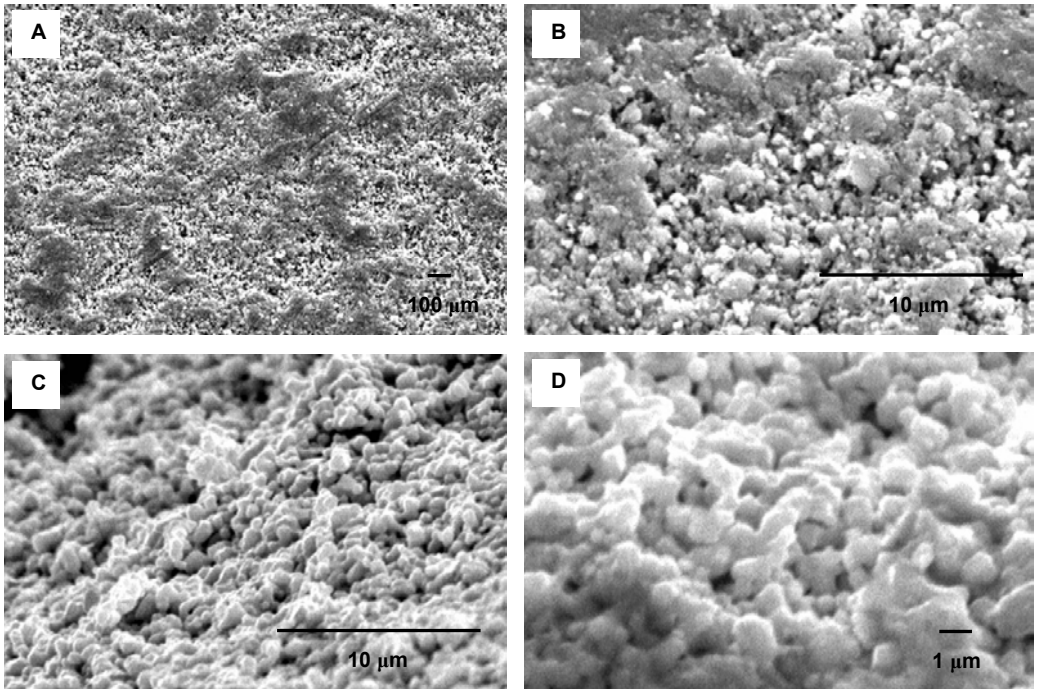

Figure 7.2. SEM SE mode micrographs of a sintered compact of “as-received” Nanopowder A, no etchant, at 1,000X (A), 5,000X (B), 4,700X (C), and 7,500X (D).

The compact formed from the “as-received” Nanopowder A without HF etching (see Figure 7.2) exhibits none of the formations observed on the surface of the HF etched compact. Solidification and grain growth is observed in the micrographs of the surface (A and B). This was also observable within the fracture surface images (C and D). The short duration of sintering at 1473K had resulted in a large amount of crystallite necking and growth which was clearly visible in all of the micrographs along with some degree of porosity. No atypical grain growth was observed in this compact.

The HF etched compact of the “as-received” Nanopowder B (see Figure 7.3) exhibited a similar morphology for the new phase discovered. The shapes observed were random and likely dependent upon the manner of the HF etchant application and surface composition. One of these phases was viewed under SE and BSE modes (see micrographs B and C). A slight variance was noted between the surface and the new phase in the backscatter micrograph, therefore denoted a variance in average atomic number between the two phases.

The compact formed from the “as-received” Nanopowder B without HF etching (see Figure 7.4) exhibited none of the formations observed on the surface of the HF etched compact. No atypical grain growth was observable either along the surface or along the fracture surface. A large degree of solidification was observable on the surface where sintering temperature was achieved quicker than within the bulk. The facture surface of the bulk, where a lesser degree of solidification was noticeable, and still exhibited growth in the form of latter stage necked crystallites and a porous structure.

The compact formed from the “as-received” Nanopowder C (see Figure 7.5) which was HF etched, also exhibited the formation of another phase on the surface. This new phase had a different morphology from that observed with the previous solid state synthesized nanopowders (see Figures 7.5 and 7.6). A more solidified clamshell shape was observed in Figure 7.5. The associated backscatter micrograph showed a definite variance in atomic number between the surface and the new phase.

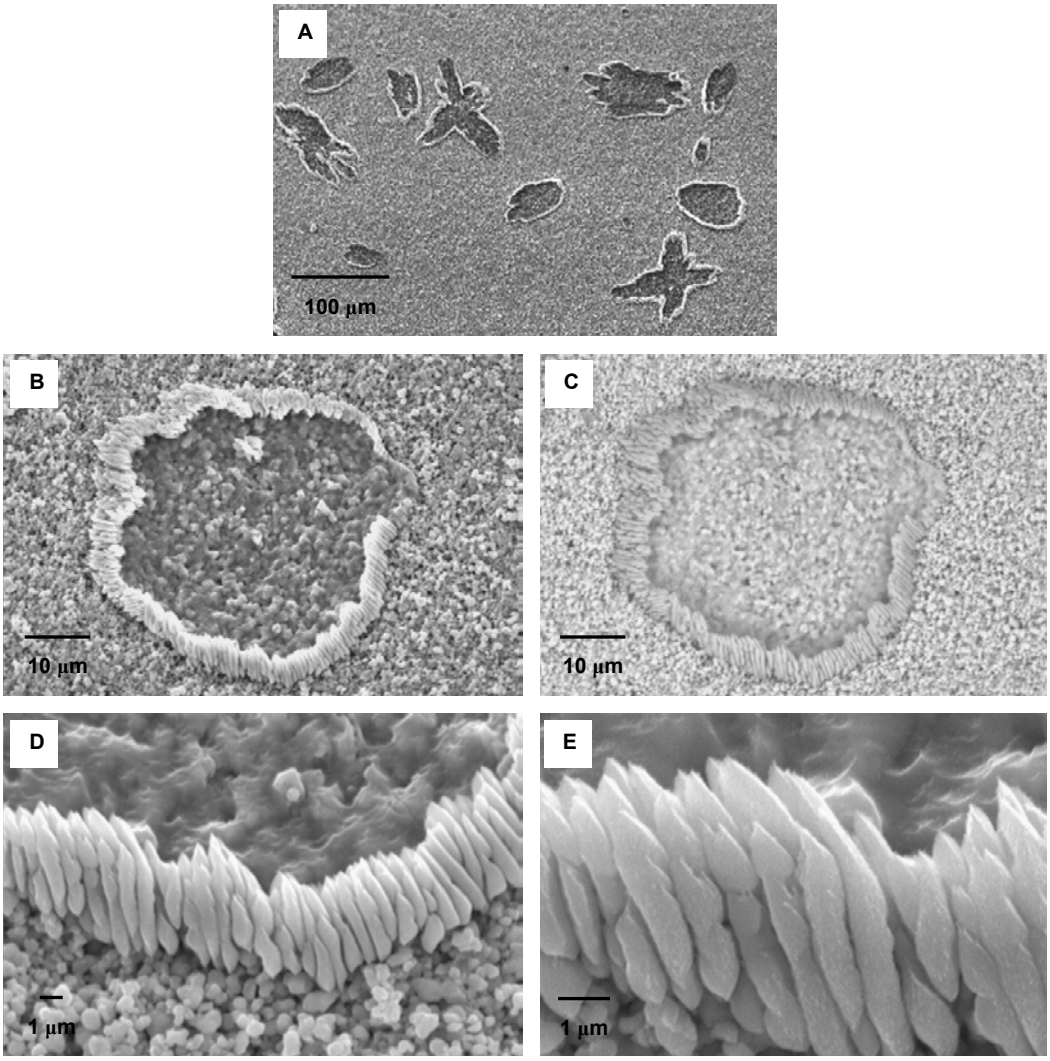

Figure 7.3. SEM micrographs of a sintered compact of “as-received” Nanopowder B, 2% HF etched, at 250X SE (A), 1,500X SE (B), 1,500X BSE (C), 5,000X SE (D), and 11,500X SE (E).

Other shapes were evident on the etched surface (see Figure 7.6). These shapes also exhibited a variance in the average atomic number between the surface and the new phase. The darker phase in backscatter mode would have a lower average atomic number than the brighter phase. Higher atomic number elements would interact to a greater degree since the yield of the collected backscattered electrons increases with the specimen's atomic number. The surface parent material (barium titanate) was therefore of higher average atomic number than the new phase. An exchange of fluorine atoms for oxygen atoms

during the HF etching may have occurred. An examination using SEM EDS may possibly prove this assumption correct.

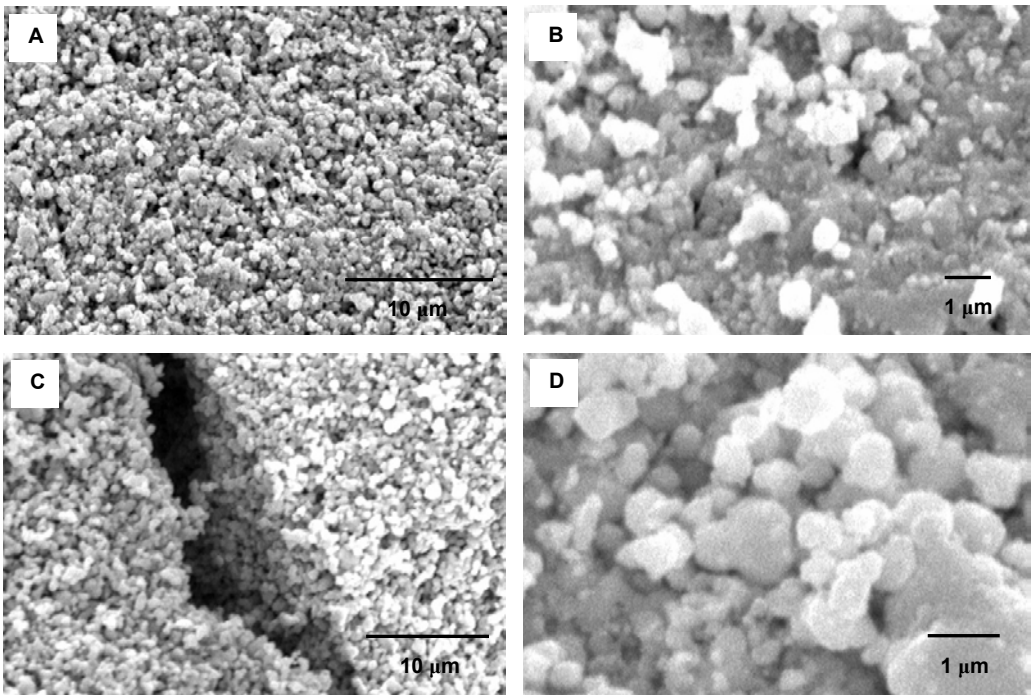

Figure 7.4. SEM SE mode micrographs of a sintered compact of "as-received" Nanopowder B, no etchant, at 3,000X (A), 10,000X (B), 3,000X (C), and 17,000X (D).

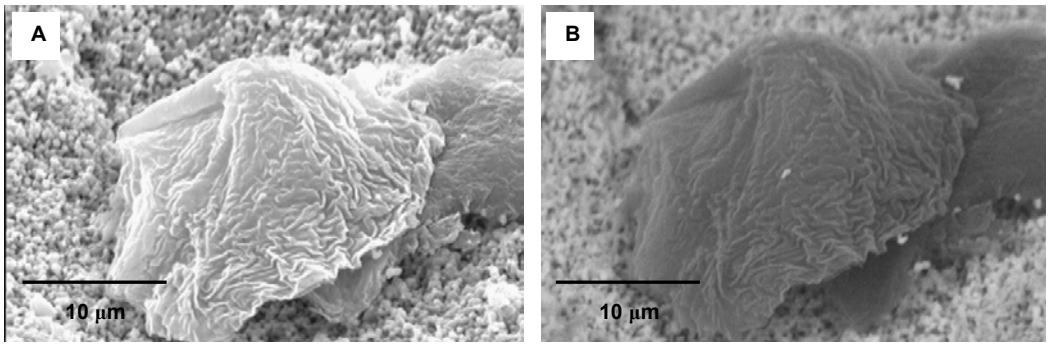

Figure 7.5. SEM micrographs of a sintered compact of "as-received" Nanopowder C, 2% HF etched, at 3,300X in SE (A) and BSE (B) modes.

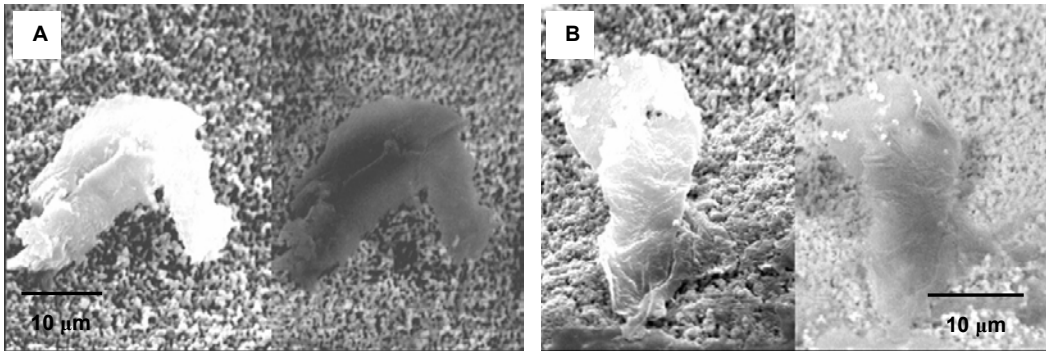

Figure 7.6. SEM micrographs of a sintered compact of “as-received” Nanopowder C, 2% HF etched, at 1,800X (A) and 2,200X (B). SE and BSE modes are left and right respectively in each micrograph.

The compact produced from the “as-received” Nanopowder C, without etching, Figure 7.7, exhibited a large amount of surface porosity in micrograph A. The fracture surface views, micrographs B and C, showed growth in the form of latter stage necking; however, larger developing grains were not observed. Sintering to an intermediate stage had produced an interconnected bulk through the necking of the small crystallites with little perceptible grain growth. Porosity was highly evident within the bulk as well as along the surface. The micrograph of the surface showed no evidence of the formations observed on the surface of the HF etched compact.

The compact formed from the “as-received” Nanopowder D (see Figure 7.8) which was HF etched, also exhibited the formation of another phase on the surface. This new phase had a different morphology from that observed with the previous three nanopowders. The new phase was formed of numerous clusters on the surface of the compact as seen in micrograph A. Higher magnification images of these clusters in micrographs B and C, show a fibrous structure comprised of needle-like ferns. This event occurred close to equilibrium conditions when the clusters grew at the expense of dissolving the smaller grained surface.

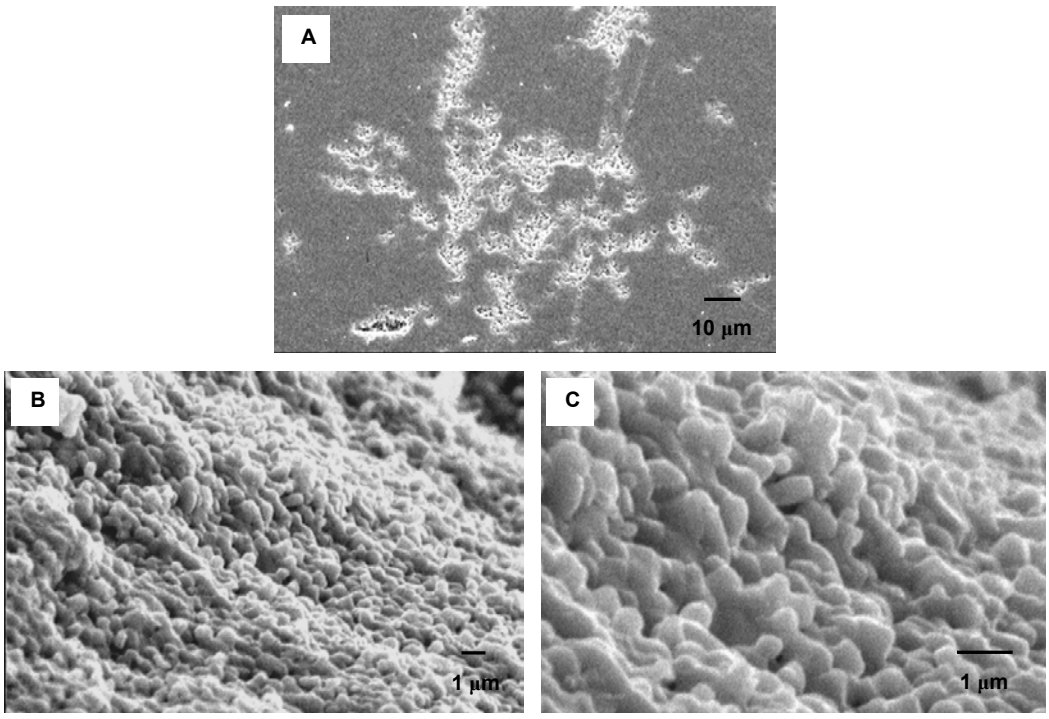

Figure 7.7. SEM SE mode micrographs of a sintered compact of “as-received” Nanopowder C, no etchant, at 900X (A), 6,200X (B), and 13,300X (C).

The new phase developed within the few second duration of the HF etching process. The clusters originated along porous regions of the surface. These regions are more disordered, of a higher energy state and represent more reactive sites for the growth of the new phase. The large number of clusters may be due to the high degree of porosity of the Nanopowder D compact and the large number of smaller grains within this porous region as observed in the micrographs of the unetched sample.

The compact produced from the “as-received” Nanopowder D, without etching, exhibited an extraordinary amount of surface porosity (see Figure 7.9). The high magnification micrograph, C, shows atypical grain growth, large grains among numerous much smaller grains, and better illustrates the high degree of porosity.

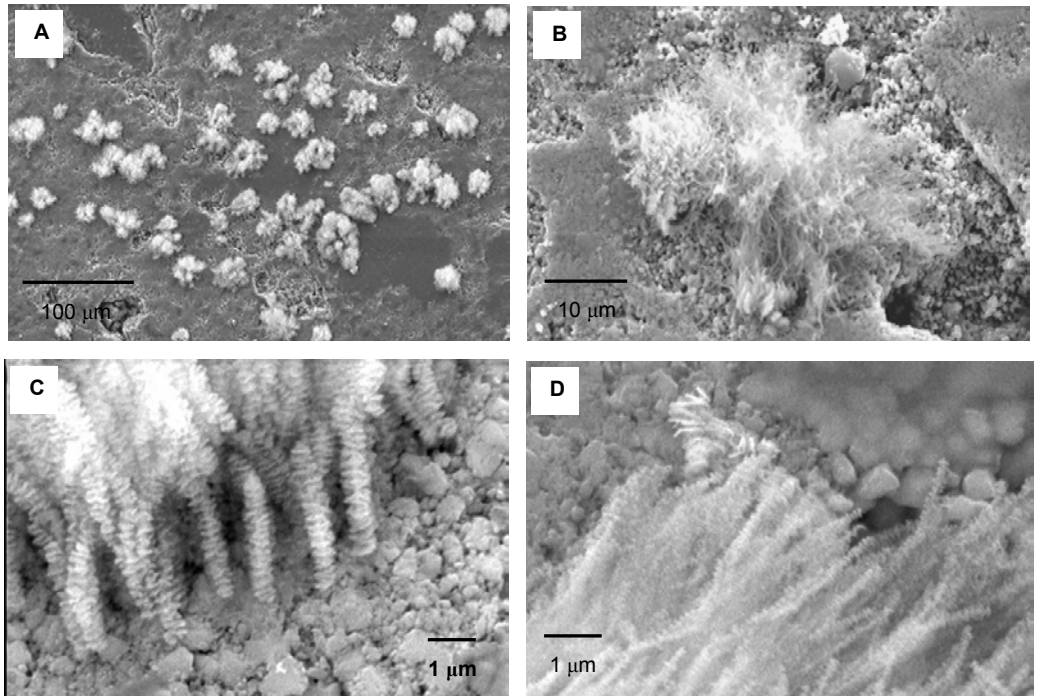

Figure 7.8. SEM SE mode micrographs of a sintered compact of "as-received" Nanopowder D, 2% HF etched, at 750X (A), 1,850X (B), 11,000X (C), and 13,000X (D).

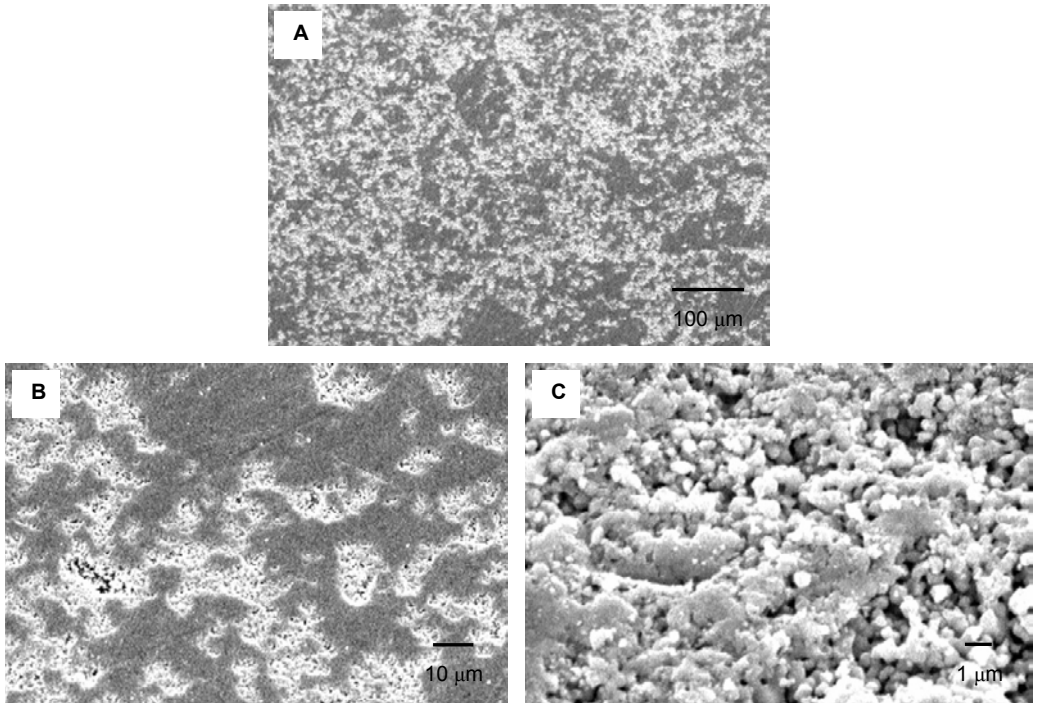

Figure 7.9. SEM SE mode micrographs of the surface of a sintered compact of "as-received" Nanopowder D, no etchant, at 170X (A), 875X (B), and 5,700X (C).

The fracture surface analysis, images of the bulk (see Figure 7.10) displayed the high degree of atypical grain growth. The majority of these large grains exceeded 100 μm in size as seen in micrograph C. Additionally, there existed a large number of the smaller grains as seen in micrographs B and C. The high degree of necking observed with the previous nanopowder (C) was absent here. The structure was disjointed and the compacts were very frangible.

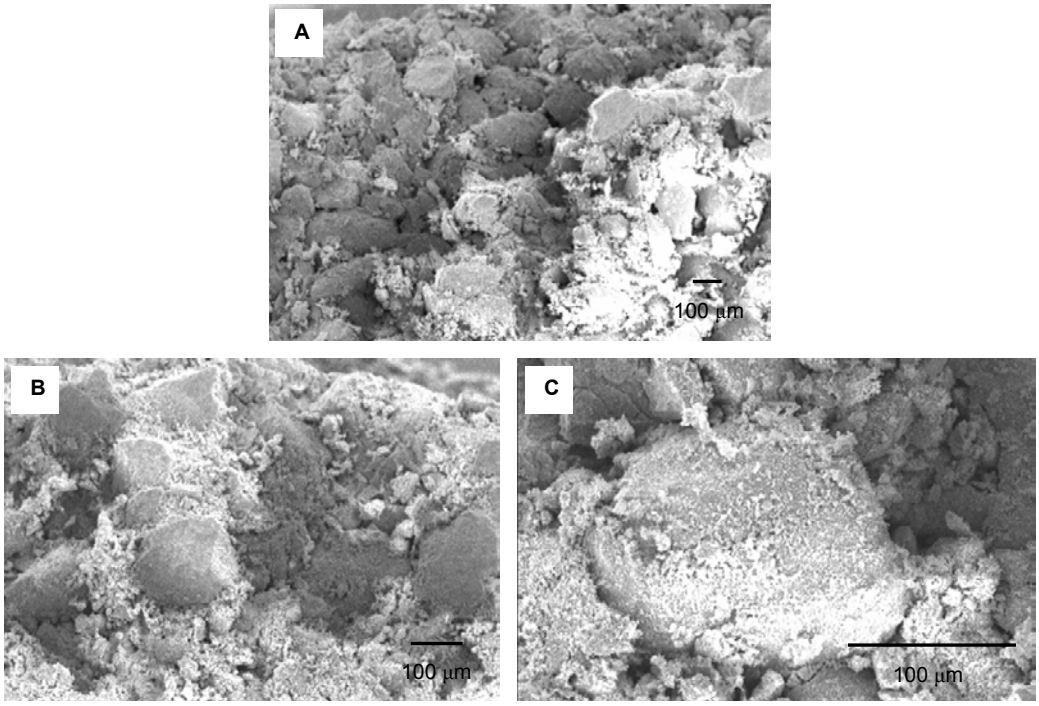

Figure 7.10. SEM SE mode micrographs of the bulk of a sintered compact of "as-received" Nanopowder D, no etchant, at 65X (A), 120X (B), and 390X (C).

The compact formed from the "as-received" Nanopowder E (see Figure 7.11 and 7.12) which was HF etched, also exhibited the formation of another phase on the surface. The new phase had morphology similar to that observed previously; a needle formation originating from the small grains of the surface of the compact. Similar to previous compact samples, the new phase was exhibited as the darker phase in backscatter mode.

The new phase was fairly prevalent on the etched surface (see Figure 7.12, micrograph A). The fibrous needle formations in micrograph B approach 10 μm in length and there appears to be no preferential orientation as was observed with previous compact samples. The compact was granular with a small grain size which yielded a large volume of porous regions that were the originating sites of new phase growth. Agglomerate growths litter the surface, with some of these agglomerates as sites for the growth of the new phase in micrograph C and D.

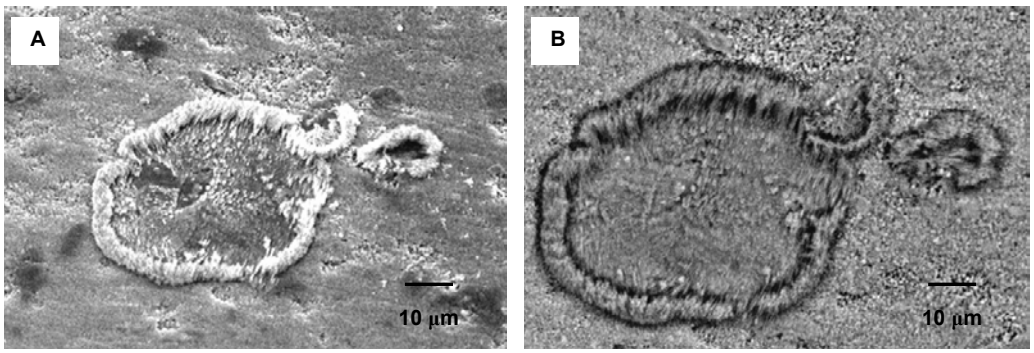

Figure 7.11. SEM micrographs of a sintered compact of "as-received" Nanopowder E, 2% HF etched, at 1,500X in SE (A) and BSE (B) modes.

The compact produced from the "as-received" Nanopowder E, without etching, exhibited an extraordinary amount of fine surface porosity (see Figure 7.13, micrographs A and B). The high magnification micrograph (B) better illustrates this high degree of fine porosity. The fracture surface images in micrographs C and D show that the bulk also contained a large degree of porosity. Atypical grain growth, large grains among numerous much smaller grains, was observed in micrograph D. This was an uncommon finding during analysis.

Necked grains and growth of smaller grains is observable in micrograph B, yielding some densification of the compact. Necking was not as prevalent as that observed with the Nanopowder C compact. The compacts produced from

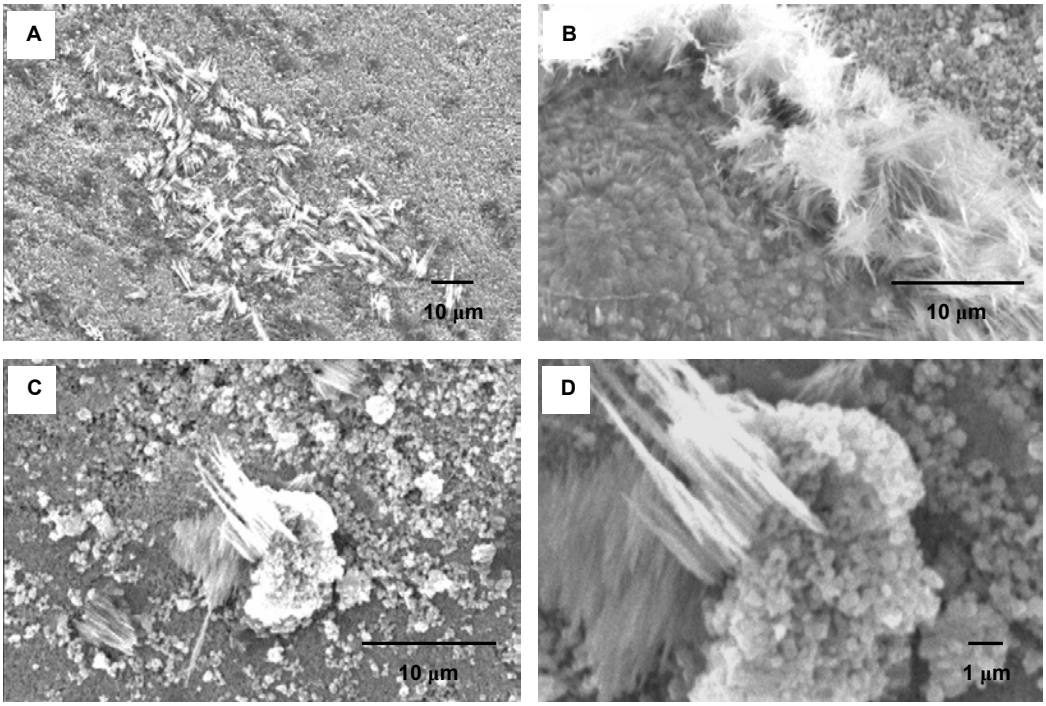

Figure 7.12. SEM SE mode micrographs of a sintered compact of “as-received” Nanopowder E, 2% HF etched, at 500X (A), 3,000X (B), 3,000X (C), and 7,500X (D).

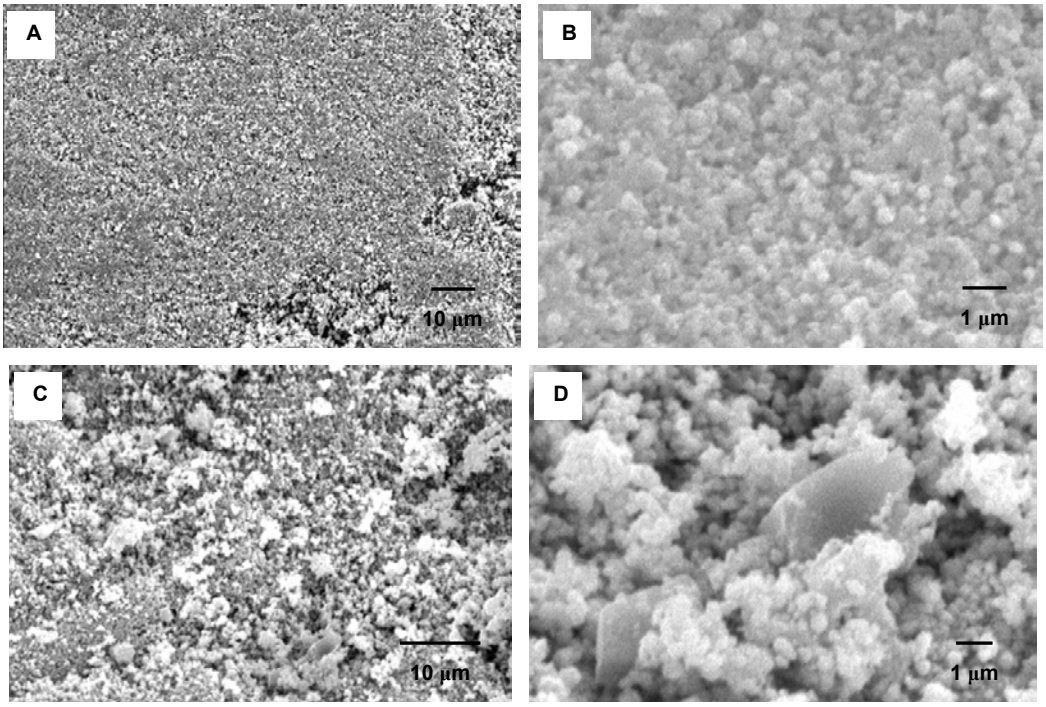

Figure 7.13. SEM SE mode micrographs of a sintered compact of “as-received” Nanopowder E, no etchant, at 100X (A), 10,000X (B), 1,800X (C), and 7,000X (D).

Nanopowder E were also quite frangible, however, not to the same degree as with the compacts from Nanopowder D.

The compact formed from the “as-received” Nanopowder F (see Figure 7.14) which was HF etched, also exhibited the formation of another phase on the surface. The new phase had morphology different to that observed previously. A smooth glassy formation originated from the small spherical grains of the surface of the compact. Near the edge of the compact in micrograph B the parent titanate and new glassy phase formed a cement blend.

The glassy phase formation covered spherical nubs along the surface ending in rings that surrounded the sphere in micrograph C. This glassy phase was a thin layer in micrograph D which covered the majority of the surface of the compact. None of the previous morphologies of the new phase observed were present.

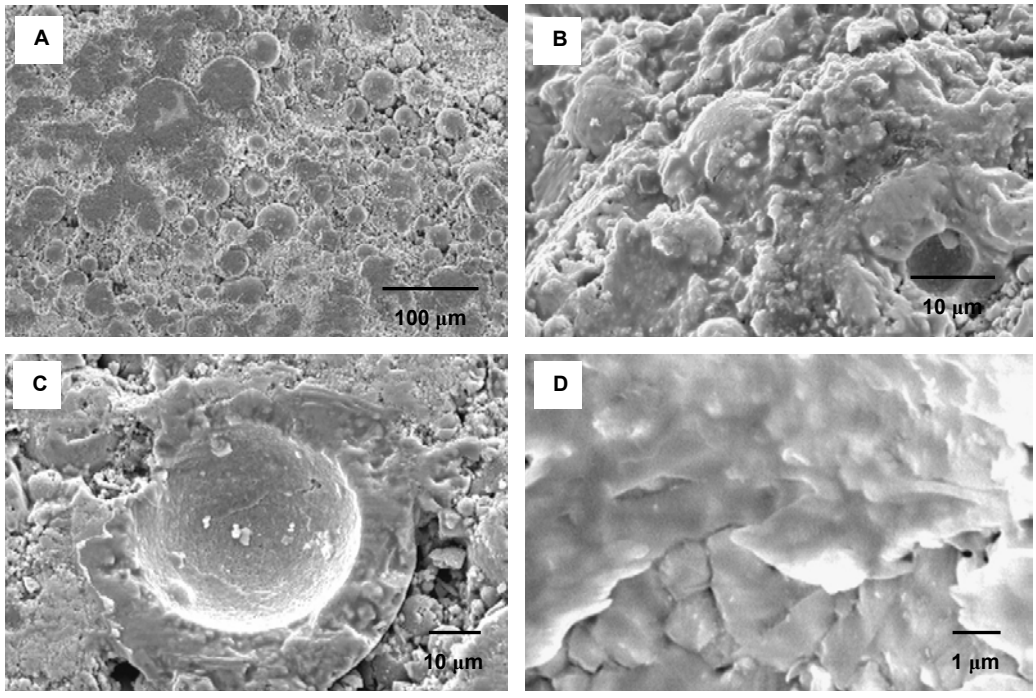

Figure 7.14. SEM SE mode micrographs of a sintered compact of “as-received” Nanopowder F, 2% HF etched, at 225X (A), 2,000X (B), 1,200X (C), and 11,000X (D).

The compact produced from the “as-received” Nanopowder F, without etching, exhibited surface and bulk porosity (see Figure 7.15). This compact exhibited a high degree of atypical growth in the form of sintered spheres. The spherical agglomerates described in previous sections of this study had become a collection of individual separate units through densification during sintering. This was similar to the observances made during the calcine study of this nanopowder. The agglomerated spheres absorbed smaller crystallites during their growth in micrograph C. The spheres grew atypically producing interagglomerate pore coarsening and microcrack formation. The largest sphere formation observed was approximately 60 μm with sizes ranging to 1 μm observed.

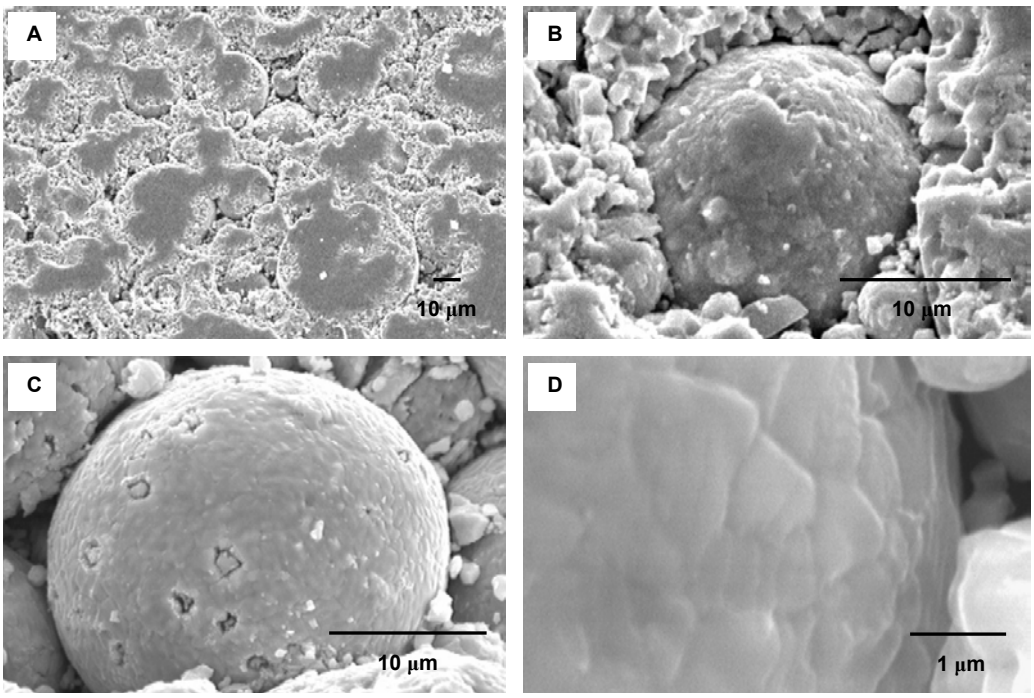

Figure 7.15. SEM SE mode micrographs of a sintered compact of “as-received” Nanopowder F, no etchant, at 600X (A), 3,900X (B), 3,600X (C), and 22,000X (D).

These large sintered spheres were composed of individual grains and may be observed in micrograph D. The individual grains that comprised the sphere

approached one micron in size. The initial crystallite size of this nanopowder was 40 nm; therefore, growth within the spheres was rapid during the time and temperature parameters used. Growth within the spheres was without atypical grain growth. The atypical growth was a product of the presence of the spherical agglomerates within the nanopowder. The pressure in forming the compacts was not high enough to distort or eliminate these spherical agglomerates. The compact was, therefore, formed of closely packed agglomerated spheres of varying sizes. A flattened spherical morphology is still observable at the surface after pressing and sintering (see figure 7.15, micrograph A).

SEM energy dispersive spectroscopy (EDS) was used in an attempt to identify the new phase that developed during the HF etching of each of the nanopowder compacts. The plot in Figure 6.16 indicates the presence of barium, titanium, oxygen, gold and palladium. The latter two elements are indicative of the 1.5 minute sputtering with 70:30, by weight, gold-palladium that was applied to the sample prior to SEM examination. The other elements are the constituents of barium titanate and expected to be present. The titanium Kα and Kβ peaks are close to the Lα and Lβ1 peaks; titanium 4.508 KeV and 4.931 KeV Kα and Kβ peaks versus barium Lα and Lβ1 peaks 4.465 KeV and 4.827 KeV. To aid in differentiating between the two elements there exist the barium Lβ2 and Lδ1 peaks at a slightly higher energy level.[141]

The EDS plot of the new phase (see Figure 7.17) indicates the presence of barium, titanium, fluorine, oxygen, gold and palladium. Again the latter two elements present due to the sputter coating. Barium, titanium and fluorine are the major constituents of the new phase. The plot provides evidence for an exchange of fluorine for oxygen at the surface of the compacts during the etching process. This may indicate the presence of one of two phases; titanium oxydifluoride ($TiOF_2$) or barium fluoride (BaF) according to the following chemical reactions:

$$BaTiO_3 + 2HF \longrightarrow TiOF_2 + BaO + H_2O \qquad (5.1)$$

$$BaTiO_3 + 2HF \longrightarrow BaF_2 + TiO_2 + H_2O \qquad (5.2)$$

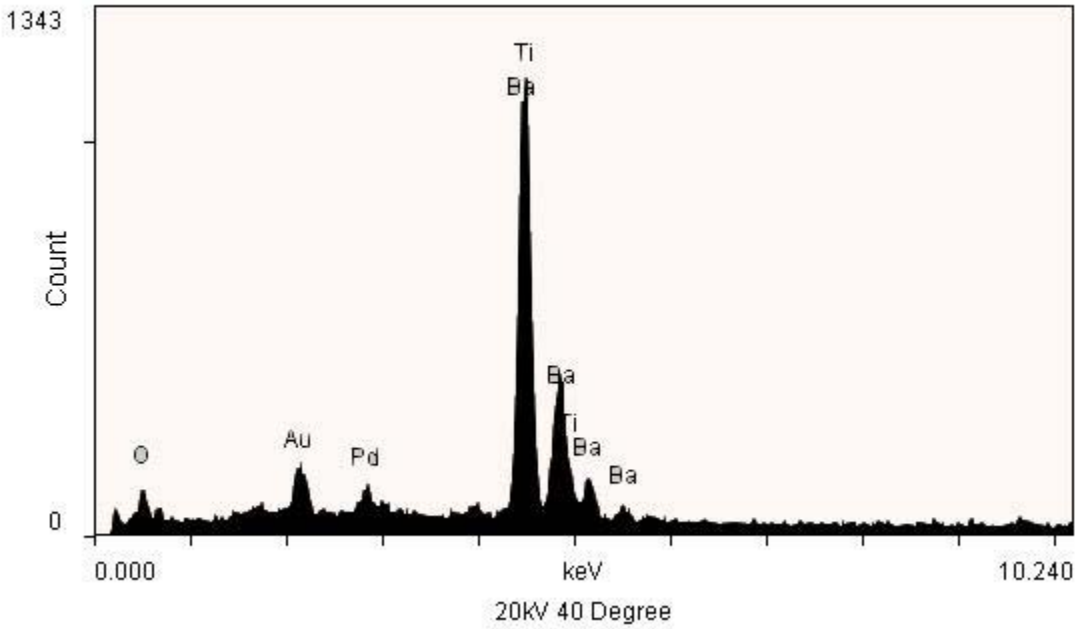

Figure 7.16. SEM EDS plot of the surface of the compact not affected by the new phase that developed during HF etching.

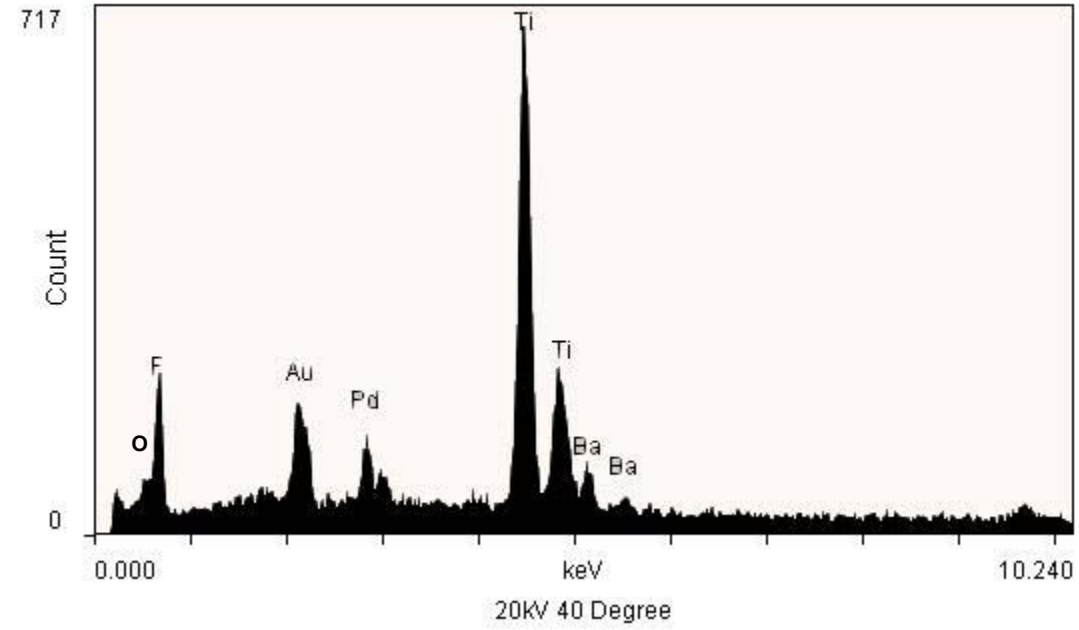

Figure 7.17. SEM EDS plot of the new phase formed on the surface of the compact during the HF etching process.

This new phase developed rapidly in a nearly 2-dimensional array in some instances, as with the fern-like growth on the Nanopowder C compact. The dendritic growth observed may have developed due to rapid crystallization in the presence of the solvent etchant which retained the heat necessary for crystallization. The morphology observed was similar to that discussed by Banfield and Navrotsky in their investigations of quickly forming fluorites on hydrocarbons.[140]

Barium fluoride has a cubic structure with a density of 4.89 g/cm^3 and is colorless.[128(p.4-47)] Titanium oxydifluoride has a simple cubic structure with a random distribution of one oxygen atom and two fluorine atoms per unit cell, is white in appearance, and has a calculated density of 3.09 g/cm^3.[128(p.4-48)]

The ionic radii sum of the Ti – X distances in $TiOF_2$, where X is either oxygen or fluorine atoms, was reported as 2.08 Å and 2.04 Å respectively.[141] These distances are similar to the cubic phase Ti – O octahedron in barium titanate that was previously described in section 3.2. The similar structure and bond distances would aid in the rapid exchange of fluorine for oxygen atoms along a titanium rich surface.

The average atomic number for barium titanate, barium fluoride and titanium oxydifluoride are 20.4, 24.7 and 12, respectively. Using backscatter imaging in the SEM, barium fluoride would appear brighter than the lower average atomic number of barium titanate and titanium oxydifluoride. Titanium oxydifluoride has a lower average atomic number than barium titanate and would appear darker under SEM backscatter imaging. Various levels of fluorine stoichiometry in $TiOF_{2\pm}$ have been reported.[142] This as well aids in deducing the correct resultant product during the etching process since differing levels of backscatter contrast was observed within the nanopowder samples examined. The surface reaction that occurred during HF etching would therefore be best expressed through the first chemical reaction with the product of titanium oxydifluoride.

7.3.3 Sintered Compacts of 473K Calcined Nanopowders

Each nanopowder was calcined for one hour at 473K. Compacts were formed using 0.5 gram from the calcined powder and subsequently sintered for one hour at the previously specified temperature. No etchant was used prior to scanning electron microscopy of the samples. Polishing was accomplished when the frangible nature of the compacts did not lead to disintegration of the surface.

The fracture surfaces of the compact formed from the 473K calcined sample of Nanopowder A (see Figure 7.18) illustrated an interconnected network of porosity and evidence of atypical grain growth. The porous network was observed in micrograph B. The majority of crystallites were observed in a later stage of necking; well developed necked connections have formed. The growth of large grains was evident in the lowest magnification micrograph. These large grains exhibited crystal faceting in micrograph C, which is generally observed with low temperature sintering in the absence of a liquid phase.[143-44] The lack of this type of diffusion path, the dissolution and reprecipitation through a wetting liquid, produces a faceted surface as opposed to a decrease in a radius of curvature of grains that arises from the driving force of liquid driven sintering as given by the Kelvin equation.[70]

The highly irregular morphology observed with the initial nanopowder was no longer evident. The grain formations were nearly spherical without appreciable growth with exception of the atypical grains. Sintering had provided the thermal energy necessary for crystallite reorientation and in the process necking with adjacent grains.

The fracture surfaces of the compact formed from the 473K calcined sample of Nanopowder B (see Figure 7.19) illustrated an interconnected network of porosity and rare evidence of atypical grain growth. The surface of the compact in micrograph A was coarse and frangible and failed to polish. The fracture surfaces in micrographs B and C indicated the interconnected network of porosity observed with Nanopowder A. The large atypical faceted grains observed in micrographs C and D were a rarity. No other atypical grains were observed during the examination of the compact.

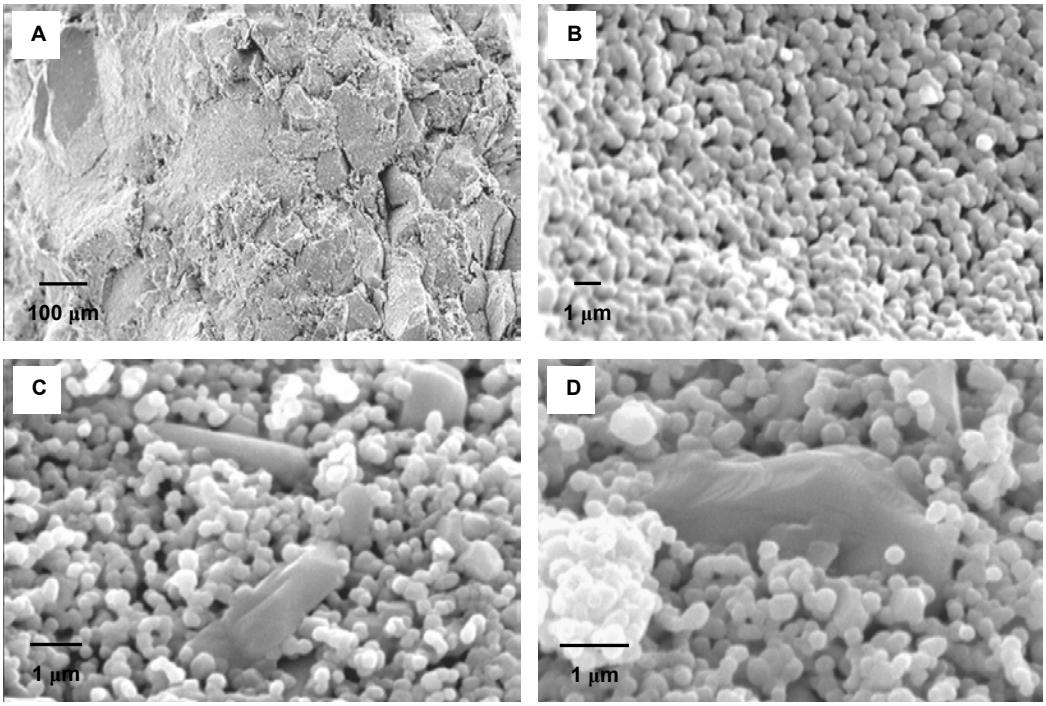

Figure 7.18. SEM SE mode micrographs of a sintered compact of 473K calcined Nanopowder A at 100X (A), 6,700X (B), 12,000X (C), and 16,000X (D).

As with the previous solid state nanopowder the irregular morphology of the starting nanopowder was absent. An interconnected spheroidal morphology existed. This compact does not appear to have the same degree of necking as that of the previous compact.

The compact produced from the 473K calcine of Nanopowder C fractured during the attempt at polishing the surface (in Figure 7.20, micrograph A). Upon closer examination of the fracture interior in micrograph B the presence of an atypical grain was observed. The stresses surrounding this large grain was the probable cause for the failure of the compact during polishing and one reason for attempts at avoiding this type of growth in commercial applications.

Looking at the image in micrograph C, it appears that the development of large grains had initiated. The large developing grain is 100 μm in size and would be considered an atypical growth. Numerous clusters of this type were observed in development. Closer examination of this type of developing structure showed that it is comprised of a necked network of small grains.

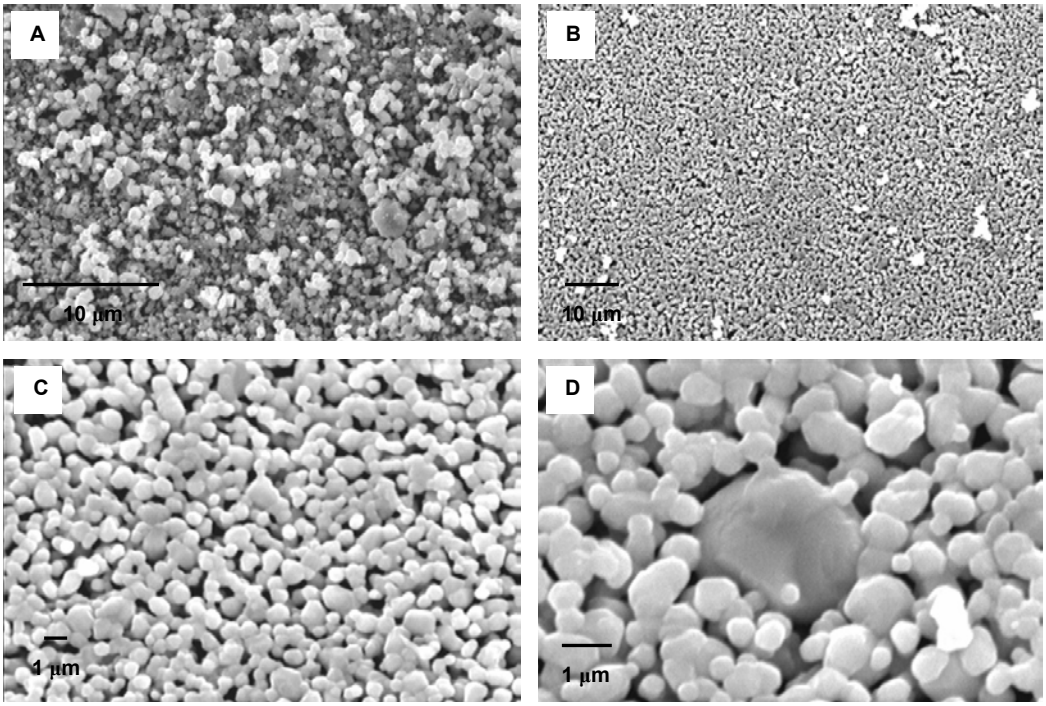

Figure 7.19. SEM SE mode micrographs of a sintered compact of 473K calcined Nanopowder B at 3000X (A), 1,200X (B), 5,400X (C), and 11,500X (D).

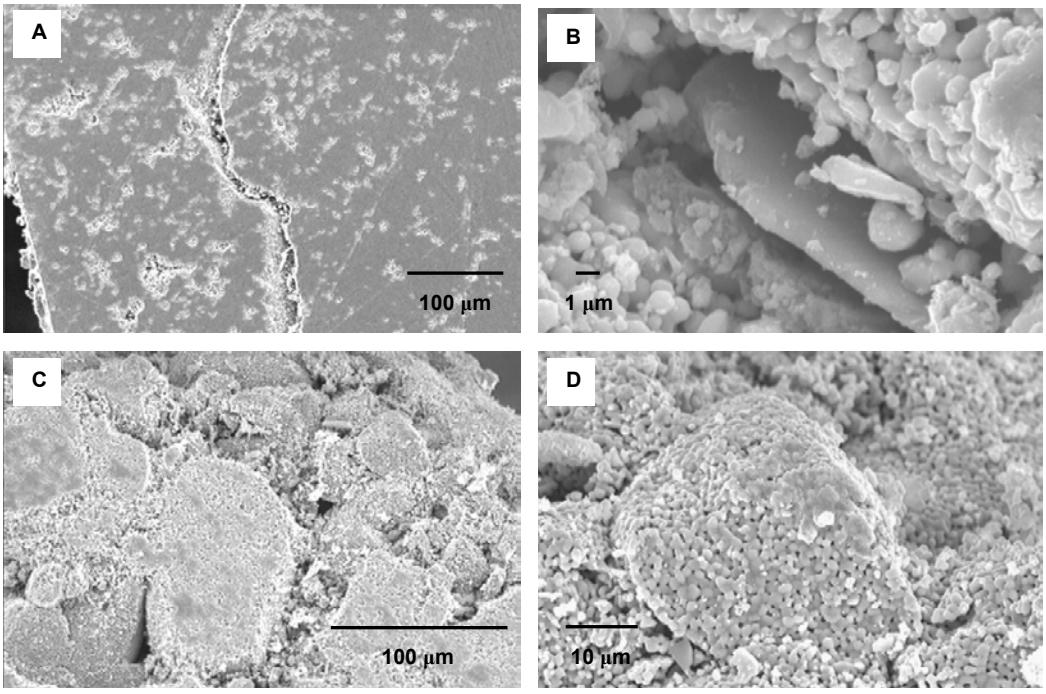

Figure 7.20. SEM SE mode micrographs of a sintered compact of 473K calcined Nanopowder C at 220X (A), 6,500X (B), 400X (C), and 1,600X (D).

There exists a possibility for entrapped porosity as this atypical grain continues developing. Additionally, large voids are forming in the boundaries between these large developing grains; several are observable in micrograph C. Pores located at grain edges are slowly removed through the diffusion process. They may, however, aid in transport through a process of shearing the grain edges as stress builds aiding the driving force to decrease the grain surface energy.[145]

The surface of the compact formed from the 473K calcine of Nanopowder D (see Figure 7.21, micrograph A) appeared smooth under low magnification. The higher magnification in micrograph B indicates a porous surface of interconnected small grains. As with the previous compacts there existed a large degree of porosity. In the micrographs of the fracture edges (C, D and E) large developing atypical grains are observable. Many well exceed 100 μm in size. These were the majority constituent of the structure of the compact. Examination of the surface of one of these large grain developments, small grains are networked together and have begun grain growth in micrograph F. This growth was not observed with the previous compact. The large voids observed in the previous compact are also absent here.

The fracture edges of the compact formed from the 473K calcined Nanopowder E (see Figure 7.22) illustrate microporosity within the necked network of the small developing grains. The surface was coarse and gritty; no polishing was attempted since particulate was easily removed under a gentle finger rub.

Grain growth was evident considering the initial size of this nanopowder was 70 nm. No atypical growth was observed with this compact. The grain growth appeared uniform in its development. Large voids were not observed and with the uniform development of the grain growth, it would not be expected to occur. The necking network was not as extensive as with previous compacts. A large volume of porosity was suspected with regard to the surfaces in the micrographs. These two items may explain the coarse fragile nature of the compact surface.

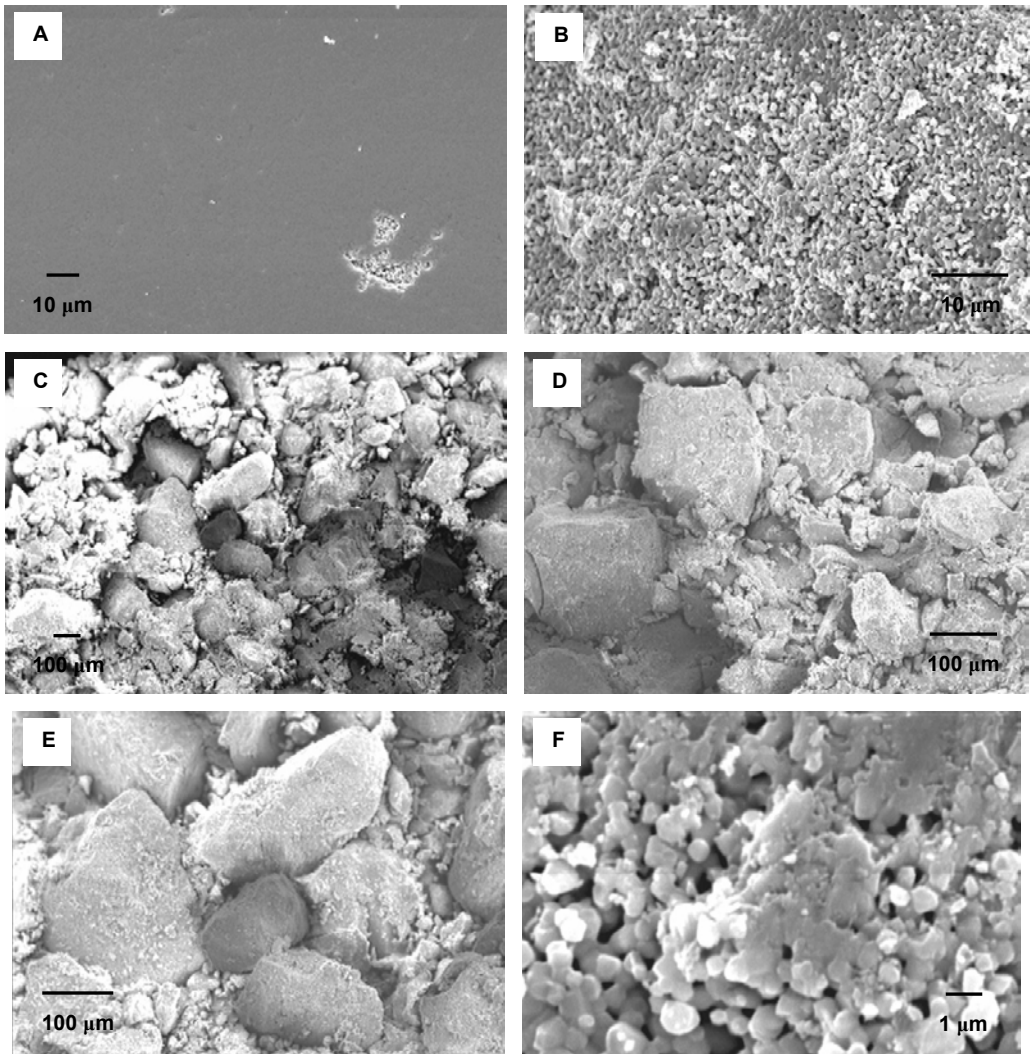

Figure 7.21. SEM SE mode micrographs of a sintered compact of 473K calcined Nanopowder D at 700X (A), 1,800X (B), 65X (C), 150X (D), 160X (E), and 8,500X (F).

The final compact examined of the 473K calcined nanopowders (see Figure 7.23) was of Nanopowder F. The development of large spherical grains that was observed with the "as-received" compact was not present here. The largest observed sphere approached 40 μm. The sizes of observable spherical shapes had a more uniform distribution of sizes. The spherical morphology, however, produced regions of pore coalescence forming large voids, evident here in micrographs C and D. The appearance of the spherical morphology was a result of sintered agglomerates present in the calcined nanopowder. These

sintered agglomerates along with pore coalescence were observed by others during the sintering of high purity barium titanate.[146]

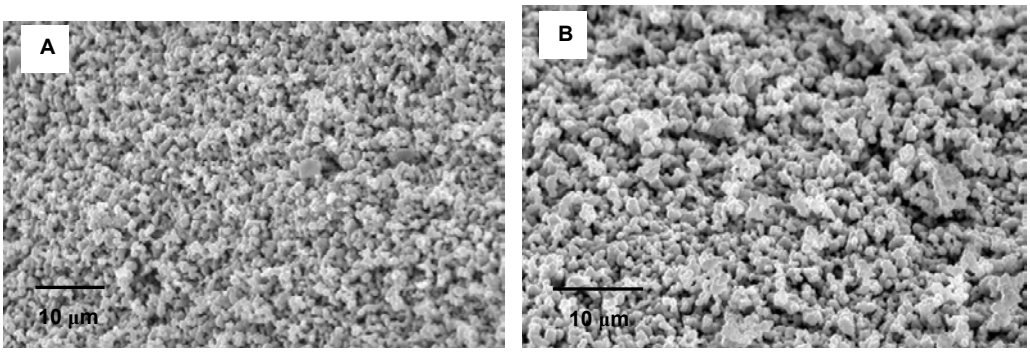

Figure 7.22. SEM SE mode micrographs of a sintered compact of 473K calcined Nanopowder E at 1,600X (A) and 2,000X (B).

The developing spherical structures were comprised of small faceted grains in micrographs C and D. The size of the grains was large compared to the 40 nm size of the initial starting nanopowder. Growth, therefore, was rapid with the smallest of the nanopowders indicating a large reduction of surface energy and a high reactivity. The grain boundary separating two of these small grains was observable in micrograph E. Numerous smaller crystallites were situated along this boundary and, with additional time at sintering temperature, would most likely be absorbed by one of the adjoining grains.

The growth of one of the small grains through a series of built up steps was observed in the last micrograph. The contours of each step were readily seen. The SEM lacks the necessary resolution to determine the relative dimensions of these steps. The steps appear to be of somewhat uniform thickness. Interestingly, after close examination of micrograph E several screw dislocations among the developing steps may be located. These dislocations are observed in regions where steps end prematurely in the side of another step.

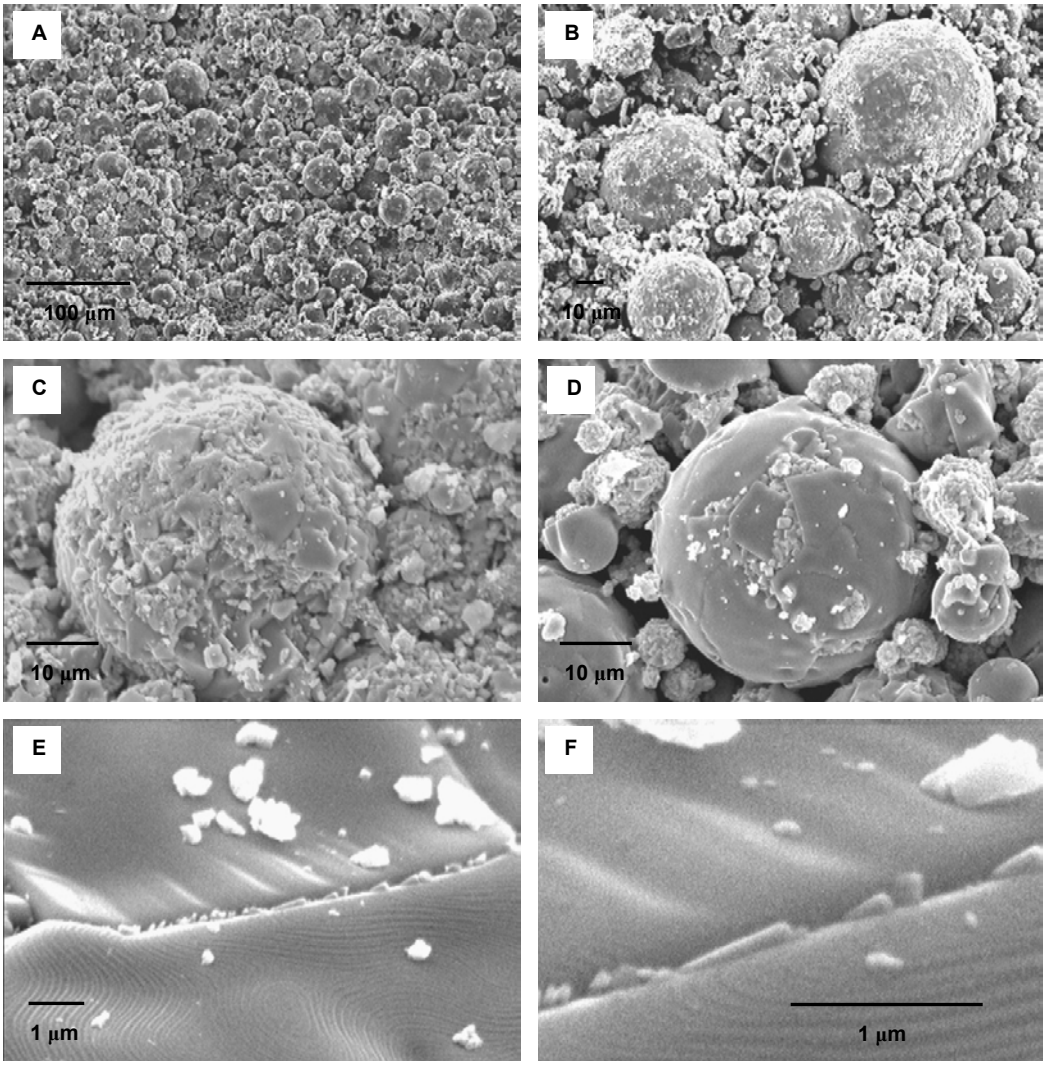

Figure 7.23. SEM SE mode micrographs of a sintered compact of 473K calcined Nanopowder F at 240X (A), 560X (B), 1,700X (C), 1,700X (D), 13,600X (E), and 44,000X (F).

7.3.4 Sintered Compacts of 773K Calcined Nanopowders

Each nanopowder was calcined for one hour at 773K. Compacts were formed using 0.5 gram from the calcined powder, and subsequently sintered for one hour at the previously specified temperature. No etchant was used prior to scanning electron microscopy of the samples. Polishing was accomplished when the frangible nature of the compacts did not lead to disintegration of the surface. The fracture surfaces were of greater interest in studying the state of densification and the nature of structural development within the compacts after an intermediate stage of sintering.

The fracture surfaces of the compact formed from the 773K calcined sample of Nanopowder A (see Figure 7.24) indicated slightly more grain size development as compared to the compacts produced from the 473K calcine. The degree of interconnected necking was less possibly due to the slight increase in grain growth. The increase in density between the 473K and 773K calcine samples was likely due to this grain growth.

The degree of porosity appeared to be unchanged as compared to the compact produced from the 473K calcine. Comparing the similar magnification images in Figure 7.18, micrograph B and Figure 7.24, micrograph C, the size of the pores observed with this compact was larger. This may be due to the different average size of the grains; the spacing between the larger grains being slightly bigger than that observed with smaller grains. The structural morphology of both compacts was similar.

The large difference was in the number of located atypical grains. Atypical grains were prevalent in the 473K calcined compact. Atypical grains, however, were rarely observed in the 773K calcined compact (see micrograph A).

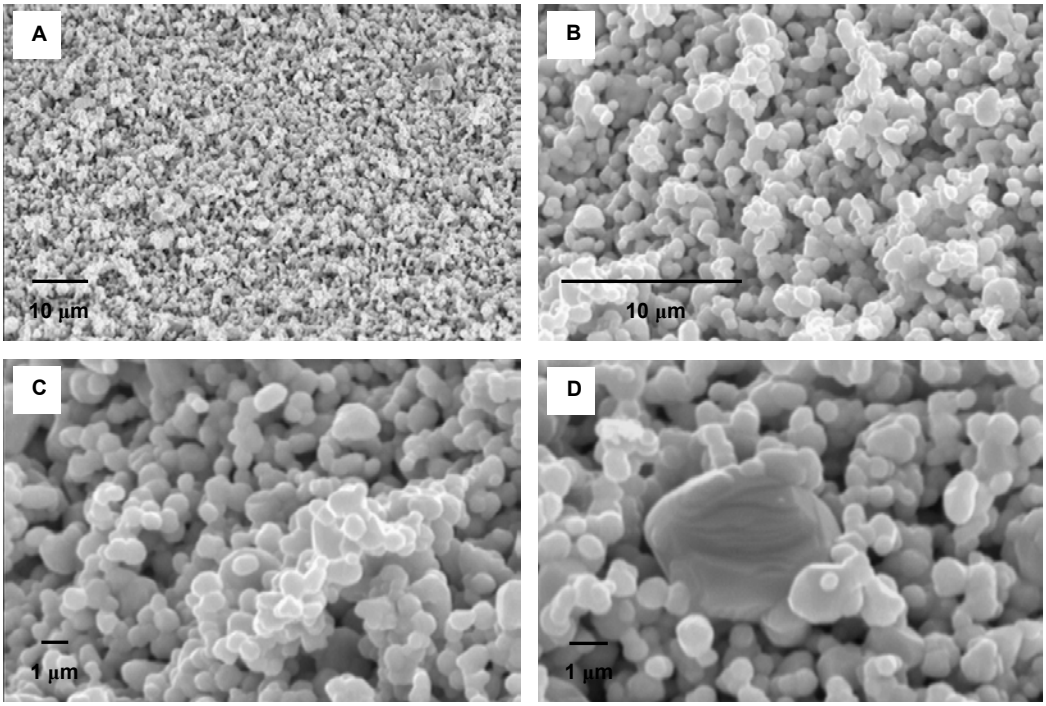

Figure 7.24. SEM SE mode micrographs of a sintered compact of 773K calcined Nanopowder A at 1200X (A), 4,000X (B), 6,400X (C), and 8,000X (D).

The fracture surfaces of the compact formed from the 773K calcined sample of Nanopowder B (see Figure 7.25) exhibited far less porosity than that observed with the 473K calcined compact (see Figure 7.19). A higher degree of connectivity between the particles was noted. The individual crystal size had not changed much, approximately one micron in size. The greater interconnected structure had led to an increase in density over that observed with the 473K calcined compact. No atypical grain growth was observed during SEM examination. The particle sizes observed were uniform throughout the compact.

The density values of Nanopowder C were the highest of any compact type. The difference between the 473K and 773K calcine produced compacts was slight, 4.91 g/cm^3 versus 4.97 g/cm^3. This difference may be from the lack of large developing grains and their associated large pores as observed in the 473K compact. The uniform structural development of the 773K calcine produced a compact yielding a slightly denser body.

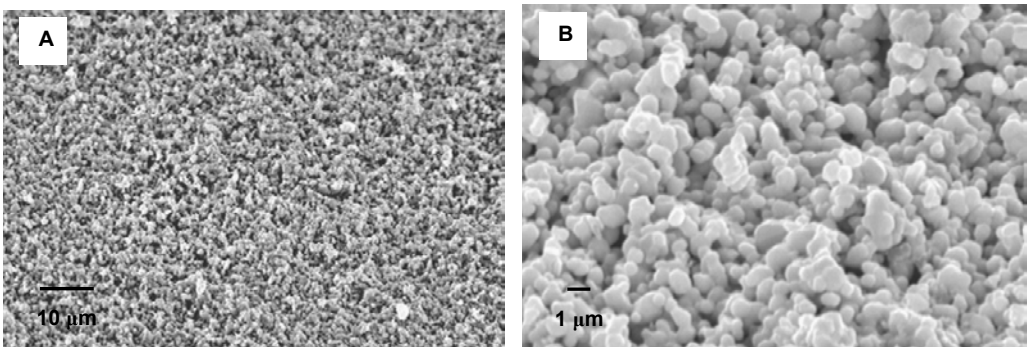

Figure 7.25. SEM SE mode micrographs of a sintered compact of 773K calcined Nanopowder B at 1200X (A) and 5,500X (B).

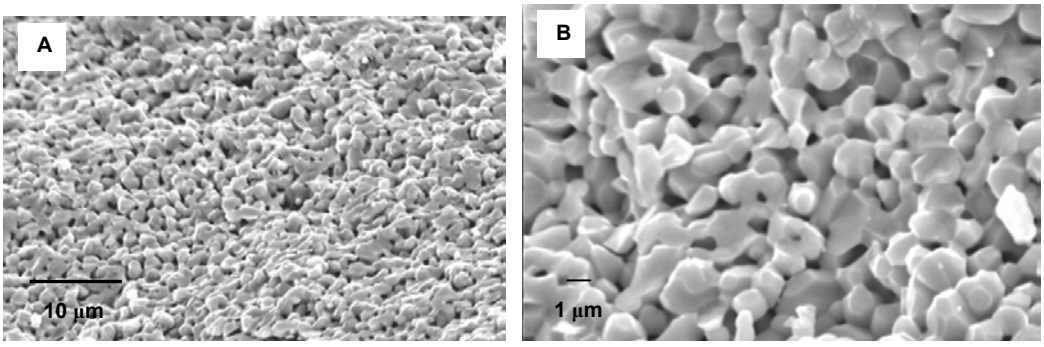

Figure 7.26. SEM SE mode micrographs of a sintered compact of 773K calcined Nanopowder C at 2000X (A) and 5,000X (B).

Nanopowder D (see Figure 7.27) exhibited no change from the observances of the 473K calcined produced compact. The development of large atypical grains was again evident. During the nanopowder SEM analysis, in section 2.4 (see Figure 2.30), it was established that this nanopowder was not highly agglomerated. A well developed interconnected network was observed here and with the 473K prepared compact. The large atypical growths may be regions where the interconnected porosity collapsed first; grains would grow more rapidly in these regions giving rise to the atypical formations observed.

The compacts formed of Nanopowder E after the 473K and 773K calcine had the same density. Their structures, however, were very different. No atypical growth was observed with the 473K calcine compact. The results here

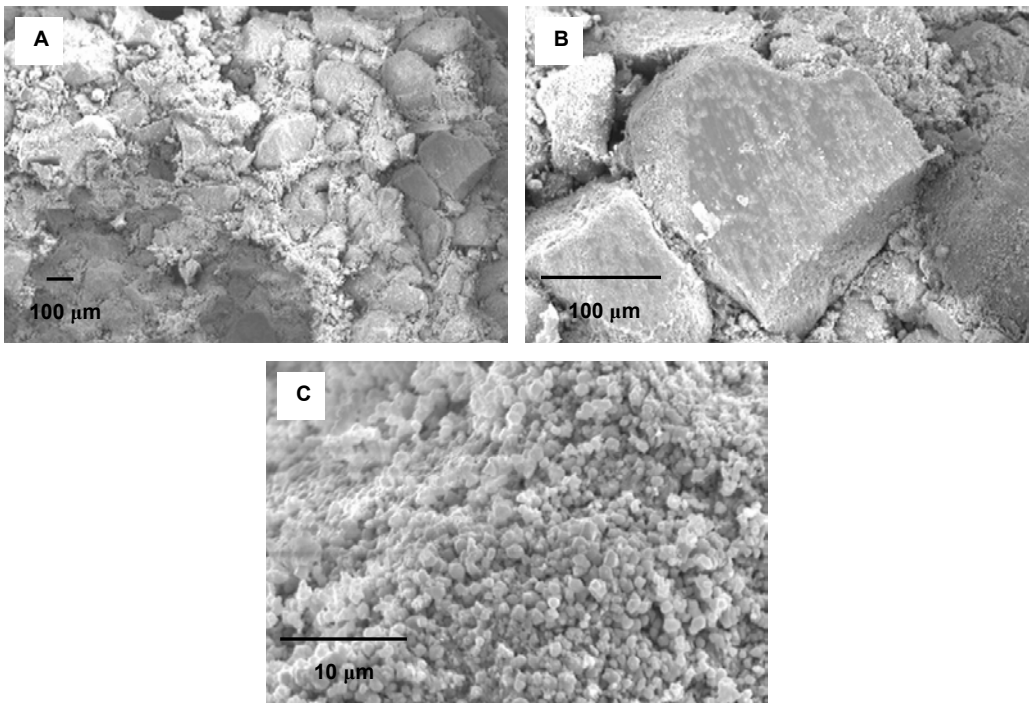

Figure 7.27. SEM SE mode micrographs of a sintered compact of 773K calcined Nanopowder D at 85X (A), 275X (B), and 3,000X (C).

(see Figure 7.28) exhibited a large degree of atypical growth, both elongated and equiaxed abnormal grains. Micrographs D and E are higher magnification images of surface areas of large atypical growths. The elongated bar shape development was similar to that observed by others.[143,147] This type of elongated growth behavior was indicative of a Ti-excess nanopowder. However, the temperature used in this study was below that required to achieve a liquid phase. The previously mentioned high moisture content of the samples, static air during sintering, and the high reactive surface area of the small crystallites may account for the growths observed. Lee and Chun observed that faceting was one of the necessary conditions for elongated atypical growth with barium titanate. This type of atypical growth was also observed by Schmelz; sintering at 1573K produced (111) twin faceted crystallites of a few hundred microns.[148]

Agglomerates were observed with this nanopowder in section 2.4 (see Figure 2.31) which was the most probable cause of the large developing

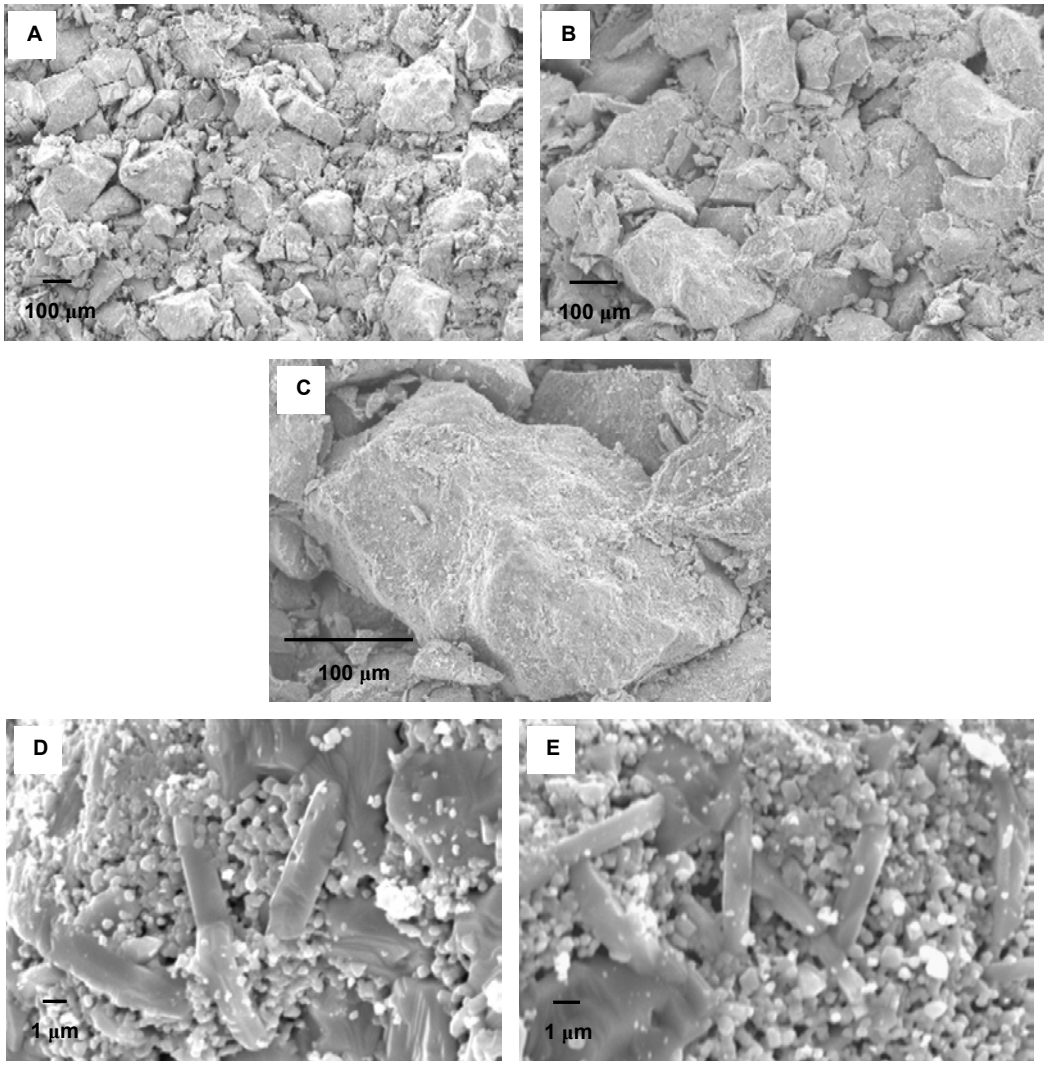

Figure 7.28. SEM SE mode micrographs of a sintered compact of 773K calcined Nanopowder E at 70X (A), 110X (B), 300X (C), 5,300X (D), and 6,000X (E).

equiaxed grains observed here. These agglomerates may be regions where the collapse of interconnected porosity began the quickest thereby initiating the atypical growth.

The compact formed from the 773K calcined Nanopowder F (see Figure 7.29) exhibited the spherical grain development observed previously. The largest of the spheres was similar to that observed with the 473K compact. The grain growth within the spheres, however, was greater; ten micron grains were

observed. The higher temperature calcine had aided in grain growth proving the crystallites of this nanopowder had highly reactive surfaces.

The decrease in density observed with increasing calcine temperature was a result of the development of the large sphere morphology and its accompanying large volume pores. The more difficult removal of internal porosity, formed as large spheres absorb smaller spheres, as observed in Figure 6.22, also hinders densification.

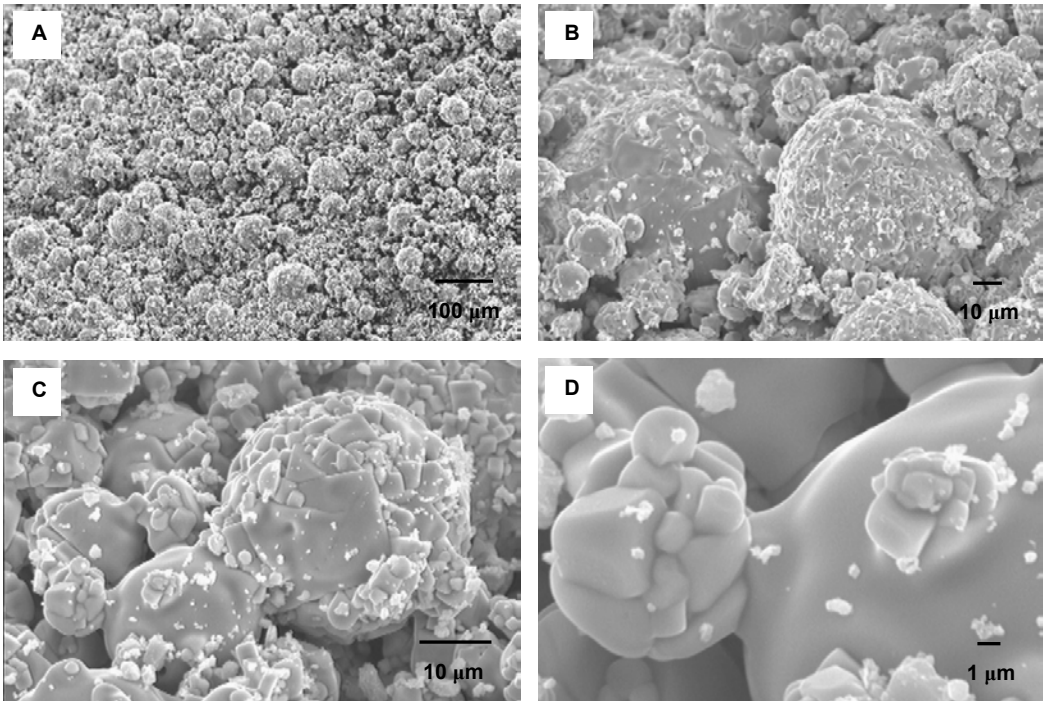

Figure 7.29. SEM SE mode micrographs of a sintered compact of 773K calcined Nanopowder F at 130X (A), 650X (B), 1,600X (C), and 5,300X (D).

7.3.5 Sintered Compacts of 1173K Calcined Nanopowders

Each nanopowder was calcined for one hour at 1173K. Compacts were formed using 0.5 gram from the calcined powder, and subsequently sintered for one hour at the previously specified temperature. No etchant was used prior to scanning electron microscopy of the samples. Polishing was accomplished when the frangible nature of the compacts did not lead to disintegration of the surface. The fracture surfaces were of greater interest in studying the state of densification and the nature of structural development within the compacts after an intermediate stage of sintering.

The compact produced from the high temperature calcine of nanopowder A (see Figure 7.30) exhibited a similar structural network as observed with the previous calcine produced compacts. There was a slight decline in density of this group as compared with the previous Nanopowder A compact lots. Slight increase in grain growth was observed here with the attendant reduction in the

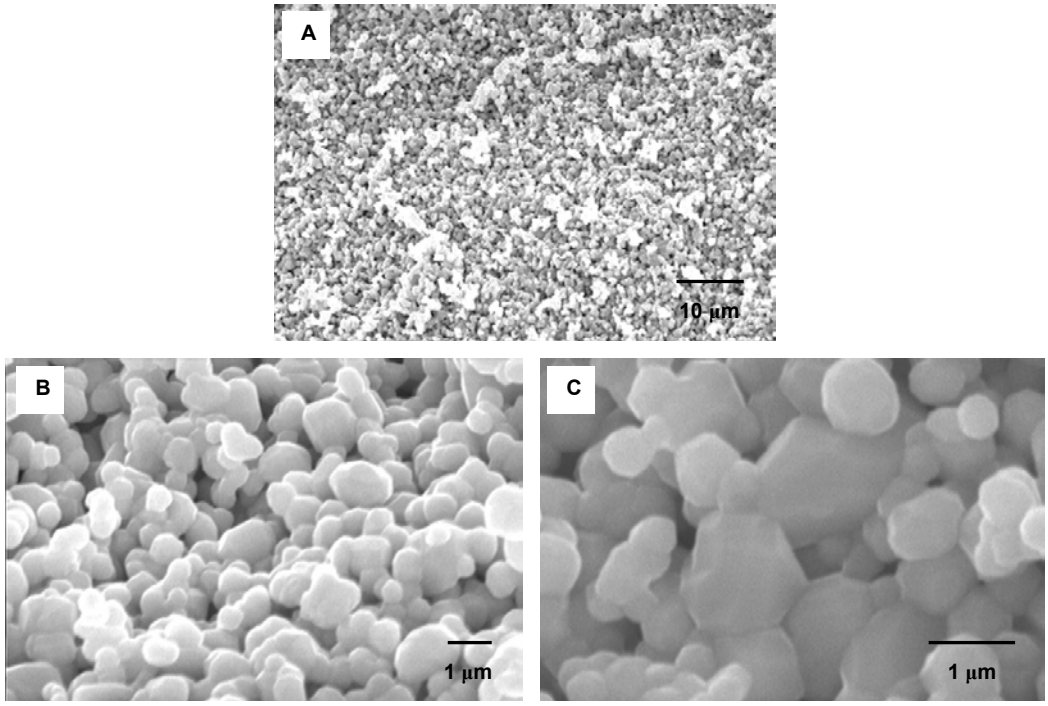

Figure 7.30. SEM SE mode micrographs of a sintered compact of 1173K calcined Nanopowder A at 1,500X (A), 10,000X (B), and 20,000X (C).

number of pores, however, these pores appeared larger. The larger pore volume was the reason for the lower density. No atypical grain growth was observed with this compact. Nearly uniform equiaxed growth typifies this sample.

The compacts formed from Nanopowder B were the only set of compacts that the calcination exhibited beneficial effects with improved densification. More grain growth and interconnectivity and the accompanying decrease in porosity typify this compact (see Figure 7.31). Atypical growth was absent with all types of compacts formed of this nanopowder. An interconnected network was observed with all compact types exhibiting increasing degrees of grain growth and connectivity from “as-received” through this, the 1173K calcine prepared compact. A slow but continued reduction in porosity was the most likely reason for the improvement in density.

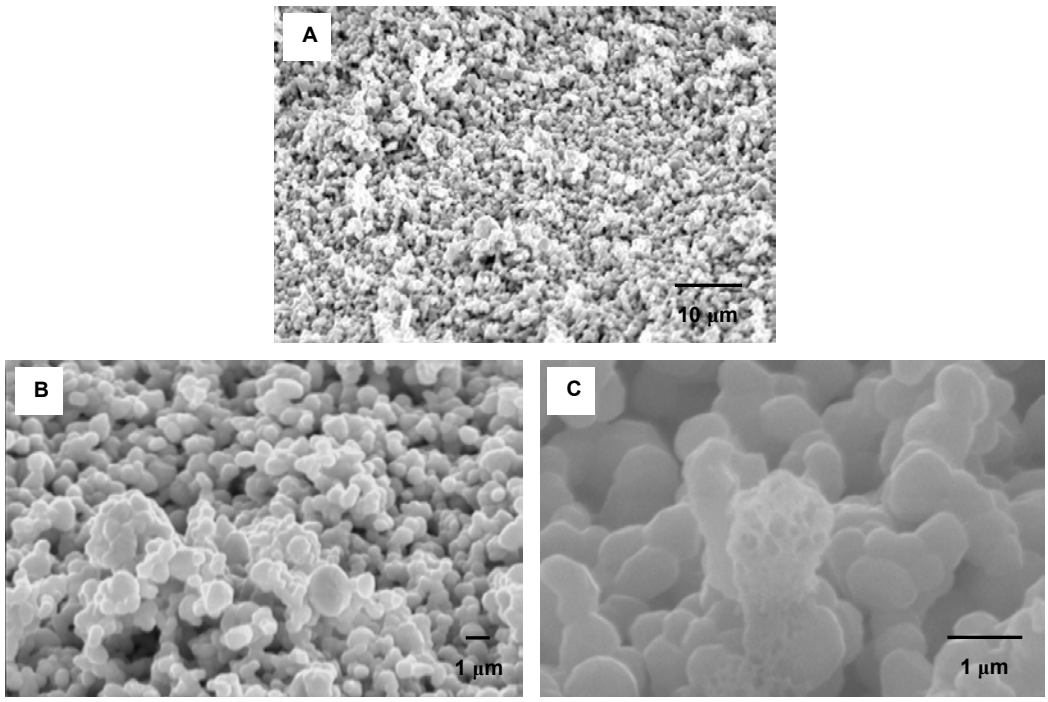

Figure 7.31. SEM SE mode micrographs of a sintered compact of 1173K calcined Nanopowder B at 1,500X (A), 5,300X (B), and 17,000X (C).

The sintering of the 1173K calcine produced compact of Nanopowder C (see Figure 7.32) formed the densest body of all of the 1173K calcined nanopowders. The density, 74.1% D_{th}, was not the greatest achieved during the intermediate sintering study. The well connected structure of this compact, micrograph B and C, contained little visible porosity and this correlated with the density calculated.

Necking was readily evident within the calcined nanopowder as imaged in the SEM prior to pressing compacts (see Figure 6.18). The spherical nature of this nanopowder was no longer observed due to the vast amount of growth that occurred through necking of the crystallites. An irregular shape was the common morphology of the crystallites. This growth and necking during calcination was the prelude to the result observed here with the sintered compact; low porosity, moderate growth and the full interconnected structure.

There were no changes due to the 1173K calcine and subsequent compact sintering of Nanopowder D (see Figure 7.33) as compared to the

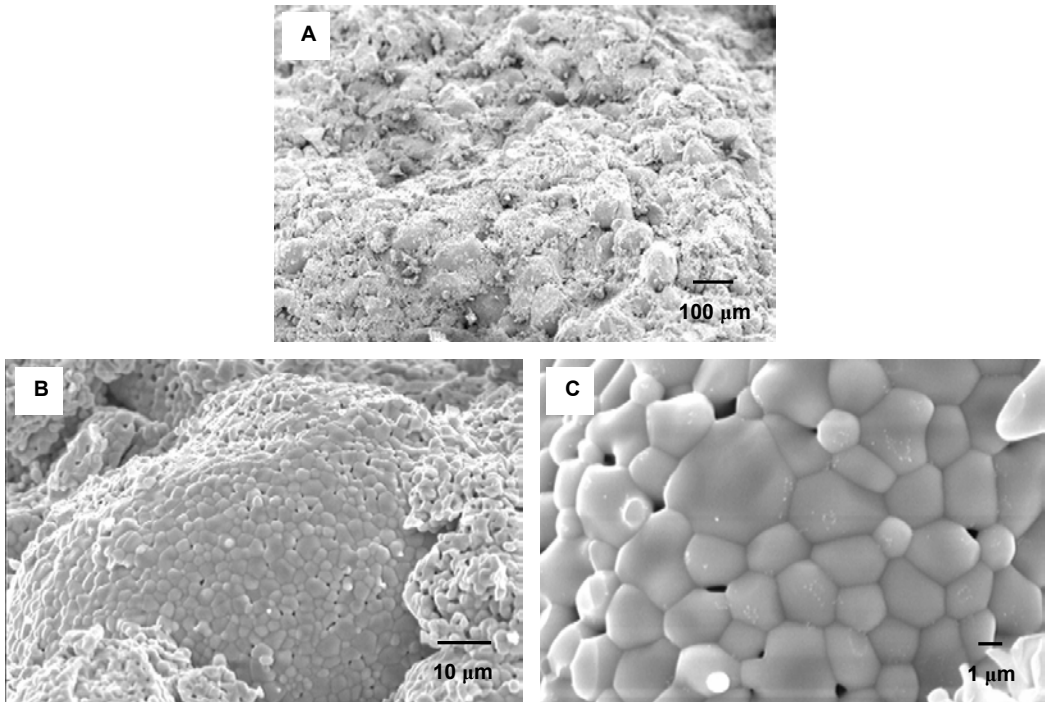

Figure 7.32. SEM SE mode micrographs of a sintered compact of 1173K calcined Nanopowder C at 100X (A), 1,200X (B), and 5,500X (C).

previous compacts. The development of large atypical grains was again evident. Additionally, large faceted grains were evident in micrographs C and D. Both an irregular collapse of local porous networks and the atypical growth of faceted grains produced large singular pores, micrograph D, that resulted in a low density compact. It is likely that the growth and shrinkage of the compacts containing faceted grains was largely by the attachment to ledges and kinks along faceted surfaces and limited not by diffusion rates but by the rate at which nucleation occurred along these faceted surfaces.[149]

Elongated atypical grains typified the compact formed of 1173K calcined Nanopowder E (see Figure 7.34). These grains were more prominent and bigger for this higher calcine temperature produced compact. These findings were similar to the 773K calcine temperature produced compact studied. This compact resulted in an average calculated density of 64.1% D_{th}, the least dense compact of those formed from the 1173K calcinations.

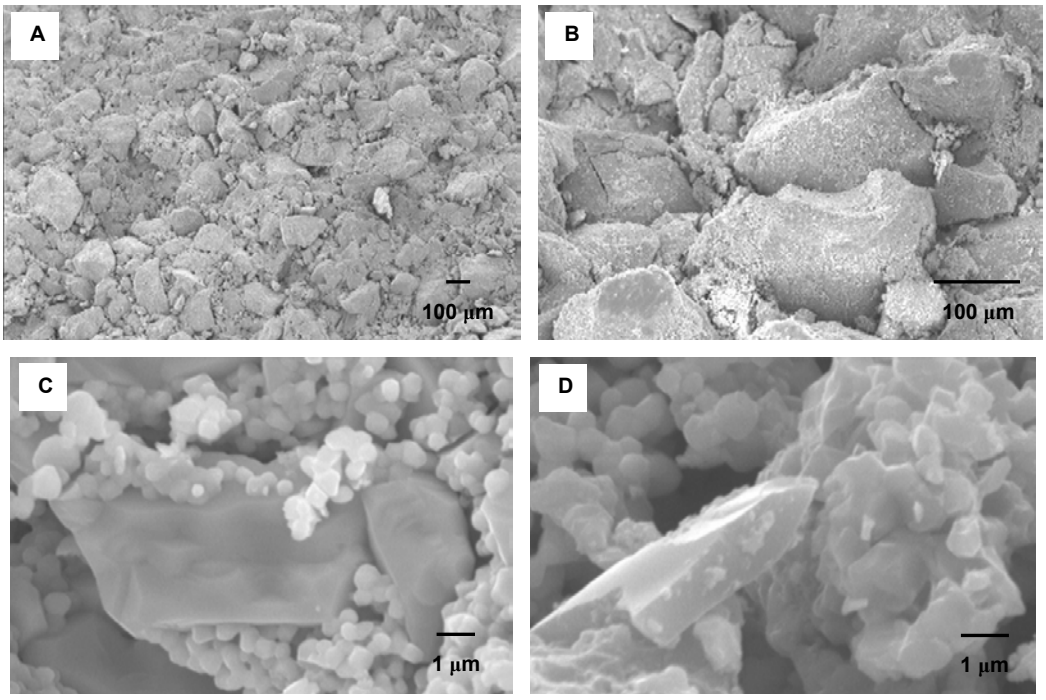

Figure 7.33. SEM SE mode micrographs of a sintered compact of 1173K calcined Nanopowder D at 50X (A), 200X (B), 7,800X (C), and 11,000X (D).

The final nanopowder examined of the 1173K calcinations, Nanopowder F, continued to exhibit the spherical agglomerated grain morphology (see Figure 7.35). Sphere size was larger than with the 773K study; spheres with a 20 – 30 micron diameter observable. Individual spheres were comprised of grains approaching 10 microns in size, micrographs B and C. The sphere in micrograph C was a nearly formed single grain with a few small grains still evident on the surface. Grain growth within the spheres was rapid; nearly 10 micron sized grains grown from the 40 nm initial crystallite size in one hour at a temperature well below eutectic.

A comparison of calculated density between the 773K calcine produced compacts and the compacts of the 1173K study demonstrated that the higher calcine temperature aided in producing a denser body. The micrographs here compared with those of Figure 7.29 of the 773K calcine study, show greater grain growth with less porosity. The growth of the individual grains within the spherical agglomerates was the likely cause for the increased densification and the slight increase in measured density.

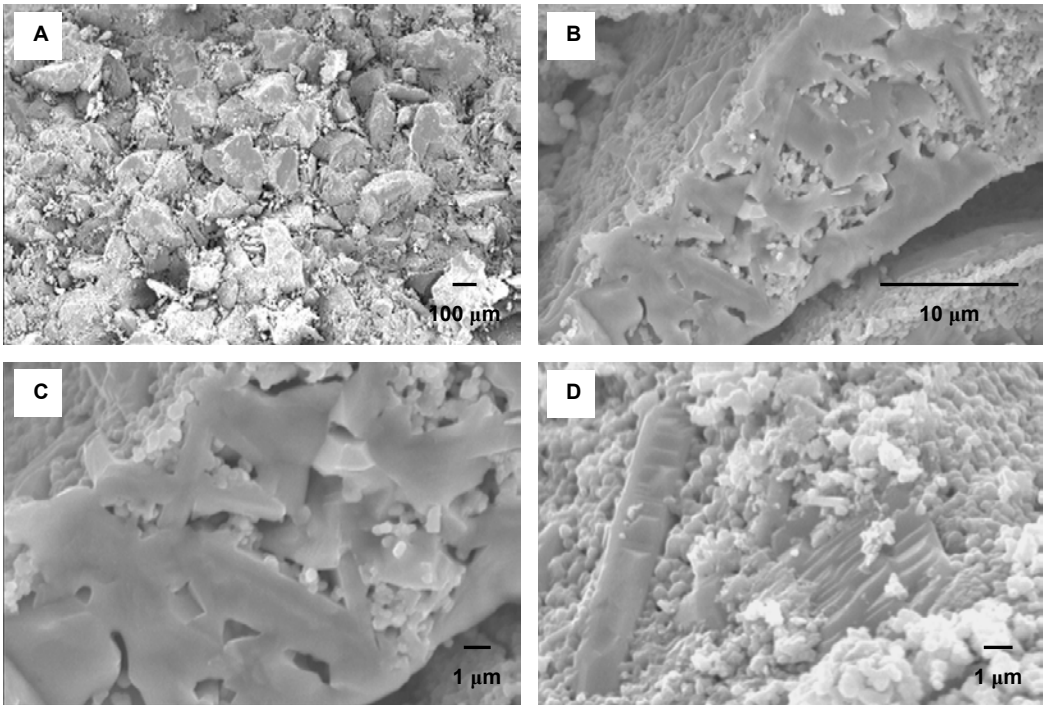

Figure 7.34. SEM SE mode micrographs of a sintered compact of 1173K calcined Nanopowder E at 100X (A), 3,000X (B), 6,000X (C), and 7,000X (D).

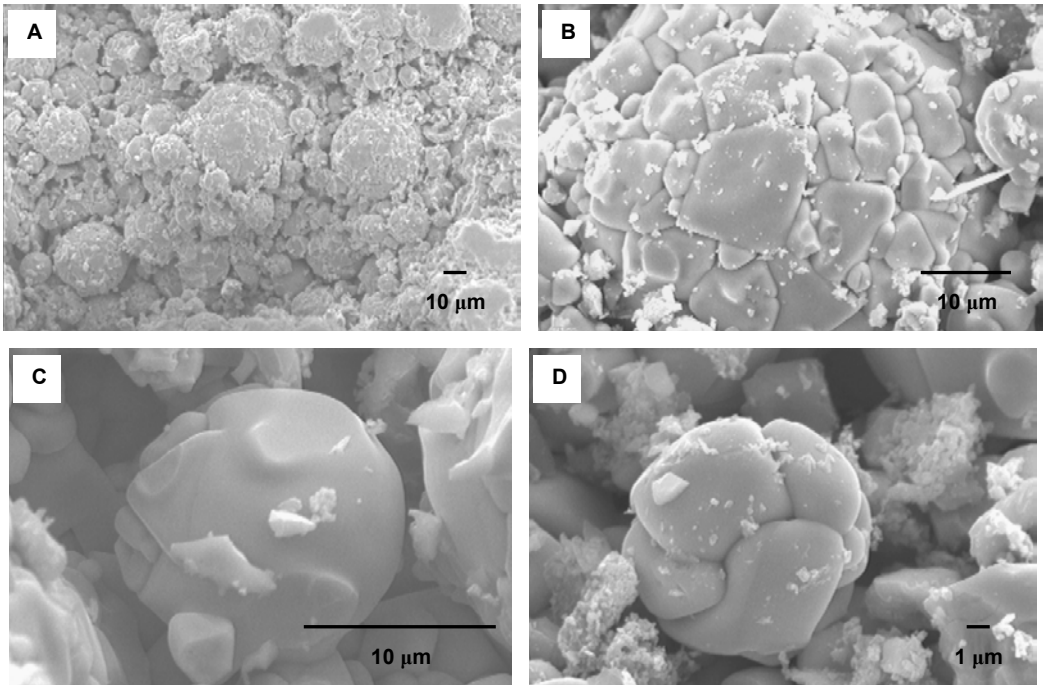

Figure 7.35. SEM SE mode micrographs of a sintered compact of 1173K calcined Nanopowder F at 500X (A), 2,000X (B), 4,400X (C), and 5,000X (D).

7.4 Summary

The results of the calcining, and subsequent pressing of compacts, without dispersants, and intermediate stage sintering were reported. The varied calcinations of the nanopowders produced sintered compacts with densities ranging from 58.8% to 86.7% of theoretical density. The compacts produced were of an interconnected porous structure. Although frangible compacts were the result for many of the nanopowders examined, a fully sintered compact might produce a solid structure of interconnected porous nature with a high surface to volume ratio; filters would be an end product of this type of production. The sintered compacts of the solid state nanopowders could be best described in this manner.

Incorporating the reduction of carbonate during the calcination of the nanopowders prior to compaction and sintering, results generally support lower carbonate levels with increased density. Nanopowder F had the largest reduction of carbonate during calcining as observed during the vibrational spectroscopic analysis. This nanopowder, however, contained a large quantity of spherical agglomerates that resisted fracture during pressing of the compacts. These agglomerates did sinter quite well with larger equiaxed grain growth than the other nanopowders. This grain growth, however, was observed to occur mostly within the spherical agglomerates. The result was large volume remnant pores at sphere junctions that reduced density throughout the sintering study.

An increase in both grain size and pore size was observed. Carbone and Reed observed similar results with $BaTiO_3$ sintering at 1488K.[150] This was the result of the agglomerated crystallites which sintered rapidly producing an agglomeration of the microporosity initially present. Neck growth between crystallites within the agglomerates was observed. Additionally, the densification of the agglomerates and their subsequent bridging produced the larger pores observed. As a result, there existed a range of porosity sizes present in the compacts.

The reduction in compact density correlated with the increasing calcine temperature of Nanopowder C. This finding was contrary to all of the other

nanopowders. The “as-received” samples produced the densest compacts while the highest temperature calcine produced the least dense compact. The 1173K calcination of Nanopowder C produced large irregularly shaped clusters. This and the additional grain growth during sintering were offset by the presence of large porosity as well as microporosity between the smaller interconnected grains yielding compacts of lower density.

Nanopowder D, after calcining for one hour at 1173K, exhibited equiaxed atypical growth of the crystallites unlike the other nanopowders. Upon sintering the large developing grains had an associated large interspaced porosity. The consequence of this atypical growth was a lack of densification with any of the compacts of Nanopowder D origin.

Faceted atypical growth of idiomorphic grains was observed with compacts produced with Nanopowder E. It was likely that the growth and subsequent shrinkage of the compacts containing faceted grains was largely by the attachment to ledges and kinks along the faceted surfaces and limited not by diffusion rates but by the rate at which nucleation occurred along these faceted surfaces. These straight edged boundaries are of lower surface energy. The driving force for growth was the lower surface energy of the larger grains compared to the higher energy of the small radius curved grains. Atypical idiomorphic grain growth developed at the expense of uniform densification of these compacts.

Nanopowder F was a case unto itself. It was the smallest average crystallite sized nanopowder having an accompanying large free surface energy. Spherical agglomerates were observed during all stages of calcination and subsequent sintering. These spheres were a result of free surface energy reduction. As was predicted, these large solid agglomerates resisted fracture and breakdown during the compaction of compacts. Sintering occurred through the densification of these spherical agglomerates. Large spheres necked and nearly fully absorbed smaller spheres. This process indicates one source of internal porosity in a solid. As one developing region absorbs another the boundary between them incorporates a quantity of vacancies, or porosity. These

vacancies must diffuse through the developing solid to the surface where they are annihilated.

At the intermediate stage of sintering studied herein, this process had resulted in highly porous structures and reduced density of the compacts. The pore space in the densifying compacts was located at grain boundaries, was interconnected and represented a large fraction of the grain diameter size. As the calcine temperature increased, larger grains developed within the spherical agglomerates upon sintering. Sphere densification developed rapidly from the initial 40 nm crystallites, 10 micron sized grains formed. The ensuing development of large pores accompanied the large spheres, thus hindering densification.

The presence of agglomerates acted as seeds for the secondary recrystallization, or atypical growth, observed with many of the nanopowder compacts. As initial particle size increases the incidence of larger than average particles decreases and consequently greater difficulty in the nucleation of secondary recrystallization. However, with many of the nanopowders examined, the agglomerates were larger than the average crystallite size, hence the development of atypical growth.

Previous analysis had indicated that the relative growth rates of large and small grains were not sufficiently different to cause a broadening of the size distribution if mobility of all interfaces were the same.[151-152] One concludes, therefore, that other causes of local variations in growth rate exist; nonuniformity of impurity content, presence of liquid phases, or porosity need be raised to explain the atypical growths observed. The inhomogeneous packing of the nanopowders could lead to variations in the densification observed with denser packed regions subsequently exhibiting more rapid grain growth through less pore pinning of the interfaces.

Anisotropies in interfacial energy and mobility may also cause atypical growth. The interfaces of the large atypical grains exhibited preferential faceting. The flat faces of these atypical growths suggest a crystallographic orientation of lower energy and thus preferential nucleation sites for continued growth.

8. Conclusions

The “as-received” nanopowders were examined by means of x-ray diffraction. All nanopowders exhibited a crystalline structure; no amorphous attributes were displayed in the diffraction patterns. A tetragonal structure was confirmed through the diffraction patterns for Nanopowders A and B. The balance of the nanopowders showed evidence of having the anomalous room temperature cubic phase.

The data corroborate previous literature in answering the question: Is there a critical size below which the cubic phase is stable at room temperature? The tetragonal Nanopowders A and B were the largest in this study, being in excess of any of the previously published critical particle sizes for anomalous room temperature cubic phase. However, these two powders were synthesized through the solid state method. The other nanopowders, C through F, exhibited the anomalous room temperature cubic structure and are also in agreement with the literature since all were below the largest critical particle size reported, 190 nm. This critical size though may be coupled to synthesis methods that incorporate water in their processes. The water content, from the synthesis process, may be distorting the lattice causing residual strain in the crystallites.

The data also corroborates previous literature in answering the question: Can stabilization of the anomalous room temperature cubic phase occur through the ubiquitous incorporation of hydroxyl groups in hydrothermally derived barium titanate? Each of the nanopowders that exhibited the anomalous room temperature cubic phase contained incorporated water as a result of the synthesis process. The TGA traces showed evidence of the removal of this water from each of the Nanopowders C through F.

The data supports an answer to the question: Are the nanocrystals a true cubic phase as they appear to be according to XRD or are the hydrothermally synthesized nanopowders pseudo-cubic structures as referred to in the literature? The data substantiated the hypothesis that the cause of the room temperature cubic phase was a hydroxyl strain stabilized pseudocubic structure.

SEM examination of each of the “as-received” nanopowders was accomplished. A general estimate of particle size and distribution was made for all but the smallest nanopowders, E and F. The largest degree of agglomeration was observed with Nanopowders E and F. Unusual spherical agglomerates were observed in the micrographs of Nanopowder F. It was suggested that this spherical agglomerate form was achieved through attractive interactions due to van der Waals forces in an attempt of the crystallites to reduce large individual free surface energy through sphere formation.

The TEM study of the “as-received” nanopowders confirmed the particle size of the nanopowders as calculated from the BET analysis with the exception of Nanopowder F. The crystallite size as observed by TEM was 40-45 nm as opposed to the BET calculated value of 67 nm. This size difference was associated with porosity trapped within the spherical agglomerates. Approximately one-third of the surface area of the particles was encapsulated within the agglomerates during the BET analysis. The agglomerates, therefore, could be considered as large individual crystals during the BET analysis.

In the darkfield imaging residual strain was observed with the hydrothermal nanopowders. The solid state nanopowders exhibited no contrast variation that would present evidence for residual strain. The strain was proposed to be a result of defects in the nanopowders formed during their synthesis, primarily in the form of lattice hydroxyls. The nanocrystals were so small that structural defects prevent the completion of the room temperature tetragonal phase, which led to high strains within the crystallites. The internal strain then was due to the tetragonal to cubic deformation observed with XRD and TEM electron diffraction and apparently resulted from the incorporated hydroxyl defect.

TEM diffraction patterns of the “as-received” nanopowders were indexed and confirmed the tetragonal phase for the solid state synthesized nanopowders. The cubic phase was confirmed for the hydrothermally synthesized nanopowders, and was in agreement with the XRD analysis.

The exposure of the nanopowder surfaces to ambient atmosphere caused a hydrolysis reaction with the humidity. Hydroxyl groups are formed which in turn form hydrogen bonds with surrounding molecular water yielding two adsorbed phases: liquid water and compressed vapor above.[153] The surface, therefore, became covered with several layers of hydrogen bonded water with the lattice gas phase directly above. The proton was then capable of migrating throughout the lattice by means of the Grotthuss mechanism thereby becoming an impurity charge carrier.

The removal of the molecular water, surface and lattice hydroxyls, and carbonates was investigated in the preliminary HT-DRIFT study. The presence of CO_2 evolution was first observed at 573K, 300 degrees lower than previously noted in the literature. The majority of the carbonate present in the nanopowders was removed after a half-hour at 1173K. The removal of the carbonate in addition to moisture during the heat treatment provided open sites for the readsorption of moisture during the cooling phase.

The readsorption of H_2O and OH groups was investigated in the H_2O study. All of the nanopowders exhibited evidence of readsorption of moisture upon cooling. The HT-FT-IR studies indicated that readsorption of lattice hydroxyl ions occurs with <6 ppm available moisture in the gas flow utilized in this study. The spectral evidence clearly showed the affinity of moisture for the readsorption onto the nanopowder surfaces. The solid state nanopowders, A and B, contained a higher concentration of moisture after heat treatment than was present initially. The vibrational wavenumber related to the bend deformation of H_2O at 1630 cm^{-1} dissipated by 873K with each of the nanopowders. This band was observed in the cooled spectra of each of the nanopowders signifying the readsorption of molecular moisture to the surfaces of the nanopowders.

It was interesting to note that, in observing the spectral region 3350 cm^{-1} to 3600 cm^{-1}, the distribution of OH groups in the lattice had changed significantly with Nanopowders C through F. A single OH related band was observed at ~3509 cm^{-1} in the room temperature spectra of nanopowders C through E. Upon

cooling after heat treatment three bands were observed at 3509 cm^{-1}, 3475 cm^{-1} and 3451 cm^{-1} in the final spectra of Nanopowders C through E. The three bands observed with the room temperature spectrum of Nanopowder F (3509 cm^{-1}, 3492 cm^{-1} and 3451 cm^{-1}) transformed to 3509 cm^{-1}, 3475 cm^{-1} and 3451 cm^{-1} upon cooling after heat treatment, the same bands as observed in the final spectrum of the other three nanopowders. These OH related bands were indicative of a cubic to tetragonal phase transition for nanopowders C through E as a result of the heat treatment and a redistribution of the OH groups to a tetragonal phase of Nanopowder F.

The lower 773K heat treatment resulted in four bands with each of Nanopowders C through F upon cooling. These results may be indicative of a local atomic displacement from cubic symmetry; distortion of the titanium atom away from the centrosymmetric position in the direction of a face of the oxygen octahedron. The observed four bands would be indicative of the resultant four bond lengths of the distorted cubic unit cell as described by Pirc and Blinc, but slightly off from the [111] direction. A Ti-ion position of (0.51, 0.51, 0.53) would yield four Ti – O bond lengths and the associated four bands observed. Eight possible regions would exist, for a displaced Ti-ion towards an oxygen octahedral face. It was presumed therefore, that the titanium atoms were displaced from their cubic centrosymmetric positions. This suggested that after the 773K treatment the minimum potential for the Ti-ion was a non-centrosymmetric location in a cubic unit cell.

The singular OH band near 3509 cm^{-1} observed with the spectra of the hydrothermal nanopowders indicated the possibility of multiple degenerate Ti – O bond related positions for these hydroxyls prior to elevated temperature treatment, therefore denoting a room temperature cubic structure. Three separate OH bands of differing intensities were observed in the spectra of these nanopowders after 1173K heat treatment. This provided evidence for the concept of a repositioning of the hydroxyls into energy states associated with Ti – O bond related positions having three different bond lengths, indicative of the tetragonal phase.

Although dehydroxylation occurred at the temperatures utilized in this study, defects were not completely eliminated, as observed in the mesoscopic structure of Nanopowder F. The complete elimination of lattice strains arising from the removal of the hydroxyl content and subsequent lattice rearrangement of residual point defects may not occur. The elimination of these lattice strains was important in stabilizing the room temperature tetragonal phase. The nucleation and growth of strain free crystallites occurred during the calcination of the nanopowders which involved rearrangement of the lattice.

Strain was evident with Nanopowders C, D, and E after the 473K and 773K calcines. It was not until after the 1173K calcine that these samples began to exhibit a large reduction in the levels of strain. Although the dehydroxylation occurred during lower temperature heat treatments, defects were not removed within the lattice at these lower temperatures. HT-DRIFT indicated the presence of OH^- at the lower calcine temperatures.

The presence of barium carbonate as a compound in all of the nanopowders was indicated by spectroscopic analysis. Nanopowder F incorporated the largest amount of carbonate which was only just above the detection limit for XRD. The XPS data indicated that the barium carbonate was a majority constituent of a contamination layer present with all of the nanopowders. The data indicated that the depth of this contamination layer was 10 Å to 18 Å. Incorporating the reduction of carbonate during the calcination of the nanopowders prior to compaction and sintering, resulted generally to support lower carbonate levels with increased density of the sintered bodies.

In Section 3.2 of the vibrational analysis, a mesoscopic state was suggested for the surfaces of Nanopowder F. All of the peaks in the initial XPS spectrum of Nanopowder F were broader and less well defined than that observed with the other nanopowders. This indicated a much broader energy distribution of all of the 4d transitions and supported the presumption of the mesoscopic state for the surfaces of this nanopowder.

The strain reduction in Nanopowder F was initiated during the 473K calcine. The proposed mesoscopic structure of this nanopowder would suggest a higher free energy surface state. A high concentration of mesomolecules, incomplete barium titanate unit cells, that comprised the structure of the surfaces of the nanocrystallites would account for an elevated excess surface energy. Additionally, the small crystallites, 40 nm average particle size, are on the order of 100 unit cell dimensions or 300 atoms across. The combination of a high energy state and short lattice dimensions would indicate a lower thermal barrier for atomic transport, especially near the surface where a disordered state existed. The high area surface and its associated high surface tension would be the first region for rearrangement. This rearrangement and relaxation among the lattice beneath the surface layer thereby produced a reduction in the observed strain after the lower calcine temperature.

At the intermediate stage of sintering studied herein, this process resulted in highly porous structures and low density compacts. Incorporating the reduction of carbonate during the calcination of the nanopowders prior to compaction and sintering, resulted generally to support lower carbonate levels with increased density. Nanopowder F had the largest reduction of carbonate during calcining as observed during the vibrational spectroscopic analysis. This nanopowder, however, contained a large quantity of spherical agglomerates that resisted fracture during pressing of the compacts. These agglomerates did sinter quite well with larger equiaxed grain growth than the other nanopowders. Sintering however, occurred through the densification of these spherical agglomerates in conjunction with individual grain growth. The ensuing development of large pores that accompanied the large spheres thus hindered densification. The result was large volume remnant pores at sphere junctions that reduced density throughout the sintering study.

The presence of agglomerates acted as seeds for the secondary recrystallization, or atypical growth, observed with many of the nanopowder compacts. As initial particle size increased the incidence of larger than average particles decreased and consequently greater difficulty in the nucleation of

secondary recrystallization. However, with many of the nanopowders examined, the agglomerates were larger than the average crystallite size, hence the development of atypical growth. The inhomogeneous packing of the nanopowders also aided in variations in the densification observed with denser packed regions subsequently exhibiting more rapid grain growth through less pore pinning of the interfaces. Anisotropies in interfacial energy and mobility may also cause atypical growth. The interfaces of the large atypical grains exhibited preferential faceting. The flat faces of these atypical growths suggest a crystallographic orientation of lower energy and thus preferential nucleation sites for continued growth.

The discussion on the room temperature crystallite structure of nanocrystalline barium titanate includes not only the effect of surface states, but also involves residual strain as discussed previously. This study is in partial agreement with Begg.[22] The possible mechanisms to explain the stabilization of the anomalous cubic room temperature phase are 1) the strains imposed by the presence of point defects: the protonic impurities and their associated cation vacancies, and 2) the role of surface states and structural changes.

At the highest temperature used in this study (1173K) moisture and the accompanying hydroxyls were mostly removed. Spectral evidence was obtained indicating that the reorientation of surface states occurred. Further, SEM and TEM supported this finding with visual evidence of interface rearrangement. HT-XRD produced results that indicated the readsorption of moisture during the slow cooling from high temperature soaks. This had the effect of impeding the transition to tetragonal symmetry, and resulted in cubic symmetry upon cooling through T_c to room temperature.

Although the 1173K temperature level does not allow a high degree of cation diffusion, the reorientation of the crystallite interfaces was observed in conjunction with the presence of room temperature tetragonal symmetry upon cooling and a reduction of incorporated protonic impurities. This data, therefore, substantiated the hypothesis that the cause of the room temperature cubic phase was a hydroxyl strain stabilized pseudocubic structure.

9. Future Work

(1) The high surface area of the nanopowders produced a high degree of agglomeration of the crystallites. A study to investigate the necessary levels of dispersant to attain fully dispersed crystallites to improve their sintering behavior would prove valuable.

(2) Extending this last concept, investigation of intermediate and final stages of sintering of the nanopowders utilizing processing additives to improve compact green densities and result in high density sintered bodies would be valuable to commercial processes.

(3) During the TEM studies, the nanopowders were highly affected by condensing the beam on groups of crystallites. Condensing the beam on a blank area had the effect of burning a hole in the formvar backing. The effect of a condensed beam on a group of crystallites would cause internal fluctuations with some of the crystallites, thereby released moisture and relieved residual strain. A reduction of strain was observed with darkfield imaging in similarly affected crystallites. A real-time monitoring of the nanopowders during this analysis would assist in the understanding of hydroxyl removal and the accompanied strain reduction in the crystallites.

(4) The propensity for many of the nanopowders to form an interconnected network of grains was noted. This resulted in a large volume interconnected network. A study to investigate the possibility of forming high density sintered compacts that contain these interconnected nanoporous channels. A possible application of such porous solids is filter substrates.

(5) Incorporating the aspect of nanoporosity, small compacts formed for use in investigating nanofluid dynamics through the formed nanochannels.

(6) XPS analysis of the surface states of calcined nanopowders and of intermediate stage sintered compacts would add to the data incorporated herein. The data may have greater application with nanoporous filters and nanofluidic applications.

References

1. X. Feng, M. S. H. Chu, H. E. Rast, and B. C. Foster, “Nanoparticles in Chip Miniaturization,” *Ceram. Trans.*, **137**, 59-74 (2003).

2. S. Wada, H. Chikamori, T. Noma, T. Suzuki, and T. Tsurumi, “Synthesis of Nanometer-sized Barium Titanate Crystallites Using a Modified Low Temperature Direct Synthesis Method and Their Characterization,” *J. Ceram. Soc. Jpn.*, **108** [8] 728-35 (2000).

3. R. Waser, “Electronic Properties of Grain Boundaries in $SrTiO_3$ and $BaTiO_3$ Ceramics,” *Solid State Ionics*, **75**, 89-99 (1995).

4. S. W. Lu, B. I. Lee, and L. A. Mann, “Carbonation of Barium Titanate Powders Studied by FT-IR Technique,” *Mater. Lett.*, **43** [3] 102-05 (2000).

5. J. F. Fernandez, P. Duran, and C. Moure, “Barium Titanate Processing: Effect of Raw Material Nature on their Synthesis and Sintering Behaviour,” pp. 172-76 in Euro-Ceramics, Vol. 1, *Processing of Ceramics*. Edited by G. de With, R. A. Terpstra and R. Metselaar. Elsevier, New York 1989.

6. W. Zhu, C. C. Wang, S. A. Akbar, and R. Asiae, “Fast-Sintering of Hydrothermally Synthesized $BaTiO_3$ Powders and Their Dielectric Properties,” *J. Mater. Sci.*, **32** [16] 4303-07 (1997).

7. G. Arlt, D. Hennings, and G. de With, “Dielectric Properties of Fine-Grained Barium Titanate Ceramics,” *J. Appl. Phys.*, **58** [4] 1619-25 (1985).

8. N. Bernaben, A. Lerche, B. Thierry, J. C. Niepce, and R. Waser, “Pure Barium Titanate Ceramics: Crystalline Structure and Dielectric Properties as a Function of Grain Size,” pp. 203-210 in Fourth Euro Ceramics, Vol. 5, *Electroceramics*. Edited by G. Gusmano and E. Traversa. Gruppo Editoriale Faenza Editrice, Italy 1995.

9. E.-W. Shi, C.-T. Xia, W.-Z. Zhong, B.-G. Wang, and C.-D. Feng, “Crystallographic Properties of Hydrothermal Barium Titanate Crystallites,” *J. Am. Ceram. Soc.*, **80** [6] 1567-72 1997.

10. Y. Waseda and A. Muramatsu, *Morphology Control of Materials and Nanoparticles*; p. 246. Springer, Berlin, 2004.

11. R. W. Siegel, “What Do We Really Know About the Atomic-Scale Structures of Nanophase Materials?” *J. Phys. Chem. Solids*, **55** [10] 1097-1106 **(**1994).

12. M. B. Bush, “Modeling of Nanophase Materials,” *Mater. Sci. Eng.*, **2** [1] 127-34 (1993).

13. N. Setter and R. Waser, “Electroceramic Materials,” *Acta Mater.,* **48** [1] 151-78 (2000).

14. H. Gleiter, “Nanostructured Materials: Basic Concepts and Microstructure,” *Acta Mater.*, **48** [3] 1-29 (2000).

15. M. H. Leipold and E. R. Blosser, “The Role of Composition in Ultrafine-Grain Ceramics,” pp 99-107 in *Ultrafine-Grain Ceramics*. Edited by J. J. Burke, N. L. Reed, and V. Weiss. Syracuse University Press, Syracuse, NY, 1970.

16. A. J. Mountvala, “Electrical and Magnetic Behavior of Ultrafine-Grain Ceramics,” pp 367-89 in *Ultrafine-Grain Ceramics*. Edited by J. J. Burke, N. L. Reed, and V. Weiss. Syracuse University Press, Syracuse, NY, 1970.

17. R. S. C. Smart and J. Nowotny, “Fundamental and Applied Aspects of Ceramic Interfaces,” pp 1-11 in *Ceramic Interfaces Properties and Applications*. Edited by R. S. C. Smart and J. Nowotny. IOM Communications, London, 1998.

18. D. Bonnell, “Atomic Structure of Transition Metal Oxide Surfaces from STM,” *Prog. Surf. Sci.*, **57** [3] 187-252 (1998).

19. S. Schlag and H.-F. Eicke, “Size Driven Phase Transition in Nanocrystalline $BaTiO_3$,” *Solid State Commun.*, **91** [11] 883-87 (1994).

20. K. Uchino, E. Sadanaga, and T. Hirose, “Dependence of the Crystal Structure on Particle Size in Barium Titanate,” *J. Am. Ceram. Soc.*, **72** [8] 1555-58 (1989).

21. H.-I. Hsrang and F.-S. Yen, “Effect of Crystallite Size on the Ferroelectric Domain Growth of Ultrafine $BaTiO_3$ Powders,” *J. Am. Ceram. Soc.*, **79** [4] 1053-60 (1996).

22. B. D. Begg, E. R. Vance, and J. Nowotny, “Effect of Particle Size on the Room-Temperature Crystal Structure of Barium Titanate,” *J. Am. Ceram. Soc.,* **77** [12] 3186-92 (1994).

23. W.-S. Cho, “Structural Evolution and Characterization of $BaTiO_3$ Nanoparticles Synthesized from Polymeric Precursor,” *J. Phys. Chem. Solids*, **59** [5] 659-66 (1998).

24. I. J. Clark, T. Takeuchi, N. Ohtori, and D. C. Sinclair, “Hydrothermal Synthesis and Characterization of $BaTiO_3$ Fine Powders: Precursors, Polymorphism and Properties,” *J. Mater. Chem.*, **11** [11] 83-91 (1999).

25. D. Hennings and S. Schreinemacher, “Characterization of Hydrothermal Barium Titanate,” *J. Eur. Ceram. Soc.*, **9** [1] 41-46 (1992).

26. A. Kruth and J. T. S. Irvine, “Water Incorporation Studies on Doped Barium Cerate Perovskites,” *Solid State Ionics*, **162-63**, 83-91 (2003).

27. N. Bonanos, “Transport Properties and Conduction Mechanism in High-Temperature Protonic Conductors,” *Solid State Ionics*, **53-56** [Part II] 967-74 (1992).

28. T. Norby, “Proton Conduction in Oxides,” *Solid State Ionics*, **40-41** [Part II] 857-62 (1990).

29. H.-P. Abicht, D. Völtzke, R. Schneider, J. Woltersdorf, and O. Lichtenberger, “Defect Chemistry of the Shell Region of Water-Milled $BaTiO_3$ Powders,” *Mater. Chem. Phys.*, **55** [3] 188-92 (1998).

30. F. Valdivieso, M. Pijolat, C. Magnier, and M. Soustelle, “Kinetic Study and Modeling of Coarsening in a $BaTiO_3$ Powder at 850ºC,” *Solid State Ionics*, **83** [3-4] 283-92 (1996).

31. B. Lee and J. Zhang, “Preparation, Structure Evolution and Dielectric Properties of $BaTiO_3$ Thin Films and Powders by an Aqueous Sol-Gel Process,” *Thin Solid Films*, **388** [1-2] 107-13 (2001).

32. T. Takeuchi, K. Ado, T. Asai, H. Kageyama, Y. Saito, C. Masquelier, and O. Nakamura, “Thickness of Cubic Surface Phase on Barium Titanate Single-Crystalline Grains,” *J. Am. Ceram. Soc.*, **77** [6] 1665-68 (1994).

33. X. Li and W.-H. Shih, “Size Effects in Barium Titanate Particles and Clusters,” *J. Am. Ceram. Soc.*, **80** [11] 2844-52 (1997).

34. C. W. Oatley, “The Detective Quantum Efficiency of the Scintillator/Photomultiplier in the Scanning Electron Microscope,” *J. Microsc.*, **139** [Part 2] 153-66 (1985).

35. J. W. Edington, *Practical Electron Microscopy*. Van Nostrand Reinhold, New York, 1976.

36. C. Davisson and L. H. Germer, “Diffraction of Electrons by a Crystal of Nickel,” *Phys. Rev.* **30** [6] 705-15 (1927).

37. C. J. Davisson, “Are Electrons Waves?” *J. Franklin Inst.*, **205**, 597-623 (1928).

38. R. E. Seidel and M. E. Winter, “The New Microscopes,” *J. Franklin Inst.*, **237** [3] 103-30 (1944).

39. P. B. Hirsch, A. Howie, R. B. Nicholson, D. W. Pashley, and M. J. Whelan, *Electron Microscopy of Thin Crystals*; pp. 188-350. Spottiswoode/Ballantyne, London, 1965.

40. R. Vivekanandan and T. R. N. Kutty, “Characterization of Barium Titanate Fine Powders Formed from Hydrothermal Crystallization,” *Powder Technol.*, **57** [3] 181-92 (1989).

41. E.-W. Shi, C.-T. Xia, W.-Z. Zhong, B.-G. Wang, and C.-D. Feng, “Crystallographic Properties of Hydrothermal Barium Titanate Crystallites,” *J. Am. Ceram.* Soc., **80** [6] 1567-72 (1997).

42. Steven P. Ostrander, “Anomalous Permittivity in Fine-Grain Barium Titanate”; Ph.D. Thesis. Alfred University, Alfred, NY, 1997.

43. T. Tunkasiri, “A Study of Structure and Microstructure of Barium Titanate Ceramics Using T.E.M. and S.E.M.,” *J. Sci. Fac. Chiang Mai Univ.*, **6** [1] 1-9 (1992).

44. W. Herschel, “Heating Power Among the Various Colors in the Solar Spectrum,” *Philos. Trans. R. Soc. London*, **18**, 688-89 (1800).

45. J. D. Ingle, Jr. and S. R. Crouch, *Spectrochemical Analysis*; pp. 35-43. Prentice Hall, Saddle River, NJ, 1988.

46. C. E. Meloan, *Elementary Infrared Spectroscopy*; p. 119. Macmillan, New York, 1963.

47. C. Noguera, *Physics and Chemistry at Oxide Surfaces*; Ch. 2. Cambridge University Press, Cambridge, England, 1996.

48. S. Dorfman, D. Fuks, and E. Kotomin, "Comparative Study of [100] Surface Relaxations of Perovskite Titanates," *Thin Solid Films*, **318**, 65-68 (1998).

49. V. F. Kiselev and O. V. Krylov, *Adsorption Processes on Semiconductor and Dielectric Surfaces I*; pp. 17-23. Springer-Verlag, Berlin, 1985.

50. H. S. Nalwa, *Handbook of Nanostructured Materials and Nanotechnology, V2: Spectroscopy and Theory*; p. 179. Academic Press, San Diego, CA, 1999.

51. S. Wada, T. Suzuki, and T. Noma, "Role of Lattice Defects in the Size Effect of Barium Titanate Fine Particles," *J. Ceram. Soc. Jpn.*, **104** [5] 383-92 (1996).

52. P. Duran, D. Gutierrez, J. Tartaj, and C. Moure, "Densification Behaviour, Microstructure Development and Dielectric Properties of Pure $BaTiO_3$ Prepared by Thermal Decomposition of (Ba,Ti)-Citrate Polyester Resins," *Ceram. Int.*, **28** [3] 283-92 (2002).

53. T. Iwaoka, S.-H. Wang, and P. F. Griffiths, "Diffuse Reflectance Infrared Spectrometry of Inorganic Materials," *Spectrochim. Acta*, **41A** [1-2] 37-41 (1985).

54. Handbook of Analytical Techniques, Vol. II; pp. 494-95. Edited by H. Günzler and A. Williams. Wiley-VCH, New York, 2001.

55. H. H. Kung, *Transition Metal Oxides: Surface Chemistry and Catalysis*; p. 7. Elsevier, Amsterdam, 1989.

56. P. Hollins, "The Influence of Surface Defects on the Infrared Spectra of Adsorbed Species," *Surf. Sci. Rep.*, **16** [2] 53-94 (1992).

57. P. Jones and J. A. Hockey, “Infra-red Studies of Rutile Surfaces,” *Trans. Faraday Soc.*, **585**, 2669-78 (1971).

58. M. Primet, P. Pachat, and M.-V. Mathieu, “Infrared Study on the Surface of Titanium Dioxides. I. Hydroxyl Groups;” *J. Phys. Chem.*, **75** [9] 1216-26 (1971).

59. H. P. Boehm, M. Schneider, and F. Arendt, “Bestummung des Aktiven Wasserstoffs, Thermische Entwässerung und Rehdroxylierung,” *Z. Anorg. Allg. Chem.*, **352** [3-4] 156-67 (1967).

60. G. Busca, V. Buscaglia, M. Leoni, and P. Nanni, “Solid-State and Surface Spectroscopic Characterization of $BaTiO_3$ Fine Powders,” *Chem. Mater.*, **6** [7] 955-61 (1994).

61. C. Hérard, A. Faivre, and J. Lemaître, “Surface Decontamination Treatments of Undoped $BaTiO_3$ - Part I : Powder and Green Body Properties,” *J. Eur. Ceram. Soc.*, **15** [2] 135-44 (1995).

62. P. Coufová, J. Novák, and N. Hlasivcová, “Hydroxyl as a Defect of the Perovskite $BaTiO_3$ Lattice,” *J. Chem. Phys.*, **45** [9] 3171-74 (1966).

63. J. C. Berg, *Wettability*; pp. 94-96. Marcel Dekker, New York, 1993.

64. R. S. Bradley, “Polymolecular Adsorbed FIlms. Part II. The General Theory of the Condensation of Vapours on Finely Divided Solids,” *J. Chem. Soc.*, **139**, 1799-1804 (1936).

65. M. W. Urban, *Vibrational Spectroscopy of Molecules and Macromolecules on Surfaces*; pp. 94-96. Wiley, New York, 1993.

66. R. Vivekanandan, S. Philip, and T. R. N. Kutty, “Hydrothermal Preparation of $Ba(Ti,Zr)O_3$ Fine Powders,” *Mater. Res. Bull.*, **22** [1] 99-108 (1987).

67. J. D. Ingle, Jr. and S. R. Crouch, *Spectrochemical Analysis*; p. 419. Prentice Hall, Saddle River, NJ, 1988.

68. X. Li, H. Zhang, S. Li, W. Fan, and M. Zhao, “IR Transmission Spectra of Nanocrystalline Powder Materials of the Composite Oxides $La_{1-x}Sr_xFe_{1-y}Co_yO_3$ with the Perovskite Structure,” *Mater. Chem. Phys.*, **41** [1] 41-45 (1995).

69. A. Morell and J.-C. Niepce, “$BaTiO_3$ -Based Materials for M.L.C. Capacitors Applications,” *J. Mater. Educ.*, **13** [3] 173-232 (1991).

70. W. D. Kingery, H. K. Bowen, and D. R. Uhlmann, *Introduction to Ceramics*; pp. 967-72. Wiley & Sons, New York, 1976.

71. D. V. Miller, J. H. Adair, and R. E. Newnham, “Dissolution of Barium from Barium Titanate in Non-Aqueous Solvents,” *Ceram. Trans.*, **1** [Part A] 493-500 (1988).

72. F. Jona and G. Shirane, *Ferroelectric Crystals*; pp. 133-41. Macmillan, New York, 1962.

73. W. Cochran, “Crystal Stability and the Theory of Ferroelectricity,” *Phys. Rev. Lett.,* **3** [9] 412-14 (1959).

74. E. A. Kotomin, E. Heifats, S. Dorfman, D. Fuks, A. Gordon, and J. Maier, “Comparitive Study of Polar Perovskite Surfaces,” *Surf. Sci.*, **566-68** [Part I] 231-35 (2004).

75. S. Kapphan, J. Koppitz, and G. Weber, “O-D and O-H Stretching Vibrations in Monodomain $SrTiO_3$,” *Ferroelectrics*, **25** [1-2] 585-88 (1980).

76. L. J. Bellamy and A. J. Owen, “A Simple Relationship between the Infra-Red Stretching Frequencies and the Hydrogen Bond Distances in Crystals,” *Spectrochim. Acta,* **25A** [2] 329-33 (1969).

77. V. E. Henrich and P. A. Cox, *The Surface Science of Metal Oxides*; Ch. 6. Cambridge University Press, Cambridge, 1994.

78. E.-W. Shi, C.-T. Xia, W.-Z. Zhong, B.-G. Wang, and C.-D. Feng, “Crystallographic Properties of Hydrothermal Barium Titanate Crystallites,” *J. Am. Ceram. Soc.*, **80** [6] 1567-72 (1997).

79. G. Busca, V. Buscaglia, M. Leoni, and P. Nanni, “Solid-State and Surface Spectroscopic Characterization of $BaTiO_3$ Fine Powders,” *Chem. Mater.*, **6** [7] 955-61 (1994).

80. H.-J. Freund and R. P. Messmer, “On the Bonding and Reactivity of CO_2 on Metal Surfaces,” *Surf. Sci.*, **172** [1] 1-30 (1986).

81. M. C. B. López, G. Fourlaris, B. Rand, and F. L. Riley, “Characterization of Barium Titanate Powders: Barium Carbonate Identification,” *J. Am. Ceram. Soc.*, **82** [7] 1777-86 (1999).

82. L. H. Little, *Infrared Spectra of Adsorbed Species*; pp. 74-84. Academic Press, London, 1966.

83. P. F. Souter and L. Andrews, “A Spectroscopic and Theoretical Study of the Reactions of Group 6 Metal Atoms with Carbon Dioxide,” *J. Am. Chem. Soc.*, **119** [31] 7350-60 (1997).

84. L. Andrews, M. F. Zhou, B. Y. Liang, J. Li, and B. E. Bursten, “Reactions of Laser-Ablated U and Th with CO_2: Neon Matrix Infrared Spectra and Density Functional Calculations of OUCO, OThCO, and Other Products,” *J. Am. Chem. Soc.*, **122** [46] 11440-49 (2000).

85. J. Castro-Rodriguez, H. Nakai, L. N. Zakharov, A. L. Rheingold, and K. Meyer, “A Linear, O-Coordinated n^1-CO_2 Bound to Uranium,” *Science*, **305** [5691] 1757-59 (2004).

86. G. H. Jeung, “Activation of CO_2 Coordinated to a Cr Atom,” *Mol. Phys.*, **65** [3] 669-77 (1988).

87. G. H. Jeung, “Activation of CO_2 Coordinated to a Ti Atom,” *Mol. Phys.*, **67** [4] 747-56 (1989).

88. D. H. Gibson, “Carbon Dioxide Coordination Chemistry: Metal Complexes and Surface-Bound Species. What Relationships?” *Coord. Chem. Rev.*, **185-86**, 335-55 (1999).

89. P. Hollins, “The Influence of Surface Defects on the Infrared Spectra of Adsorbed Species,” *Surf. Sci. Rep.*, **16**, 51-94 (1992).

90. J. Castro-Rodriguez, H. Nakai, L. N. Zakharov, A. L. Rheingold, and K. Meyer, "A Linear, O-Coordinated η^1-CO_2 Bound to Uranium," *Science*, **305** [5691] 1757-59 (2004).

91. P. F. Souter and L. Andrews, "A Spectroscopic and Theoretical Study of the Reactions of Group 6 Metal Atoms with Carbon Dioxide," *J. Am. Chem. Soc.*, **119** [31] 7350-60 (1997).

92. K. Nakamoto, *Infrared Spectra of Inorganic and Coordination Compounds, 2*nd ed. Wiley-Interscience, New York, 1970.

91. P. J. Lucchesi and W. A. Glasson, "Infrared Investigation of Bound Water in Hydrates," *J. Am. Ceram. Soc.*, **78** [7] 1347-48 (1956).

92. K. S. Mazdiyasni, R. T. Dollof, and J. S. Smith, "Preparation of High-Purity Submicron Barium Titanate Powders," *J. Am. Ceram. Soc.*, **52** [10] 523-26 (1969).

93. P. J. Launer, "Tracking Down Spurious Bands in Infrared Analysis," pp. xvii-xxi in *Laboratory Methods in Infrared Spectroscopy*. Edited by R. G. J. Miller and B. C. Stace. Heyden & Son, London, 1972.

94. J. A. Lercher, C. Colombier, and H. Noller, "Acid-Base Properties of Alumina-Magnesia Mixed Oxides, Part 4. Infrared Study of Adsorption of Carbon Dioxide," *J. Chem. Soc., Faraday Trans.*, **80** [1] 949-59 (1984).

95. J. A. Gadsden, *Infrared Spectra of Minerals and Related Inorganic Compounds*; p.62. Butterworth, London, 1975.

96. *Infrared Spectra Handbook of Minerals and Clays*; p. 75. Edited by J. R. Ferraro. Sadtler Research Lab, Bio-Rad Laboratories, Philadelphia, 1982.

97. J. T. Last, "Infrared-Absorption Studies on Barium Titanate and Related Materials," *Phys. Rev.*, **105** [6] 1740-50 (1957).

98. *Laboratory Methods in Infrared Spectroscopy*; p. xvii. Edited by R. G. J. Miller and B. C. Stace. Heyden & Son, London, 1972.

99. P. J. Launer, "Tracking Down Spurious Bands in Infrared Analysis," p. xviii in *Laboratory Methods in Infrared Spectroscopy*. Edited by R. G. J. Miller and B. C. Stace. Heyden & Son, London, 1972.

100. S. W. Lu, B. I. Lee, and L. A. Mann, “Characterization of Carbonate on $BaTiO_3$ Ceramic Powders,” *Mater. Res. Bull.*, **35** [8] 1303-12 (2000).

101. D. Lee and R. A. Condrate, “The Effect of Protective Organic Thin Film Coatings on $BaTiO_3$ Powders with Respect to Aqueous Processing,” *Mater. Res. Soc. Symp. Proc.*, **458**, 385-88 (1997).

102. S. W. Lu, B. I. Lee, and L. A. Mann, “Carbonation of Barium Titanate Powders Studied by FT-IR Technique,” *Mater. Lett.*, **43** [3] 102-05 (2000).

103. M. H. Frey and D. A. Payne, “Synthesis and Processing of Barium Titanate Ceramics from Alkoxide Solutions and Monolithic Gels,” *Chem. Mater.*, **7** [1] 123-29 (1995).

104. P. Coufová, J. Novák, and N. Hlasivcová, “Hydroxyl as a Defect of the Perovskite Lattice,” *J. Chem. Phys.*, **45** [9] 3171-74 (1966).

105. M. H. Frey and D. A. Payne, “Grain-Size Effect on Structure and Phase Transformations for Barium Titanate,” *Phys. Rev.* B: Condens. Matter, **54** [5] 3158-68 (1996).

106. S. Wada, T. Suzuki, and T. Noma, “Role of Lattice Defects in the Size Effect of Barium Titanate Fine Particles - A New Model,” *J. Ceram. Soc. Jpn.*, **104** [5] 383-92 (1996).

107. R. Waser, “Solubility of Hydrogen Defects in Doped and Undoped $BaTiO_3$,” *J. Am. Ceram. Soc.*, **71** [1] 58-63 (1988).

108. C. Hérard, A. Faivre, and J. Lemaître, “Surface Decontamination Treatments of Undoped $BaTiO_3$ - Part I : Powder and Green Body Properties,” *J. Eur. Ceram. Soc.*, **15** [2] 135-44 (1995).

109. U. S. Secretary of Commerce, “NIST Chemistry WebBook” (1991) National Institute of Standards and Technology. Accessed on: November, 2001. Available at: <http://webbook.nist.gov/chemistry>

110. X. Li, H. Zhang, M. Zhao, and Y. Zheng, “EPR Spectra of Nanocrystalline Composite Oxide $LaFeO_3$ with the Perovskite Structure,” *Mater. Chem. Phys.*, **38** [2] 157-61 (1994).

111. X. Li, H. Zhang, X. Liu, S. Li, and M. Zhao, “XPS Study on O(1s) and Fe(2p) for Nanocrystalline Composite Oxide $LaFeO_3$ with the Perovskite Structure,” *Mater. Chem. Phys.*, **38** [4] 355-62 (1994).

112. X. Li, H. Zhang, S. Li, W. Fan, and M. Zhao, “IR Reflectance Spectra on High-Pressure Compacted Nanocrystalline La-Sr-Fe-Co Oxides,” *Mater. Chem. Phys.*, **42** [2] 120-28 (1995).

113. X. Li, H. Zhang, S. Li, W. Fan, and M. Zhao, “IR Transmission Spectra of Nanocrystalline Powder Materials of the Composite Oxides $La_{1-x}Sr_xFe_{1-y}Co_yO_3$ with the Perovskite Structure,” *Mater. Chem. Phys.*, **41** [1] 41-45 (1995).

114. F.-X. Cai, J.-F. Meng, G.-T. Zou, “Study on the “Soft” Optical Phoon and Structural Phase Transition of $Bi_{2-x}A_xTi_4O_{11}$,” *Chin. Sci. Bull.*, **39** [17] 284-90 (1994).

115. S. Klauer and M. Wöhlecke, “Incorporation of Hydrogen in Cubic and Uniaxial Oxidic Crystals Deduced from Polarized Raman Scattering,” *Phys. Rev. B*: *Condens. Matter* **49** [1] 158-81 (1994).

116. S. Kapphan and G. Weber, “IR-Absorption Study of H- and D-impurities in $BaTiO_3$ Crystals,” *Ferroelectrics,* **37** [1-4] 673-76 (1981).

117. R. Pirc and R. Blinc, “Off-Center Ti Model of Barium Titanate,” *Phys. Rev. B*, **70** [13] 134107-1 – 134107-8 (2004).

118. N. Agmon, “The Grotthuss Mechanism,” *Chem. Phys. Lett.*, **244** [5-6] 456-62 (1995).

119. A. L. Samgin, “Lattice-Assisted Proton Motion in Perovskite Oxides,” *Solid State Ionics*, **136-37**, 291-95 (2000).

120. W. Münch, G. Seifert, K. D. Kreuer, and J. Maier, “A Quantum Molecular Dynamics Study of the Cubic Phase of $BaTiO_3$ and $BaZrO_3$,” *Solid State Ionics*, **97** [1-4] 39-44 (1997).

121. D. M. MacBride, C. G. Malone, J. P. Hebb, and E. G. Cravalho, “Effect of Temperature Variation on FT-IR Spectrometer Stability,” *Appl. Spectrosc.*, **51** [1] 43-51 (1997).

122. P. R. Griffiths and J. A. de Haseth, *Fourier Transform Infrared Spectrometry*; p. 274. Wiley, New York, 1986.

123. C. E. Meloan, *Elementary Infrared Spectroscopy*; p. 119. Macmillan, New York, 1963.

124. S. Pinchas and I. Laulicht, *Infrared Spectra of Labeled Compounds*; p. 79. Academic Press, New York, 1971.

125. M. Glerup, F. W. Poulsen, and R. W. Berg, "Vibrational Spectroscopy on Protons and Deuterons in Proton Conducting Perovskites," *Solid State Ionics*, **148** [1-2] 83-92 (2002).

126. E. P. Hunter and S. G. Lias, "Evaluated Gas Phase Basicities and Proton Affinities of Molecules: An Update," *J. Phys. Chem. Ref. Data*, **27** [3] 413-656 (1998).

127. R. N. Compton, P. W. Reinhardt, and C. D. Cooper, "Collisional Ionization of Na, K and Cs by CO_2, COS and CS_2: Molecular Electron Affinities," *J. Chem. Phys.*, **63** [9] 3821-27 (1975).

128. D. R. Lide, *CRC Handbook of Chemistry and Physics*, 71st ed.; p. 4-47, 4-48, and 14-19. CRC Press, Boston, 1991.

129. D. Bonnell, "Atomic Structure of Transition Metal Oxide Surfaces from STM," *Prog. Surf. Sci.*, **57** [3] 187-252 (1998).

130. C. J. Powell and A. Jablonski, *NIST Electron Inelastic-Mean-Free-Path Database – Version 1.1 [CD-ROM]* National Institute of Standards and Technology, Gaithersburg, MD, 2000.

131. W. K. Ford, J. Anderson, G. V. Rubenacker, J. E. Drumheller, C. T. Chen, M. Hong, J. Kwo, and S. H. Liou, "Physical Processing Effects on Polycrystalline $YBa_2Cu_3O_x$," *J. Mater. Res.*, 4 [1] 16-22 (1989).

132. H. van Doveren and J. A. Th. Verhoeven, "XPS Spectra of Ca, Sr, Ba and Their Oxides," *J. Elec. Spect.*, 21 [3] 265-73 (1980).

133. J. F. Moulder, W. F. Stickle, P. E. Sobol, and K. D. Bomben, *Handbook of X-ray Photoelectron Spectroscopy*. Physical Electronics, Eden Prairie, MN, 1995.

134. W. F. Egelhoff, Jr., “Core Level Binding Energy Shifts at Surfaces and in Solids,” *Surf. Sci. Rep.*, 6 [6-8] 253 (1987).

135. Y.-M. Chiang, D. P. Birnie, III, and W. D. Kingery, *Physical Ceramics*; pp. 38-41. Wiley & Sons, New York, 1997.

136. L. Bragg and G. F. Claringbull, *Crystal Structures of Minerals*; pp. 128-31. Cornell University Press, Ithaca, NY, 1965.

137. B. Pawelec, “Surface Processes and Composition of Metal Oxide Surfaces,” pp.111-31 in *Metal Oxides: Chemistry and Applications*. Edited by J. L. G. Fierro. Taylor & Francis, Boca Raton, FL, 2006.

138. Materials Science Monographs, Vol. 80, *Structure and Properties of Ceramics*; pp. 135-37. Edited by A. Koller. Elsevier, Amsterdam, 1994.

139. F. Valdivieso, M. Pijolat, C. Magnier, and M. Soustelle, “Kinetic Study and Modelling of Coarsening in a $BaTiO_3$ Powder at 850ºC,” *Solid State Ionics*, **83** [3-4] 283-92 (1996).

140. J. F. Banfield and A. Navrotsky, *Nanoparticles and the Environment*; pp. 107-33. Mineralogical Society of America, Washington, DC, 2001.

141. K. Vorres and J. Donohue, “The Structure of Titanium Oxydifluoride,” *Acta Crystallogr.*, **8** [1] 25-26 (1955).

142. J. H. Moss and A. Wright, A., **“**Titanium (IV) Oxydifluoride,” *J. Fluorine Chem.*, **5** [*2*] 163-67 (1975).

143. B.-K. Lee, S.-Y. Chung, and S.-K. L. Kang, “Grain Boundary Faceting and Abnormal Grain Growth in $BaTiO_3$,” *Acta* Mater., **48** [7] 1575-80 (2000).

144. S. B. Lee, W. Sigle, and M. Ruhle, “Investigation of Grain Boundaries in Abnormal Grain Growth Structure of TiO_2-excess $BaTiO_3$ by TEM and EELS,” *Acta Mater.*, **50** [8] 2151-62 (2000).

145. A. Koller, *Structure and Properties of Ceramics*; pp. 119-42. Elsevier, Amsterdam, 1994.

146. P. Duran, J. Tartaj, and C. Moure, “Sintering Behaviour and Microstructural Evolution of Agglomerated Spherical Particles of High-Purity Barium Titanate,” *Ceram. Int.*, **29** [4] 419-25 (2003).

147. J.-K. Liou, M.-H. Lin, and H.-Y. Lu, “Crystallographic Facetting in Sintered Barium Tatanate,” *J. Am. Ceram.* Soc., **85** [12] 2931-37 (2002).

148. H. Schmelz and A. Meyer, “The Evidence of Anonalous Grain Growth Below the Eutectic Temperature in $BaTiO_3$ Ceramics,” *Ceram. Forum*, **59** [8/9] 436-40 (1982).

149. M.-H. Lin, J.-F. Chou, and H.-Y. Lu, “The Rate-Determining Mechanism in the Sintering of Undoped Nonstoichiometric Barium Titanate,” *J. Eur. Ceram. Soc.*, **20** [4] 517-26 (2000).

150. T. J. Carbone and J. S. Reed, “Microstructure Development in Barium Titanate: Effects of Physical and Chemical Inhomogeneities,” *Am. Ceram. Soc. Bull.*, **58** [5] 512-15 (1979).

151. C. V. Thompson, H. J. Frost, and F. Spaepen, “Relative Rates of Secondary and Normal Grain Growth,” *Acta Metall.*, 35 [4] 887-90 (1987).

152. D. J. Srolovitz, G. S. Grest, and M. P. Anderson, “Computer Simulation of Grain Growth – V. Abnormal Grain Growth,” *Acta Metall.*, 33 [12] 2233-47 (1985).

153. D. T. Ewing and C. H. Spurway, “The Density of Water Adsorbed on Silica Gel,” *J. Am. Chem. Soc.*, **52** [12] 4635-41 (1930).

154. B. D. Cullity, *Elements of X-Ray Diffraction*; p.501-02. Addison-Wesley, Boston, 1978.

155. M. P. Seah and W. A. Dench, “Quantitative Electron Spectroscopy of Surfaces: A Standard Data Base for Electron Inelastic Mean Free Paths in Solids,” *Surf. Interface Anal.*, **1** [1] 2-11 (1979).

156. B. Pujilaksono, U. Klement, L. Nyborg, U. Jelvestam, S. Hill, and D. Burgard, “X-ray Photoelectron Spectroscopy Studies of Indium Tin Oxide Nanocrystalline Powder,” *Mater. Charact.*, **54** [1] 1-7 (2005).

157. K. Suzuki and K. Kijima, “Optical Band Gap of Barium Titanate Nanoparticles Prepared by RF-plasma Chemical Vapor Deposition,” *Jpn. J. Appl. Phys.*, **44** [4A] 2081-82 (2005).

158. D. Briggs and J. T. Grant, *Surface Analysis by Auger and X-ray Photoelectron Spectroscopy*; p.31-32. IM Publications, Trowbridge, UK, 2003.

Appendices

A.1 Indexing Diffraction Patterns

Crystallography of the specimen can be analyzed through electron diffraction techniques. The information provided by a diffraction pattern will determine whether the specimen is crystalline and provide the crystal system and characteristic symmetry of the specimen if it is crystalline. Using the separation between the diffraction spots of the diffraction pattern, the interplanary spacings in the crystallite can be determined.

Consider the geometry of a simulated selected area diffraction pattern, Figure A.1, which shows the camera length 'L' which is characteristic of the optics of the microscope. Starting with Bragg's law:

$$2d \sin\theta = n\lambda , \tag{A.1}$$

and consider that for low order diffractions of 120 kV electrons the angle θ ~ 1º. For such small angles, sin θ ~ tan θ ~ ½ tan 2θ. By the geometry of Figure A.1:

$$\tan 2\theta = \frac{r}{L} . \tag{A.2}$$

Substitution of this into Bragg's law achieves the equation used in solving electron diffraction patterns:

$$rd = n\lambda L . \tag{A.3}$$

Equation (A.3) is used to determine the interplanary spacing (d) by measuring the separation of the diffraction spots (r). The value of the product λL (the camera constant) must be known. A close approximate value of the camera constant can be found by calculating the product of the relativistic wavelength of the accelerated electrons and the camera length as indicated by the instrument.

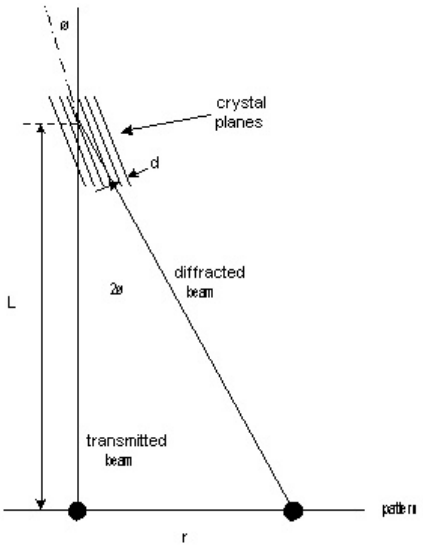

Figure A.1. Geometry for electron diffraction and definition of 'camera length'.

The process used in solving diffraction patterns was the method of ratios. Once obtaining electron diffraction patterns the Miller indices of the planes that gave rise to the reflections in the pattern must be assigned and the zone axis direction determined.

A table of the ratios of known d-spacings from the crystal with the inclusive angles is constructed. The angles may be calculated using the interplanar angle formulas:[154]

cubic:
$$\cos\phi = \frac{h_1h_2 + k_1k_2 + l_1l_2}{\left[\left(h_1^2 + k_1^2 + l_1^2\right)\left(h_2^2 + k_2^2 + l_2^2\right)\right]^{1/2}} \qquad \text{(A.4)}$$

and

tetragonal: $$\cos\phi = \frac{\frac{1}{a^2}\left(h_1h_2 + k_1k_2\right) + \frac{1}{c^2}\left(l_1l_2\right)}{\left\{\left[\frac{1}{a^2}\left(h_1^2 + k_1^2\right) + \frac{1}{c^2}\left(l_1^2\right)\right]\left[\frac{1}{a^2}\left(h_2^2 + k_2^2\right) + \frac{1}{c^2}\left(l_2^2\right)\right]\right\}^{1/2}}. \quad \text{(A.5)}$$

Considering the number of possible planes involved, these formulas were entered in a spreadsheet forming a table of ratio values and angles.

The second step was determining the R spacing for each diffracted spot in the pattern, Figure A.2. The d-spacing, the distance between planes in a crystal, is related to the R spacing through the following equation:

$$d = \frac{\lambda L}{R} \quad \text{(A.6)}$$

where L is the camera length, λ is the wavelength of the electrons and R is the distance in mm between diffraction spots on the negative. Measure the included angle between pairs of spots. The camera constant, or magnification factor between real space and reciprocal space (λL) may be considered a constant when solving an individual pattern; the relationship of the ratio between two planes in a crystal may be express as

$$\frac{d_1}{d_2} = \frac{R_2}{R_1}. \quad \text{(A.7)}$$

Ratios of R spacings and their accompanying angles were calculated and compared to the table of ratio values.

The ratio and the inclusive angle must match for all spots for a correct solution. In this manner, the correct solution of a diffraction pattern could be accomplished.

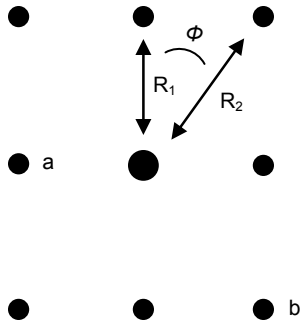

Figure A.2. Simplified diffraction pattern indicating R spacings and included angle with transmitted spot in the center.

Once the Miller indices were assigned to the diffraction patterns the zone axis was determined. The zone axis, [uvw], was the direction normal to the diffraction pattern. Using two indexed diffraction spots that are not directly opposite of the transmitted spot, spots a and b in Figure A.1. The selected indices were written out twice, one set above the other, then strike out the first and last numbers as shown in the following example.

$$\begin{array}{cccccc} \cancel{h_1} & k_1 & l_1 & h_1 & k_1 & \cancel{l_1} \\ \cancel{h_2} & k_2 & l_2 & h_2 & k_2 & \cancel{l_2} \end{array} \qquad \text{(A.8)}$$

Cross multiply in pairs to achieve the zone axis:

$$k_1l_2 - l_1k_2,\ l_1h_2 - h_1l_2,\ h_1k_2 - k_1h_2.$$

The zone axis may be checked by multiplying the vectors representing the planes in the diffraction pattern by the zone axis. The two are perpendicular and the result should be 0. For planes hkl with zone axis uvw:

$$hu + kv + lw = 0. \qquad \text{(A.9)}$$

A.2 The Infrared Spectrum

The invisible light described by Sir William Herschel, what is now known as the infrared spectrum because of its dispersed position relative to the visible red, is the basis of current infrared vibrational spectroscopic techniques. The spectroscopic method is based on the principle that absorption of light whose wavelength corresponds to the bond energy will often lead to an atom being displaced from its equilibrium position in the molecule. A restoring force which increases with the displacement, similar to a spring as with Hooke's law, the chemical bond is therefore formally similar to a spring that has weights, atoms, attached to its two ends. This system possesses a natural vibrational frequency which depends on the masses of the weights and the stiffness of the spring.

The chemical bond vibrational motions, phonons, are, unlike a spring, quantized. Only vibrations having certain discrete energies are allowed, Figure A.3. The natural frequencies of these bonds correspond to those of infrared light. Each wavelength of infrared light that excites the vibrational motion of a particular bond will be absorbed by the molecule. In general, the stronger the bond and the lighter the atoms it connects, the higher will be its natural stretching frequency and the shorter the wavelength of light absorbed.

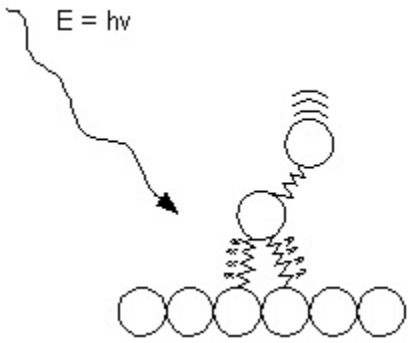

Figure A.3. Only vibrations having certain discrete energies are allowed.

Molecules absorbing energy are able to vibrate, therefore, at specific frequencies predetermined by their structure, bond force constants, and the

masses of the atoms present. The vibrations that are infrared active are those which lead to a net change in the dipole moment of the molecule:

$$\mu = q \cdot r \tag{A.10}$$

where $\mu \rightarrow$ dipole moment,
$q \rightarrow$ charge,
and $r \rightarrow$ separation.

As an example, carbon disulfide (CS_2) is a linear molecule that exhibits both infrared active and infrared inactive vibrations:[123]

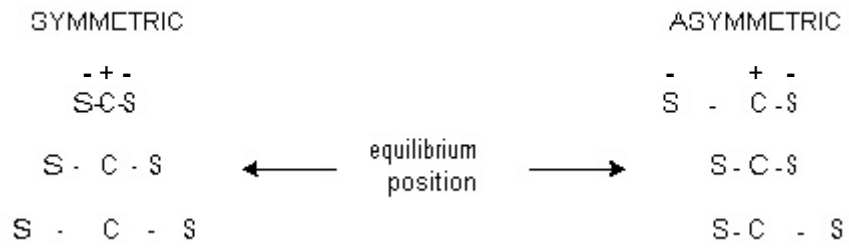

The symmetric stretching motion does not produce a net change in the dipole moment of the molecule. The molecule remains charge balanced throughout the stretching motion since the sulfur atoms are equidistant from the carbon atom. Both of the sulfur atoms move simultaneously toward, then away from, the carbon atom. The asymmetric stretch however does exhibit a net change in the dipole moment of the molecule as shown above. The vibration brings the carbon atom closer to one of the sulfur atoms, then the other, producing a charge imbalance and net dipole moment.

For simple two atom molecules, the classical vibrational frequency, υ, is related to the bond strength and masses of the atoms through:

$$\upsilon = \sqrt{k \big/ 4\pi^2 \mu} \tag{A.11}$$

$k \rightarrow$ force constant
$\mu \rightarrow$ reduced mass

where $$\mu = \frac{m_1 m_2}{m_1 + m_2} \tag{A.12}$$

The interaction of light of frequency υ on a diatomic molecule whose masses are m_1 and m_2 should result in absorption of that light.

A phonon is a single quantum of vibrational energy in the crystal lattice. Atoms in solid materials are constantly vibrating at high frequencies. The vibrations are coupled due to the bonding of neighboring atoms. The vibrations therefore are coordinated in a way that traveling lattice waves are produced which propagate through the crystal. There are generally three modes, or polarizations, of the atomic vibrations: acoustic or longitudinal waves, with the atoms vibrating along the line of atoms, and two optical or transverse waves, with the atoms vibrating perpendicular to the line of atoms.[45]

Acoustic waves occur in all crystalline materials and are produced by neighboring atoms or ions moving in the same direction, but by slightly differing amounts, so that the spacing between the atoms or ions remains relatively constant. Acoustical modes do not generate electric fields since both positive and negative ions are moving in the same direction at the same time, Figure A.4. There is no net dipole moment produced by the acoustic wave.

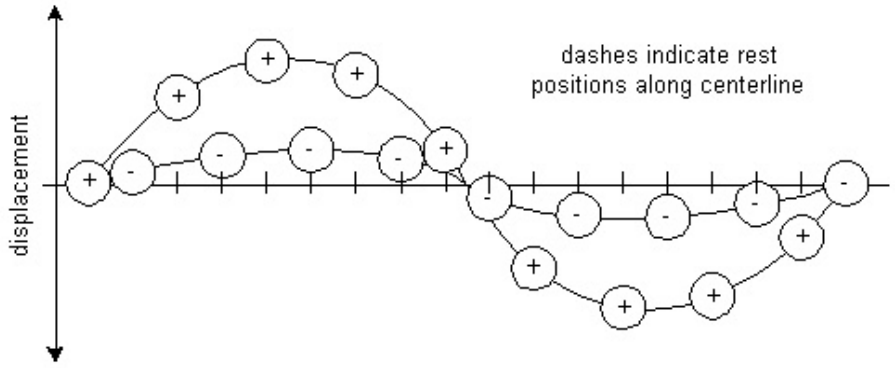

Figure A.4. The acoustic wave exhibits no net dipole moment as it propagates through the lattice.

Optical waves, however, occur when neighboring atoms or ions move out of phase with one another resulting in local oscillating dipole electric fields within the crystal, Figure A.5, having a period and frequency of the lattice vibration of about 10^{15} Hz. These waves are of higher frequency than acoustic waves and are responsible for optical scattering in a crystal. These optical modes couple strongly with externally applied fields. This coupling is important because of the

strong interactions with infrared electromagnetic radiation, hence the term 'optical' phonons. Molecular vibrational modes mix with the radiation field producing coupled excitations known as polaritons.

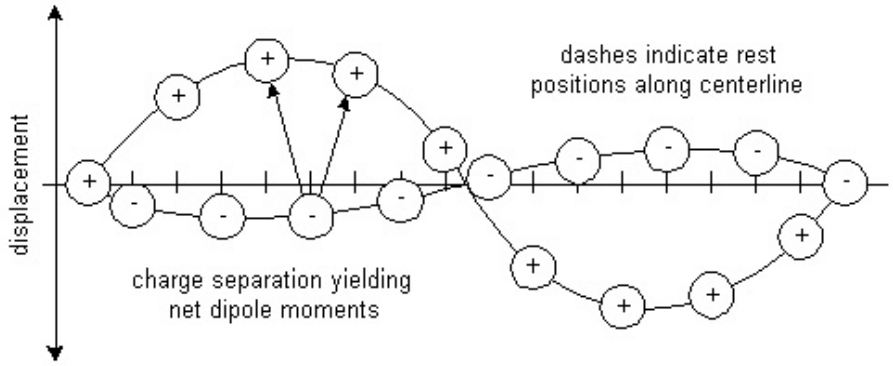

Figure A.5. The optical wave exhibits a net dipole moment as it propagates through the lattice.

Infrared spectroscopy examines the absorption of light whose wavelength corresponds to the bond energy of a molecule. By plotting the degree of absorption as a function of wavelength, one obtains the infrared spectrum of the molecule which allows the distinction between the bonds that are present. The reciprocal centimeter (cm^{-1}), or wavenumber, is the unit most commonly used in vibrational spectroscopy. This unit is derived from energy and is related to the frequency and wavelength by:

$$E = nh\nu \text{, where } \nu = c/\lambda . \tag{A.13}$$

Substituting,

$$E = nh\left(c/\lambda\right) = nhc\tilde{\upsilon} , \tag{A.14}$$

$$\text{where } \tilde{\upsilon} = 1/\lambda = \nu/c = E/hc . \tag{A.15}$$

Note the distinction between the symbol for frequency (ν, nu) and the symbol for the wavenumber ($\tilde{\upsilon}$).[46]

A.3 Calculation of Surface Layer Contamination Thickness Using XPS Data

The atomic percentage of the elements present in a sample can be determined by dividing the peak area by the sensitivity factor and expressing the result as a fraction of the summation of all of the normalized peak intensities.

$$atomic\% = \left(\frac{I_A / F_A}{\sum \left(I_i / F_i \right)} \right) \times 100 \qquad \text{(A.16)}$$

This assumes a homogenous sample within the volume analyzed. When a sample may not be homogenous, this is still a valuable means of comparing similar samples.

Factors affecting the spectra of XPS for the quantification of analysis results include the cross-section from which the emission of ejected electrons arises and the escape depth of the electrons. The cross-section is dependent upon the element, the orbital from which the electron is ejected, and the energy of the exciting radiation ($h\nu$). The escape depth of an electron ejected from an atom depends on its kinetic energy, the nature of the sample (density, number of valence electrons, band gap), and spectrometer related factors. These factors include the transmission function (work function – Φ), which is the proportion of electrons transmitted through the spectrometer as a function of kinetic energy, and the efficiency of the detector, which is the proportion of electrons striking the detector which are detected.

The inelastic mean free path of an electron (IMFP) is the distance the electron will travel before interacting with another atomic particle. The electron's attenuation length (λ) is related to the IMFP and varies as $\sqrt{E}$. Seah and Dench,[155] after analysis of the inter-element and inter-compound effects, showed that λ was related to atom size and devised the following relations:

for elements: $$\lambda = \frac{538}{E_A^2} + 0.41\left(a_A E_A\right)^{0.5} \quad \text{(A.17)}$$

for inorganic compounds: $$\lambda = \frac{2170}{E^2} + 0.72\left(aE\right)^{0.5} \quad \text{(A.18)}$$

Generally, the attenuation length is roughly 90% of the IMFP. Various data bases exist from which IMFP values can be obtained. The NIST Electron Inelastic-Mean-Free-Path Database[129] is one such data base. The IMFP of various ejected electrons were calculated using this data base, as calculated using the Tanuma, Powell, and Penn (TPP) equation and the Gries equation.

The TTP equation is considered a more accurate representation of IMFP than the Gries equation. The TTP equation incorporates several factors that represent the nature of a sample: density, number of valence electrons, and band gap. The band gap of the samples in this study may be approximated using the valence band region of the XPS spectra.[156] The intercept of the slope of the low eV side of the valence peak with the abscissa yields the band gap. Since a close analysis of this region of the spectrum for each nanopowder was not accomplished, only a rough measured estimate could be made from the survey spectra. The results are listed in Table A.3.1. The results were reasonable considering that the band gap increases with decreasing particle size.[157]

Table A.3.1. Band Gap Measured From the Nanopowder XPS Survey Spectra

Nanopowder	Band Gap	Nanopowder	Band Gap
A	2.95 eV	D	3.51 eV
B	3.15 eV	E	3.66 eV
C	3.15 eV	F	4.15 eV

The Gries equation incorporates atomic based factors and requires the user to input only the sample density for the calculation of the IMFP. The IMFP for the ejected electrons passing through the barium carbonate component was calculated using the Gries equation.

The data from XPS analysis provides information on which elements were present and their respective binding energies. IMFP data bases incorporate the electron kinetic energy in reporting IMFP. The relationship between the binding energy and the kinetic energy is represented as

$$KE = h\nu - BE - \Phi \qquad \text{(A.19)}$$

where hν is the excitation energy, BE is the binding energy, and Φ is the work function of the spectrometer. The work function of a spectrometer is generally between 4 – 5 eV.[158] A value of 4.5 eV was used in calculating the kinetic energy of the respective electron transitions of the elements in this study.

Calculation of the IMFP for ejected electrons must incorporate the relative passage through each component of the sample material. The IMFP was longer passing through the carbonate than when passing through the titanate. For example, a barium 3d3 electron ejects with approximately 688 eV in kinetic energy. This translates into an IMFP of 15.96 Å in titanate and 20.56 Å in carbonate. In contrast, a barium 4d electron ejects with approximately 1392 eV in kinetic energy, and an associated IMFP of 26.93 Å in titanate and 34.70 Å in carbonate.

A balance needed to be met between the relative IMFP's of electrons from the different elements and the possible distance of travel through the different compounds. An acceptable result for one element could exclude another element. Iterations continued until mutually inclusive results were arrived at for the thickness of the layers of carbonate and adsorbed species.